Transactions of the ASME®

Technical Editor
H. L. JULIEN (1998)

Associate Technical Editors
Advanced Energy Systems
M. J. MORAN (1999)
Gas Turbine
D. COOKE (1999)
H. NELSON (1999)
J. PETERS (1999)
Internal Combustion Engines
D. ASSANIS (1999)
Power
D. LOU (1998)

BOARD ON COMMUNICATIONS
Chairman and Vice President
R. MATES

OFFICERS OF THE ASME
President, **KEITH B. THAYER**
Executive Director, **D. L. BELDEN**
Treasurer, **J. A. MASON**

PUBLISHING STAFF
Managing Director, Engineering
CHARLES W. BEARDSLEY
Director, Technical Publishing
PHILIP DI VIETRO
Managing Editor, Technical Publishing
CYNTHIA B. CLARK
Managing Editor, Transactions
CORNELIA MONAHAN
Production Coordinators
VALERIE WINTERS
COLIN MCATEER
Production Assistant
MARISOL ANDINO

Transactions of the ASME, Journal of Engineering for Gas Turbines and Power (ISSN 0742-4795) is published quarterly (Jan., April, July, Oct.) for $185.00 per year by The American Society of Mechanical Engineers, 345 East 47th Street, New York, NY 10017. Periodicals postage paid at New York, NY and additional mailing offices. POSTMASTER: Send address changes to Transactions of the ASME, Journal of Engineering for Gas Turbines and Power, c/o THE AMERICAN SOCIETY OF MECHANICAL ENGINEERS, 22 Law Drive, Box 2300, Fairfield, NJ 07007-2300.
CHANGES OF ADDRESS must be received at Society headquarters seven weeks before they are to be effective. Please send old label and new address.
PRICES: To members, $40.00, annually: to nonmembers, $185.00. Add $40.00 for postage to countries outside the United States and Canada.
STATEMENT from By-Laws. The Society shall not be responsible for statements or opinions advanced in papers or . . . printed in its publications (B7.1, par. 3).

INDEXED by Applied Mechanics Reviews and Engineering Information, Inc. Canadian Goods & Services Tax Registration #126148048

Journal of Engineering for Gas Turbines and Power

Published Quarterly by The American Society of Mechanical Engineers

VOLUME 120 • NUMBER 2 • APRIL 1998

TECHNICAL PAPERS

(Contents continued on outside back cover)

This journal is printed on acid-free paper, which exceeds the ANSI Z39.48-1992 specification for permanence of paper and library materials. ♾™

♻ 85% recycled content, including 10% post-consumer fibers.

(Contents continued)

The Development of the Whittle Turbojet

C. B. Meher-Homji
Bechtel Corporation,
Houston, TX 77056-2166

Sir Frank Whittle passed away on August 8, 1996, at the age of 89, in Maryland. His work in developing the turbojet can truly be said to represent one of the greatest mechanical engineering achievements in the last 70 years. The development of the turbojet demanded that Whittle face almost insurmountable technical and institutional challenges. The technical challenges included developing centrifugal compressor pressure ratios of 4:1 from the prevailing technology level of 2.5:1, increasing compressor efficiencies from 65 to 80 percent while designing for combustion intensities that were 10 times the prevailing state of the art in boiler technology. He was also responsible for utilizing a vortex turbine design approach. The institutional challenges that he faced included changing a paradigm on aircraft propulsion technology and nurturing Power Jets Ltd. to produce excellent engine designs with minimal resources in terms of money, technical manpower, and governmental support. It is the object of this paper to document the epic long-drawn-out struggle fought by Sir Frank against entrenched technical opinion, which ultimately resulted in the turbojet revolution. The technical aspects of his pioneering work with emphasis on the problems he encountered will also be discussed.

1.0 Introduction

1.1 Historical Antecedents. The turbojet revolution was pioneered by Sir Frank Whittle in England and Hans von Ohain in Germany, their work being extensively documented by Constant (1980), Schlaifer (1950), von Ohain (1979), Scott (1995), and Jones (1989). Both these pioneers, who envisioned flight speeds in excess of 500 mph at altitudes of 30,000 feet, had revolutionary ideas as students, and developed their engines without the help of the traditional aeroengine companies. In order to put the development of the Whittle jet into a historical context, it is necessary to trace the course of Whittle's thinking as well as the theoretical and practical developments in the field of gas turbines before the Second World War.

The history of jet propulsion starts with the inventions of Hero of Alexandria (circa AD 60) who developed the first reaction-type turbine. In 1791 John Barber invented a Watt-type beam engine driven by a primitive gas turbine via reduction gearing. In 1900, Stirling Moss in the U.S, worked on a Doctoral Thesis on gas turbines and upon joining General Electric (GE), designed and built one by 1907, albeit with poor performance. He then turned to his pioneering work on turbochargers for aircraft piston engines. In France, C. Lemale and R. Armengaud, who worked at the Société Anonyme des Turbomoteurs, designed a crude gas turbine, which achieved an overall efficiency of 3 percent by 1906. From 1905 through 1940, the Brown Boveri Corporation of Zurich designed and built several pioneering gas turbines. In 1919, when the gas turbine was an established prime mover, the British Air Ministry asked Dr. W. J. Stern to report on the prospect for the use of gas turbines for aircraft propulsion. His study was flawed in its assumptions and he concluded that the gas turbine was not a feasible proposition.[1] This report was to have an adverse impact on Whittle's quest for support years into the future.

Dr. A. A. Griffith, a brilliant scientist working at England's Royal Aircraft Establishment (RAE) worked in the 1920s on developing groundbreaking aerodynamic theory where he treated turbomachine blades as airfoils. He built a small, 4 inch diameter, single stage axial compressor driven by an axial turbine. Griffith played an important part in gas turbine development but, as we will see later, initially rejected Whittle's concept, thereby delaying Government assistance at a most critical juncture.

1.2 Whittle's Early Work. As a flight cadet attending the Royal Air Force College at Cranwell in 1928, Whittle wrote a thesis titled "Future Developments in Aircraft Design." In this thesis he proposed a propulsion concept that utilized a piston engine driven compressor to blow air over fuel jets exhausting the high temperature air through a propulsion nozzle. In October 1929, he realized that he could increase the blower pressure ratio and replace the piston engine by a turbine. Whittle approached Britain's air ministry with his concept but was told that it was not feasible. This assessment was made by Griffith, who was eager to pursue his own complex gas turbine scheme[2] and failed to see the elegant simplicity of Whittle's engine.

On January 16, 1930, Whittle filed for Patent No. 347206 for "Improvements in Aircraft Propulsion" (Fig. 1). This figure depicts a single-shaft turbojet with an axial-centrifugal compressor, tubular combustor and two-stage turbine. Between 1934 and 1936, he studied for his Tripos at Cambridge and in 1935, allowed his patent to lapse because the Air Ministry would not pay the £5 renewal fee. Whittle, however, doggedly pursued his goal and in March, 1936, a company called Power Jets Ltd. was launched with a nominal capital of £ 10,000 with Whittle acting as the Chief Engineer. In May 18, 1935, he filed for Patent No 459980 for an experimental turbojet, which would be called the WU. Whittle proceeded to design a double entry compressor with a 19 in. diameter made of high-strength aluminum alloy and having 30 vanes. The compressor was to be driven by a 16.4 in. turbine operating at 17,750 rpm. The mass flow rate was to be 26 lb/sec and the pressure ratio 4.4:1. Whittle recognized that the area of greatest technical risk was in the combustor where an exceedingly large heat release had

[1] Stern based his computations on industrial technology, taking, for example, 1250 lb for fuel pumps and drive gears!

Contributed by the International Gas Turbine Institute and presented at the 42nd International Gas Turbine and Aeroengine Congress and Exhibition, Orlando, Florida, June 2–5, 1997. Manuscript received at ASME Headquarters February 1997. Paper No. 97-GT-528. Associate Technical Editor: H. A. Kidd.

[2] Griffith started work at RAE at Farnborough in 1915 and had made fundamental contributions to airfoil theory. He focused on an exceedingly complex model of an axial flow gas turbine (a turboprop) and could not appreciate the fact that Whittle's centrifugal design had an inherent simplicity that would help promote its success.

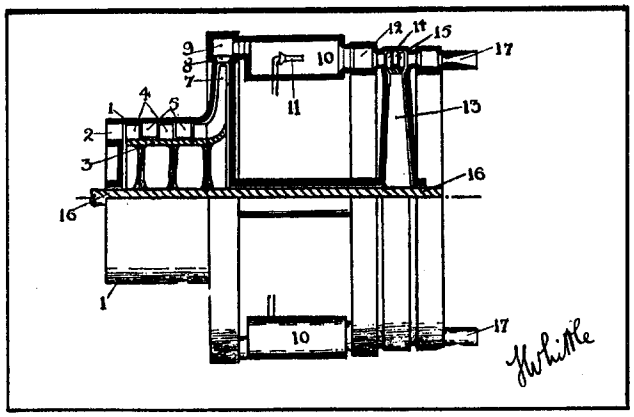

Fig. 1 Whittle's patent drawing, filed January 16, 1930, showing a two-stage axial compressor followed by a one-stage centrifugal compressor. A straight through burner and a two-stage axial turbine on one disk is shown.

to be achieved in a very small volume.[3] After talking to several burner manufacturers, Whittle was able to get the assistance of Laidlaw Drew and Co. to work on a small research contract.

It is interesting to note that the German jet engine development program was, on the other hand, very well funded. In 1938, Helmut Schelp had to *pressure* German aeroengine companies into accepting funds for studies on jet engines. The German jet engine development program that resulted in the Junkers Jumo 004B, the world's first production jet engine under the leadership of Anselm Franz, is documented by Meher-Homji (1997).

2.0 Brief History of Whittle's Engines

2.1 Design and Development of the WU Engine. In June 1936, the British Thomson-Houston Co (BTH) of Rugby was awarded the contract for the detailed design and construction of the WU. Operating under severe financial constraints, Whittle recognized he could not afford component testing and therefore had to take a bold risk and attempt to run a complete engine.[4] His initial experiments on combustion were run with very crude combustion equipment, as illustrated in Fig. 2. As reported by Jones (1989), these experiments produced deafening noise and thick clouds of fuel vapor and smoke. Reportedly,

[3] Whittle's aim was to burn 3.3 gal/min in a volume of 6 cu. ft.

[4] Component testing was considered but the quotations for compressor test sets were £28,000, far beyond the means of Power Jets.

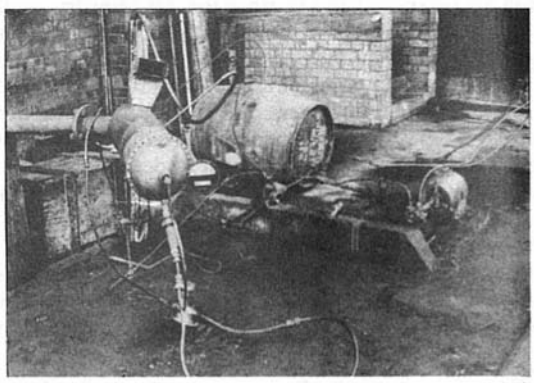

Fig. 2 Crude combustion test rig at the BTH factory. This shows the budgetary constraints that Whittle was working under. Deriving a satisfactory combustion chamber was one of the greatest challenges Whittle faced (Whittle, 1945).

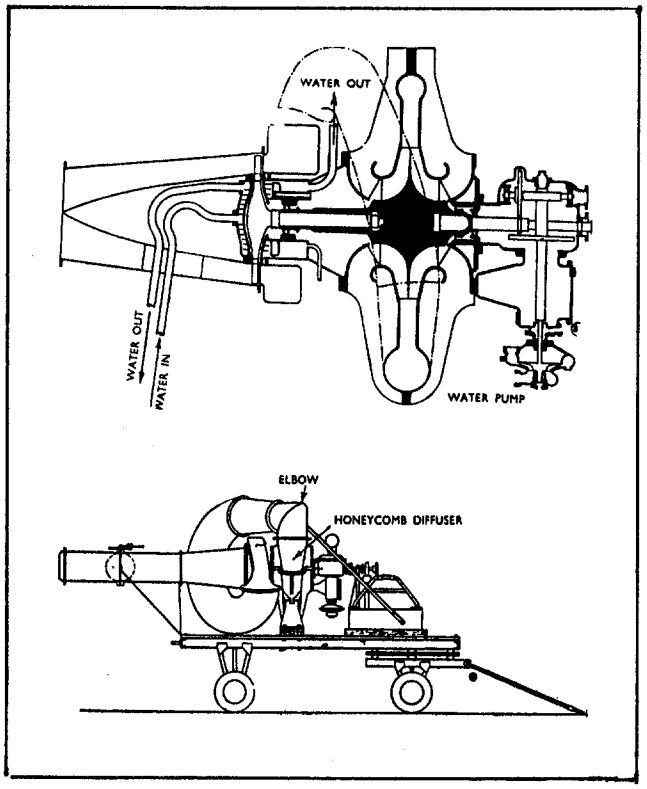

Fig. 3 First model of the experimental engine and the test stand on which it was mounted. This unit had a large double-sided impeller with 30 vanes and a honeycomb diffuser and a single combustor. The single stage turbine disk was cooled by water jackets. Mass flow through the machine was 26 lb/sec. The jet pipe extended through an open window. Key data on the W.U and W.1 may be found in the appendix.

Power Jet's engineering drawings were recognizable by the smell of fuel oil with which they became impregnated.

On April 12, 1937, the first few runs of the WU engine were made. These were eventful because in several instances, the turbine accelerated with a rising shriek to 8000 rpm even with the fuel valve closed. This uncontrolled and noisy acceleration caused considerable concern as it was usually accompanied by patches of red heat being visible on the combustor and flames emanating from the jet pipe. Finally, it was determined that fuel pump tests conducted prior to engine light-off resulted in an accumulation of fuel in the bottom of the combustion chamber, which ignited, causing the uncontrolled acceleration. Figure 3 illustrates the assembly of the first model of the experimental engine and the test stand on which it was to be used. The engine had a single large combustor of helical form. Tests showed that the compressor and turbine efficiencies were below design expectations. This engine also suffered from a series of mishaps, including one in which the compressor impeller rubbed its casing at 12,000 rpm, causing the engine to come to a stop in about 1.5 seconds.

After the testing on the first WU engine was completed in August 1937, BTH was given an order for a complete reconstruction in which the major changes were an improved compressor diffuser, a new combustion system, and modification of the turbine blading to conform to free-vortex design principles.[5]

The second version of the experimental engine was tested in April and May of 1938 and demonstrated that the turbine designed by Whittle on free vortex principles had an efficiency

[5] Whittle had always believed in the importance of this type of blading and was amazed when he found that turbine designers had not utilized it. Whittle was unaware of Griffith's work in this area. Griffith had concluded in 1926 that free vortex blading was needed.

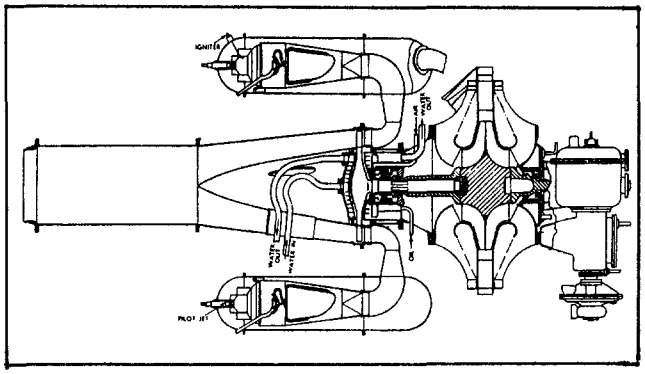

Fig. 4 Engine layout of the third experimental unit. This unit had ten reverse-flow combustion chambers.

of 84 percent. The second version of the engine failed after only 4 hours of running. The major problem was still in the combustion system.

In the third version of the experimental engine, ten counterflow combustors were used instead of a single combustion chamber. The engine layout is shown in Fig. 4. The use of multiple combustors allowed bench testing of a single combustor utilizing blowers existing at the BTH plant. From 1938 to 1940 most of the experimental work focused on combustion. Experiments were made on a system that vaporized the fuel before injection. In October 1940, an atomizer burner and flame tube were designed and used satisfactorily on the third experimental engine.

2.2 Design of the W.1X through the W.2B. In July 1939, Power Jets Limited were promised a contract for a flight engine designated as the W.1 and in August 1939, Gloster Aircraft Company was awarded a contract for the design of an experimental aircraft that would be powered by the W.1. In late 1939, even while the development work was continuing on the W.1, the Government promised to pay for the development of a more ambitious W.2, which would power the twin engine Gloster Meteor fighter.

Whittle started the development of the W.1 engine in July 1939 with a design goal of 1200 lb of thrust. The aerodynamic design of the W.1 was similar to the WU third version. The first W.1 called the W.1X was put on test in December 1940, and experience on this engine was put into the design of the W.1 engine, which powered the E28/39 jet illustrated in Fig. 5. The first flight occurred on May 15, 1941. The first test flight, with test pilot Jerry Sayer at the controls, lasted 17 minutes.[6]

[6] The British Air Ministry did not send an official photographer to film this historic event.

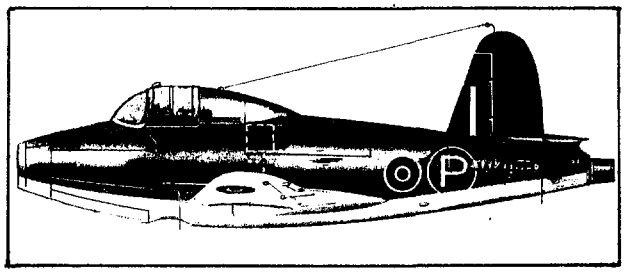

Fig. 5 The Gloster E28/29 Experimental airplane. Powered by the Whittle W.1 engine designed by Power Jets Limited and built by BTH, this was the first British jet to fly. Designed by George Carter, this aircraft was popularly known as the "Squirt." It also served as a test bed for several subsequent Whittle engines. The aircraft had tricycle wheels, was of all-metal construction, and had a wingspan of 29 ft and a length of 25 ft.

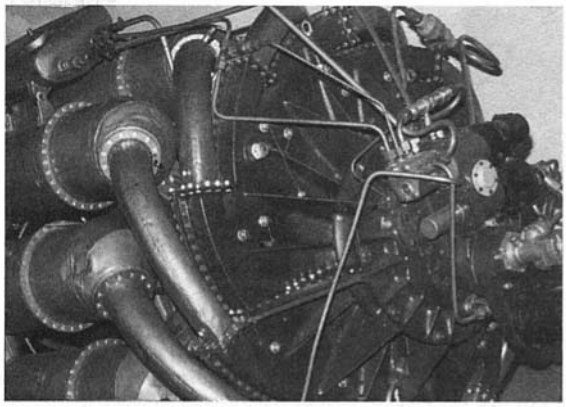

Fig. 6 Inlet section of the W.1X. This engine was subsequently shipped to GE in 1941 and is currently on display at the Smithsonian Air and Space Museum.

The successful flight provided an impetus for the British Government to lay definitive plans for the W.2B, which was to be the production engine for the Gloster Meteor.[7] The inlet section of the W.1X that powered this aircraft for its taxiing trials is shown in Fig. 6.

In early 1940, the Rover Company was given a contract for the production of Whittle engines as the Government did not feel that Power Jets had the experience or the personnel for quantity production. By April 1940, prototype drawings of the W.2, which was to be the production engine, were handed over to Rover. Shortly after the handover of the drawings, Whittle performed a detailed analysis of his design and became convinced that this design was liable to be a complete failure.[8] Whittle then began working on a revised design, known as the W.2B. By the Fall of 1941, Rover was almost ready to begin production of the W.2B and set up a special factory at Barnoldswick. Unfortunately, both technical and political problems developed relating to this design.

The first W.2B delivered surged at outputs over 1000 lb thrust and also suffered from turbine blade failures.[9] On the political side, relationships between Power Jets Ltd. and Rover started to deteriorate rapidly, mainly over disagreements with respect to Rover's right to make independent design modifications to the engine. In fall 1941, Power Jets was deprived of authority over the design of the production engine and was limited to research and development activities and Rover was authorized to make design changes without Power Jet's approval. Rover proceeded with work on its version of the W.2B engine. By December 1941, it had put on test the W.2B Mark II, which incorporated a 10 vane diffuser designed in consultation with Rolls Royce, and a new turbine with fewer and broader blades. The engine attained a thrust of 1510 lb without surging.

2.3 Power Jets and the W.2/500. In March 1942, Power Jets Limited designed a new engine designated the W.2/500. This engine retained the new diffuser of the W.2B Mark II and

[7] This flight made a significant contribution in speeding up jet engine development work in Britain. Rolls Royce, which had a program some time before 1939 when it hired A. A. Griffith from RAE, started to apply considerable resources to its development. In June 1941 The Bristol Engine Company undertook a survey of the gas turbine field and by the spring of 1942 had completed the design for what would become the Theseus turboprop. Metropolitan Vickers worked on an axial RAE design that resulted in the F2 engine. De Havilland Aircraft Company worked on the development of the Goblin which powered the Vampire.

[8] This arose from an over-ambitious design where the exhaust velocity was too close to Mach 1 so that the component efficiencies were not achieved, and exhaust velocities reached critical values at well below full speed. Surging of the compressor and high exhaust gas temperatures made it impossible to run at over 75 percent of the design rpm.

[9] In July 1942, GE sent Rover several sets of turbine blades made from Hastalloy B, which were superior to Rex 78. A little later the British alloy Nimonic 80 was introduced.

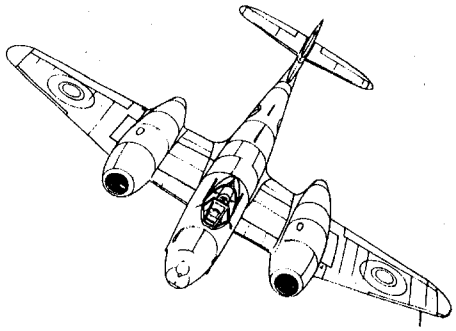

Fig. 7 The Gloster Meteor was the only Allied jet fighter to become operational during World War II. This single seat jet fighter was powered by two Whittle W.2 engines built by Rolls Royce (Welland I). The Meteor had a maximum speed of 410 mph at 10,000 ft and a operational ceiling of 40,000 ft. It had midwing nacelles for the engines, tricycle landing gear, a pressurized cabin, and four 20 mm nose cannon.

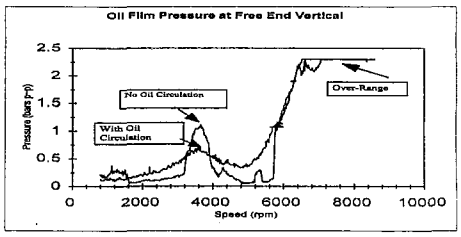

Fig. 8 The W.2/700 engine made by Power Jets Ltd. This was the last engine to be built by Power Jets. It was rated at 2500 lb thrust.

included a new blower case and a new turbine design. On its first run in September 1942, the W.2/500 attained 1755 lb thrust.

2.4 Rolls Royce as the Producer of Whittle Type Jet Engines. In late 1942, Rolls Royce, which had a long history of reciprocating aero engine successes, but had been struggling with Dr. A. A. Griffith's gas turbine designs, took over the jet engine effort at Rover and toward the end of 1942, the direction of Rover staff and works facilities was in the hands of Rolls Royce.[10] Ultimately the W.2B/23 was put into production and named the Welland, the first of Rolls Royce "River Class" jet engines. On June 12, 1943, the Meteor, shown in Fig. 7 was flown with two Welland engines. The Welland was put into production in October 1943 and deliveries were first made in May 1944. Production engines were rated at 1600 lb thrust, weighed 850 lb and had a specific fuel consumption of 1.12 lb/hr/lb thrust. With this engine, the Meteor could attain speeds of 410 mph. The first production Meteors were delivered to Squadrons in July 1944 and were used against German V-1 flying bombs (Shacklady, 1962).

Based on experience with the Merlin engine's supercharger, Rolls Royce felt that the air flow through the Welland could be increased by 40 percent and changes were made, ultimately resulting in the Rolls Royce Derwent. As blower casings that were already made for the Welland had to be used to facilitate rapid production, the increase in thrust was only 25 percent, achieved by the use of a new impeller adopted with some modifications from Whittle's W.2/500, a new diffuser designed by Rolls Royce, and a scaled-up turbine. The Derwent I was first tested in July 1943 and in 1944, it attained thrust of 2000 lbs. Approximately 500 Derwent I engines were produced.[11]

In 1943, the course of Power Jet's activities started to diverge from Rolls Royce. After the W.2/500 of 1942, Power Jets built the W.2/700 illustrated in Fig. 8, which included important changes in the compressor, the introduction of a completely new diffuser (known as the type −16 diffuser) and blower casing. With these modifications, the W.2/700 compressor finally attained Whittle's aim of 80 percent efficiency while deriving a pressure ratio of 4:1. There were several problems with impeller vibration and failures which are discussed ahead. In the four years that had elapsed since the first flight trials of the W.1 engine, Power Jets Ltd. had tripled the thrust of the engine with no increase in size and a 70 percent increase in weight (Whittle, 1954) (see appendix).

In 1944 Power Jets Ltd. was nationalized. Engine development work continued with emphasis on the W.2/700 engine. Nationalization resulted in a serious drop in morale and the pioneering Power Jets team started to lose heart with conflicts developing regarding the role of the company. Whittle felt that engine development should be a goal, while others were content to view the organization as a research and development establishment. In January 1945, Whittle was invited to become a member of the board of Power Jets (R&D). It was at this time that the Gas Turbine Technical Advisory and Coordinating Committee was formed to direct the course of gas turbine activities in the UK. In April 1945 it started to become clear that Power Jets would not have the right to design and build experimental engines and that it was expected to focus on fundamental research and component development. The company that boldly strode forth with technology which no established company would invest resources in, was now stripped of the right to design or build jet engines. On January 22, 1946, Whittle submitted his letter of resignation from the board of Power Jets (R&D) Ltd. As he predicted, the brilliant team of engineers that had pioneered jet engines in Britain, finally broke up and were hired by other firms working on gas turbines.

Whittle's basic engine design features lived on at Rolls Royce. The Nene, designed by Dr. Stanley Hooker, first ran in 1944, and had some new features but still retained 80 percent of the Power Jet design ideas. The engine was rated at 4500 lb thrust. A scaled-down version of the Nene known as the Derwent V was made. Figure 9 shows a cutaway of the Rolls Royce Nene.

3.0 Technical Features of Whittle's Engines

Whittle had the genius to know that to achieve success, his designs had to be simple, robust and have the best chance for rapid development. Whittle's designs were masterpieces of simplicity in design[12] and construction and low in weight. His designs utilized the same general layout and maintained an outer diameter of 42 in. while increasing the thrust over successive models from 850 lb to 2400 lb. The Rolls Royce Welland initially was similar to the W.2B utilizing reverse-flow combustors. The design was only later modified to a straight-through design for the Derwent.

[10] As reported by Hooker (1984), Lord Hives and Hooker of Rolls Royce met at a pub for dinner with S. B. Wilks of Rover. Hives is reported to have told Wilks, "You give us this jet job and I will give you our tank engine factory at Nottingham." A decision was made on the spot and the deal was done.

[11] The Derwent I was used on the Meteor III, which had a speed of 460 mph or 50 mph more than the Welland-powered Meteor.

[12] When Whittle pointed out the virtue of the simplicity of the engine to Lord Hives of Rolls Royce, Hives is reported to have drily remarked, "Wait until we have worked on it for a while; we will soon design the simplicity out of it!" (Hooker, 1984). Looking at today's complex aeroengines, this was a prophetic statement!

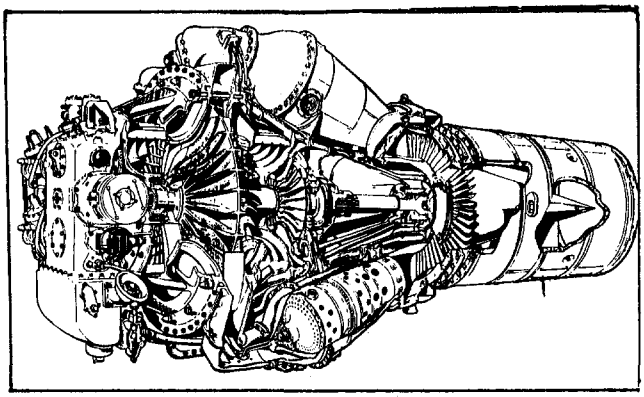

Fig. 9 Cutaway of the Rolls Royce Nene. Designed by Sir Stanley Hooker, this engine was similar in layout to the Derwent but had nine combustors. The strong influence of Whittle's design can be noted. It was rated at 5000 lb thrust and had a mass flow of 80 lb/sec.

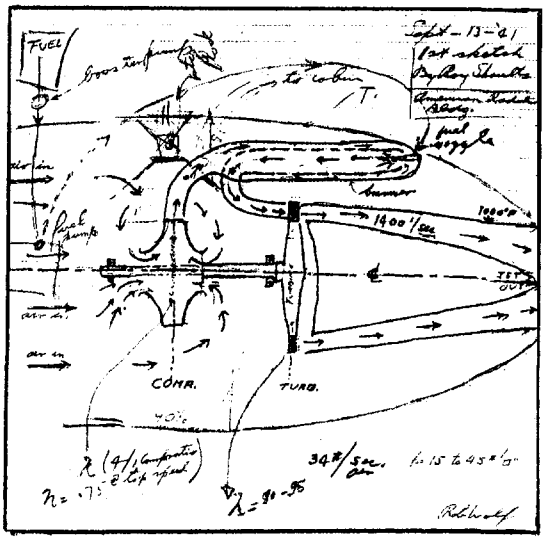

Fig. 10 Sketch made by Roy Shoults of GE to explain the fundamentals of the Whittle propulsion jet to Bell Aircraft engineers. This sketch indicates mass flow rate of 34 lb/sec, compressor η of 75 percent, turbine η of 90 percent and turbine efflux velocity of 1400 ft/sec (Ford, 1992).

3.1 Double-Sided Centrifugal Impellers. Whittle's choice of a double-sided centrifugal compressor was chosen to obtain the maximum possible breathing capacity in proportion to size. The first experimental engine (WU) had a compressor tip diameter of 19 in. and had 30 blades. Whittle chose the largest number of blades possible based on manufacturing limitations in order to minimize the blade loading.

3.2 Reverse Flow Combustors. There were several reasons why Whittle elected to use reverse-flow combustors for his early developments. These included:

(*i*) To permit the use of a short shaft, which required only two bearings and eliminated the need for a flexible coupling.
(*ii*) To eliminate an expansion joint between the compressor and turbine.
(*iii*) To provide for even air flow to the primary combustion zone.
(*iv*) To screen the turbine blades from direct flame radiation.

3.3 Vortex Design of Turbine Blades. Whittle assumed that the BTH engineers were designing the turbines based on vortex theory and was amazed when one day, in the course of discussions, they stated that the consequence of a blade design change would be an increase in thrust load on the bearing from 180 to 1800 lb. When he asked the engineers what they assumed was the difference in the pressure between the blade root and the tip he was astounded by the response, which was "what pressure difference?" BTH engineers had not assumed vortex flow from the turbine nozzles and therefore had not designed the blades with adequate twist. Whittle's insistence on this design approach soured relationships with some BTH engineers, who resented this young engineer instructing them on how to design turbines.[13]

4.0 The Whittle Engine in the USA

Upon declaration of World War II, Sir Henry Tizard,[14] who was Chairman of the British Aeronautical Research Council, proposed sharing jet technology with the United States and started official talks. US military intelligence had, however, been filing reports about jet propulsion work in both England and Germany and Major General Hap Arnold visited Britain to examine this technology. In May 1941, Arnold put in a formal request for jet technology. On July 21, 1941, Roxby Cox and Roy Shoults of GE visited the Ladywood Works and the Gloster factory. A decision was made to mass produce this engine in the US and GE was chosen to build the engine. As reported by Ford (1992), a GE delegation visited Washington on September 4, and was handed a sheaf of drawings with Hap Arnold reportedly stating "Gentlemen, I give you the Whittle Engine." GE committed to build a working engine within six months. Bell Aircraft was commissioned to build a prototype jet fighter. Roy Shoults' sketch of the Whittle engine made to explain the concept to Bell designers in September 1941 is illustrated in Fig. 10 (Ford, 1992).

In October 1, 1941, the W.1X was flown to the US in a B-24 bomber and made its way to Bldg. 34 North at the GE, Lynn Massachusetts facility. On October 16, the W.1X was fired up.[15] In a remarkable engineering effort, the GE team made some modifications to the design and within six months ran an engine on March 18, 1942. Later, Whittle visited Boston to help solve a problem with burning bearings.[16] In August, GE delivered two engines (designated the I-A) to Bell Aircraft and the first flight of the Bell P-59 was made on October 1, 1942, exactly one year after the W.1X left Britain. An excellent description of the initial US jet engine work is made by Ford (1992).

5.0 Engineering Success Through Failure

With this brief encapsulation of the history of engine development, it is easy for one to gain the impression that the course of engine development was easy and logical. This was hardly the case and there were numerous problems that had to be surmounted by Whittle and his team, with minimal resources and funds and always under intense time pressure. Several problems were the result of pushing the state of the art. Several setbacks were the results of bad luck, lack of funds, which

[13] Whittle points out that some of these differences stemmed from the differences in background. He was a pilot and an engineer looking for ways to save weight and robustness of the design under varying operating conditions. The BTH engineers were designers of large stationary steam turbines and several of them had no exposure to modern aerodynamic theory.

[14] Sir Henry Tizard was Chief Scientific Advisor to the British Government before WW II and was instrumental in ensuring the timely development and deployment of radar technology. He had to fight against detractors of this groundbreaking technology and had experienced, the skepticism and opposition similar to that leveled against Whittle's enterprise.

[15] This was the first jet engine to ever run in the US. The W.1 X is now at the National Air and Space Museum, Washington DC.

[16] This was caused by the inadvertent omission of a oil passage from the Rover drawings that were sent to the US.

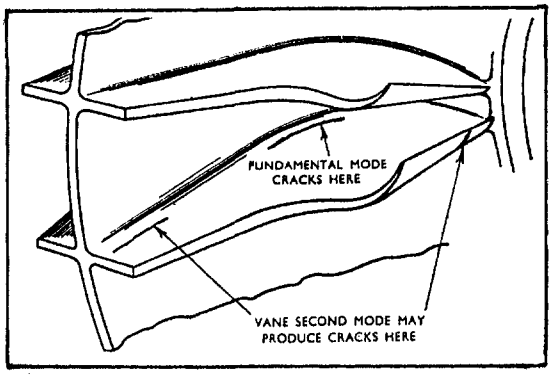

Fig. 11 Position of centrifugal impeller vane cracks (Vosey, 1945)

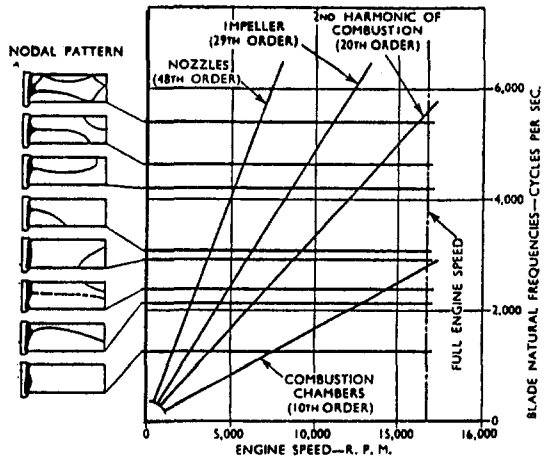

Fig. 13 Interference diagram for the W.2/800 engine. Turbine blades at 700°C (Vosey, 1945).

forced cannibalization of parts, or environmental factors. Whittle believed, for example, that several of the early bearing failures that occurred at the dilapidated Ladywood Works were the result of a "rain" of foundry sand derived from the roof of the workshop, which was formerly a foundry! Some of the serious problems faced are presented below.

5.1 Impeller, Turbine Blade, and Disk Failures. There were several problems pertaining to impeller vibration and cracks, which have been covered by Vosey (1945). Problems started with the W.2/500 engine. Whittle found out that at 14,000 rpm the engine produced a "howling" sound. Tests showed that even a short run at the howling speed would result in resonance cracks over the length of its junction with the impeller disk as shown in Fig. 11. A front view of a wrecked Power Jets W.2/500 engine caused by a impeller failure is illustrated in Fig. 12. Several methods of fundamental importance in analyzing blade and impeller vibration were developed. Problems also plagued turbine blading, especially with later versions of the Whittle engines specifically in the W.2/800 where the blade lengths had increased. A Campbell diagram for the W.2/800 is illustrated in Fig. 13.

The initial disks that utilized the De Laval type fixation method were subject to failure as shown in Fig. 14. This failure occurred on the W.U engine in February 1941.[17] The use of a fir-tree arrangement and better blade materials resolved this problem on future engines.

In another case, the W.1 engine, which was putting in considerable time both on the E28 test aircraft and on the bench, suddenly encountered turbine blade failures. The mystifying factor in this case was that the location of the crack was not consistent (as would be expected by a fatigue type problem), occurring at times at the root, midspan, and at the blade tip. Whittle suspected that this was the effect of a thermocouple located three feet *downstream* from the turbine that was causing fluctuations in blade loading. Upon removal of the thermocouple, the blade failure problem disappeared (Whittle, 1979).

5.2 Combustion Problems. The first model of the experimental engine had severe problems with hot spots and improper heat distribution. Whittle made an attempt to utilize the primus principle and the single combustion chamber was fitted with a vaporizer. On this engine, poor compressor delivery pressure compounded the problem and diffusers were fitted to improve compressor performance. Numerous tests and modifications were attempted on the flame tubes, vaporizers, baffle systems and spray patterns. Whittle (1945) states that in January 1939 alone, ten types of vaporizer were tried in the combustion rig and nine flame tube modifications made. There were also problems with repeatability of results derived from the test rigs on the engine. Whittle struggled hard with the combustion problem until the fall of 1940 when Mr. Isaac Lubbock, head of Shell Fulham Laboratory who was advising Power Jets, developed and tested a combustor utilizing atomized spray injection. Power Jets continued development of this combustor, and from that point, the combustion problems diminished. A combustion chamber with a vaporizer as well as the Shell type combustion

[17] This failure occurred after a run time of 169 hours.

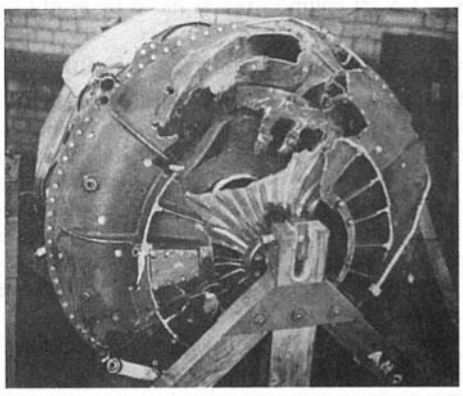

Fig. 12 Failure of compressor impeller on W.2/500 engine

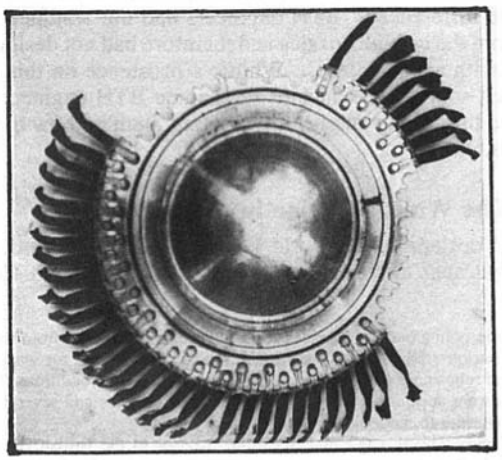

Fig. 14 Disk failure of the third model of the experimental engine. Later engines utilized fir tree type attachments instead of the De Laval type attachments shown here.

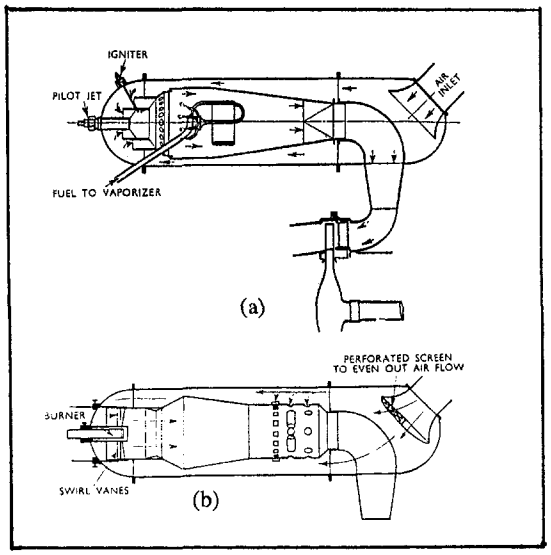

Fig. 15 (*a*) Vaporizer-type combustor, (*b*) shell-type combustor with atomizer (Whittle, 1945)

chamber is shown in Fig. 15. The combustors and jet pipe end of the W.1X are depicted in Fig. 16.

6.0 Sir Frank Whittle, Coinventor of the Jet Engine

Sir Frank Whittle (Fig. 17) was born in Coventry on June 1, 1907, and at the age of 16 became an apprentice with the Royal Air Force. Throughout his life, he had a strong sense of curiosity and was a voracious reader. During his school years, he became acquainted[18] with Stodola's classic work "Steam and Gas Turbines." He later became a cadet in the RAF college

[18] Even though he could not fully comprehend this text at such an early age, it gave him some insight into the construction of turbines. Later as a scholar at Cambridge University, he received the two volumes as a prize and then could fully understand them.

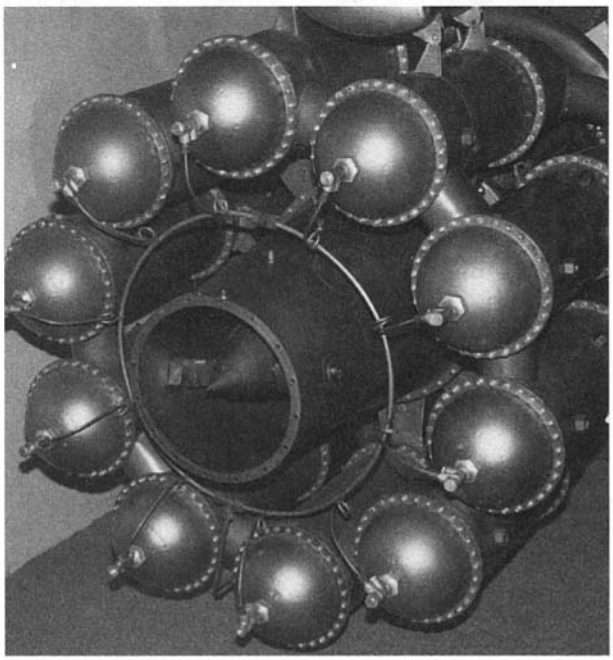

Fig. 16 Exhaust end of the Power Jet Ltd. W.1X showing the 10 combustor cans and exhaust cone

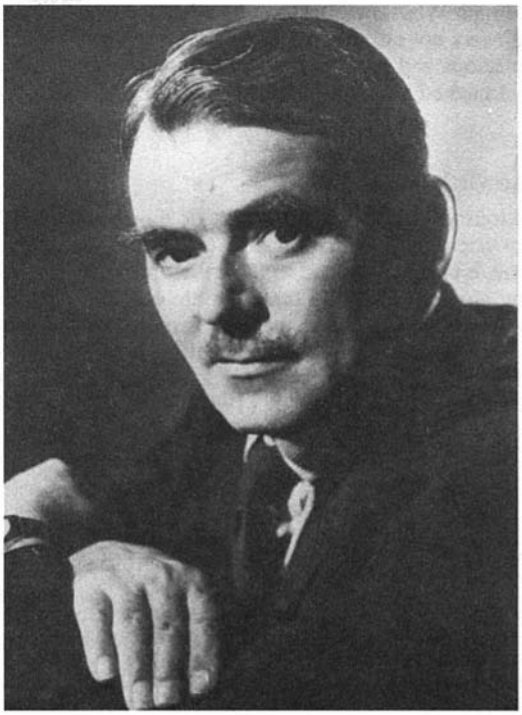

Fig. 17 Sir Frank Whittle, OM, KBE, CB, FRS, coinventor of the turbojet (Whittle, 1954)

in Cranwell. At Cranwell he prepared his thesis, laying the groundwork for the turbojet, for which he received a patent in 1932. In March 1936 he, along with others, formed Power Jets Ltd. The first Whittle centrifugal jet ran in a test stand in 1937 and the first flight in the Gloster E29/39 occurred two years later on May 15, 1941. Whittle was knighted in 1948, which was also the year he retired from the RAF.

Between 1948 and 1952 he worked as a consultant for British Overseas Airway Corporation and for various oil companies. He moved to the US in 1976 and worked as Navair research professor for the US Naval Academy in Annapolis, Maryland, where he wrote a textbook on Gas Turbine Aerothermodynamics (Whittle, 1981). Sir Frank was accorded numerous honors from all over the world, including nine honorary Doctorates, and was elected to Fellowship of the Royal Society in the UK. He was the recipient of the Tom Sawyer Award of the ASME.

In addition to his prolific contributions to the early development of turbojets, Whittle had 27 patents to his credit, covering areas such as high-bypass engines (turbofans) filed in 1936, and turbodrills used for oilfield applications. A detailed biography of Sir Frank Whittle has been written by Golley (1987).

7.0 Closure

This paper has covered the pioneering work of Sir Frank Whittle with an emphasis on the numerous problems and challenges he faced in the development of a reliable turbojet. As is typical with most paradigm shifts, he had to fight not only against difficult technical problems but also against the traditionalists who were convinced of the superiority of reciprocating engines. It is interesting to note that all the major aeroengine manufacturers started their jet engine work based on Whittle's designs (Singh, 1996). The Rolls Royce Welland, Derwent, Nene, and Tay were based on the Whittle designs. Pratt and Whitney entered the gas turbine field after the war using the Rolls Royce Nene as a basis for their J-42 and J-48. General Electric started their Jet engine work based on the Whittle designs and developed the I-A, J-31 and J-33.

Sir Frank Whittle will always be a beacon of encouragement to engineers not only for his engineering brilliance but also for the tenacious and epic battle that he fought against officialdom and entrenched technical opinion to make possible the jet engine.

Acknowledgments

Obviously, in a historical report of this kind, considerable use has been made of historical texts and technical reports and these have been referenced to the extent possible. Included are the autobiography of Sir Frank Whittle entitled "Jet" and his classic paper presented for the First James Clayton Lecture in 1945 at the Institute of Mechanical Engineers in the UK. The excellent work of Jones (1989), Schlaifer (1950), Constant (1980), Boyne (1980), Golley (1987), Ford (1992), and Gunston (1995) is recommended to those wishing to pursue this topic further.

References

Boyne, W., and Lopez, D., eds., 1979, *The Jet Age: 40 Years of Jet Aviation,* Smithsonian Institute, Washington.

Constant, E. W., II, 1980, *The Origins of the Turbojet Revolution,* John Hopkins Univ. Press.

Constant, H., 1948, *Gas Turbines and Their Problems,* Todd Publishing Group, UK.

Ford, D., 1992, "Gentlemen, I Give You the Whittle Engine," *Air and Space,* Oct./Nov.

Golley, J., 1987, *Whittle—The True Story,* Smithsonian Institution Press, Washington DC.

Gunston, B., 1995, *The Development of Jet and Turbine Aero Engines,* Patrick Stephens, Ltd., UK, 1995.

Gunston, B., 1995, *World Encyclopedia of Aero Engines,* Patrick Stephens, Ltd., UK, 1995.

Hooker, Sir Stanley, 1984, *Not Much of an Engineer,* Airlife Publishing.

Jones, G., 1989, *The Birth of Jet Powered Flight,* Methuen, London.

Meher-Homji, C. B., 1997, "The Development of the Junkers Jumo 004B—the World's First Production Turbojet," ASME JOURNAL OF ENGINEERING FOR GAS TURBINES AND POWER, Vol. 119, pp. 783–789.

Neville, L. E., and Silsbee, N. F., 1948, *Jet Propulsion Progress,* McGraw-Hill.

Schlaifer, R., 1950, *Development of Aircraft Engines,* Graduate School of Business Administration, Harvard University, Boston.

Scott, P., 1995, "Birth of the Jet Engine," *Mechanical Engineering,* Jan., pp. 66–71.

Shacklady, E., 1962, *The Gloster Meteor,* Macdonald and Co., London.

Singh, R., 1996, "Fifty Years of Civil Aero Gas Turbines," Fiftieth Anniversary Lecture, Cranfield University, U.K., June 5.

Von Ohain, H., 1979, "The Evolution and Future of Aeropropulsion Systems," 40 Years of Jet Engine Progress, Boyne, W. J., and Lopez, D. S., eds., National Air and Space Museum, Smithsonian, Washington.

Vosey, R. G., 1945, "Some Vibration Problems in Gas Turbine Engines," *Proc. Institution of Engineers,* Vol. 153, 1945—Lectures on the Development of the Internal Combustion Turbine.

Whittle, Sir Frank, 1954, *Jet—The Story of a Pioneer,* Philosophical Library, Inc, 1954.

Whittle, F., 1945, "The Early History of the Whittle Jet Propulsion Gas Turbine," First James Clayton Lecture of the Institution of Mechanical Engineers, UK, Oct. 5.

Whittle, Sir Frank, 1979, "The Birth of the Jet Engine in Britain," in: *The Jet Age: 40 Years of Jet Aviation,* Smithsonian Institute, Washington, Boyne, W., and Lopez, D., eds.

Whittle, Sir Frank, 1981, *Gas Turbine Aerothermodynamics,* Pergamon Press.

APPENDIX

Leading Particulars of the W.U and the W.1 Engines

	W.U (first version)	W.1
COMPRESSOR		
Tip Dia., in.	19	19
Tip Width, in.	2	2
Eye OD/ID, in	10.75/5.5	10.75/5.5
No. of Blades	30	29
Material	Hiduminium RR 59	Hiduminium RR 59
TURBINE		
Mean Blade Dia., in.	14	14
Blade Length, in.	2.4	2.4
No. of Blades	66	72
Blade chord, in.	0.8	0.8
Material of Blade	Stayblade	Rex 78
Material of Disc	Stayblade	Stayblade
Max speed, RPM	17,750	17,750

Growth in Whittle Engines, W.1 through the W.2/700

ENGINE	Thrust, Lbs.	SFC, lb./hr/lb.	Jetpipe Temp, C
W.1	950	1.37	597
W.2/500	1,755	1.13	606
W.2/700	2,487	1.05	647

Note:

1 Engine speed for all engines was 17,500 rpm. Overall diameter was the same.
2 W.2/700 data for final version, with Nimonic 80 blading, blade height of 3.63", and mass flow rate of 47.15 lb/sec

Investigation of Vapor-Phase Lubrication in a Gas Turbine Engine

K. W. Van Treuren

D. N. Barlow

W. H. Heiser

Department of Aeronautics,
United States Air Force Academy,
Colorado Springs, CO 80840

M. J. Wagner

N. H. Forster

Fuels and Lubrication Division,
Aero Propulsion and Power Directorate,
Wright-Patterson AFB, OH 45433

The liquid oil lubrication system of current aircraft jet engines accounts for approximately 10–15 percent of the total weight of the engine. It has long been a goal of the aircraft gas turbine industry to reduce this weight. Vapor-Phase Lubrication (VPL) is a promising technology to eliminate liquid oil lubrication. The current investigation resulted in the first gas turbine to operate in the absence of conventional liquid lubrication. A phosphate ester, commercially known as DURAD 620B, was chosen for the test. Extensive research at Wright Laboratory demonstrated that this lubricant could reliably lubricate rolling element bearings in the gas turbine engine environment. The Allison T63 engine was selected as the test vehicle because of its small size and bearing configuration. Specifically, VPL was evaluated in the number eight bearing because it is located in a relatively hot environment, in line with the combustor discharge, and it can be isolated from the other bearings and the liquid lubrication system. The bearing was fully instrumented and its performance with standard oil lubrication was documented. Results of this baseline study were used to develop a thermodynamic model to predict the bearing temperature with VPL. The engine was then operated at a ground idle condition with VPL with the lubricant misted into the #8 bearing at 13 ml/h. The bearing temperature stabilized at 283°C within 10 minutes. Engine operation was continued successfully for a total of one hour. No abnormal wear of the rolling contact surfaces was found when the bearing was later examined. Bearing temperatures after engine shutdown indicated the bearing had reached thermodynamic equilibrium with its surroundings during the test. After shutdown bearing temperatures steadily decreased without the soakback effect seen after shutdown in standard lubricated bearings. In contrast, the oil-lubricated bearing ran at a considerably lower operating temperature (83°C) and was significantly heated by its surroundings after engine shutdown. In the baseline tests, the final bearing temperatures never reached that of the operating VPL system.

Introduction

The development of gas turbines operating without a conventional liquid lubrication system has been a research objective for several decades. Potential benefits of eliminating the liquid lubrication system include reductions in cost, weight, engine cross-sectional area, and maintenance. Additional benefits are possible if the lubrication method also increases the operating temperature of the main shaft bearings, reducing thermal gradients, and therefore, thermal stresses in the rotating components of the engine. Currently, bearing temperatures in gas turbines are limited to approximately 204°C due to thermal limitations of the liquid lubricant. To maintain a 204°C operating temperature, the bearing compartment is cooled with compressor air, heat shielding is added to critical locations, and the lubricant is cooled via a fuel/oil heat exchanger. In advanced engines the use of these thermal management tools becomes increasingly more difficult.

Previous efforts to develop a high-temperature lubrication system focused primarily on solid lubricants delivered as powders (Macks et al., 1951; Anderson, 1965; Wilson, 1962; Wallerstein, 1965) or as lubricant films transferred from the sliding surfaces of bearing cages (Devine et al., 1961; Dayton, 1971; Boes, 1978; Gardos, 1984). Both of these methods provide adequate lubrication for lightly loaded, low-speed applications. However, both methods have demonstrated limited success at conditions required for a gas turbine engine, i.e., bearing speeds of 1.5 to 2.5 MDN (MDN = shaft diameter (mm) × shaft rpm/10^6) and bearing stress loads of 1.0 to 2.0 GPa. Bearing wear, cage fracture, and seizure due to thermal growth are the common modes of failure in high-speed, solid-lubricated bearings.

During the 1980s and early 1990s a new form of lubrication known as vapor phase lubrication began to show promise as an alternative high-temperature lubrication concept (Graham and Klaus, 1985; Gunsel, 1986; Klaus et al., 1989, 1990; Maki and Graham, 1990, 1991; Klaus and Duda, 1991; Graham et al., 1993; Rao, 1993; Morales et al., 1994; Hanyaloglu and Graham, 1994). To accomplish VPL, a small quantity of organophosphorus material is vaporized and transported to a metallic bearing surface where the vapors chemically react with the surface to form the lubricating film. Analyses of bearings, lubricated with a tertiary-butylphenyl phosphate, DURAD 620B, indicate that the lubricating film is primarily composed of condensed phosphates and graphite (Forster, 1996a). The phosphate serves as an antioxidant and binder for the lubricant. The extremely high flash point of the lubricant also allows a thin layer of liquid lubricant to exist in the bearing contact at extremely high temperatures.

During the 1990s Wright Laboratory initiated an extensive in-house research program to investigate vapor phase lubrication for use in gas turbine bearings. The primary emphasis of this research was to identify nontoxic vapor lubricants that can successfully lubricate rolling element bearings in an air environment (Forster, 1996a, b). Over the past five years the technology has evolved to the point where gas turbine bearings can be reliably lubricated for periods of several hours. This period of

Contributed by the International Gas Turbine Institute and presented at the 42nd International Gas Turbine and Aeroengine Congress and Exhibition, Orlando, Florida, June 2–5, 1997. Manuscript received at ASME Headquarters February 1997. Paper No. 97-GT-3. Associate Technical Editor: H. A. Kidd.

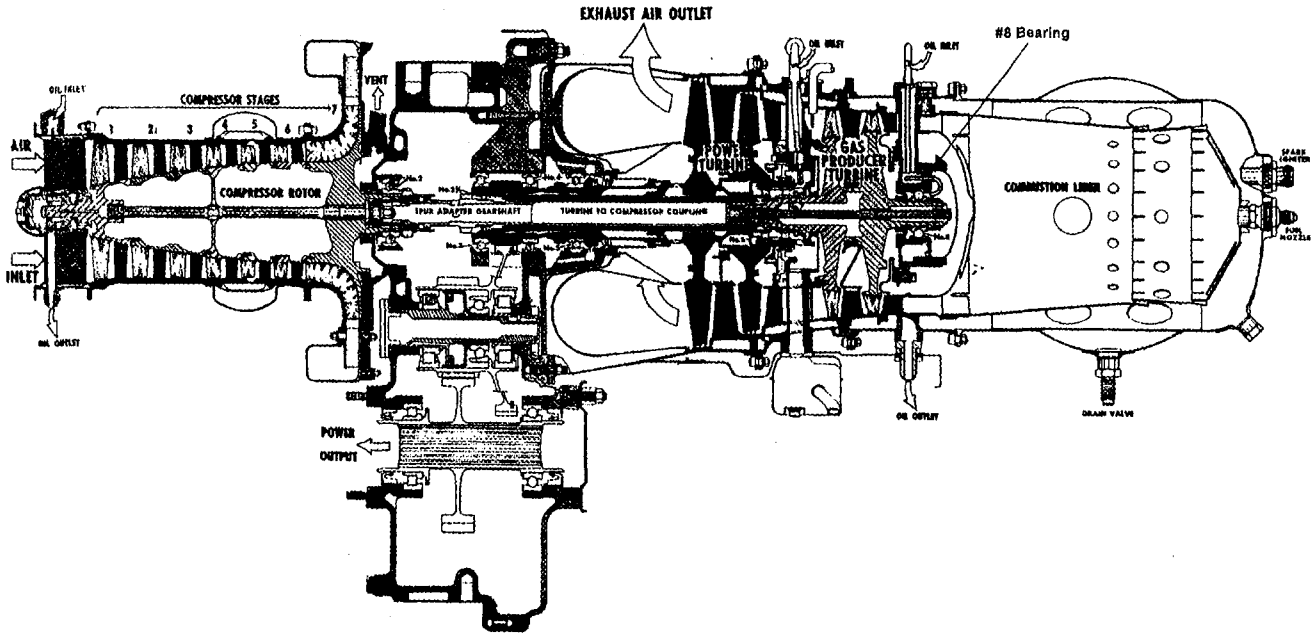

Fig. 1 Allison T63 Turboshaft Engine (Allison, 1981)

operation is sufficient for consideration of the technology in expendable class engines. One of the key shifts in the vapor phase approach has been delivering the lubricants as an oil mist rather than in the vapor phase. The increased momentum of an oil mist droplet allows better penetration of the pressure differential created by windage in high-speed bearings. Upon entering the bearing, the bearing surface temperature provides the heat input required to complete vaporization and to initiate the chemical reactions. The oil mist delivery approach also provides additional cooling of the bearing.

High-Speed Bearing Rig Tests

The Allison T63 turboshaft engine is an excellent platform to test VPL because of its small size and wide use in the commercial and military helicopter market (Fig. 1). The #8 bearing in the T63 (Fig. 2) was chosen to test VPL because its design places the #8 bearing immediately downstream of the combustor, providing a harsh temperature environment for the bearing cavity, and because the #8 bearing can be isolated from the other bearings in the liquid lubrication system. A shroud around the bearing housing is supplied with cooling air from the compressor. The shroud serves to shield the bearing housing from direct combustor flow, but at this location, high cooling rates for the bearing are still required to maintain normal operating temperatures. The T63 #8 bearing is a 20 mm bore split outer race bearing, with M50 steel balls and races, and a one piece cage of silver plated 4340 steel. It is typical of existing bearings currently used with conventional oil lubrication systems.

Prior to engine testing, single-bearing rig tests were performed to establish safe operating limits, thereby reducing risk to the engine. This was considered necessary because the bearing is designed to operate with standard liquid lubrication at outer race temperatures below 150°C, and temperatures with VPL were expected to be in excess of 260°C. The T63 #8 bearing, its support, and the vapor mist system were installed in the High-Speed Bearing test rig. The rig is an air turbine driven test stand designed to test complete bearings at speeds up to 55,000 rpm. Operating conditions in the engine were simulated by blowing hot air over the bearing compartment and applying a constant thrust load of 267 Newtons to the bearing outer race. The rig could not simulate the rapid heating experienced in the engine, so the bearing was preheated to a steady-state temperature for 30–45 minutes prior to each test. All tests began with a slow (10–15 minute) ramp up to the engine idle speed of 35,000 rpm, and then operation at idle to establish steady-state conditions. From there, heater and speed controls were adjusted to establish other desired operating conditions. The precision to which any given test condition could be maintained was ±14°C in bearing temperature and ±1000 rpm in speed. Bearings were generally run until a sharp increase in friction was detected, as indicated by a rapid decrease in rig speed (~1000 rpm/s) and a rapid increase in outer race temperature (~3°C/s).

A total of eight bearings were rig tested. Results are summarized in Table 1. Setup and procedural errors, which are believed to have caused premature suspension to bearing tests 1, 3, 4, and 6, are noted. Visual inspection of the bearing cages revealed wear at the cage-outer land and ball pocket surfaces in all cases, similar to the engine bearing. The bearing races and rolling elements varied in condition, but were all worn more severely than the engine bearing. This was attributed to the considerably longer run times and more severe test conditions experienced by the rig bearings.

Nomenclature

C_p = specific heat, J/kgK
h_{load} = heat load coefficient, W/°C
$\dot{m}$ = fluid mass flow rate, kg/s
MDN = shaft diameter, mm × shaft rpm/10^6
$\dot{Q}_{oil}$ = oil heating rate, W
$\dot{Q}_{air}$ = air heating rate, W
$\dot{Q}_{vap}$ = Durad heating rate, W
$T_{bearing}$ = #8 bearing temperature, °C
T_{exit} = #8 vapor outlet temperature, °C
T_{inlet} = #8 vapor inlet temperature, °C
$T_{surrounding}$ = #8 bearing air cavity temperature, °C
T_{T3} = compressor bleed temperature, °C
T_{T5} = intra-turbine temperature, °C

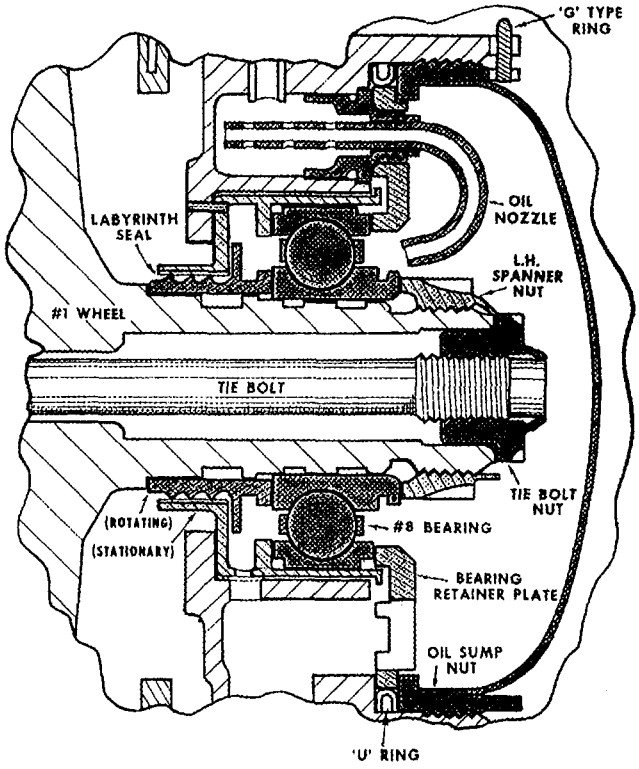

Fig. 2 Side view of #8 bearing housing (Allison, 1981)

Based on the series of bearing rig tests and the success demonstrated during bearing test eight, it was concluded that safe and continuous operation of the bearing could be achieved at outer race temperatures below 379°C at speeds from idle to full power (35,000–51,000 rpm). Continuous engine operation at temperatures above the limit was deemed inadvisable. The greater wear of the races and balls of the rig bearings indicates that improved materials for these components will be required for extended life at higher temperatures. Finally, although the engine races and balls showed virtually no wear, its cage was worn similarly to the rig bearings. This indicates that cage wear is a problem at much less severe conditions than race and ball wear. Therefore, a primary focus of future efforts should be on the improvement of cage lubrication.

T63 Experimental Setup

With the success of the High-Speed Bearing Rig tests, the next step was to test VPL under engine operating conditions. These experiments were conducted on an Allison T63-700 turboshaft engine. The engine test cell was equipped with a complete engine control system and with a SUPERFLOW SF-740 data acquisition system capable of 320 channels of data. The engine was fully instrumented and all normal engine health parameters monitored. The acquisition system also incorporated a dynamometer to measure engine torque during testing. In addition to the standard instrumentation, the #8 bearing was fully instrumented to provide information on the operating conditions during both oil lubrication and VPL operations (Fig. 3). The bearing housing contains five support struts. Two of these struts are ordinarily used to feed the lubricant to the bearing and remove the lubricant from the bearing. Another of the struts was modified to allow seven *K*-type thermocouple leads to pass through to the bearing and bearing housing. Three thermocouples were in contact with the bearing outer race. Two thermocouples were placed in the return sump cavities around the bearing to monitor the fluid temperatures after the fluid passed through the bearing but before it exited the bearing housing. Another thermocouple was located in the air cavity between the heat shield and the bearing sump cap. The interior strut temperature was also monitored to determine whether the fluid temperature increased prior to reaching the bearing as a result of passing through the strut. Lubricant inlet and outlet temperatures were measured just prior to entering and just after exiting the bearing housing.

Prior to using VPL in the engine, the bearing temperatures using the conventional oil lubrication system were determined. The engine was operated under various load conditions (ground idle, flight idle, and full throttle at maximum continuous operation) to characterize engine performance completely and to have sufficient data to compare conventional lubrication operation with VPL.

After the baseline oil tests were accomplished, the #8 bearing was isolated from the engine oil system by coupling the #8 oil inlet line to the exit line that completed the oil system. The oil intake line was replaced with a line from the mister. The mister, an Alemite Model 4955, was attached to the test rig. A tertiary-butylphenyl phosphate (TBPP) lubricant, DURAD 620B, was chosen as the lubricant for this test. The lubricant was preheated to 93°C to reduce its viscosity and allow better misting. The mister used 0.00066 m^3/s of shop air at 1.72 bar (gage) and was set to supply 13 ml of lubricant per hour, according to research done during the High-Speed Bearing Rig tests. To increase the flow of the mist to the bearing, the highly restrictive oil nozzle in the bearing compartment was removed and replaced by one with a larger diameter (3 mm) vapor injection nozzle, which permitted greater mist. After passing through the bearing, any unused lubricant was passed directly into the engine exhaust. Toxicology studies conducted at the Armstrong Lab determined that DURAD 620B is nontoxic in liquid form. Tests of decomposition rates were conducted at Wright Labora-

Table 1 High-Speed Test Rig results

Bearing	Speed (rpmx1000)	Bearing Temp (C)	Run Time (hr)	Comments
1	38	385-391	0.6*	extended preheat cycle without lube, unintended
2	38	338-354	12.0	
3	33	304-346	0.08*	bearing misalignment; alternate lube.
4	33	327-416	0.4*	bearing misalignment.
5	38	382-416	2.7*	
6	38	327-349	0.7	extended preheat cycle without lube, unintended
	40	338-343	0.1	
	43	343-360	0.01*	
			0.8 Total	
7	38	399-416	3.3*	
8	35-39	332-377	4.7	
	40-50	316-343	3.5	
	50-55	299-354	8.9	
	55	349-379	3.1	
	55	379-418	0.6	
	55	418-443	0.05*	
			20.9 Total	
				*Test terminated due to sudden friction increase

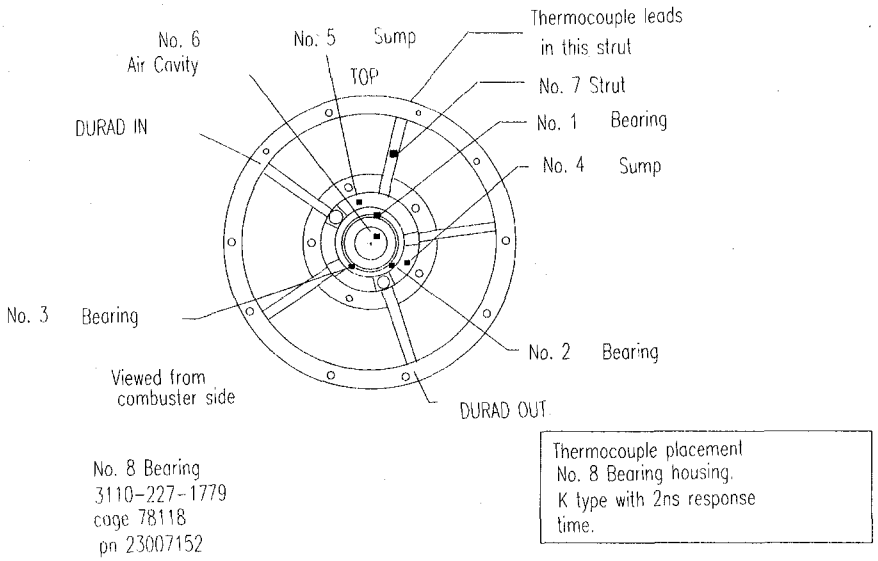

Fig. 3 T-63 #8 bearing housing instrumentation

tory. At vapor temperatures representative of exhaust gas temperatures, slow decomposition rates were measured, resulting in low toxicity at these temperatures. Venting the vapors to the engine exhaust is safe since the quantity of lubricant, 13 ml/h, is small and consequently poses no significant environmental impact when diluted in the exhaust air stream.

Theory

Tests with the oil lubrication system provided the baseline data for comparison with the vapor-phase test. In the liquid lubricant tests it was determined the bearing operated at a steady-state condition of 83°C at the ground-idle condition. Knowing this temperature and the temperatures of the other thermocouples in the bearing compartment, it was possible to develop a model to predict what the bearing temperature would be using a VPL system at the same engine operating conditions. Knowing the temperature difference of the oil across the bearing (inlet and exit), the flow rate of oil, and the specific heat of the oil at the average temperature, the total energy absorbed by the oil can be calculated:

$$\dot{Q}_{\text{oil}} = \dot{m} C_{p_{\text{oil}}} (T_{\text{exit}} - T_{\text{inlet}})$$

The heating rate was found to be 582 W at ground-idle conditions. This value was used to calculate a characteristic heat loading coefficient, h_{load}. This coefficient is simply the energy transfer rate to the oil divided by the difference between the temperature of the air cavity surrounding the bearing and the temperature of the bearing race:

$$h_{\text{load}} = \frac{\dot{Q}_{\text{oil}}}{(T_{\text{bearing}} - T_{\text{surrounding}})}$$

The energy transport mechanism for the vapor-phase flow is not as great as in the liquid case. Energy transport is expected to be a function of both the thermal conductivity and heat capacity of the fluid. Comparing VPL to oil lubrication, the thermal conductivity and the specific heat of air are less than that of oil ($k_{\text{oil}}/k_{\text{air}} \sim 10$, $C_{p\text{oil}}/C_{p\text{air}} \sim 2$). As a result, the energy transport from the bearing to the fluid is less for VPL than for the liquid lubrication case. In reality, h_{load} is expected to be a lower value. It was optimistically assumed that h_{load} would be the same for the VPL case as that of the oil. With this assumption it was possible to develop an equation to predict the temperature of the bearing. The energy pickup in the VPL case is given as follows:

$$\dot{Q}_{\text{vap}} + \dot{Q}_{\text{air}} = h_{\text{load}} (T_{\text{bearing}} - T_{\text{surrounding}})$$

The energy absorption due to vaporization was found to be several orders of magnitude smaller than the energy transfer rates caused by the air and therefore is considered negligible in the remainder of the calculations. The mass flow of air was calculated as 0.00081 kg/s from the specifications set forth in the mister user's manual. The VPL bearing temperature was predicted using the following equation:

$$\dot{m} C_{p_{\text{air}}} (T_{\text{exit}} - T_{\text{inlet}}) = h_{\text{load}} (T_{\text{bearing}} - T_{\text{surrounding}})$$

T_{inlet} and T_{exit} are the temperatures of the vapor as it enters and leaves the bearing assembly. The value of T_{inlet} was assumed to be the same as the temperature of the lubricant in the mister, 93°C. From the oil system data and the equation for energy pickup for the VPL system with air only, it was possible to make estimates for T_{exit} and $T_{\text{surrounding}}$. In the oil lubrication tests, T_{exit} was found to be approximately the mean of the bearing temperature and T_{inlet} at each operating point. Likewise, $T_{\text{surrounding}}$, the temperature of the area surrounding the bearing, was found to be approximately the mean of the turbine intrastage gas temperature, T_{T5}, and the compressor bleed air temperature, T_{T3}, which is used to cool the bearing housing. In predicting bearing temperature under VPL operation, $T_{\text{surrounding}}$ and T_{exit} are therefore defined as:

$$T_{\text{surrounding}} = \frac{T_{T5} + T_{T3}}{2}$$

$$T_{\text{exit}} = \frac{T_{\text{bearing}} + T_{\text{inlet}}}{2}$$

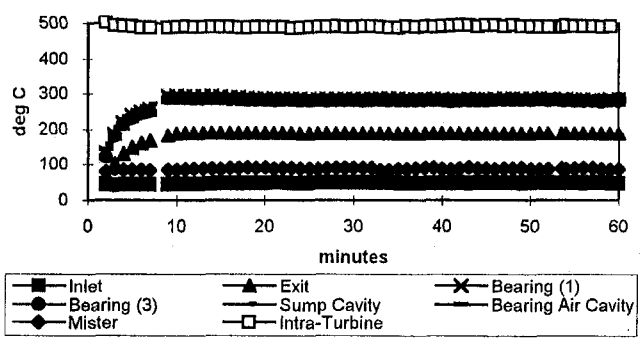

Fig. 4 T63 temperature–time histories

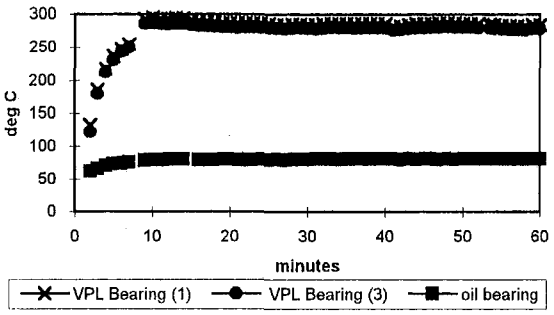

Fig. 5 VPL and oil bearing temperature comparison

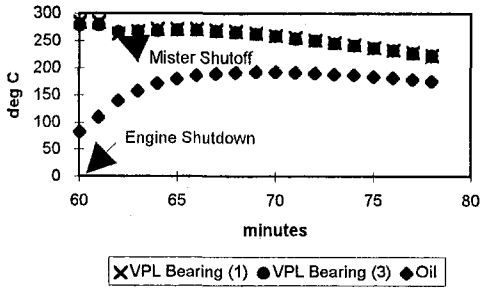

Fig. 6 T63 #8 bearing soak back temperatures

Using the data from the oil system test, a bearing temperature of 306°C for the ground-idle condition was predicted for VPL operation. This temperature was well below the 379°C operating limit determined from the bench tests, so it was concluded that limiting engine operation for the VPL test to ground idle would permit a safe test with reasonable risk. Although differences in the transport mechanisms involved with liquid and vapor lubrication were not considered in the h_{load} value, the $T_{bearing}$ calculated is relatively insensitive to differences in h_{load}. If h_{load} is decreased by 83 percent the calculated temperature of the bearing increases by only 2 percent. This provided confidence in the predicted bearing temperature, despite the uncertainty in the assumptions.

Experimental Results

Engine Test Results. The first steady-state test of a VPL system in a turbine engine was conducted on 19 March 1996 in the test cell of the United States Air Force Academy Aeronautics Laboratory. The test lasted 60 minutes and was conducted with the T63 engine at ground-idle. The results are given in Fig. 4. The first 13 minutes of the test showed the bearing temperature rising steadily as it reached equilibrium. The VPL bearing reached a state of equilibrium at 283°C, a temperature somewhat below that predicted by the model. Figure 4 compares the temperature profiles of the bearing race, the bearing sump cavity, the bearing compartment air cavity, vapor inlet and exit ports, and the intraturbine temperature, T_{T5}. These data showed that, as expected, the bearing operated at temperatures very close to the temperature of the bearing air cavity. The bearing air cavity and assembly are actively cooled by compressor bleed air, maintaining a temperature below T_{T5}. Figure 5 compares the bearing temperature of a liquid and vapor-lubricated bearing. Once equilibrium was achieved, the bearing temperature remained virtually constant for the remainder of the test. A comparison of the VPL system with the liquid lubrication system showed little change in other engine operating parameters. Table 2 gives a comparison of important measured parameters in the #8 bearing at virtually the same operating condition. The small differences in torque and T_{T5} are not considered significant due to deviations in ambient air temperatures between runs.

Another item for consideration in the bearing is the soak back performance. Soak back occurs after the engine is shut down and the lubricant no longer carries the energy away from the bearing housing. For this reason, normal turbine engines experience a large rise in bearing temperature for about 10 minutes after engine shut-down.

Soak back affects the formation of deposits from the lubricant in a liquid lubrication system. For expendable engines, soak back is irrelevant since the engine is only intended to be used once, for short duration. Since the VPL bearing operated at extremely high temperatures, there was only a small thermal gradient between the bearing and its surroundings. Therefore, soak back was not experienced. Figure 6 shows the soak back for the #8 bearing after the oil and VPL tests. The VPL bearing shows a steady decrease in temperature with time, indicating it was in thermal equilibrium with its surroundings. The small dip in the VPL curve at the beginning of the soak back curve is due to the mister, which was still supplying some cooling air, before being turned off.

Bearing Analysis. After the engine test was completed, the bearing was removed from the engine and the outer race cut in half so the bearing could be disassembled and the components inspected. Three levels of inspection were performed. First, each component was visually inspected for defects at 1× to 10× magnification, according to overhaul shop procedures (ref. T.O. 44B-1-15, T.O. 44B-1-102). This was to determine if they would be considered serviceable in an operational aircraft engine. Next, each component was viewed at 120× to 600× magnification with a Scanning Electron Microscope (SEM) to evaluate surface finish and the geometry of any defects found. Finally, Energy Dispersive X-ray (EDX) measurements of surface elements were made to check for the formation of a deposition film, as indicated by the presence of phosphorus.

When the engine was disassembled for bearing removal, it was discovered that the tip of the vapor injection nozzle was worn. It appeared that thermal expansion of the nozzle had caused it to come in contact with the retaining nut on the bearing

Table 2 Comparison of oil and VPL systems at ground idle

PARAMETER	OIL	VPL
Torque (N-m)	35.2	34.8
TT5 (deg C)	497	491
Average #8 Bearing (degC)	83	283
#8 Bearing Oil Sump (deg C)	91	294
#8 Bearing Air Cavity (deg C)	67	274

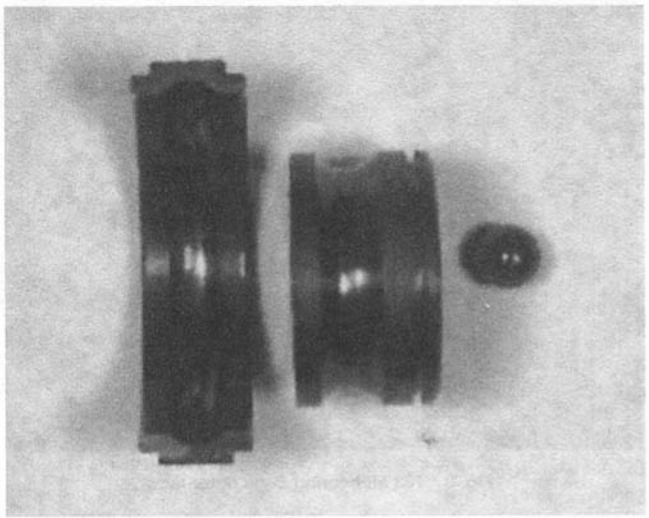

Fig. 7 T63 #8 bearing outer race, inner race, and ball

inner race. In general, this did not appear to affect bearing performance, but minor defects found in the balls and races have been attributed to nozzle debris entering the bearing.

The balls, outer race and inner race all passed visual inspection (Fig. 7). They appeared smooth and light brown in color, with a slight wear track visible, which is normal. The land surface of the outer race showed signs of cage rubbing, but was still smooth and uniform. The only visible defect was a light scratch in the ball track of the inner race, which ran for one-third of the circumference. The scratch was not detectable when a 0.762 mm radius scribe was dragged across it, so the race was still serviceable. Under the SEM, at 150× magnification, the scratch revealed a series of indentations, characteristic of debris damage, as from the nozzle debris. The outer race and balls showed similar indentations in the wear track under the SEM. Phosphorus was present in the raceways of both races, indicating the formation of a deposition film.

The cage showed signs of wear at the outer land riding surfaces and in the ball pockets (Fig. 8). The wear was limited to smearing of the silver plating. This is expected at marginal lubrication conditions at these areas of sliding contact. The outer land was worn for the entire circumference on the forward and aft sides of the ball pockets. The ball pockets were worn around their entire circumference for one half of the cage thickness. A definite ridge could be felt with a 0.762 mm radius scribe between the worn and unworn areas. Although the silver plating on the cage performed its designed function, the cage would not be acceptable for reinstallation in an operational engine. The EDX measurements of the worn areas revealed that a substantial amount of silver was still present. Phosphorus was also present, indicating the formation of a deposition film on the land and ball pocket surfaces.

Conclusions

This experiment demonstrated, for the first time, the ability to run a VPL system in an operating turboshaft engine and represents the first known tests in which a gas turbine engine was run without a liquid lubricant. VPL is a possible option for future use in the design of modern turbine engines, offering significant weight and cost savings, as well as significant improvements in engine performance due to the increase in temperature capability. For expendable class engines used in air-launched cruise missiles, the weight reduction of a vapor lubrication system compared to a liquid lubrication system is approximately 15 percent of the turbine engine weight. A similar reduction in engine cost could be expected.

Future VPL work will include the development of a self-contained mister system using engine bleed air. Tests will also include operation at conditions above ground idle, requiring careful monitoring of bearing temperatures so as not to exceed the 379°C temperature limit determined by the High-Speed Bearing Rig tests. Future tests will also include alternative bearing materials allowing operation above this temperature limit. There is also a need to demonstrate the application of VPL in a bearing that operates at a colder temperature, such as the #1 bearing in the T63.

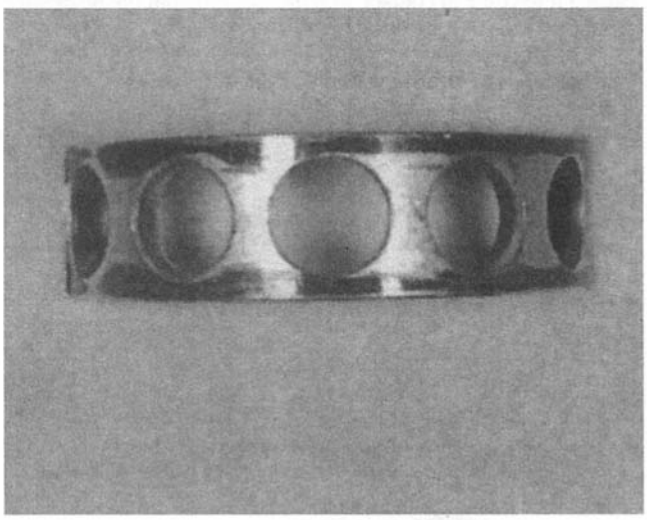

Fig. 8 T63 #8 bearing cage outer land

Acknowledgments

The authors are grateful to the United States Air Force for supporting this important research. A special thanks goes to Mr. Jerry Stermer, who modified the bearing housing and prepared the T63 engine for operation at the Air Force Academy. Also, thanks to 2LT Mark Mitchum for his contributions to the VPL research effort at the Air Force Academy (Mitchum, 1996).

References

Allison Gas Turbine Division, 1981, TM 55-2840-231-23.

Anderson, W. J., 1965, "Advanced Bearing Technology," NASA SP-38, Bisson, E. E., and Anderson, W. J., eds., pp. 309–370.

Boes, D., 1978, "Development of Light Weight Solid Lubricated Bearing Retainers," Air Force AFAPL-TR-78-72.

Dayton, R. D., 1971, "Experimental Investigation of Ag-Hg-WTFE-$MoSe_2$ Solid Lubricated Ball Bearings for High Speed, High Temperature, and High Load Applications," AFAPL-TR-71-100.

Devine, M. J., Lamson, E. R., and Bowen, J. H., 1961, "The Lubrication of Ball Bearings With Solid Films," ASME Paper No. 61-UBS-11.

Forster, N. H., 1996a, "High Temperature Lubrication of Rolling Contacts With Lubricants Delivered From the Vapor Phase and as Oil-Mists," Ph.D. Thesis, University of Dayton, OH.

Forster, N. H., 1996b, "Rolling Contact Testing of Vapor Phase Lubricants," AGARD-CP-589, pp. 15-1, 15-8.

Gardos, M. N., 1984, "Solid Lubricated Rolling Element Bearings Final Report," AFWAL-TR-83-4129.

Graham, E. E., Nesarikar, A., Forster, N. H., and Givan, G. D., 1993, "Vapor Phase Lubrication of High Temperature Bearings," *Lubr. Eng.*, Vol. 49, No. 9, pp. 713–718.

Graham, E. E., and Klaus, E. E., 1985, "Lubrication from the Vapor Phase at High Temperatures," *ASLE Trans.*, Vol. 29, pp. 229–234.

Gunsel, X. Y., 1986, "Development and Evaluation of a High-Temperature Lubrication System," Ph.D. Thesis, Pennsylvania State University.

Hanyaloglu, B., and Graham, E. E., 1994, "Vapor Phase Lubrication of Ceramics," *Lubr. Eng.*, Vol. 50, No. 10, pp. 814–820.

Klaus, E. E., and Duda, J. L., 1991, "Vapor Phase Lubrication Development for Engines," *SAE Publ. SP-256*, pp. 541–550.

Klaus, E. E., Phillips, J., Lin, S. C., Wu, N. L., and Duda, J. L., 1990, "Structure of Films Formed During the Deposition of Lubrication Molecules on Iron and Silicon Carbide," *Trib. Trans.*, Vol. 33, pp. 25–32.

Klaus, E. E., Jeng, G. S., and Duda, J. L., 1989, "A Study of Tricresyl Phosphate as a Vapor Delivered Lubricant," *Lubr. Eng.*, Vol. 45, pp. 717–723.

Macks, E. F., Nemeth, Z. N., and Anderson, W. J., 1951, "Preliminary Investigation of Molybdenum Disulfide—Air-Mist Lubrication of Roller Bearings Operating to DN Values of 1×10^6 and Ball Bearings Operating to Temperatures of 1000°F," NACA RM ES1 631.

Maki, J. F., and Graham, E. E., 1990, "Vapor Phase Deposition on High Temperature Surfaces," *Trib. Trans.*, Vol. 33, No. 4, pp. 595–603.

Maki, J. F., and Graham, E. E., 1991, "Formation of Solid Films From the Vapor Phase on High Temperature Surfaces," *Lubr. Eng.*, Vol. 47, pp. 199–206.

Mitchum, M., 1996, "T63 Vapor-Phase Lubrication," AIAA Region V student paper.

Morales, W., Hanyaloglu, B., and Graham, E. E., 1994, "Infrared Analysis of Vapor Phase Deposited Tricresyl Phosphate (TCP)," NASA Tech. Rept. TM-106423.

Rao, A. M. N., 1993, "Identification of an Alternative Lubricant for Vapor Phase Lubrication," M.S. Thesis, Cleveland State University, OH.

Wallerstein, S., 1965, "Application of a Gas Powder Lubrication System to a Gas Turbine Engine," AFAPL-TR-65-43.

Wilson, D. S., 1962, "Powdered and Gaseous Lubricants for Use in Ball Bearings at Temperatures From Room Temperature to 1200°F," ASD-TDR-62-465, Beane, G. A., and Berkey, K. L., eds., pp. 201–209.

Reliability of a Conceptual Ceramic Gas Turbine Component Subjected to Static and Transient Thermomechanical Loading

P. S. DiMascio

R. M. Orenstein

Power Generation Engineering,
GE Power Systems,
Schenectady, NY 12345

H. Rajiyah

Mechanics of Materials,
GE Corporate R&D,
Schenectady, NY 12301

A three year program to evaluate the feasibility of using monolithic silicon nitride ceramic components in gas turbines was conducted. The use of ceramic materials may enable design of turbine components which operate at higher gas temperatures and/or require less cooling air than their metal counterparts. The feasibility evaluation consisted of the following three tasks: (1) expand the material properties database for candidate silicon nitride materials; (2) demonstrate the ability to predict ceramic reliability and life using a conceptual component model; and (3) evaluate the effect of proof testing on conceptual component reliability. The overall feasibility goal was to determine whether established life and reliability targets could be satisfied for the conceptual ceramic component having properties of an available material. Fast and delayed fracture reliability models were developed and validated via thermal shock and tensile experiments. A creep model was developed using tensile creep data. The effect of oxidation was empirically evaluated using four-point flexure samples exposed to flowing natural gas combustion products. The reliability and life-limiting failure mechanisms were characterized in terms of temperature, stress, and probability of component failure. Conservative limits for design of silicon nitride gas turbine components were established.

Introduction

A three year program to evaluate the feasibility of using monolithic silicon nitride ceramic components in gas turbines was conducted by GE Power Systems (GEPS). The use of ceramics in advanced gas turbines is desirable because candidate materials possess greater strength, stiffness, and oxidation resistance at temperatures between 1000 and 1400°C than state-of-the-art metal superalloys. This may enable design of components which operate at higher gas temperatures and/or require less parasitic cooling air than their metal counterparts.

Monolithic ceramics, which can be fabricated into complex shapes (e.g., turbine airfoils and seals) at relatively low cost, were surveyed. Sintered silicon nitride offered the advantages of higher fracture toughness, thermal conductivity, and resistance to thermal shock than other candidate materials. However, it was not known how the potential loss of material strength over time by creep, fatigue, and oxidation mechanisms would affect component reliability. Furthermore, monolithic ceramic materials typically fail in a catastrophic manner during overstress conditions, such as thermal shock, from a random population of flaws which are introduced during processing, machining, or service. It was therefore necessary to quantitatively characterize the reliability and life-limiting failure mechanisms in candidate materials in terms of temperature, stress, and probability of component failure. This enabled conservative limits for design of ceramic components to be established as well as definition of requirements for proof tests to ensure that each component possessed a prescribed minimum strength level prior to service.

Contributed by the International Gas Turbine Institute and presented at the International Gas Turbine & Aeroengine Congress & Exhibition, Orlando, FL, June 2–5, 1997. Manuscript received by the ASME Headquarters July 1997. Paper No. 97-GT-284. Associate Technical Editor: H. A. Kidd.

The program was sponsored jointly by the Electric Power Research Institute (EPRI) and the Gas Research Institute (GRI). Participating laboratories included GE Corporate Research and Development (GECRD), Materials Performance analysis, Inc. (MPa), the National Institute of Standards and Technology (NIST), the Pennsylvania State University (PSU), and the University of Dayton Research Institute (UDRI).

The feasibility evaluation consisted of the following three tasks: (1) expand the material properties database for candidate ceramic materials; (2) demonstrate the ability to predict ceramic life and reliability using a conceptual component model; and (3) evaluate the effect of proof testing on conceptual component life and reliability. The overall feasibility goal was to determine whether established life and reliability targets could be satisfied for the conceptual ceramic component having properties of an available material.

Ceramic Reliability and Life Prediction

The material characterization tests used for developing predictive models are given in Table 1. The first objective was to validate a fast fracture (i.e., time independent) reliability prediction method using notched rectangular plates that were thermally shocked in a fluidized bed. The ultimate objective was to apply time and cycle-dependent reliability prediction methods to a conceptual ceramic turbine shroud as subjected to (1) steady-state thermomechanical loading during baseload gas turbine operation, and (2) transient thermal shock loading during a full load turbine trip, i.e., a rapid shutdown from the baseload condition.

Materials Selection. State-of-the-art silicon nitride materials were surveyed prior to selecting two candidate materials for further characterization. Only commercially available material grades were considered. The selected materials were SN-88

Table 1 Material characterization tests

TEST	TEST SPECIMEN	TEST PURPOSE
Fast Fracture Strength	• Buttonhead tensile • Flat tensile • Type A Flexure • Type B Flexure (notched) • JIS Flexure	• Estimate material strength parameters for component reliability prediction • Identify reliability-limiting fracture origin distributions
Static Fatigue Strength	• Buttonhead tensile • Flat tensile	• Estimate material fatigue parameters for component reliability prediction
Dynamic Fatigue Strength	• Buttonhead tensile • Flat tensile • Type B Flexure	
Cyclic Fatigue Strength	• Buttonhead tensile • Type B Flexure (notched)	
Fast Fracture Strength following Burner Rig Aging	• Type A Flexure	• Estimate material strength parameters for component reliability prediction • Identify reliability-limiting fracture origins following aging to 10,000 hours
Tensile Creep Strength	• Buttonhead tensile • Flat tensile	• Determine material creep parameters for component life prediction • Characterize changes in materials following creep testing to 10,000 hours

(NGK Insulators, Ltd., Nagoya, Japan) and AS-800 (Allied Signal Ceramic Components, Torrance, CA). Both materials contained elongated grains of beta-phase silicon nitride, which served to increase fracture toughness and fatigue crack growth resistance. Both materials also contained crystalline grain boundary phases, which served to increase creep and fatigue crack growth resistance.

SN-88 test specimens were machined from billets which were cold isopressed, sintered, and preoxidized via a passivation heat treatment. AS-800 test specimens were machined from billets which were pressure slip cast and sintered. All machining was performed by West Advanced Ceramics (Ithaca, NY). The SN-88 was extensively characterized using the tests in Table 1, which are described below in greater detail. This material was considered relatively mature since it was developed in the late 1980s. The AS-800 was in an earlier state of development and was therefore characterized less extensively than the SN-88. Predictive models were based upon SN-88 thermomechanical and fracture properties.

SN-88 Strength Evaluations. Tensile tests were conducted in fast fracture, fatigue, and creep modes using buttonhead specimens measuring 165 mm in length, with gage dimensions of $35 \times 6.3\ \phi$ mm, and flat specimens measuring 76 mm in length, with gage dimensions of $19 \times 2.5 \times 2.5$ mm. Test temperature ranged from 20 to 1400°C. Tensile specimens were machined in a direction parallel to the gage axis and were heat treated following machining. Data censoring was used to estimate material strength parameters for discrete populations of fracture origins (e.g., pores, large grains, and metallic inclusions) in the specimens tested in fast fracture mode. Pooled data (i.e., not censored for flaw type) were used to estimate material fatigue parameters in the specimens tested in static and dynamic fatigue modes. Creep behavior was thoroughly characterized using flat specimens tested from 1150 to 1400°C. The strength of two groups of buttonhead specimens was evaluated in dynamic fatigue mode, one group following 1000 h of creep loading at 1200°C and the second group following 5000 tension-compression fatigue cycles at 900°C. Strength changes for specimens which survived these interrupted loading tests were small.

Flexure tests were conducted in fast fracture mode using three standard specimen sizes. Type A specimens measured 23 mm $\times$ 1.5 mm $\times$ 1 mm and were loaded in four-point flexure using an inner span of 10 mm and an outer span of 20 mm. Type B specimens measured 50 mm $\times$ 4 mm $\times$ 3 mm and were loaded in four-point flexure using an inner span of 20 mm and an outer span of 40 mm. JIS specimens measured 36 mm $\times$ 4 mm $\times$ 3 mm and were loaded in four-point flexure using an inner span of 10 mm and an outer span of 30 mm. The Type A and Type B flexure specimens were machined in directions either parallel or transverse to the loading axis and heat treated following machining. The JIS specimens were prepared by NGK and were machined in a direction parallel to the loading axis. The JIS flexure data from 90 tests were evaluated to estimate temperature-dependent Weibull moduli and temperature-dependent Weibull scale parameters for two volume-distributed fracture origins, pores, and large grains (Rajiyah et al., 1996). The data were pooled over the temperature range of 25 to 1204°C.

Flexure tests were conducted in fast fracture mode at room temperature using Type A specimens ground transverse to the loading axis which were aged in small gas-fired burner rigs. The

Nomenclature

A = specimen fatigue crack growth constant
B = material fatigue crack growth constant
D = dimensional (i.e., finite element geometry)
DPM = defects per million
K_T = notch correction factor
m = Weibull modulus (shape parameter)
N = fatigue crack growth exponent
n_f = cycles to failure
$n_{\min}$ = minimum cycles to failure
P_f = probability of failure
POF = probability of failure
P_s = probability of survival
t_f = time to failure
$t_{\min}$ = minimum time to failure
V_{eff} = effective volume
ΔT = temperature difference during thermal shock
ϕ = diameter
σ = standard deviation of the mean
σ_{ap} = applied stress
σ'_{ap} = time/cycle-dependent applied stress (for P_f)
σ''_{ap} = time/cycle-dependent applied stress (for t_f)
σ_o = Weibull scale parameter
σ_p = proof stress

specimens were exposed in cross flow to natural gas combustion products at atmospheric pressure and 0.1 mach (33 m/s) velocity for periods up to 10,033 hours. Aging temperature ranged from 982 to 1204°C. The specimens were removed from the burner rig and air quenched three times per week. Strength before and after aging is shown in Fig. 1. The data for all aging temperatures and times were pooled in this plot, yielding Weibull moduli of 19.9 and 18.6 for unaged and aged material, respectively. Mean strength of the aged SN-88 increased, as functions of both aging temperature and time, by an average of ~5 percent. This strength change was statistically significant. Weibull modulus decreased by approximately the same factor, but this change was not statistically significant. The typical fracture origins were independent of both aging temperature and time. An adherent oxide film of 2–3 μm thickness was present following aging at each condition. It was hypothesized that the flexure strength of the SN-88 increased during aging due to a flaw healing mechanism such as crack-tip blunting by oxidation products, and that the strength of the SN-88 was controlled by the same fracture origins (e.g., pores, inclusions, large grains, machining-induced damage, etc.) in the unaged and aged material. These data and observations imply that the reliability of SN-88 components in service will not degrade due to oxidation at temperatures up to 1204°C. However, the effects of water vapor on oxidation at gas turbine operating pressures were not characterized by these tests.

Flexure tests were conducted in dynamic fatigue mode using Type B specimens. Test temperature ranged from 700 to 1250°C. These tests did not provide data that could be used for estimation of material fatigue parameters due to creep relaxation effects at temperatures above 700°C. Notched Type B flexure specimens were prepared from thermal shock test plates. These specimens were tested in fast fracture, dynamic fatigue, and cyclic fatigue modes at room temperature. The strength of the notched Type B specimens is compared to the strength of unnotched Type A specimens in Fig. 2. Weibull moduli of 23.5, 19.9, and 21.4 were estimated for Type A (parallel machined), Type A (transverse machined) and notched Type B specimens, respectively. A correction factor (K_T) of 1.8 to account for the stress concentration at the notch, as determined by finite element analysis, was applied to the fracture stresses. Strength of the notched specimens (scaled for effective volume and area) was equivalent to strength of the unnotched specimens, which implies that the fracture origins at the notches in the thermal shock plates were equivalent to the fracture origins expected at the machined surfaces of the conceptual component.

Thermal Shock Reliability Model. A life-limiting condition for ceramic gas turbine components is fast fracture during a full load turbine trip. An atmospheric thermal shock test rig was constructed for the purposes of proof test development and reliability model validation (Rajiyah et al., 1996). The rig consisted of an electric furnace, an air-fluidized bed of alumina particles, and an elevator apparatus which rapidly transferred the specimen from the furnace to the fluidized bed. Fully machined SN-88 plates measuring 100 × 90 × 6 mm were used for thermal shock experiments. The plates were insulated on the flat faces to produce a condition of one-dimensional heat flow which maximized the transient thermal stress.

SN-88 plates in unnotched and notched configurations were tested. The plate configurations are shown in Fig. 3. Notches were required in order to introduce stresses high enough to fracture the material. The notches subtended an angle of 90 deg and had a depth of 6 mm. Notch radius was 0.76 ± 0.13 mm. Notches were ground using a 1200 grit diamond wheel and hand polished following machining. Other surfaces were ground using a 320 grit diamond wheel.

The test plates were heated at 5°C/min and held at a temperature in the furnace for a soak period of one hour to initially ensure temperature equilibrium. The soak temperature was increased in 100°C increments. Later experiments were performed using soak temperature increased in 25°C increments. These experiments were all considered to be "single cycle" in nature, i.e., it was assumed that subcritical crack growth did not occur prior to catastrophic fracture. Five unnotched silicon nitride plates were shocked from furnace soak temperatures up to 1365°C to room temperature without fracture. The Aremcolox™ (zirconium phosphate) platform support and insulating plates failed at 1365°C, which defined the upper temperature limit of the test rig. Thirteen notched silicon nitride plates were fractured from furnace soak temperatures between 675 and

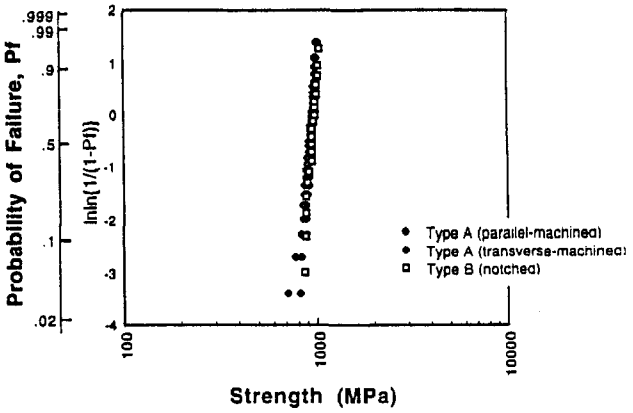

Fig. 2 Flexure strength of unnotched and notched SN-88 silicon nitride at room temperature

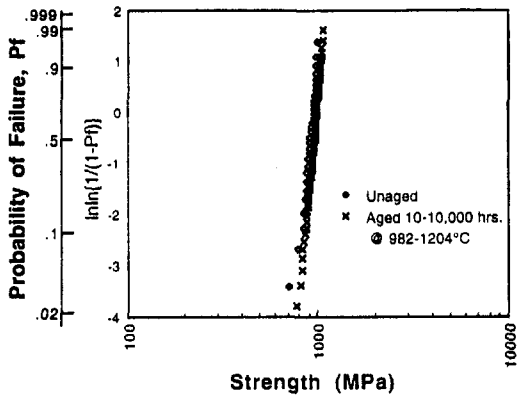

Fig. 1 Flexure strength of SN-88 silicon nitride at room temperature before and after burner rig aging

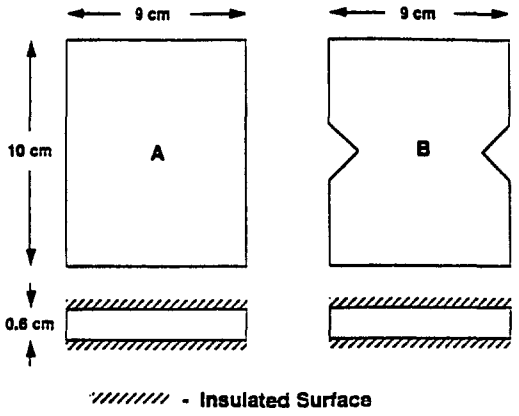

Fig. 3 Configuration of unnotched and notched SN-88 silicon nitride thermal shock test plates

800°C. All plates fractured into two intact pieces, with the fracture origin always in the center of one of the notches. The fracture origins were identified using optical microscopy and SEM. Machining-induced damage was positively identified as the fracture origin on four of the plates. Inclusions, pores, large grains, and "white spots" were present at or near the fracture origins on certain plates. These may have been associated with machining-induced damage, however.

Transient temperature and stress distributions were predicted for unnotched and notched plates using finite element modeling in ANSYS (Swanson Analysis System, Inc.). Quenches from various furnace temperatures into the fluidized bed at room temperature were modeled. The ANSYS output files were used with CARES/LIFE (Powers et al., 1992) to calculate the probability of fracture for a given ΔT ($\equiv$ the difference between the furnace temperature and the fluidized bed temperature) for various volume and surface-distributed fracture origins. The reliability predictions were much more sensitive to the accuracy of the finite element model than to the material strength parameters. The finite element model was refined several times. The earliest model (Rajiyah et al., 1996) contained approximately 5000 elements and did not accurately define the notch radius. This model was therefore designated as "crude". The model was refined first by including accurate geometry representing the notch radius and by increasing the number of elements at the notch to a "moderate" level. This model was designated as "accurate," and contained approximately 10,000 elements. The model was further refined by increasing the number of elements at the notch to a "high" level. The most refined finite element model contained approximately 20,000 elements. Figure 4 shows the predictions for the various models based upon the strength parameters estimated for large grains (Weibull modulus = 26.5).

The predicted reliability of notched SN-88 plates for various volume and surface-distributed fracture origins is shown in Fig. 5. Predictions based upon pooled surface-distributed fracture origins and volume-distributed large grains all matched the experimental data very well. The estimated Weibull moduli for these strength distributions were 19.9, 21.4, and 26.5 for the unnotched (i.e., smooth) surface, notched surface, and large grains, respectively. Predictions based upon volume-distributed pores and metallic inclusions did not match the experimental data. The estimated Weibull moduli for these strength distributions were 8.4 and 9.5, respectively. The best prediction of the experimental data was obtained using strength parameters estimated at a 50 percent level of confidence from notched Type B flexure data. The predictions at the 5 percent, 50 percent, and 95 percent confidence levels for these data were indistinguishable. It was concluded that the thermal shock reliability of the notched plates was controlled by the surface-distributed fracture origins (e.g., machining-induced damage, etc.) present in the machined notches. These results were considered to be adequate validation of the fast fracture reliability method, given that a 5 percent error in estimated stress will result in a 300 percent error in estimated probability of failure for a material with a Weibull modulus of 20 (Wachtman, 1989).

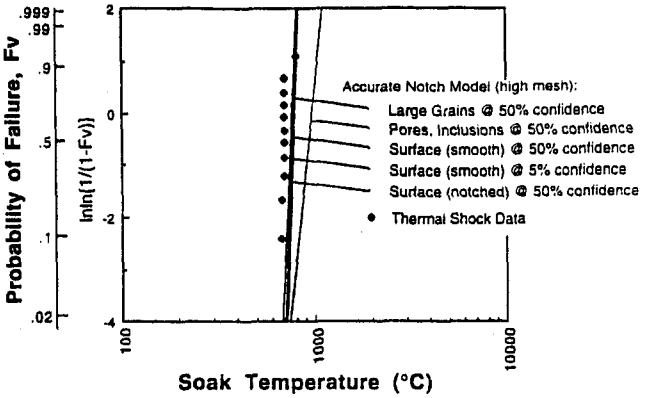

Fig. 5 Effect of material strength parameters on the reliability prediction for notched SN-88 silicon nitride plate

Time-Dependent Fracture Reliability Model. Calculations based upon Weibull Uniaxial Theory were used to evaluate the influence of strength and fatigue crack growth parameters on predicted component reliability. Equations for time-dependent fatigue are given in the appendix. Equations of a similar form were used for cycle-dependent fatigue. Effective stresses and effective volumes for a conceptual SN-88 component were derived from time-independent CARES/LIFE analyses. A multiaxial stress function was used that related the stresses predicted from three-dimensional finite element analysis to one-dimensional stresses in uniaxial strength tests. Material strength parameters, m and σ_o, were estimated from censored fast fracture data, i.e., strength was uniquely dependent upon fracture origin. Material fatigue parameters, N and B, were estimated from pooled 900°C static fatigue data, i.e., changes in strength were not dependent upon fracture origin. It was assumed that the Weibull modulus, m, was invariant with temperature and time. Changes in Weibull scale parameter, σ_o, which resulted from fatigue crack growth, were accommodated through transformed (time or cycle-dependent) applied stress functions, σ'_{ap} and σ''_{ap}.

The method for prediction of time-dependent component reliability under static loading was tested by predicting the minimum life of SN-88 buttonhead tensile specimens at 1200°C. The experimental and predicted static fatigue results are shown in Fig. 6. Of 15 tensile creep tests performed on buttonhead

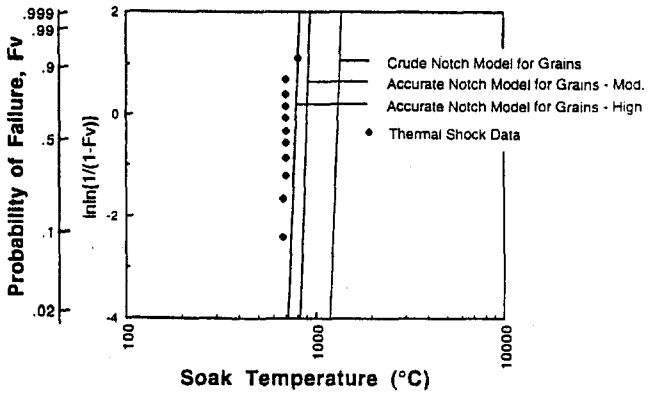

Fig. 4 Effect of finite element model on the reliability prediction for notched SN-88 silicon nitride plate

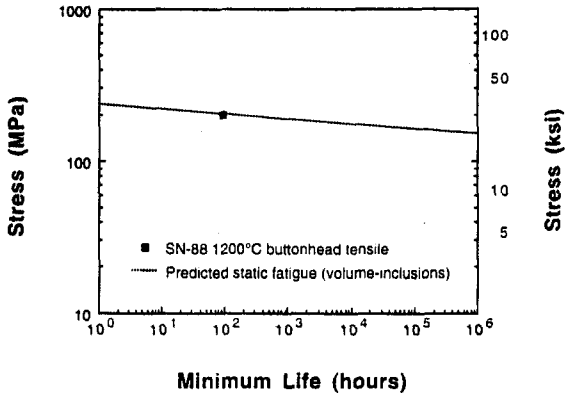

Fig. 6 Minimum static fatigue life of SN-88 buttonhead tensile specimens predicted using Weibull uniaxial theory

specimens at 1200°C and 200 MPa, one specimen failed from a metallic inclusion at 92 hours. This represents a probability of failure, P_f, of 0.067. The other 14 specimens survived until the test was terminated at 1000 hours. Predicted -3σ creep life for this test condition was ~9,000 h; therefore, it was assumed that the early failure was caused by static fatigue. The prediction was based upon fatigue parameters estimated from flat tensile static fatigue data. Strength parameters were estimated from 1200°C buttonhead tensile data censored for inclusions. It was assumed that no interaction between creep and static fatigue occurred.

The method for prediction of cycle-dependent component reliability under transient loading was tested by predicting the minimum life of SN-88 buttonhead tensile specimens at 900°C. The experimental and predicted cyclic fatigue results are shown in Fig. 7. Of 30 buttonhead tensile cyclic fatigue tests performed, two specimens failed from metallic inclusions at 12 and 42 cycles, respectively, at a stress of 400 MPa. This represents a P_f of 0.2, since only 10 specimens were tested at 400 MPa. The other 28 specimens survived until the test was terminated at 5000 cycles. The prediction was based upon fatigue parameters estimated from notched Type B flexure data. Strength parameters were estimated from 900°C buttonhead tensile data censored for inclusions.

The sensitivity of the fatigue life prediction to errors in the estimated material parameters, m, σ_o, N, and B, and to errors in the numerically calculated effective volume, V_{eff}, was assessed parametrically, i.e., by varying one parameter at a time while holding all others constant. It was found, for both static and cyclic loading, that the predictions were most sensitive to errors in the Weibull modulus, m, followed by errors in the Weibull scale parameter, σ_o, the fatigue crack growth exponent, N, the effective volume, V_{eff}, and the fatigue crack growth constant, B. However, the predictions were more sensitive to errors in the specimen fatigue constant, $\ln A$, than to errors in the Weibull modulus. This parameter, along with N, is estimated directly from fatigue data, implying the need for a large quantity of data for highly accurate predictions. It can be shown that the data requirements for a given level of prediction accuracy increase in proportion to the quantity $\{\exp[(N-2)/m]\}$.

Turbine Shroud Concept Model

A conceptual model of a ceramic inner turbine stator shroud for a Frame 7FA gas turbine was utilized to predict hypothetical ceramic component life and reliability. The shroud configuration is shown in Fig. 8. Material properties of SN-88 silicon nitride were used to predict shroud temperatures, stresses, and reliability. A conceptual model was needed because the probabilistic design method is dependent upon volume and surface integrals for performing component reliability analyses. The

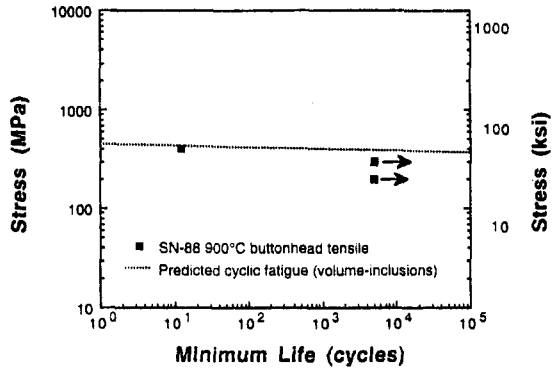

Fig. 7 Minimum cyclic life of SN-88 buttonhead tensile specimens predicted using Weibull uniaxial theory. Arrows indicate runouts at 5000 cycles.

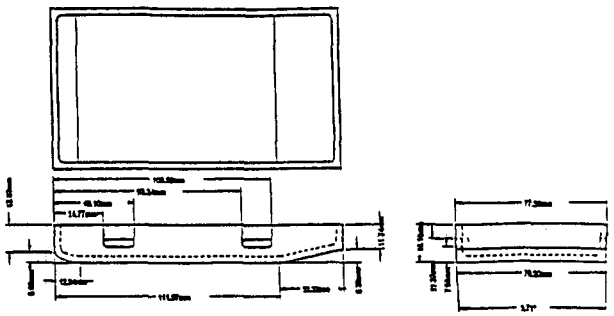

Fig. 8 Configuration of conceptual SN-88 silicon nitride inner turbine stator shroud

conceptual model was developed without performing detailed component design for the following reasons: (1) temperature and stress allowables for candidate silicon nitride materials were not known at the time the shroud concept was developed; and (2) it was considered premature to engage significant design resources prior to establishing feasibility of utilizing ceramic components in gas turbines.

Stress and reliability analyses for the conceptual shroud were performed using ANSYS and CARES/LIFE, respectively, for the following two cases: (1) steady-state thermomechanical loads during baseload gas turbine operation, and (2) transient thermal shock loading during a full load turbine trip. The analysis methods were described previously (Rajiyah et al., 1996). The method for predicting component reliability during a turbine trip was validated via thermal shock analyses and experiments. The thermal shock studies indicated the need for a highly refined finite element mesh. As a result, unique models of the conceptual shroud were developed and optimized for analyzing the two cases of interest. Both finite element models constituted a symmetric half of the conceptual shroud divided by a plane perpendicular to the axial centerline.

Stress Models. Predicted temperatures and stresses for the conceptual shroud are given in Table 2. Predicted stress levels, for both steady-state and transient conditions, were significantly increased over those predicted by previous analysis due to the refined meshes. CARES/LIFE calculated an effective stress based on the combination of a particular flaw shape (Penny-shaped crack) and fracture criterion (Shetty's mixed mode). These effective stresses were the multiaxial equivalent Mode One (i.e., crack opening) stresses. Reliability calculations were performed in CARES/LIFE at the Gaussian integration points of each element. Both the ANSYS nodal stresses and the CARES/LIFE effective stresses are given in Table 2. The effective stresses were used to calculate conceptual shroud reliability.

For steady-state analyses, the finite element model consisted of 14,500 elements out of which 8000 elements were three-dimensional brick elements (for volume reliability predictions) and 6500 elements were two-dimensional shell elements (for surface reliability predictions). The mesh was refined most

Table 2 Predicted conceptual SN-88 shroud temperatures and stresses

	Steady-state (Baseload)	Turbine Trip (t = 1.5 sec.)
Temperature, °C (°F)	496-1073 (924-1964)	
Max.ANSYS Nodal Stress, MPa (ksi) @ Temp., °C (°F)	228 (33.1) @ 552 (1026)	295 (42.8) @ 542 (1007)
Max.CARES/LIFE Eff.Stress, MPa (ksi) @ Temp., °C (°F)	246 (35.7) @ 552 (1026)	294 (42.6) @ 542 (1007)

highly at the mounting holes where the highest stress under steady-state conditions existed.

For transient analyses, the finite element model consisted of 14,000 elements out of which 9500 elements were three-dimensional brick elements (for volume reliability predictions) and 4500 elements were two-dimensional shell elements (for surface reliability predictions). The mesh was refined most highly at the axial edge facing the flowpath where the highest stress under transient conditions existed. The simulation of a full load turbine trip was performed by assuming that the gas temperature on all surfaces of the conceptual shroud decreased instantly to the compressor discharge gas temperature of 371°C, with no change in mass airflow rate (i.e., no change in hot side or cold side heat transfer coefficients). The maximum stresses occur 1.5 s following the turbine trip.

Reliability Models. The reliability of the conceptual shroud over 72,000 h and 5000 cycles was predicted using CARES/LIFE and spreadsheet calculations. The CARES/LIFE analyses were used to determine effective stresses and effective volumes for spreadsheet (i.e., off-line) calculations of time and cycle-dependent component reliability. On-line CARES/LIFE calculations of time and cycle-dependent component reliability showed that the off-line predictions were conservative by a factor of two. Effective volumes were 9.5 mm^3 for the steady-state condition and 254 mm^3 for the transient condition. CARES/LIFE used the ANSYS outputs to calculate reliability for each element. A mixed-mode fracture criterion based upon shear-sensitive Batdorf Multiaxial Theory was used. The probability of survival for each element was assumed to be a mutually exclusive event, and, thus, the overall component reliability was the product of all the calculated element survival probabilities. Lower bound Weibull scale parameters estimated at 90 percent levels of confidence were used to apply conservative estimates of material strength. Three volume-distributed fracture origins (pores, metallic inclusions, and large grains) were analyzed. Weibull moduli were 8.4, 9.5, and 26.5, respectively. Fractographic information to censor strength data for discrete surface-distributed fracture origins was not available. Therefore, surface analyses were performed based upon Weibull moduli of 18.7 and 11.5, which were estimated from fast fracture flexure strength data censored for transversely ground surfaces and edges, respectively. It was determined that volume-distributed pores limited reliability of the conceptual SN-88 shroud under both steady state and transient conditions.

The effect of using censored versus pooled strength data on the time-dependent reliability prediction is shown in Fig. 9 for the reliability criterion, $P_f = 63 \times 10^{-6}$ following 72,000 hours of baseload gas turbine operation. This criterion is approximately equivalent to a -4σ (long-term) variation in component reliability without proof testing. The key difference between the predictions based upon pooled strength data and the predictions based upon censored strength data was the Weibull modulus. The Weibull modulus estimated from SN-88 strength data censored for volume-distributed pores was 8.4, whereas the Weibull modulus estimated from pooled SN-88 strength data was 10.4. The stress allowable based upon the pooled strength data was much less conservative than the stress allowable based upon the censored strength data. It is therefore recommended that censored data be used when possible in order to calculate conservative stress allowables for design purposes.

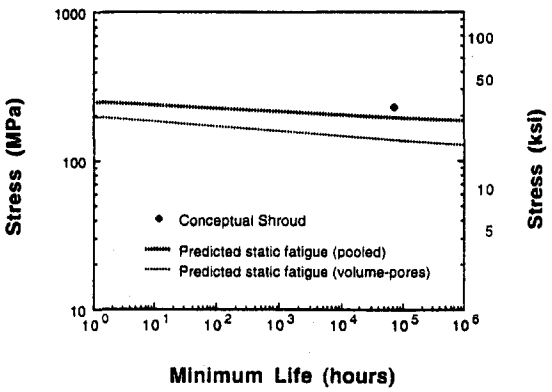

Fig. 9 Effect of using pooled SN-88 buttonhead tensile strength data on the stress-time allowables for a conceptual shroud probability of failure of 63×10^{-6} in 72,000 hours without proof testing. Shroud stress given is from ANSYS nodal output.

Reliability of the conceptual SN-88 shroud over extended periods of gas turbine operation was not expected to be reduced by the effects of creep and oxidation. Creep was not limiting because the conceptual shroud was thermally constrained at temperatures above 1000°C. Dynamic fatigue tests following creep for 1000 hours showed that creep did not affect fatigue crack growth behavior. Oxidation was found to increase material strength and not affect Weibull modulus following burner rig aging to >10,000 hours. Therefore, the effects of creep and oxidation were not considered in the conceptual shroud reliability calculations.

Both creep and oxidation are deterministic in nature if only the evolution of new fracture origins is involved, i.e., fatigue crack growth from preexisting fracture origins is not accelerated. As such, these phenomena can be characterized using temperature-stress-time parameters. The SN-88 creep data was parameterized and found to be very reproducible. AS-800 creep data was much less reproducible; creep tests on more recent material are in-progress. Unlike characterization of fatigue crack growth, these parameters need not be merged with the original fracture strength in order to predict component life and reliability. Therefore, prediction of ceramic component life for cases where creep or oxidation is limiting (and do not change the fatigue behavior of the material) can be handled in the same manner as for metal components.

Effect of Proof Testing on Component Reliability and Life. The following two types of proof tests were considered: (1) a simulation of the steady-state stresses present during baseload turbine operation; and (2) a simulation of the transient stresses present during a full load turbine trip. The simplest analysis was that in which the stress distribution in the proof tests perfectly duplicated the stress distribution in the gas turbine. Weibull Uniaxial Theory coupled with the effective stresses and effective volumes from CARES/LIFE was used to evaluate the residual static and cyclic life as functions of applied stress for selected proof stress levels of 450 MPa (steady state) and 350 MPa (transient). These represent 75 percent and 19 percent overstress conditions based upon the ANSYS nodal stresses for the steady state and transient conditions, respectively. Equations used for the steady-state analysis are given in the appendix. The analyses were based on volume-distributed pores in SN-88. The effect of proof testing on the steady-state stress allowable for a conceptual shroud probability of failure of zero in 72,000 h is shown in Fig. 10. The effect of proof testing on the transient stress allowable for a conceptual SN-88 shroud probability of failure of zero in 5000 cycles is shown in Fig. 11. Yields of >95 percent were predicted for the conceptual shroud following proof testing at these stress levels.

The fluidized bed thermal shock rig was considered for developing a transient proof test. Analytical simulations were performed using ANSYS. To simulate the thermal transient in the gas turbine during a trip, all faces of the conceptual shroud were insulated except the gas side. The component was subjected to thermal shocks in the fluidized bed rig from various soak temperatures in order to determine the proof test condition which would result in the highest residual reliability. Maximum soak temperature was 1204°C in order to minimize oxidative degradation to the material. The highest stress predicted for

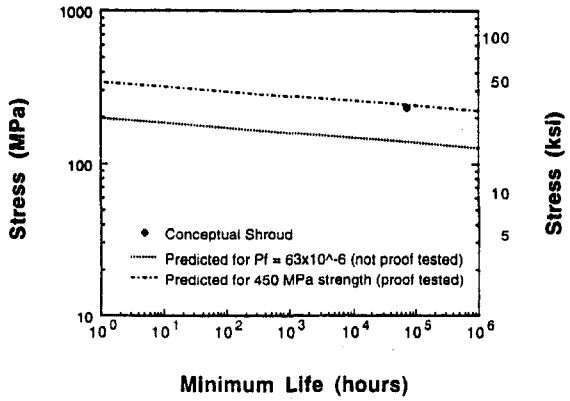

Fig. 10 Effect of proof testing on the stress-time allowable for a conceptual SN-88 shroud probability of failure of zero in 72,000 hours. Shroud stress given is from ANSYS nodal output.

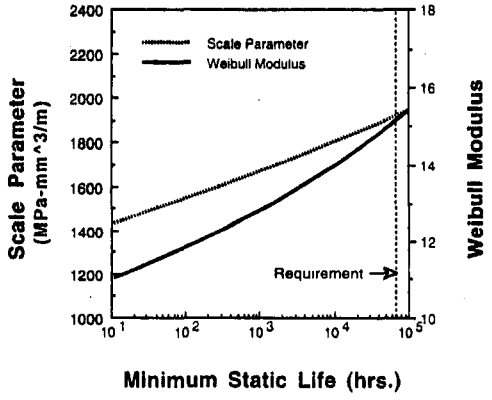

Fig. 12 Required material strength parameters for a conceptual SN-88 shroud probability of failure of 63×10^{-6} in 72,000 hours without proof testing

quenching from 1204°C to −196°C (the temperature of liquid nitrogen, which could be used to cool the fluidized bed) was only 162 MPa. This would not be sufficient for conceptual shroud life assurance at a design stress of 295 MPa.

It was concluded that mechanical proof tests would be needed and could be developed to simulate both the steady state and trip conditions in order to assure 72,000 hours and 5000 cycles minimum component life. However, the challenge of developing mechanical proof tests to simulate either the static or transient gas turbine case with respect to matching both stress alignment and effective volume/area, in order to maximize both residual reliability and proof test yield, may be significant. As a result, mechanical proof test development and reduction to practice was not undertaken.

The requirements for proof testing may be eliminated if improved materials with either increased tensile Weibull modulus or increased tensile strength (i.e., Weibull scale parameter) were available. The requirements for the conceptual shroud were evaluated parametrically against the baseline properties (Weibull modulus = 8.4, Weibull scale parameter = 1024 MPa-$mm^{3/m}$). These requirements are shown in Fig. 12 for the time-dependent reliability criterion, $P_f = 63 \times 10^{-6}$ following 72,000 hours of baseload gas turbine operation. The required Weibull modulus and Weibull scale parameter for this criterion were >16 and >2000 MPa-$mm^{3/m}$, respectively. The required Weibull modulus and Weibull scale parameter for the cycle-dependent reliability criterion, $P_f = 63 \times 10^{-6}$ following 5000 cycles, were >13 and >1900 MPa-$mm^{3/m}$, respectively.

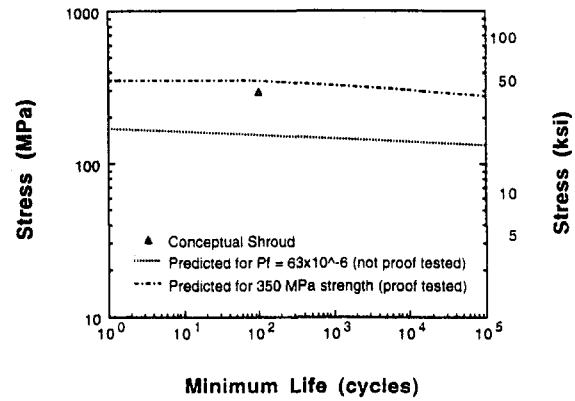

Fig. 11 Effect of proof testing on the stress-cycles allowable for a conceptual SN-88 shroud probability of failure of zero in 5000 cycles. Shroud stress given is from ANSYS nodal output.

Summary and Conclusions

Two state-of-the-art monolithic silicon nitride materials were characterized and evaluated for potential application in gas turbines. Both materials offer significant improvements over state-of-the-art single crystal superalloys in terms of creep, cyclic fatigue, and oxidation resistance at temperatures in the range of 1000 to 1200°C. The reliability and life-limiting failure mechanisms were characterized in terms of temperature, stress, and probability of component failure. A conceptual ceramic inner turbine stator shroud having the properties of SN-88 silicon nitride was used for evaluation purposes. Highly refined finite element and risk integration analyses were performed using ANSYS and CARES/LIFE, respectively.

Conservative limits for design of silicon nitride gas turbine components were established using models to predict fracture of SN-88, which may result from static fatigue, cyclic fatigue, or creep. The models were validated via thermal shock and tensile experiments. The stress limits for components that are not proof tested were based upon a Six Sigma design approach, using a reliability criterion of $P_f = 63 \times 10^{-6}$ following 72,000 h of baseload operation or 5000 cycles. This criterion was derived from established acceptability limits for normally distributed material failure data, and was applied to ceramic material failure data which obeys a two-parameter Weibull distribution. The stress limits for components that are proof tested were based upon power law crack growth criteria and proof stress levels that guarantee acceptable component life.

Delayed fracture, from either static or cyclic fatigue, was determined to be the limiting failure mechanism in either material for proof tested components. Fast fracture was limiting for components that are not proof tested. Reliability of SN-88 was limited by volume-distributed pores. Reliability of AS-800 was limited by pores and metallic inclusions, although these occurred at a lower frequency than in SN-88. The probabilistic fracture model for SN-88 was conservative for predicting life and reliability of AS-800 components. Creep rupture life of the two materials was similar, although SN-88 was affected by creep at a lower temperature and could tolerate higher plastic strain prior to fracture than AS-800.

Proof testing will be required in order to meet part life requirements for the conceptual shroud using either material. Overstress conditions of 75 percent and 19 percent for the steady state and transient conditions, respectively, are needed for SN-88. If proof tests that perfectly match the service stress distributions can be developed, yields of >95 percent are predicted. A detailed component cost evaluation was not performed; however, this proof test yield is expected to be acceptable for meeting the product cost target. Significantly lower yields were predicted if the proof tests do not perfectly match the service stress

distributions, as may be the case for static components such as turbine stator shrouds. Therefore, proof test development and/or material process development will be required to ultimately establish commercial feasibility for the shroud application. Improvement in tensile fast fracture strength, in terms of either Weibull modulus or Weibull scale parameter, is needed to reduce or eliminate the proof test requirements.

Acknowledgments

This work was supported by the Electric Power Research Institute (EPRI) and the Gas Research Institute (GRI) under EPRI Contract No. WO8512-05. The authors wish to acknowledge the support and encouragement of W. Bakker of EPRI and R. Petrich, formerly of GRI. The materials suppliers, NGK Insulators, Ltd. and AlliedSignal Ceramic Components are recognized for their contributions of material properties and strength data. Special thanks are extended to A. Prabhu and W. Tucker of GECRD for stress and reliability analyses; L. Inzinna of GECRD for thermal shock testing; I. Ur-Rahman of GEPS for creep modeling; D. Woodford and D. van Steele of MPa for stress relaxation testing; W. Leucke and S. Wiederhorn of NIST for creep and fracture testing; D. Shelleman and R. Tressler of PSU for evaluations of oxidized material; and N. Hecht and D. McCullum of UDRI for creep and fracture testing.

References

Rajiyah, H., Inzinna, L. P., Trantina, G. G., Orenstein, R. M., and Cutrone, M. B., 1996, "Thermal Shock Analysis and Testing of Simulated Ceramic Components for Gas Turbine Applications," ASME JOURNAL OF ENGINEERING FOR GAS TURBINE AND POWER, Vol. 118, No. 2, pp. 308–312.

Powers, L. P., Starlinger, A. and Gyekenyesi, J. P., 1992, "Ceramic Component Reliability With the Restructured NASA/CARES Computer Program," ASME Technical Paper No. 92-GT-383.

Wachtman, J. B., Jr., ed., 1989, *Structural Ceramics, Treatise on Materials Science and Technology,* Vol. 29, Academic Press, Inc., San Diego, CA, pp. 67.

APPENDIX

Equations for Predicting Time-Dependent Reliability and Life

POF @ 72,000 hour Life (Without Proof Test).

$$P_f = 1 - \exp\left[-V_{\text{eff}} * \left(\frac{\sigma'_{ap}}{\sigma_o}\right)^m\right]$$

$$\text{where } \sigma'_{ap} = \left[\frac{t_{\min} * \sigma_{ap}^N}{B} + \sigma_{ap}^{(N-2)}\right]^{1/(N-2)} \quad (1t)$$

Life @ POF = 63 DPM (Without Proof Test).

$$t_f = B * \frac{\sigma''^{(N-2)}_{ap} - \sigma^{(N-2)}_{ap}}{\sigma^N_{ap}} \quad (2t)$$

$$\text{where } B = \frac{A}{\sigma_o^{(N-2)}}\left[\frac{V_{\text{eff}}}{\ln(1-0.5)^{-1}}\right]^{(N-2)/m}$$

B is calculated using properties of test specimen.

$$\sigma''_{ap} = \sigma_o * \left[\frac{\ln(1-P_f)}{-V_{\text{eff}}^{(1/m)}}\right]$$

σ'' is calculated using properties of component.

σ_{ap} = Design Stress

$P_f = 0.000063$

$t_f = A * \sigma^{-N}$

Minimum Life With Proof Testing (Perfect Stress Alignment).

$$t_{\min} = \frac{B}{\sigma_{ap}^2}\left[\left(\frac{\sigma_p}{\sigma_{ap}}\right)^{N-2} - 1\right] \quad \text{where } \sigma_p = \text{Proof Stress} \quad (3t)$$

Proof Stress for 72,000 h Minimum Life.

$$\sigma_p = \sigma_{ap} * \left[1 + \frac{t_{\min} * \sigma_p^2}{B}\right]^{1/(N-2)} \quad (4t)$$

Proof Test Yield.

$$P_s = \exp\left[-V_{\text{eff}} * \left(\frac{\sigma_p}{\sigma_o}\right)^m\right]$$

$$\text{where } P_s = \text{Probability of Survival during proof test} \quad (5t)$$

Analysis of the Temperature Profile of Ceramic Composite Materials Exposed to Combined Conduction–Radiation Between Concentric Cylinders

A. Tremante
Departamento de Conversión y Transporte de Energía.

F. Malpica
Departamento de Termodinámica y Fenómenos de Transferencia.

Universidad Simón Bolívar, Caracas, Venezuela.

A numerical study is made of the thermal characteristics of semitransparent materials exposed to simultaneous conduction and radiation between concentric cylinders. For extremely high-temperature applications, where radiative transfer plays an important role, ceramic-matrix composites, considered as semitransparent materials, are being explored for potential use in turbine and compressor components, spacecraft structures, engine control systems and nuclear reactors. Through the use of a gray model and the two-flux method, specialized equations are developed that generate a system of nonlinear ordinary differential equations. To facilitate the solution of this system, an iterative strategy is adopted. In order to demonstrate the versatility and accuracy of the proposed methodology, the results of several numerical experiments are presented and compared with benchmark solutions.

1 Introduction

It is a well-known fact that there are some industrial applications in which heat is transported within a medium by conduction and radiation simultaneously. Radiation processes must usually be formulated by means of integral equations. This implies that any point within the medium the solution is influenced by other processes occurring throughout the entire medium. Due to this global nature of radiative transport, geometry plays a major role in the solution of this kind of problems. This peculiarity is contrasted with conduction processes, which are formulated in terms of differential equations. Here, a solution is affected by interactions occurring in the vicinity of any point within the medium. Of course, this behavior renders a local character to the conductive mechanism. Therefore, when radiation is coupled with conduction, the descriptive energy equation becomes a nonlinear integro-differential equation having both global and local components. In general, an exact solution of an equation of this type is seldom possible and the analyst has to resort to a variety of numerical approximations. The literature review will be restricted to the problem under study. It deals with an absorbing and emitting layer of a gray medium contained between two nonblack concentric cylinders.

During the last decade, important efforts have resulted in significant advances in structural materials and analysis. To achieve such advances, developments in high-temperature materials, like ceramic composites, are considered key for potential use in turbine rotor blades, nozzle vanes (Parks et al., 1991), rocket engines and space structures (Upadhya, 1992). Therefore, fiber-reinforced ceramic matrix composites are receiving increased attention (Tan et al., 1991; Mah et al., 1987) owing to their high-temperature capabilities (Abdullah and Das-Gupta, 1990) and the toughening properties provided by the fibrous reinforcement (Mah et al., 1985).

The interaction between conduction and radiation mechanisms was first investigated by Viskanta and Grosh (1962a, b) who obtained numerical solutions by way of an iterative method. Additional heat transfer results using a simplified procedure have been presented by Einstein (1963). Meanwhile, the finite element method was attempted by Fernandes and Francis (1982).

Alternatively, Wang and Tien (1966) used perturbation techniques and a differential method for two limiting cases where either radiation or conduction tend to be predominant. The accuracy of the P–N differential approximation was examined by Ratzel and Howell (1982), where the P-1 and P-3 approximations yielded a fourth-order and sixth-order differential equation, respectively.

On the other hand, the analysis of combined conduction and radiation in a plane layer and nongravity participating medium was performed by Crosbie and Viskanta (1971) and by Echigo et al. (1971) using numerical methods.

The primary purpose of this study is to present an analysis for the combined conduction and radiation in an annular layer of a gray participating medium using a two-flux model. This model is based on the idealization that the medium may be described by only two uniform fluxes (Sidall, 1974), one in the forward direction and the other in the backward direction of the radial coordinate. This approach converts the equation of radiative transfer into two coupled nonlinear differential equations of second order (Tremante and Malpica, 1994), instead of a nonlinear integro-differential equation (Siegel and Howell, 1992). Then, the resulting system of differential equations can be solved as a two-point boundary value problem, using a variable order, variable step size finite difference method with deferred corrections (Pereira, 1982). Since ceramics for gas turbines have refractive indices of about 1 to 4, the present study is only for a layer where its refractive index is equal to 1. Higher refractive index values could be deferred to subsequent work, until theoretical and/or experimental data for ceramic composite materials between concentric cylinders are available. Therefore, the influence of the conduction–radiation parameter, optical thickness and wall emissivity are investigated in detail and the results compare well with those reported in the literature and they are presented in graphic and tabular form in the last section.

Contributed by the International Gas Turbine Institute and presented at the 42nd International Gas Turbine and Aeroengine Congress and Exhibition, Orlando, Florida, June 2–5, 1997. Manuscript received at ASME Headquarters March 1997. Paper No. 97-GT-390. Associate Technical Editor: H. A. Kidd.

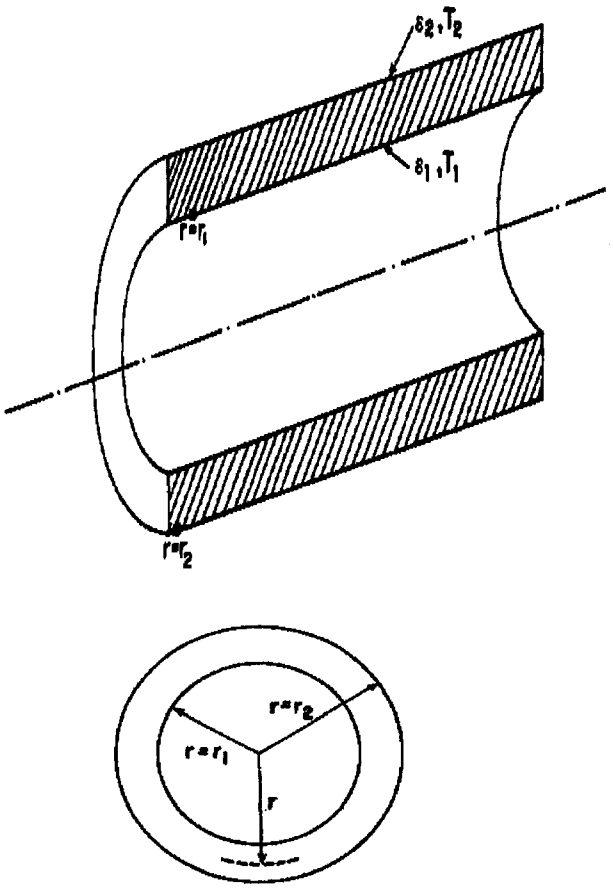

Fig. 1 Physical geometry

2 Problem Formulation

Consider a concentric cylinder configuration separated by a conducting and radiating participating medium. The medium absorbs and emits energy and is assumed to be gray. A sketch of the physical system is illustrated in Fig. 1.

Under the above-mentioned idealizations, the equation of the conservation of energy is written as

$$-\frac{k}{r}\frac{d}{dr}\left(r\frac{dT}{dr}\right)+\frac{1}{r}\frac{d}{dr}(q_r r)=0. \tag{1}$$

where q_r denotes the radiative heat flux inside the medium.

The boundary conditions are given by

$$r=r_1,\quad T=T_1 \tag{2}$$

$$r=r_2,\quad T=T_2 \tag{3}$$

A relation between the radiative heat flux q_r and the temperature T provided by the conduction heat flux has to be inserted into Eq. (1). This relation is of the integral form, leading to a nonlinear integro-differential equation as stated by Siegel and Howell (1992). Correspondingly, an approximate solution, for the resulting equation in one dimension, requires a numerical computation involving an iterative process between the differential and integral terms.

As was pointed out previously, the alternate model investigated here is based on the assumption that radiation in the medium may be represented by two uniform fluxes, one in the forward hemisphere and the other in the backward hemisphere. In principle this formulation replaces the equation of transfer by two coupled nonlinear ordinary differential equations in cylindrical coordinates. That is

$$\frac{1}{r}\frac{d}{dr}(q_r r)=\kappa_a(4E_b-G) \tag{4}$$

$$\frac{dG}{dr}=-A\kappa_a q_r \tag{5}$$

where G is the total incident radiation and A is a constant. The numerical values assigned to A are 3 for the Milne-Eddington model (M-E) and 4 for the Schuster and Schwarzschild model (S-S) (Sidall, 1974).

Combining Eqs. (1) and (4) yields

$$\frac{k}{r}\frac{d}{dr}\left(r\frac{dT}{dr}\right)=\kappa_a(4E_b-G) \tag{6}$$

On the other hand, multiplying Eq. (5) by r and differentiating with respect to this same variable leads to an expression that has been introduced into Eq. (4). The end results is

$$\frac{1}{r}\frac{d}{dr}\left(r\frac{dG}{dr}\right)=-A\kappa_a^2(4E_b-G) \tag{7}$$

At this point, inspection of Eqs. (6) and (7) reveals that this coupled set of ordinary differential equations describes a differential formulation for simultaneous effect of radiation and conduction in an annular region. Tremante and Malpica (1994) studied the same case for a gray planar medium.

The boundary conditions for temperature are Eqs. (2) and (3). Meanwhile, the boundary conditions for the radiant energy are given by

$$r=r_1 \Rightarrow G_1+2\left(\frac{2}{\epsilon_1}-1\right)q_{r1}=4E_{b_1} \tag{8}$$

$$r=r_2 \Rightarrow G_2+2\left(\frac{2}{\epsilon_2}-1\right)q_{r2}=4E_{b_2} \tag{9}$$

where q_r is expressed by Eq. (5) (Sidall, 1974).

Nomenclature

A = constant
E_b = emissivity power of a black body
G = total intensity of incident radiation, W/m^2
G^* = dimensionless total intensity of incident radiation = $G/\sigma T_1^4$
I = intensity of radiation, W/m^2 str
k = thermal conductivity, W/m°K
N = dimensionless conduction–radiation parameter = $k\kappa_a/4\sigma T_1^3$
r = cylindrical coordinate, m
R = optical depth = $\kappa_a r$
q_k = conductive heat flux, W/m^2
q_r = radiative heat flux, W/m^2
q_t = total heat flux, W/m^2
Q_t = dimensionless total heat flow defined by Eq. (18)
T = temperature, °K
ϵ = emissivity of the surface
η = dimensionless position coordinate = $(R-R_1)/(R_2-R_1)$
θ = dimensionless temperature = $(T-T_2)/(T_1-T_2)$
κ_a = absorption coefficient, 1/m
σ = Stefan–Boltzmann constant, W/m^2°K^4

Subscripts

1 = refers to outer temperature cylinder
2 = refers to inner temperature cylinder

Superscripts

* = refers to dimensionless parameters

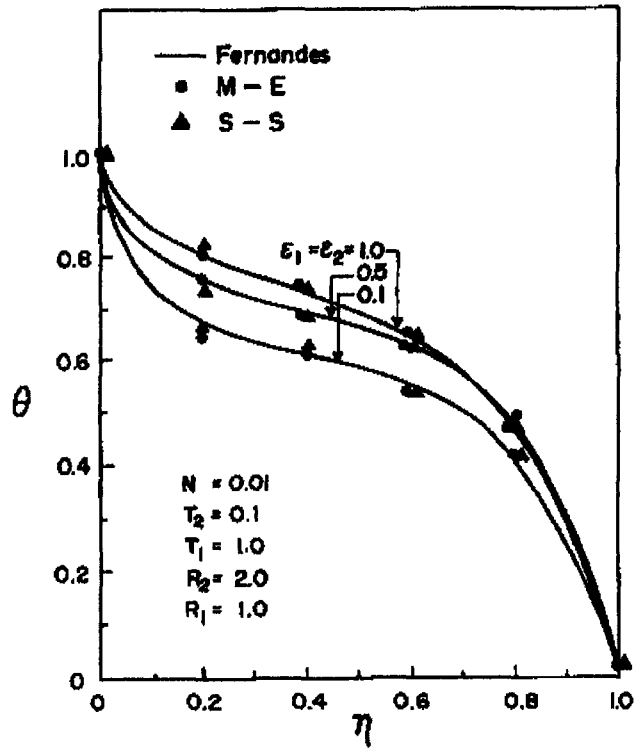

Fig. 2 Dimensionless temperature profile for several wall emmissivities

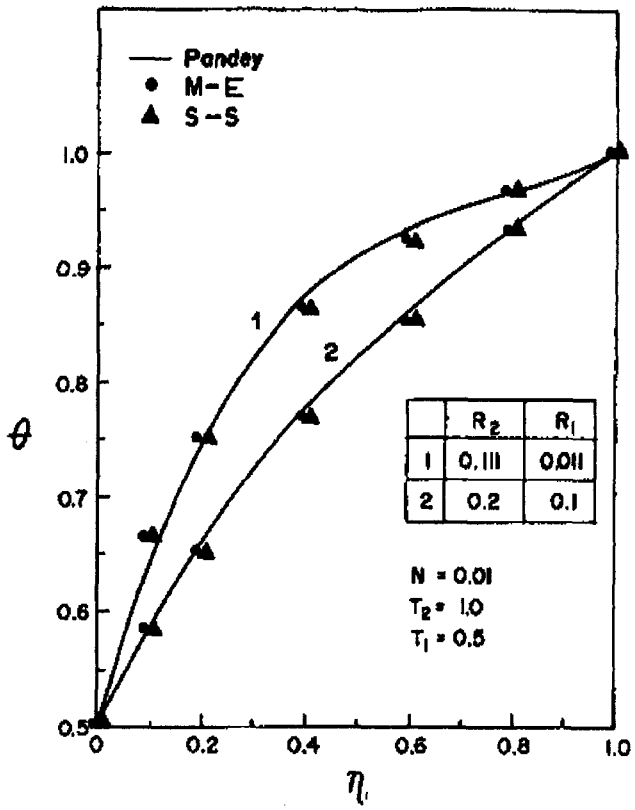

Fig. 4 Dimensionless temperature profile for $N = 0.01$

The above-defined problem will be reformulated in terms of dimensionless variables and parameters. Accordingly, introducing

$$N = \frac{\kappa_a k}{4\sigma T_1^3} \quad \theta = \frac{T - T_2}{T_1 - T_2} \quad \eta = \frac{R - R_1}{R_2 - R_1} \tag{10}$$

Eqs. (6) and (7) may be rewritten as follows

$$\frac{(1-\theta_2)}{(R_2-R_1)^2}\frac{d^2\theta}{d\eta^2} + \frac{1-\theta_2}{[(R_2-R_1)\eta + R_1](R_2-R_1)}\frac{d\theta}{d\eta} = \frac{1}{N}\left[[(1-\theta_2)\theta + \theta_2]^4 - \frac{dG^*}{d\eta}\right] \tag{11}$$

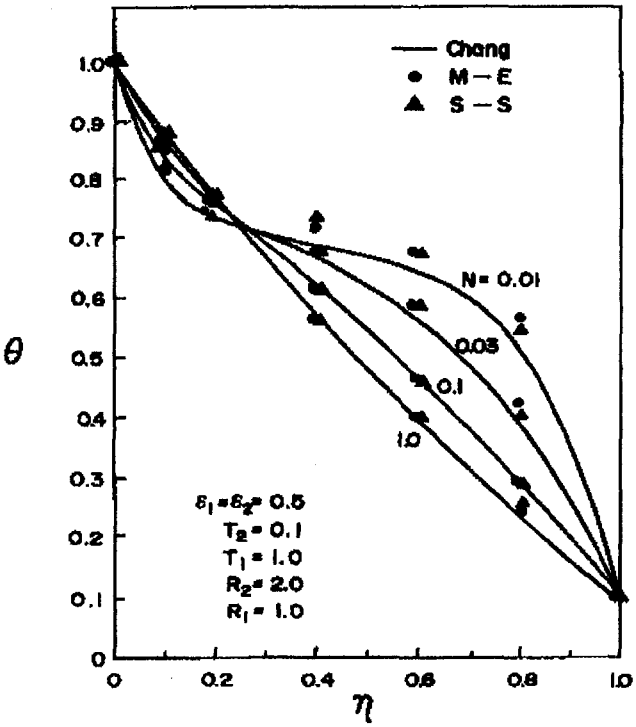

Fig. 3 Dimensionless temperature profile for several values of N

and

$$\frac{1}{(R_2-R_1)^2}\frac{d^2G^*}{d\eta^2} + \frac{1}{[(R_2-R_1)\eta + R_1](R_2-R_1)}\frac{dG^*}{d\eta} = -A[4[(1-\theta_2)\theta + \theta_2]^4 - G^*] \tag{12}$$

Likewise, the associated boundary conditions are transformed to

$$\eta = 0 \Rightarrow \theta_1 = 1 \tag{13}$$

$$\eta = 1 \Rightarrow \theta_2 = 0 \tag{14}$$

and

$$\eta = 0 \Rightarrow G_1^* = 4 - 2\left(\frac{2}{\epsilon_1} - 1\right)q_{r1}^* \tag{15}$$

$$\eta = 1 \Rightarrow G_2^* = 4\theta_2^4 - 2\left(\frac{2}{\epsilon_2} - 1\right)q_{r2}^* \tag{16}$$

where the dimensionless radiative heat flux is given by

$$q_r^* = -\frac{1}{A(R_2-R_1)}\frac{dG^*}{d\eta} \tag{17}$$

The total dimensionless heat flow between the concentric cylinders may be computed from the relation

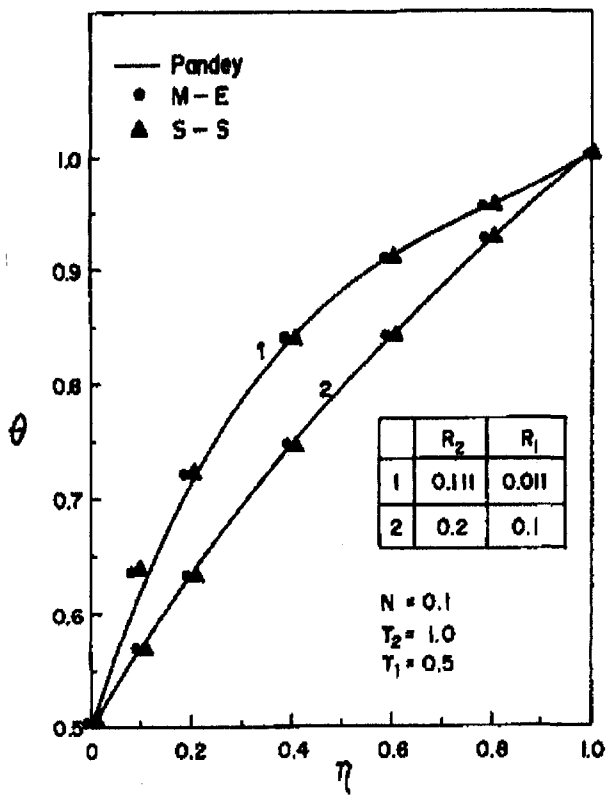

Fig. 5 Dimensionless temperature profile for $N = 0.1$

$$Q_t = q_r^* + q_k^* \tag{18}$$

where q_k^* is the conductive component defined as

$$q_k^* = -\frac{4N(1-\theta)}{(R_2 - R_1)}\frac{d\theta}{d\eta} \tag{19}$$

while the radiative component is given by Eq. (17).

The nonlinear problem expressed by the coupled ordinary differential Eqs. (11) and (12) subject to set of boundary conditions Eqs. (13)–(16), can be solved as a two-point boundary value problem, using a variable order, variable step size finite difference method with deferred corrections (Pereira, 1982). The solution algorithm utilizes a nonuniform grid network and produces as outputs the numerical distributions of the dependent variables and their derivatives in the radial interval. In all the calculations a relative tolerance not greater than 10^{-6} was used at all mesh points as a convergence criterion. Typical values of CPU time were not greater than 8 seconds for a compatible PC-486 computer.

3 Results and Conclusions

In order to assess the validity of the two-flux model in an annular gray medium and the accuracy of the computational algorithm, a nonuniform grid with 21 spacing was selected for comparison purposes. Results for the temperature distribution for several combinations of N, θ_2, and R_2 were verified by comparing them to results of other investigators who used more accurate expressions for the radiative heat flux.

The influence of the wall emissivities for dominant radiation ($N = 0.01$) is illustrated in Fig. 2. The results seem to agree with those of Fernandes and Francis (1982). To illustrate better the behavior of N, Fig. 3 has been prepared using an intermediate value of $\epsilon_1 = \epsilon_2 = 0.5$. For large values of N, the heat transfer is dominated by conduction and the curves are seen to be practically linear with η. As the thermal radiation becomes the dominant mode of heat transfer (small N) the curves depart from the linearity as N decreases. Comparison with the results reported by Chang and Smith (1970) shows a good agreement, except for the case of $N = 0.01$ which is close to conditions of pure radiation, and Eq. (11) becomes stiff.

A comparison of local temperatures for dominant radiation and radius ratios of up to 10 is depicted in Figs. 4 and 5. Here, the results are in a good qualitative agreement with those of Pandey (1982, 1989).

Results for the dimensionless total heat flux calculated at the inner wall are listed in Table 1 for a wide variety of parameters. Also included are the dimensionless radiative heat flux, as well as the temperature differentiation at the same inner wall. Here minor deviations are observed between the results for Fernandes and Francis (1982) using the finite element method for the solution of the integro-differential equation and our results using a differential formulation relying on the two-flux model. This trend is consistent with the comparisons of local temperatures examined in the figures. In general, it may be said that the Schuster–Schwarzschild model (S-S) gives better results than the corresponding model of Milne-Eddington (M-E) using the results of Fernandes and Francis (1982) as comparison.

The present paper gives the basis for further studies of Ceramic Composite Materials in cylindrical media, which have refractive indices greater than 1 and are considered nongray. This is because the two-flux model can be generalized for sev-

Table 1 Results evaluated at the inner wall

N	$\frac{d\theta}{d\eta}$			q^{r*}			Q_t		
	present work S-S	present work E-E	Fernandes Francis 1982	present work S-S	present work E-E	Fernandes Francis 1982	present work S-S	present work E-E	Fernandes Francis 1982
				$\epsilon_1 = \epsilon_2 = 0.1$					
0.05	-2.189	-2.252	-2.118	0.077	0.079	0.076	2.572	2.650	2.500
0.1	-1.769	-1.806	-1.731	0.076	0.079	0.076	1.960	2.004	1.921
0.5	-1.397	-1.405	-1.388	0.076	0.079	0.076	1.435	1.445	1.426
				$\epsilon_1 = \epsilon_2 = 0.5$					
0.05	-1.748	-1.836	-1.728	0.377	0.404	0.368	3.633	3.858	3.566
0.1	-1.503	-1.553	-1.499	0.384	0.411	0.372	2.464	2.581	2.430
0.5	-1.331	-1.342	-1.333	0.395	0.421	0.379	1.528	1.552	1.523
				$\epsilon_1 = \epsilon_2 = 1.0$					
0.05	-1.298	-1.392	-1.366	0.755	0.853	0.731	5.073	5.655	5.019
0.1	-1.204	-1.257	-1.273	0.786	0.882	0.748	3.168	3.461	3.144
0.5	-1.248	-1.259	-1.274	0.831	0.926	0.773	1.664	1.722	1.660

$R_2 = 2.0$, $R_1 = 1.0$, $T_1 = 1.0$, $T_2 = 0.1$.

eral spectral bands (Siegel and Spuckler, 1994). Also, ceramic components can be exposed to convection and/or radiation and/or be in a multilayered geometry, so other more general boundary conditions could be studied. Reinforced ceramics would be expected to have optical thicknesses larger than those considered here. However, temperature distribution and heat fluxes could be obtained for typical values of Ceramic Matrix Composite emissivity, thermal conductivity, and spectral absorptivity. Therefore, the two-flux model can be generalized and used to calculate a wide range of combined conduction–radiation problems. Finally, the main goal of this work is to provide a simple but reliable predictive method to the engineer, faced with the task of analyzing thermal effects and predicting optical properties in ceramic composite materials, considered semitransparent media when radiation plays an important role.

References

Abdullah, M. J., and Das-Gupta, D. K., 1990, "Electrical-Properties of Ceramic Polymer Composites," IEEE *Transactions on Electrical Insulation,* Vol. 25, No. 3, pp. 605–610.

Cess, R. D., 1964, "The Interaction of Thermal Radiation With Conduction and Convection Heat Transfer," *Advances in Heat Transfer,* Vol. 1, Academic Press, New York, pp. 1–50.

Chang, J., and Smith, R. S., 1970, "Steady and Transient Heat Transfer by Radiation and Conduction in a Medium Bounded by Two Coaxial Cylindrical Surfaces," *International Journal of Heat and Mass Transfer,* Vol. 13, pp. 69–74.

Crosbie, A. L., and Viskanta, R., 1971, "Interaction of Heat Transfer by Conduction and Radiation in a Nongray Planar Medium," *Wärme- und Stoffübertragung,* Vol. 4, pp. 205–212.

Echigo, R., Hasewaga, S., and Miyazaki, Y., 1971, "Composite Heat Transfer With Thermal Radiation in Nongray Medium. Part I: Interaction of Radiation With Conduction," *Int. J. Heat Mass Transf.,* Vol. 14, pp. 2001–2015.

Einstein, T. H., 1963, "Radiant Heat Transfer to Absorbing Gases Enclosed Between Parallel Flat Plates With Flow and Conduction," NASA TR, Vol. R154.

Fernandes, R., and Francis, J., 1982, "Combined Conductive and Radiative Heat Transfer in an Absorbing, Emitting, and Scattering Cylindrical Medium," ASME *Journal of Heat Transfer,* Vol. 104, pp. 594–599.

Higenyi, J. K., 1980, "Higher Order Differential Aproximation of Radiative Energy Transfer in a Cylindrical Media," Ph.D. Thesis, University of Texas.

Mah, T. I., et al., 1985, "High-Temperature Mechanical-Behavior of Fiber-Reinforced Glass-Ceramic-Matrix Composites," *Journal of the American Ceramic Society,* Vol. 68, No. 9, pp. 248–251.

Mah, T. I., et al., 1987, "Recent Developments in Fiber-Reinforced High-Temperature Ceramic Composites," *American Ceramic Society Bulletin,* Vol. 66, No. 2, pp. 304.

Pandey, D. K., 1982, "Radiative Transfer in Concentric Cylindrical Media," Ph.D. Thesis, University of Illinois.

Pandey, D. K., 1989, "Combined Conduction and Radiation Heat Transfer in Concentric Cylindrical Media," *J. Thermophysics,* Vol. 3, No. 1, pp. 75–82.

Parks, W. P., et al., 1991, "Potential Applications of Structual Ceramic Composites in Gas Turbines," ASME JOURNAL OF ENGINEERING FOR GAS TURBINES AND POWER, Vol. 113, pp. 628–634.

Pereira, V., 1982, "Codes for Boundary Value Problems in Ordinary Differential Equations," *Lecture Notes in Computer Science,* Vol. 76, pp. 67–88.

Ratzel, A. C., and Howell, J. R., 1982, "Heat Transfer by Conduction and Radiation in One-Dimensional Planar Media Using Differential Approximation," ASME *Journal of Heat Transfer,* Vol. 104, pp. 388–391.

Sidall, R. G., 1974, "Flux Methods for the Analysis of Radiant Heat Transfer," *J. Institution Fuel,* Vol. 47, pp. 101–109.

Siegel, R., and Howell, J. R., 1992, *Thermal Radiation Heat Transfer,* 3rd ed., Hemisphere, Washington, DC.

Siegel, R., and Spuckler, C. M., 1994, "Approximate Solution Methods for Spectral Radiative Transfer in High Refractive Index Layers," *Int. J. Heat Mass Transfer,* Vol. 37, Suppl. 1, pp. 403–413.

Tan, T. M., et al., 1991, "Engineering Design of Tough Ceramic Matrix Composites for Turbine Components," JOURNAL OF ENGINEERING FOR GAS TURBINES AND POWER, Vol. 113, pp. 312–317.

Tremante, A., and Malpica, F., 1994, "Contribution of Thermal Radiation to the Temperature Profile of Ceramic Composite Materials," ASME JOURNAL OF ENGINEERING FOR GAS TURBINES AND POWER, Vol. 116, pp. 583–586.

Upadhya, K., 1992, "Ceramics and Composites for Rocket Engines and Space Structures," *Journal of the Minerals, Metals & Materials Society,* Vol. 44, No. 5, pp. 15–18.

Viskanta, R., and Grosh, R. J., 1962a, "Effect of Surface Emissivity on Heat Transfer by Simultaneous Conduction and Radiation," *Int. J. Heat Mass Transf.,* Vol. 5, pp. 729–734.

Viskanta, R., and Grosh, R. J., 1962b, "Heat Transfer by Simultaneous Conduction and Radiation in an Absorbing Medium," ASME *Journal of Heat Transfer,* Vol. 84, pp. 63–72.

Wang, L. S., and Tien, C. L., 1966, "Study of the Interaction Between Radiation and Conduction by a Differential Method," *Proc. Int. Heat Transfer Conference,* Vol. 5, pp. 190–196.

Development of a Hydrogen-Fueled Combustion Turbine Cycle for Power Generation

R. L. Bannister
Westinghouse Power Generation,
4400 Alafaya Trail,
Orlando, FL 32826-2399

R. A. Newby

W. C. Yang

Westinghouse Science and
Technology Center,
1310 Beulah Road,
Pittsburgh, PA 15235-5068

Consideration of a hydrogen based economy is attractive because it allows energy to be transported and stored at high densities and then transformed into useful work in pollution-free turbine or fuel cell conversion systems. Through its New Energy and Industrial Technology Development Organization (NEDO) the Japanese government is sponsoring the World Energy Network (WE-NET) Program. The program is a 28-year global effort to define and implement technologies needed for a hydrogen-based energy system. A critical part of this effort is the development of a hydrogen-fueled combustion turbine system to efficiently convert the chemical energy stored in hydrogen to electricity when the hydrogen is combusted with pure oxygen. The full-scale demonstration will be a greenfield power plant located seaside. Hydrogen will be delivered to the site as a cryogenic liquid, and its cryogenic energy will be used to power an air liquefaction unit to produce pure oxygen.

To meet the NEDO plant thermal cycle requirement of a minimum of 70.9 percent, low heating value (LHV), a variety of possible cycle configurations and working fluids have been investigated. This paper reports on the selection of the best cycle (a Rankine cycle), and the two levels of technology needed to support a near-term plant and a long-term plant. The combustion of pure hydrogen with pure hydrogen with pure oxygen results only in steam, thereby allowing for a direct-fired Rankine steam cycle. A near-term plant would require only moderate development to support the design of an advanced high pressure steam turbine and an advanced intermediate pressure steam turbine.

Introduction

The development of a comprehensive global energy system based on renewable and/or nuclear energy using hydrogen as a storage and transportation medium is a necessary step towards realization of a pollution-free civilization. To this end, the Japanese government, through its New Energy and Industrial Technology Development Organization (NEDO) has created the World Energy Network (WE-NET) Program, a 28-year effort from 1993 to 2020, directed at research and development of the technologies needed to develop a hydrogen-based energy conversion system (MITI, 1993). A part of this effort is directed toward research and development of a hydrogen-fueled combustion turbine system (NEDO, 1994) which can efficiently convert the chemical energy stored in hydrogen to electricity via a heat engine in which the hydrogen is combusted with pure oxygen.

Westinghouse is working to develop a hydrogen-fueled combustion turbine system designed to meet the goals set by the WE-NET Program (Bannister et al., 1996). These goals include greater than 70.9 percent low heating value (LHV)[1] thermal efficiency, a reliability-availability-maintainability (RAM) equivalent to current base-loaded natural gas-fired combined cycles, and elimination of CO_2, NO_x, and SO_x during power generation. Other turbine manufacturers developing hydrogen-fueled power generation cycles under the WE-NET program are: Toshiba and Mitsubishi Heavy Industries (NEDO, 1996).

Basic technologies and concepts to support the hydrogen-fueled combustion turbine are to be first demonstrated in a pilot plant in the 50–60 MW size range which will have greater than 64.9 percent thermal efficiency. This is to be followed by the full-scale 500 MW demonstration plant startup in 2020. The demonstration plant will meet all the above mentioned requirements for the WE-NET Program.

The full-scale demonstration will be at a new Japanese power plant to be located seaside. Ambient temperature and pressure are 15°C (59°F) and 1.013 bar (14.7 psi), respectively. Relative humidity is 60 percent, and 21°C (70°F) sea water is available for cooling. Chemically pure hydrogen and oxygen are to be provided as gases at ambient temperature and at whatever pressure is needed for injection into the turbine's combustor. It is assumed that the hydrogen is delivered to the site as a cryogenic liquid, but that the cryogenic energy is used to power an air liquefaction unit which in turn produces the pure oxygen.

WE-NET intends to construct a total hydrogen energy system. From production using renewable energy such as hydraulic power and solar energy, to transportation to high demand areas via ship by converting hydrogen into other transportable energy mediums, including chemical mediums such as methanol, ammonia, etc., to utilization. Pure hydrogen is a clean fuel; however, it is expensive to make. Within the WE-NET Program, hydrogen production technology, using renewable energy research, has been conducted by others on water electrolysis, photoelectrochemical (conversion of water directly into hydrogen), and thermochemical (production of carbon-free hydrogen utilizing nuclear heat) conversion methods. Solid polymer electrolyte water electrolysis has been selected as the hydrogen production method for the WE-NET Program (NEDO, 1995), in part, because of its high energy conversion efficiency (90 percent is the development target).

Rankine Cycle Selection

To meet NEDO's thermal efficiency requirement of greater than 70.9 percent, a number of different cycle concepts were developed and analyzed. Each cycle model included the essen-

[1] All efficiency values in this paper will be LHV.

Contributed by the International Gas Turbine Institute and presented at the International Gas Turbine & Aeroengine Congress & Exhibition, Orlando, FL, June 2–5, 1997. Manuscript received by the ASME Headquarters July 1997. Paper No. 97-GT-14. Associate Technical Editor: H. A. Kidd.

tial process equipment blocks needed to predict thermal performance, including compressors, expanders, combustors, heat exchangers, pumps, flow mixers, and flow splitters. Once assembled, the models were run to determine performance of each cycle as a function of at least two independent variables, cycle pressure ratio, and expander inlet temperature. The sensitivity of cycle performance to other process variables was examined as indicated by the configuration of the cycle. The cycle configuration itself was in some cases altered to take into account the performance trends suggested by the sensitivity studies or to try variations offering potential thermodynamic advantages.

A consistent set of assumptions was used for the analysis of power systems so that the results could be consistently evaluated. The key assumptions involve: performance of individual components, supply conditions of fuel and oxidant, fixed cycle conditions, property data and calculation methods, and a set of simplifying assumptions provided by NEDO.

It was decided that the power system would be based upon the mechanical conversion of hydrogen energy to electricity, rather than by a chemical or magnetohydrodynamic (MHD) conversion. In other words, the cycle was to be based upon a turbine expander to capture the mechanical energy of expansion of hot gas. The cycle could not be based upon fuel cells, MHD channels, or other nonmechanical converters of thermal energy. This narrowed the field of potential systems and corresponding development issues to those that could be derived from present day combustion and turbine technologies.

Determination of the optimum system began by first identifying all thermodynamic cycles and configuration options that could be used for practical, high efficiency power generation. The systems identified were categorized into three basic cycle types. The first cycle type was the conventional combined cycle that includes a heat recovery steam generator (HRSG). This cycle was studied only for purposes of comparison to the other cycle types, since it would produce NO_x emissions due to combustion in a high nitrogen content environment. The pure oxygen was provided only to facilitate a direct comparison to the other (closed) cycle types, since in a real system the hydrogen could be combusted with the compressor discharge air.

The second cycle type studied was the direct heated closed combined cycle which differs from the conventional combined cycle, since the topping cycle (combustion turbine) exhaust gas is not discharged to the atmosphere, but reingested by the combustion turbine compressor after it is discharged from the HRSG to form a closed working fluid loop. Prior to reingestion by the compressor, the gas is cooled and water is condensed and removed from the flowpath. Several options for topping cycle working fluids were investigated.

Table 1 Alternative system performance results*

No.	Cycle Description	Thermal Efficiency (%)	Max. Working Fluid Pressure (bar)
1.	Conventional Combined Cycle	67.0	59.0
2.	Closed Combined Cycle, Helium-Steam	64.8	13.0
3.	Closed Combined Cycle, Nitrogen-Steam	66.9	51.0
4.	Closed Combined Cycle, Hydrogen-Steam	66.7	44.0
5.	Closed Combined Cycle, Steam	68.3	78.0
6.	Rankine Cycle	68.7	500.0
7.	Rankine Cycle, Feedwater Heating	69.4	500.0
8.	Rankine Cycle, Feedwater Heating, Double Reheat	77.2	500.0

* 1700°C Class Combustion Turbine

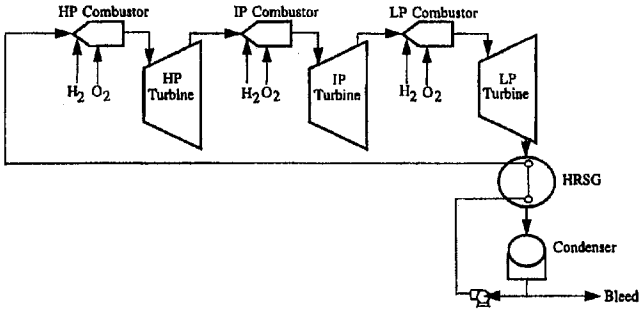

Fig. 1 General rankine cycle

The third type of cycle analyzed was the Rankine cycle. Many different schemes for feedwater heating were considered. The selected scheme involved the heating of the feedwater with the low pressure turbine exhaust gas, similar to a HRSG in a conventional gas turbine combined cycle. The combustion of pure hydrogen with pure oxygen results only in steam, thereby allowing for a direct-fired Rankine steam cycle.

From the three types of cycles, eight specific systems were analyzed using the simplifying assumptions. The results are shown in Table 1. From the table, it can be seen that the open combined cycle performance is similar to that of the closed combined cycles, and that the Rankine cycles show the most promise toward achieving the 70.9 percent thermal efficiency goal.

A general Rankine cycle is shown in Fig. 1. In concept, it consists of several turbine expansion stages having hydrogen-fueled reheats. Like conventional steam power plants, the general cycle expands steam from very high pressure down to the vacuum condenser conditions. A recuperator or HRSG uses low-pressure (LP) turbine exhaust to generate recycle steam, and no gas compression is required in the cycle. This general cycle can be arranged into a large number of configurations having variations in steam heat interchange and reheat conditions, each having relative advantages and disadvantages.

The other cycles considered, such as closed combined cycles with various working fluids, can only achieve 70.9 percent efficiency if they utilize advanced bottoming cycles with a condensing HRSG. Within our study, it was determined that the advanced bottoming cycles require working fluids such as chlorofluorocarbons and hydrocarbons. Use of advanced bottoming cycles with these working fluids adds environmental and safety issues to the plant, increases the complexity and development requirements for the plant, and still does not reach net plant efficiencies as high as those that can be achieved by a good Rankine cycle. Thus, only Rankine cycles were considered as candidates for the hydrogen-fired combustion turbine system.

Rankine Cycle Evaluation

Several forms of the Rankine cycle were evaluated: one and two reheat stages, HRSG operated at condenser vacuum conditions following a condensing LP turbine, and HRSG operated at atmospheric pressure, exhausting to a condensing LP turbine.

Turbine closed-loop steam cooling was incorporated into the cycle models, and improved estimates of component performance factors were applied. Initial screening studies were performed with all combustion stages operating at 1600°C, and subcritical steam generated in the HRSG. The screening studies showed that two reheat stages with a vacuum HRSG provided the greatest cycle efficiency, but this cycle is also the most complex and has the greatest development requirements. The primary concerns with this cycle are the large number of LP

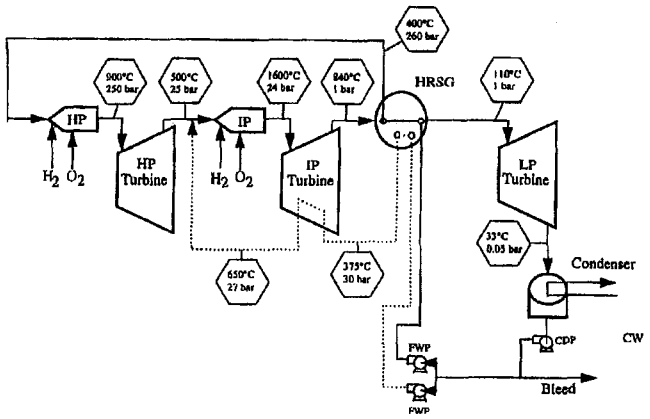

Fig. 2 Near-term reference cycle

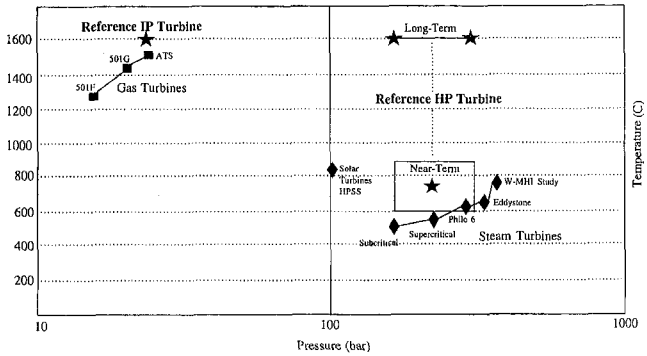

Fig. 4 Status of turbine technology

combustors required, the large LP turbine blades, and the large and complex HRSG.

A strategy was formulated for the selection of a specific Rankine reference system, which included that the number of developmental components and the complexity of the plant should be minimized. Also, a near-term plant and long-term plants should be selected and evaluated. The designation near-term implies that the technology applied is an adaptation of current technology requiring only moderate development effort, while long-term implies that the technology applied is a major advancement in technology requiring extensive development effort. Applying this strategy, the following reference plant characteristics were selected:

- single reheat stage,
- HRSG operates at atmospheric pressure, producing supercritical steam
- developmental components are the HP and IP combustors and turbines
- the near-term reference plant HP turbine inlet conditions are limited to 600–900°C, 200–300 bar
- long-term reference plant HP turbine inlet conditions are 1600°C, 200–300 bar
- near-term and long-term reference plant IP turbine inlet conditions are 1600°C, 17–25 bar

Process flow diagrams for the near-term and long-term reference plants are shown in Figs. 2 and 3. Representative temperatures and pressures are also listed at various locations on the flow diagrams. In the near-term plant, Fig. 2 hydrogen and oxygen are combined stoichiometrically in the HP combustor and mixed with recycle steam to produce a 900°C combustion product at a nominal pressure of 250 bar. This is expanded through the uncooled HP turbine, producing an exhaust having nominal conditions of 500°C and 25 bar. This exhaust stream is combined with IP turbine cooling steam and then mixes with the IP combustion products to moderate their temperature to 1600°C. The IP turbine expands the combustion stream to exhaust conditions of about 840°C and 1 bar. The IP turbine exhaust stream is cooled in the HRSG down to about 110°C before being expanded through the LP turbine to about 33°C and the condenser pressure. A bleed stream of water is taken from the water condensate. A split feedwater pump provides high-pressure water to the HRSG to produce high-pressure steam for recycle, and intermediate-pressure water to the HRSG to produce intermediate-pressure cooling steam for the IP turbine.

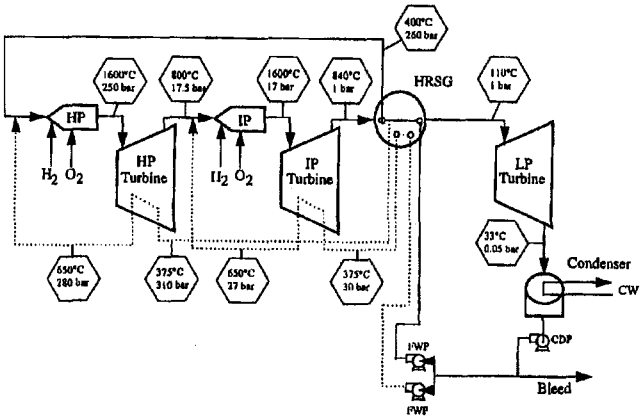

Fig. 3 Long-term reference cycle

Figure 3 shows the long-term reference plant process diagram. The differences between the long-term plant and near-term plant diagrams are primarily related to the HP turbine. The long-term plant HP combustor produces a 1600°C, 250 bar stream to be expanded in the HP turbine. The HP turbine expansion stream is at about 800°C and 17.5 bar, as compared to the 24 bar exhaust pressure in the near-term plant. If the HP turbine exhaust pressure in the long-term plant were 24 bar, the exhaust temperature would be about 1000°C and the connecting ducting from the HP turbine to the IP combustors would be much more complex in their design. In contrast to the near-term plant, the long-term plant HRSG must produce additional steam cooling streams at several pressure levels to cool the HP turbine. The flow diagram shows only a single representative cooling stream for the HP turbine.

The status of current steam turbine and combustion turbine technology with respect to inlet temperature and pressure conditions is plotted in Fig. 4 and is compared to the HP and IP turbine conditions required in the near-term and long-term reference plants. Conventional steam turbine conditions (subcritical and supercritical) are indicated in the figure, as well as points for two high-temperature steam turbines that have been operated in the past, Philo 6 and Eddystone 1 (Bannister and Silvestri, 1989). Advanced steam turbine conditions considered in previous Westinghouse, and Mitsubishi Heavy Industries engineering studies are also shown (Silvestri et al., 1992). The conditions of a recent 100 hour demonstration test of the Solar Turbines High Performance Steam System (HPSS) are also marked on the figure. The near-term plant HP turbine is close to, or within the range of current steam turbine technology. In contrast, the long-term plant HP turbine is a large technology step above both current steam turbine practice and advanced combustion turbine developments. Figure 4 also shows operating conditions for three Westinghouse combustion turbines: the 501F, an established combustion turbine system, the 501G, the latest Westinghouse combustion turbine, and the ATS, the next commercialization in the year 2000 (Bannister et al., 1994). The reference plant IP turbine has conditions close to the conditions of ad-

vanced combustion turbines being developed for natural gas fuels.

Conceptual Design

The conceptual design of the reference plant was developed by using several design tools and sources of engineering experience. Commercial process simulators (Aspen Plus™) and power cycle simulators (GateCycle™) have been used to develop the reference plant process flow diagrams and thermal performance estimates. Westinghouse proprietary design codes are being used to design and size turbines, combustors, and the HRSG. Advanced combustion turbine engineering experience resulting from current development programs in the United States (Little et al., 1993) and advanced steam turbine engineering experience (Bannister et al., 1987) resulting from past studies and testing at Westinghouse is being used to extrapolate current technology to the demands of the reference plant.

The conceptual design procedure for the reference plant was iterative. The selected reference plant configuration and an initial list of estimated component performance factors were applied to generate process flow diagrams and materials and energy balances. This initial set of data was used to conceptually design and size the major equipment in the reference plant power island. This was followed by generating an initial plant layout configuration. The initial equipment designs and plant layouts provided the basis to make better estimates of the set of component performance factors, and these were again applied with the system model to generate a second, improved process flow diagram and materials and energy balances. This iteration has been repeated several times, with additional modifications to improve the reference plant feasibility and performance made, as needed. The iterations will continue until converging to an acceptable reference plant having high feasibility and optimized performance. The final form of the plant will be used as the basis to estimate the cost of electricity, to identify the component development needs, and to formulate a pilot plant plan.

The scope of the reference plant conceptual design is limited to the power block. Some of the key technical assumptions are as follows

- 100 percent pure hydrogen and oxygen were assumed to be provided—contaminants might be present that must be considered in the design.
- The HP turbine efficiency was assumed at a representative value for HP steam turbines (92 percent)—the small size of the HP turbine blades in some cases would reduce this efficiency to lower values.
- The HP turbine and IP turbine closed-loop steam cooling needs have been estimated at about 5 percent and about 10 percent in the cycle calculations—the uncertainties in these cooling needs and their impact on the plant efficiency needs to be ascertained.
- The generator efficiency is assumed to be 99.2 percent—this value is about 0.2 percent greater than current Westinghouse generator technology.

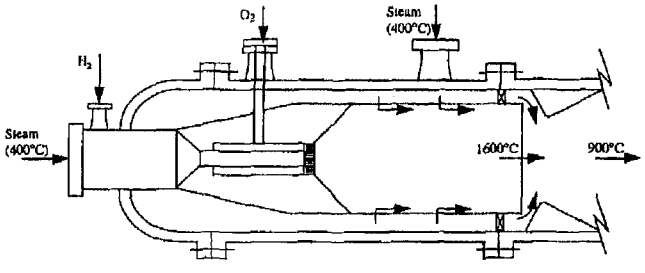

Fig. 5 HP combustor concept

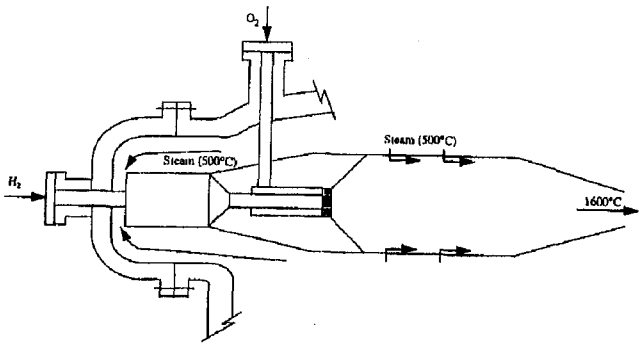

Fig. 6 IP combustors concept

Combustors

Combustors have been designed to premix hydrogen fuel with recycle steam, generating a low-heating value fuel gas similar to low-heating value fuel gases produced in solid fuel gasification systems. The combustors proposed apply principles similar to combustors developed for low-heating value fuels. The combustor should have no ignition difficulties at the steam-hydrogen ratios needed. The cooling of the combustor is by steam impingement and film cooling techniques. In the conceptual designs, the combustor design velocity, residence time and intensity have been selected from prior experience.

The combustor concepts are illustrated in Figs. 5 and 6. The HP combustors would be placed external to, but closely coupled with the HP turbine expanders. As Fig. 5 shows, the hydrogen and recycle steam are premixed in an inlet chamber. The low-heating value fuel flows through an axially located tube, and an annular tube carries oxygen. Both fuel gas and oxygen flow through swirlers, producing an intensely back-mixing zone for the primary combustion. The mixed temperature of the combustion products is about 1600°C. Cooling steam also passes through the combustor liner, keeping the liner at an acceptable temperature. Additional dilution steam passes through swirlers surrounding the primary zone outlet and into a highly-mixed quench zone where the temperature is dropped to the desired outlet temperature (600–900°C in the near-term plant).

The IP combustors are located internal to the turbine casing, and they apply the same combustion concept as used for the HP combustors. Hydrogen fuel is premixed with the HP turbine exhaust steam and cooling steam that has flowed through the turbine to cool the turbine components. In the high-intensity mixing zone, the combustion products are diluted to 1600°C by the combustor liner cooling steam. The combustor liners and transitions would be made from high-alloy steels with thermal barrier coatings, or would be of ceramic construction.

Turbines

Conceptual designs of the HP and IP turbines have been developed. The steam cooling flows for the HP and IP turbines have been estimated based on the turbine cooling surface estimates and using experience from steam-cooled combustion turbines. Specific estimates for cooling steam leakage rates have also been applied.

The HP turbine is a single-flow, impulse-type turbine. The long-term HP turbine requires steam-cooled internals and multiple cylinders, and is an advanced steam turbine configuration requiring extensive development effort. The near-term HP turbine has, at most, only limited cooling needs and is an adaptation of existing steam turbine configurations. The long-term HP turbine has very small blade sizes, with the first-stage blade being comparable to the smallest size currently manufactured by Westinghouse. The long-term HP turbine blades also require internal cooling.

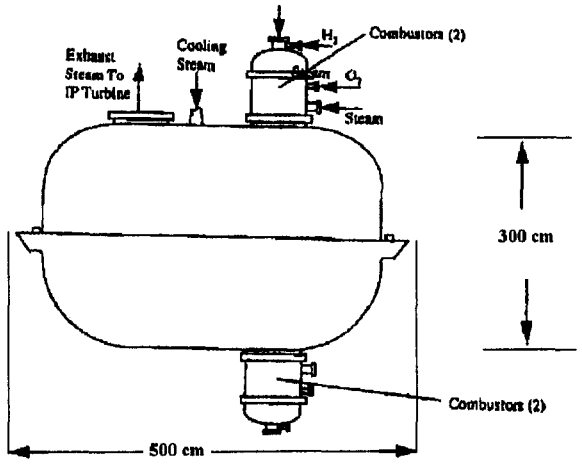

Fig. 7 Near-term turbine outline drawing

A representative near-term HP turbine outline drawing is shown in Fig. 7. Its overall appearance is much like a conventional HP steam turbine, but with four external combustors located at the four steam inlet nozzles. Two outlet nozzles exhaust steam to the IP turbine. A nozzle is also shown for the small steam cooling that may be needed for the 900°C turbine inlet case, while none is needed for the 600°C turbine inlet case. The overall dimensions shown are representative of the full range of near-term HP turbines considered.

The long-term HP turbine would require a complex longitudinal design. It would take on the appearance of an advanced combustion turbine. Complexity arises because controlled flows of cooling steam must be supplied to almost all of the vanes and blades, and the cooling steam must be provided at several pressure levels requiring separate chambers within the turbine casing. The development requirements for the long-term HP turbine would be extensive.

An IP turbine outline conceptual drawing is shown in Fig. 8. Its overall appearance is that of a combustion turbine, except that exhaust steam from the HP turbine enters axially through an annular region at the front of the IP turbine. Sixteen combustors are located within the casing. Nozzles are shown to provide vane cooling steam and blade cooling steam.

Heat Recovery Steam Generator

The HRSG has two functions in the near-term plant: to generate intermediate pressure steam (375°C, 30 bar) for cooling the IP turbine, and to generate high pressure recycle steam (400°C, 250–250 bar). The HRSG is very compact due to the large temperature differences between the shell-side and tube-side fluids. Since the HRSG is designed for atmospheric-pressure duty, its design can be very much like a conventional HRSG for combustion turbines. The inlet gas temperature is higher than conventional HRSG practice, but the design can apply

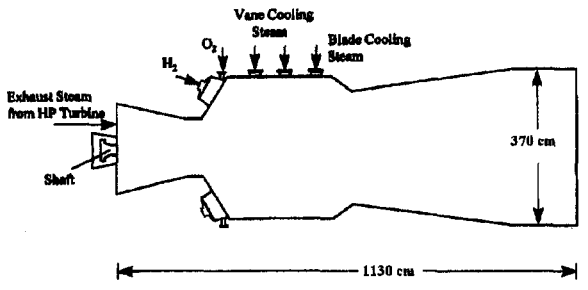

Fig. 8 IP turbine outline drawing

Table 2 HRSG conceptual characteristics

Status of technology	Conventional
Inlet gas flow (kg/s)	175
Inlet gas temperature (°C)	835
Inlet gas pressure (bar)	1.1
Heat transferred (kJ/s)	290,000
HP steam flow (kg-s)	100
IP cooling steam flow (kg/s)	17
HP heat transfer surface area (m^2)	25,000
HRSG length (m)	20 (includes exhaust diffuser)
HRSG width (m)	11
HRSG height (m)	12
HRSG pressure drop (bars)	0.03

conventional furnace steam generator principles. Table 2 lists the major characteristics of the HRSG for representative operating conditions. It requires about 25 percent of the heat transfer surface needed in a conventional HRSG for a combustion turbine application raising the same flow rate of steam.

Materials

Fuel for combustion turbines has traditionally been hydrocarbon based. However, a relatively small number of combustion turbines in the United States have been fueled with hydrogen enriched gaseous hydrocarbon fuels, but the hydrogen content of these refinery-by-product fuels is relatively low, typically less than 6 percent hydrogen by weight (40 percent by volume).

The combustion of relatively pure hydrogen in combustion turbines poses special material problems. The hydrogen rich environment can promote metal deterioration. The higher flame temperature associated with hydrogen can cause significant damage to the materials currently employed in turbines. The higher water vapor content can create special problems with heat recovery equipment. New materials and designs will be needed to successfully burn hydrogen fuels in combustion turbines.

The selection of acceptable materials for the combustors and expanders relate directly to the degree that the component structures can be cooled. Cooling of the hot structures must maintain the surface temperatures and average structure temperatures at acceptable levels to satisfy the life design requirements with respect to surface oxidation/corrosion, creep rupture, and low cycle fatigue. In addition, the selection of materials for the combustors, expanders, and heat exchangers must consider the stability of the material surface protective layers, hydrogen ingress, hydrogen embrittlement, and high-temperature steam/stress corrosion cracking in the specific environments of each cycle. Although power systems have not yet required materials for service under these specific conditions, some materials have been developed for somewhat similar service conditions in specialized engine systems. The materials technology basis for hydrogen-fueled turbines is the following.

1450–1500°C Temperature. This is representative of the conditions of the state-of-the-art cooling and materials for next generation of combustion turbines now in early demonstration phases. Materials (superalloys), coatings (e.g., Yttria-stabilized zirconia, alumina, TiN) have been recently developed for these conditions.

1600–1700°C Temperature. Materials and coating have been developed for these conditions for short-time applications such as rockets. Advanced materials, such as single crystal and directionally solidified alloys, refractory metals, and ceramics, are now being developed for these conditions. Advancements in technology will apply ceramic inserts for leading edges and platforms, as well as eventually ceramic vanes and blades.

Table 3 Reference plant thermal performance

	Long-term plant		Near-term plant	
HP Turbine				
Combustion temperature (°C)	1600	1600	900	600
Inlet pressure (bar)	300/195	300/195	300/210	300/210
Net power (MWe)	199/184	150/137	111/101	83/75
IP Turbine				
Combustion temperature (°C)	1600	1600	1600	1600
Inlet pressure (bar)	17/18	24/24	24	24
Net power (MWe)	261/275	310/321	344/352	370/375
LP Turbine				
Net power (MWe)	50/53	50/54	55/58	59/61
Plant Efficiency (%)	73.5/71.9	75.6/74.0	73.5/72.1	72.5/71.2

Generating Efficiency

Plant heat and materials balances and cycle calculations have been generated for the reference plants at 500 MWe. The reference plants, both near-term and long-term, apply stoichiometric combustion in both of the combustion stages. No hydrogen or oxygen preheat is used in the plants and no feedwater heating is used; this provides a simple, compact plant configuration.

Table 3 lists several reference plant performance factors for the long-term plant and the near-term plant. The table lists the HP turbine combustion temperature, inlet pressure (2 pressure levels considered), and the net power generated; the IP turbine combustion temperature, inlet pressure (2 levels), and the net power generated; the LP turbine net power; and the plant net efficiency. Near-term plant combustion temperatures ranging from a minimum of 600°C to a maximum of 900°C are considered in the table.

Comparison of these results show that the near-term plant can achieve the program goal of greater than 70.9 percent efficiency, even with a HP turbine combustion temperature (600°C) that is at a level of current steam turbine technology. The long-term plant has an efficiency that is comparable to that of the near-term plant with a 900°C combustion temperature in the HP turbine. This situation arises because of two factors: (1) the cooling requirements of the long-term HP turbine reduce the plant efficiency about 0.5 percent below that of the plant, if no cooling were required; (2) the expansion ratio of the HP turbine in the long-term plant was increased so that the exhaust temperature from the HP turbine would be at a lower, more practical temperature. This second factor reduced the plant efficiency about 1.8 percent compared to what it would be at the near-term HP turbine expansion ratio. If the HP turbine expansion ratio were fixed as in the near-term plant, the net plant efficiencies would be 75.5 percent (300 bar case) to 73.8 percent (195 bar case). These results, depicted in Fig. 9 imply that the benefits in developing the long-term HP turbine capabilities may be small.

Variations in two component performance assumptions were also investigated: the HP turbine adiabatic efficiency and turbine cooling requirements. In the base set of performance assumptions, the HP turbine was assumed to have an efficiency of 92 percent for both the long-term and near-term conditions. The HP turbine blades are relatively small in the near-term plant. Thus, 92 percent efficiency for the HP turbine is optimistic for the reference plant. Reduced values for the HP turbine efficiency were assessed, and results are plotted in Fig. 10 for the near-term plant and for the long-term plant. These results indicate that reducing HP turbine efficiency down to less than 85 percent has only a small influence on the net plant efficiency and does not change any of the conclusions drawn from the cycle calculations. This results because the HP turbine produces only about 10 to 40 percent of the total plant power.

The steam cooling rates for the HP and IP turbines were increased above the values estimated in the base calculation. Doubling the IP turbine steam cooling rate requirement from about 10 to 20 percent would reduce the net plant efficiency almost 1 percent. Tripling the long-term HP turbine cooling need from about 5 percent to 15 percent would reduce the net plant efficiency about 1 percent. Thus, increased turbine cooling rates can have a significant impact of the net plant efficiency, but the Reference Plant could achieve the 70.9 percent net efficiency goal even with significantly higher cooling needs.

Other variations in the reference plant configuration were also considered: fuel/oxidant preheating, feedwater heating, all oxygen through the HP combustor, additional turbine reheat stage, reduced IP turbine exhaust pressure, and LP turbine placed before the HRSG.

Table 4 outlines the results from these variations. The only variation worth further consideration is the option of feeding

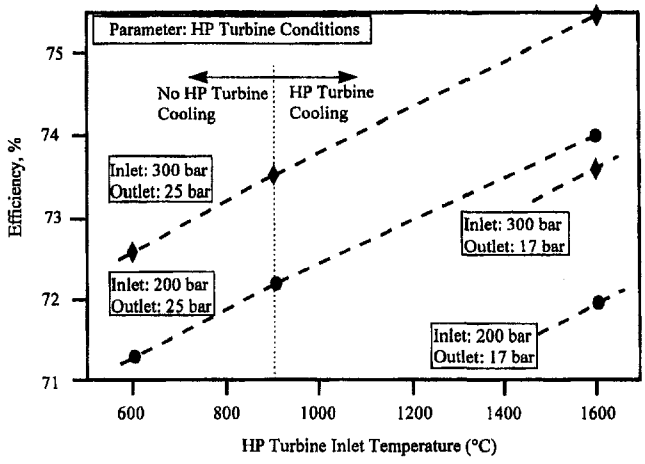

Fig. 9 Reference plant efficiency trends with base assumptions

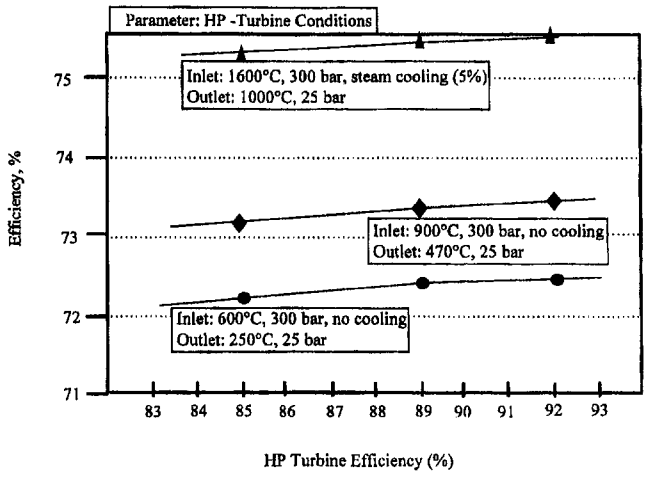

Fig. 10 Influence of HP turbine efficiency on plant net efficiency

Table 4 Reference plant alternative configurations thermal performance

Configuration Variation	Consequences
Fuel/oxidant Preheating	No benefit
Feedwater Heating	No Benefit
All Plant Oxygen Through HP Turbine	Efficiency increase 0.5-0.6% Chemistry control not needed in HP turbine Need to modify IP combustor arrangement
Additional Turbine Reheat	Small increase in efficiency Increased cost and complexity
HRSG Placed After LP Turbine	Significant increase in efficiency Increase cost Increased development needs

all of the plant oxygen to the HP turbine combustor. This results in a significant increase in plant efficiency (about 0.5%) while eliminating the need for combustor chemistry control in the HP stage. Use of this configuration would require the IP combustor arrangement to be modified since all of the oxygen would be premixed with the HP turbine exhaust steam. The other variations having some potential benefits would also have increased costs, complexity and development needs.

Environmental Performance

The Reference Plant environmental performance is superior to that of power generation using other fuels, having very low NO_x emissions, sulfur oxide emissions, particulate emissions, toxic species emissions, and green-house gas emissions. The generation of solid waste and liquid/sludge wastes would also be negligible. The only significant emissions could result from fuel or oxygen contaminants, or from noise.

Plant safety is another area of concern in the reference plant. Based on industrial and defense experience, it is expected that the handling and safety requirements for hydrogen will be comparable in scope and cost to that of other liquid fuels (e.g., methane and gasoline). The plant safety systems required for the hydrogen/oxygen environment in the reference plant will differ considerably from those in a conventional combustion turbine combine-cycle power plant, but the safety technology is available and economical.

Impurities that may enter the Reference Plant at various locations are of concern both from their environmental impact and their impact on the plant reliability, and availability maintenance. Impurities may be introduced with the oxygen supply, with the fuel hydrogen supply, through the condenser from the sea water coolant, or internally by corrosion of materials in the flow path. The oxygen generated by air separation will generally contain as much as 0.1 volume percent argon, and traces of nitrogen, depending on the design and operation of the air separation system. The air supply that is drawn from for air separation may also contain various contaminants, and any component in the air supply that is heavy relative to oxygen will tend to remain with the oxygen.

Hydrogen can be produced by many methods, with electrolysis expected to generate the most pure hydrogen. Contaminant levels in the hydrogen depend on the nature of the specific producer's electrolysis system, as well as the nature of the hydrogen transport equipment. Typically, contaminants expected in the electrolysis hydrogen might have levels as high as 0.1 percent oxygen, 0.14 percent nitrogen, 50 ppm methane, and traces of mercury.

Salts would be the most severe contaminants with respect to corrosion potential, and salts would be likely to be introduced into the recycle water system through the sea water-cooled condenser. Once salts enter the system, corrosion products could exist in the turbine exhausts in particulate, liquid, or gaseous forms. The turbine exhaust might also contain either excess hydrogen or excess oxygen, and traces of unburned hydrocarbons, NO_x, CO_2, and CO resulting from hydrogen fuel and oxygen contaminants.

The control of contaminants can best be undertaken at the condenser. Here, noncondensible gases and vapors can be separated and compressed for either recycled or disposed. An ion exchange, deep bed polisher can be used to efficiently remove ions from the recycle water. This is commercial technology. The power consumption for the polisher is associated only with the additional feedwater pressure drop resulting, and this is estimated from commercial practice to be about 3 bars. This pressure drop will have a negligible impact on the net plant efficiency. Power consumption for the regeneration of the ion exchange media (probably done off-site) would be treated as an operating cost for the system.

Conclusions

The development of a heat engine power plant system with a 70.9 percent efficiency of conversion of hydrogen chemical energy to electricity can be accomplished within the time frame of the WE-NET Program. The selected near-term plant, (See Table 3, HP turbine combustion temperature is 600°C) along with the identified performance enhancements, assures a system which meets all of the requirements of the program while managing risk, cost, and complexity to arrive at a practical power generation system.

The near-term conceptual plant layout, Fig. 11, was prepared based on conceptual equipment sizing. The HP turbine, IP turbine, LP turbine and generator are arranged on a single shaft. The HRSG is depicted as a conventional HRSG. The overall 500 MWe Reference Plant is compact and simple in configuration.

A key feature of the near-term Reference Plant is that the only developmental components are the HP and IP combustors and turbines. The near-term plant is only a moderate extrapolation of current and developing steam turbine and combustion turbine technologies. Other development needs for the reference plant can be dealt with through engineering studies (optimum HRSG design, optimum plant integration, plant controls, etc.).

The near-term plant HP turbine development needs center on the combustor (combustion phenomena and design features) and materials selection. The near-term HP turbine design will be an adaptation of conventional HP steam turbine designs, and component cooling needs will be very limited. The IP turbine development needs to focus on the combustor and materials development. In the IP turbine, the component cooling needs are extensive (airfoils, cylinder, blade rings, rotor, bearings). The cooling design follows from closed-loop steam cooling

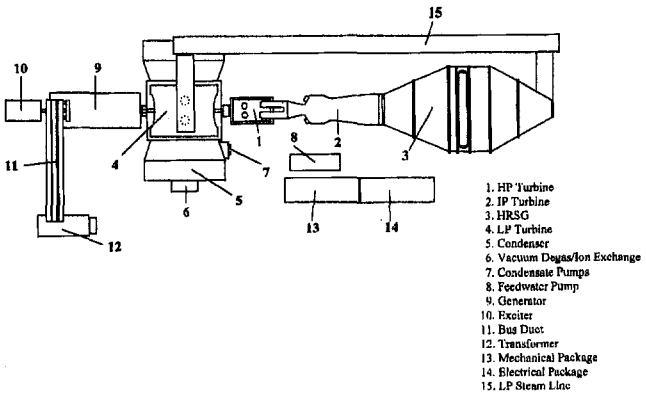

Fig. 11 Near-term reference plant layout

features currently under development for advanced combustion turbines operating under similar temperature and pressure conditions (Diakunchak et al., 1996).

HP and IP combustion development will focus on the nature of the hydrogen combustion products and the control of its chemistry, as well as on the combustor operability: flame stability, ignition, flame detection, and combustion induced oscillations. Combustor liner and transition cooling will also be part of the combustor development testing using available techniques.

Materials testing will focus on the durability of candidate materials during exposure to the hydrogen combustion products at simulated commercial operating duty conditions (hydrogen embrittlement, oxidation, stress corrosion cracking corrosion deposits, creep rupture). The development of appropriate corrosion coatings and thermal barrier coatings and their associated bond coating will be a major part of the materials program. The initial testing would consider advanced combustion turbine Ni-based superalloys (single crystal and directionally solidified), and advanced combustion turbine thermal barrier coatings (e.g., yttria-stabilized zirconia, alumina limited use of ceramic components (ring segments, combustor liners and transitions, vane and blade leading edges), and would consider the stability of candidate ceramic materials and alternative ceramic forms in simulated combustion-steam environments (e.g., zirconia in composite forms, tile forms, and fibrous insulating forms).

Verification tests would be performed at sub-scales sufficient to generate data that can be interpreted for full conditions. The verification tests would address the HP and IP combustors and the IP turbine cooling features (combustor and transition, cylinder, blades and vanes, rotor, bearing and seals) with the components made from optimum materials and thermal barrier coatings. Rotating tests of the turbines with integrated hydrogen combustion would ultimately be required to demonstrate the operability and performance of the non-integrated components and to develop confidence for the technology in industry.

Material issues must be resolved if a reliable and efficient system is to be developed. It is felt, though, that the development challenges discussed can be overcome, resulting in a significant step forward in the development of a pollution-free global energy system.

Acknowledgments

The studies described in this paper were performed under a contract from the Japanese New Energy and Industrial Technology Development Organization (NEDO). The program is administered through the Central Research Institute of Electric Power Industry (CRIEPI) as a part of the International Clean Energy Network Using Hydrogen Conversion (WE-NET) Program.

References

Bannister, R. L., Huber, D. J., Newby, R. A., and Paffenbarger, J. A., 1996, "Hydrogen-Fueled Combustion Turbine Cycles," ASME Paper 96-GT-247.

Bannister, R. L., Cheruvu, N. S., Little, D. A., and McQuiggan, G., 1994 "Turbines for the Turn of the Century," *Mechanical Engineering,* Vol. 116, No. 6, pp. 68–75.

Bannister, R. L., Silvestri, G. J., Hizume, A., and Fujikawa, T., 1987, "High-Temperature Supercritical Steam Turbines," *Mechanical Engineering,* Vol. 109, No. 2, pp. 60–65.

Bannister, R. L., and Silvestri, G. J., 1989, "The Evolution of Central Station Steam Turbine," *Mechanical Engineering,* Vol. 111, No. 2, pp. 70–78.

Diakunchak, I. S., Bannister, R. L., Huber, D. J., and Roan, F., 1996, "Technology Development Programs for the Advanced Turbine Systems Engine," ASME Paper 96-GT-5.

Little, D. A., Bannister, R. L., and Wiant, B. C., 1993, "Development of Advanced Turbine Systems," *ASME Cogen Turbo Power '93 Proceedings,* IGTI-Vol. 8, pp. 271–280.

Agency of Industrial Science and Technology in Ministry of International Trade and Industry (MITI), 1993, "Comprehensive Approach to the New Sunshine Program Which Supports the 21st Century," *Sunshine Journal,* No. 4, pp. 1–6.

New Energy and Industrial Technology Development Organization (NEDO), 1996, "Subtask 8 Development of Hydrogen-Combustion Turbine, Study for an Optimum System for Hydrogen-Combustion Turbine," 1995, *Annual Technical Results Report.*

New Energy and Industrial Technology Development Organization (NEDO), 1995, International Clean Energy Network Using Hydrogen Conversion (WE-NET), 1994, *Annual Summary on Results.*

New Energy and Industrial Technology Development Organization (NEDO), 1994, International Clean Energy Network Using Hydrogen Conversion (WE-NET), 1993 *Annual Summary Report on Results.*

Silvestri, G. J., Bannister, R. L., Fujikawa, T., and Hizume, A., 1992, "Optimization of Advanced Steam Condition Power Plants," ASME JOURNAL OF ENGINEERING FOR GAS TURBINES AND POWER, Vol. 114, pp. 612–620.

Biomass Gasification for Gas Turbine-Based Power Generation

M. A. Paisley

D. Anson

Battelle,
505 King Ave.,
Columbus, OH 43201

The Biomass Power Program of the US Department of Energy (DOE) has as a major goal the development of cost-competitive technologies for the production of power from renewable biomass crops. The gasification of biomass provides the potential to meet this goal by efficiently and economically producing a renewable source of a clean gaseous fuel suitable for use in high-efficiency gas turbines. This paper discusses the development and first commercial demonstration of the Battelle high-throughput gasification process for power generation systems. Projected process economics are presented along with a description of current experimental operations coupling a gas turbine power generation system to the research scale gasifier and the process scaleup activities in Burlington, Vermont.

Introduction

The history of biomass fueled power systems is as old as the steam engine. In the early days, and for decades afterwards, wood was a common fuel, and was used in fairly simple combustion systems with little preparation other than size reduction and some air drying. As steam technology developed and competition from other fuels increased, the characteristics of wood and other biomass fuels became better understood, and these characteristics increasingly came to control the design of the power system.

Biomass Fuel Characteristics

Biomass fuels are characterized by high and variable moisture content, low ash content, low density, and fibrous structure. In comparison with other fuels, they are regarded as of low quality despite low ash content and very low sulfur content. A major concern in using biomass in more thermodynamically advanced (high-temperature) equipment is the relatively high percentage of alkali in the ash. The significance of alkalis is their propensity to form, in combination with other elements, mixed sulfates and other salts having low fusion points and high corrosive potentials. Table 1 gives some examples of biomass fuel ash composition. It should be noted that the compositions can vary greatly from those listed because in many cases there is contamination by adventitious material picked up during handling. Also alkali levels, notably potassium, may be much higher than reported because of losses during analysis [1]. The numbers quoted are an amalgam from various sources and have been rounded to total nearly 100 percent in each case. They indicate that grasslike materials have high silica contents and generally high alkali, whereas woods tend to have high calcium content and less alkali. It is significant that poplar, which is potentially suitable for fuel wood plantations, has a high potassium content compared to pine and maple.

Many older wood-burning steam power plants use steam temperatures below 400°C (750°F) and sometimes below 300°C (570°F) so ash behavior is a minor concern as long as sulfur-bearing secondary fuels (oil or coal) are not used. When back pressure turbines are used to provide process steam as well as power, good overall energy utilization is possible, typically 70 percent or more, but the electrical output is only 10–15 percent. With condensing turbines (no process steam supply) the electrical efficiency may be 15–20 percent. In more modern plants, especially those of larger size (over 50 MW capacity) steam temperatures up to 480°C (900°F) have been used and electrical efficiencies around 25 percent can be reached, but with increasing concern about the formation of glassy ash deposits and superheater corrosion.

The latest generation of electric power plant utilizes gas turbines combined with steam turbines to utilize the exhaust heat. With support from the DOE's Advanced Turbine Systems program, thermal efficiencies of 60 percent are being targeted [2] while 58 percent has been attained [3] in large utility scale systems. In the small sizes (5–20 MW) combined cycle efficiencies are over 40 percent [4]. These efficiency levels are unattainable by the direct use of biomass fuels because of the high sensitivity of gas turbines to erosion by solid particles, deposit formation by dust, and corrosion by molten ash or salts. Attempts have been made to operate modified gas turbines by direct combustion of wood [5], but even with turbine inlet temperatures (TIT) as low as 750°C (1380°F) serious problems have been experienced with the fuel ash [5]. A TIT of 750°C represents a large departure from normal modern gas turbine practice in which a TIT of 980–1200°C is more usual. Figure 1 illustrates how gas turbine performance falls off with lower TIT. Biomass conversion to a clean essentially ash-free form, usually by gasification and purification, is necessary to obtain high efficiency.

Biomass Derived Fuel Gases

As well as the ash behavior, the chemical composition and the heating value of the fuel gas affect its suitability as a turbine fuel. Chemical composition, especially hydrogen content, affects flame speed, which can cause problems in the distribution of heat release in the combustor and eventually flash back and overheating. The presence of nitrogen compounds makes it difficult to attain low NO_x emission levels [6]. To some extent it is possible to modify the combustion system to suit specific fuels, but this increases turbine cost.

Problems in the utilization of solid fuels and their derivatives have recently been discussed by DeCorso et al. [7] who found that, although many processes have been proposed for producing "clean" fuels from coal and biomass, acceptable levels of fuel impurities have not yet been adequately defined, particularly in the context of advanced gas turbines using high-strength materials with undemonstrated corrosion resistance. While the problems may be somewhat less severe in more modestly rated industrial gas turbines, it is nevertheless true that properties of fuels derived from biomass are vital to the successful operation of gas turbine-based biomass fueled plants. Specifically, the following are desirable, and in some cases essential, characteristics:

Contributed by the International Gas Turbine Institute and presented at the 42nd International Gas Turbine and Aeroengine Congress and Exhibition, Orlando, Florida, June 2–5, 1997. Manuscript received at ASME Headquarters February 1997. Paper No. 97-GT-5. Associate Technical Editor: H. A. Kidd.

Table 1 Examples of biomass ash compositions

Specie	Ash, %	Ash Composition, %						
		Al_2O_3	CaO	Fe_2O_3	MgO	Na_2O	K_2O	SiO_2
Bagasse	2-3	18	4.5	14.4	3.3	0.8	4.1	46.6
Corn Cob	2-3	-	0.8	0.1	8	0.6	40	50
Corn Stalk	5-10	6	14	1.4	18	20	0.1	40
Wheat Straw	10-15	1.7	10	1.9	2.5	1.2	25	46
Poplar	2-3	1	47	0.5	4.4	0.2	20	2.6
Pine	2-3	4.5	49	3.5	0.5	0.4	2.6	32.5
Maple	3-5	4	56	2	20	-	6	10

- The fuel gas must have very low ash content (equivalent to less than 1 ppm at the turbine inlet).
- The ash must not contain significant amounts of alkali (alkali concentration below 10^{-8} at the turbine inlet).
- The burning characteristics (flame speed, heating value) of the fuel should not be too different from those used in standard gas turbines designed for natural gas or petroleum liquid fuels.
- The heating value of the fuel should be high enough to permit attainment of the design turbine inlet temperature.
- Combined nitrogen in the fuel should be low to avoid formation of fuel derived NO_x.

Relatively clean fuel gas can be derived from biomass either by gasification (through a partial oxidation process) or by pyrolysis. Pyrolysis involves thermal decomposition of the biomass into volatile and solid fractions, without oxidation. The volatile fraction in this case is of higher heating value than gases obtained by partial oxidation, but only a part of the input combustible (the volatile fraction) is transformed to the gaseous (or vapor) form. All of the combustible material can be gasified by oxidation. The volatiles produced in pyrolysis can also be in the form of condensible tars, which require further treatment. These difficulties have been largely overcome by a rapid pyrolysis process developed by Battelle, with support from DOE. This process depends on very rapid heating of the raw biomass to minimize tar formation, and on the efficient use of the solid residue (or char) as a heat source for the pyrolysis process. Compared with air-blown partial oxidation processes, this process produces a gas of much higher heating value, and it does not require the oxygen separation usually necessary for production of medium Btu gas. This gas has been demonstrated to be interchangeable with natural gas as a gas turbine fuel, firing a small (200 kW) Solar gas turbine with only minor modifications to the fuel feed system [8]. Fuel changeover is achieved simply by operation of a solenoid valve, which switches the fuel supply.

Gas Cleanup

While there are a number of routes by which biomass can produce an acceptable combustion turbine fuel gas, the critical stage in the process is treatment of the gas to remove impurities. Established methods, used for many years in the gas-making industry, use wet scrubbing methods; these can remove solid particles, soluble gases, soluble salts, and condensible liquids, to produce high levels of fuel purity. Their disadvantages relate to disposal of contaminated water, and the associated heat losses. Alternative methods, currently under development [9], involve cooling the gas to below 600°C (1100°F) to allow condensation of volatile salts, followed by filtration to remove solids and chemical sorption of alkali and sulfur over regenerable reactants. With biomass feedstock sulfur sorption is generally not an issue. Hot gas clean up methods are becoming more effective, but there remain some problems with filter reliability and pressure drop over long operating periods. Filters do not remove condensible vapors, which contribute to the heating value of the product gas but can adversely affect fuel control systems if they condense, and also lead to soot formation. Feeding hot fuel gas to the turbine can avert condensation in the fuel system, but presents some obvious problems in fuel system design. Nitrogen compounds are not removed in hot gas treatments. Overall, wet gas treatments present fewer problems to the turbine, but carry an efficiency penalty.

In the case of the Battelle gasifier described below, the relatively high heating value of the gas minimizes the sensible heat loss in the scrubbing operation. Also, the condensible fraction of the gas is very low (on the order of 0.5 percent), and the condensates are predominantly of low boiling point and immiscible in water. Thus, water treatment is simplified and toxic effluents eliminated. Condensibles can be fed to the process combustor.

In a further development of the Battelle process, a novel hot-gas conditioning catalyst (DN34) has been developed that converts these condensible products to noncondensible forms. This catalyst permits the use of a dry gas cleanup without the problems associated with a high fuel gas temperature in high-pressure gasifiers or, as in the case of the Battelle atmospheric pressure process, will result in the elimination of the gas scrubbing operation and replace it with a simple water cooler prior to gas compression. The resulting gas can be used in virtually any gas turbine with minimal or no modification to the engine.

The Battelle Biomass Gasification Process

The Battelle biomass gasification process, licensed in North America by Future Energy Resources Corporation (FERCO) in Atlanta, GA, produces a medium-Btu product gas without the need for an oxygen plant. The process schematic in Fig. 2 shows the two reactors and their integration into the overall gasification process. This process uses two physically separate reactors: (1) a gasification reactor in which the biomass is converted into a medium-Btu gas and residual char, and (2) a combustion reactor that burns the residual char to provide heat for gasification. Heat transfer between reactors is accomplished by circulating sand between the gasifier and the combustor.

The Battelle/FERCO Process, unlike conventional gasification processes, takes advantage of the inherently high reactivity of biomass feedstocks. The reactivity of biomass is such that throughputs in excess of 14,600 kg/h-m^2 (3000 lb/hr-ft^2) can be achieved. In other gasification systems throughput is generally limited to less than 1000 kg/h-m^2 (200 lb/hr-ft^2).

The basic uniqueness of the process compared to other biomass gasification processes is that it was designed to exploit the unique properties of biomass while the other processes were

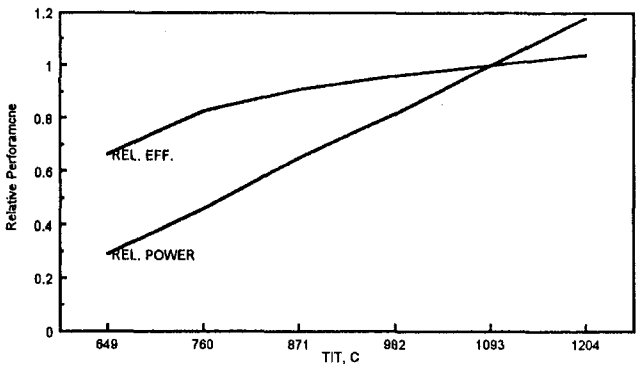

Fig. 1 Effect of TIT on performance

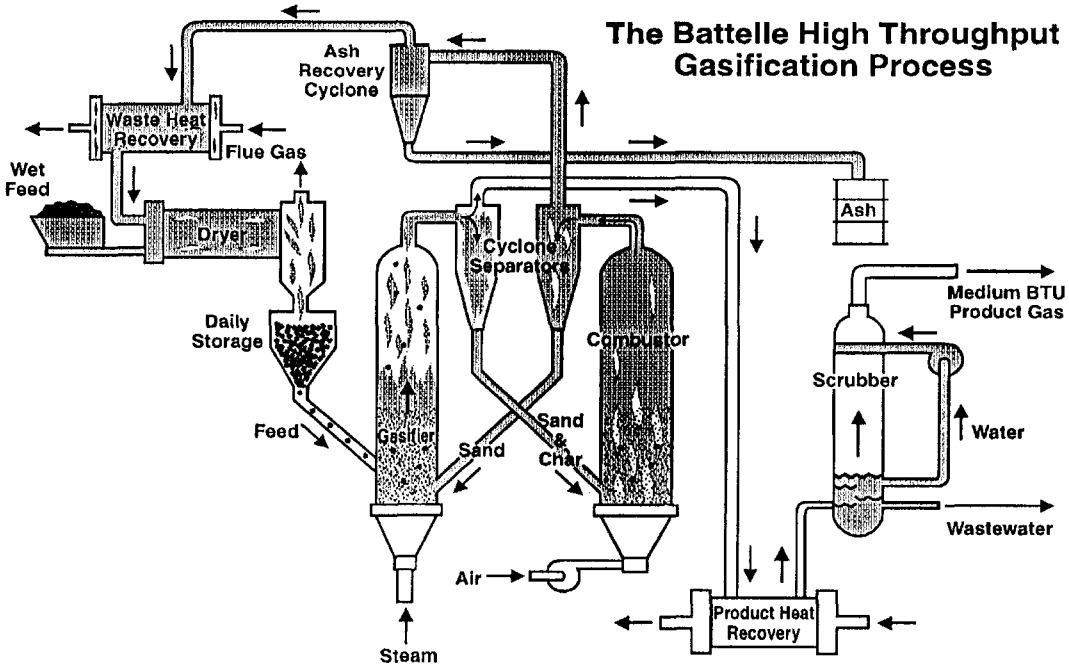

Fig. 2 Schematic of the Battelle/FERCO gasification process

either developed for coal gasification or were heavily influenced by coal gasification technology.

Technology Status. The process has been under development since the late 1970s and has been extensively tested with woody biomass, herbaceous crops (switch grass), and a highly prepared RDF. Recent testing in Battelle's 10 ton per day Process Research Unit (PRU) has coupled a small-scale gas turbine power-generation system to the PRU gasifier. This testing has demonstrated the feasibility of biomass gasification for power generation, and has identified areas that require further investigation to improve the projected performance of a commercial scale gasification power generation system.

A Commercial Scale Demonstration Plant. Based on the successful operation in the PRU, a decision was made to scale up the process to a commercial scale. A scale of 200 tons per day (dry) was chosen for the scale-up plant to provide both scale-up data and an economically viable gasification power generation system after the initial performance data was collected.

The commercial scale demonstration of the Battelle Gasification process is under way at the McNeil Generating station in Burlington, Vermont. In the first phase of the project, a 200 ton per day gasifier based on the Battelle technology will be constructed and operated at the McNeil site. The product gas produced during initial operation will be used in the existing McNeil power boilers. In the second phase, a gas combustion turbine will be installed to accept the product gas from the gasifier and form an integral part of a combined cycle system.

The construction of the gasification plant is under way and is expected to be completed in the early part of 1998.

The DN34 Gas Conditioning System

Battelle has developed a low-cost, disposable cracking catalyst (DN34) that can be used to condition the product gas prior to its use in a power generation system. DN34 is a proprietary catalyst described in US Patent 5,494,653.

Results of Testing With DN34. Tar concentrations measured in the product gas from the Battelle gasifier are typically 16 g/m^3. These tars are highly aromatic in character and are relatively insoluble in water. As discussed above, these tars can be removed by conventional water-based scrubbing; however, such scrubbing methods can leave significant amounts (up to 30 percent of the incoming tar) of tar behind in the product gas. By providing hot gas conditioning of the product gas using DN34, significant improvement in the quality of the product gas can be realized. By combining DN34 with a water-based direct contact cooler, no measurable condensibles or particulates remain in the gas.

Integrated Biomass-Based Power Supply

To achieve the best overall efficiency, the Battelle gasification system must be carefully integrated into a combined cycle power generator. This permits effective recovery of heat from the pyrolyzer and its associated heat source, and of course it also utilizes the exhaust heat from the gas turbine.

Figure 3 shows in schematic form how this integration can be achieved. The gas turbine uses a turbine inlet temperature of 1090°C (2000°F) and a pressure ratio of 10:1. The plant conditions assumed in this case are consistent with current practice for relatively small industrial scale power plants with electrical outputs in the range 5 to 15 MW. The plant has not been optimized and some further improvement in output would certainly be possible. The gross thermal efficiency is 36 percent, and the overall electrical efficiency allowing for gearing and electrical losses is 34.5 percent. After deducting power for auxiliaries, the net output would be about 32 percent. This is a substantial improvement over a wood-fired steam plant operating at the same steam conditions, which would provide less than half the power at 15 percent efficiency, before deducting auxiliary power.

Industrial power plants frequently operate in a cogeneration mode, supplying both process heat and electrical power. From Fig. 3 it can be deduced that the pyrolyzer/gas turbine system could supply electrical power form the gas turbine at about 23 percent efficiency (before auxiliaries) and could also deliver over 60 percent of the input fuel energy as process heat. The overall utilization of thermal energy in this case is around 80 percent, which compares well with cogeneration systems based on natural gas. The power-to-heat ratio, which is over 0.35, is also very good, although lower than could be obtained with

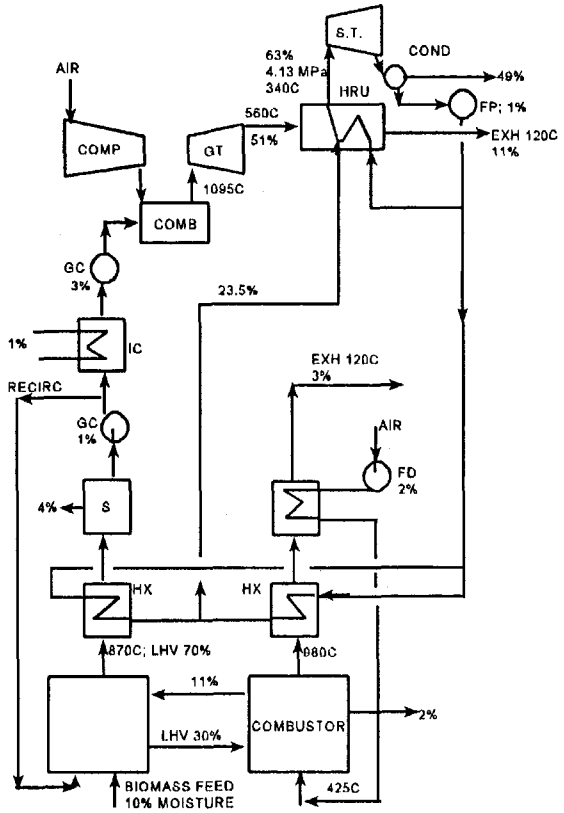

Fig. 3 Biomass gasification combined cycle schematic

LEGEND:
COMP Compressor
GT Gas turbine
COMB Combustor
ST Steam turbine
COND Condenser
FP Feed pump
EXH Exhaust
IC Intercooler
S Scrubber
GC Gas compressor
HX Heat exchanger
FD Forced draft fan
HRU Heat recovery unit
Note: % figures refer to heat energy relative to LHV of the fuel fed to the gasifier; temperatures in °C.

natural gas, at around 0.5. Where an industrial site has traditionally used biomass waste to produce steam only, usually at less than 80 percent efficiency, a change to cogeneration, with imports of electrical energy, could be very profitable.

When considering biomass as fuel for power generation on a larger scale, say upward of 25 MW, schemes rather more sophisticated than that shown in Fig. 3 are appropriate. Consonni and Larson [10], for example, examined a number of gasification/combined cycle operations based on the use of aeroderivative gas turbines. They assumed a gas turbine inlet temperature (TIT) of 1232°C (2250°F), and a pressure ratio of 19.4:1 with a steam turbine operating between inlet conditions of 60 atm (900 psi), 450°C (842°F), and exhaust temperature of 95°F (0.82 psi). Using the Battelle/FERCO gasifier concept, a net efficiency of 42.5 percent based on LHV of the fuel was predicted. It is interesting that direct air-blown gasification yielded gases that had insufficient heating value to permit achievement of the same turbine inlet temperature. For these cases the TIT was reduced to 1000°C (2012°F), resulting in slightly lower net power output than with the Battelle/FERCO system. Efficiencies were 45.2 percent for a pressurized gasifier, and 41.9 percent for a near-atmospheric pressure gasifier.

More advanced versions of the Battelle gasifier/combined cycle system probably would not use a pressurized gasifier because it would be necessary to pressurize both the pyrolyzer vessel and the FBC unit. Pressurization would not greatly reduce the size of the pyrolyzer, and it would become necessary to recover energy from the FBC exhaust stream through a pressure recovery turbine. These complications would hardly, if at all, be offset by the savings in gas compression costs, which use less than 9 percent of the input energy because of the relatively high heating value of the gas. Meanwhile, the net efficiency of 42.5 percent quoted earlier represents a target that can be obtained using available technologies with virtually no modification to current turbine designs.

In all of the systems outlined above, the moisture content of the biomass feed is important. With partial combustion systems it affects the product gas quality; hydrogen content increases with fuel moisture, changing the heating value, mean molecular weight, and flame speed, as well as affecting the overall gasification efficiency. With the Battelle system the gas quality is virtually unaffected by fuel moisture, but the FBC must supply additional heat to evaporate the moisture, and this heat is a major component of the scrubber loss. Thus, it is important to ensure that the biomass feed is as dry as possible, preferably in the 10–20 percent range. The exhaust gas streams must be utilized to supplement air drying if these values are to be attained.

Projected Economics of a Cogeneration System

The production of product gas in the indirectly heated gasifier coupled with the relatively high efficiency of gas turbine power production provides the potential for a cogeneration system that can be readily applied to existing industrial sites. A conceptual process design was developed and based on the following criteria: (1) electrical production of approximately 50 MW; (2) basing the design on an industrial gas turbine system; (3) using a dual pressure steam cycle; (4) using steam generator exhaust gas for chip drying [11].

For this evaluation, a GE MS 6001 (B) was chosen as the gas turbine. The decision to use this turbine system was based on the desire to have a currently available turbine system rather than optimizing the turbine pressure ratio. The MS 6001 turbine has a pressure ratio of 11.8 and a thermal efficiency (LHV) of 31.4 percent.

Projected Economics

An economic analysis was done for installation of this system into an existing industrial site. Based on such an installation, capital costs were built up from FOB equipment costs and

Table 2 Operating cost estimate—818 TPD combined cycle plant

Operating Costs:
Load Factor = 0.9 (Base-Loaded Plant)
Fuel - Whole Tree Chips - Delivered Cost of $16/ton wet
Capital Charge Rate = 0.200
Operation and Maintenance - Personnel = 12 @ $15/hr
Supplies Per Year for Operation and Maintenance
GT/SP Plant - 1 % of Capital Cost;
Gasification Plant - 5 % of Capital Cost
Power Delivered/Year = 441.5×10^6 kWh

Cost Component	Cost	
	$/Yr	Cents/kWh
Capital	11.6×10^6	2.63
Fuel	7.17×10^6	1.62
Oper. & Maintenance		
Personnel	0.56×10^6	0.13
Purchased Supplies	1.18×10^6	0.27
Total	20.51×10^6	4.65

factored battery limit installation costs to develop the total physical plant costs. Total installed equipment costs on a dollars per installed kilowatt basis, including a conditioning catalyst system, were estimated to be $1037/kW, less than projections for a new central power station.

Operating costs for system are shown in Table 2 along with the cost of power. For the cash flow analysis used in developing the estimate for the cost of power, a capital charge rate of 20 percent was used, which is equivalent to a 20 percent ROI, which results in a power selling price of $0.047/kWh.

Conclusions

The gasification/gas turbine power system provides both power costs and system efficiencies that surpass a biomass direct combustion system, typically having a process efficiency in the range of 17 percent with corresponding power costs. The system has a low risk associated with it since the primary power system components, gas compression, and gas turbine have all been demonstrated commercially with similar fuels. The gasifier, combustor, and scrubbers have not been commercially demonstrated, but based on the current testing at Battelle, data will be available to result in a manageable risk for these components as well. The integration of the systems is simplified due to the relatively high heating value of the Battelle product gas minimizing the modifications necessary to use the medium-Btu gas in a gas turbine.

References

1 Zicherman, J. B., and Thomas, R. J., "Analysis of Loblolly Pine Ash Materials." Paper No. 3574, Journal Series of North Carolina State University, Ag. Experimental Station, 1972.

2 Webb, H. A., Parsons, E. L., and Borjuror, R. A., "Advanced Turbine Systems Program and Coal Applications," ASME Paper No. 93-GT-356, 1993.

3 Dodman, K., ed., "Gas Turbine Development Emphasizes Improved Efficiency," *Power Engineering International,* Mar./Apr. 1996.

4 DeMoss, T. B., ed., "They're Here (almost): The 60% Efficient Combined Cycle," *Power Engineering,* July 1996.

5 Ragland, K. W., Misra, M. K., Aerts, D. J., and Palmer, C. A., "Ash Deposition in a Wood Fired Gas Turbine," ASME JOURNAL OF ENGINEERING FOR GAS TURBINES AND POWER, Vol. 117, 1995, p. 509.

6 Tarig, A. S., and Purvis, M. R. I., "NO_x Emissions and Thermal Efficiencies of Small Biomass Fueled Combustion Plant With Reference to Process Industries in a Developing County," *International Journal of Energy Research,* Vol. 20, 1996, p. 41–55.

7 DeCorso, M., Newby, R., Anson, D., Wenglarz, R., and Wright, I., "Coal/Biomass Fuels and the Gas Turbine: Utilization of Solid Fuels and Their Derivatives," ASME Paper No. 96-AT-76, 1996.

8 Paisley, M. A., and Overend, R. P., "Biomass Gasification for Power Generation," presented at the EPRI 13th Conference on Gasification Power Plants, Oct. 1994.

9 Judkins, R. R., Stinton, D. P., and DeVan, J. H., "A Review of the Efficiency of Silicon Carbide Hot Gas Filters in Coal Gasification and Pressurized Fluidized Bed Combustion Environments," ASME JOURNAL OF ENGINEERING FOR GAS TURBINES AND POWER, Vol. 118, 1996, p. 500.

10 Consonni, S., and Larson, E. D., "Biomass-Gasifier/Aeroderivative Gas Turbine Combined Cycles. Part B: Performance Calculations and Economic Assessment," ASME JOURNAL OF ENGINEERING FOR GAS TURBINES AND POWER, Vol. 118, 1996, p. 517.

11 Paisley, M. A., and Farris, G., "Commercialization and Development of a Biomass Gasification Power System," presented at the EPRI Conference on New Power Generation Technology, Oct. 1995.

Effects of Temperature on Formation of Insolubles in Aviation Fuels

W. J. Balster

E. G. Jones

Innovative Scientific Solutions, Inc.,
2786 Indian Ripple Road,
Dayton, OH 45440-3638

Ten aviation turbine fuels (five Jet-A fuels, three JP-5, one JP-8, and one JPTS) were stressed at 185 and 225°C in a single-pass heat exchanger. On the basis of several criteria applied at 185°C, these fuels cover a broad thermal-stability range from lesser-quality fuels to the most stable JPTS fuel. Three of these fuels contain significant concentrations of dissolved metal (copper, >30 ppb). The surface and bulk insolubles formed from each fuel have been quantified using surface-carbon burnoff of tubing sections and of in-line filters. The total insolubles measured at 185 and 225°C fall in the range 0.3–7.5 μg/mL and 0.1–2 μg/mL, respectively. In general, the greater the quantity of insolubles formed at 185°C, the greater its reduction at 225°C. Possible explanations for this effect are offered, and implications relative to understanding surface fouling are discussed.

Introduction

Aviation fuel in modern military aircraft serves as the primary heat sink to cool subsystems; this application and its enhancement by fuel recirculation prior to combustion can lead to deleterious surface and bulk fuel fouling (Edwards et al., 1992). Below 300°C surface fouling originates as insoluble autoxidation products that collect on heat exchangers, nozzles, and servocontrols. For understanding and reducing fouling, experimental methods are required for quantitative assessment of insolubles. The distribution of bulk fuel and wall temperatures under turbulent flow that exists in aircraft fuel lines results in complicated chemical test conditions. Simulations conducted under simpler, but well-defined, test conditions can be valuable in quantifying insolubles. One approach taken in this laboratory has been to study both autoxidation and fouling that occur during slow flow of fuel through a single-pass heat exchanger. In this manner, data interpretation is simplified by the imposition of flow conditions that are laminar and reaction conditions that are nearly isothermal. Quantification of surface and bulk insolubles is accomplished by surface-carbon burnoff of heat-exchanger tubing segments and in-line filters, respectively.

The effects of temperature on fuel-fouling kinetics are very complex. Autoxidation rates increase with temperature; however, the integrated quantity of insolubles does not necessarily increase. For example, studies in this laboratory (Jones and Balster, 1994) of one Jet-A fuel over the temperature range 145–225°C have shown surface insolubles to have a pronounced inverse temperature dependence. In order to assess the importance of bulk-fuel temperature in the formation of insolubles, we have conducted experiments to quantify insolubles formed in ten fuels at 185 and 225°C. The results of this temperature study are reported herein.

Experimental Arrangement

Ten aviation fuels covering a broad spectrum of thermal stability and currently of interest to the USAF are summarized in Table 1, along with some pertinent fuel properties. All experiments were conducted using the NIFTR single-pass heat exchanger, which has been described previously (Jones and Balster, 1993, 1995). The configuration consisted of a stainless-steel tube (0.318 cm o.d., 0.216 cm i.d.) clamped tightly within a copper block to maintain constant wall temperature. In order to maintain a single reaction phase, all studies were carried out at high pressure (>2.3 MPa). Autoxidation was studied using a gas-chromatographic technique developed by Rubey et al. (1995) for monitoring O_2. The disappearance of O_2 was tracked as a function of fuel residence time in a heated tube of fixed length (0.81 m) maintained at 185°C. Residence times were varied by changing the flow rate. Analogous experiments could not be performed at 225°C because of the short reaction times.

In fouling studies, fuel was pumped at a constant flow rate through a 1.8 m heated tube and Ag membrane in-line filters (0.45 and 0.20 μm). After the 72 h test period, the heated tube was cut into 5.1 cm segments. Tubes were then rinsed with heptane, treated for 24 h at 130°C in a vacuum oven, and subjected to conventional surface-carbon burnoff (LECO RC 412). Reaction time associated with each segment was calculated from tubing dimensions and flow rate, assuming plug flow. A flow rate of 0.25 mL/min provided ~23 min of isothermal stressing at 185°C for 1.08 L of fuel. A flow rate of 1.5 mL/min provided more than 3 min of stressing at 225°C for 6.48 L of fuel. Reaction conditions became isothermal at this higher temperature only after the reaction time exceeded that associated with the first three data points (~15 cm into the block). Reaction times allowed conversion of all dissolved O_2 and completion of the primary deposition processes at each temperature. Data are presented as the total integrated sum of tubing carbon (in units of micrograms per milliliter) as a function of stress duration. The quantity of surface carbon reproduces within 20 percent; the minimum detectable surface carbon is estimated to be 0.1 μg/mL.

Bulk insolubles were collected over the entire 72 h test period on in-line filters; the filters were rinsed with heptane and evaluated for surface carbon in the same manner as the tube segments. Total bulk insolubles (expressed in units of micrograms per milliliter) represented an average over the complete stress duration. Filter housings located ~10 cm from the heat exchanger remained at room temperature for the 185°C experiments and within 20°C of room temperature for the 225°C experiments. In both cases the measured filterables include additional contributions arising from fuel cooling. The dispersant additive obtained from Betz Laboratories was used at a concentration of 100 mg/L.

Contributed by the International Gas Turbine Institute and presented at the International Gas Turbine & Aeroengine Congress & Exhibition, Orlando, FL, June 2–5, 1997. Manuscript received by the ASME Headquarters July 1997. Paper No. 97-GT-218. Associate Technical Editor: H. A. Kidd.

Table 1 Fuel properties

fuel no.	class	JFTOT temp., K	total S ppm	dissolved metals, ppb*
3084	Jet-A	541	527	Cu, 35; Fe, <5
3119	Jet-A	(fails)	1000	Cu, 7; Fe, 26
2985	JP-5, Hydrotreated	535 (fails)	233	Cu, 14; Fe, 18
2962	JP-5		438	
2963	JP-5, Cu-Doped 2962	505 (fails)	438	Cu, 98; Fe, 60
2827	Jet-A, Straight Run	539	790	Cu, <5; Fe, 8
2934	JP-8	539	755	Cu, 34; Fe, <5
2747	Jet-A, Hydrotreated	605	37	Cu, <5
2922	Jet-A, Hydrotreated	550	210	Cu, 7; Fe, <5
2976	JPTS	700	<5	

* Measurements made for USAF using graphite furnace Zeeman/5000 System Atomic Absorption Spectrometer by United Technologies, Pratt and Whitney.

Results and Discussion

Autoxidation and Insoluble Formation at 185°C. The disappearance of O_2 as a function of reaction time is given in Fig. 1 for seven of the ten fuels studied. The selected plots include the slowest and fastest oxidizing fuels and, for clarity in presentation, exclude the three most stable fuels. Time required for total reaction ranges from 1.5 min for the copper-doped JP-5 fuel to ~15 min for a straight-run Jet-A fuel. The integrated quantity of surface deposits, given in Fig. 2, shows a strong dependence on autoxidation, based on the fact that deposition occurs primarily during oxidation and becomes negligible soon after O_2 depletion. For example, deposition is complete after 2 and 15 min, respectively, for the two fuels mentioned above, which exhibited the largest difference in autoxidation rates.

The quantity of deposits is dependent on the nature of the fuel, the reaction temperature, and the amount of dissolved O_2 present. No simple dependence on the rate of autooxidation is apparent. Striebich and Rubey (1994) have found that the amount of dissolved O_2 in air-saturated fuel is approximately fuel independent; thus, the total amount of deposits and filterables evaluated for any fuel following complete O_2 conversion can be used as a relative measure of its thermal stability at that temperature (Jones et al., 1995). The quantity of bulk and surface insolubles increases markedly after a five-fold increase in dissolved O_2, as seen in Fig. 3. The higher concentration is obtained by sparging the initial fuel with pure O_2. Similarly, reductions by a factor of ~20 in surface insolubles from POSF-2827 fuel have been reported at this temperature after sparging of the initial fuel with helium (Jones and Balster, 1993).

Insoluble Formation at 225°C. Autoxidation at this temperature occurs too rapidly for measurement by our experimental methods. However, from reported Arrhenius parameters (Pickard and Jones, 1996), the slowest oxidizing fuel (POSF-2827) consumes all dissolved O_2 within 0.5 min. The deposition behavior of the seven selected fuels shown in Fig. 4 indicates two distinct regions. In the first, or major region, deposition occurs rapidly during the initial minute of stressing and corresponds to the time associated with O_2 depletion; this region encompasses the time needed for the fuel to achieve isothermal

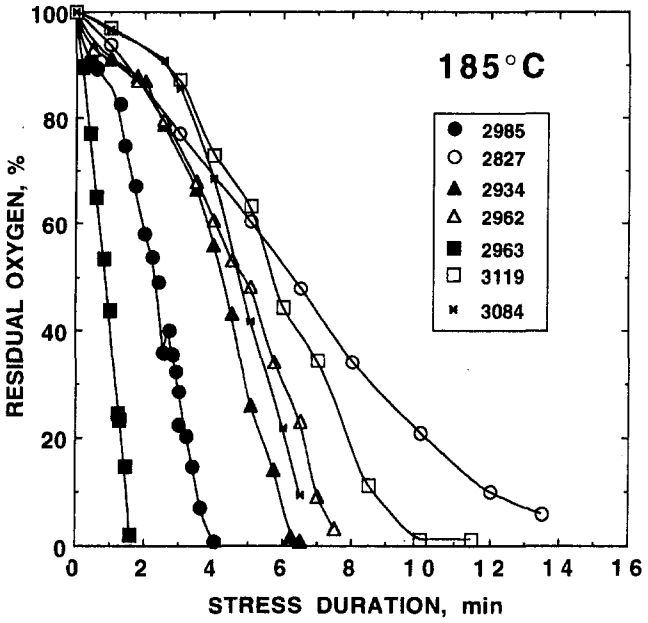

Fig. 1 Depletion of dissolved O_2 at 185°C in air-saturated fuels

reaction conditions. In the second, or post-oxidation region, deposition occurs much more slowly and is negligible at 185°C. We attribute the first primarily to fast autoxidation reactions and the second to slow agglomeration of small particles coming out of solution.

Relative Comparison of Fuel Thermal Stability at 185 and 225°C. The integrated quantity of surface and bulk insolubles for the 10 fuels studied is summarized in Figs. 5(*a*) and 5(*b*) for reaction at 185 and 225°C, respectively. Fuels having the lowest thermal stability at 185°C (namely, POSF-3119, -3084, -2827, and -2934) also have the highest concentration of sulfur (see Table 1). Fuels containing many components having heteroatoms such as sulfur, nitrogen, and oxygen have lower thermal stability (Hazlett, 1991). This arises because such components are frequently aromatic and react during autoxidation to form polar products having reduced solubility. Sulfur-containing components are well known as inhibitors because of their ability to destroy hydroperoxides (ROOH) and, thereby, reduce self-initiation. The destruction of ROOH has been implicated in insoluble formation in kerosenes by Kendall and Mills (1986) and in jet-fuel blends by Jones et al. (1996a).

The large differences in thermal stability observed at 185°C are not apparent at 225°C. At the higher temperature all of the fuels, with the exception of JPTS, form similar quantities of insolubles within an experimental range of ±0.5 μg/mL. The thermal stability of the more stable fuels does not change significantly with increasing temperature. However, that of the less stable fuels is relatively improved as the temperature increases. The data presented are consistent with autoxidation processes as the source of insolubles. This view is further supported by the fact that the copper-doped fuel, POSF-2963, forms surface deposits much faster than its undoped complement, POSF-2962,

Nomenclature

JFTOT = jet-fuel thermal-oxidation test
JPTS = thermally stable jet fuel
Jet-A = commercial kerosene fuel
JP-8 = kerosene fuel with additive package consisting of icing inhibitor, static-charge dissipator, and corrosion inhibitor
JP-5 = high-flash-point kerosene
NIFTR = near-isothermal flowing test rig
POSF = jet-fuel designation, see Table 1
QCM = quartz crystal microbalance
USAF = United States Air Force
8Q405 = proprietary dispersant from Betz Laboratories

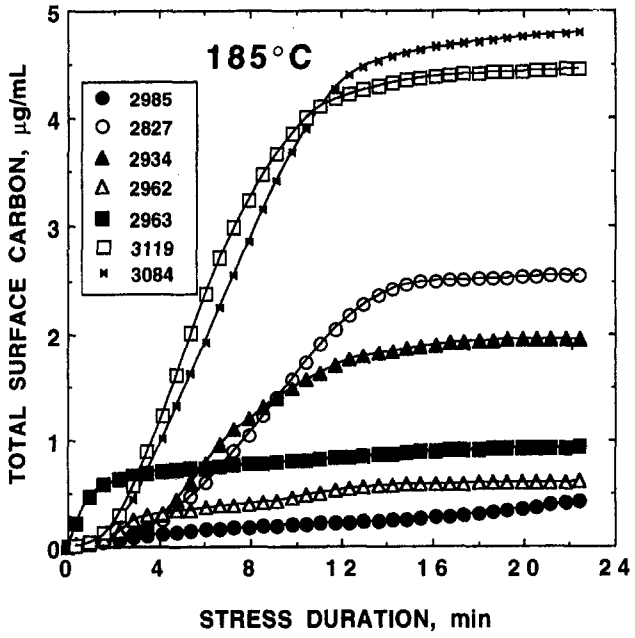

Fig. 2 Total surface deposition at 185°C in air-saturated fuels

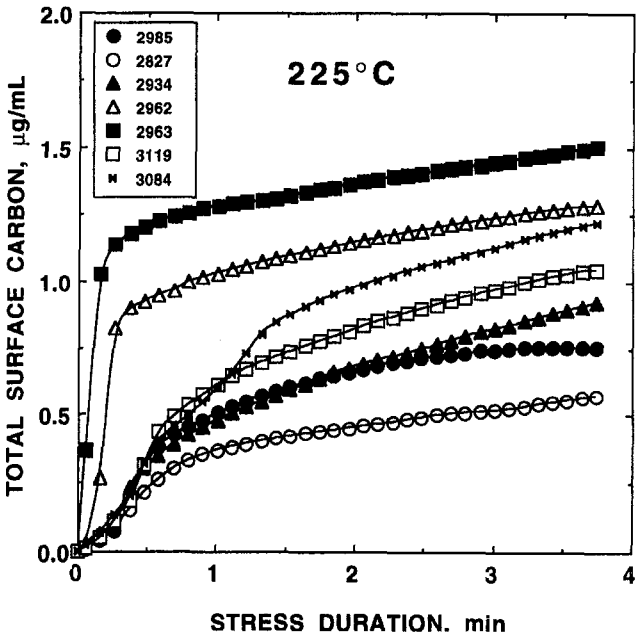

Fig. 4 Total surface deposition at 225°C in air-saturated fuels

or any of the other fuels. This can occur only as a result of the well-known catalytic role of metal cations in accelerating autoxidation by dissociating ROOH (Pedersen, 1949). Thus, any explanation of thermal-stability changes must involve ROOH and free-radical chemistry.

Effect of Dissolved Oxygen at 225°C. Considering the relatively small quantity of insolubles measured, it is important to investigate the importance of dissolved O_2 at 225°C. We have conducted tests after the initial fuel has been sparged with N_2 for 30 min. O_2 measurements under these conditions indicated ~15 percent of the air-saturated value. The deposition behavior of N_2-sparged fuels is given in Fig. 6. Despite the large reduction in dissolved O_2, the corresponding total insolubles were reduced on an average only to 61 percent of the air-saturated values, with a mean deviation of 17 percent. The greatest observed reduction to 37 percent of the air-saturated value occurred for POSF-2934 and the least to 81 percent occurred for POSF-2962.

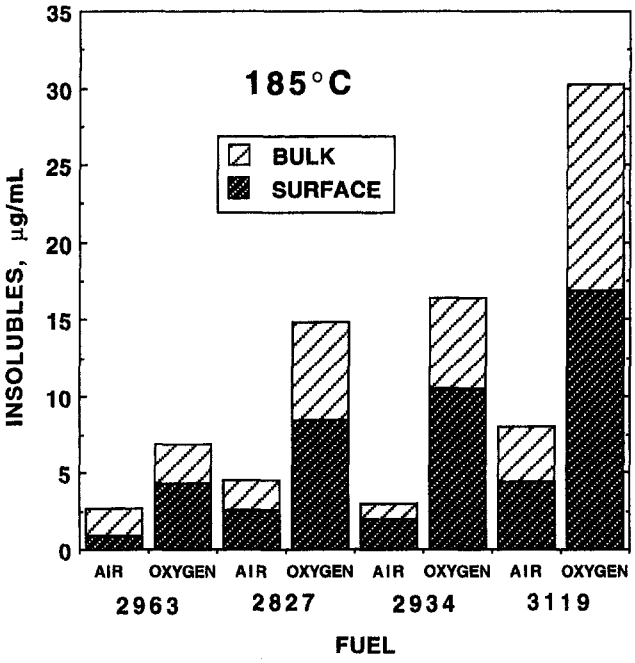

Fig. 3 Effect of dissolved O_2 on insolubles at 185°C

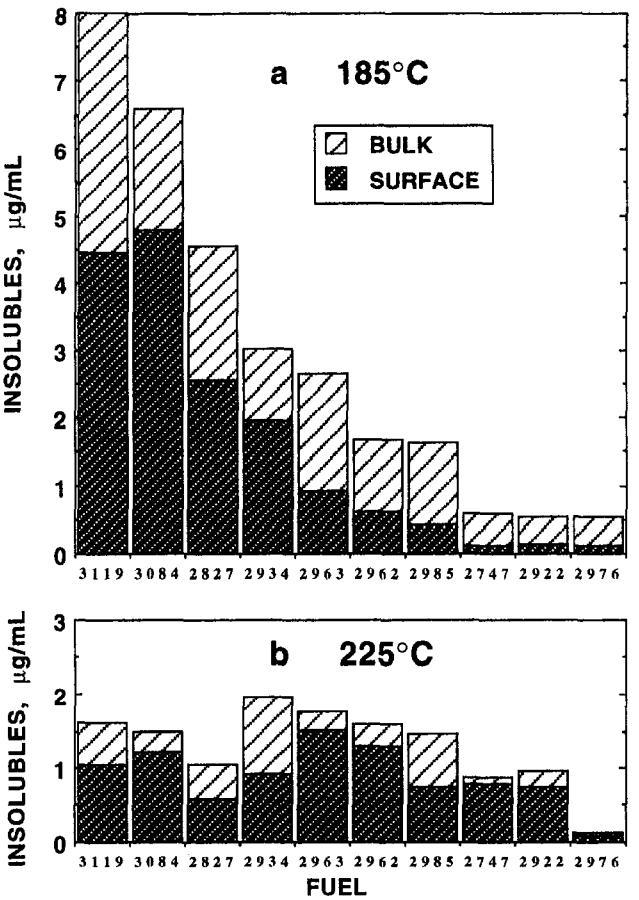

Fig. 5 Quantity of bulk and surface insolubles at 185 and 225°C

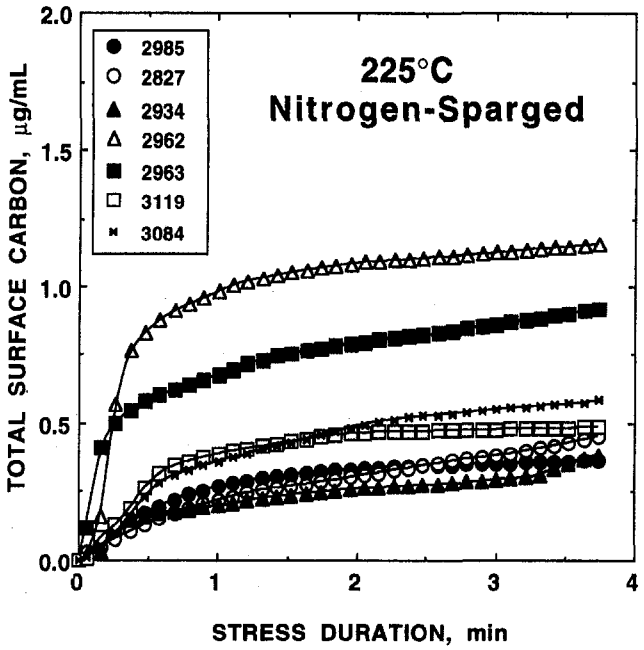

Fig. 6 Total surface deposition at 225°C in N_2-sparged fuel

The dependence of total bulk and surface insolubles on dissolved O_2 is given in Fig. 7 for four fuels, including data for O_2-sparging. It appears that for all of these fuels, some small amount of insolubles (on the order of 1 μg/mL) is formed—even under conditions of reduced O_2. Taylor and co-workers in a series of papers (Taylor, 1974; Taylor, 1976; Taylor and Frankenfeld, 1978; Frankenfeld and Taylor, 1980) have addressed the effects of deoxygenation on deposition in fuels. The suppression of deposits by deoxygenation was found to vary considerably among fuels and was found to depend on the distribution of trace sulfur, nitrogen, and oxygen-containing components.

Deoxygenation and its ramifications are beyond the scope of this study, but some comments can be made based on the current results. First, most of the deposition involving N_2-sparged or air-saturated fuel occurs primarily during oxidation and declines following O_2 depletion (see Figs. 4 and 6). This suggests that all deposition in the autoxidative region (<300°C) requires the presence of some O_2. The deoxygenation observations are explained according to the following reaction scheme:

$$RH + O_2 \rightarrow R^{\bullet} + (HOO^{\bullet}) \quad \text{Initiation} \qquad (1)$$

Case 1. Sufficient O_2 (air-saturated; conventional autoxidation).

$$R^{\bullet} + O_2 \rightarrow ROO^{\bullet} \quad \text{Propagation} \qquad (2)$$

$$ROO^{\bullet} + RH \rightarrow ROOH + R^{\bullet} \quad \text{Propagation} \qquad (3)$$

$$ROO^{\bullet} + ROO^{\bullet} \rightarrow \text{Non-radicals} \quad \text{Termination} \qquad (4)$$

$$ROOH \rightarrow RO^{\bullet} + HO^{\bullet} \quad \text{Self-Initiation} \qquad (5)$$

$$ROO^{\bullet}, ROOH + \text{Heteroatomics} \rightarrow \text{Insolubles} \qquad (6)$$

Case 2. Limited O_2 (N_2-sparged).

$$R^{\bullet} + \text{Olefins} \rightarrow \text{Polymerization} \rightarrow \text{Insolubles} \qquad (7)$$

Free radicals are first formed in the initiation reactions (1) and (5). In Case 1 (air-saturated fuel), insolubles from lesser quality fuels originate from the interaction of early autoxidation products such as peroxy radicals, $ROO^{\bullet}$, and ROOH with polar fuel components as in reaction (6). The small amount of insolubles formed from hydrotreated fuels probably does not originate from reaction (6) but rather from polar oxidation products. In Case 2 (N_2-sparged fuel), some O_2 is necessary for the initiation reaction (1); but at such low O_2 concentrations, the initial free radicals do not undergo propagation reactions (2) and (3) to form $ROO^{\bullet}$ and ROOH. They can, however, react with olefins in free-radical polymerization to produce insoluble oligomers that may contribute to surface fouling. Such polymerization reactions would not be significant at higher O_2 concentrations because O_2 serves as a polymerization inhibitor (Vollmert, 1973).

Possible Explanation of Dependence of Thermal Stability on Temperature. Two primary effects are proposed to account for the observed temperature dependence. The first is a chemical effect related to the least stable oxidation product, ROOH. Autoxidation in hydrotreated fuels is very similar to that in pure hydrocarbons and is dominated by the formation of ROOH, as in reactions (1)–(5). Because hydrotreatment removes natural antioxidants, hydrotreated or specialty fuels require the addition of synthetic antioxidants such as hindered phenols or phenylenediamines to improve storage stability (Turner et al., 1988). The absence of natural inhibitors in hydrotreated fuels reduces the importance of reaction (6), and only small quantities of insolubles are formed, as evidenced by the behavior of the treated fuels POSF-2747, -2922, and -2976. The lesser-quality fuels having heteroatom impurities such as sulfur react with $ROO^{\bullet}$ and ROOH, slowing autoxidation and leading ultimately to insolubles. At higher temperatures, the homolysis reaction (5), dissociation of ROOH on hot stainless-steel surfaces (Jones et al., 1996b), and other oxidation processes can compete with reaction (6), thereby limiting the quantity of insolubles. For hydrotreated fuels in which reaction (6) is not important, similar temperature effects would not be expected.

The second effect is a physical one, relating to the solubility and agglomeration of polar autoxidation products. Solubility is expected to increase with temperature, consistent with the current observations of reduced insolubles. The importance of agglomeration in deposition is demonstrated by observed reductions in insolubles with the use of detergent/dispersant additives at 140°C (Zabarnick and Grinstead, 1994) and at 185°C (Jones and Balster, 1995). There was, approximately, a 50 percent reduction observed using the dispersant additive 8Q405 at

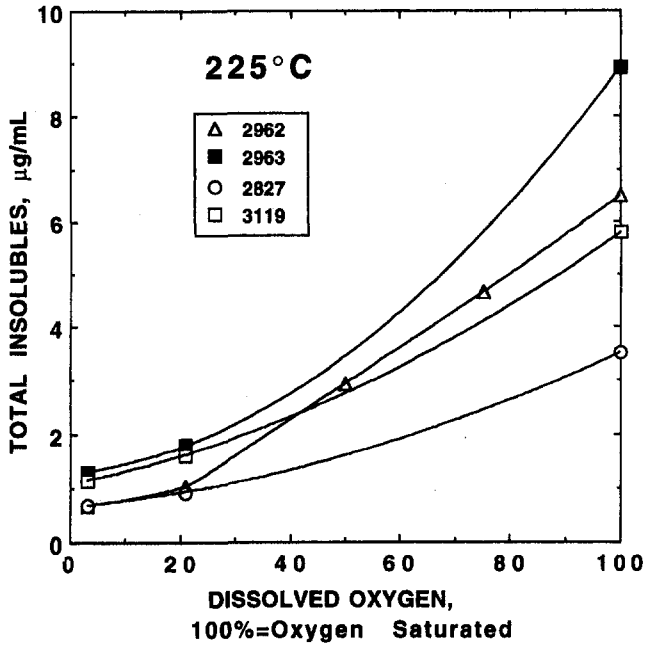

Fig. 7 Dependence of total insolubles on dissolved O_2 at 225°C

Table 2 Effect of 8Q405 (100 mg/L) at 225°C

fuel no.	surface, μg/mL	bulk, μg/mL	total, μg/mL
2963	1.50	0.27*	1.77*
2963, treated	0.80	~0*	0.80*
2962	1.29	0.31	1.60
2962, treated	0.65	0.47	1.12
2827	0.57	0.46	1.03
2827, treated	0.29	0.28	0.57

* Correction made for inherent bulk insolubles.

185°C for fuels POSF-2827, -2934, -2980, -3084, and -3119. We have also studied 8Q405 at 225°C; the results, given in Table 2, indicate similar reductions at the higher temperature.

Summary and Conclusions

The formation of surface insolubles at 185 and 225°C is found to occur predominantly during O_2 depletion and is attributed to autoxidation reaction products. At 225°C, an increase in the dissolved O_2 results in a corresponding increase in insolubles; however, reducing dissolved O_2 to 15 percent of the air-saturated value effects only slight reductions. It is argued in the latter case that some small amount of O_2 is needed for free-radical initiation, but the mechanism of surface fouling under deoxygenation switches from autoxidation to free-radical polymerization. This situation is not anticipated to occur under normal fuel conditions unless deoxygenation efforts are made.

In cases where all dissolved O_2 is consumed, we find that a broad range of fuels produces 0.3–7.5 μg/mL of surface insolubles at 185°C and 0.1–2 μg/mL at 225°C. The inverse dependence on temperature occurs for fuels having lower thermal stability, and it is attributed to reduced steady-state concentrations of ROOH and increased solubility at the higher temperatures. This has implications for ranking fuels based on the relative quantity of insolubles measured isothermally. It would appear that quantification of insolubles at 225°C does not provide a sufficient dynamic range of either bulk or surface insolubles for identifying unstable fuels. Because of demonstrated ability to flag unstable fuels and to quantify the effectiveness of additives, lower-temperature isothermal methods such as the QCM at 140°C (Zabarnick and Grinstead, 1994) and the NIFTR at 185°C (Jones and Balster, 1995) are preferred.

Acknowledgment

The authors would like to acknowledge Ms. L. Balster for conducting the O_2 depletion experiments and Mrs. M. Whitaker for editorial assistance. This work was funded by Wright Laboratory, Aero Propulsion and Power Directorate, Wright-Patterson Air Force Base, Ohio, under USAF Contract No. F33615-95-C-2507 and by the Air Force Office of Scientific Research.

References

Edwards, T., Anderson, S. D., Pearce, J. A., and Harrison, W. E., 1992, "High Temperature Thermally Stable JP Fuels—An Overview," AIAA Paper 92-0683. Presented at the AIAA 30th Aerospace Sciences Meeting and Exhibit, 6–9 January, Reno, NV.

Frankenfeld, J. W., and Taylor, W. F., 1980, "Deposit Formation from Deoxygenated Hydrocarbons, 4, Studies in Pure Compound Systems," *Industrial and Engineering Chemistry Product Research and Development,* Vol. 19, pp. 65–70.

Hazlett, R. N., 1991, *Thermal Oxidation Stability of Aviation Turbine Fuels,* ASTM Monograph 1, American Society for Testing and Materials, Philadelphia, PA.

Heneghan, S. P., and Zabarnick, S., 1994, "Oxidation of Jet Fuels and the Formation of Deposits," *Fuel,* Vol. 73, pp. 35–43.

Jones, E. G., and Balster, W. J., 1993, "Phenomenological Study of the Formation of Insolubles in a Jet-A Fuel," *Energy and Fuels,* Vol. 7, pp. 968–977.

Jones, E. G., and Balster, W. J., 1994, "Formation of Insolubles in a Jet-A Fuel: Temperature Effects," *Preprints-American Chemical Society, Division of Petroleum Chemistry,* Vol. 39, pp. 78–81.

Jones, E. G., and Balster, W. J., 1995, "Surface Fouling in Aviation Fuel: Short vs. Long-Term Isothermal Tests," *Energy and Fuels,* Vol. 9, pp. 610–615.

Jones, E. G., Balster, L. M., and Balster, W. J., 1995, "Quantitative Evaluation of Jet-Fuel Fouling and the Effect of Additives," *Energy and Fuels,* Vol. 9, pp. 906–912.

Jones, E. G., Balster, L. M., and Balster, W. J., 1996a, "Thermal Stability of Jet-A Fuel Blends," *Energy and Fuels,* Vol. 10, pp. 509–515.

Jones, E. G., Balster, L. M., and Balster, W. J., 1996b, "Autoxidation of Aviation Fuels in Heated Tubes: Surface Effects," *Energy and Fuels,* Vol. 10, pp. 831–836.

Kendall, D. R., and Mills, J. S., 1986, "Thermal Stability of Aviation Kerosenes: Techniques to Characterize Their Oxidation Properties," *Industrial and Engineering Chemistry Product Research and Development,* Vol. 25, pp. 360–366.

Pickard, J. M., and Jones, E. G., 1996, "Kinetics of the Autoxidation of a Jet-A Fuel," *Energy and Fuels,* Vol. 10, pp. 1074–1077.

Pedersen, C. J., 1949, "Inhibition of Deterioration of Cracked Gasoline during Storage," *Industrial and Engineering Chemistry,* Vol. 41, pp. 924–928.

Rubey, W. A., Striebich, R. C., Tissandier, M. D., Tirey, D. A., and Anderson, S. D., 1995, "Gas Chromatographic Measurement of Trace Oxygen and Other Dissolved Gases in Thermally Stressed Jet Fuel," *Journal of Chromatographic Science,* Vol. 33, pp. 433–437.

Striebich, R. C., and Rubey, W. A., 1994, "Analytical Method for the Detection of Dissolved Oxygen," *Preprints-American Chemical Society, Division of Petroleum Chemistry,* Vol. 39, pp. 47–50.

Taylor, W. F., 1974, "Deposit Formation from Deoxygenated Hydrocarbons, 1, General Features," *Industrial and Engineering Chemistry Product Research and Development,* Vol. 13, pp. 133–138.

Taylor, W. F., 1976, "Deposit Formation from Deoxygenated Hydrocarbons, 2, Effect of Trace Sulfur Compounds," *Industrial and Engineering Chemistry Product Research and Development,* Vol. 15, pp. 64–68.

Taylor, W. F., and Frankenfeld, J. W., 1978, "Deposit Formation from Deoxygenated Hydrocarbons, 3, Effects of Trace Nitrogen and Oxygen Compounds," *Industrial and Engineering Chemistry Product Research and Development,* Vol. 17, pp. 86–90.

Turner, L. M., Kamin, R. A., Nowack, C. J., and Speck, G. E., 1988, "Effect of Peroxide Content on the Thermal Stability of Hydrocracked Aviation Fuel," *Proceedings of 3rd International Conference on Stability and Handling of Liquid Fuels,* Institute of Petroleum, London, pp. 338–349.

Vollmert, B., 1973, *Polymer Chemistry,* Springer-Verlag, New York, NY, p. 62.

Zabarnick, S., and Grinstead, R. R., 1994, "Studies of Jet Fuel Additives Using the Quartz Crystal Microbalance and Pressure Monitoring at 140°C," *Industrial and Engineering Chemistry Research,* Vol. 33, pp. 2771–2777.

Characterization of Oscillations During Premix Gas Turbine Combustion

G. A. Richards
gricha@fetc.doe.gov

M. C. Janus
Federal Energy Technology Center,
3610 Collins Ferry Road,
Morgantown, WV 26507-0880

The use of premix combustion in stationary gas turbines can produce very low levels of NO_x emissions. This benefit is widely recognized, but turbine developers routinely encounter problems with combustion oscillations during the testing of new premix combustors. Because of the associated pressure fluctuations, combustion oscillations must be eliminated in a final combustor design. Eliminating these oscillations is often time-consuming and costly because there is no single approach to solve an oscillation problem. Previous investigations of combustion stability have focused on rocket applications, industrial furnaces, and some aeroengine gas turbines. Comparatively little published data is available for premixed combustion at conditions typical of an industrial gas turbine. In this paper, we report experimental observations of oscillations produced by a fuel nozzle typical of industrial gas turbines. Tests are conducted in a specially designed combustor capable of providing the acoustic feedback needed to study oscillations. Tests results are presented for pressures up to 10 atmospheres, with inlet air temperatures up to 588 K (600 F) burning natural gas fuel. Based on theoretical considerations, it is expected that oscillations can be characterized by a nozzle reference velocity, with operating pressure playing a smaller role. This expectation is compared to observed data that shows both the benefits and limitations of characterizing the combustor oscillating behavior in terms of a reference velocity rather than other engine operating parameters. This approach to characterizing oscillations is then used to evaluate how geometric changes to the fuel nozzle will affect the boundary between stable and oscillating combustion.

Introduction

Lean premix combustion is now accepted as a standard approach to reduce NO_x emissions from stationary gas turbine combustors. The lean-premix (LPM) combustor is designed to avoid high-temperature, stoichiometric combustion that produces NO_x by the thermal mechanism. With careful premixing of fuel and air, it is possible to achieve both excellent NO_x and CO emissions. Development programs from several turbine vendors include various versions of the LPM concept to achieve the lowest possible pollutant emissions (Alsup et al., 1995).

Although premixing fuel and air can produce very low NO_x emissions, practical application of LPM combustion is restricted by the problem of operating very close to the lean flammability limit. Slight changes in operating conditions can lead to sudden flame extinction, or to excessive CO emissions. This problem of flame static stability is often addressed by adding a smaller pilot flame to anchor the main premix flame. By operating the pilot flame closer to stoichiometric, the main flame can be maintained even during momentary upsets. The drawback is that the pilot contributes to NO_x emissions.

In addition to static stability, LPM combustors must achieve dynamic stability, meaning the combustion must not oscillate. It has been common experience that operation near the lean-extinction limit is often accompanied by oscillating combustion. Oscillation must be eliminated in a final combustor design because the associated pressure fluctuations can shorten the engine component lifetime. Keller (1995) discusses the significance of this problem, and points out that operation near the lean limit is especially prone to oscillation problems. Near the lean limit, minor variations in fuel/air ratio lead to appreciable variations in combustor reaction rate. When these variations in reaction rate couple to acoustic modes, significant pressure oscillations can occur with frequencies ranging from hundreds to thousands of Hertz.

Few studies of LPM combustion oscillation have been reported at representative gas turbine conditions. In practice, the task of studying (and eliminating) combustion oscillation in a gas turbine is complicated by the specific acoustic response of a given combustor design. Thus, no general trends have been proposed to describe the effect of usual gas turbine parameters such as inlet air temperature, operating pressure, and equivalence ratio. The effect of these parameters is not well understood. Consequently, tests of proposed oscillation remedies are complicated because it is difficult to specify an appropriate test matrix.

In this paper, we report observations of oscillations from a premix combustor that is specially designed to study oscillations at gas turbine operating conditions. Test results are presented for pressures to 10 atmospheres, with inlet air temperatures to 589 K (600 F). Results are compared to expectations from a simple model for combustion oscillations.

Background

Previous studies of combustion oscillations have focused on various technical applications. During the 1960s, considerable research was devoted to solving the problem of combustion oscillations in liquid rocket motors. An excellent review of this research was published in 1972 by Harrje and Reardon. Recent progress in liquid rocket combustion oscillations is described in the text edited by Yang and Anderson (1995). Routine problems with oscillating combustion during industrial burner development are discussed in the textbook by Putnam (1971). Schadow and Gutmark (1991) summarize a series of studies on the oscillations due to periodic vortex shedding in dump combustor

Contributed by the International Gas Turbine Institute and presented at the International Gas Turbine & Aeroengine Congress & Exhibition, Orlando, FL, June 2–5, 1997. Manuscript received by the ASME Headquarters July 1997. Paper No. 97-GT-244. Associate Technical Editor: H. A. Kidd.

applications. Candel (1992) reviews the oscillating mechanism in a number of burner applications.

Few previous studies have analyzed oscillations from premixed, swirl-stabilized flames that are typical of modern gas turbine combustors. Sivasegaram and Whitelaw (1991) studied oscillating combustion in swirl-stabilized flames, but the focus of the research was not on the discrete-tone oscillations that are typical of LPM combustors. Richards and Yip (1995) report preliminary data from a laboratory-scale burner that incorporates swirl-stabilization and a pilot flame similar to many gas turbine fuel nozzles. These authors showed that some oscillations could be described by the time-lag approach (described later). However, these lab-scale tests were limited to one atmosphere pressure and ambient inlet air temperature. A small number of articles report combustion oscillations at gas turbine conditions (Mehta et al., 1990a, b), but focus on liquid-fueled aeroengine applications.

The exact features of specific burner configurations introduce a variety of mechanisms responsible for sustaining combustion oscillations. Variations in heat release can result from changes in mixing, changes in the supply of fuel and/or air, vortex shedding, or other mechanisms. In a practical application, it is often difficult to identify the mechanism responsible for variations in the heat release because several mechanisms can occur simultaneously, or may be dominant at different operating conditions. For example, pressure disturbances in a combustion chamber will change the instantaneous delivery of fuel and air or both, and all of these will affect the heat release. To date, there has been no general approach to account for the combined variation of these and other parameters. Feiler and Heidman (1967) proposed that stability behavior can be analyzed with a linear combination of the various mechanisms, but this method ignores the interaction between mechanisms.

No matter what the specific mechanism, all oscillations involve a feedback between variation in the local heat release rate $Q(t)$ and the acoustic pressure field inside the combustor $P(t)$. The well-known Rayleigh criterion (Rayleigh, 1878) states that oscillations will be likely if the changes in heat release are in phase with the acoustic pressure disturbances. Conversely, oscillations are dampened if the heat release fluctuations are out of phase with pressure oscillations. It is necessary to integrate across the entire combustor volume to evaluate the cumulative effect of local fluctuations because P and Q are functions of both space and time. For clarity in this discussion, we consider just the time dependence.

The Rayleigh criterion has been the cornerstone for the development of many analyses of combustion oscillations. As early as 1956, Merk developed a linear analysis for premixed combustion oscillations that predicted stable and oscillating regions as a function of burner heat output. Merk proposed that heat release variation would result from changes in flame structure produced by acoustic pressure disturbances. The time delay between the pressure disturbance and the heat release variation determined the phase, and, therefore, whether the system was stable or likely to oscillate. In a similar fashion, characterization of oscillating combustion in liquid rockets was also recognized to depend upon a time delay (or time lag) between acoustic pressure and the subsequent variation in heat release rate (Crocco and Cheng, 1956). As explained by Harrje and Reardon (1972), the time lag and the gain of the system (denoted by n) have been widely used to explain experimental data from rocket oscillations. Likewise, Putnam's approach to solving oscillations in industrial burners relies on determining the time lag between $P(t)$ and $Q(t)$; see Putnam (1971).

Based on these earlier studies, it is reasonable to expect that oscillations from LPM combustors can be characterized by a simple time lag approach. Figure 1 shows a schematic of the important processes, for a specific case, where a sinusoidal pressure disturbance produces a sinusoidal variation in the air flow, but 180 degrees out of phase with the pressure. As shown,

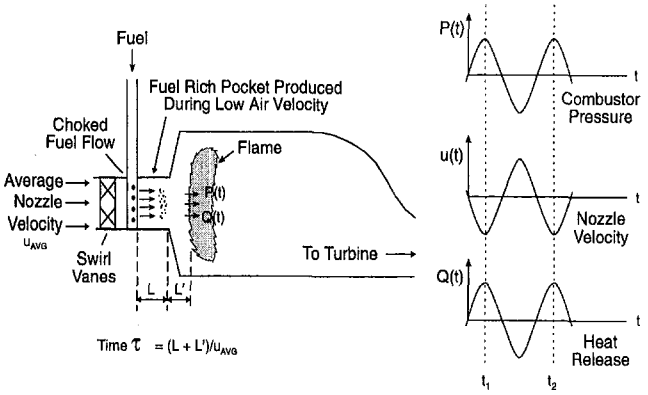

Fig. 1 Schematic of processes in an example oscillation. In this example, the pressure $P(t)$ changes the air flow. The air velocity $U(t)$ is 180 deg out of phase with the combustor pressure, and produces a fuel-rich pocket at time t_1. This pocket arrives at the flame to increase $Q(t)$ at time t_2.

the time lag τ is estimated as the distance between the point of fuel injection and flame front divided by the average axial velocity:

$$\tau = (L + L')/U_{avg}, \tag{1}$$

where L is the distance from the fuel injection point to the tip of the nozzle, L' is the distance from the tip of the nozzle to the flame front, and U_{avg} is the average velocity of mixture in the fuel nozzle.

In this example, a positive pressure fluctuation in the combustor produces a momentary decrease in air flow. We assume that the fuel supply is choked, so that the fuel flow rate does not change as the pressure varies. Thus, the reduced air flow receives a proportionally higher amount of fuel, creating a fuel-rich pocket. This richer pocket will arrive at the flame front with a time lag given by (1). If this "extra" fuel produces an immediate increase in the heat release, oscillations will be most likely when the peak of the pressure fluctuation is in phase with the increased heat release; i.e., when the time lag $t_2 - t_1$ is an integer multiple of the acoustic period. This criterion for oscillations can be stated as

$$(\text{time lag})/(\text{acoustic period}) = 1, 2, 3 \ldots \tag{2}$$

Noting that the acoustic period is the reciprocal of frequency f, and using (1), we have

$$(\text{time lag})(\text{frequency}) = 1, 2, 3 \ldots \text{ or,}$$

$$f(L + L')/U_{avg} = 1, 2, 3 \ldots \tag{3}$$

This is a restatement of Rayleigh's criterion, and it again requires that the heat release and pressure fluctuations should be in phase to promote oscillations. In practice, it is not necessary that the heat release and pressure be exactly in phase to drive oscillations. Some driving will occur for heat release fluctuations that lead or lag the pressure by as much as $\frac{1}{4}$ of the acoustic cycle (Putnam, 1971). Thus, there is a range of plus/minus 0.25 around each integer in the series (3) where driving is possible, but driving is greatest for the integer values where the pressure and heat release are exactly in phase.

The criterion (3) is specific to the example where positive pressure produces an immediate decrease in air flow, and assumes that the fuel-rich pocket produces an immediate increase in reaction rate when it arrives at the flame front. In practice, other mechanisms for variable heat release can complicate the criterion for oscillations such that the series expressed by (2) will have numeric values other than 1, 2, 3 . . . , etc. Richards and Yip (1995) show that a similar criterion can be developed which accounts for the fuel system impedance, or can also

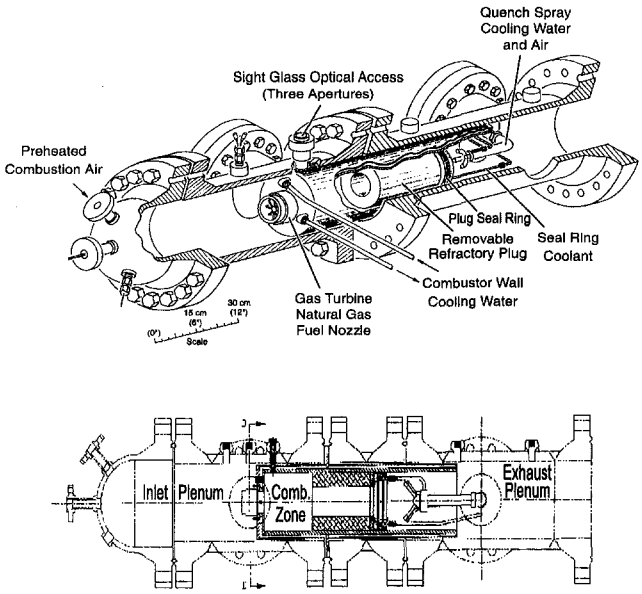

Fig. 2 Cutaway and cross-section view of the experimental combustor

describe oscillations apparently linked to transport of tangential velocity from the fuel nozzle swirl vane. Putnam (1971) analyzed industrial burners and showed how to account for the geometry of the flame front in determining the numeric series.

Although the numeric series (3) will be different for different situations, the idea that oscillations can be characterized using the average nozzle velocity provides a convenient starting point to analyze data from gas turbine tests. In a gas turbine, the fuel nozzle mass flow, pressure, and inlet air temperature are all variables. This complicates evaluation of nozzle stability because tests must be conducted over a wide range of parameters. In contrast, if Eq. (3) is valid, tests can be conducted over a range of nozzle velocities, rather than independent values of mass flow, pressure, or inlet air temperature.

The proposed approach is complicated by the flame standoff distance L'. Clearly, as the equivalence ratio rises, or as the inlet air temperature is increased, the premixed flame speed will rise, and the flame standoff will decrease. The geometry of the flame will introduce further complication in determining L'. Although these complications are recognized, in this paper we will evaluate the stability behavior of a fuel nozzle based on the simple concept of a fixed flame standoff. The experimental description is provided in the next section.

Experimental Description

A cutaway view of the experimental combustor is shown in Fig. 2. Combustion facilities at the Federal Energy Technology Center (FETC) can supply up to 1.4 kg/s (3 lbm/s) of unvitiated inlet air at temperatures up to 840 K (1050 F) and pressures up to 30 atmospheres. The experiment described here is limited to pressures up to 10 atmospheres by certain components in the pressure vessel design. The facilities include gas sampling capabilities for major species such as NO_x, CO, and UHC. (See Halow et al. (1994) for a complete description of the facility capabilities.)

Preheated combustion air enters the combustor inlet plenum and is diffused by a series of three perforated plates (not shown) located at the left end of the plenum. Air passes through the premixing fuel nozzle and into the combustion zone. The combustion zone is enclosed by a water-cooled liner with 19.8 cm (7.80 in) inside diameter. The water-cooled liner is fitted with a removable refractory plug. The plug inside diameter of 10.4 cm (4.10 in) forms an exhaust "neck" that provides an acoustic response. The plug length is 22.9 cm (9.00 in). The combination of the combustion zone volume and the mass of gas in the exhaust neck approximates a classic acoustic Helmholtz resonator. As described by Richards et al. (1997), the water-cooled walls and the refractory plug form a "hard" acoustic boundary. The use of hard acoustic boundaries (as opposed to an air-cooled liner) provides appreciable acoustic feedback, and, therefore, promotes the occurrence of oscillations near the natural frequencies of the systems. The rationale for the acoustic design of this test combustor is described in Richards et al. (1997). After the refractory plug, cooling water is sprayed into the exhaust stream to quench the combustion products that exhaust through a back-pressure control valve.

The combustor dynamic pressure was recorded with a Kistler Model 206 pressure transducer mounted outside the pressure vessel. This avoids the need to locate the transducer in a high-temperature environment. To prevent signal distortion by the connecting tube, we used the transducer connection described by Mahan and Karchmer (1991) and Englund and Richards (1984). The transducer was mounted on a small side branch of 4.8 mm (0.188 in) ID tube connected to the combustor interior. The side branch was located 61 cm (24 in) from the combustor interior, with 10 m (33 ft) of terminating tubing attached beyond the point of the transducer side branch. In other words, the transducer was mounted on a small side branch of a very long tube. The long tube approximates an infinite waveguide so that pressure signals are transmitted down the waveguide but dissipated by the length of tubing beyond the side branch. Mahan and Karchmer (1991) show that this approach to signal measurement produces little signal distortion and typically less than 1 dB attenuation for frequencies below 1000 Hz.

The oscillating heat release was recorded using a fiber optic probe to view the emission from the electronically excited hydroxyl radical (OH*). For this radical, the radiative decay to ground state occurs approximately one microsecond after formation during combustion reactions (Gaydon, 1974). Because the excited state exists only momentarily during the combustion reaction, radiative emission (310 nm) is a measure of the combustion heat release. Many studies have shown that OH* emission is proportional to heat release; see Mehta et al. (1981), Keller and Saito (1987), Keller et al. (1990), and Samaniego et al. (1995) for more details. Here, we are concerned only with the phase of the heat release relative to the pressure, so no attempt is made to calibrate the OH* signal to the actual heat release. The fiber optic probe used here was made from a sapphire rod (1.6 mm) (0.063 in) inserted through the pressure vessel in a standard compression fitting using graphite ferrules. (See Richards et al. (1997) for details of the probe construction.)

The probe was located 2.54 cm (1 in) downstream of the fuel nozzle exit plane, viewing across the combustor diameter in a conic region with a 15 deg included angle. This viewing angle does not record emissions from the entire flame region, but was taken as a representative measure of the fluctuating heat release near the fuel nozzle. The ends of the sapphire rod were polished to allow coupling to a UV-transmissive fiber optic cable. The cable was terminated at the focal point of a UV transmissive lens, which allowed beam expansion to 25.4 mm (1 in). An interference filter (310 nm) and photomultiplier tube (PMT) are used to record the signal from the fiber optic probe. The PMT amplifier response was essentially linear over the range of frequencies of interest (less than 2 kHz).

Both the OH* and pressure signals were recorded using a TEAC RD-135T digital tape recorder with a sampling rate of 12 kHz. Signals were analyzed for frequency content, correlation, and root-mean-square (RMS) values using standard signal analysis software available on the TEAC recorder or on a desktop personal computer.

The fuel nozzle was designed to quickly investigate geometric changes in the nozzle design. The assembled nozzle is shown

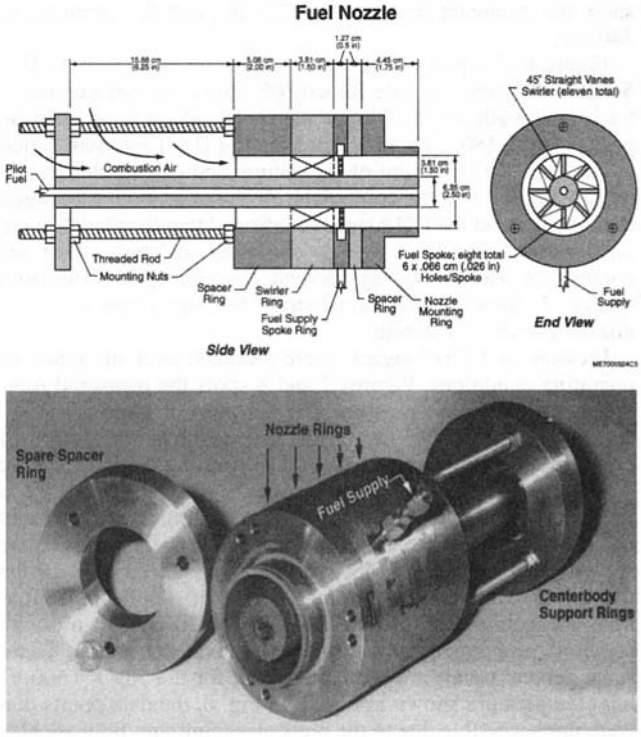

Fig. 3 Sketch and photographs of the fuel nozzle. The fuel nozzle is comprised of various "rings" which can be stacked on the threaded rods to produce different nozzle geometries. Eleven straight-blade vanes (set at 45 deg) provide swirl.

in Fig. 3. The nozzle consists of a series of rings stacked on three threaded rods as shown. The nozzle centerbody is cantilevered from a support ring attached to the end of the threaded rods. Up to the maximum centerbody length, the threaded rods can be fitted with various spacer rings to study the effect of different nozzle geometries. Pilot fuel is injected through the centerbody on the nozzle axis. Pilot fuel was used for ignition only, and not during the combustion tests reported here. Combustion air passes through the annular region between the centerbody and surrounding rings. Eleven straight-blade vanes generate swirl in the nozzle annulus and provide mechanical support for the centerbody. The vanes are set at 45 deg to the nozzle axis, and are 0.32 cm (0.13 in) thick. The main fuel is injected by eight fuel spokes manufactured from standard 0.32 cm ($\frac{1}{8}$ in) stainless steel tubing. Fuel is distributed to each spoke by an annular passage inside the ring. Each fuel spoke has six 0.066 cm (0.022 in) holes perpendicular to the axis of the nozzle. These holes were sized to insure that the fuel supply would be choked at the point of fuel injection during most operating conditions. Thus, oscillations produced by this fuel nozzle are not the result of fuel system acoustics.

We point out that practical fuel nozzles are typically not choked, and, therefore, fuel system acoustics may be a consideration in combustion oscillations. However, for development purposes, it is possible to choke the fuel supply and to characterize other oscillating mechanisms as done here. Comparison to the unchoked nozzle behavior will then help identify the contribution of fuel system acoustics versus other mechanisms. As explained earlier, the combined effect of various mechanisms may complicate data interpretation, and this complication was avoided by choking the fuel supply.

The fuel (natural gas) was supplied from the local gas company, and pumped to 4.1 MPa (600 psig) prior to metering and injection to the fuel nozzle. The high fuel pressure allowed choking the fuel nozzle even at relatively low fuel flow rates, but still allowing operation at higher flow rates. The (nominal) fuel composition was 94 percent CH_4, 4 percent C_2H_6, 1 percent C_3H_8, and 1 percent inerts and higher hydrocarbons. Equivalence ratios reported here were established with a precision of better than plus/minus 0.01 at each operating condition. Fuel and air flow rates are metered by standard orifice runs. The absolute accuracy of all flow loops was better than 97 percent, compared to flow-proving performed with sonic nozzle flow meters.

Shih et al. (1996) have recently shown that the level of premixing is an important consideration in characterizing combustion oscillations. We recognized that tests conducted with inadequate premixing would not be representative of LPM combustor design. To ensure that the nozzle described in Fig. 3 produced a uniform flow of premixed fuel and air, we conducted a series of cold-flow studies using CO_2 as a tracer gas. Using the same nozzle velocity as in the hot-flow tests, CO_2 was injected at the same volume flow rate as fuel used in the actual hot flow tests. A sampling probe made from 3.2 mm (0.125 in) tubing was then used to traverse the exit plane of the nozzle. The measured CO_2 concentration was essentially flat across the nozzle face, indicating that premixing was complete. We mention that an initial nozzle design incorporated vanes that were half of the length of those shown in Fig. 3. The cold-flow premixing studies showed that the shorter vanes did not produce a uniform velocity downstream of the vanes, and the resulting CO_2 concentration was not uniform. In contrast, the longer vanes used here produced very uniform premixing.

Before studying the oscillating characteristic of the fuel nozzle, a limited number of combustion test points were sampled for CO and NO_x emissions. These data are presented as further validation that the fuel nozzle was indeed providing excellent premixing. Emissions were measured in the exhaust stack after the combustion gases were quenched by the spray cooling water. Stack temperature established by quenching was maintained at less than 477 K (400 F) to minimize any post-quench reactions. The sampling probe (not shown in Fig. 2) was located more than 3 m (10 ft) from the quench point but prior to the backpressure control valve. The sampling probe is a 6.4 mm (0.25 in) tube placed across the diameter of the exhaust stack, with multiple holes drilled along the length of the probe to ensure that the extracted sample is a spatial average of the stack gases. Measurements are reported on a dry basis corrected to 15 percent oxygen after assuring mass closure from the flow loops versus the measured CO_2 concentration. Figure 4 is a plot of NO_x and CO emissions as a function of equivalence ratio. The reported emissions are typical of premixed burner designs (Lovett and Mick, 1995), and, as expected, flame blowoff occurred for an equivalence ratio near 0.52. These combustion data affirm

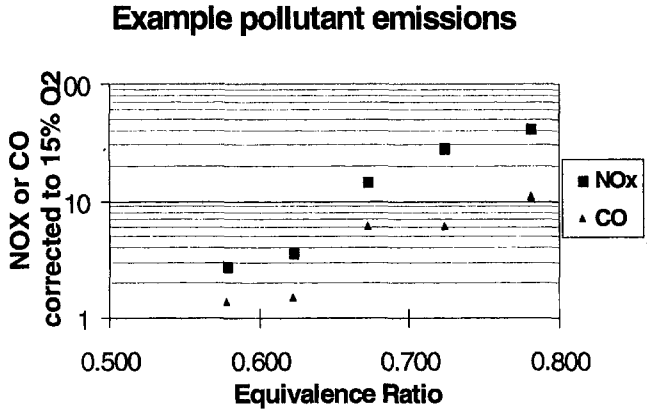

Fig. 4 NO_x and CO emissions (PPMV, corrected to 15% O_2, dry basis) as a function of equivalence ratio. Experimental conditions are 5 atmospheres pressure, 533 K (500 F) inlet air temperature, 40 m/s reference velocity.

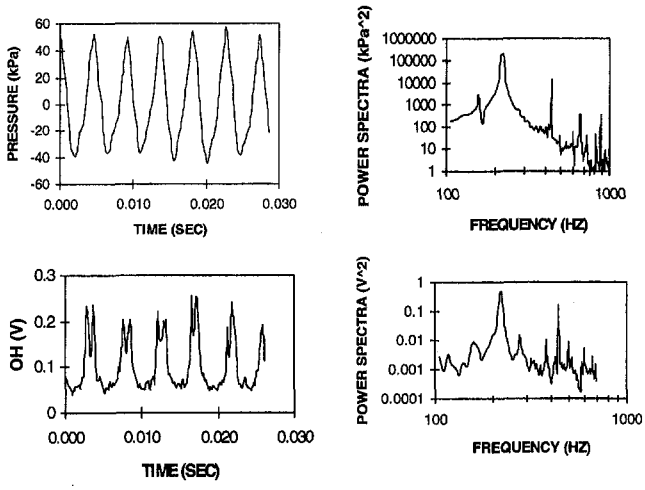

Fig. 5 Example of oscillation. Tests conditions: 7.5 atmospheres, 533 K inlet temperature, equivalence ratio 0.77, (average) nozzle velocity 30 m/s. The OH* signal represents the oscillating heat release. The spectra show that the dominant frequency of oscillation is 220 Hz at this condition. Other operating conditions produced appreciable RMS signals (i.e., greater than 0.5 percent of the operating pressure) between 180 and 250 Hz.

the excellent premixing observed in the cold-flow studies described above.

Experimental Results

As explained above, oscillating characteristics of the nozzle were recorded as a function of the nozzle reference velocity. The range of various test parameters is shown below. Because of the desire to choke the fuel supply at even relatively low fuel flows, some higher flow operating conditions were not accessible due to limits on the maximum fuel supply pressure. Likewise, some low air-flow conditions were inaccessible due to the minimum flow requirements of the combustion air preheater. Aside from these limitations, tests were conducted at the following conditions:

Inlet Air Temperature: 533, 589 K (500, 600 F)
Pressure: 5, 7.5, 10 atmospheres
Equivalence Ratio: 0.59, 0.63, 0.67, 0.71, 0.77
Nozzle Velocity: 30, 40, 50, 60 m/s (98, 131, 164, 197 ft/s)

Over this range of parameters, oscillations with frequencies ranging from approximately 190 Hz to 240 Hz were observed, depending upon operating conditions. Figure 5 is an example of the time history of one oscillation. The nozzle velocity is 30 m/s, with other conditions indicated on the figure. The figure shows both the history of the oscillating pressure and the heat-release fluctuation as measured by the flame OH* emission. The pressure signal was phase shifted to account for the remote transducer location by simply accounting for the speed of sound traveling in the connecting tube.[1] In accordance with Rayleigh's criterion, the pressure and OH* signals are approximately in phase, driving significant oscillations. The "dual peak" signal in the OH* time history shows that the heat-release fluctuation includes some complex features that we did not investigate further for this paper, but are the subject of current analysis. The spectra corresponding to both pressure and OH* signals show the dominant frequency of 220 Hz, and the harmonic at 440 Hz.

Figure 6 is a plot of the same combustor signals as in Fig. 5, but with a higher nozzle velocity (50 m/s). Here, the combustor is essentially steady. Notice the spectra show weak acoustic peaks at 150, 180, 215, 225, 269, and 454 Hz. This small signal is the result of excitation of the natural acoustic modes by the air moving through the combustor. A cross correlation between the pressure and the OH* signal confirmed that the signals were only weakly correlated at this condition, indicating that the combustion was not driving the weak acoustic signal. Compared to Fig. 5, these results demonstrate the significant effect of nozzle velocity on stability.

Pressure and OH* signals were recorded over the range of operating conditions. Figures 7 and 8 show the measured root-mean-square (RMS) pressure as a function of nozzle velocity and equivalence ratio. The vertical scale is the normalized RMS pressure expressed as a percent of the operating pressure. Figure 7 shows results for an inlet temperature of 533 K (500 F) at pressures 5, 7.5, and 10 atmospheres. Data points which could not be reached due to limits on the fuel supply pressure are shown as having zero RMS, with an "X" placed through the data point. Comparing the graphs, note that significant oscillations are confined to nozzle velocities of 30 and 40 m/s and are most pronounced at the highest equivalence ratios. These same general trends are seen in the data for the 589 K (600 F) inlet temperature shown in Fig. 8. In Fig. 8, the data points that were not accessible due to the preheater minimum flow are also marked with an "X".

We point out that the higher inlet temperature cases do show a modest reduction in RMS pressure along the 40 m/s velocity. In a study of the effect of inlet air temperature, Janus et al. (1997) have shown that increased inlet temperature should move the stability boundary to lower values of nozzle velocity. This behavior is approximately evident when comparing Figs. 7 and 8, but not very distinct. More data, at a finer spacing of velocity, would be needed to clearly capture this behavior.

Aside from the similarity in the general shape of the instability regions, Figs. 7 and 8 also show that the normalized RMS pressure is approximately similar at different operating pressures. For example, if we compare the data in Fig. 7 at 40 m/s, 0.77 equivalence ratio, the RMS pressure is a constant 5 percent for operating pressures of 5, 7.5, and 10 atmospheres. Thus, the actual RMS scales directly with the operating pressure. This observation is consistent with results from other stud-

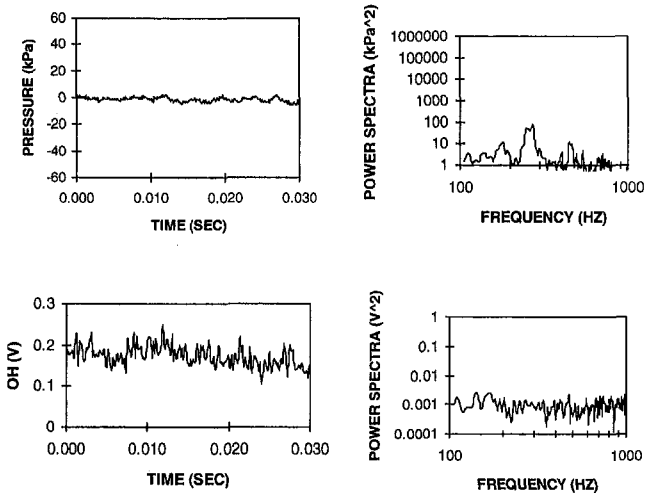

Fig. 6 Combustor signals at 50 m/s nozzle velocity. Other conditions are the same as in Fig. 5. Combustion is steady at these conditions. Spectral peaks in the pressure signal are due to acoustic excitation of resonant frequencies.

[1] The infinite waveguide transmits the signal from the combustor to the transducer side branch. The delay for this transmission is simply the length to the side branch, divided by the speed of sound in the tube. We estimated the speed of sound at the average temperature of the combustion air supply because the waveguide tube is bathed by the (heated) air supply over most of its length. Based on these assumptions, the delay is 1.4 ms.

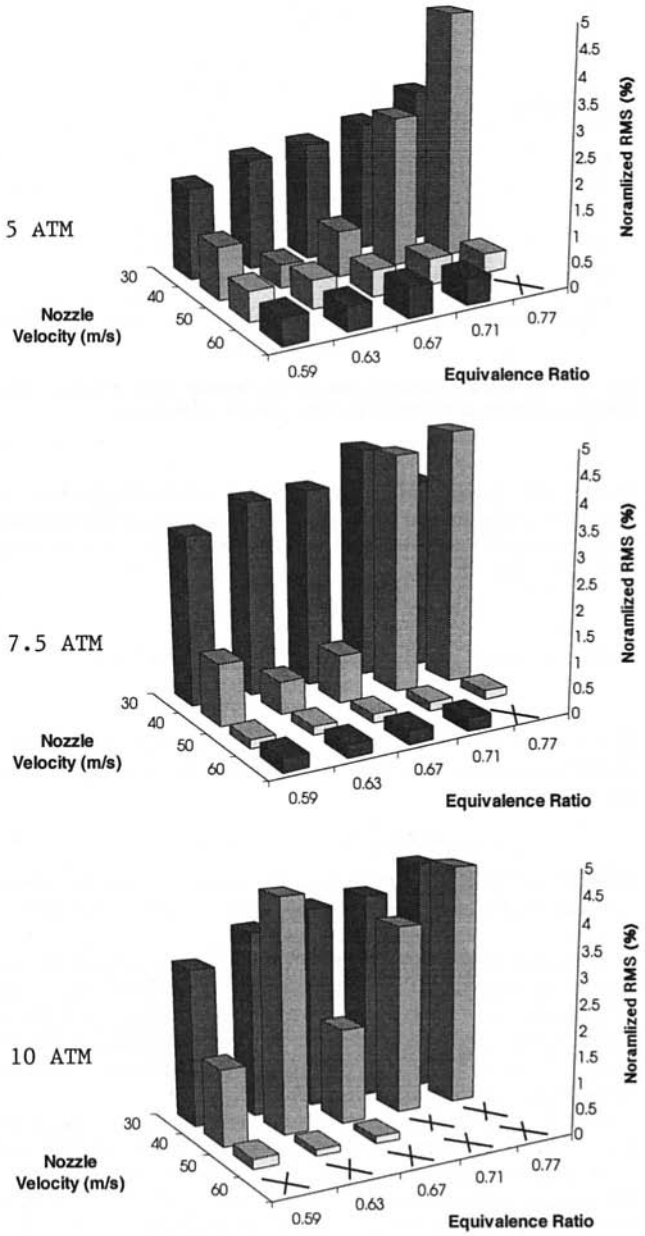

Fig. 7 **Root-mean-square (RMS) pressure as a function of nozzle velocity and equivalence ratio. The RMS pressure is expressed as a percentage of the operating pressure. Inlet air temperature: 533 K. Conditions marked with 'x' were not accessible.**

ies. Based on theoretical considerations, Narayanaswami and Richards (1996) have shown that RMS pressure in an oscillating (pulse) combustor will scale directly with pressure as long as the mixing and chemical reaction rate in the combustor are not appreciably affected by operating pressure. In an experimental study of pressurized pulse combustion, Gemmen et al. (1995) showed that the normalized RMS pressure was only a weak function of operating pressure, and the observed dependence was explained by modest changes in the chemical reaction rate.

Thus, useful estimates of the expected RMS pressure at various operating pressures can be directly scaled from data at other operating pressures. For example, small-amplitude oscillations encountered during low-cost atmospheric pressure tests should not be dismissed during combustor development because the actual RMS may be unacceptably large during pressurized testing. It is emphasized again that this conclusion depends on the specific mixing and reaction response to changes in operating pressure, and may need to be tested experimentally in specific cases. Nevertheless, the data in Figs. 7 and 8 show that in this nozzle (which is typical of LPM combustor designs) the RMS can be approximately estimated by scaling from various pressures.

The shape of the instability region for all plots in Figs. 7 and 8 shows a surprisingly consistent series of trends, with a few interesting exceptions. It is particularly instructive to compare the behavior of the RMS versus equivalence ratio at a nozzle velocity of 40 m/s. Generally, the RMS reduces to a minimum at equivalence ratio 0.63, but a notable exception occurs for the 10 atmosphere 533 K case (Fig. 7). Here, the RMS is very large, almost 5 percent. Why is this point anomalous? A careful analysis of the time history at this operating condition revealed that the limit cycle oscillation was unstable and would intermittently alternate between low and high RMS values. A plot of the combustor pressure during several of these transitions is shown in Fig. 9. Notice that the oscillation amplitude cycles at a very low frequency so that the measured RMS plotted in Fig. 7 is really not a meaningful characterization of the oscillation.

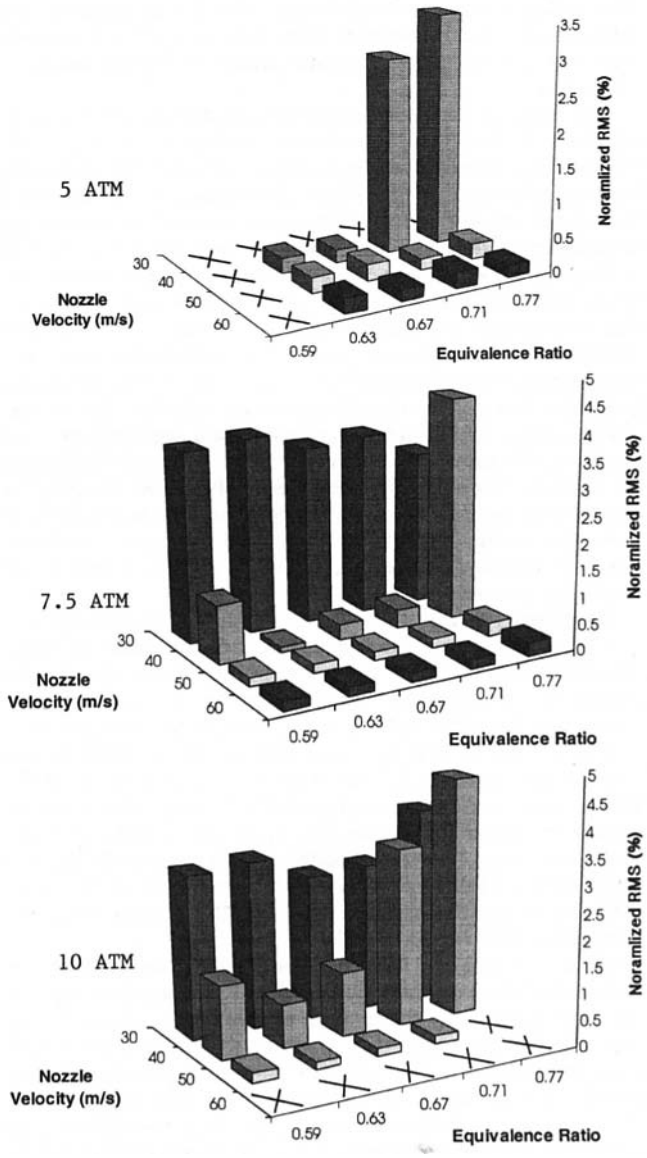

Fig. 8 Root-mean-square (RMS) pressure as a function of nozzle velocity and equivalence ratio. The RMS pressure is expressed as a percentage of the operating pressure. Inlet air temperature: 589 K. Conditions marked with 'x' were not accessible.

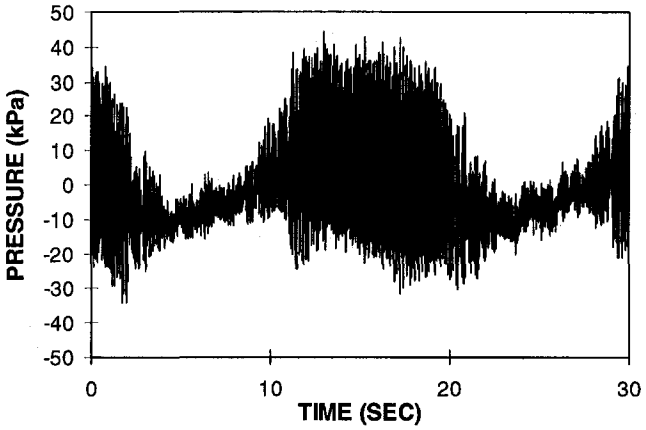

Fig. 9 Time history of oscillating pressure at anomalous condition (40 m/s reference velocity, 10 ATM, 533 K inlet temperature, equivalence ratio 0.63). Note that the time scale is 30 s. The amplitude of the oscillation varies substantially during this 30 s period.

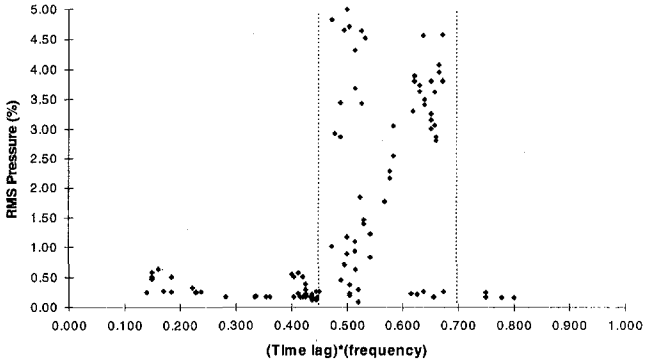

Fig. 10 Plot of RMS pressure versus the product of time lag and frequency. All of the data shown in Figs. 7 and 8 are included.

This behavior was observed during several tests occurring on different days at this operating point, confirming that the results were not a peculiar experimental artifact occurring during a single test.

This irregular oscillation apparently exists right at the boundary between steady and oscillating combustion. Knoop et al. (1996) have recently reported control of so-called hysteresis boundaries in step-stabilized flame oscillations. These hysteresis boundaries are difficult to characterize because the oscillating amplitude may depend on the history of the combustor operation so that slight disturbances can either stabilize or activate oscillations. Although it is not clear that conditions associated with Fig. 9 constitute a formal hysteresis boundary,[2] the irregular behavior of the combustor provides a caution that unwitting operation near the oscillation boundary can lead to significant problems. Very slight changes in nozzle velocity (due to machining errors in new engines, or combustor seal wear in older engines) can move the combustor from stable to oscillating combustion. These types of boundaries should be identified in new combustor testing, with appropriate nozzle changes to move the nozzle velocity away from the irregular condition. Plots of combustor dynamics, as shown in Figs. 7 and 8, are useful for this purpose.

Oscillations produced by a simple time lag should obey Eq. (3). As already stated, we cannot precisely determine the flame standoff distance L', and we cannot accurately account for the change in L' as operating conditions change. Recognizing these limitations, Fig. 10 is a plot of Eq. (3) for all the data presented in Figs. 7 and 8. We estimated that the flame standoff was constant and equal to 2.5 cm (1.0 in), and we plotted all the RMS data as a function of the nozzle velocity, and observed peak in the frequency spectra. The figure shows that significant oscillations were indeed confined to a small range of the product (time lag) × (frequency). When this product is in the range 0.45 to 0.70, oscillations were observed. Outside this range, the RMS pressure was very small.

Figure 10 suggests that the oscillations observed here are indeed described by a simple time lag. When the time lag was the correct fraction of the acoustic period, oscillations occurred. The time lag was changed by studying the effect of the nozzle velocity on stability. The time lag can also be changed by increasing L (the length of the fuel nozzle). According to (3), if we increase L, then oscillations given by a specific constant will occur at a higher velocity. For example, we showed in Fig. 10 that the stability boundary occurred when the product of frequency and transport time was 0.45. If we denote our original nozzle geometry with subscript "a", and a second geometry with subscript "b", then

$$f_a(L_a + L')/U_{\text{avg},a} = 0.45, \tag{4}$$

and for a second nozzle geometry "b" we also have

$$f_b(L_b + L')/U_{\text{avg},b} = 0.45. \tag{5}$$

If we assume that the oscillating frequency is not changed appreciably between the two nozzles, then along the stability boundary

$$U_{\text{avg},b} = U_{\text{avg},a}(L_b + L')/(L_a + L'). \tag{6}$$

Thus, if we lengthen the nozzle, we should see the boundary between stable and oscillating combustion move to a higher velocity.

We tested this hypothesis experimentally. We added a spacer ring to our original fuel nozzle geometry (Fig. 3) so that L was extended by 1.9 cm (0.75 in). Again, estimating $L' = 2.5$ cm (1.0 in), Eq. (6) predicts that the stability boundary at 40 m/s would move to 52 m/s. To confirm this prediction, we repeated some of the tests shown in Fig. 7.

Figure 11 is a plot of the same operating conditions as in Fig. 7, at 7.5 atmospheres pressure. Figure 11 shows that the oscillating boundary has moved from approximately 40 to 50 m/s nozzle velocity, as predicted by Eq. (6). Also note that some of the data at 30 m/s has a small amplitude. For this

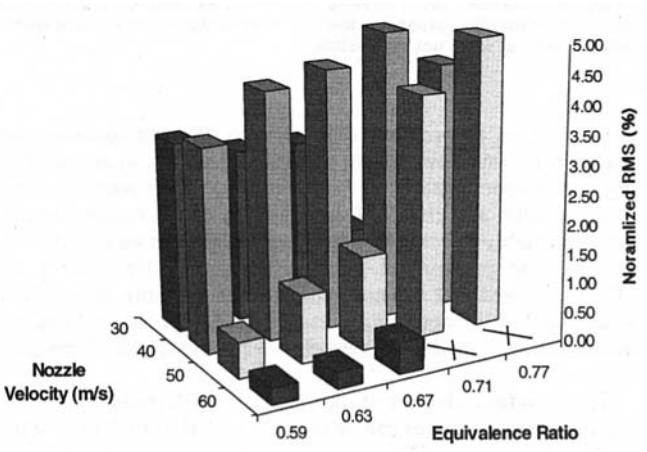

Fig. 11 RMS pressure from longer nozzle. The RMS pressure is expressed as a percentage of the operating pressure. Operating conditions compare directly to data from Fig. 7 at 7.5 atmosphere pressure. Notice the change in the location of the stability boundary: oscillations are activated at 50 m/s in this figure, but are absent at 50 m/s in Fig. 7.

[2] A hysteresis is identified as a subcritical Hopf bifurcation point. See Strogatz (1994) for a discussion of these issues.

nozzle length, the product of frequency and transport time at 30 m/s was 0.72. From Fig. 10, this is again the boundary between stable and oscillating combustion, and we would expect that oscillations should be weak, or irregular.

For practical application, these results show the value of describing the oscillations with a time lag model. Reasonable predictions of the effect of changing nozzle geometry can be made after gathering basic information on the oscillating behavior of the fuel nozzle. If plots such as Figs. 7 and 8 can be gathered from an engine or test stand, it may be possible to move the oscillating region out of the operating map by changing the fuel nozzle length or nozzle velocity.

We caution that many subtleties can complicate this approach. The flame standoff (L') can change abruptly with relatively minor changes in nozzle geometry or operating conditions. Prior work on the flame standoff distance (Ferguson and Keck, 1979) may be qualitatively helpful, but exact predictions of L' are complicated by the recognition that the flame is not a flat surface. The acoustic response of the combustor may include several modes so that various frequency-time lag products need to be considered in defining the stability boundaries. We have also artificially choked the fuel supply in this test combustor, eliminating fuel-feed variation as a possible mechanism for variation in heat release. Recognizing these limitations, the time lag approach provides a good starting point to understand more complex mechanisms and to propose modifications to solve instability problems.

Summary and Future Work

In this study, we used a simple time lag model to experimentally characterize combustion oscillations produced by a premix fuel nozzle. The combustor was specially designed to provide an acoustic environment suitable for investigating these oscillations. The fuel nozzle uses a modular design to allow rapid investigation of the effect of nozzle geometry.

The time lag model suggests that the nozzle velocity should play a determining role in oscillations. Thus, oscillation data were gathered as a function of nozzle velocity for pressures of 5, 7.5, and 10 atmospheres, with inlet air temperatures of 533 K and 589 K (500 F and 600 F). Results showed that the conditions which produced oscillations changed only slightly with pressure and inlet air temperature. For many cases, the oscillation amplitude scaled directly with pressure. This suggests that small oscillations encountered during low-pressure testing may scale to unacceptably large oscillations during higher-pressure operation. At the boundary between stable and oscillating combustion, we observed some intermittent behavior where the oscillation amplitude would rise and fall over several seconds. This irregular behavior emphasizes the need for engineers to identify stability boundaries in new combustors and then ensure that the regular operating conditions are well-removed from the oscillating boundary. Using the approach described here, we were able to characterize the stability boundary from the time-lag model and then propose how changes in the nozzle geometry would affect the boundary between oscillating and steady combustion. An experimental test of this approach proved successful for this fuel nozzle and combustor.

We close by noting that the experimental approach used here was tested on just two fuel nozzle geometries. Although the fuel nozzle and operating conditions were representative of current LPM combustor design, more testing is needed to confirm the value of this approach in a wider range of nozzle geometries, with multiple combustor acoustic modes, or with multiple mechanisms driving the variation in heat release. We are presently conducting additional tests using variations on the fuel nozzle geometry (Fig. 3) to evaluate these issues.

Acknowledgments

The authors wish to thank Dr. Don Cha for help in conducting cold-flow mixing studies on the initial fuel nozzle design. We also gratefully acknowledge Mr. Rick Griffith, Mr. Mike Dera, and Mr. Keith Dodrill for help with experimental development and operation.

References

Alsup, C. T., Zeh, C. M., and Blazewicz, S., eds., 1995, "Proceedings of the Advanced Turbine Systems Program Review Meeting, DOE/METC-96/1023, NTIS/DE96000561 and NTIS/DE96000562, (2 Vols.) National Technical Information Service, Springfield, VA.

Candel, S. M., 1992, "Combustion Instabilities Coupled by Pressure Waves and Their Active Control," *The Twenty-Fourth (International) Symposium on Combustion,* The Combustion Institute, Pittsburgh, PA, pp. 1277–1296.

Crocco, L., and Cheng, S. I., 1956, "Theory of Combustion Instability in Liquid Propellant Rocket Motors," *AGARD Monograph,* No. 8, Butterworths, London.

Englund, D. R., and Richards, W. B., 1984, "The Infinite Line Probe," *Proceedings of the 30th International Instrumentation Symposium,* Instrument Society of America, Research Triangle Park, NC, pp. 115–124.

Feiler, C. E., and Heidman, M. F., 1967, "Dynamic Response of Gaseous-Hydrogen Flow System and its Application to High-Frequency Combustion Instability," NASA TN D-4040, National Technical Information Service, Springfield, VA.

Ferguson, C. R., and Keck, J. C., 1979, "Stand-Off Distances on a Flat Flame Burner," *Combustion and Flame,* Vol. 34, pp. 85–98.

Gemmen, R. S., Janus, M. C., Richards, G. A., Norton, T. S., and Rogers, W. A., 1995, "Achieving Improved Cycle Efficiency Via Pressure Gain Combustors," ASME Paper 95-GT-63, presented at the IGTI/ASME Gas Turbine and Aeroengine Congress and Exposition, June 5–8, Houston, TX.

Halow, J. S., Maloney, D. J., and Richards, G. A., 1994, "METC Combustion Research Facility," *Proceedings of the Advanced Turbine Systems Annual Program Review Meeting,* DOE/OR-2025.

Harrje, D. T., and Reardon, F. H., 1972, "Liquid Propellant Rocket Combustion Instability," NASA SP-194.

Janus, M. C., Richards, G. A., Yip, M. J., and Robey, E. H., 1997, "The Effect of Ambient Conditions and Fuel Composition On Combustion Stability," ASME paper 97-GT-266, presented at the IGTI/ASME Gas Turbine and Aeroengine Congress and Exposition, June 2–5, Orlando, FL.

Keller, J. J., 1995, "Thermoacoustic Oscillations in Combustion Chambers of Gas Turbines," *AIAA Journal,* Vol. 33, No. 12, pp. 2280–2287.

Keller, J. O., and Saito, K., 1987, "Measurement of the Combusting Flow in a Pulse Combustor," *Combustion Science and Technology,* Vol. 53, pp. 137–163.

Keller, J. O., Bramlette, T. T., Westbrook, C. K., and Dec, J. E., 1990, "Pulse Combustion: The Quantification of Characteristic Times," *Combustion and Flame,* Vol. 79, pp. 151–161.

Knoop, P., Culick, F. E. C., and Zukoski, E. E., 1996, "Extension of the Stability of Motions in a Combustion Chamber by Non-Linear Active Control Based on Hysteresis," available from the National Technical Information Service, Springfield, VA., DOE/MC/29061-96/C0701.

Lovett, J. A., and Mick, W. J., 1995, "Development of a Swirl and Bluff-Body Stabilized Burner for Low-NOx, Lean-Premixed Combustion," ASME Paper 95-GT-166: also presented at the IGTI/ASME Gas Turbine and Aeroengine Congress and Exposition, June 5–8, Houston, TX.

Mahan, J. R., and Karchmer, A., 1991, "Combustion and Core Noise," in *Aeroacoustics of Flight Vehicles: Theory and Practice, Volume 1: Noise Sources,* NASA Langley Research Center, available from AIAA Technical Library.

Mehta, G. K., Ramachandra, M. K., and Strahle, W. C., 1981, "Correlations Between Light Emission, Acoustic Emission, and Ion Density in Premixed Turbulent Flames," *The Eighteenth (International) Symposium on Combustion,* The Combustion Institute, Pittsburgh, PA. pp. 1051–1059.

Mehta, J., Mungur, P., Dodds, W., Bahr, D., and Clouser, S., 1990a, "Fuel Effects on Gas Turbine Combustor Dynamics," AIAA Paper No. 90-1957: also presented at the 26th Joint Propulsion Conference, July 16, Orlando, FL.

Mehta, J., Mungur, P., Dodds, W., Bahr, D., and Clouser, S., 1990b, "Thermoacoustics of Unsteady Combustion," AIAA Paper No. 90-3928, also presented at the 13th Aeroacoustics Conference, October 22–24, Tallahassee, FL.

Merk, H. J., 1956, "An Analysis of Unstable Combustion of Premixed Gases," *Sixth Symposium (International) on Combustion,* The Combustion Institute, Pittsburgh, PA, pp. 500–512.

Narayanaswami, L., and Richards, G. A., 1996, "Pressure-Gain Combustion: Part 1—Model Development," ASME JOURNAL OF ENGINEERING FOR GAS TURBINES AND POWER, Vol. 118, pp. 461–468.

Putnam, A. A., 1971, *Combustion Driven Oscillations in Industry,* American Elsevier Publishers, New York, NY.

Rayleigh, J., 1878, "The Explanation of Certain Acoustical Phenomena," *Royal Institute Proceedings,* Vol. VIII, pp. 536–542.

Richards, G. A., Gemmen, R. S., and Yip, M. J., 1996, "A Test Device for Premixed Gas Turbine Combustion Oscillations," DOE/METC-96/1027 (DE96004367), National Technical Information Service, Springfield, VA.

Richards, G. A., and Yip, M. J., 1995, "Oscillating Combustion from a Premix Fuel Nozzle," presented at the Combustion Institute/American Flame Research Committee Meeting, April 23–26, San Antonio, TX.

Samaniego, J. M., Egolfopoulos, N., and Bowman, C. T., 1995, "CO_2 Chemiluminescence in Premixed Flames," *Combustion Science and Technology,* Vol. 109, pp. 183–203.

Schadow, K. C., and Gutmark, E., 1991, "Combustion Instability Related to Vortex Shedding in Dump Combustors and Their Passive Control," *Progress in Energy and Combustion Science,* Vol. 18, pp. 195–205.

Shih, W.-P., Lee, J., and Santavicca, D. A., 1996, "Stability and Emission Characteristics of a Lean Premixed Gas Turbine Combustor," *The Twenty-Sixth (International) Symposium on Combustion,* The Combustion Institute, Pittsburgh, PA, pp. 2771–2778.

Sivasegaram, S., and Whitelaw, J. H., 1991, "The Influence of Swirl on Oscillations in Ducted Premixed Flames," *Combustion and Flame,* Vol. 85, pp. 195–205.

Strogatz, S. H., 1994, *Nonlinear Dynamics and Chaos,* Addison-Wesley Publishing Co., Reading, MA, pp. 215–252.

Yang, V., and Anderson, W., eds., 1995, *Liquid Rocket Combustion Instability,* The American Institute of Aeronautics and Astronautics, Cambridge, MA.

R. C. Steele[1]

J. H. Tonouchi

D. G. Nicol

D. C. Horning

P. C. Malte
malte@u.washington.edu

D. T. Pratt

Combustion Laboratories,
Department of Mechanical Engineering,
Box 352600,
University of Washington,
Seattle, WA 98195-2600

Characterization of NO_x, N_2O, and CO for Lean-Premixed Combustion in a High-Pressure Jet-Stirred Reactor

A high-pressure jet-stirred reactor (HP-JSR) has been built and applied to the study of NO_x and N_2O formation and CO oxidation in lean-premixed (LPM) combustion. The measurements obtained with the HP-JSR provide information on how NO_x forms in lean-premixed, high-intensity combustion, and provide comparison to NO_x data published recently for practical LPM combustors. The HP-JSR results indicate that the NO_x yield is significantly influenced by the rate of relaxation of super-equilibrium concentrations of the O-atom. Also indicated by the HP-JSR results are characteristic NO_x formation rates. Two computational models are used to simulate the HP-JSR and to provide comparison to the measurements. The first is a chemical reactor model (CRM) consisting of two perfectly stirred reactors (PSRs) placed in series. The second is a stirred reactor model with finite rate macromixing (i.e., recirculation) and micromixing. The micromixing is treated by either coalescence-dispersion (CD) or interaction by exchange with the mean (IEM) theory. Additionally, a model based on one-dimensional gas dynamics with chemical reaction is used to assess chemical conversions within the gas sample probe.

Introduction

This is the first study to use a high-pressure jet-stirred reactor (HP-JSR) to examine pollutant formation. The present HP-JSR has been designed for 15 atm, although in the present work the maximum pressure treated is 7.1 atm. The pressure range of 1 to 7 atm, though less than the 10 to 15 atm range of heavy-duty combustion turbines, is useful, since most of the sensitivity in the relaxation of superequilibrium O-atom, and thus NO_x formation, lies in the 1 to 7 atm range.

Because the jet-stirred reactor (JSR) is useful for gaining information on chemical effects for high-intensity combustion, it was decided to extend its operation from the usual pressure of 1 atm to high pressure. In this regard, it is worth recalling that the JSR has assisted in the understanding of gas turbine combustion since the development of the first JSR in the 1950s. Early on, the JSR was used to study flameout and global oxidation rates, and since the 1970s, the JSR has been used to study pollutant formation. The JSR is advantageous for the present work because it simulates the pollutant chemistry of LPM combustion turbines. In LPM combustors, the NO_x mainly forms in the shear layers and adjacent recirculation zones, which are regions of superequilibrium free radical concentrations. The JSR contains the following features: its flow-field consists of one or more strong jets (i.e., shear layers) and one or more recirculation zones, and it is filled with superequilibrium free radical concentrations.

The challenge facing the JSR designer is attainment of the well-stirred reactor (WSR) condition, which is defined as spatial uniformity in the time-mean temperature and species concentrations. The WSR condition requires that the characteristic chemical time of the event being examined, in this case NO_x formation, be long compared to the characteristic mixing times in the JSR. There is substantial evidence that the WSR condition is essentially satisfied for NO_x formation in the 1 atm JSR operated lean.

The WSR condition is attained at 1 atm because free radical recombination rates are relatively slow, and, thus, high levels of O, H, and OH concentrations essentially fill the reactor uniformly. This is implied by Fig. 1, due to Nicol (1995). In this figure, the time for the O-atom to relax from its peak concentration (which occurs near the end of the premixed flame zone) to 110 percent of its thermochemical equilibrium concentration is plotted versus pressure for a typical LPM combustion fuel-air ratio. Figure 1 is based on chemical reactor modeling, i.e., a perfectly stirred reactor (PSR) followed by a plug flow reactor (PFR), though essentially equivalent behavior to that shown may be obtained by one-dimensional, laminar flame modeling. The chemical kinetic mechanism used is that of Miller and Bowman (1989). For 1 atm, the relaxation time shown in Fig. 1 is about 20 ms, which is long compared to the mean residence time of 2 to 4 ms of the JSR, and, thus, to the characteristic mixing times of the JSR. Since the NO_x formation in LPM combustion is strongly influenced by the O-atom behavior through both the nitrous oxide and Zeldovich mechanisms (Nicol et al., 1995), the JSR is essentially a WSR with respect to NO_x formation. For pressures in the vicinity of 5 atm and greater, however, Fig. 1 shows that the O-atom relaxation time is short, about 1 to 2 ms. Thus, a high pressure JSR operated lean at 2 to 4 ms, as the case here, cannot be a WSR with respect to NO_x formation. In particular, the characteristic chemical time is not long compared to the mixing time of the large recirculation eddy. In order to attain the WSR condition, the HP-JSR must be operated at a residence time of 0.5 ms or less. (A 0.5 ms HP-JSR is under development.)

Attention is focused on the O-atom because it has a greater impact on NO_x formation than the other major free radicals in flames, i.e., H-atom and OH (Nicol, 1995). For LPM combustion, the O-atom accounts for at least about 50 percent of the NO_x formed by the nitrous oxide pathway (through the reaction

[1] Present Affiliation: Solar Turbines, Inc., 2200 Pacific Highway, P.O. Box 85376, San Diego, CA 92186-5376.

Contributed by the International Gas Turbine Institute and presented at the 41st International Gas Turbine and Aeroengine Congress and Exhibition, Birmingham, United Kingdom, June 10–13, 1996. Manuscript received by the ASME Headquarters February 1996. Paper No. 96-GT-128. Associate Technical Editor: J. N. Shinn.

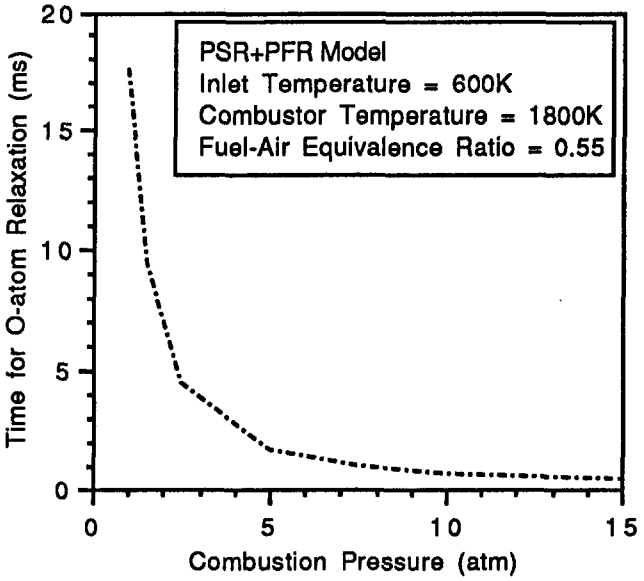

Fig. 1 O-atom relaxation time versus pressure (Nicol et al., 1995)

$N_2O + O \rightarrow 2NO$), and the O-atom accounts essentially for all of the NO_x formed by the Zeldovich pathway (through the reaction $N_2 + O \rightarrow NO + N$, followed by oxidation of the N-atom to NO). The H-atom accounts for the balance of the NO_x formed by the nitrous oxide pathway (through the reaction $N_2O + H \rightarrow NO + NH$, followed by oxidation of the NH radical to NO). Also, the H-atom destroys N_2O, and thus, influences the N_2O concentration in the combustion reactor (through the reaction $N_2O + H \rightarrow N_2 + OH$). However, since the H-atom is of less importance overall than the O-atom in establishing NO_x formation in LPM combustion and since the trend of H-atom relaxation is generally similar to that of the O-atom, the H-atom relaxation is not explicitly treated herein.

The other free radical of significance to NO_x formation is CH. Modeling indicates that the CH radical has a very short lifetime (of order 0.1 ms) in LPM combustion (Nicol, 1995), is confined to the flame zone, and does not survive into post-flame zones (as occurs for O, H, and OH). Although there is evidence for the formation of prompt NO_x in LPM combustion (by the reaction $CH + N_2 \rightarrow HCN + N$, followed by oxidation of the HCN and N-atom to NO), the short lifetime of the CH radical and chemical reactor modeling (Nicol et al., 1995) indicate that prompt NO_x is not a major source of NO_x in LPM combustion, unless the fuel-air equivalence ratio is greater than about 0.65, or the residence time of the combustion reactor is very short. For the present study, the prompt mechanism is regarded as a secondary source of NO_x, the nitrous oxide and Zeldovich mechanism are assumed to account for most of the NO_x, and the relaxation time of the O-atom is assumed to define the characteristic time for NO_x formation under the influence of high concentrations of free radicals.

The non-WSR nature of the HP-JSR has provided impetus for the development and application of two models. The first is a chemical reactor model (CRM) in which two perfectly stirred reactors (PSRs) placed in series are used to simulate the reactor. The second model is a stirred reactor with finite rate macromixing (i.e., recirculation) and micromixing. The micromixing is treated by either coalescence-dispersion (CD) or interaction by exchange with the mean (IEM) theory. In addition, a probe model based on one-dimensional gas dynamics with chemical reaction is used to assess probe chemical conversions.

In the following sections of this paper, the HP-JSR system is described; the experimental results for the combustion of methane are presented, discussed, and compared to the literature; and the computational models are described briefly and compared to the measurements. Results are given and discussed for NO_x, N_2O, and CO. The paper provides an understanding of how NO_x forms in high-pressure, jet-stirred combustion, and it provides a useful comparison to other laboratory results, including results for practical LPM combustors.

Experimental Setup and Approach

The experimental facility and high-pressure, jet-stirred reactor (HP-JSR) are described by Steele (1995). The facility consists of the pressure vessel (i.e., cylinder) in which the HP-JSR, its premixing chamber, and its electrical air heater are located, and it consists of the equipment for the distribution, metering, and control of the air and fuel. Figure 2 shows the pressure vessel with the HP-JSR and the premixing chamber. The pressure vessel also contains ports (not shown in Fig. 2) for the insertion of the thermocouple and gas sampling probes through the side wall of the pressure vessel into the HP-JSR. The dimensions of the components shown in Fig. 2 are as follows: pressure vessel (stainless steel): height is 1 m (nominal), inside diameter is 127 mm, and wall thickness is 9.5 mm; premixing chamber (stainless steel): height is 240 mm, inside diameter is 25 mm, distance from point of fuel injection holes to nozzle block is 115 mm, and diameter of each of the 4 fuel injection holes is 1 mm; jet-stirred reactor (Zirconia): outside diameter is 64 mm, outside height is 51 mm, inside diameter at widest point is 12.7 mm, and inside height is 22.2 mm; and nozzle block (Inconel): height is 9.5 mm, and diameter of jet is 1 mm.

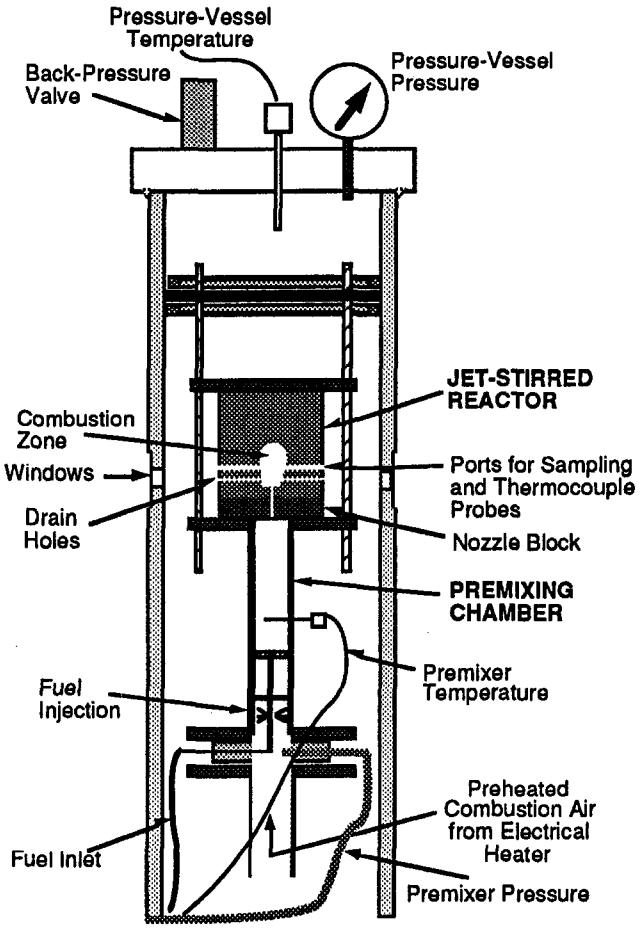

Fig. 2 Schematic of HP-JSR with premixing chamber

Air from a mechanical compressor, of maximum pressure 7.5 atm, is filtered and forced to flow through the pressure vessel. This air dilutes and carries away the effluent of the HP-JSR. The pressure level of the pressure vessel is controlled by a back-pressure valve located at the exit of the pressure vessel. Although the pressure within the HP-JSR is slightly greater than the pressure of the air in the pressure vessel, the nominal pressure of the HP-JSR, which is the pressure reported below, is taken to equal the pressure of the air in the pressure vessel. The pressure vessel and other components are designed for a pressure of 15 atm, though for the present study, because of the limitation of the mechanical compressor used, the maximum pressure tested is 7.1 atm.

The combustion air for the HP-JSR is provided either from bottled air or from a separate stream from the mechanical compressor. This air is preheated and injected into the premixing chamber (see Fig. 2). This chamber serves the following two functions: (1) the gaseous fuel (from bottles) and the combustion air are premixed; and (2) the high pressure required to create the high velocity jet of the HP-JSR is attained. For experiments with a HP-JSR pressure of 6.5 atm or less and a residence time of 4 ms or greater, the mechanical compressor provides the combustion air. For experiments of greater pressure levels and/or shorter residence times, the pressure of the mechanical compressor is inadequate, and bottled air is used as the combustion air. The bottled air is tested for traces of N_2O, and only bottles with negligible levels of N_2O are used. The fuel/air mixture entering the HP-JSR is assumed to be perfectly premixed. Several features of the design support this assumption: (1) the high pressure drop and small size of the jets which inject the fuel into the premixing chamber; (2) the baffle plates used in the premixing chamber; (3) the residence time in the premixer is long (i.e., at least 0.2 s); and (4) the small size of the premixed fuel/air jet entering the HP-JSR.

The shape of the HP-JSR chamber is identical to that shown by Steele et al. (1995) for the 1 atm JSR. The HP-JSR is stirred by the centered, high velocity jet of 1 mm diameter. The Mach number of the inlet jet is nominally sonic for 2 ms operation, and nominally 0.5 for 4 ms operation. The jet is directed upwards, entrains recirculating gas, and is reflected at the reactor's back wall, thereby creating a strong downwards recirculation. The flow pattern within the HP-JSR is identical to that shown by Steele et al. (1995) for the 1 atm JSR with a single, centered jet. The volume of the HP-JSR is 2 cc; that is, all dimensions are one-half the dimensions of the 1 atm, 16 cc JSR used by Steele et al. (1995). Gases exit the reactor through 6 holes, including 4 holes (each of diameter 2.4 mm) at the bottom of the reactor, and 2 holes (each of diameter 3.2 mm) at 64 percent elevation, which is the same elevation as the holes for the thermocouple and sampling probes. The bottom holes encourage the gas to fully recirculate. Application of jet entrainment formulas (Beér and Chigier, 1983) shows that the average fluid particle makes about 4 to 6 cycles of the reactor. (A reactor nozzle with small, multiple jets would permit a greater number of cycles. Such a nozzle was recently built for the HP-JSR. For the 1 atm JSR, Steele et al. (1995) reported little difference in the NO_x yield of the single and multiple jet configurations.)

The small (2 cc) volume minimizes the size and cost of the high pressure rig, and the cost of the fuel and air. No detriment has been found from this approach. Because of the high loading at high pressure, the HP-JSR operates nearly adiabatically. Measurements for 1 atm show that the 2 cc JSR gives the same NO_x as a function of combustion temperature as JSRs tenfold to a hundred-fold larger (see Steele et al., 1995).

Combustion temperature is measured by a small type-R thermocouple. The thermocouple bead is coated with ceramic material to prevent catalytic reaction, giving a bead diameter of about 1 mm, and the measured temperature is corrected for heat loss by calculation. The correction is small (i.e., about 30 to 40°C) because the HP-JSR chamber approximates a black-body cavity. Unless stated otherwise below, the temperature reported is that measured (and corrected) for the recirculation zone of the HP-JSR. In this zone the temperature is uniform, and has attained its peak value (see Fig. 3), which is close to that for adiabatic equilibrium.

Gas sampling is conducted with a microprobe. Two probes have been developed; one a quartz tube (Steele, 1995), the other a ceramic tube (Horning, 1996). With each, the inlet of the tube is closed to a very small diameter so that the inlet flow is choked, and a small segment of supersonic flow is obtained before the flow undergoes shock recompression to the back pressure of about 0.3 atm imposed by the sampling pump. External cooling of the probe is obtained by permitting a small amount of the pressure-vessel air to escape and flow rapidly

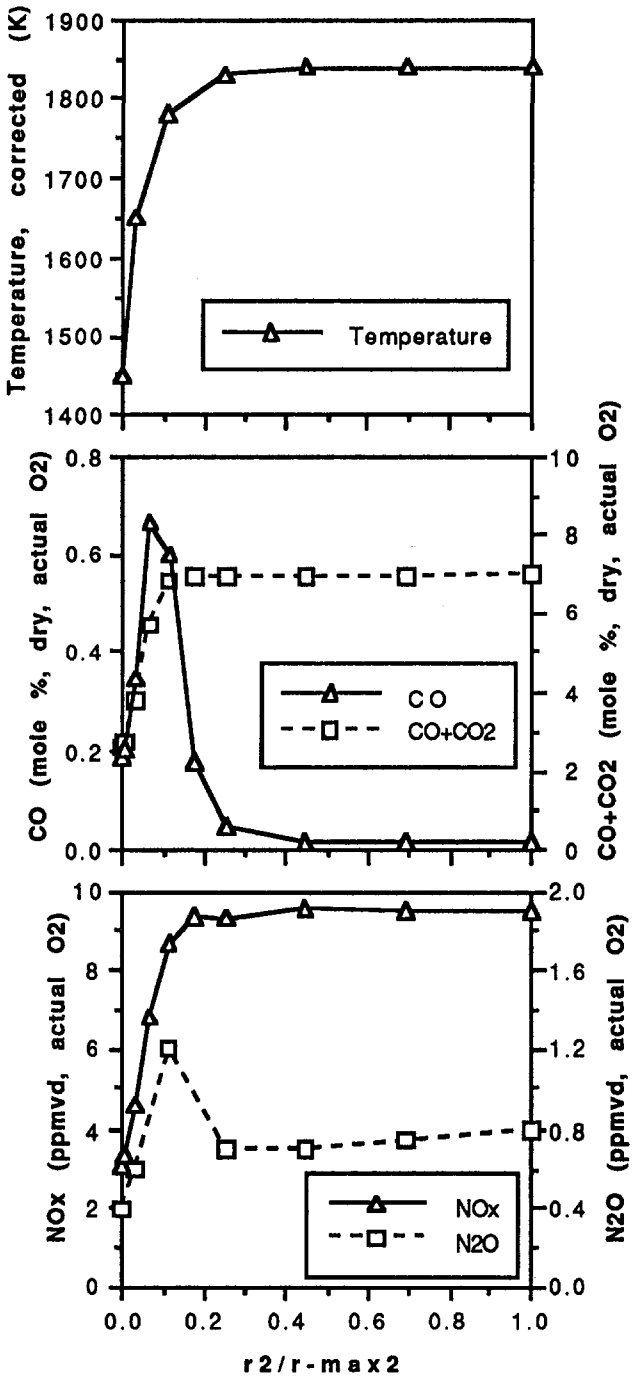

Fig. 3 Typical HP-JSR profiles from centerline to the inside wall

over the probe as it passes through the port in the side wall of the pressure vessel. The useful lifetime of a quartz probe is about 8 hours. The failure mode of the quartz probe is devitrification, which is accelerated by high pressure. In order to obtain improved lifetime, a ceramic probe has been developed (Horning, 1996). Both probes have undergone extensive modeling with the probe model. Unless stated otherwise, the species data given below are for the recirculation zone of the reactor, and were obtained with the quartz probe. For sampling from the recirculation zone of the HP-JSR (with CO concentration of order 100 ppmv), the modeling indicates that chemical conversions within the probe are small. Essentially, NO_x is conserved, though conversion of NO to NO_2 occurs. Loss of N_2O is less than 10 percent (relative), and CO oxidation is 10 to 20 percent (relative).

The gas sample line connecting the sample probe to the gas analyzers is wrapped with heating tape and maintained at a temperature sufficient to prevent condensation and loss of NO_2 by absorption into water. The water is removed in ice cooled impingers, while maintaining minimum gas (e.g., NO_2) contact with the water. Sampling with newly dried impingers gives identical results to sampling with wet impingers, indicating a negligible loss of NO_2 in this work. Analysis is by process gas analyzers (chemiluminescence for NO_x, NDIR for CO and CO_2) and by electron capture gas chromatography for N_2O. The uncertainty estimated for the NO_x measurements is ±20 percent (relative).

Experimental Results and Discussion

The measurements reported herein are for methane burned over the combustion temperature range of 1550 to 1850 K and the pressure range of 1 to 7.1 atm. The combustion temperature was varied by varying the fuel-air ratio (for the particular inlet temperature). The 1 atm JSR results for methane fuel, though reported previously by Steele et al. (1995), are summarized below in order to provide completeness to the present paper and a benchmark for comparison of the HP-JSR results. The complete experimental results are contained in the theses of Steele (1995) and Horning (1996).

Summary of Results on NO_x Formation for 1 atm Combustion of Methane. The NO_x data obtained for 1 atm methane combustion cover the fuel-air equivalence (ϕ) range 0.46 to 0.7, the combustion temperature range 1550 to 1850 K, and the residence time range 1.6 to 7.2 ms, for inlet temperatures of 300 and 600 K (nominal) and for both single and multiple jet configurations (Steele, 1995; Steele et al., 1995). The NO_x data vary exponentially with combustion temperature and linearly with residence time, and they agree well with the following best fit expression:

$$NO_x(\text{ppmvw, actual } O_2)/\tau(\text{ms}) = 2.29 \times 10^6 \exp(-24290/T(K)), \quad (1)$$

where τ(ms) is the JSR residence time in milliseconds, $T(K)$ is measured (corrected) combustion temperature in degrees Kelvin, and the NO_x is expressed as parts per million by volume, wet basis (ppmvw), assuming no O_2 correction.

The 1 atm NO_x data are very well modeled by assuming the JSR to be a PSR at the experimental temperature and residence time (Steele, 1995). This finding, the linear dependency of the NO_x on residence time shown by Eq. (1), and the high levels of CO observed throughout the JSR (Steele, 1995) give substantial evidence for the superequilibrium free radicals (O, OH, and H) filling the JSR and affecting an essentially uniform NO_x formation rate. That is, the whole JSR is a flame zone. Thus, Eq. (1) may be taken as the NO_x formation rate for 1 atm high-intensity, lean-premixed, methane-air flame zones. In applying Eq. (1), the user must decide the residence time of the flame zone (i.e., the time over which high free radical concentrations persist). This is either the combustor residence time (as the case with the 1 atm JSR) or the O-atom relaxation time (see Fig. 1), whichever is smaller.

If only the 600 K inlet temperature data are curve fit, Eq. (1) becomes $NO_x/\tau = 1.28 \times 10^7 \exp(-27230/T)$. The comparison of this expression with Eq. (1) indicates that the overall NO_x activation energy increases slightly with increasing inlet temperature. That is, for the highest combustion temperatures, the NO_x concentration is slightly higher for the 600 K inlet temperature than for 300 K. This tendency is also noted in PSR modeling. However, for a 1 atm JSR with a large inlet jet (Williams, 1995), and thus relatively slow jet eddy mixing, the NO_x is found to decrease with increasing inlet temperature (for fixed combustion temperature). This behavior may be a response of the NO_x chemistry to the decreased fuel/air ratio permitted by the higher inlet temperature. Adjustment of the 600 K data to a dry, 15 percent O_2 basis changes Eq. (1) to $NO_x/\tau = 4.22 \times 10^5 \exp(-22115/T)$.

Reactor Uniformity. Representative profiles of temperature, CO, CO + CO_2, NO_x, and N_2O for the HP-JSR are shown in Fig. 3. These measurements were obtained by Horning (1996) for the case of 6.5 atm pressure, 4 ms residence time (nominal), and 300 K inlet temperature (nominal), using the ceramic sampling probe. The corrected temperature for the recirculation zone is 1840 K; the fuel-air equivalence ratio is 0.7. The profiles extend from the centerline (0) to the inside wall (1.0) of the HP-JSR, and indicate two-zone behavior. Except for the jet (centerline) zone, the HP-JSR is uniform in temperature and NO_x. The outer 70 percent of the HP-JSR, on the r^2 basis shown, is uniform in all quantities. This is the recirculation zone.

The CO profile is indicative of the two-zone behavior. The CO forms in the jet, reaches peak concentration in the jet boundary layer, and then oxidizes and reaches a low (though greater than equilibrium) concentration in the recirculation zone. Since O-atom and CO concentrations are well correlated in LPM combustion (Nicol, 1995), the CO profile may be taken as an indicator of the O-atom behavior and the zones of high and low free radical concentrations. By this reasoning, the highest rate of NO_x formation occurs mainly in the jet boundary layer. This situation is different from that argued above for the 1 atm JSR, which is NO_x formation dispersed throughout the reactor and recirculation zone.

The recirculation zone temperature of Fig. 3 is relatively high, 1840 K. Profile measurements (not shown here) have also been obtained for lower combustion temperatures (Steele, 1995; Horning, 1996). For these experiments, the profile trends for temperature, NO_x, and CO + CO_2 are similar to the profiles in Fig. 3. However, the CO behavior in the outer part of the lower-temperature reactor changes from the flat profile of Fig. 3. Particularly, the CO close to wall increases due to the flow of less-reacted gas from the jet zone into the outer region of the recirculation zone. At lowest temperatures (less than 1650 K) and shortest residence times (2 ms nominal), high CO concentrations (of magnitude 3000 ppmv) fill the recirculation zone. In this case, the dispersion of super-equilibrium CO throughout the HP-JSR is similar to the behavior observed in the 1 atm JSR. Also, at the lower combustion temperatures, the N_2O does not relax from its peak concentration but remains at elevated concentration throughout recirculation zone (Horning, 1996).

Probe modeling of sampling from regions of high CO concentration (and thus, high free radical concentrations) shows that the CO conversion to CO_2 can be as great as 60 percent (relative), compared to 10 to 20 percent conversion stated above for sampling from the recirculation zone (with CO concentration of order 100 ppmv). Thus, the high CO measurements should be treated qualitatively rather than quantitatively. The NO_x and

N_2O conversions remain negligible to small, as stated above for the low-CO recirculation zone.

Results for High Pressure Combustion of Methane. The measurements for the HP-JSR cover the pressure range 1 to 7.1 atm and the combustion temperature range 1550 to 1850 K, and have residence times of 2 and 4 ms nominal (1.6 to 4.5 ms actual) and inlet temperatures of 300 and 600 K nominal (297 to 605 K actual). Figure 4 shows the complete dataset for the NO_x and N_2O concentrations for the 1 to 7.1 pressure range from the work of Steele (1995). About one-half of the data for 1.0 atm were obtained in the 16 cc (1 atm) JSR. All other data were obtained in the 2 cc HP-JSR. (As shown by Steele et al. (1995) JSR size does not affect NO_x.) At the top of the band of the NO_x data, most of the points are for 1 atm; whereas, at the bottom of the band most of the points are for 7.1 atm. That is, the NO_x exhibits a slightly negative dependency on pressure. This tendency is also noted in the data of Joshi et al. (1994). Analysis of the NO_x data in Fig. 4, assuming an NO_x pressure (P) dependency of

$$NO_x \approx P^n \tag{2}$$

gives $n = -0.20$ as the average value, and $n = -0.10$ to -0.35 as the range.

The 1 atm data plotted in Fig. 4 are subject to the linear increase in NO_x with residence time expressed by Eq. (1). However, the high pressure (4.7 and 7.1 atm) data are nearly neutral with respect to residence time; the doubling of the residence time from 2 to 4 ms (nominal) causes an increase of 0 to 20 percent (relative) in the NO_x. This nearly neutral result may be explained by the O-atom behavior discussed above. High concentrations of free radicals no longer fill the whole reactor, and thus, the free radical relaxation time rather than reactor residence time affects the NO_x yield. Although the rate of NO_x formation in the high free radical region of the HP-JSR is about five-fold greater than for the 1 atm JSR, this effect is neutralized by the fast relaxation of the free radicals at high pressure.

For high free radical zones of 1800 K temperature, the rate of NO_x formation is about 2 ppmvd (15 percent O_2) per millisecond at 1 atm (based on Eq. (1)), and about 10 ppmvd (15 percent O_2) per millisecond at 7 atm (based on chemical reactor modeling by Nicol (1995) and Horning (1996).

With respect to inlet temperature, the HP-JSR NO_x data show little to no sensitivity to the doubling in inlet temperature from 300 to 600 K (nominal).

The N_2O data plotted in Fig. 4 show a greater scatter than the NO_x data, and indicate three regimes of behavior: 1 atm, high pressure/low temperature, and high pressure/high temperature. The 1 atm data show a slight decrease with increasing temperature; also, the highest data are for 2 ms residence time, the lowest for 4 ms. The 4.7 and 7.1 atm N_2O data are 3 to 4 fold greater than the 1 atm data, except for the high temperature regime. When the combustion temperature is high (i.e., about 1800 K and greater) and the residence time is sufficient (i.e., 4 ms), the N_2O has an opportunity to relax towards its equilibrium concentration. High pressure promotes this effect; the data points (filled triangles) at 1850 K and 0.6 to 0.7 ppmvw are for the case of 7.1 atm and 4 ms. For 2 ms residence time, however, the N_2O remains in the 2 to 3 ppmvw range for all temperatures, since the time is inadequate for relaxation towards equilibrium.

Although much of the NO_x forms from oxidation of the N_2O, especially for combustion temperatures below 1800 K (see Nicol et al., 1995), a correlation between the NO_x and N_2O is not evident from Fig. 4. This is because the formation of NO_x from N_2O also depends on the O-atoms (and H-atoms).

Comparison to LPM Combustion Turbine Data. In Fig. 5, the NO_x data from Fig. 4 are adjusted to a dry, 15 percent O_2 basis and compared to best-fit results from the recent gas

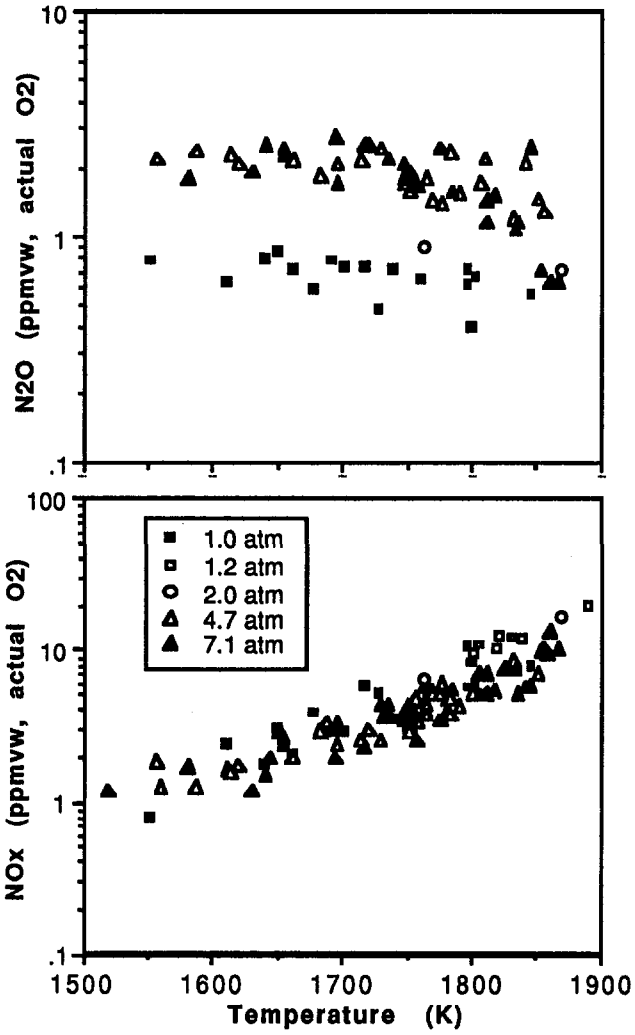

Fig. 4 Complete NO_x and N_2O datasets for methane combustion over the 1 to 7.1 atm pressure range. Residence time = 2 and 4 ms (nominal). Inlet temperature = 300 and 600 K nominal. The 1 atm data are for 2 cc and 16 cc JSRs, using both single and multiple inlet jets. Data for all other pressures are for the 2 cc, single jet HP-JSR.

turbine literature. (The best-fit curves are ours.) The jet-stirred reactor data are bracketed by those data from the literature which either have a nil to weak pressure dependency or are for an engine premixer/combustor run at 1 atm. This includes the following: (1) the data of Leonard and Stegmaier (1993) obtained for a porous-plate laboratory combustor, for which insignificant dependency of the NO_x on pressure, inlet temperature, and overall residence time was reported; (2) the data of Joshi et al. (1994) obtained using prototype premixers and combustor segments, which indicate a slightly negative pressure exponent (Eq. (2)) similar to that stated above for the HP-JSR data; and (3) the data of Sattelmayer et al. (1990) for the double-cone combustor run at 1 atm. The data of Snyder et al. (1994) for the high penetration premixer also lie relatively close to the jet-stirred reactor data. For certain regimes, the Snyder et al. data show a weak, though generally somewhat positive pressure dependency of the NO_x. The tendency of the NO_x emissions of the practical premixers/combustors (Joshi et al., Sattelmayer et al., Snyder et al.) to lie a factor 1 to 2 above the laboratory data (of this study and Leonard and Stegmaier, 1993) is attributed to more nearly perfect premixing possible in the laboratory rigs than in the practical hardware. Other data plotted are from Snyder et al. (1994) for the low penetration premixer, Aigner et

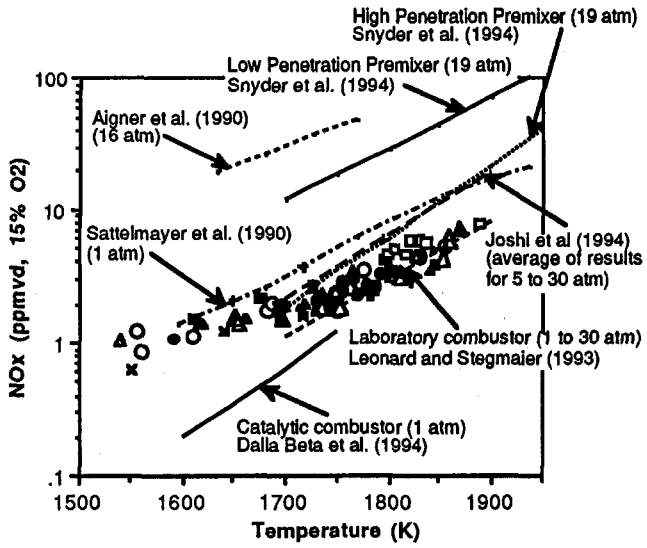

Fig. 5 Comparison of complete NO_x dataset to recently published NO_x data for LPM combustors

al. (1990) for the double-cone burner, and Dalla Betta et al. (1994) for a laboratory catalytic combustor.

For the complete jet-stirred reactor database, over the temperature range of 1700 to 1900 K, the Arrhenius-type best fit is

$$NO_x(\text{ppmvd, 15 percent } O_2) = 1.72 \times 10^6 \exp(-23650/T(K)), \quad (3)$$

corresponding to an overall activation energy of NO_x formation of 47.0 kcal/gmol. The Leonard and Stegmaier data correspond to an overall activation energy of 57 kcal/gmol. Other results plotted in Fig. 5 give overall activation energies in the range from 35 to 70 kcal/gmol.

Chemical reactor modeling has been used by Nicol (1995) to determine NO_x overall activation energies for the 1700 to 1900 K range. The combustor is simulated by a PSR (of either incipient-blowout or 2 ms residence time) followed by a PFR (plug flow reactor). Total residence time is 6 ms. The results given below in Table 1 show that the NO_x activation energy is sensitive to the chemical kinetic mechanism, the pressure level, and the residence time split. The greater activation energies for the blowout PSR are due to the relatively long residence time of the PFR, and, thus, the opportunity for post-flame, thermal NO_x formation. Thermal NO_x, i.e., NO_x formation due to the Zeldovich mechanism under the influence of equilibrium O-atom, has an activation energy of 135 kcal/gmol. If thermal NO_x is eliminated from the computation, and only the NO_x due to superequilibrium free-radical attack on the N_2 (in the Zeldovich, nitrous oxide, and prompt mechanisms) is considered, the range of the activation energies for the full range of conditions of Table 1 is narrowed; 47.7 to 55.5 kcal/gmol by the MB mechanism (indicating little pressure sensitivity), and 54.2 to 77.6 by the DB mechanism.

Table 1 Overall activation energies of NO_x formation

PSR Residence Time (ms)	Pressure Range	
	1 to 10atm	10 to 30atm
	Miller-Bowman (1989) Mechanism (MB)	
blowout	56.8	71.0
2.0	48.8	60.4
	Drake-Blint (1991) Mechanism (DB)	
blowout	65.1	90.5
2.0	56.6	83.8

Chemical Reactor Modeling of the HP-JSR

Chemical reactor modeling for the HP-JSR is based on two PSRs in series (Steele, 1995). This configuration is used in order to simulate the two-zone behavior implied by the O-atom relaxation (Fig. 1) and the CO profile (Fig. 3). The first PSR is used to provide a relatively small zone of high free-radical concentrations and high NO_x formation rate. The second PSR is used to simulate the significantly reduced free-radical activity of the relatively large recirculation zone.

The ratio of volumes of the two PSRs is selected so that the minimum CO concentration measured in the recirculation zone is matched to the modeled result for the second PSR. The temperature is matched also. The volume of the two PSRs is set equal to the volume of the HP-JSR. The CO loss in the probe is modeled and is included as part of the matching.

Alternatives to the two-PSRs-in-series configuration have been evaluated for the HP-JSR (Steele, 1995; Horning, 1996). The replacement of the second PSR with a PFR permits too much CO oxidation, and, thus, gives too low of CO concentration exiting the reactor. This implies that the recirculation zone of the HP-JSR has sufficient mixing to prevent the CO from relaxing to its equilibrium concentration. If the PFR is made

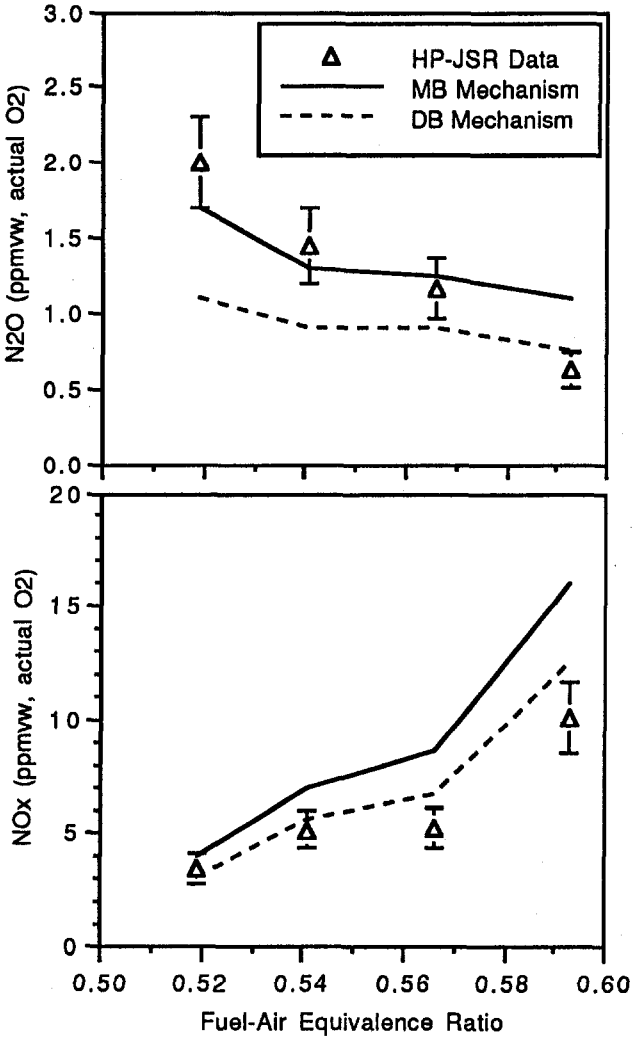

Fig. 6 Comparison of two-PSR model to measurement. Pressure = 7.1 atm, residence time = 3.9 ms, inlet temperature = 605 K. Respective combustion temperatures are 1745, 1810, 1835, and 1865 K.

small and, consequently, the initial PSR is made large, the minimum CO of the recirculation zone is matched, but the NO_x becomes unrealistically large. (The model of a large PSR and a small PFR does work acceptably for the 1 atm JSR.) The addition of recycle of some of the exit gas of the second PSR into the initial PSR gives too large of CO concentration in the second PSR. On the other hand, if recycle is added to the PSR-followed-by-PFR model, the problem of too low of exit CO returns. The two-PSRs-in-series model works best for methane burned at temperatures below about 1800 K. For higher temperatures, the addition of a small PFR zone after the second PSR gives best agreement to the measured CO (Horning, 1996). The small PFR zone simulates additional relaxation of the CO in the recirculation zone of the HP-JSR. The effect of the small PFR zone on the NO_x prediction is nil.

Results obtained by the two-PSRs-in-series configurations are shown in Fig. 6. The NO_x and N_2O modeled for the second PSR are compared to the data measured for the recirculation zone. Two chemical kinetic mechanisms have been used in this analysis: the Miller and Bowman (1989) mechanism (MB), and the Drake and Blint (1991) mechanism (DB). The trends in the measured NO_x are reproduced by the model. The modeled results obtained with the DB mechanism lie relatively close to the measured NO_x. On the other hand, the measured N_2O is most closely reproduced by the MB mechanism. This implies that the DB mechanism may under predict the NO_x formed via the nitrous oxide pathway, and may compensate for this by over predicting the NO_x formed by the prompt pathway.

Finite Mixing Modeling of the HP-JSR

A reactor model which includes finite rate macromixing and micromixing effects is applied in this section. This numerical model, developed by Tonouchi and Pratt (1995), involves a particle-tracking, control volume approach. The model and its application are described by Tonouchi (1996). The jet and recirculation zones of the HP-JSR are divided into several control volumes having the same axial length. The amount of macromixing within the HP-JSR is modeled using the recirculation ratio R, which is defined as the ratio of the mass flow rate of the jet at the reactor's back wall to the inlet jet mass flow rate.

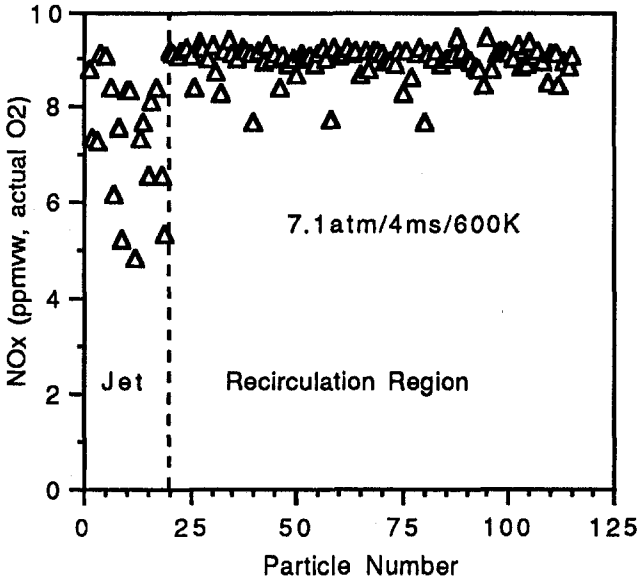

Fig. 7 Application of the finite-rate mixing model to HP-JSR. Pressure = 7.1 atm, residence time = 4 ms, inlet mixture temperature = 600 K, fuel-air equivalence ratio = 0.58. Results are presented as a scatterplot "snapshot" of particle NO_x concentrations. The mean particle NO_x in the jet element is 7.5 ppm. The mean particle NO_x value in the recirculation region is 9.0 ppm.

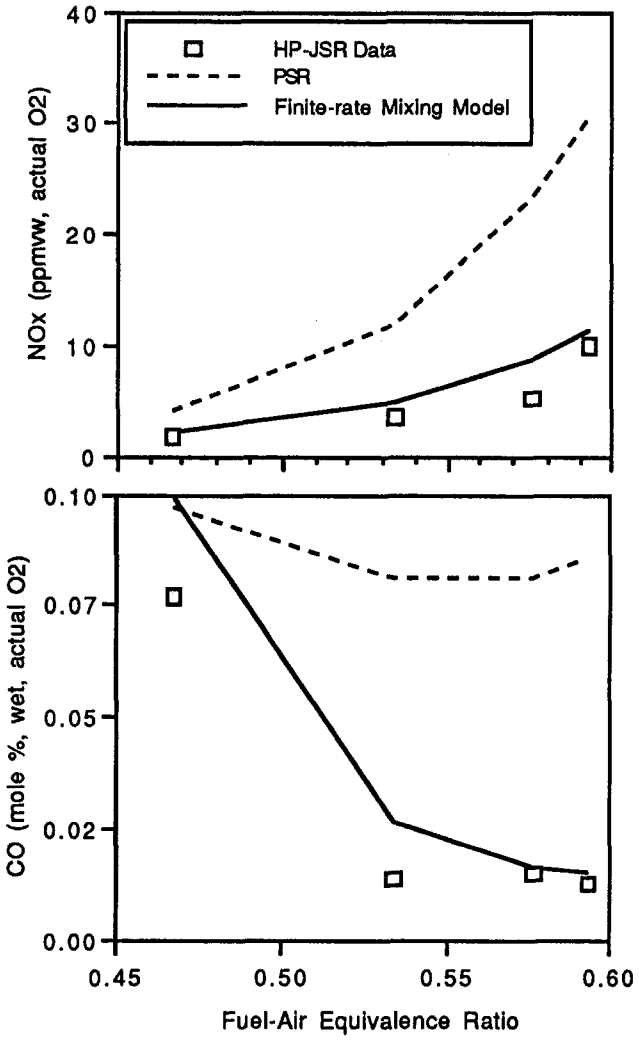

Fig. 8 Comparison of the finite-rate mixing model and the PSR model to the experimental data of Steele (1995). Pressure = 7.1 atm, residence time = 4 ms, and inlet temperature = 600 K.

Finite-rate micromixing within each control volume is modeled using either the CD or IEM theory. In the CD approach, micromixing is simulated by randomly pairing particles to mix (coalesce and disperse). During this CD event, the extensive properties of the paired particles are averaged, while between CD encounters the particles undergo batch reaction. The number of pair encounters for a given time Δt is given by $\beta \Delta t N_{cv}$, where N_{cv} is the number of particles in the control volume, and β is the CD mixing frequency or the reciprocal of the turbulent mixing time. The ratio of β to the feed frequency (i.e., the reciprocal of the mean residence time) is the micromixing parameter I_m. The parameter I_m is prescribed for each control volume by estimating the CD mixing frequency β as the ratio of the local turbulent dissipation rate to the local turbulent kinetic energy. The resulting algebraic expression for I_m requires an estimate of the size of the velocity fluctuations. For the purposes of modeling the experimental data, the rms values of the velocity fluctuations are estimated to be 25 percent of the local mean velocity of the gases flowing in the control volume.

In the IEM theory, the particles' physical properties are determined from an evolution equation that includes the mean properties of the control volume. The IEM algorithm used in this model is similar to the approach used by Correa (1993). In the IEM model, the micromixing parameter is the IEM mixing frequency w. This mixing frequency is related to the CD mixing frequency by a factor of 2 (Villermaux, 1986).

Figures 7 and 8 show the application of the finite mixing model to the HP-JSR data for 7.1 atm pressure, 600 K inlet temperature, and 4 ms residence time. The chemical kinetic mechanism used is the 24 step/16 species reduced mechanism of Nicol (1995), which is based on the Miller and Bowman (1989) mechanism. The reduced mechanism retains the essential features of methane oxidation and NO_x formation by the Zeldovich and nitrous oxide reactions. The value of R estimated for this application is 6.5, the micromixing is treated by the CD theory, and the reactor is assumed adiabatic. For reference, results obtained by modeling the HP-JSR as a single, adiabatic PSR are also plotted. In this case, the full Miller and Bowman (1989) mechanism is used.

Figure 7 is a scatterplot of NO_x for one instant ("snapshot") for a fuel-air equivalence ratio of 0.58. The scatterplots are for the jet control volume and adjacent recirculation region control volume corresponding to the sample probe path. This figure indicates a low variation of NO_x in the recirculation zone. Figure 8 shows the predictions of the finite-rate mixing model and the PSR model. The finite-rate mixing model results are for the recirculation region control volume corresponding to the sample probe path. The results plotted for NO_x and CO generally show close agreement to the experimental data, and, thus, indicate that the data are influenced by finite-rate mixing effects. Essentially, the same results (not shown) are obtained when the IEM micromixing model is used (Tonouchi, 1996). The results for temperature and N_2O predicted by the finite rate mixing model, though not plotted in Fig. 8, also generally show close agreement to the experimental data. Additionally, although predictions of NO_x by the two-PSRs-in-series model are not shown in Fig. 8, the results in Fig. 8 may be directly compared to the two-PSRs-in-series results of Fig. 6. This comparison may be made because Figs. 6 and 8 pertain to the same experimental conditions (though the measurements were taken on different days).

Conclusions

The high-pressure, jet-stirred reactor (HP-JSR) has been described and shown to exhibit distinct two zone behavior. The HP-JSR provides useful data and insight on NO_x formation for high-intensity, LPM combustion. In particular, the results show how NO_x formation varies as a function of the primary combustion variables, including combustion temperature, pressure, inlet temperature, and residence time, and indicate that the NO_x formation is sensitive to the free radical relaxation rate. Also indicated are characteristic rates of formation of NO_x for LPM flame zones.

Two models have been developed. One is the two-PSRs-in-series model, which conveniently permits evaluation of the HP-JSR, and may be useful generally for the prediction of species concentrations in high-intensity, high-pressure flames. The other is the finite mixing model, which reproduces the HP-JSR species concentrations quite well, and indicates the degree to which finite mixing affects the HP-JSR. The finite mixing model shows promise for future application to high-intensity, high-pressure combustion.

Acknowledgments

The ATS Program of the U.S. Department of Energy is thanked for the support of the computational components of this study. Additionally, the Asea Brown Boveri Company is thanked for the gift of a Graduate Fellowship to the University of Washington, which has supported the fabrication and operation of the HP-JSR facility.

References

Aigner, M., Mayer, A., Schiessel, P., and Strittmatter, W., 1990, "Second-Generation Low-Emission Combustors for ABB Gas Turbines: Test Under Full-Engine Conditions," presented at the Gas Turbine and Aeroengine Congress, Brussels, Belgium, ASME Paper No. 90-GT-308.

Beér, J. M., and Chigier, N. A., 1983 *Combustion Aerodynamics,* R. E. Krieger Publishing Co., Malabar, FL.

Correa, S. M., 1993, *Combust. and Flame,* Vol. 93, pp. 41–60.

Dalla Betta, R. A., Schlatter, J. C., Nickolas, G. G., Yee, D. K., and Shoji, T., 1994, "New Catalytic Combustion Technology for Very Low Emissions Gas Turbines," presented at the Gas Turbine and Aeroengine Congress, The Hague, The Netherlands, ASME Paper No. 94-GT-260.

Drake, M. C., and Blint, R. J., 1991, *Combust. Science and Technol.* Vol. 75, pp. 261–285.

Horning, D., 1996, "Pollutant Formation by Lean-Premixed Combustion in a High Pressure Jet-Stirred Reactor," M.S. thesis, University of Washington, Seattle, WA.

Joshi, N. D., Epstein, M. J., Durlak, S., Markovits, S., and Sabla, P. E., 1994, "Development of a Fuel Air Premixer for Aero-Derivative Dry Low Emissions Combustors," presented at the Gas Turbine and Aeroengine Congress, The Hague, The Netherlands, ASME Paper No. 94-GT-253.

Leonard, G., and Stegmaier, J., 1993, "Development of an Aeroderivative Gas Turbine Dry Low Emissions Combustion System," presented at the Gas Turbine and Aeroengine Congress, Cincinnati, OH, ASME Paper No. 93-GT-288.

Miller, J. A., and Bowman, C. T., 1989, *Prog. in Energy and Combust. Science,* Vol. 15, pp. 287–338.

Nicol, D. G., Steele, R. C., Marinov, N. M., and Malte, P. C., 1995, ASME JOURNAL OF ENGINEERING FOR GAS TURBINES AND POWER, Vol. 117, pp. 100–111.

Nicol, D. G., 1995, "A Chemical Kinetic and Numerical Study of NO_x and Pollutant Formation in Low-Emission Combustion," Ph.D. dissertation, University of Washington, Seattle, WA. (Available from University Microfilms, Ann Arbor, MI.)

Sattelmayer, T., Felchlin, M. P., Haumann, J., Hellet, J., and Styner, D., 1990, "Second-Generation Combustors for ABB Gas Turbines: Burner Development and Tests at Atmospheric Pressure," presented at the Gas Turbine and Aeroengine Congress, Brussels, Belgium, ASME Paper No. 90-GT-162.

Snyder, T. S., Rosfjord, T. J., McVey, J. B., Hu, A. S., and Schlein, B. C., 1994, "Emission and Performance of a Lean-Premixed Gas Fuel Injection System for Aeroderivative Gas Turbine Engines," presented at the Gas Turbine and Aeroengine Congress, The Hague, The Netherlands, ASME Paper No. 94-GT-234.

Steele, R. C., 1995, "NO_x and N_2O Formation in Lean-Premixed Jet-Stirred Reactors Operated From 1 to 7 atm," Ph.D. dissertation, University of Washington, Seattle, WA. (Available from University Microfilms, Ann Arbor, MI.)

Steele, R. C., Jarrett, A. C., Malte, P. C., Tonouchi, J. H., and Nicol, D. G., 1997, "Variables Affecting NO_x Formation in Lean-Premixed Combustion," ASME JOURNAL OF ENGINEERING FOR GAS TURBINES AND POWER, Vol. 119, pp. 102–107.

Tonouchi, J. H., and Pratt, D. T., 1995, "A Finite-Rate Macromixing, Finite-Rate Micromixing Model for Premixed Combustion," paper presented at the 1995 Fall Meeting of the Western States Section/The Combustion Institute, Stanford, CA.

Tonouchi, J. H., 1996, "Macromixing and Micromixing in Lean Premixed Combustion," Ph.D. dissertation, University of Washington, Seattle, WA. (Available from University Microfilms, Ann Arbor, MI.)

Villermaux, J., 1986, *Encyclopedia of Fluid Mechanics,* Gulf Publishing Company, West Orange, NJ.

Williams, J. T., 1995, "NO_x Formation in a Stirred Reactor with Large Jets," M.S. thesis, University of Washington, Seattle, WA.

Results of Experiments and Models for Predicting Stability Limits of Turbulent Swirling Flames

S. Hoffmann
Siemens-KWU,
D-45466 Mülheim,
Federal Republic of Germany

B. Lenze
Engler-Bunte-Institut,
Universität Karlsruhe,
D-76128 Karlsruhe,
Federal Republic of Germany

H. Eickhoff
DLR, D-51170,
Cologne,
Federal Republic of Germany

Swirling flames are used in many industrial applications, such as process furnaces, boilers, and gas turbines due to their excellent mixing, stability, emission, and burnout characteristics. The wide-spread use of swirl burners in the process and energy industries and, in particular, new concepts for the reduction of NO_x emissions, raises the need for simple-to-use models for predicting lean stability limits of highly turbulent flames stabilized by internal recirculation. Based on recently published experimental data of the first author concerning the reaction structures of swirling flames operating near the extinction limit, different methods for predicting lean blow-off limits have been developed and tested. The aim of the investigations was to find stabilization criteria that allow predictions of blow-off limits of highly turbulent recirculating flames without the requirement for measurements in those flames. Several similarity criteria based on volumetric flow rates, burner size, and material parameters of the cold gases were found to be capable of predicting stability limits of premixed and (in some cases) nonpremixed flames at varying swirl intensities, burner scales and fuel compositions. A previously developed numerical field model, combining a $k-\epsilon$ model with a combined "assumed-shape joint-PDF"/eddy-dissipation reaction model was also tested for its potential for stability prediction.

Introduction

Stability, emission, and burnout characteristics of swirling flames are used in many industrial applications, such as process furnaces, boilers, and gas turbines due to their excellent mixing. The swirl-induced formation of a central recirculation zone with heat and chemically active species plays the essential role in the stabilization processes in those highly turbulent natural gas flames. The wide-spread use of swirl burners in combustion systems and new concepts for thermal NO_x reduction by ultra lean premixed combustion or/and for fuel NO_x reduction by air staging (rich/lean combustion zones) raises the need for simple models to predict lean stability limits of turbulent flames with inner recirculation. Different methods for the prediction of lean blow-off limits that do not require field measurements in flames or cold flows will be discussed.

Basic Relations for Reactions, Stability, and Modeling

Structures of Reaction in Swirling Flames. The results of our investigations concerning the reaction structures in turbulent swirling flames published in [1, 2] show that intense turbulence in the shear layer between the recirculation zone and the forward flow results in a well-mixed "distributed reaction zone," where fluid elements with different reactivities can coexist. Measurements at different flow rates show that aerodynamically controlled parameters like the mean flow and mixing fields are invariant against Reynolds number variations, while flame characteristics, which are influenced by the chemical reactions such as temperature and species concentrations, show strong variations with flow rate, especially at relatively low Reynolds numbers. Results of experimental and numerical investigations of the stabilization [2, 3] reveal that reactions in swirling flames occur at relatively low turbulent Damköhler numbers, indicating that the flames are kinetically controlled even at relatively low burner loads. We have shown [11] for the swirling flames that the reactions are to be located mainly in the Well-Stirred Reactor (WSR) Regime. It is not surprising, therefore, that the processes leading to blow-off of swirling flames resemble those observed in well-stirred reactors: Increased burner loads result in a shortening of residence time inside the stabilization zone, causing a decrease of burnout and temperature due to the reduced heat release finally resulting in flame blow-off.

Methods for Predicting Stability Limits

Peclet Number Model. The stability limits of premixed and nonpremixed recirculating flames can be described by Peclet numbers based upon the blow-off velocity u_i or the laminar flame speed S_l, respectively [4, 5, 6]:

$$\mathrm{Pe}_{ui} \sim \mathrm{Pe}_{Sl}^{n} \tag{1}$$

$$\mathrm{Pe}_{ui} = (u_i \cdot L_{char})/a \tag{2}$$

$$\mathrm{Pe}_{Sl} = S_l \cdot D/a \tag{3}$$

where the theoretical value of n is equal to 2.

Due to the experimentally proven Reynolds number invariance of the fully turbulent flowfield, the characteristic length scale L_{char} is the length of the inner recirculation zone being proportional to the burner diameter D for geometrically similar burner configurations. Furthermore, the tangential velocities w are proportional to the swirl number S_0 and the axial exit velocity u_0, so that a characteristic tangential velocity $w = u_0 \cdot S_{0,th}$ was considered as a reasonable parameter for a characteristic velocity.

With this and when $u_i = u_o$ the Peclet numbers can be written as:

Contributed by the International Gas Turbine Institute and presented at the 42nd International Gas Turbine and Aeroengine Congress and Exhibition, Orlando, Florida, June 2–5, 1997. Manuscript received at ASME Headquarters February 1997. Paper No. 97-GT-396. Associate Technical Editor: H. A. Kidd.

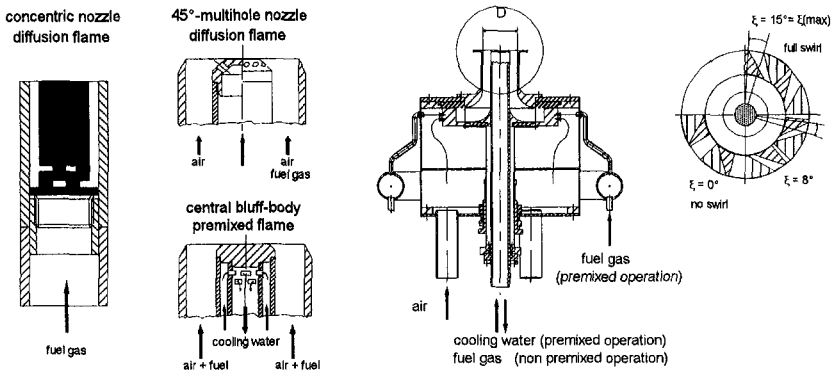

Fig. 1 Swirl burner for premixed and nonpremixed operation

$$(u_0 \cdot S_{0,th} \cdot D)/a = \mathrm{Pe}_w \sim \mathrm{Pe}_{Sl}^2 = \{(S_l \cdot D)/a\}^2 \quad (4)$$

$$(u_0 \cdot S_{0,th})/D \sim S_l^2/a \quad (5)$$

Equation (5) allows prediction of stability limits for premixed burners of different scales based on burner size, flow rate, and parameters of the cold gases only and operating with different fuels and swirl intensities. For nonpremixed combustion, variations of the momentum ratio of gas to air flow cause variations of the average mixing field due to the different mixing behavior of the fuel.

The Peclet number model requires values of the laminar burning velocities as an input, whereby values of S_l published in the literature are sometimes not consistent, and for some fuels no data are available. Moreover, errors in flow rate measurements that lead to some scatter of the stability measurements also cause errors in S_l, which was derived according to the blow-off air ratio. In order to avoid those difficulties, the Peclet number expression can easily be transformed to obtain

$$(u_0 \cdot S_{0,th})/D \propto S_l^2/a \quad (6)$$

If only one type of fuel is being considered, the laminar burning velocity and thermal conductivity depend on the initial air ratio only, so that they can be substituted by an empirical function λ [11, 13]:

$$(u_0 \cdot S_{0,th})/D = F\{\lambda\} \quad (7)$$

In Eqs. (6) and (7) D/u_0 represents a typical residence time in the stabilization zone of the flame, and $S_{0,th}$ takes into account the effect of air entrainment. This simplified relationship enables prediction of stability limits of burners of different size at varying swirl intensities. The only input data needed are the nozzle diameter and blow-off data of a geometrically similar model burner for the determination of the λ-function.

Chemical Reactor Modeling. For swirling flames, the intense turbulence in the near field of the burner leads to the existence of a well-mixed "distributed reaction zone" in the shear layer between the recirculation zone and the fresh combustible mixture. The processes that cause the flame blow-off resemble those observed in well-stirred reactors (WSR), which leads to the idea of a relation between the blow-off limits of well-stirred reactors and swirling flames.

The critical residence time τ_{WSR} of an adiabatic WSR given by the reactor volume divided by the flow rate at the extinction limit only depends on fuel type, stoichiometry and inlet temperature and is not influenced by the reactor volume. Hence, τ_{WSR} may also be interpreted as a characteristic chemical reaction time scale for the relevant oxidation reactions. The WSR calculations were performed using the PSR code by Glarborg et al. [7] and a detailed reaction mechanism by Miller and Bowman [8]. To reduce the computational effort, only the reactions of the C–H–O system were considered.

Following the previous considerations, the residence time in the stabilization zone τ_{Flame} can be expressed by the typical length scale of the burner divided by a characteristic velocity, provided that geometric similarity exists. In the present, the burner diameter and the bulk burner exit velocity were used as characteristic parameters. Comparison of both time scales proves that they are well correlated with each other, giving the opportunity to predict blow-off velocities of geometrically similar burners operated with different fuels based on the knowledge of τ_{WSR} and the stability diagram of a model burner.

Numerical Field Models. Previous investigations [2, 3] showed that correct prediction of the general characteristics and stability limits of swirling flames can only be achieved if the mean flowfield and the turbulent mixing are adequately pre-

Nomenclature

a = thermal conductivity, m^2/s^2
B = blockage ratio = $d_0^2/(D^2 - d_0^2)$
c_μ = dimensionless constant [Eq. (1)]
D = burner diameter, m
Da = Damköhler number
Ka = Karlowitz number
k = turbulent kinetic energy, m^2/s^2
L_{char} = characteristic lengthscale, m
L_t = turbulent length, m
m = constant
n = exponent [Eq. (3)]
Pe_{ui} = Peclet number based on blow-off velocity
Pe_{Sl} = Peclet number based on laminar flame speed
r = radial distance, m
S = flame speed m/s
S_0 = initial swirl number
$S_{0,th}$ = theoretical swirl number
T = temperature °C
u = axial velocity, m/s
v = radial velocity, m/s
w = tangential velocity m/s
x = axial distance, m
ϵ = turbulent dissipation energy, m^2/s^3
λ = excess air factor
ξ = angle of swirl generator
τ = residence time s

Subscripts

air = air
char = characteristic
f = fuel
i = blow-off
fl = flame
l = laminar
WSR = well-stirred reactor
0 = burner exit
s = flame velocity
t = turbulent
th = theoretical

dicted. In the numerical model considered, this has been achieved by accounting for the swirl-induced attenuation or amplification of turbulence by means of a Richardson number correction applied to the $k-\epsilon$ model, in which the axisymmetric transport equations for the following variables were solved: velocity, turbulence energy and its dissipation rate, mixture fraction and its fluctuation, enthalpy, fuel concentration, CO-concentration, and temperature fluctuations. The partial differential equations were solved by a semi-implicit finite volume algorithm following Patankar and Spalding. A second-order differencing procedure (QUICK) on a fine grid allowed the prediction of the small recirculation zone along the central bluff body, which is important for calculation of the stabilization limits. We captured the major features by a PDF approach accounting for fluctuating of temperature (T) and mixture fraction (f) and statistical correlations of related quantities. The reaction mechanism used was the two-step methane mechanism following Westbrook and Dryer [9]. In the numerical model, the actual shape of the PDF was calculated from values of f, f'^2, T and T'^2 in a way that approximates the experimental findings, as explained in [3].

The effective reaction rate is calculated by superposition of the joint-PDF (JPDF) reaction rate with the eddy break-up (EBU) reaction rate. In [3] it has shown that the reaction model is suitable for premixed and nonpremixed systems, provided that the aerodynamic model is able to predict the flow and mixing field correctly. Stability limits had to be determined iteratively by the numerical code, which required a considerable computational effort.

Experiments

The experiments on enclosed and nonenclosed as well as premixed and nonpremixed flames were performed for geometrically similar burners. A "Movable-Block" swirl generator

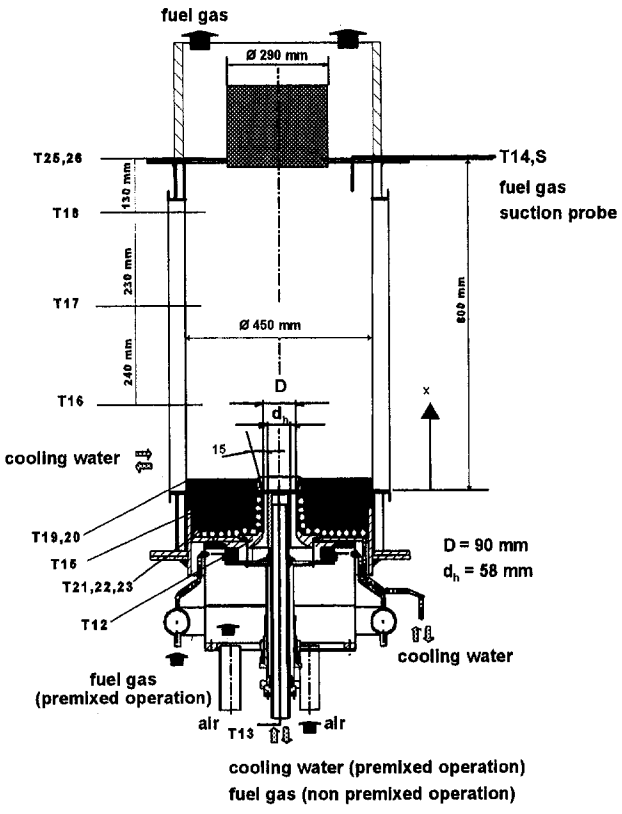

Fig. 2 Water-cooled furnace with burner, fuel gas exit, and temperature (T) and suction (S) probe location

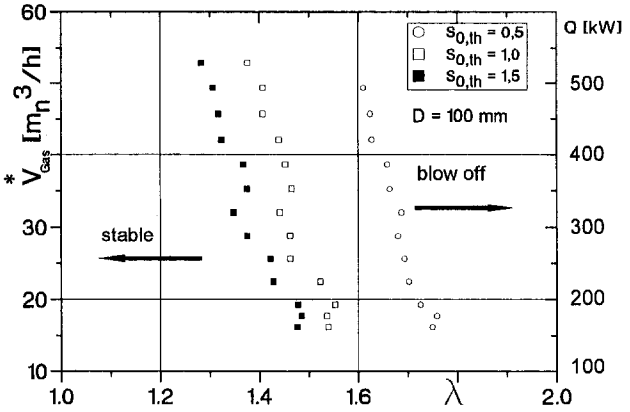

Fig. 3 Stability limits of unconfined swirling premixed flames as a function of air equivalence ratio λ and theoretical swirl number $S_{0,th}$

allowed for continuous adjustment of the theoretical swirl number between values of 0 and 2 [10] (Fig. 1). Burners with nozzle diameters between 60 and 100 mm were operated at thermal loads of 250 up to 750 kW and Reynolds numbers > 60,000.

For the diffusion flames fuel gas was supplied through the central bluff-body, the blockage ratio B being 0.33, and injected into the concentric, swirling air flow by means of interchangeable 45 deg multihole nozzles or a concentric gas ring. For premixed flames fuel gas was injected radially upstream of the swirler through eight nozzles in order to provide complete mixing in the burner exit plane and a watercooled central bluff-body was installed in order to keep the geometry comparable to that of the diffusion flame experiments with the same blockage ratio [11]. All experiments have been made with temperature of fuel and air of 20°C.

The measurements in the near field of the burner included the determination of the velocity and temperature fields as well as mean values of volumetric concentrations of the relevant stable species at different flow rates. In addition, the blow-off limits were determined for a variety of swirl numbers, air-to-fuel ratios, and fuel gas compositions. A counter-type two-color LDV working in backscattering mode was used for the velocity measurements; magnesia oxide particles with diameters of about 1 micron served as tracer seeds. The turbulent temperature fields were measured using electronically compensated thermocouples with diameters of 50 and 100 μm [12], the compensation of thermal inertia resulting in a dynamic range of about 1 kHz. Commercial gas analyzers were used for the concentration mea-

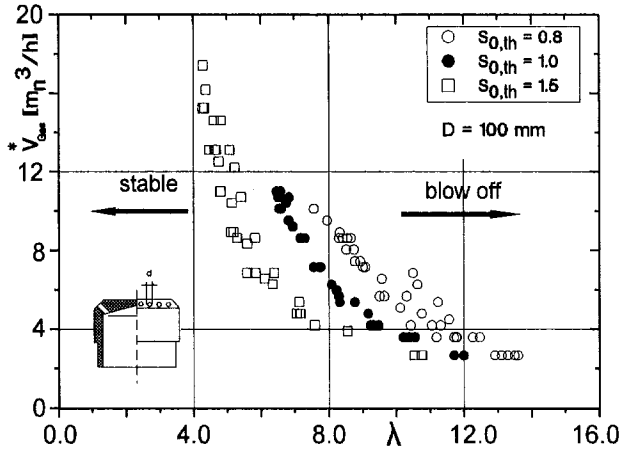

Fig. 4 Stability limits of swirling diffusion flames as a function of air equivalence ratio λ and theoretical swirl number $S_{0,th}$

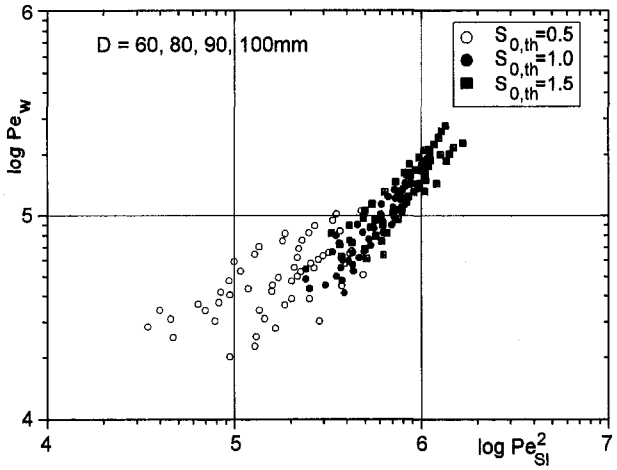

Fig. 5 Correlation of stability data based on Peclet numbers (Eq. (4)), for premixed swirling flames

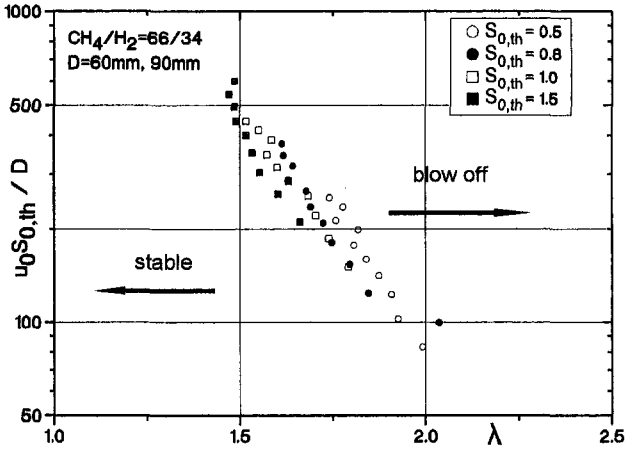

Fig. 7 Correlation of stability data based on the simplified relation Eqs. (7) and (8) for premixed swirling flames (fuel: 66 percent CH_4, 34 percent H_2) in dependence on λ

surements. Sampling was nearly isokinetic by watercooled stainless-steel suction probes, which could be turned into the mainstream direction by means of stepping motors. More detailed descriptions of the experimental setup are given in [1, 2, 11]. At least some experiments have been made with enclosed flames with a burner of $D = 90$ mm and a watercooled combustion chamber of 500 mm diameter and 1000 mm length and a central plate in the chamber exit, so that the flue gases flow out of the furnace by a ring and no recirculation flow from outside the furnace can influence the reaction zone (Fig. 2).

The results of the detailed velocity, temperature, and concentration measurements in the region of the length of the flame L ($L \approx 3.5D$) have been presented in [11 and 14].

Results

The experiments show the basic influences on flame stability limits and assess the stability models for unconfined burning flames. Figure 3 shows that the results of stability measurements on unconfined, premixed swirling flames at different initial swirl numbers. Combustion is stable for conditions left of the given data points. At a given swirl number the regime of stable combustion is shifted toward smaller air ratios with increasing thermal load due to the higher kinetic rates of the mixture. Increasing swirl leads to a higher entrainment of air, resulting in lower flame temperatures and flame speeds and in decreasing of the limits of stable combustion in free jet flames. The blow-off curves in Fig. 4 reveal that the same behavior can also be observed in the case of nonpremixed swirling flames. In the whole range of swirl numbers, the diffusion flames display higher stability limits than the comparable premixed flames. This is due to the fact that fuel concentration is higher in the stabilizing recirculation zone.

Figure 5 shows stability data evaluated according to the Peclet number relation, based on flame speeds determined on a Bunsen flame. The Peclet number dependency correlates the measurements for three different swirl numbers and four burner sizes rather satisfactorily. In Fig. 6, the stability data of Fig. 5 are presented as a function of the excess air factor λ in a semilogarithmic diagram. It can be seen that the inverse characteristic residence time $u_0 \cdot S_{0,th}/D$ is well reproduced by an exponential function of the form

$$(u_0 \cdot S_{0,th})/D = \exp\{m \cdot \lambda + B\} \qquad (8)$$

with a reduction of the scatter of correlation and with m and B as empirical constants. In order to analyze the influence of kinetic rates or laminar burning velocities on the stability limits of recirculating flames, additional measurements were carried out using different mixtures of natural gas (95 percent CH_4) and hydrogen or nitrogen. In the case of hydrogen-doped flames, higher content of H_2 leads to a widening area of stable operation due to the lower fuel lean ignition limit of H_2 compared to CH_4. Figure 7 presents corresponding curves for a fuel mixture of 66 percent CH_4 and 34 percent H_2. The stability data are again represented by a single straight line, only the empirical constants of the exponential function had to be adapted for this different fuel. The stability data presented in Fig. 8 show that Eq. (8) is

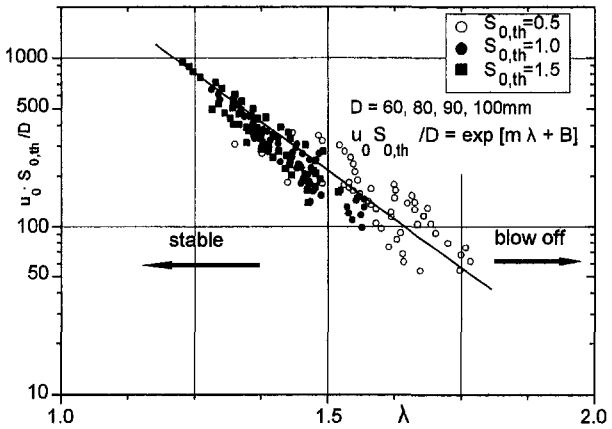

Fig. 6 Correlation of stability data based on the simplified Eq. (8) for swirling premixed flames

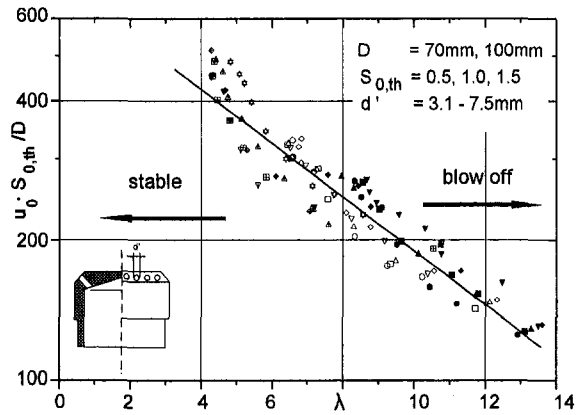

Fig. 8 Correlation of stability data based on the simplified relation (8) for swirling diffusion flames

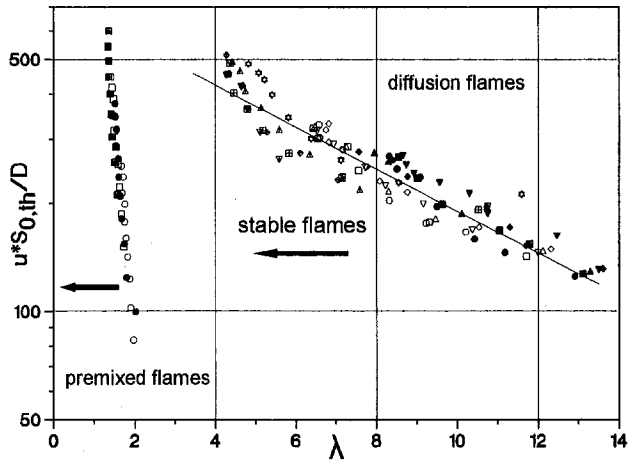

Fig. 9 Correlation of stability data based on the simplified relation for swirling flames in dependence on λ

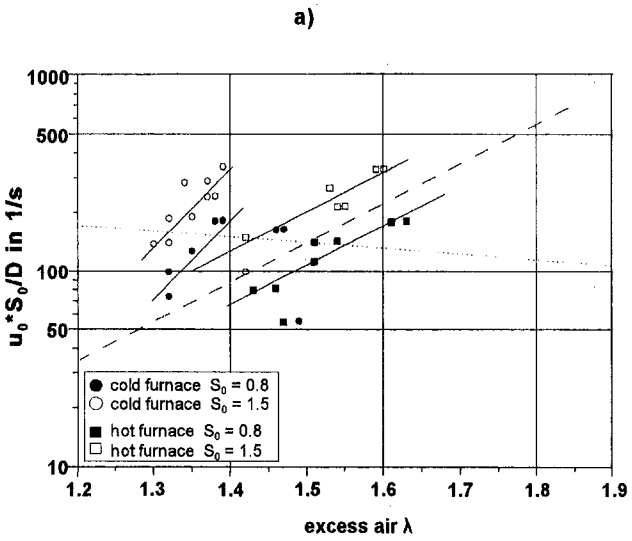

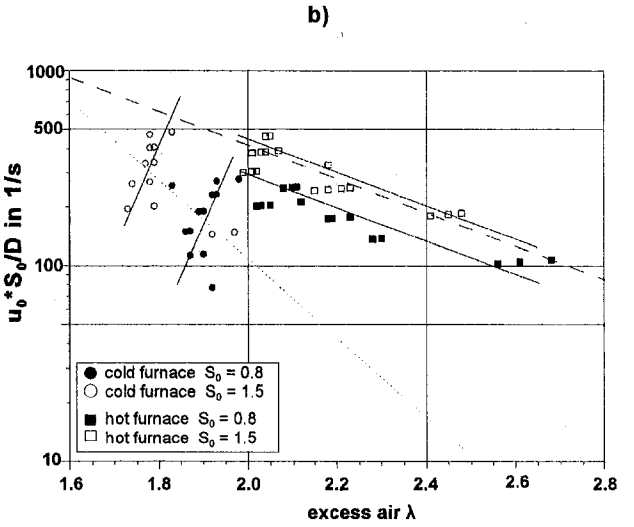

Fig. 11 Stability limits of enclosed premixed swirling flames in a hot and cold combustion furnace: (*a*) premixed; (*b*) diffusion flame

also applicable to nonpremixed flames. Using Peclet number based models, the stability limits of geometrically similar turbulent flames of different size operated with different fuels can be predicted on the basis of stability measurements on a model burner. Furthermore, the simplified model offers the opportunity to predict the stability limits of diffusion flames. However, the constants of the exponential function have to be adapted to every combination of burner system and fuel.

In Fig. 9 the results of premixed and non-premixed flames have been comprehended with regard to the stability and the diagram shows that premixed flames are stable in a small excess air ratio regime only while the non-premixed flames burn stably up to excess air factors of about 14 and more, depending on the load, swirl parameter, and burner diameter. The limits of stabilization for smaller λ values could not be measured because the combustion air supply was limited to about 1200 m^3/h, which causes relatively low exit velocities (45–70 m/s) at the comparatively large experimental burners with diameters of 80–100 mm in the back.

The comparison between the characteristic residence times at the blow-off limit of turbulent flames and of WSRs, which are displayed in Fig. 10, shows that the time scales are well correlated. This offers the opportunity to predict the stability limits of swirling flames for varying burner scales and different fuels, based on stability measurements with a model burner and calculated values of τ_{WSR}.

Figure 11 shows measured stability points of different enclosed flames (premixed Fig. 11(*a*) and diffusion Fig. 11(*b*)) in dependence on excess air factor with hot (1500°C) and cold (100°C) combustion chamber walls.

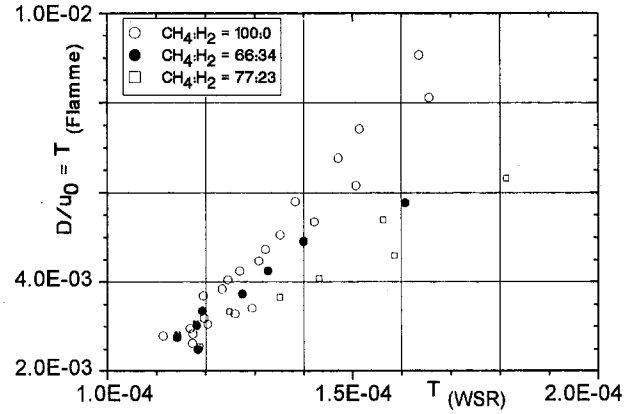

Fig. 10 WSR modeling: correlation of characteristic residence time (τ_{Flame} and τ_{WSR})

The results show differences between free and enclosed swirling flames and the model of Hoffmann regarding Eq. (8) is not usable without the consideration of the influence of inner and outer more or less hot flue gas recirculation, which can influence the stabilization of the enclosed flames by increasing the temperatures but decreasing the optimal stabilization condition of fuel and oxygen concentrations in the mixture of fuel-air-fluegas.

The experimentally and numerically collected stability data, as presented in Fig. 12, illustrate that the numerical field model treats this type of flames reasonably well throughout the whole range of blow-off velocities, swirl levels, and burner sizes [7]. The accuracy of the predictions is comparable to the ones obtained with the Peclet criteria. The numerical model is not restricted to geometrically similar systems but can also predict stability limits of different burner shapes, thus giving the opportunity to optimize the construction of burners.

Conclusions

Results from a great number of experiments and detailed mathematical modelling can be summarized as follows:

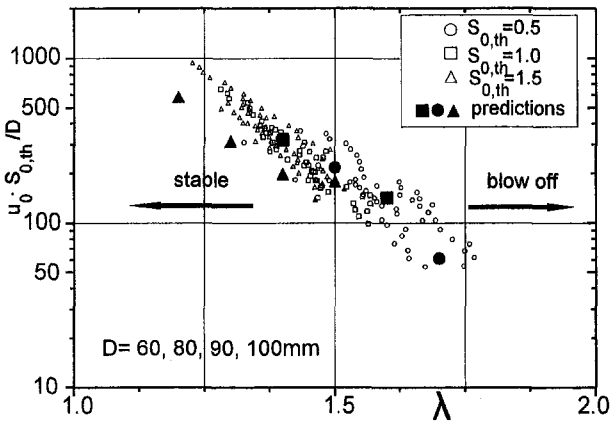

Fig. 12 Stability limits calculated from a numerical (JPDF) field model (experimental results: open symbols; predictions: filled symbols) for different burner diameter *D* and swirl parameter $S_{0,th}$

- Reaction processes in high-Reynolds-number swirl-stabilized turbulent flames are determined by finite kinetic reaction rates, since flame conditions correspond to relatively low turbulent Damköhler numbers.
- The stabilization mechanisms of the flames considered resemble those observed in a well-stirred reactor, the finite kinetic rates being the limiting factor for flame stability.
- Several simple-to-use methods for the prediction of stability limits of highly turbulent nonenclosed flames with internal recirculation zones have been developed and tested with respect to their suitability of predicting the lean blow-off limits based on volumetric flow rates, burner geometry, and material coefficients of the cold gases only. Experiments covering a wide range can very well be correlated by a unique relation such as Eqs. (6), (7) and (8).
- WSR models for premixed and nonpremixed-free flames agree with the experimentally derived correlations fairly well.
- Also numerical predictions of stability limits of free-burning flames by a numerical Joint-Probability-Density-Function (JPDF) based model agree with measurements as well.
- The results of enclosed flames measured in furnaces with cold (100°C) and hot (1500°C) combustion chamber walls differ from the relations obtained by the nonenclosed free flames.

Dedication

This work is dedicated to the 65th birthday of Professor W. Leuckel.

Acknowledgments

The investigations were conducted in the frame of projects DFG LE 399/7-1,2 and DFG-SFB167, TP A9. The authors wish to express their gratitude to the Deutsche Forschungsgemeinschaft (DFG) for their financial support.

References

1 Hoffmann, S., and Lenze, B., "Investigations Concerning Stability Mechanism of Unconfined Swirling Premixed Flames," *Archivum Combustionis,* Vol. 12, No. 1–4, 1992, pp. 45–57.

2 Philipp, M., Hoffmann, S., Habisreuther, P., Lenze, B., and Eickhoff, H., "Experimental and Numerical Study Concerning Stabilization of Strongly Swirling Premixed and Nonpremixed Flames," *24th Symposium (Int.) on Comb.,* Pittsburgh, 1992, pp. 361–368.

3 Philipp, M., "Experimentelle und theoretische Untersuchungen zum Stabilitätsverhalten von Drallflammen mit zentraler Rückströmzone," Ph.D. Thesis, Universität Karlsruhe, 1991.

4 Minx, E., "Über die Stauscheibenstabilisierung turbulenter Diffusionsflammen an Brennern mit zentraler Brennstoff- und ringförmiger Luftzufuhr," *Ph.D. Thesis, Universität Aachen, 1969.*

5 Rawe, R., "Über die Drallstabilisierung freibrennender, turbulenter Diffusionsflammen mit zentraler, radialer Gaszufuhr," Ph.D. Thesis, Ruhr-Universität Bochum, 1978.

6 Prade, B., and Lenze, B., "Experimental Investigation in Extinction of Turbulent Non-Premixed Disk Stabilized Flames," *24th Symposium (Int.) on Combustion,* Sydney, Australia, July 5–12, 1992, The Combustion Institute, Pittsburgh, 1992, pp. 369–375.

7 Glarborg, P., Kee, R. J., Grear, J. F., and Miller, J. A., "A Fortran Program for Modelling Well-Stired Reactors," Sandia National Laboratories, Albuquerque, NM, Sandia Report Sand 86-8209, 1986.

8 Miller, J. A., and Bowman, C. T., *Prog. Energy Comb. Sci.,* Vol. 15, No. 4, 1989, pp. 287–338.

9 Westbrook, C. K., and Dryer, F. L., "Simplified Reaction Mechanisms for the Oxidation of Hydrocarbon Fuels in Flames," *Combustion Sci. and Tech.,* Vol. 27, 1981.

10 Leuckel, W., "Swirl Intensities, Swirl Types and Energy Losses of Different Swirl Generating Devices," IFRF Doc No. G 02/a/16, Nov. 1967.

11 Hoffmann, S., "Untersuchungen des Stabilisierungsverhaltens und der Stabilitätsgrenzen von Drallflammen mit innerer Rückströmzone," Ph.D. Thesis, Universität Karlsruhe, 1994.

12 Günther, R., "Turbulence Properties of Flames and Their Measurement," *Prog. Energy Combust. Sci.,* Vol. 9, 1983, pp. 105–154.

13 Hoffmann, S., Habisreuther, P., Lenze, B., and Eickhoff, H., "Lean Stability Limits of Turbulent Swirling Natural Gas Flames," *Proc. International Gas Research Conference,* Cannes, 1995, pp. 11–18.

14 Hoffmann, S., and Lenze, B., "Das Strömungs-und Reaktionsfeld sowie Stabilisierungseigenschaften in Drallflammen unter dem Einflußder inneren Rückstromzone," DFG-Bericht AZ Le 399/7-1 ÷ 8-1, FIZ, Karlsuhe, 1996.

Sensor-Based Analyzer for Continuous Emission Monitoring in Gas Pipeline Applications

P. F. Schubert

D. R. Sheridan

M. D. Cooper

A. J. Banchieri

Advanced Sensor Devices,
430 Ferguson Drive,
Mountain View, CA 94043

Continuous emissions monitoring of gas turbine engines in pipeline service have typically been monitored using either laboratory derived instruments (CEMS), or predicted using data from low cost sensors on the engines and algorithms generated by mapping engine performance (PEMS). A new cost-effective system developed under a program sponsored by the Gas Research Institute (Chicago) combines the advantages of both systems to monitor engine emissions in gas transmission service. This hybrid system is a sensor-based analyzer that uses a sensor array, including a newly developed NO_x sensor, to directly monitor NO_x, CO, and O_2 emissions at the stack. The gases are measured hot and wet. The new systems were installed and tested on a gas-fired Rolls Royce Spey turbine engine and on Ingersoll-Rand KVG-410 and Cooper GMVH-10 reciprocating engines in gas transmission service. These systems passed the Relative Accuracy Test (Part B) required under U.S. EPA regulations (40 CFR 60).

Introduction

In the U.S., the Clean Air Act and its amendments have required installation of continuous emissions monitoring systems (CEMS) for NO_x and other combustion products on a wide variety of large emissions sources. These monitoring requirements are just beginning to impact the natural gas pipeline industry through the operating permit programs. Many CEM systems employed in other applications can be adapted for use in the pipeline industry. However, the traditional systems tend to be expensive and to require significant ongoing maintenance. These needs include the need to operate in unattended facilities, the potential to be mounted in the compressor station's hazardous classified areas (Class 1, Division 1, and Class 1, Division 2 areas), to have a probe that is insensitive to stack vibration, and to provide a wide dynamic range to accommodate the varying engine operating conditions characteristic of pipeline applications. As a result, alternative monitoring methods have been sought to address the cost and maintenance issues as well as to more effectively meet the needs of gas transmission engines and their compressor stations.

Predictive emission monitoring systems (PEMS) were developed to substitute an array of low cost sensors for the traditional laboratory derived CEM systems. The sensors used vary considerably depending on the predictive system supplier. Installation of a predictive emissions monitoring system has three distinct phases: sensor installation, system mapping, and predictive monitoring. During sensor installation, the selected sensors for system monitoring are installed on the engine. On newer engines, many of the required sensors are already present as part of the control system. However, on older engines, new sensors must be installed directly on the engine. Mapping begins after the sensors are installed. During mapping, actual engine emissions and sensor readings are measured instrumentally over a wide range of engine operating conditions. The emissions-sensor reading correlation is then used during normal system operations to predict the actual emissions. Because these systems potentially offer a lower cost alternative to monitoring, while at the same time providing useful information on engine operating conditions, this type of monitoring has been widely tested.

The development of a true NO_x sensor allows the user to directly measure NO_x like the traditional instrumental approaches, while achieving the potentially lower installed cost from the sensor based predictive monitoring approach. In order to achieve this lower cost, it is necessary to package the array of sensors in a system that does not require the air conditioned shelter traditionally required for CEM systems. Therefore, the system has been designed for direct exposure to the weather for most applications. Where continuous emissions monitoring is required for pipelines, it is typically NO_x, oxygen, and sometimes CO which must be monitored. Sensors for each of these gases are in the array. A schematic showing the instrument configuration is shown in Fig. 1.

Since most U.S. pipelines utilize a considerable variety of engines for transmission, it was desirable to test the effectiveness of the new analyzer on a set of engines that are representative of the range of emissions found in the industry. The following three engines were selected: a Rolls Royce Spey gas turbine engine; a Cooper GMVH-10 reciprocating engine; and an Ingersoll-Rand KVG-410 reciprocating engine. Characteristics of these systems are given in Table 1. The typical NO_x emissions from these engines vary from a low of about 50 ppm to a high of about 4000 ppm.

In order to confirm the performance of the analyzer, a relative accuracy test was conducted at each of the sites. The tests compared reference method results to the analyzer results. In each case, the analyzer successfully passed the relative accuracy test standards.

Sensor Technology

The continuous emissions monitor (CEMcat™ analyzer) uses two catalytic sensors: one to measure NO_x and one to measure CO. Oxygen is monitored using well-known electrocatalytic zirconium oxide sensor technology. These three sensors are placed within a single heated manifold which contains critical flow orifices to ensure constant flow across each sensor.

The catalytic sensors were both developed specifically for use in combustion systems. Both sensors have the same basic design, but use significantly different catalysts to detect their target gases. These spark-plug sized sensors have two discrete functional portions: a catalytic sensor element and a reference

Contributed by the International Gas Turbine Institute and presented at the 41st International Gas Turbine and Aeroengine Congress and Exhibition, Birmingham, United Kingdom, June 10–13, 1996. Manuscript received by the ASME Headquarters February 1997. Paper No. 96-GT-481. Associate Technical Editor: J. N. Shinn.

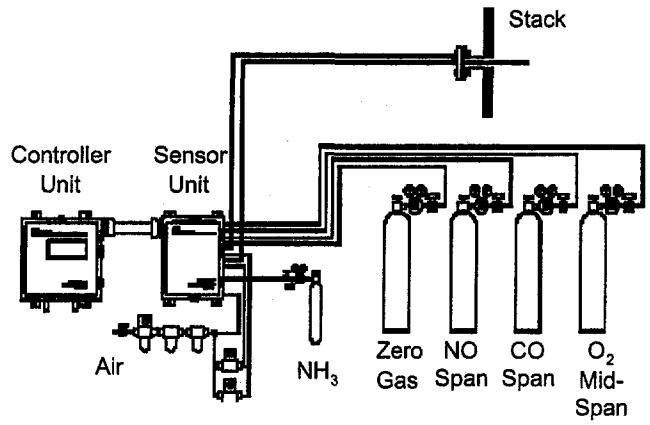

Fig. 1 Schematic of the sensor-based analyzer installation on an engine exhaust stack. The CEM unit consists of a sensor units and a controller unit, each housed in a NEMA 4X type box.

Table 1 Characteristics of engines used in system field tests

Engine Type	Turbine	Reciprocating	Reciprocating
Manufacturer	Rolls Royce	Cooper	Ingersoll-Rand
Model	Spey	GMVH-10	KVG-410
Location	Washington	Louisiana	Texas
Horsepower	16,500	2200	2000
Typical Emissions Ranges			
NOx (ppm)	52–165 ppm	200–300 ppm	2500–4000
CO (ppm)	30–90	50–150	700–6500
O_2 (%)	15–16	14–15	0.2–0.4

sensor element (Fig. 2). The catalytic element consists of a stainless steel sheath covering a resistive temperature device (RTD). A thin catalytic coating is then applied to the sheath. The catalyst for the CO sensor is a precious metals based material. The NO_x sensor uses a vanadium-based material (Dalla Betta and Sheridan, 1994). The reference element has the same construction as the catalytic element, but is coated with an inactive ceramic coating.

The catalyst coating is designed to selectively react to the gas being measured on its surface, giving off heat (an exothermic reaction). The difference in the resistance of the RTD in the active catalytic element relative to the reference RTD is measured using a bridge circuit. This resistance difference is directly proportional to the concentration of the monitored gas in the total gas stream. Both sensor gives a signal of about 1 Ω at 1000 ppm of the target molecule. A 90 percent of full scale reading is achieved in 30 s.

In order to ensure that the reaction rate is high and that condensation does not occur, the sensors are operated at approximately 300°C (572°F). The elevated temperature is maintained

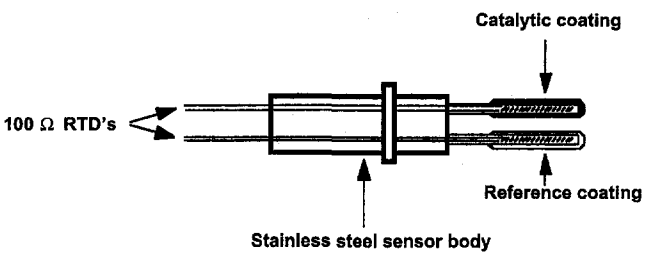

Fig. 2 Catalytic sensor schematic. The sensor has two probes, each consisting of a sheathed RTD covered by a coating. One is coated with a catalytic material, and the other with an inactive material. The gas being measured reacts on the active catalyst coating and heat is released. The heat difference between the active and reference probes is used to determine the concentration of the gas of interest in the total gas stream.

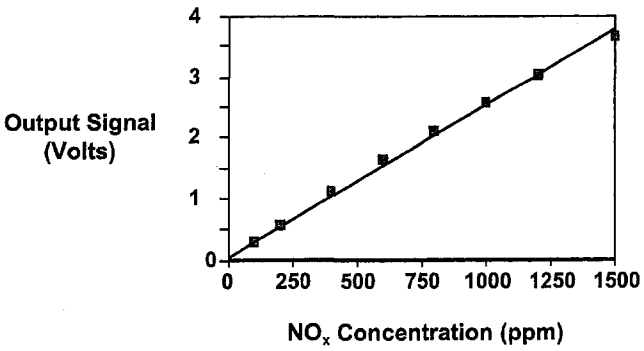

Fig. 3 Linearity of the NO_x Measurement. The NO_x sensor shows excellent linearity over the 0 to 1500 ppm range measured

by housing the sensor in a heated module. The module also serves as a heat exchanger to equilibrate the exhaust gas sample temperature with the sensor temperature. This allows the sensors to give accurate concentrations readings, even if there is considerable variation in the engine's exhaust temperature.

The NO_x Sensor. The active catalyst on the NO_x sensor is a vanadium-based catalyst related to the selective catalytic reduction catalysts (SCR) used for catalytic NO_x reduction from industrial sources. This catalyst is capable of reducing both NO and NO_2 on its surface in the presence of ammonia, as shown in Eqs. (1) and (2).

$$2\ NO + 2\ NH_3 + 1/2\ O_2 \rightarrow 2\ N_2 + 3\ H_2O$$

$$\Delta H^{\circ}_{600K} = -97.1\ \text{kcal/mol} \quad (1)$$

$$2\ NO_2 + 2\ NH_3 \rightarrow 2\ N_2 + 3\ H_2O + 1/2\ O_2$$

$$\Delta H^{\circ}_{600K} = -83.1\ \text{kcal/mol} \quad (2)$$

For these reactions, trace levels of ammonia are introduced directly into the sensor chamber as a co-reagent. For a source with 50 to 250 ppm of NO_x emissions, less than 454 g (1 lb.) of ammonia represent a year's supply. The lack of interfering reactions in the reducing environment of the sensor makes the system highly specific for NO_x. Since both NO and NO_2 react on this catalyst, the sensor is a true NO_x sensor. Conversion of NO_2 into NO (which is required for chemiluminescence based analyzers) is unnecessary. The NO_x sensor shows a linear response to NO_x over a very broad range (Fig. 3), and can effectively measure NO_x between 0 and 10,000 ppm with an accuracy of ±2 ppm under ideal laboratory conditions.

A two-fold excess of ammonia is supplied to the sensor to ensure complete reaction, and to provide a substantial dynamic range during process upsets. Since ammonia also oxidizes over the catalyst, as shown in Eq. (3), the sensor reading is corrected for the ammonia reaction.

$$2\ NH_3 + 3/2\ O_2 \rightarrow N_2 + 3\ H_2O$$

$$\Delta H^{\circ}_{600K} = -75.4\ \text{kcal/mol} \quad (3)$$

The NO_x sensor response does show a dependency on the oxygen content of the sample stream (Fig. 4). In addition, the NO_x sensor has a dependency on the water content of the gas stream (Fig. 5).

This dependency is not unexpected given the presence of oxygen and water in the NO and NO_2 reductions. The effect is significant, primarily at oxygen concentrations below about 5 percent. The oxygen dependency is corrected using the reading of the oxygen sensor from the sensor array. The water dependency is corrected using actual measured water content, or calculated water content based on fuel flow and excess oxygen levels.

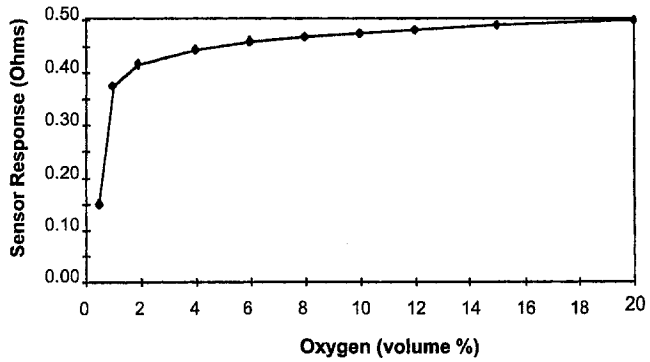

Fig. 4 NO_x sensor dependency on oxygen concentration. The response of the sensor as a function of oxygen concentration is shown for a sample with 500 ppm NO_x at 304 C.

The CO Sensor. The CO sensor uses a precious-metal-based catalyst to oxidize CO to CO_2 as shown in Eq. 4.

$$CO + 1/2\ O_2 \rightarrow CO_2 \quad \Delta H^{\circ}_{600K} = -67.6\ \text{kcal/mol} \quad (4)$$

Oxygen present in the exhaust gas serves as the required co-reagent for this oxidation reaction. If there is insufficient oxygen in the exhaust stream, then additional air can be provided to ensure complete reaction.

As with the NO_x sensor, the CO sensor has a very broad linear range and similar accuracy. Figure 6 shows linear performance of the CO sensor from 0 to 1500 ppm of CO, although CO concentrations up to 3 to 5 percent can be measured using this sensor. This type of catalytic CO sensor has been manufactured by Advanced Sensor Devices (ASD) under the Sonoxco name for about 13 years, and it has been used in large quantities in combustion control applications.

Experience in combustion control applications has shown that these precious metal based sensors also respond to unburned hydrocarbons in the exhaust gases. For example, methane can oxidize over the catalyst as shown in Eq. (5).

$$CH_4 + 2\ O_2 \rightarrow CO_2 \quad +2\ H_2O \quad (5)$$

However, the catalyst has been optimized to minimize the sensor's response to hydrocarbons. In pipeline applications, methane typically represents more than 90 percent of the unburned hydrocarbon present in the exhaust stream. Since the CO sensor's response to CO is 150 times greater than its response to methane, there is little effect from these hydrocarbons on the CO measurement. This allows the sensor based continuous emissions monitor to meet regulatory requirements in most applications.

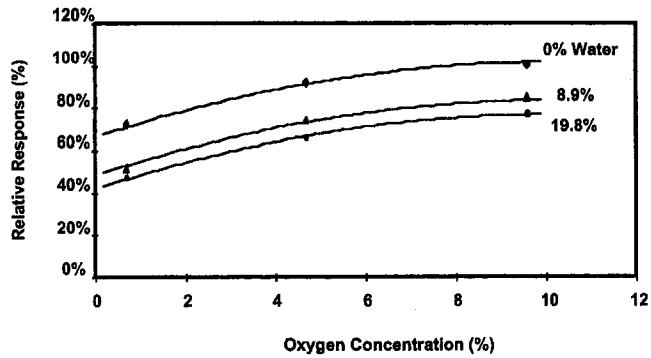

Fig. 5 NO_x sensor dependency on water and oxygen concentration. The response of the sensor as a function of water and oxygen concentration is shown for a sample with 500 ppm NO_x at 304 C.

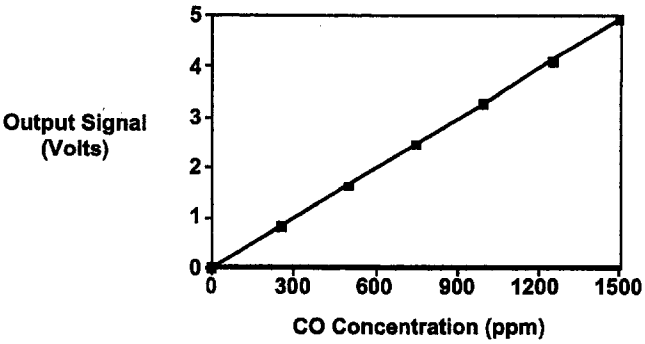

Fig. 6 Linearity of the CO Measurement. The CO sensor shows excellent linearity over the 0 to 1500 ppm range measured.

The Oxygen Sensor. The new continuous emissions monitor uses a high performance electrocatalytic zirconium oxide (ZrO_2) based oxygen sensor. These sensors are well characterized, and have been extensively used in emissions monitoring and combustion control applications (Jahnke, 1993). Although the oxygen sensor is housed in the same 300°C (572°F) sensor module as the two catalytic sensors, it has its own integral heater which operates at about 850°C (1550°F). The high temperature allows the zirconium oxide to operate as a conduit for oxygen between the higher concentration reference side and the lower concentration sample side. The concentration of oxygen is then determined from the electromotive force (emf) produced by this process.

Analyzer Design

The three sensors have been incorporated into an analyzer designed to take advantage of their performance features. The analyzer consists of two NEMA 4X type enclosures (Fig. 1), the controller unit, and the sensor unit. The controller unit contains the system's microprocessor, power supply, I/O modules, analog and digital circuit boards, and keypad/display. The microprocessor converts analog signals from the sensors to a digital form that can be transmitted to the user's data acquisition system using the continuous emissions monitor's RS 485 serial communication port using the MODBUS communication protocol. The microprocessor also controls the daily calibration of the unit. The unit can be programmed using the keypad/display or remotely via the serial port. The microprocessor converts the continuous raw output of the sensor array into compensated, one-minute-average readings for each gas. The regulations require at least one reading per 15 minute period—so this rate is much higher than required.

The sensor unit houses the three sensors, the dual stage air driven aspirator, and the solenoid valves. The dual stage aspirator uses 2 scfm of clean, dry, oil free plant air, and draws a sample out of the stack and through the sensor module. Air driven aspirators were selected because they have no moving parts, which eliminate maintenance problems frequently encountered with other sample collections systems.

Solenoid valves are the only moving parts in the entire continuous emissions monitor, and are used to introduce the calibration gases for the daily calibration. Since they are located on the clean, dry calibration gases, they are not subject to corrosion and plugging, which is the most frequent failure mode for solenoid valves.

Several different analyzer configurations are possible. The sensor unit can be directly mounted on the exhaust stack, eliminating any need for heated sample lines. The controller unit can then be mounted up to 46 meters (150 feet) from the sensor unit. However, in all three pipeline installations, the controller and sensor units were mounted side by side at ground level, and a short heated sample line (<8 meters, 25 feet) was used

Table 2 Installed system configuration

Engine Type	Turbine	Reciprocating	Reciprocating
Manufacturer	Rolls Royce	Cooper	Ingersoll-Rand
Analyzer Location	Indoor	Outdoor	Outdoor
Purge System	Yes	No	No
Sample Line Length (m)	8	6	5

to take the sample from the exhaust stack mounted probe to the sensor unit. In the turbine application, a Bebco purge system was installed between the two enclosures. This purge system ensured that a positive pressure was maintained in both monitor enclosures, and allowed the entire system to be installed in a Class 1, Division 2 area. The analyzer is designed so that the keypad and readout on the control unit can be accessed without breaking the seal of the unit. The use of the short heated sample line and purge allowed the entire unit to be located in a convenient place within the turbine room. The analyzers on the reciprocating engines were not purged. The configurations of each of the systems is given in Table 2.

Performance Testing

The objective of the field testing was to demonstrate that the sensor-based analyzer was capable of meeting the standards of existing U.S. Environmental Protection Agency regulations (U.S. EPA, 1992). This was determined by conducting a Relative Accuracy Test (Appendix B of the regulations) at each of the field trial sites. These tests were each conducted by third party source testers. In each test, the source tester's sample probe was located approximately one foot above the CEMcat analyzer's probe on the engine's exhaust stack. Both probes extended to the approximate center of the stack. The source testers measured NO and NO_2 using reference method 7E. Reference method 10 was used to monitor CO, and reference method 3A was used for oxygen. Moisture was determined gravimetrically.

The source tester's measurements were compared against the CEMcat analyzer's total NO_x, CO, and oxygen obtained from the hot wet exhaust gas. The CEMcat analyzer used calculated water content based on fuel value F factors, and measured oxygen concentrations. NO_x and CO were reported and compared in units of ppm, while oxygen and water were reported and compared in units of volume percent.

The relative accuracy test consisted of nine separate side-by-side comparisons of the continuous emissions monitoring system against the reference method. Each trial lasted a minimum of 21 minutes. Before and after each trial, the source tester re-checked their instrument calibration. The CEMcat system was not adjusted during the test.

The relative accuracy test produces nine separate mean differences (d_i) and one overall average mean difference (d) for each species under comparison. The final calculation of relative accuracy is as follows:

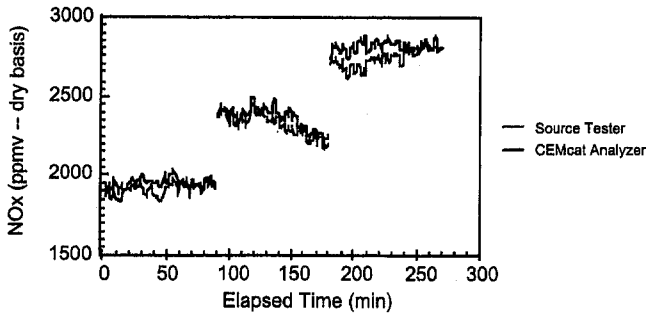

Fig. 7 Relative accuracy test results for NO_x on Ingersoll-Rand internal combustion engine. The CEMcat™ sensor based analyzer results track the source tester over a broad range of concentrations.

Relative Accuracy

$$= (|d| + |CC|)/\text{Reference Method Mean}*100 \quad (4)$$

The value CC, or confidence coefficient, is a statistical means to compensate for variations in the data spread between the CEMS and the source tester. Specifically, it is the product of the student t for a 95 percent confidence interval ($t = 2.306$ for nine tests) and the standard deviation (Sd) of the mean difference between the CEMS and the reference method (d), divided by the square root of the number of trials (n), i.e.,

$$CC = (t_{0.95}) \cdot \frac{Sd}{\sqrt{n}} \quad (5)$$

For the turbine engine and the Cooper reciprocating engine, the engine conditions were kept constant throughout the tests. However, with the Ingersoll-Rand engine, the operating conditions were varied so that each set of three trials was made under a different set of operating conditions. This effectively tested the systems dynamic range and accuracy.

The overall relative accuracies obtained in the test of the turbine and the reciprocating engines are given in Table 3. The U.S. regulations (40 CFR part 60) require a relative accuracy of 20 percent for NO_x, 10 percent for CO, and either 20 percent for oxygen or 1 percent absolute difference for oxygen. The data show that the analyzer is capable of meeting these accuracy requirements.

The test with the Ingersoll-Rand engine required the analyzer to measure both NO_x and CO over a very wide range of operating conditions. The NO_x level varied between approximately 1900 ppm and 2800 ppm while the CO emissions varied between 770 ppm and 5400 ppm. The results of each trial are shown in Figs. 7 and 8. The data show that the analyzer met the relative accuracy standards for this engine, and tracked the levels from the source tester over the entire range. Considering that the CO emissions varied by a factor of 8, this represents a significant achievement for the CO sensor.

Table 3 Relative accuracy test results under constant engine conditions for the Rolls Royce Spey turbine engine and the Cooper GMVH-10 recirpocating engine

Engine	Gas	Reference method (ppm)	CEMcat™ sensor (ppm)	Difference	Relative accuracy
Rolls Royce	NOx	110.8 ppm	120.5 ppm	9.7 ppm	11.2%
Turbine	CO	60.1 ppm	58.1 ppm	−2.0 ppm	6.7
	O_2	15.6%	14.5%	11.1%	8.9
Cooper	NOx	286.2 ppm	289.3 ppm	3.1 ppm	2.8%
Recip.	CO	80.0 ppm	77.9 ppm	−2.1 ppm	5.0
	O_2	14.6%	14.7%	0.1%	1.6
In-Rand	NOx	2324 ppm	2283 ppm	−41 ppm	0.08%
Recip.	CO	2946 ppm	2982 ppm	36 ppm	4.8
	O_2	0.28%	0.31%	0.03%	

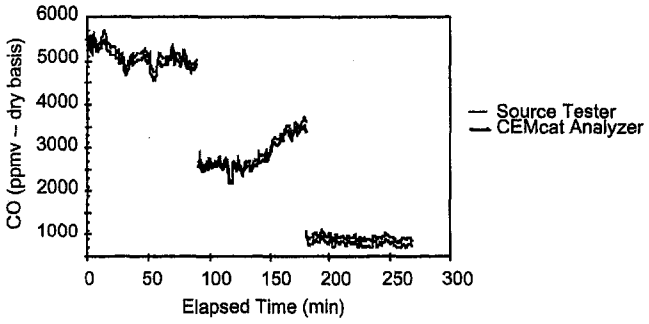

Fig. 8 Relative accuracy test results for CO on Ingersoll-Rand internal combustion engine. The CEMcat™ sensor based analyzer results track the source tester over a broad range of concentrations.

Conclusions

The pipeline industry uses a wide range of engines in its transmission operations. Serving the monitoring needs of this industry with a single type of analyzer requires a system that is capable of effectively monitoring a wide variety of engine types under a wide variety of load conditions. The tests conducted with the sensor-based analyzer demonstrate that the system can operate on turbines and reciprocating engines that are representative of the types that are commonly used within the pipeline industry. The tests further demonstrated that even when the engine operating conditions were varied and the emissions levels changed considerably, the sensor-based analyzer tracked the engine emissions.

The ability to track engine emissions with this sensor-based analyzer not only means that the system can be used to meet regulatory requirements for emissions monitoring, but it provides potential for control and diagnostic uses. The 4-20 mA output of the monitor could be fed into the station's DCS system and used to adjust engine operations to ensure that the system stays below the regulatory limits for emissions. Work on these control applications is just beginning.

Acknowledgments

The authors wish to acknowledge the Gas Research Institute and Southern California Gas Company for financial support of the emissions monitor, and the U.S. Department of Energy for support in developing the NO_x sensor. We also wish to acknowledge the efforts of Diana Rostrup-Nielsen, and Charles Schramm of Advanced Sensor Devices in sensor and instrument development and testing.

References

Dalla Betta, R. A., Sheridan, D. R., 1994, U.S. Patent 5 314 828, assigned to Catalytica, Inc., May 1994.

Jahnke, J. A., 1993, *Continuous Emissions Monitoring*, VanNostrand Reinhold, NY, pp. 108–109.

U.S. EPA, 1992, "Specifications and Test Procedures for SO2 and NO_x Continuous Emission Monitoring Systems in Stationary Sources," *Code of Federal Regulations*, Chap. 1, Title 40, Part 60, Appendix B, Performance Specification 2, pp. 1108–1115, 1218–1219.

Developing Centrifugal Compressor Train Optimization Models for Performance Evaluation

S. M. Summers
Senior Engineer,
BP Exploration (Alaska) Inc.,
Anchorage, AK 99519

Recent advances in numerical optimization software now allow problems arising in the evaluation of complex centrifugal compressor train performance to be solved readily by machinery users. Analyses of compressor operations often require consideration of multiple nonlinear constraints involving pressure, temperature, flow rate, composition, and power. Based on these constraints, the operational boundaries of the machinery must be evaluated. Frequently operating points of greatest interest exist where one of the operational variables, such as flow rate, is maximized subject to operational constraints. A methodology is proposed that can be used to apply commercially available optimization software to problems of this type. A review of gas equation of state relationships needed to determine thermodynamic properties is provided, as well as methods for calculating compressor discharge pressure based on polytropic head and efficiency. Recycle control is considered and a model is proposed.

Introduction

The task of evaluating how a centrifugal compressor will operate in a given process frequently reduces to evaluating machine performance at operating points, which are defined by process constraints. These constraints usually involve pressure or temperature and may be flow dependent. Compressor performance, on the other hand, is characterized by polytropic head, which is thermodynamically related to pressure and temperature and is also flow dependent. In situations where compressor flow is known, the associated system pressures and temperatures can easily be calculated. Unfortunately, evaluating compressor performance in the context of plant operations often involves situations where the flow is unknown and must be determined based on pressure or temperature constraints, which are also flow dependent. In this case, a lengthy iteration is required to find the operating point where compressor performance characteristics and system constraints are simultaneously satisfied. This situation may be further complicated when gas turbines are used as machinery drivers and the effect of compressor recycle control is considered. In fact, the problem may become sufficiently complex that interactions between the compressors, turbines, and recycle controllers may not be clearly understood at all.

This provides the motivation for the development of a numerical methodology, which can be used to find machinery operating points while simultaneously satisfying operational constraints. In the usual case, where many viable solutions may exist, this methodology should also be able to optimize the solution with respect to some defined objective function.

If we consider the necessary features of such a methodology, two aspects of the problem are apparent. The first of these is the need for a system model that can be used with a numerical optimization routine, and the second is the optimization routine itself.

Contributed by the International Gas Turbine Institute and presented at the 42nd International Gas Turbine and Aeroengine Congress and Exhibition, Orlando, Florida, June 2–5, 1997. Manuscript received at ASME Headquarters February 1997. Paper No. 97-GT-241. Associate Technical Editor: H. A. Kidd.

It is the intent of this paper to describe in detail one such model, which was developed for use with a commercially available optimization program. It is not the goal of this paper to describe the techniques used to perform numerical optimization; however, a brief discussion of optimization methodology is presented to familiarize the reader with the topic.

The Optimization Problem. Describing compressor performance as part of an operating plant usually requires that several simultaneous constraints be satisfied while some other operational variable is maximized. A likely situation might involve a plant that wishes to maximize gas processing rate subject to constraints involving compressor discharge pressure. To achieve this objective, suction pressure, inlet flow rate, and compressor speed might be manipulated. Mathematically this problem can be formulated as a constrained optimization, where the objective function, which is to be maximized, is the compressor flow rate and the constraints involve power and delivery pressure.

Assuming that a suitable model for the system can be established, a numerical optimization program can be used to maximize the objective function subject to the constraints. This optimization program, or optimizer, will have to be capable of dealing with compressor characteristics and operating constraints that are nonlinear. Until recently, development costs and computing requirements limited the application of such routines; however, today these programs are increasingly available as features included in popular numerical computation software packages (Grace, 1993). Because of their ready availability and the powerful set of subroutines offered with these packages options exist for users to develop optimization models for their own compressor installations.

The specific compressor operating scenario to be considered is from an actual Arctic oil production facility. At this facility two parallel three-stage gas compression trains are driven by gas turbines and are used to process natural gas as shown in the flow diagram of Fig. 1. All compressors have associated recycle valves and controllers. Each of the three stages, which constitute a machinery train, are connected by a common drive shaft. From a process perspective, the two trains are tied together between stages such that interstage pressures are equal-

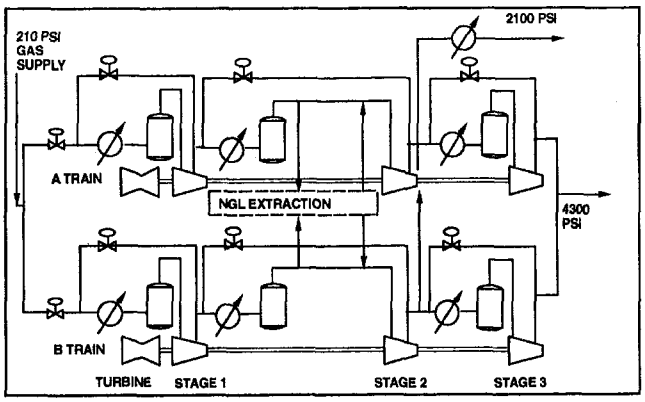

Fig. 1 Three-stage parallel train compression process with natural gas liquids extraction after first stage. Intermediate gas extraction after second and third stage.

ized. The process includes a natural gas liquids extraction plant, which is fed from the discharge of the first stage. In this process heavy hydrocarbon components are removed from the gas stream prior to entering the second stage, thereby reducing the molecular weight of the gas in the later compression stages. Flow-rate dependent delivery pressure constraints exist for both the second and third stages.

Clearly a large number of operating parameters influence overall system performance. Some of these are: ambient temperature, molecular weight, interstage pressure drop, recycle control settings, and performance characteristics of individual compressors. Because so many parameters affect system performance, efforts that were undertaken to determine relationships between operating variables and gas processing rate experimentally were only partially successful. Testing difficulties arose because of process noise and ever-changing process conditions. Modeling provided a means of overcoming these difficulties and allowed the effects of operating variables to be quantified. In several circumstances these effects were surprising and proved to be counterintuitive to operational personnel.

Thermodynamic Relationships. To model a system such as this it is necessary to introduce several thermodynamic relationships. As a first step we must select a suitable equation of state, which in this analysis will be the Redlich–Kwong equation, Eq. (1). This two-parameter cubic equation of state provides a relatively simple means of obtaining thermodynamic properties. With little additional work other similar, but slightly more complex, three-parameter cubic equations of state including the Soave form of the Redlich–Kwong equation or Peng–Robertson equation could be used (Reid et al., 1987). All of these equations can be manipulated to form cubic polynomials similar to Eq. (2). From this equation the compressibility is found as a root of the polynomial. In the case of a superheated vapor, the polynomial has one real root and two complex roots, whereas for a saturated mixture three real roots will be found, where the largest root is associated with the gas phase and the smallest root is associated with the liquid phase (Henley and Seader, 1981). Since the model being developed will deal only with superheated gases it will not be necessary to distinguish between real roots.

$$p = \frac{R \cdot T}{v - b} - \frac{a}{v^2 + bv} \tag{1}$$

With $Z = p \cdot v / R \cdot T$ a cubic equation may be defined:

$$Z^3 - Z^2 + (A^* - B^* - B^{*2}) \cdot Z - A^* \cdot B^* = 0 \tag{2}$$

$$A^* = \frac{a \cdot p}{R^2 \cdot T^2} \tag{3}$$

$$B^* = \frac{b \cdot p}{R \cdot T} \tag{4}$$

$$a = \frac{0.42748 \cdot R^2 \cdot T_c^{2.5}}{p_c \cdot T^{1/2}} \tag{5}$$

Nomenclature

ACFM = actual cubic ft per minute
C_p = specific heat, Nm/kg K (ft lbf/lbm R)
C_v = specific heat, Nm/kg K (ft lbf/lbm R)
CKF_aY = flow metering constants, kg/s (lbm/min)
H_p = polytropic head, Nm/kg (ft lbf/lbm)
K = control parameter, usually 0.5
$\dot{M}$ = mass flow, kg/s (lbm/min)
MW = molecular weight, kg/kg mol (lbm/lb mol)
P_{gas} = compressor power, W (hp)
$P_{turbine}$ = turbine power, W (hp)
Q = flow, standard m^3/day (ft^3/day)
Q_a = flow, actual m^3/min (ft^3/min)
Q_{min} = flow minimum, standard m^3/day (ft^3/day)
$Q_{recycle}$ = flow recycle, standard m^3/day (ft^3/day)
R = gas constant = $8314/MW$ Nm/kg K ($1545/MW$ ft lbf/lb R)
R_u = gas constant = 8314 N m/kg mol K (1545 ft lbf/lb mol R)
S = speed, fraction of rated speed
SCFD = standard cubic ft per day
T = temperature, K(R)
T_{amb} = ambient temperature, °C (°F)
Z = compressibility
a = acoustic velocity = $\sqrt{kg_cZT_1R_u/MW}$
b = surge control safety margin
d = orifice diameter, cm (in.)
$f_{objective}$ = optimization objective function
f_1 = functional relation based surge data
f_2, f_3 = constraint functions
$g_{constraint}$ = constraint evaluation vector
g_c = dimensional constant, 1 SI units (32.2 lbm ft/lbf sec^2)
h = enthalpy, Nm/kg (ft lbf/lbm)
h_w = orifice pressure drop, cm (in H_2O)
k = isentropic exponent
n = polytropic exponent
p = pressure, N/m^2 (lbf/ft^2)
s = entropy, Nm/kg K (ft lbf/lbm R)
s_s = proximity to surge
s_c = proximity to surge control
u = internal energy, Nm/kg (ft lbf/lbm)
v = specific volume, m^3/kg (ft^3/lbm)
y = mole fraction
σ = polytropic group = $n/n - 1$
η_p = polytropic efficiency
ΔP_o = flow variable, fraction of transmitter range
ρ = density, gm/cm^3 (lbm/ft^3)

Subscripts/Superscripts

a = actual, m^3/min (ft^3/min)
ave = average of inlet and outlet
i = component or increment
ref = reference state at low pressure
std = standard conditions
1 = inlet or stage one
2 = outlet or stage two
3 = stage three
A = machinery train A
B = machinery train B
v = evaluated at constant volume
p = evaluated at constant pressure
o = evaluated at low-pressure state
$'$ = invariant form based on inlet conditions

$$b = \frac{0.08664 \cdot R \cdot T_c}{p_c} \tag{6}$$

When gas mixtures are being considered, mixing rules must be applied to determine a_m and b_m. The simplest mixing rules apply to the Redlich–Kwong equation and are given in Eqs. (7) and (8) where for hydrocarbon pairs the parameter k_{ij} is usually zero.

$$a_m = \sum_i \sum_j y_i \cdot y_j \cdot (a_i \cdot a_j)^{1/2} \cdot (1 - k_{ij}) \tag{7}$$

$$b_m = \sum_i (y_i \cdot a_i^{1/2})^2 \tag{8}$$

Using either mixture or pure substance values for a and b, departure functions can be calculated for the desired thermodynamic properties of enthalpy, internal energy, and entropy based on the equation of state resulting in Eqs. (9), (10), and (11). These departure functions allow accurate calculation of properties at pressures where the assumption of ideal gas behavior is no longer valid. The departure functions are combined with low-pressure ideal gas relations to give Eq. (12) to (15) where the thermodynamic quantity calculated is relative to a low-pressure reference state:

$$h - h^o = p \cdot v - R \cdot T - \frac{3 \cdot a}{2 \cdot b} \cdot \ln\left(\frac{v + b}{v}\right) \tag{9}$$

$$u - u^o = -\frac{3 \cdot a}{2 \cdot b} \cdot \ln\left(\frac{v + b}{v}\right) \tag{10}$$

$$s - s^o = R \cdot \ln\left(\frac{v - b}{v}\right) - \frac{a}{2 \cdot b \cdot T} \times \ln\left(\frac{v + b}{v}\right) + R \cdot \ln\left(\frac{v}{v^o}\right) \tag{11}$$

$$\Delta h = (h^o - h_{p1})_{T_1} + \int_{T_1}^{T_2} C_p^o \cdot dT - (h^o - h_{p1})_{T_2} \tag{12}$$

$$\Delta u = (u^o - u_{p1})_{T_1} + \int_{T_1}^{T_2} C_v^o \cdot dT - (u^o - u_{p1})_{T_2} \tag{13}$$

where

$$C_v^o = C_p^o - R \tag{14}$$

$$\Delta s = (s^o - s_{p1})_{T_1} + \int_{T_1}^{T_2} \frac{C_p^o}{T} \cdot dT - (s^o - s_{p1})_{T_2} \tag{15}$$

Data for C_p^o are readily available for a wide variety of gases in the form of third-order polynomials, Eq. (16) (Reid et al., 1987):

$$C_p^o = c_0 + c_1 \cdot T + c_2 \cdot T^2 + c_3 \cdot T^3 \tag{16}$$

where for gas mixtures,

$$C_{pm}^o = \sum_i y_i \cdot C_p^o \tag{17}$$

With the forgoing equations in hand, numerically evaluating enthalpy, internal energy, and entropy at any pressure or temperature is a straightforward task.

Polytropic Head. Polytropic head is the quantity usually provided by equipment manufacturers to describe compressor performance. Data are typically in the form of a family of curves showing head as a function of flow, Q_a, and compressor speed, S, where flow is usually expressed in units of volume at actual inlet flowing conditions.

For the purposes of developing a system model, these curves can be conveniently reduced to Eq. (18), which is a polynomial in Q_a, S, and Q_a/S. This polynomial has eight constants, which are found by performing a multivariable linear regression on manufacturer data:

$$H_p = c_1 Q_a^4 + c_2\left(\frac{Q_a}{S}\right)^2 + c_3\left(\frac{Q_a}{S}\right) + c_4 Q_a^2 + c_5 Q_a + c_6 S^2 + c_7 S + c_8 \tag{18}$$

A plot of this polynomial is shown in Fig. 2. In Fig. 2 constant speed lines describing polytropic head as a function of flow have been extended from minimum and maximum flow values as horizontal lines using relations given in Eqs. (19) and (20). Although this is not representative of actual compressor performance, these equations allow polytropic head to be fully defined for all speeds and flows. This avoids computational difficulties that may arise if polytropic head is calculated for an unusually large or small flow rate, which is outside of the compressor's normal operating range. Of course, precautions need to be taken to ensure that data are not erroneously used from these regions in any final solution obtained.

for $Q \le Q_{\min}$, $H_p = H_p|_{Q_{\min}}$ where

$$Q_{\min} = 9000 \cdot S^{1.5} \tag{19}$$

for $Q \ge Q_{\max}$, $H_p = H_p|_{Q_{\max}}$ where

$$Q_{\max} = 13000 \cdot S^{1.5} \tag{20}$$

Polytropic Efficiency. Polytropic efficiency curves may be dealt with in a completely analogous manner to the polytropic head curves just described. Using the same polynomial form, Eq. (21) is obtained:

$$\eta_p = c_1 Q_a^4 + c_2\left(\frac{Q_a}{S}\right)^2 + c_3\left(\frac{Q_a}{S}\right) + c_4 Q_a^2 + c_5 Q_a + c_6 S^2 + c_7 S + c_8 \tag{21}$$

As before, the constant speed curves are extended as horizontal lines outside the normal operating range of the compressor, Fig. 3.

The polytropic head and efficiency curves just introduced are based on manufacturer data, which, strictly speaking, are only valid for one set of specified inlet conditions. Since it is our intent to use these curves under inlet conditions that will differ from those originally specified, it is worthwhile commenting on the errors that will be introduced. Four types of error will arise because of differences in Mach number, Reynolds number, capacity speed ratio and, most importantly for multistage compressors, volume ratio effects (ASME, 1992). Should we decide

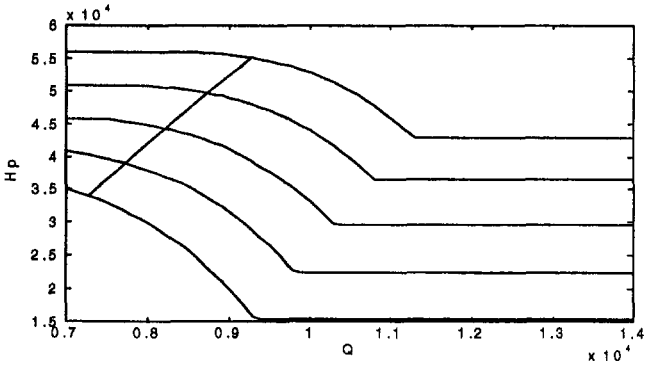

Fig. 2 Polytropic head (ft.lbf/lbm) versus flow (ACFM) for speeds 0.85, 0.90, 0.95, 1.0, and 1.05

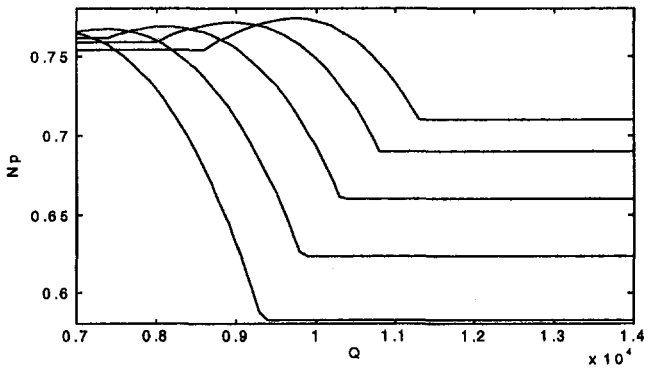

Fig. 3 Polytropic efficiency versus flow (ACFM) for speeds 0.85, 0.90, 0.95, 1.0, and 1.05

to deal with these errors rigorously, a model of the compression process that considers each impeller of the compressor would be needed; therefore, a family of curves similar to those just presented would be required (Sapiro, 1982; Gresh, 1991). For the present analysis it will be assumed that the deviation from originally specified conditions will be small, thereby allowing a single curve to be used.

It is worth noting that when significant variations in inlet conditions are expected, Eqs. (18) and (21) can be made invariant to inlet Mach number with relative ease. To accomplish this, independent and dependent variables are converted to their invariant forms using design inlet conditions and regressed using Eqs. (18) and (21). In this case, invariant forms of the variables become $Q_a' = Q_a/a$, $S' = S/a$, $\eta_p' = \eta_p$ and $H_p' = H_p/a^2$ (Batson, 1996). For simplicity, these invariant forms have omitted terms involving the impeller diameter. When this characteristic length is included the invariant forms become dimensionless.

Calculating Discharge Pressure. Accurately relating polytropic head and efficiency to inlet and outlet pressures and temperatures is one of the principle difficulties associated with developing a compressor model. In the situation being considered, we are given polytropic head and efficiency from manufacturer curves and an unknown pressure and temperature must be found. Let us consider first the more common situation, which is that of finding an unknown polytropic head and efficiency given inlet and outlet conditions. If we assume the compression path follows that of a polytropic process, $pv^n = \text{const}$, then the familiar polytropic head expression given in Eq. (22) is found. Here it is assumed that the polytropic exponent and thus the isentropic exponent k can be adequately described by averages taken at the inlet and the outlet (Lapina, 1982).

In our case since the head and efficiency are known, Eq. (22) can be easily rearranged to solve for pressure, where Eq. (23) is used to find the polytropic exponent:

$$H_p = Z_{\text{ave}} \cdot \frac{R_u}{MW} \cdot T_1 \cdot \frac{n_{\text{ave}}}{(n_{\text{ave}} - 1)} \times [(p_2/p_1)^{(n_{\text{ave}}-1)/n_{\text{ave}}} - 1] = \eta_p \cdot \Delta h \quad (22)$$

$$\frac{n_{\text{ave}}}{n_{\text{ave}} - 1} = \frac{k_{\text{ave}}}{k_{\text{ave}} - 1} \cdot \eta_p \quad \text{where} \quad k = \frac{C_p/C_v}{1 - \dfrac{Z}{p}\dfrac{\partial Z}{\partial p}\Big|_T} \approx \frac{C_p}{C_v} \quad (23)$$

It is noteworthy that average compressibility and polytropic exponent values have been used. The rationale behind this is that the compressibility decreases continuously as the gas pressure increases. Average compressibility values tend to account for this behavior. The same reasoning applies to average values for the polytropic exponent although, in this case, the exponent of the pressure ratio in Eq. (22) offsets changes in the polytropic term (Lapina, 1982).

In Eq. (23), the isentropic exponent k may be taken as the low-pressure ratio of specific heats without too great a loss in accuracy. It should, however, be pointed out that the correct form of k is as given in Eq. (23) (*Fluid Meters,* 1971). At high pressures, approaching the critical point, real gas k values become quite large. Because of this and the averaging approach used, the more accurate form of the isentropic exponent does not always yield better overall results when compared to the simpler ratio of specific heats given in Eq. (22). This point is at least partly support by Edminster (1961).

In the case where Eq. (22) is rearranged to solve for an unknown discharge pressure and temperature, the average compressibility and ratio of specific heats cannot be found until the unknown pressure and temperature are found. The necessary iterative solution is easily accomplished and converges rapidly. Equations (22) and (23) can give surprisingly good results, usually within 2–3 percent, of values obtained using more rigorous methods.

For greater accuracy, the unknown pressure and temperature may be calculated directly using Eq. (25) (Sorenson, 1983). Where the polytropic path is defined such that, "the ratio of reversible work input to enthalpy rise is a constant" (*Power Test Code,* 1992) or as a differential equation, Eq. (24). Using the thermodynamic relations given earlier, an unknown pressure and temperature can be calculated that satisfy Eq. (25). To do this, we start from a known pressure temperature point and calculate the isentropic enthalpy change $\Delta h_{\Delta s=0}$ for an incremental pressure change. This amounts to finding an unknown temperature such that $\Delta s = 0$ for the pressure change. Next we iterate to find a second temperature point at the same pressure that results in a Δh such that $\Delta h = \Delta h_{\Delta s=0}/\eta_p$ is satisfied. This process is repeated using pressure–temperature points associated with the previous Δh as the starting point for the next increment of pressure along the compression path. The process is repeated for n increments until the entire path has been defined and the required polytropic head rise across the compressor is achieved.

$$\eta_p = \frac{v \cdot dp}{dh} \quad (24)$$

$$\eta_p \approx \frac{\sum_{i=1}^{n} \Delta h_{\Delta s=0}}{h_n - h_1} = \frac{\sum_{i=1}^{n} (h_{(i+1)ds=0} - h_{(i)})}{h_n - h_1} = \frac{H_p}{\Delta h} \quad (25)$$

Recycle Control. In modeling the overall compression system, a key component is the recycle control scheme. In the system being analyzed, recycle control is shown in Fig. 2 as the positively sloped line intersecting the constant speed curves. This line defines the minimum flow through the compressor. Rates below this minimum are unstable and will result in flow reversals or surge.

The recycle controllers being modeled utilize Eqs. (26) to (29). In these equations the parameter s_s is defined such that its value is equal to one when the compressor is operating on the surge line. Equation (26) can, therefore, be regarded as a ratio of polytropic head to flow parameter ΔP_o where f_1 is an almost linear function obtained from compressor testing or from manufacturer surge estimates.

$$s_s = \frac{K \cdot f_1(H_{p_{\text{reduced}}}) \cdot p_1}{\Delta P_o} \quad (26)$$

$$H_{p_{\text{reduced}}} = \frac{(p_2/p_1)^{\sigma} - 1}{\sigma} \quad (27)$$

$$\sigma = \frac{\ln (T_2/T_1)}{\ln (p_2/p_1)} \quad (28)$$

The control variable is then calculated:

$$s_c = s_s + b \tag{29}$$

The surge control algorithm manipulates the recycle valve of the compressor such that the proximity to surge, s_c, is maintained at a value less than or equal to one. Since s_s also uses this criterion, we recognize that the variable b creates an offset between the control variable s_c and the actual surge point defined by s_s, Eq. (29).

Because of the relative complexity of this control scheme and frequent changes made to K, b, and f_1 variables, the antisurge control algorithm was simulated exactly. This allowed model parameters to be modified in the same way that the field control settings were entered in the controllers. To do this it was necessary to scale all variables in the control equations by their respective operating ranges, just as field instrument transmitters would function. As an example, let us consider the differential pressure flow signal ΔP_o. For simulation purposes this parameter is related to compressor inlet mass flow by Eq. (30). Using Eqs. (30) and (31), ΔP_o may be calculated. Likewise, Eqs. (26) to (29) must also be evaluated using pressures and temperatures expressed as fractions of transmitter ranges:

$$\dot{M} = CKF_aYd^2\sqrt{h_w \cdot \rho_1}, \quad C = 0.03475\ (5.983) \tag{30}$$

$$h_w = \Delta P_o \times [\text{transmitter range, cm } H_2O\ (\text{inches } H_2O)] \tag{31}$$

Turbine and Compressor Power. As was the case with polytropic head and efficiency maximum available turbine power can also be characterized using a polynomial, which in this case is a function of speed and ambient temperature, Eq. (32), Fig. 4.

$$P_{\text{turbine}} = c_1 S T_{\text{amb}} + c_2 (T_{\text{amb}})^2 + c_3 (T_{\text{amb}}) + c_4 S^2 + c_5 S + c_6 \tag{32}$$

It is worth noting that the polynomial only represents maximum power available from the turbine. As before, constants are found by performing a multivariable linear regression on data from manufacturer curves.

Ultimately it is our intention to compare turbine power to the total power utilized by the compression train. Equation (33) serves this purpose and is used to calculate the thermodynamic power absorbed by individual compressors. Of course, to calculate total compressor power mechanical losses also need to be included.

$$P_{\text{gas}} = \frac{\dot{M} \cdot H_p}{\eta_p} \quad \left(P_{\text{gas}} = \frac{\dot{M} \cdot H_p}{33000 \cdot \eta_p} \right) \tag{33}$$

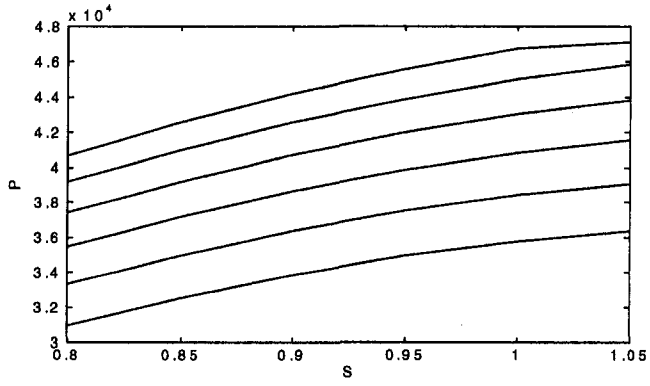

Fig. 4 Maximum turbine power (HP) versus speed (1 = 100 percent) for ambient temperatures (−40, −20, 0 20, 40, 60°F)

Building a Model. Having introduced the necessary equations required to develop a basic process simulator, let us pause to review how various system attributes might be considered in our calculations. Since our objective is to formulate a computational scheme that can eventually be turned into a computer program, our functions will henceforth be described as subroutines with their respective independent input and output variables identified. For convenience these subroutines have been given names and further organized into a three-level hierarchical structure. We shall consider first the level one thermodynamic subroutines.

Level 1: Thermodynamic Subroutines. Since the conceptual basis for these subroutines has already been discussed in detail no further attention will be given to them here. These relationships are summarized in Table 1.

Level 2: Machine Level Subroutines. We are now prepared to introduce the level 2 subroutines, which deal with the behavior of the individual compressors and which are listed in Table 2. The first of these subroutines, "look_up" and "turbine_power," contain little more than the coefficients of the respective polynomials that describe head and efficiency for the various compressors or, in the case of the gas turbine driver, the output power. The latter routines "surge_speed," "surge_flow," and "stage_perform," need to be explained in greater detail.

Considering first the subroutine "surge_speed," we note that the objective of this routine is to calculate the minimum flow through a given gas compressor. The compressor will have associated with it a set of recycle control variables K, b, and f_1, which define a surge control line based on the criterion $s_c = 1$ as described earlier. Given a set of input variables, the subroutine is to calculate a value of s_c and compare this value to one. In the case where $s_c < 1$, the machine has a flow rate greater than the minimum flow and the recycle controller is inactive.

In the case where $s_c > 1$, the flow rate being provided to the machine is below the minimum required. In this case, recycle flow is present at some unknown rate. To find the recycle flow, the inlet flow corresponding to $s_c = 1$ must first be found at the specified operating speed. Once this flow is known, the recycle rate can be determined as the difference between the minimum required rate defined by the condition $s_c = 1$ and the rate being fed to the compressor from the upstream source. The only difficulty arising is that criterion s_c is not a function of speed but rather p_1, T_1, p_2, T_2 and ΔP_o; therefore, we cannot solve directly for the quantity ΔP_o.

In the author's work, the task of finding the flow where the condition $s_c = 1$ was satisfied at a given speed was accomplished using a second subroutine "surge_speed," in combination with "surge_flow." In this case, "surge_speed" performed an interation, at a constant speed, using "surge_flow."

In the iteration just described, it is noteworthy that the reduced polytropic head specified by Eq. (27) is not the same polytropic head found using the polynomial in "look_up." Rather the form of Eqs. (27) and (28) requires that compressor outlet pressures be calculated so that the reduced polytropic head can be found.

The last of the level 2 subroutines is "stage_perform." This subroutine is used to simulate the performance of an actual compressor. Not unexpectedly, it makes use of all of the subroutines introduced thus far. The set of input variables to this subroutine includes inlet pressure, temperature, compressor speed, and flow rate. The basic function of the subroutine is described in the pseudo code fragment in Table 3, where "( )" define subroutine input variables and "[ ]" define returned variables.

Level 3: System Level Subroutines. At this point we have developed a series of subroutines that are able to describe the thermodynamic performance of a single compressor given a set

Table 1 Level 1 subroutines

Name	Subroutine function	Input Variables	Output Variables
z_find	calculates compressibility	p,T,C_p a_m,b_m,MW	Z
h_find	calculates enthalpy	p,T,C_p a_m,b_m,MW	$h-h_{ref}$
u_find	calculates internal energy	p,T,C_p a_m,b_m,MW	$u-u_{ref}$
s_find	calculates entropy	p,T,C_p a_m,b_m,MW	$s-s_{ref}$
k_find	calculates ratio of specific heats	p,T,C_p a_m,b_m,MW	k
p_find	calculates unknown pressure and temperature	p_1,T_1,H_p,η_p a_m,b_m,C_p,MW	p_2,T_2

of input variables, p_1, T_1, Q, and S. We have not, however, come up with a strategy to connect multiple compressors in some cohesive scheme. This is the function of the last two system level subroutines, which we shall call the level 3 subroutines, Table 4. The first of these is "opt_form." The function of this subroutine is sequentially to execute "stage_perform" for each of the six compressors in the process.

The sequence of progression is important and is from low to high pressure stages. As this is done, unknown discharge pressures and temperatures are calculated and populated in a state table, which looks much the same as Table 5. The subroutine "opt_form" also performs mass continuity calculations so that flow variables are reduced to the minimum independent set, which in this case is Q_{1A}, Q_{1B}, Q_{2A} and Q_{3A}. Here we recognize that mass passing through lower compression stages must equal the total passing through higher stages less any extracted flows that are known constants.

Upon executing the subroutine "opt_form," using a set of manipulated variables, including Q_{1A}, Q_{1B}, Q_{2A}, Q_{3A}, S_A, S_B, p_{11A}, p_{11B} and T_{amb}, the state table can be completely populated. At this point, the table will accurately represent the operating characteristics of individual compressors; however, it would not necessarily satisfy system operating constraints such as equilibrium discharge pressure between trains, maximum absorbed horsepower, or minimum delivery pressure requirements. In addition, the objective function $Q_{3A} + Q_{3B}$ would not yet be maximized. Restating this another way, we would have a physical model of the machinery where operational characteristics of the compressors at a machine level were met; however, characteristics of the process system or process constraint would not be met. In the latter case the degree to which these constraints were violated would be easily determined using values already available from the state table.

We also observe that by manipulating the input variables used in "opt_form" we can eventually satisfy the system level constraints while simultaneously maximizing the chosen objective function.

At this point our problem has become one of applied mathematics and can be restated as a system of objective and constraint equations as given by Eqs. (34) to (37). Constraints built into the model at a the machine level have also been noted, Eq. (37). In these equations it is important to realize that the volumes and mass flows, Q and $\dot{M}$, respectively, are forward moving flows in the process and as such do not include recycle gas that may also be present. The gas flows Q are calculated at standard conditions and in the absence of molecular weight changes behave in the same manner as mass flows.

Objective Function:

$$f_{\text{objective}} = Q_{3A} + Q_{3B} \tag{34}$$

Table 2 Level 2 subroutines

Name	Subroutine function	Input Variables	Output Variables
look_up	calculates polytropic head and efficiency	Q_a,S	H_p,η_p
turbine_power	calculates available turbine driver power	$S,T_{ambient}$	P
surge_flow	calculates minimum flow as a function of inlet and outlet pressures and temperatures.	p_1,T_1,p_2,T_2	Q_{min}
surge_speed	calculates minimum flow for compressor as a function of compressor speed and inlet conditions	p_1,T_1,Q,S	$Q_{min}\|_S$
stage_perform	calculates discharge pressure, temperature and recycle flow for a given compression stage	p_1,T_1,Q,S	H_p,η_p, p_2,T_2, $Q_{recycle}$

Table 3 Pseudo-code subroutine "stage_perform"

```
Function [H_p, η_p, p_2, T_2, Q_recycle] = stage_perform (p_1, T_1, Q, S)
[H_p, η_p] = look_up (Q, S)
[p_2, T_2] = p_find (p_1, T_1, H_p, η_p)
[Q_min] = surge_flow (p_1, T_1, p_2, T_2)
if Q_min > Q
   [Q_min|_S] = surge_speed (p_1, T_1, S)
   [H_p, η_p] = look_up (Q_min|_S, S)
   [p_2, T_2] = p_find (p_1, T_1, H_p, η_p)
   Q_recycle = Q_min|_S − Q
else
   Q_recycle = 0
end
```

Table 4 Level 3 subroutines

Name	Subroutine function	Input Variables	Output Variables
opt_form	populates all unknown variables the output state matrix for all compressors	Q_{1A},Q_{1B},Q_{2A}, Q_{3A},S_A,S_B, p_{11A},p_{11B},T_{amb} *(all system constants)*	p_{21A},p_{21B},p_{22A}, p_{22B},p_{23A},p_{23B}, T_{21A},T_{21B},T_{22A}, T_{22B},T_{23A},T_{23B}, $f_{objective}$, $g_{constraint}$
opt_setup	provides initial guess for manipulated variables	*none*	*none*

Manipulated Variables:

$$Q_{1A}, Q_{1B}, Q_{2A}, Q_{3A}, p_{11A}, p_{11B}, S_{1A}, S_{1B} \tag{35}$$

Level 3 System Level Constraints:

$$g_{\text{constraint}}(1) = p_{21B} - p_{21A} = 0$$

$$g_{\text{constraint}}(2) = p_{22B} - p_{22A} = 0$$

$$g_{\text{constraint}}(3) = p_{23B} - p_{23A} = 0$$

$$g_{\text{constraint}}(4) = P_{1A} + P_{2A} + P_{3A} - P_{\text{turbine}A} \leq 0$$

$$g_{\text{constraint}}(5) = P_{1B} + P_{2B} + P_{3B} - P_{\text{turbine}B} \leq 0$$

$$g_{\text{constraint}}(6) = f_2(Q_{1A} + Q_{1B}) - p_{22} \leq 0,$$

$$g_{\text{constraint}}(7) = f_3(Q_{1A} + Q_{1B}) - p_{23} \leq 0, \tag{36}$$

where $f_2 \approx 2100$ psi, $f_3 \approx 4300$ psi.

Level 2 Machine Level Constraints:

$$S_{1A} = S_{2A} = S_{3A}$$

$$S_{1B} = S_{2B} = S_{3B}$$

$$Q_{1A} \geq Q_{1A\min}, \quad Q_{2A} \geq Q_{2A\min}, \quad Q_{3A} \geq Q_{3A\min}$$

$$Q_{1B} \geq Q_{1B\min}, \quad Q_{2B} \geq Q_{2B\min}, \quad Q_{3B} \geq Q_{3B\min}$$

$$\dot{M}_{2B} = \dot{M}_{1A} + \dot{M}_{1B} - \dot{M}_{2A} - \dot{M}_{\text{extraction flow1}}$$

$$\dot{M}_{3B} = \dot{M}_{2A} + \dot{M}_{2B} - \dot{M}_{3A} - \dot{M}_{\text{extraction flow2}} \tag{37}$$

Recapping the level 3 constraints, Eq. (36), the first three equations specify that discharge pressures of machines must be at equilibrium between trains A and B. The following two equations specify the requirement that absorbed compressor power be less than maximum available turbine power and finally the last two equations set minimum requirements for discharge pressures on the second and third stages. Examining these equations, it is apparent that they have been written in open form so that the degree to which constraints are violated at intermediate stages of the optimization may be calculated.

It is also noteworthy that the decision to build level 2 constraints into the model and leave other constraints at the system level, where they eventually are resolved by the optimization program, was arbitrary. In fact all of the constraints could have been left for the optimizer to solve.

Once a model has been developed, a numerical optimization routine must be utilized with the model. In the author's work, the system model "opt_form" was passed to the optimization program using subroutine "opt_setup," where "opt_setup" provided initial guesses for manipulated variables and constants needed for the calculations to proceed, Table 4. The optimization program then used "opt_form" to generate numerical partial derivatives of the objective function with respect to each of the manipulated variables. These partial derivatives were used to estimate new values for the manipulated variables which would maximize the objective function. Clearly when constraints were encountered by the program, the direction of change in the manipulated variables was modified so that these constraints would be avoided. Many methods exist for performing these numerical procedures as discussed by Reklaitis et al. (1983) and Grace et al. (1993).

Table 5 Sample optimization at +50°F ambient temperature

OPERATION STATE						
train	A	A	A	B	B	B
stage	1	2	3	1	2	3
Tamb °F	50	50	50	50	50	50
speed (1=100%)	0.93	0.93	0.93	0.94	0.94	0.94
Qfeed *	154	201	145	184	128	133
Qrecycle *	27	0	0	0	58	0
Qinlet *	181	201	145	184	186	133
Qinlet ACFM	8029	2963	543	8355	2690	494
MW	23.6	22.5	22.5	23.6	22.5	22.5
p1 psig	210	606	2026	210	606	2026
p2 psig	656	2051	4142	656	2051	4142
t1 °F	75	72	85	84	65	82
t2 °F	238	261	191	249	267	192
Poly head(ft)	42217	47401	24056	43022	47384	23942
η polytropic	0.77	0.74	0.68	0.76	0.69	0.65
stage power(hp)	13149	16262	6460	13731	16112	6156
A total (hp)	35872	35872	35872	N/A	N/A	N/A
B total (hp)	N/A	N/A	N/A	35999	35999	35999

* Flows are expressed in million standard cubic feet or as otherwise noted.

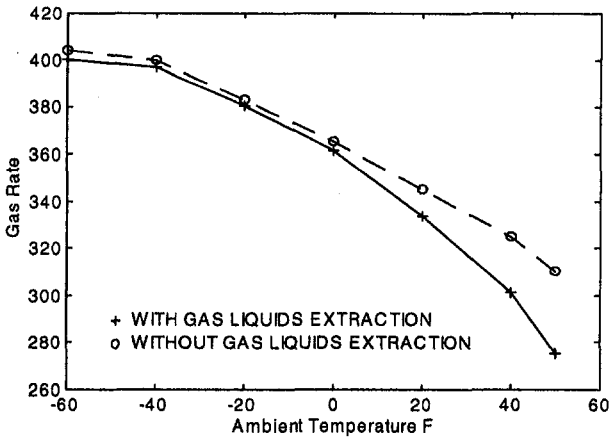

Fig. 5 Third-stage gas rate (10^6 SCFD) versus ambient temperature (°F)

Results

The results of a typical optimization performed at 50°F are given in Table 5. Similar optimizations performed over a range of ambient temperatures are also presented in Fig. 5. From Fig. 5 it is apparent that gas processing capacity rapidly deteriorates as ambient temperature increases and available turbine power decreases. Table 5 gives some insight into why this is the case. In Table 5 it is apparent that recycle valves are open in the first and second stages of the A and B trains, respectively. As can be seen in Fig. 5, this leads to a steeper reduction in gas processing capacity as ambient temperatures increase than would be otherwise expected. This behavior begins to occur at approximately 0°F, which accounts for the change in the slope of Fig. 5 at this point. Considering this system behavior further, it is apparent that absorbed power of the first and second stages cannot be reduced by decreasing throughput and can only be decreased by reducing speed. In actuality, both of these actions are taken by the optimizer in an effort to maximize gas processing rates while meeting system constraints.

The situation just described has been made considerably more complex by the activity of the recycle controllers and the fact the available gas turbine horsepower is insufficient to assure that these controllers are inactive at all ambient temperatures. It is noteworthy that this was, in fact, the original design intent for the system; however, upon start up it was discovered that the margins required for surge control were larger than expected. These margins were as much as 12 percent of the compressor inlet flow at surge and far greater than the 6–7 percent expected. This can, in part, be attributed to the multistage design and closely coupled operation of the two parallel trains.

Because of the sharp decline in gas processing rates observed with increasing ambient temperature, various operational scenarios were investigated for maximizing plant throughput. Interestingly, it was discovered that plant gas processing rates could be increased if the natural gas liquids extraction process operating between the first and second stage was turned off, as

shown in Fig. 5. This result was counterintuitive and highlighted why such a model was useful.

In general, actual plant operation conformed quite closely to simulation predictions. This was particularly true when competing operational strategies were compared. In these cases, the overall calibration of the model was somewhat less important.

References

Batson, B. W., 1996, "Invariant Coordinate Systems for Compressor Control," ASME Paper No. 96-GT-240.

Compressors and Exhausters PTC 10, 1992, ASME, New York.

Edminster, W. C., 1961, *Applied Hydrocarbon Thermodynamics,* Gulf Publishing Co., Houston, TX.

Fluid Meters: Their Theory and Application, 1971, ASME, New York.

Grace, A., 1993, *Optimization Toolbox,* The Math Works, Inc. Natick, MA.

Gresh, T. M., 1991, *Compressor Performance,* Butterworth Heinemann, Stoneham, MA.

Henley, J. H., and Seader, J. H., 1981, *Equilibrium Stage Separation Operations in Chemical Engineering,* Wiley, New York.

Lapina, R. P., 1982, *Estimating Centrifugal Compressor Performance,* Gulf Publishing Co., Houston, TX.

Principles of Operation Series III Controller, 1993, Compressor Controls Corporation, Des Moines, IA.

Reid, R. C., Prausnitz, J. M., and Poling, B. E., 1987, *Properties of Gases and Liquids,* 4th ed., McGraw-Hill, New York.

Reklaitis, G. V., and Ravindran, 1983, A., and Ragdell, K. M. *Engineering Optimization Methods and Applications,* Wiley, New York.

Sapiro, L., 1982, *Centrifugal Gas Compressors Basic Aero-Thermodynamic Concepts for Selection and Performance Evaluation,* Solar Turbines Incorporated, San Diego, CA.

Sorenson, H. A., 1983, *Energy Conversion Systems,* Wiley, New York, pp. 159–160.

Design of a Semiclosed-Cycle Gas Turbine With Carbon Dioxide–Argon as Working Fluid

I. Ulizar
Industria de Turbopropulsores—Ajalvir,
Torrejon de Ardoz,
Madrid, Spain

P. Pilidis
School of Mechanical Engineering,
Cranfield University,
Cranfield, Bedford, United Kingdom

The main performance features of a semiclosed-cycle gas turbine with carbon dioxide–argon working fluid are described here. This machine is designed to employ coal synthetic gas fuel and to produce no emissions. The present paper outlines three tasks carried out. First, the selection of main engine variables, mainly pressure and temperature ratios. Then a sizing exercise is carried out where many details of its physical appearance are outlined. Finally the off-design performance of the engine is predicted. This two-spool gas turbine is purpose built for the working fluid, so its physical characteristics reflect this requirement. The cycle is designed with a turbine entry temperature of 1650 K and the optimum pressure ratio is found to be around 60. Two major alternatives are examined, the simple and the precooled cycle. A large amount of nitrogen is produced by the air separation plant associated with this gas turbine and the coal gasifier. An investigation has been made on how to use this nitrogen to improve the performance of the engine by precooling the compressor, cooling the turbine nozzle guide vanes, and using it to cool the delivery of the low-pressure compressor. The efficiencies of the whole plant have been computed, taking into account the energy requirements of the gasifier and the need to dispose of the excess carbon dioxide. Hence the overall efficiencies indicated here are of the order of 40 percent. This is a low efficiency by current standards, but the fuel employed is coal and no emissions are produced.

Introduction

The continuing concern over the emission of greenhouse gases coupled with the ever-increasing demand for electrical energy poses a very difficult challenge to power engineers. One possible solution to these conflicting requirements, if solid fossil fuels are to be employed, is to collect and dispose of the emissions in a controlled way.

An internal combustion semiclosed power cycle, where the working fluid is carbon dioxide, with oxygen and fuel injected in the combustion chamber and excess carbon dioxide collected at the outlet seems to be a very attractive environmental proposition. Such a cycle has a dual advantage. By collecting and storing safely the excess carbon dioxide, the emission of greenhouse gases is controlled. By having a clean fuel and no air in the working fluid, there are no emissions of oxides of sulfur and nitrogen.

This proposition becomes particularly attractive when coal is considered. This fuel is in plentiful supply and when gasified it can be a very clean source of energy. The major drawbacks of such a cycle are the complexity of the equipment and the significant reduction in efficiency caused by the need to produce pure oxygen.

This paper describes the physical aspects of such a machine and how to capitalize on the integration of the machine and the gasifier. Of particular interest is the use of the large amount of cold nitrogen produced by the air separation plant required to produce pure oxygen for the gas turbine and the gasifier.

The Engine

This paper describes an internal combustion turbine where the working fluid is carbon dioxide, the main mass of which is recirculated in the engine. The choice of working fluid is dictated by the fuel, based on coal, and the requirement to make carbon dioxide collection an easy process.

Heat addition is achieved by injecting oxygen and coal gas fuel in the combustion chamber. To keep a constant mass flow through the device, water is collected at the outlet of the cooler and some carbon dioxide is extracted at the HPC delivery. This gas is compressed to 60 atm for efficient collection. All calculations include this compression work. The background of such a device was reported in [6].

Figure 1 shows the engine selected. It is a two-spool gas generator where the low-pressure turbine drives the LPC and the load. The coal gasifier energy requirements have been included and the machine has been optimized to account for them. The predictions outlined here have been produced with a developed version of GTSI [5]. It works on the main principles of TURBOMATCH [4], the Cranfield gas turbine simulation

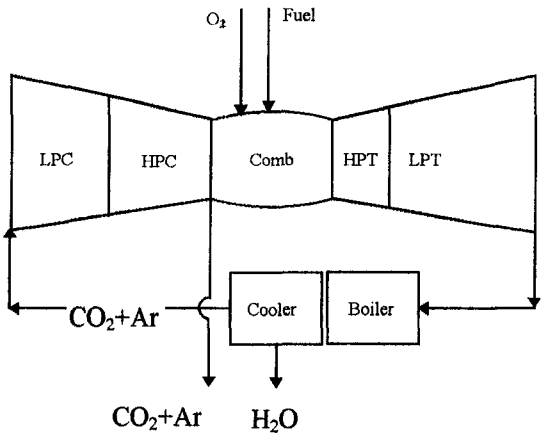

Fig. 1 Diagram of the semiclosed cycle engine

Contributed by the International Gas Turbine Institute and presented at the 42nd International Gas Turbine and Aeroengine Congress and Exhibition, Orlando, Florida, June 2–5, 1997. Manuscript received at ASME Headquarters March 1997. Paper No. 97-GT-129. Associate Technical Editor: H. A. Kidd.

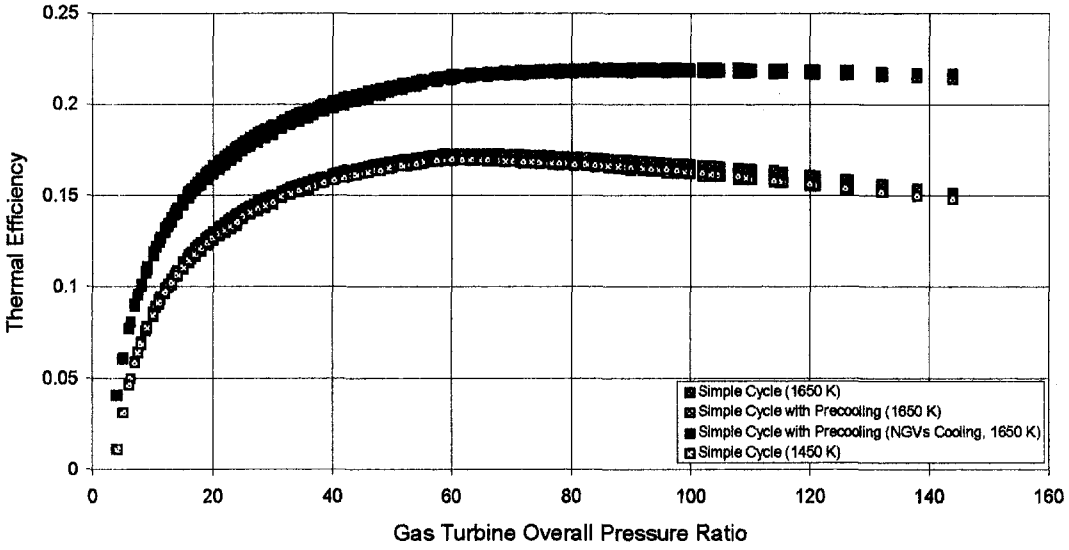

Fig. 2 Gas turbine thermal efficiency

program. The gas properties are calculated based on what is published in [2 and 6].

Advanced Engine Cycle

From the outset it was clear that a special turbine would need to be designed for this duty. Using existing equipment would result in high losses. A study was carried out and it was found that the use of existing air-breathing equipment would incur a thermal efficiency penalty of 10 percent [2]. The design of the engine studied here was made with a turbine inlet temperature of 1650 K as a benchmark. This high temperature presupposes clean gas fuel.

A cycle such as that reported in [6] without accounting for the coal gasifier energy requirements would yield thermal efficiencies of 26 and 48 percent for the gas turbine and the combined cycle, respectively.

Similar cycles are shown in Figs. 2, 3, and 4 for a pressure ratio of 48, labeled Simple Cycle-1450 K. Each value of overall pressure ratio is represented by a clusters of points representing the various splits of LPC and HPC pressure ratios to give one given value of overall pressure ratio. Figures 2 and 3 show the thermal efficiencies of the simple cycle and the combined cycle, respectively. Figure 4 shows the specific work of the gas turbine. If the coal gasifier energy requirements are included, the simple cycle efficiency would be about 17 percent (instead of 26, without allowing for the gasifier energy inputs, as reported in [6]) and combined cycle efficiency would be about 36 (instead of 46 reported previously). These figures are shown for the purposes of comparison.

It is interesting to observe that the simple cycle efficiency is not much better with the higher turbine entry temperature of 1650 (Fig. 2). This is because of the additional compressor work required to elevate the pressure of the gas fuel to that required for entry into the combustor. In such a machine the fuel and oxidant flow is predicted to be in excess of one tenth of the working fluid. The combined cycle efficiency is better, however, by about one percent because of the higher exhaust mass flow of the gas turbine.

The performance of the cycle is heavily penalized by the requirement of emissions control. Its efficiency is 15 to 20 percent lower than state-of-the-art, currently available, combined cycle equipment. The need to operate with carbon dioxide

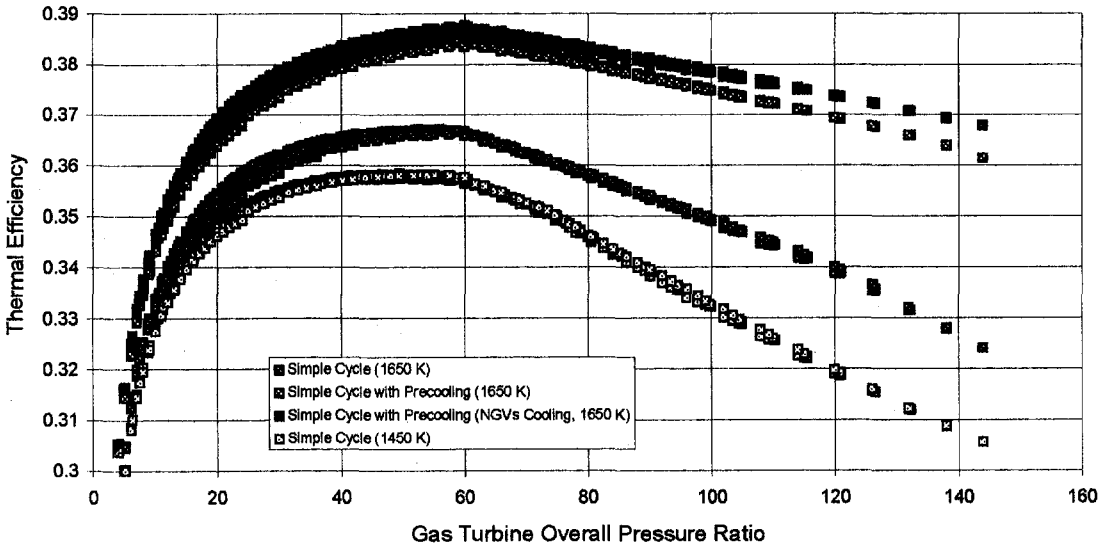

Fig. 3 Combined cycle thermal efficiency

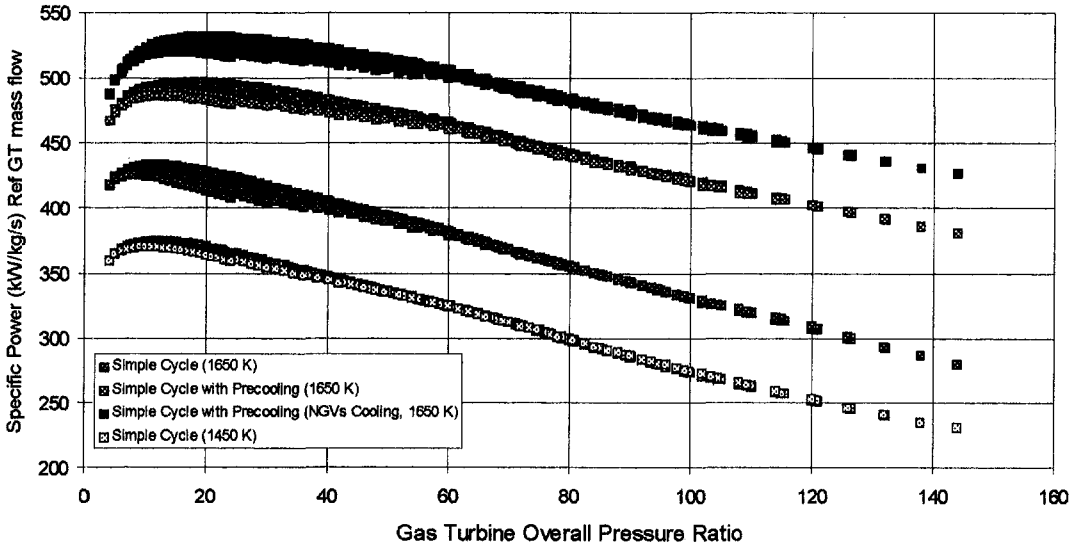

Fig. 4 Combined cycle specific power

as working fluid and to use pure oxygen for combustion results in three major energy drains:

- Power for the air separation plant
- Compression of the fuel and oxidant gases
- Compression of the gas for disposal

The steam cycles employed in the present analysis are current state-of-the-art back pressure cycles, with a steam inlet temperature and pressure of 813 K and 52.6 bar. The back pressure is 0.06 bar.

Integration With the Coal Gasifier

The 1650 K cycle described above was taken as a baseline. Three modifications were investigated to improve its performance. These entailed the use of the nitrogen produced by the cryogenic air separation plant that produces pure oxygen for the coal gasifier and the gas turbine combustor.

For each mass unit of oxygen produced for the engine, one half unit is required by the gasifier. The byproduct of this air separation plant is liquid nitrogen, in very large quantities. It can be employed to boost engine performance, as follows:

- Cooling the compressor inlet gas
- Cooling the turbine nozzles
- Cooling the LPC exit gas

Cooling the Compressor Inlet. Cooling the compressor inlet gas will bring about increased efficiency and specific power. The quantity of liquid nitrogen, produced as a byproduct of the air separation process, varies from case to case because different pressure ratios result in different fuel to gas ratios. The nitrogen to working fluid gas mass ratio ranges from 0.15 to 0.30 (Fig. 5). When it is used to cool the compressor inlet gas, the engine inlet temperature can be as low as 190 K (Fig. 6).

Introducing this compressor entry precooling, efficiency and specific work can be increased. This is illustrated in the following figures: Fig. 2 shows the thermal efficiency of the gas turbine and Fig. 3 that of the combined gas and steam cycle. It can be observed that an improvement of typically 5 percent (this equates at those levels of efficiency to a reduction of the fuel burn of approximately 25 percent) can be obtained with precooling when the pressure ratio is 60. This is the optimum or nearly the optimum pressure ratio for both cycles.

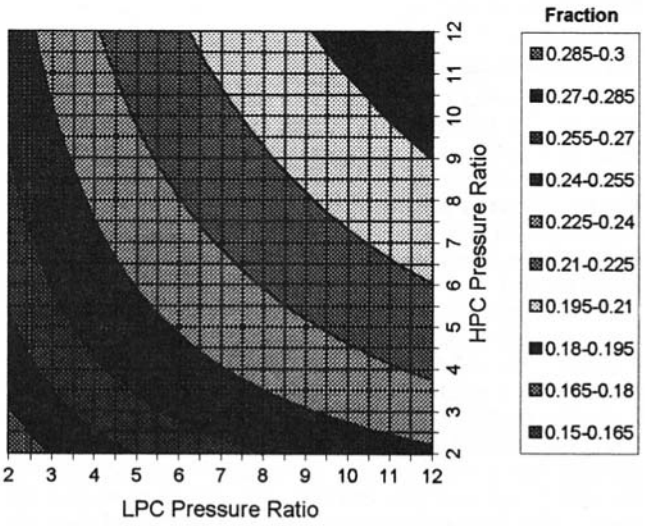

Fig. 5 Nitrogen to engine mass flow ratio simple cycle with precooling, CO_2/argon

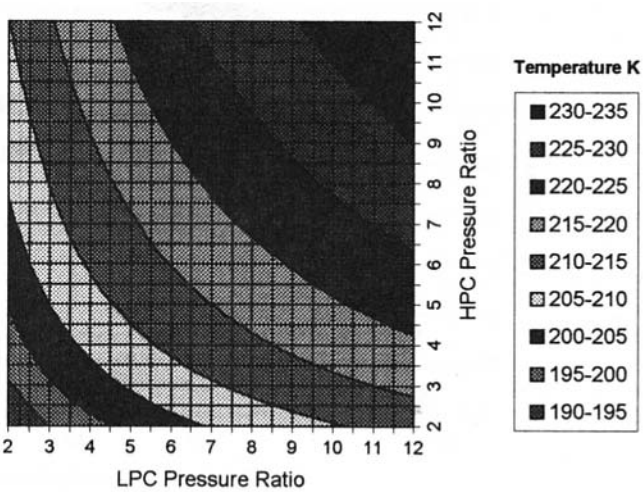

Fig. 6 LPC inlet temperature simple cycle with precooling, CO_2/argon

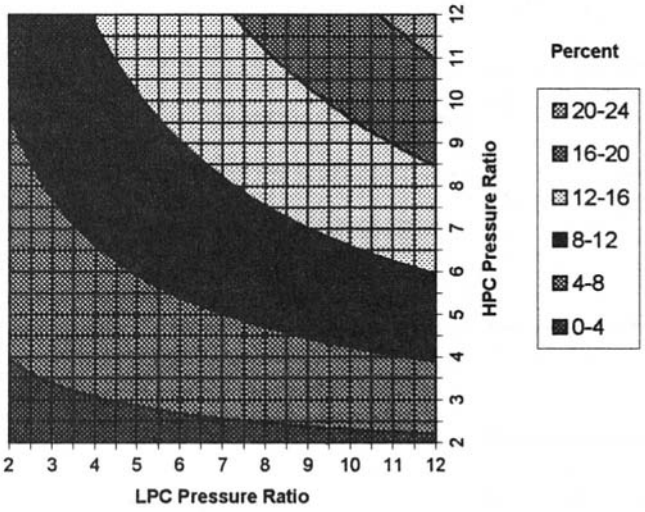

Fig. 7 HPT cooling bleed (W_{cool}/W_2, percent) simple cycle, 1650 K

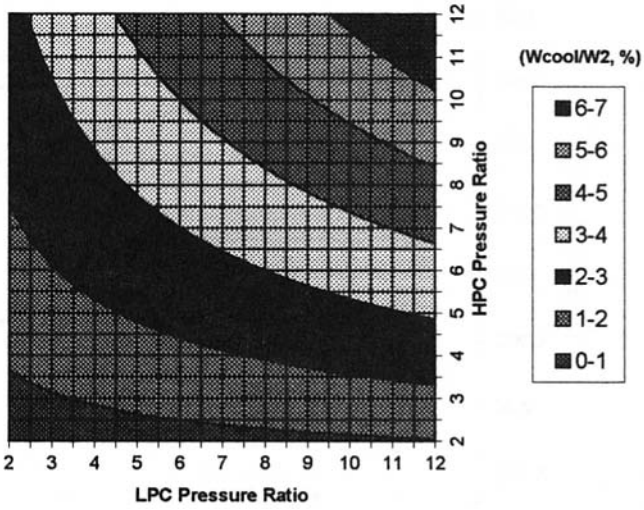

Fig. 9 HPT cooling bleed simple cycle with precooling and NGVs cooling, 1650 K

When the performance of the combined cycle is examined, it can be observed that the efficiency is nearly double that of the simple cycle. The power increase accrued from an unfired steam cycle is larger than what would be expected from a conventional combined cycle. This is because this engine experiences large energy drains of the gasifier and associated equipment. This deduction is much larger than in a conventional gas turbine. In the present case it accounts for approximately one third of the gas turbine output. It can also be observed that the combined cycle efficiency is better in the precooled case, but the difference is now much smaller, of the order of two percent. This is because the precooled gas turbine cycle has a larger specific power, therefore a lower steam to gas flow ratio.

Cooling the Turbine Nozzles. The nitrogen, once it emerges from the compressor precooler, is still very cold. This low-temperature gas can be put to further use. It could be recycled through the nozzle guide vanes of the turbine to cool the aerofoils. In the design proposed here this is achieved by means of a closed-loop circuit so that no nitrogen is injected into the main gas stream. The rotors are cooled in a conventional way (Figs. 7–9).

The benefits of such an approach would be the reduction of cooling flow extracted from the HPC delivery to cool the turbine. This would result in a higher average gas temperature in the turbine, improving the cycle characteristics.

The cooling flow can be reduced quite significantly. In the simple cycle case, turbine cooling flows can exceed 20 percent of the compressor delivery gas. When precooling is employed, this is reduced by about one third, due to the cooler compressor delivery temperature. If nitrogen is used to cool the turbine nozzle guide vanes, the requirement for cooling air is halved, when compared to the previous case.

It can be noticed that this will have a very minor effect on the efficiency of the simple cycle, but the effect on the combined cycle is of the order of one quarter to one third of a percent (Figs. 2 and 3, respectively). The effect is smaller than expected in a conventional combined cycle because part of the efficiency gain is counteracted by the need to compress more fuel gas.

Using nitrogen to cool the turbine nozzle guide vanes has small effect on efficiency, similar to using a higher turbine inlet temperature. The effect on the specific power of the cycle is quite marked, an increase of nearly 10 percent for the gas turbine alone and slightly more in the combined cycle (Fig. 4).

This effect does not include the improvement of turbine efficiency due to the reduction of the cooling flows. It is anticipated this would be between one and two percent, which would translate into a similar improvement in gas turbine thermal efficiency.

Cooling the LPC Exit Gas. Using nitrogen to cool the LPC exit gas in an intercooled cycle is another scheme that was investigated by the authors.

In this case the nitrogen left the compressor precooler, was then ducted to the intercooler between the two compressors and then to the nozzle guide vanes of the turbines. The results were marginal; there was no efficiency gain compared to the cycle with precooling and NGV cooling, even when a higher compressor pressure ratio was selected. Again the gains in efficiency were counterbalanced by the fuel compression work.

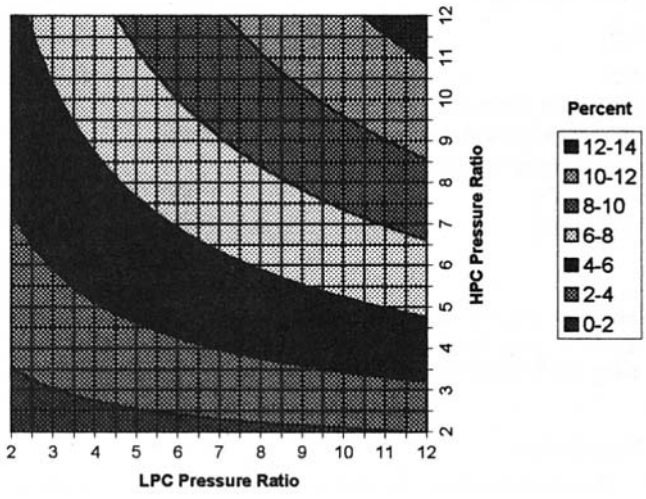

Fig. 8 HPT cooling bleed (W_{cool}/W_2, percent) simple cycle with precooling, 1650 K

Engine Design

An overall pressure ratio of 60 appears to be the optimum, or close to the optimum in every case. This figure is selected, because in addition to yielding very good efficiencies, the selection of this pressure ratio will also simplify the equipment required. 60 bar is the disposal pressure of the CO_2 in the cycle. If the gas turbine pressure ratio selected is also 60, the CO_2 can be stored directly from a bleed at the compressor delivery without the requirement for an additional compressor.

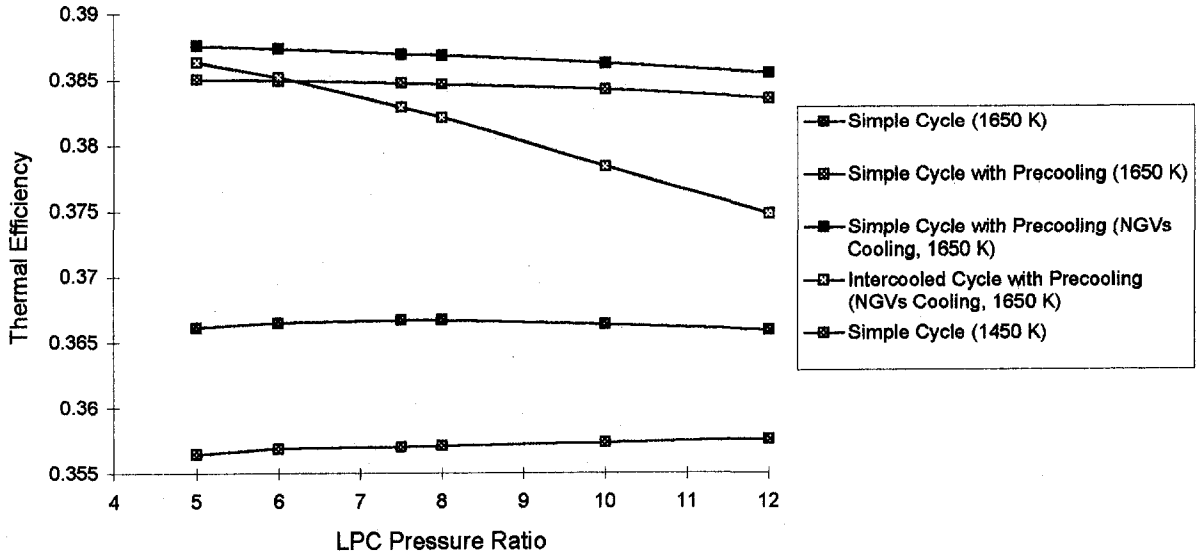

Fig. 10 Combined cycle efficiency variation with LPC pressure ratio (PR = 60)

Having selected the overall pressure ratio of 60, the authors then examined the split of LPC and HPC pressure ratios. The only constraint introduced was that no compressor would have a pressure ratio greater than 12. This is a pressure ratio, which for carbon dioxide is quite high, equivalent to the state of the art in current air breathing industrial gas turbine compressors.

Efficiency changes for different pressure ratio splits were examined and it can be seen in Fig. 10 that there is little effect on efficiency as the pressure ratio split between the two compressors changes. The only exception is that of the intercooled cycle where the lowest LPC pressure ratios give higher efficiencies.

Taking this advanced cycle as the baseline, the next step was to make an approximate estimate of component sizing. Techniques developed from those described in [1] were employed to produce the results shown in Table 1. The two engines illustrated are the simple cycle and the precooled cycle with nitrogen cooled turbine nozzle guide vanes.

The large effect, approximately 90 MW, of the energy drains of the gasifier on the nett output of the plant can be observed in Table I. The largest drains are the power for the fuel gas compression and for the air separation plant.

Table 1 Engine features for two engine models

Item	Simple Cycle	Precooled Cycle
LPC Press. Ratio	7	5
HPC Press. Ratio	8	12
Overall Press. Ratio	56	60
HPT Press. Ratio	3.2	2.6
LPT Press. Ratio	15.3	20.0
LPC Stages	9	8
HPC stages	12	14
HPT stages	2	2
LPT Stages	6	7
LPC inlet Temp (K)	300	216
HPC exit Temp (K)	708	563
HPT inlet Temp (K)	1650	1650
LPT exit Temp (K)	960	921
Gas Turbine Power (MW)	161	230
Steam Turbine Power (MW)	103	112
Nett Output (MW)	193	253
Mass Flow (kg/s)	500	500
Fuel Flow (kg/s)	52	64
ηgt	0.172	0.216
ηcc	0.367	0.388
LPC inlet diameter (m)	1.75	1.56
LPT outlet diameter (m)	2.14	2.14
Overall gas turbine length (m)	5.4	5.5
RPM HPC	5000	5000
RPM LPC	3000	3000

Off-Design Performance

Having selected the engine cycle and having performed the preliminary design, the off-design performance of the engine was predicted for the gas turbine and the combined cycle.

The results shown above are quite interesting. In both cases the turbine power includes the work required for the gasifier. These results are preliminary. An optimization of the control laws is required.

In the cycle without precooling (Table 2), the LPC pressure ratio rises and then falls. Also the speed of the LPC remains constant because it is on the power shaft connected to the electricity generator. The changes in mass flow are a result of closing the stators. In the present exercise the surge margin of the two compressors is adequate so the HPC does not require any variable stators. However, these may be necessary if further investigations reveal that the surge margin of the LPC is not satisfactory.

For the cycle with precooling (Table 3) some interesting features can be observed. The large mass flow reduction is achieved by variable stators and by the higher compressor inlet temperature resulting from the lower mass flow of nitrogen through the precooler. Also, the HPC needs only a small modulation of variable stators, such that variable inlet guide vanes would suffice. Most of the surge margin control is achieved using the variable stators of the LPC.

Conclusion

This paper describes the preliminary analysis of a semiclosed-cycle gas turbine. The working fluid is carbon dioxide and the fuel is low heating value gas synthesized from coal. The selected

Table 2 Advanced semiclosed cycle performance (simple and combined cycle—no precooling)

Mass Flow (%)	100	100	99	89	76	64	54
LPC Inlet T (K)	300	300	300	300	300	300	300
LPC P.Ratio	7.0	7.5	8.2	8.1	7.4	6.8	6.2
HPC P.Ratio	8.0	7.3	6.4	5.6	5.0	4.5	4.0
HPC Exit T(K)	709	697	692	631	664	646	628
LPC RPM (%)	100	100	100	100	100	100	100
HPC RPM (%)	100	97	94	92	89	86	83
TET (K)	1650	1550	1450	1350	1250	1150	1050
Fuel (Kg / s)	10.2	9.21	8.05	6.32	4.64	3.32	2.32
GT Power MW	161	144	121	86	53	28	11
ST Power MW	103	85	72	54	38	26	17

Table 3 Advanced semiclosed cycle performance (simple and combined cycle—with precooling)

Mass Flow (%)	100	94	78	61	48	37	29
LPC Inlet T (K)	216	225	233	241	248	255	262
LPC P.Ratio	5.0	5.2	5.0	4.4	3.8	3.5	3.1
HPC P.Ratio	12.0	10.5	8.9	7.6	6.5	5.5	4.5
HPC Exit T(K)	566	556	553	542	531	519	506
LPC RPM (%)	100	100	100	100	100	100	100
HPC RPM (%)	100	97	94	91	88	85	81
TET (K)	1650	1550	1450	1350	1250	1150	1050
Fuel (Kg / s)	12.68	10.76	8.00	5.57	3.81	2.58	1.70
GT Power MW	230	194	134	83	48	25	10
ST Power MW	112	94	71	51	37	26	17

configuration is a two-spool simple cycle gas generator with an integral power turbine.

The benefits of integration of the cycle with the gasifier are shown here. In particular, the use of the liquid nitrogen produced by the air separation plant to precool the compressor inlet. This scheme increases the overall efficiency of the gas turbine by about 5 percent and of the combined cycle by approximately 2 percent.

The analysis was extended to examine the physical features of the engine and to assess its off-design performance. Rotational speeds and size do not present any extraordinary features. It is expected that the mechanical design will present no more problems than a conventional one, although careful attention will need to be paid to the aerodynamic design.

Some control issues are noteworthy, such as the careful variable stator control to achieve surge control and mass flow modulation.

The prize offered by this type of engine is clean electricity. There are many difficulties envisaged in the development and construction of such a machine. Furthermore, its efficiency will be lower than a conventional open-cycle combined cycle gas turbine. Its development depends on the willingness to pay a premium for clean electricity.

The main issue will be an economic one. It is very difficult to make a cost estimate of such a power plant. Uncertainties in the development, the number of machines to be built, etc., contribute to this difficulty. It is clear that such a machine will be much more expensive than a conventional one. In the balance will be its higher cost and lower efficiency against its ability to use coal and its attractive environment features.

A large amount of work needs to be done to understand the fundamental principles of the machine. The current knowledge base rests on experimental and computational techniques based on air as a working fluid. This needs to be replicated for carbon dioxide. The combustion of a low calorific value fuel in an oxygen stream needs to be assessed. It may be necessary to burn with some excess oxygen to ensure all the fuel is consumed. This will require a slightly larger energy drain for the air separation plant. These and other issues need to be explored prior to any development work.

Acknowledgments

The authors are grateful to their colleagues in I.T.P. and Cranfield for their support and encouragement and to professor W. D. Morris for giving the inspiration, in an indirect way, for the idea of nitrogen precooling.

References

1 Hunter, I. H., "Design of Turbomachinery for Closed and Semiclosed Gas Turbine Cycles," M.Sc. Thesis, Cranfield University, England, 1994.

2 Keenan, J. H., Kaye, J., and Chao, J., *Gas Tables, International Version,* 2nd ed., SI Units, 1983.

3 Navaratnam, M., "The Investigation of an Aeroderivative Gas Turbine Using Alternative Working Fluids in Closed and Semiclosed Cycles," M.Sc. Thesis, Cranfield University, England, 1994.

4 Palmer, J. R., "The TURBOMATCH scheme for Gas Turbine Performance Calculations," Users' Guide, Cranfield Institute of Technology, England, 1983.

5 Ulizar, I., and Pilidis, P., "GTSI, Simulation of Gas Turbines With Unorthodox Working Fluids and Fuels," Turbomachine 96, Italian Thermotechnical Association presented at the Conference, Genova, July, 1996.

6 Ulizar, I., and Pilids, P., "A Semiclosed-Cycle Gas Turbine With Carbon Dioxide–Argon as Working Fluid," ASME JOURNAL OF ENGINEERING FOR GAS TURBINES AND POWER, Vol. 119, 1997, pp. 612–616.

The Evaporative Gas Turbine [EGT] Cycle

J. H. Horlock
Whittle Laboratory,
Madingley Road,
Cambridge CB3 0DY, United Kingdom

Humidification of the flow through a gas turbine has been proposed in a variety of forms. The STIG plant involves the generation of steam by the gas turbine exhaust in a heat recovery steam generator (HRSG), and its injection into or downstream of the combustion chamber. This increases the mass flow through the turbine and the power output from the plant, with a small increase in efficiency. In the evaporative gas turbine (or EGT) cycle, water is injected in the compressor discharge in a regenerative gas turbine cycle (a so-called CBTX plant—compressor [C], burner [B], turbine [T], heat exchanger [X]); the air is evaporatively cooled before it enters the heat exchanger. While the addition of water increases the turbine mass flow and power output, there is also apparent benefit in reducing the temperature drop in the exhaust stack. In one variation of the basic EGT cycle, water is also added downstream of the evaporative aftercooler, even continuously in the heat exchanger. There are several other variations on the basic cycle (e.g., the cascaded humidified advanced turbine [CHAT]). The present paper analyzes the performance of the EGT cycle. The basic thermodynamics are first discussed, and related to the cycle analysis of a dry regenerative gas turbine plant. Subsequently some detailed calculations of EGT cycles are presented. The main purpose of the work is to seek the optimum pressure ratio in the EGT cycle for given constraints (e.g., fixed maximum to minimum temperature). It is argued that this optimum has a relatively low value.

Gas turbine cycles are referred to as follows [Hawthorne and Davis (1956), after E. S. Taylor initially]: CHT, CBT, CHTX, CBTX, CICHTX, CICBTX, etc., where C denotes compressor; H, heater; B, burner (combustion); T, turbine; X, heat exchanger; I, intercooler. Subscripts i and r indicate reversible and irreversible, respectively.

1 Introduction

The evaporative gas turbine (EGT) cycle has a long history; recent studies have been made by Gasparovic and Hellemans (1971), Frutschi and Plancherel (1988), El-Masri (1988), Annerwall and Svedberg (1991), and Bolland and Stadhaas (1995). In what is essentially a regenerative gas turbine cycle, water is injected in an aftercooler; the air is thus evaporatively cooled before it enters the heat exchanger. The addition of the water vapor in the turbine increases the mass flow and the work output of the turbine [as in the STIG cycle (Fraize and Kenney, 1979) where steam is injected directly after water evaporation in a waste heat boiler]. In one variation of the EGT cycle, water is also added downstream of the evaporative aftercooler, even continuously to the cold stream of the heat exchanger. It is the basic thermodynamics of these EGT cycles which is studied here.

Initially (in Section 2) a *closed* regenerative cycle (CHTX, without combustion) is studied in which a single semi-perfect gas is heated in the heater (H). Since the mass flow and specific heat are the same in the two streams of the heat exchanger (X) there is no spare thermal capacity to evaporate any water injected in the cold stream of the heat exchanger. Water is therefore introduced in an evaporative aftercooler and the cycle is completed with a cooler and a condenser after the wet gas exhausts from the heat exchanger. The efficiency of this closed EGT cycle is compared with that of the basic dry CHTX cycle.

Next (in Section 3) an open cycle (CBTX, with combustion in a burner B) is considered in which, following combustion, the thermal capacity of the hot stream in the exchanger is greater than that of the cold stream. There is now capacity for water evaporation in the cold stream of the heat exchanger, as well as in an aftercooler. Again the efficiencies of the wet EGT cycle and the dry CBTX cycle are compared.

From these analyses it becomes apparent that the increased efficiency of an EGT cycle, compared with a "dry" regenerative cycle, is due primarily to the increased turbine work associated with water injection. A simple analysis is therefore developed in Section 4 for the dry CHTX cycle efficiency, to allow for increased thermal capacity in the flow through the turbine, using an approach followed by Woods (1991). This analysis suggests that optimum efficiency still occurs at low pressure ratio, although higher than the dry regenerative air standard cycle with constant specific heat. This question of the optimum pressure ratio is further developed, for the EGT cycle, in a series of numerical calculations, in Section 5.

2 A Closed EGT Cycle

Consider a closed EGT cycle based on water injected into a closed regenerative cycle, which uses a single semi-perfect gas as working fluid (Fig. 1). Water is injected irreversibly after the compressor (C) in an evaporative after cooler (AC), the exit state being just saturated. After passing through the heat exchanger (EXCH), heater (H), and turbine (T), the mixture of air and water emerges from the hot side of the regenerator to enter a first cooler CO1, which drops the temperature to T_1 and partially condenses the water vapor. The remaining water vapor must be abstracted in a separator [V], pumped out from its partial pressure up to atmospheric pressure before it is condensed (CO2). This condensate joins with that emerging from the first cooler thus completing the water part of the cycle, before it is re-injected into the compressor discharge air.

The states are as indicated by the numbers shown in Fig. 1. It may be noted that in the absence of water injection the cycle reverts to the basic gas standard cycle with a regenerator, labeled by Hawthorne and Davis (1956) as the $[CHT]_i X_r$ cycle, where the subscript i indicates irreversible compression and expansion, and the subscript r indicates that the regenerator is

Contributed by the International Gas Turbine Institute and presented at the 42nd International Gas Turbine and Aeroengine Congress and Exhibition, Orlando, Florida, June 2–5, 1997. Manuscript received at ASME Headquarters February 1997. Paper No. 97-GT-408. Associate Technical Editor: H. A. Kidd.

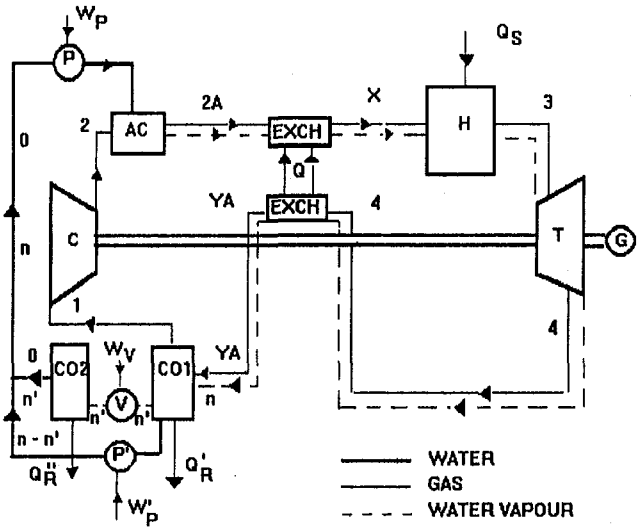

Fig. 1 Closed EGT cycle with aftercooler

essentially reversible. It is assumed to have a very large surface area and there is therefore full-temperature recovery for the cold stream from the hot stream. This is possible because the working fluid is assumed to be a semi-perfect gas with $c_p = c_p[T]$; with no abstraction of cooling air for the turbine it is implied that the thermal capacities of the cold stream and the hot stream are identical at any temperature within the heat exchanger. This condition is assumed to be maintained when water is added, the gas mixtures, hot and cold, having the same thermal capacity. Note that there is thus no further capacity for water injection and evaporation in the cold stream of the heat exchanger—all the water injection is in the aftercooler in this case.

In the analysis that follows it is assumed that the amount of water injected is small, so that the temperature levels are as determined in the original noninjection cycle, the gas temperature entropy chart for which is shown in Fig. 2. The water addition does not then change the ratio of specific heats, so that for given top and bottom temperatures and given pressure ratio, compressor and turbine exit temperatures T_2 and T_4 do not change. However, the heat exchanger temperatures, at cold stream entry and hot stream exit, are reduced [to $T_{2A} = T_{YA}$] and extra heat is required to raise the added water vapor from temperature T_X [$=T_4$] to T_3.

Specific gas [molal] enthalpies are indicated by h, specific water vapor [molal] enthalpies by h [ital], and specific [molal] water enthalpy by h_w. Since the number of moles of water injected per unit gas flow [n] is small, the partial pressures are all small fractions of local total pressure [$p/\mathrm{p} = n$] and the vapor enthalpies are functions of temperature only. For a mixture of air and water vapor the total enthalpy is $H = \mathrm{h} + nh$. Three further points on notation need to be made. First we shall refer to the enthalpy of water at ambient temperature T_1 and atmospheric pressure by subscript 0 [h_{w0}]; second the enthalpy of water at temperature T_1 and its normal saturation pressure is referred to by subscript 1 [h_{w1}]; thirdly [$n - n'$] moles of water are condensed in cooler CO1 leaving n' moles to be condensed in CO2.

A simple "first law" analysis of the cycle may now be undertaken, writing the steady flow energy equation (SFEE) for the various processes in the EGT cycle. In particular, (i) it follows from the SFEE applied to the evaporator that the quantity of water injected is

$$n = \{[\mathrm{h}_2 - \mathrm{h}_{2A}] + W_P\}/[h_{2A} - h_{w0}], \tag{1}$$

where W_P is the work input required to pump the water up to compressor discharge pressure before injection; and (ii) it may be shown that the total heat rejected in the two coolers is

$$\begin{aligned} Q_R &= Q_{R'} + Q_{R''} \\ &= [\mathrm{h}_{YA} - \mathrm{h}_1] + n[h_{YA} - h_{w0}] + W_{P'} + W_V, \end{aligned} \tag{2}$$

where $W_{P'}$, W_V are the pumping work and the extraction work as indicated in Fig. 1.

But using Eq. (1) for the amount of water injected [n], it follows that the heat rejected is

$$\begin{aligned} Q_R &= [(\mathrm{h}_2 - \mathrm{h}_1) - (\mathrm{h}_2 - \mathrm{h}_{YA}) + (\mathrm{h}_2 - \mathrm{h}_{2A}) \\ &\quad + W_P + W_V + W_{P'}] \\ &= W_C + W_P + W_V + W_{P'} \end{aligned} \tag{3}$$

since $\mathrm{h}_{2A} = \mathrm{h}_{YA}$, and $W_C = \mathrm{h}_2 - \mathrm{h}_1$. The water pumping terms W_P, $W_{P'}$ will be very small and in general may be ignored. The extraction work term, of the form

$$W_V = n'RT_1 \log_e [\mathrm{p}_1/p'_1] = n'RT_1 \log_e [1/n'], \tag{4}$$

is also very small (the limit $n' \log_e [1/n']$ goes to zero for small n'). Thus approximately

$$Q_R \approx W_C. \tag{5}$$

Further, since in this cycle the heat supplied, $Q_S = H_3 - H_X$, is equal to the turbine work output, $W_T = H_3 - H_4$, the thermal efficiency may be written

$$\begin{aligned} \eta &= [Q_S - Q_R]/Q_S \\ &\approx 1 - [W_C/W_T] \end{aligned} \tag{6}$$

which is of similar form to that for the [CHT]$_i X_r$ cycle, although the turbine work has been increased.

Nomenclature

c_p = specific heat at constant pressure
C = thermal capacity
$[CV]_0$ = calorific value at temperature T_0
h, H, h = enthalpy
n, n, n' = number of moles
p, p = pressures
q, Q = heat
R = universal gas constant
T = temperature
w, W = work
x = ratio of isentropic indices
$\alpha = \eta_C \eta_T \theta$
$\beta = 1 + \eta_C(\theta - 1)$
$\gamma = c_p/c_v$
$\epsilon = r^{(\gamma-1)/\gamma}$
η = thermal, component efficiency
η_X = heat exchanger effectiveness
θ = maximum to minimum temperature ratio

Subscripts

c = cold [air] flow
nd = nondimensional
h = hot [gas] flow
i = irreversible
r = reversible
w = water
C = compressor
DRY = cycle with no water injection
R = rejected
S = supplied
T = turbine
X = exchanger

Specific quantities [per unit mole] in lower case.

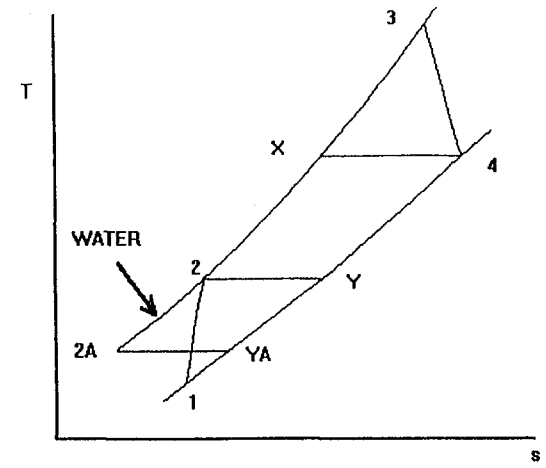

Fig. 2 *T*, *s* diagram [gas properties] for closed EGT cycle with aftercooler

Since the cycle is closed this approximate result for efficiency is more readily obtained by writing

$$Q_S = W + Q_R$$
$$= W_T - W_C + Q_R, \tag{7}$$

ignoring the small work quantities. But since $Q_S = W_T$, it follows that $Q_R = W_C$, and Eq. (6) is immediately obtained.

The first important point is that the heat rejected by the EGT cycle will be approximately the same as that rejected by the dry cycle and equal to the compressor work. Although the temperature drop in heat rejection, from T_{YA} to T_1, is less than that in the dry cycle ($T_2 - T_1$), there is an increased thermal capacity of the flow through the wet cooler compared with that through the dry one, and the total amount of heat rejected is virtually unchanged. Secondly, the efficiency expression, similar to that for the $[\mathrm{CHT}]_i X_r$ cycle, shows that the increase in efficiency of this closed EGT cycle is essentially due to the increased turbine work (and heat supplied) resulting from increasing the mass flow by water injection.

3 An Open EGT Cycle

The closed cycle analyzed in Section 2 is a somewhat artificial one. A more realistic approach involves introducing combustion in an open cycle so that with the increased thermal capacity of the turbine exhaust there is capacity for water evaporation in the cold stream of the heat exchanger, as well as in an aftercooler. It is again assumed that the heat exchanger surface area is large. (A detailed discussion of heat exchanger performance with water injection is given in another paper [Horlock, 1997b]).

Figure 3 shows this open cycle on an air/gas *T*, *s* diagram. The first stage of water injection drops the air temperature to T_{2A}. Further water is added in the cold stream of the heat exchanger and the *total* water injected is n. The hot gas leaves the heat exchanger at temperature $T_{YA} = T_{2A}$ (rather than T_Y with no water injection). The hot wet gas is now discharged downstream of the heat exchanger, and there is no requirement to introduce coolers for heat rejection, as in the closed cycle described in Section 2. n_f is the number of moles of fuel added in the combustion chamber [per unit molal flow of air]. An overbar on thermal capacity $[\bar{C}]$ represents a mean value over the appropriate temperature range following in brackets, and the subscripts h and c refer to hot gas and the cold air respectively.

Again a straightforward "First Law" analysis may be employed, using the steady flow energy equation, for the various processes in this open cycle. In particular, (i) from the SFEE applied to the after cooler plus heat exchanger it follows that

$$n = \{[T_4 - T_{2A}] - \bar{C}_c[T_4 - T_2]\}/[h_{2A} - h_{w0}]; \tag{8}$$

(ii) in combustion, the fuel energy supplied is

$$\mathrm{n}_f[CV]_0 = \bar{C}_h[T_3 - T_0] - \bar{C}_c[T_4 - T_0] + n[h_3 - h_4]; \tag{9}$$

(iii) in the exhaust stack the enthalpy drop is

$$\{\bar{C}_h[T_{2A} - T_1] + n[h_{2A} - h_1]\}.$$

But the "heat rejected" (if the water vapor were condensed at $T_1 = T_0$) would be

$$Q_R = \bar{C}_h[T_{2A} - T_1] + n[h_{2A} - h_{w1}].$$

Substituting for n from Eq. (8), assuming $h_{w1} \approx h_{w0}$, it follows that

$$Q_R = \bar{C}_h[T_4 - T_1] - \bar{C}_c[T_4 - T_2] \tag{10}$$

This may be shown to be the same as the heat rejected in the dry cycle with no water injection, when the hot gas leaves the heat exchanger at $T_Y > T_{YA}$. Because the heat exchanger is large, the cold stream leaves at T_4, so that

$$[Q_R]_{\mathrm{DRY}} = \bar{C}_h[T_Y - T_1] \tag{11}$$

But

$$\bar{C}_h[T_4 - T_Y] = \bar{C}_c[T_4 - T_2] \tag{12}$$

so that

$$[Q_R]_{\mathrm{DRY}} = \bar{C}_h[T_4 - T_1] - \bar{C}_c[T_4 - T_2]. \tag{13}$$

The rational efficiency of the open EGT open cycle is

$$\eta = \frac{W_T - W_C}{\mathrm{n}_f[CV]_0}$$
$$= \frac{\bar{C}_h[T_3 - T_4] + n[h_3 - h_4] - \bar{C}_c[T_2 - T_1]}{\bar{C}_h[T_3 - T_0] + n[h_3 - h_4] - \bar{C}_c[T_4 - T_0]}$$
$$= \frac{W_T - W_C}{W_T + [\bar{C}_h - \bar{C}_c][T_4 - T_0]} \tag{14}$$

whereas the efficiency of the dry cycle was

$$[\eta]_{\mathrm{DRY}} = \frac{[W_T]_{\mathrm{DRY}} - W_C}{[W_T]_{\mathrm{DRY}} + [\bar{C}_h - \bar{C}_c][T_4 - T_0]} \tag{15}$$

η is clearly greater than $[\eta]_{\mathrm{DRY}}$ because of the increase in turbine work, with W_C and $[\bar{C}_h - \bar{C}_c][T_4 - T_0]$ both remaining unchanged.

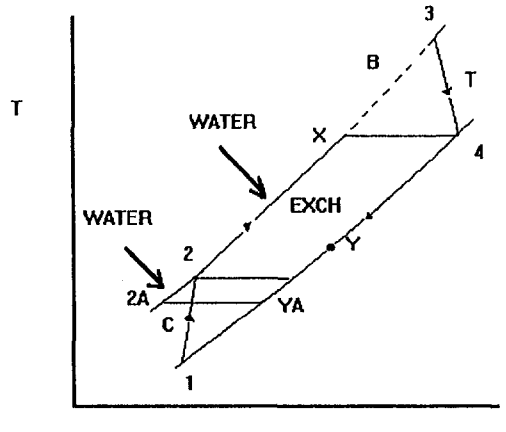

Fig. 3 *T*, *s* diagram [gas properties] for open EGT cycle with full water injection

This analysis is valid if water injection is (i) only in the aftercooler, (ii) only in the cold side of the heat exchanger, (iii) in both. The temperature T_{2A} is controlled by the amount of water injection in the aftercooler (it becomes T_2 for no aftercooler water injection). But note that T_{2A} does not appear in the expressions for Q_R and thermal efficiency.

4 The Effect of Increased Turbine Work on Optimum Pressure Ratio

The analysis of Sections 2 and 3 suggests that the EGT cycle may be similar to the $[CHT]_i X_r$ cycle but with increased turbine work due to the water injection. A preliminary study of the effect of increased W_T on the performance of the $[CHT]_i X_r$ cycle was therefore undertaken.

4.1 The Air Standard Regenerative Cycle. Hawthorne and Davis analyzed the $[CHT]_i X_r$ cycle as a part of their much fuller analysis of many "air standard" gas turbine cycles; they assumed a perfect gas with constant specific heats (c_p, c_v) as the working fluid and constant (unit) mass flow. Their simple analysis leads to the highest efficiency

$$\eta = 1 - [1/\alpha] \tag{16}$$

being obtained at very low pressure ratio ($r \to 1.0$), but when the specific work output $[w = (w_T - w_C)]$ goes to zero. However, the specific work output is a maximum when $\epsilon = r^{(\gamma-1)/\gamma} = [\alpha]^{1/2}$. The efficiency then becomes

$$\eta = 1 - [1/\alpha]^{1/2} \tag{17}$$

which is that of the $[CBT]_i$ cycle at the same pressure ratio, when the heat exchanger becomes redundant (because the turbine outlet temperature approaches that at outlet from the compressor). Thus for a recuperative cycle with a very effective heat exchanger, the designer should optimize at a pressure ratio such that ϵ lies between 1.0 and $[\alpha]^{1/2}$, in order to obtain both good efficiency and specific work output (i.e., not too large a plant).

Hawthorne and Davis then developed a graphic analysis for the $[CBTX]_i$ cycle (i.e., with the heat exchanger effectiveness $\eta_X < 1.0$). Frost et al. (1992) gave formal, complex algebraic analyses for the $[CBTX]_i$ cycle in terms of the variables r, α, and η_X, but numerical calculation is straightforward. For example, the full lines on Fig. 4 show how thermal efficiency and nondimensional specific work $[w_{nd} = w/c_p(T_3 - T_1)]$ vary with pressure ratio for $\theta = T_3/T_1 = 1473/298 = 4.94$, $\eta_T = 0.875$, $\eta_C = 0.875$ and $\eta_X = 0.85$. The thermal efficiency peaks at low r (about 4), but substantially less than that for maximum specific work, $r = 10.3$, corresponding to $\epsilon = [\alpha]^{1/2}$ (the specific work is unaltered by the value of the effectiveness of the heat exchanger).

It is also worthwhile noting that intercooling shifts the optimum pressure ratio to a slightly higher value for the air standard cycle. The dashed lines in Fig. 4 show the effect of intercooling (after a pressure ratio of $r^{1/2}$); for this $[CICHTX]_i$ cycle, the optimum pressure ratio for maximum thermal efficiency is about 7. The maximum specific work peaks at a very much higher pressure ratio (about $r = 22.3$, corresponding to $\epsilon = [\alpha]^{2/3}$).

4.2 The Effect of Change in Thermal Capacity in [CBTX] Cycles. In real gas turbine plants the mass flow and specific work of the combustion gases in the turbine are both greater than those of the air flow through the compressor (i.e., W_T increases). Since water injection similarly increases turbine work, it was thought to be worthwhile to investigate how increased W_T affects the optimum pressure ratio in the dry cycle.

Firstly, the basic approach used by Hawthorne and Davis for the $[CBT]_i X_r$ cycle (in which the turbine work output is taken as equal to the heat supplied) is adopted. But here it is developed by allowing for increased work in the turbine (due to the increased specific heat) and for different compression and expansion indices in compressor and turbine, the working fluid in the latter being a mixture of "perfect" combustion gases. This follows the work of Woods (1991).

Thus in terms of state points 12343Y1 (as in Fig. 3, but with no water injection), the turbine work, equal to the heat supplied, is

$$w_T = [c_{pc}/x]\eta_T T_3[1 - 1/(\epsilon)^x] \tag{18}$$

where $x = c_{pc}/c_{ph}$, and the ratio of the expansion indices is also $x = \{[\gamma_h - 1]/\gamma_h\}/\{[\gamma_c - 1]/\gamma_c\}$. It is assumed that the fuel addition is significant in terms of changing specific heat but not the mass flow. The compressor work is

$$w_C = c_{pc}T_1[\epsilon - 1]/\eta_C \tag{19}$$

Thus the thermal efficiency may be written as

$$\eta = 1 - [w_C/w_T] = 1 - \{[\epsilon - 1]x/\alpha[1 - 1/(\epsilon)^x]\} \tag{20}$$

where $\alpha = \eta_C\eta_T\theta$, and the nondimensional specific work as

$$w_{nd} = \{\alpha[1 - 1/(\epsilon)^x] - x[\epsilon - 1]\}/[\beta - 1] \tag{21}$$

where $[\beta - 1] = \eta_C[\theta - 1]$.

Both η and w_{nd} are increased by the specific heat capacity effect. As for the Hawthorne and Davis simplified analysis of the $[CBT]_i X_r$ cycle, the highest efficiency remains

$$\eta = 1 - [1/\alpha] \tag{22}$$

and still occurs when the pressure ratio is unity, and when the specific work is zero. Maximum specific work occurs when $\epsilon = [\alpha]^{1/[1+x]}$, which is the result derived by Woods (1991) for the specific heat capacity effect in the $[CBT]_i$ cycle.

Calculations have also been made to assess this specific heat capacity effect on the air standard $[CHTX]_i$ cycle with heat exchanger effectiveness less than unity; the dotted line on Fig. 4 show η and w_{nd} for $x = 0.875$ and $\eta_X = 0.85$. Both the thermal efficiency and the specific work are increased compared with their values in the $[CHTX]_i$ cycle. The pressure ratio for maximum efficiency is little changed but that for maximum specific work is increased to $r = 11.3$, corresponding to $\epsilon = [\alpha]^{1/1.875}$.

4.3 Discussion. Analysis for the closed and open EGT cycles suggested that the main effect of water addition should be primarily through the increase of work output from the turbine, the "heat rejection" being unchanged from that of the dry cycle. Modification of the Hawthorne and Davis analysis, as given in Section 4.2, to allow for increased turbine work (through change of gas properties), suggests that low compression ratio is still advantageous in (CHTX) cycles, there being little or no movement in pressure ratio for maximum cycle efficiency from that for the air standard cycle.

The indication from these preliminary analyses is therefore that the optimum pressure ratio for the EGT cycle, with its increased turbine work resulting from water injection, should also be quite low (in any compromise between the requirement for maximum efficiency and maximum specific work). This somewhat surprising result suggests that more detailed and realistic calculations of the EGT cycle, with water addition in an aftercooler and in the heat exchanger, were required and these are described below.

5 Calculations for "Real" EGT Cycles

Calculations are presented in this section to investigate in more detail the optimum pressure ratio for the EGT cycles. Allowance is made for the effects of

(*i*) intercooling;

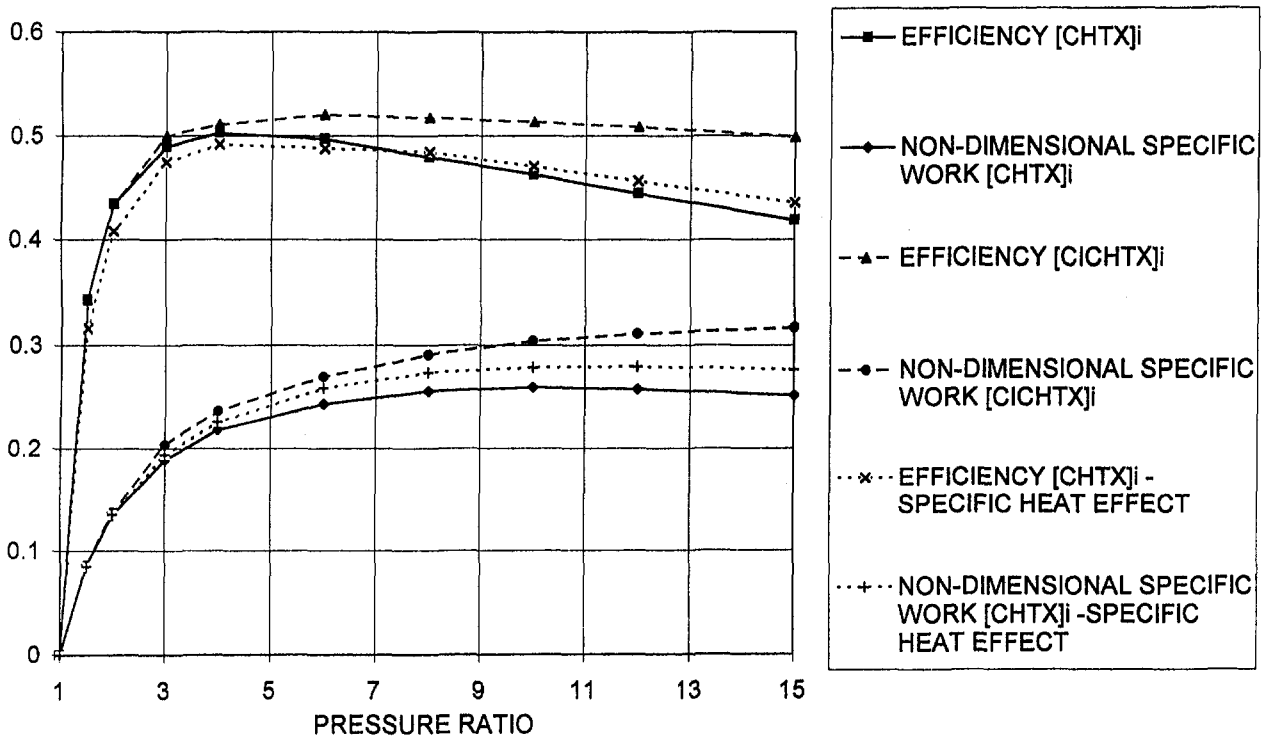

Fig. 4 Thermal efficiency and specific work of air standard cycles showing intercooling and specific heat effects

(*ii*) extraction of air at exit from the compressor for cooling the turbine;
(*iii*) water injection in the heat exchanger; and
(*iv*) additional water injection in an aftercooler.

All the calculations are for "real" open cycles (the detailed assumptions are listed in Appendix 1). The performance of dry cycles (for comparison purposes) is described in Section 5.1 and the performance of wet cycles in Section 5.2

5.1 Dry "Open Cycle" Regenerative Plants (With Burners [B] for Combustion). For the "open" cycle combustion plant $[CBT]_i X_r$, the form of the "rational" efficiency is given by Eq. (15). It is assumed that the heat exchanger has a large surface area, so that the cold stream exit temperature approaches that of the hot stream entry temperature ($T_X = T_4$), although T_Y is still greater than T_2, because $C_h > C_c$. The heat exchanger effectiveness as conventionally defined then approaches unity; here the subscript r is used to indicate this, although the exchanger is not strictly reversible, because of the temperature differences between the two streams within the exchanger (except for cold stream exit/hot stream entry). Figure 5—the full line—shows that the $[CBT]_i X_r$ efficiency peaks at low pressure ratio (about 3, not at $r \rightarrow 1.0$, as for the air standard $[CHT]_i X_r$ cycle).

The introduction of intercooling, in a $[CICBT]_i X_r$ cycle, with pressure ratio equally split between low and high-pressure compressors, raises the efficiency (the dashed line in Fig. 5). The optimum pressure ratio appears to be more or less unchanged; but the efficiency plot is flat without a clearly defined optimum.

Next, the extraction of air (from the compressor discharge flow) for turbine cooling, and how it affects the thermal efficiency and the optimum pressure ratio for the dry plant, was investigated. A simple mixing model was used (see Appendix 2), it being assumed that with say 10 percent cooling air extraction, 90 percent of the compressor air flow was burned to a higher combustion temperature and then mixed with the 10 percent cooling air, at a pressure marginally below the combustion exhaust pressure, to give the original, selected maximum temperature. It is thus implied that the first row stator is cooled and the cooling air is mixed at the trailing edge condition to give the "rotor entry" temperature. It is accepted that this model is much oversimplified, compared with other much more detailed calculations involving multistage turbine cooling (see El-Masri [1988] and Bolland and Stadhaas [1995], for example). The purpose here is to demonstrate the nature of the movement in optimum pressure ratio due to such cooling, rather than to attempt accurate prediction of overall efficiency.

The effect of turbine cooling on the real open cycle regenerative plant, $[CBT]_i X_r$, with no intercooling, is also shown in Fig. 5 (the dotted line); it is to drop the efficiency, but to shift the optimum pressure ratio from about 3 to about 6. The introduction of intercooling in this plant, to give a $[CICBT]_i X_r$ cycle, increases the thermal efficiency, as to be expected (see the chain-dotted line on Fig. 5). The optimum pressure ratio increases further, now to about 8, although the plot of efficiency with pressure ratio r is again very flat, with no sharply defined optimum condition.

Thus the effects of (*a*) intercooling and (*b*) turbine cooling are both to raise the optimum pressure ratio quite substantially, for the "dry" plant. (Similarly, increases in the optimum r would result from increased values of the pressure losses assumed in the cycle.) The Hawthorne–Davis analysis of the $[CHT]_i X_r$ air standard cycle [with its emphasis on *very* low optimum pressure ratio] is shown to be idealized; the efficiency of the real intercooled, turbine cooled plant peaks at higher pressure ratio, but one that is still in the "industrial" gas turbine plant range, rather than the "aeroderivative" gas turbine plant range (see Horlock, 1997a).

5.2 Regenerative Plants With Water Injection [EGTs]. Next the effects of water injection were investigated, on open cycle plants, all with turbine cooling, but with and without intercooling.

The effect of water injection *in the heat exchanger alone* was first calculated for the "cooled turbine" plant, without intercooling. Figure 6 (the dashed line) shows the thermal effi-

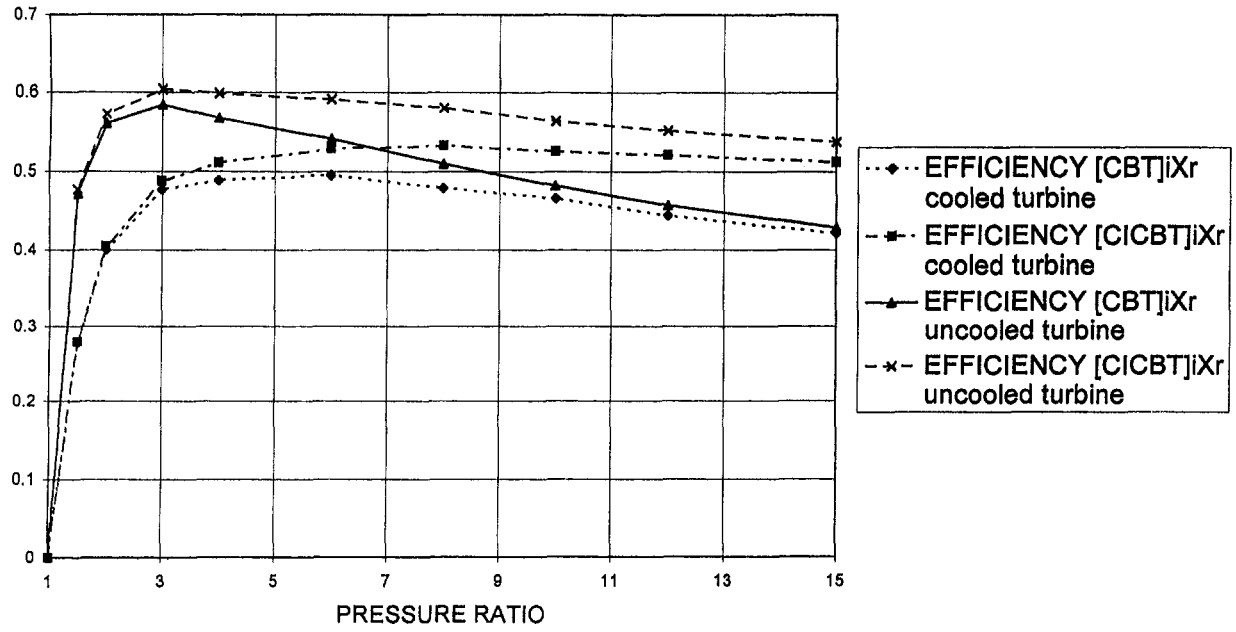

Fig. 5 Effects of intercooling and turbine cooling on dry cycle efficiency

ciency is increased compared with the dry $[CBT]_i X_r$ plant (the full line), but not by much (because the water injected, as a fraction of the air flow, is very small as is also indicated in Fig. 6); the optimum pressure ratio is little altered. For the intercooled cooled plant (also with turbine cooling) addition of water in the heat exchanger similarly raises the efficiency (the chain-dotted line) compared with the dry $[CICBT]_i X_r$ plant (the dotted line), but again there is little change in the optimum pressure ratio. The amount of water injected is again small. For both these plants, the amount of water injected per unit air flow is controlled by both the difference in thermal capacity between the hot and cold streams and the available temperature difference between turbine exit (T_4) and compressor exit (T_2). This temperature difference ($T_4 - T_2$) drops with increasing pressure ratio (r), so the water injected also decreases with increasing r.

Finally the addition of water *in both evaporative aftercooler and heat exchanger* was considered for the "cooled turbine"

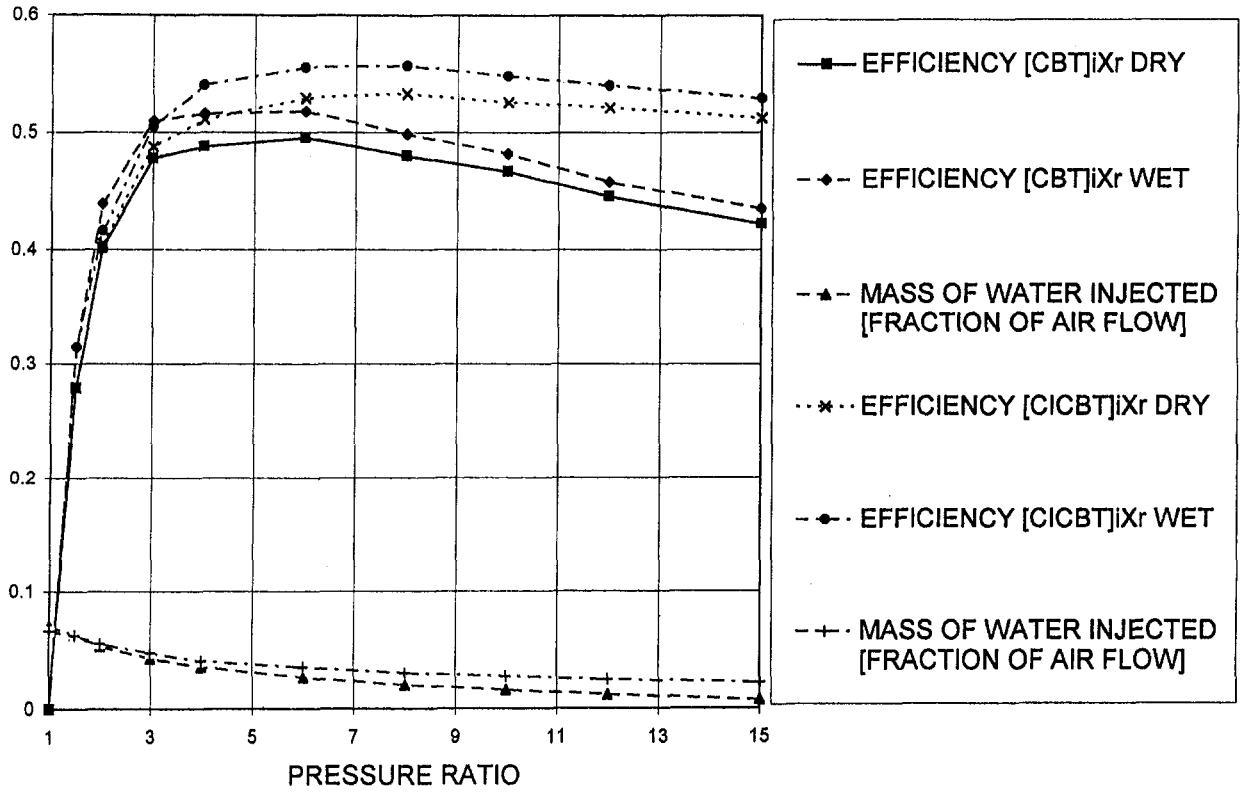

Fig. 6 Effect of water injection (in heat exchanger only) on efficiency

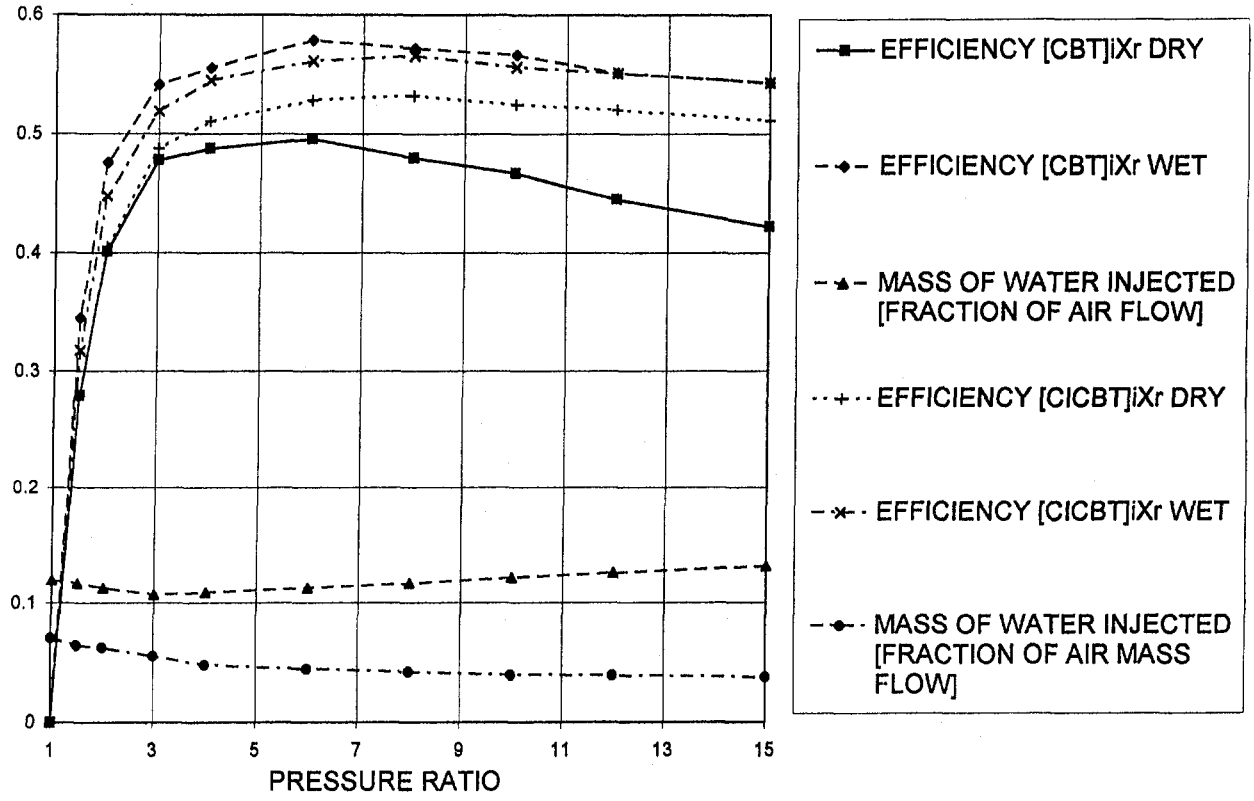

Fig. 7 Effect of full water injection on efficiency

open cycle plant $[CBT]_i X_r$, first with no intercooling and then with intercooling. Figure 7 shows that with no intercooling, substantially more water is injected and as a consequence there is a big increase in the thermal efficiency—some eight percentage points (see the dashed line). The optimum pressure ratio—originally about 6—shifts to a slightly higher value. Figure 7 also shows that the effect of full water injection in the $[CICBT]_i X_r$ intercooled, "turbine-cooled" plant is less (the chain-dotted line c.f. the dotted line). There is less cooling for the evaporative aftercooler to do, and less water is injected. A gain in efficiency of some 3 percent is indicated with little or no change in optimum pressure ratio.

6 Conclusions

It is clear from these calculations that the simplified analysis given in Section 4 is not adequate to describe what happens in a real (CBTX) plant when it is converted into an EGT plant by water injection. The earlier simple analysis, developed from Hawthorne and Davis, shows that for a dry cycle with increased turbine work (resulting from an enhanced thermal capacity of the working gas), the optimum pressure ratio should remain very low. It was thought initially that the performance of a regenerative cycle with water injection [the major effect of which is also to increase turbine work] might be similar, with peak efficiency at very low pressure ratio.

But calculations for more realistic EGT cycles, with intercooling and air extraction for turbine cooling, do not confirm this. The optimum pressure ratio of a dry $[CBTX]_i$ plant is raised from low pressure ratio to higher pressure ratio anyway by these two effects, intercooling and turbine cooling. The introduction of water injection then gives higher thermal efficiency as anticipated, but does not in general increase the optimum pressure ratio much further.

Nevertheless, the calculations described above still suggest that the optimum pressure ratios for the EGT cycles are still relatively low (in the range of 8 to 10). Bolland and Stadhaas (1995) also suggest relatively low optimum pressure ratio for the complex intercooled EGT/STIG cycle they studied [but Macchi et al. (1995) obtained somewhat higher optimum r, although their calculations were for higher maximum temperature than used here]. This would imply that water injection may be more beneficial for the industrial type of gas turbine plant than the aeroengine derivative.

Finally it should be realized that the evaporative gas turbine EGT plant is essentially a form of combined cycle plant, with heat transfer from the higher (gas turbine) cycle exhaust to a lower (steam turbine) cycle; the two turbines are combined into one and there is supplementary heat supplied to raise the water vapor to the maximum temperature. However the steam plant efficiency is much less than in the truly combined cycle plant (where there is a lower temperature of heat rejection), so it cannot be expected that the EGT plant will match the CCGT plant in thermal efficiency. Nor will the gas turbine pressure ratios for maximum efficiency be necessarily comparable [see Horlock (1992) for a summary of the performance of CCGT plants, including calculations of optimum pressure ratio].

Acknowledgments

The author is indebted to Dr. Ian Ritchey of the Industrial Power Group of Rolls Royce plc for assistance in developing this paper. In particular he drew the author's attention to the effects of intercooling and turbine cooling on optimum pressure ratio.

References

Annerwall, K., and Svedburg, G., 1991, "A Study of Modified Gas Turbine Systems with Steam Injection or Evaporative Regeneration," *Proc.* ASME COGENTURBO 6, pp. 1–8.

Bolland, O., and Stadhaas, J. F., 1995, "Comparative Evaluation of Combined Cycles and Gas Turbine Systems With Water Injection, Steam Injection, and Recuperation," ASME JOURNAL OF ENGINEERING FOR GAS TURBINES AND POWER, Vol. 117, pp. 138–147.

Cohen, H., Rogers, G. F. C., and Saravanamuttoo, H. I. H., 1987, *Gas Turbine Theory,* 3rd ed., Longmans and John Wiley, New York.

El-Masri, M. A., 1988, "A Modified High Efficiency Recuperated Gas Turbine Cycle," ASME JOURNAL OF ENGINEERING FOR GAS TURBINES AND POWER, Vol. 110, pp. 233–242.

Fraize, W. E., and Kinney, K. R., 1979, "The Thermodynamics of Steam Injection on the Performance of Gas Turbine Power Cycles," ASME JOURNAL OF ENGINEERING FOR POWER, Vol. 101, pp. 217–227.

Frost, T. H., Agnew, B., and Anderson, A., 1992, "Optimizations for Brayton-Joule Gas Turbine Cycles," *Proc. Instn. Mech. Engrs., Journal of Power and Energy,* Vol. A 206, pp. 283–288.

Frutschi, H. U., and Plancherel, A. A., 1988, "Comparison of Combined Cycles With Steam Injection and Evaporation Cycles," *Proc.* ASME COGEN-TURBO II, pp. 137–145.

Gasparovich, N., and Heddelmans, J. G., 1971, "Gas Turbines With Heat Exchanger and Water Injection in the Compressed Air," *Proc. Instn. Mech. Engnrs.,* Vol. 185.

Hawthorne, W. R., and Davis, G. de V., 1956, "Calculating Gas Turbine Performance," *Engng.,* Vol. 181, p. 361.

Horlock, J. H., 1992, *Combined Power Plants,* Pergamon Press, Oxford.

Horlock, J. H., 1997a, "Aero-engine Derivative Gas Turbines for Power Generation: Thermodynamic and Economic Perspectives," ASME *Journal of Engineering for Gas Turbines and Power,* Vol. 119, pp. 119–123.

Horlock, J. H., 1997b, "Heat Exchanger Performance With Water Injection," Flowers Conference, Florence, SG Editorial, Padova, pp. 3–14.

Macchi, E., Consonni, S., Lozza, G., and Chiesa, P., 1995, "An Assessment of the Thermodynamic Performance of Mixed Gas-Steam Cycles, Parts A and B," ASME JOURNAL OF ENGINEERING FOR GAS TURBINES AND POWER, Vol. 117, pp. 489–508.

Woods, W. A., 1991, "On the Role of the Harmonic Mean Isentropic Exponent in the Analysis of the Closed-Cycle Gas Turbine," *Proc. Instn. Mech. Engrs., Journal of Power and Energy,* Vol. A 205, pp. 287–291.

APPENDIX 1

Assumptions Made in the Calculations

The following assumptions were made in the calculations:

Compressor efficiency, 0.875
Turbine efficiency, 0.875
Maximum to minimum temperature ratio, $T_3/T_1 = 1473/298 = 4.943$
Pressure loss in combustion, $[p_2 - p_3]/p_2 = 0.03$
Pressure loss downstream of turbine, $[p_4 - p_1]/p_1 = 0.05$.
Gas properties as given by Cohen et al. [1987, Fig. 2.14].
Flow saturated at exit from the aftercooler.
Enthalpy of water vapor (at low partial pressure) a function of temperature only.
Form of rational efficiency for an open cycle as Eq. [15].

APPENDIX 2

Mixing Model for Turbine Cooling

Mass flow in compressor, 1 mole of air [subscript c].
Cooling air abstraction, 0.1 moles of air.
Combustion of remaining air (0.9 moles at T_2) with fuel (n_f moles at T_0) to give products (subscript h) at $T_{3'}$.

$$0.9h_{4c} + n_f h_{f0} = [0.9 + n_f]h_{3'h} \qquad (A1)$$

But from the definition of fuel calorific value at temperature T_0,

$$n_f h_{f0} + 0.9h_{0c} = [0.9 + n_f]h_{0h} + n_f[CV]_0 \qquad (A2)$$

Equations (A2) and (A3) yield

$$n_f[CV]_0 = [0.9 + n_f]c_{ph}[T_{3'} - T_0] - 0.9c_{pc}[T_4 - T_0] \qquad (A3)$$

The steady flow energy equation for the subsequent mixing process gives

$$[0.9 + n_f]h_{3'h} + 0.1h_{2c} = [1 + n_f]h_{3h} \qquad (A4)$$

For a selected maximum temperature T_3 Eqs. (A3) and (A4) may be solved to give n_f and $T_{3'}$ (which is not subsequently used).

A. V. Zaita
Advanced Engineering and
Research Associates, Inc.,
Technology Development Division,
2361 Jefferson Davis Hwy., Suite UL336,
Arlington, VA 22202

G. Buley
Naval Surface Warfare Center,
Carderock Division,
9500 MacArthur Blvd.,
West Bethesda, MD 20817-5700

G. Karlsons
Naval Air Warfare Center Aircraft Division,
Patuxent River,
Propulsion and Power Engineering,
22119 James Road, Mail Stop 3,
Patuxent River, MD 20670-5304

Performance Deterioration Modeling in Aircraft Gas Turbine Engines

Steady-state performance models can be used to evaluate a new engine's baseline performance. As a gas turbine accumulates operating time in the field, its performance deteriorates due to fouling, erosion, and wear. This paper presents the development of a model for predicting the performance deterioration of aircraft gas turbines. The model accounts for rotating component deterioration based on the aircraft mission profiles and environmental conditions and the engine's physical and design characteristics. The methodology uses data correlations combined with a stage stacking technique for the compressor and a tip rub model, along with data correlations for the turbine to determine the amount of performance deterioration. The performance deterioration model interfaces with the manufacturer's baseline engine simulation model in order to create a deteriorated performance model for that engine.

Introduction

Gas turbine engines represent the primary propulsion system for military and commercial aircraft. Developing an understanding of the mechanisms which deteriorate performance in gas turbine engines is the key to maintaining reliability as well as developing new engines with improved performance retention.

The United States Navy operates a substantial fleet of aircraft around the world, predominantly in corrosive salt-laden sea air. Continual operation in a corrosive environment causes performance deterioration that causes engine thrust and fuel consumption penalties and reduces the stable operating envelope. This, in turn, reduces the military readiness that is crucial to the armed services.

The commercial industry and the military services currently monitor limited engine parameters such as vibration and temperature to detect anomalies prior to failure. The acceptable level of deterioration prior to engine removal for maintenance is based on historical performance data. Aero-thermodynamic models can be used to determine additional engine performance parameters that are not measured.

A model of gas turbine engine deterioration would allow the evaluation of the overall mission performance of a system at any given point in its life and thus provide an assessment of time based war fighting capability. To date, other than the engine manufacturers who have their own in-house empirical models, a well defined methodology to predict engine performance deterioration has not been developed. To better understand this phenomenon, the US Navy and AERA Incorporated have initiated the development of a computer-based simulation that would enable the prediction of performance retention capability of aircraft engines.

The amount of engine performance deterioration is a function of the operating load, the operating environment, and the operating time. These factors are dependent on the aircraft in which the engine is installed, its usage, and its operating environment. Performance deterioration is primarily due to increased losses in the rotating components. The nonrotating components, such as the combustor, contribute to the degraded performance, but their impact tends to be accounted for in the simulation of the rotating components.

Contributed by the International Gas Turbine Institute and presented at the International Gas Turbine & Aeroengine Congress & Exhibition, Orlando, FL, June 2–5, 1997. Manuscript received by the ASME Headquarters July 1997. Paper No. 97-GT-278. Associate Technical Editor: H. A. Kidd.

Rotating component wear results in differentials in adiabatic efficiency, flow capacity, and pressure rise. This is reflected in overall system performance by thrust loss and specific fuel consumption (SFC) increase. Figure 1 shows the contribution of each component to the total SFC increase (Sallee, 1980).

The model incorporates known data of the operating condition, mission type, global location, and engine structural and thermodynamic properties to determine the rotating component performance losses in efficiency and flow capacity. The model is then integrated with a manufacturer's baseline engine simulation to deliver a deteriorated engine simulation.

Compressor Methodology

Deterioration build-up in an axial flow compressor is due to reduction in aerodynamic capability of the rotor and stator airfoils. This reduced capability decreases the total pressure rise across each stage of the compressor. By simulating the aerodynamic pressure loss increase due to deterioration, the actual accumulation of performance deterioration is modeled.

The physical changes in the compressor blades that cause the performance deterioration are due to (1) fouling, (2) erosion, and (3) rubbing wear.

Fouling is the accumulation of deposits on the blade surfaces causing an increase in surface roughness. Fouling has been observed to progress up to 40–50 percent into the compressor, primarily affecting the front stages of the compressor (Aker and Saravanamuttoo, 1989). In addition, the accumulation of deposits increases rapidly during the accumulation of operating time/cycles and then levels off to a fairly constant value where the aerodynamic forces prevent any further accumulation. Increased pressure losses due to this phenomena can be reduced by washing the engine periodically. Yet, washing the engine too often will increase engine erosion.

Erosion is the removal of material from the blades caused by solid particles colliding with the blades. This material removal causes increased tip clearances and reduced chord lengths. Erosion has been observed to be more severe in the tip region at the rear of the compressor due to centrifugal forces causing the migration of solid particles to the outer diameter (Tabakoff, 1986). The amount of erosion is also dependent upon the time spent at low altitudes. Helicopters, which operate at somewhat low altitudes over their entire mission, have relatively short engine lives in sandy areas (50 to 250 hours) (Tabakoff, 1987).

Rubbing wear is the removal of material from the rotor blade tips and knife edge seals due to contact between static and

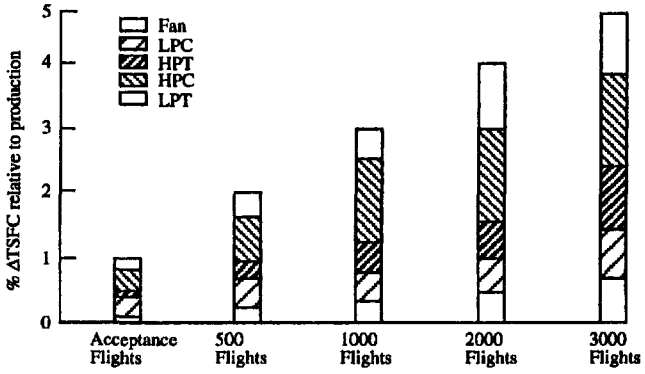

Fig. 1 JT9D-7 preformance deterioration distribution

rotating parts. Typically rubbing wear occurs when compressor blade tips rub with the compressor casing. This is usually the result of the engine rotor flexing during heavy operating loads, or in a mismatch of thermal growth between the rotors and casing. The increased loss due to this effect is more a function of engine cycles than total engine operating hours. Rubbing wear is a short-term deterioration effect. The clearances will increase to a point where rubbing no longer, or only rarely, occurs. When this happens, the performance penalty due to rubbing wear remains fairly constant. The rate of increase in clearances will be dependent upon the operating loads imposed on the engine early in its operation.

The following discussion provides an overview of the methodology that the performance deterioration model uses to compute compressor deterioration. A flowchart of the overall compressor methodology is shown in Fig. 2. The steps for the compressor methodology that are taken for each mission are listed below, and followed by a more detailed description.

Step 1. The user selects a mission profile and operating environment for the engine. For the selected mission, the number of cycles (which cause rubbing and operating loads) and the operating time at altitude are derived from the completed mission profiles. The manufacturer's cycle deck determines the undeteriorated steady-state engine mass flow and efficiency for each compressor section for use in calculating the reference points used in stage stacking routine. Weighted averages for the inlet Mach number, altitude, and power level are also calculated for each mission and are input as the operating point for running the deteriorated deck inputs from the model at the end of the procedure (Step 7).

Step 2. Adjustments are made to the operating time due to the operating environment. The adjustments are based upon the amount of ingested mass and the material erosion characteristics of the selected engine compared to that of the baseline engine used for scaling the mass flow and compressor efficiency adjustments.

Step 3. Mass flow and efficiency penalties for fouling, erosion, and wear are calculated, taking into account compressor component (Fan, LPC, HPC), stage loading, and adjusted operating time.

Step 4. The mass flow penalty is further modified to account for differences in size between the engine being studied and the engine from which the correlation curves were developed.

Step 5. The mass flow penalty for erosion and wear is then distributed for each stage across the entire compressor. The efficiency penalty is applied to the compressor section as a whole.

Step 6. Using the reference points calculated in Step 1, the nondimensional curve of flow coefficient (ϕ/ϕ_{ref}) versus pressure loading (ψ/ψ_{ref}) and the per-stage deteriorated ϕ, a new deteriorated value for ψ can be determined.

Step 7. Using the ψ from Step 6, a new stage pressure ratio is obtained, and the overall compressor pressure ratio is determined from restacking the compressor. The new pressure ratio and the efficiency changes are then input to the manufacturer's engine simulation deck. The deck uses these deteriorated values to calculate the deteriorated engine outputs.

Adjustments to Operating Time. The user selects a mission profile and a geographic area of engine operation. For this simulation, a relative relationship between the standardized data correlations and the actual environment input is used to adjust the rate of performance deterioration. The first adjustment to the operating time is based on the amount of sand ingested by the user-selected engine compared to the amount ingested by the Pratt & Whitney JT9D, which was the engine used for standardizing the data correlations. The data correlations were developed based on engine operation in the eastern United States. If the operational environment selected has a different particulate concentration than that of the data correlations, a proportional adjustment is made to the operating time accumulated. For example, if the user selected the combat air patrol mission for the F404 engine in a desert-type environment, the total amount of the sand ingested is calculated based on the following: operating time at or below 7500 feet; desert particle concentration; and F404 engine mass flow. The total amount of the sand ingested for the F404 is set up as a ratio to the amount the JT9D engine would have ingested based on the particle concentration of the data correlations (eastern United States), JT9D mass flow, and the mission operating time.

Nomenclature

A = leakage area
$CK = 1$, for $\beta_1 \leq 2\beta_0$
$CK = 0$, for $\beta_1 > 2\beta_0$
C_a = axial velocity
C_p = specific heat
K = material constants (1, 3, 12)
N = number of stages
PR_s = stage pressure ratio
P_{inlet} = turbine inlet pressure
R_t = tangential restitution ratio
R_h = hub radius
R_t = tip radius
T_{os} = stage inlet temperature
TR = temperature ratio
U = tip speed
V_1 = impact velocity
V_{inlet} = turbine specific volume inlet
W_{inlet} = inlet airflow
W_L = leakage flow
g = acceleration of gravity
j = stage number
α = contraction factor due to throttling
β_0 = angle of maximum erosion
β_1 = impingement angle
β_m = mean fluid inlet angle
ϵ_{tip} = tip loss
$\gamma = C_p/C_v$
$\Delta\eta_{\text{turb}}$ = turbine stage efficiency delta
λ = solidity
μ = overall labyrinth pressure ratio factor
ν = ratio of eroded mass to mass of the impinging particles
ω = carry-over correction factor
ϕ = flow coefficient
ρ_i = density at inlet
ρ_o = density at outlet
$\sigma = 1-3(\tau/(R_t - R_h))$
τ = tip clearance
ζ = temperature rise

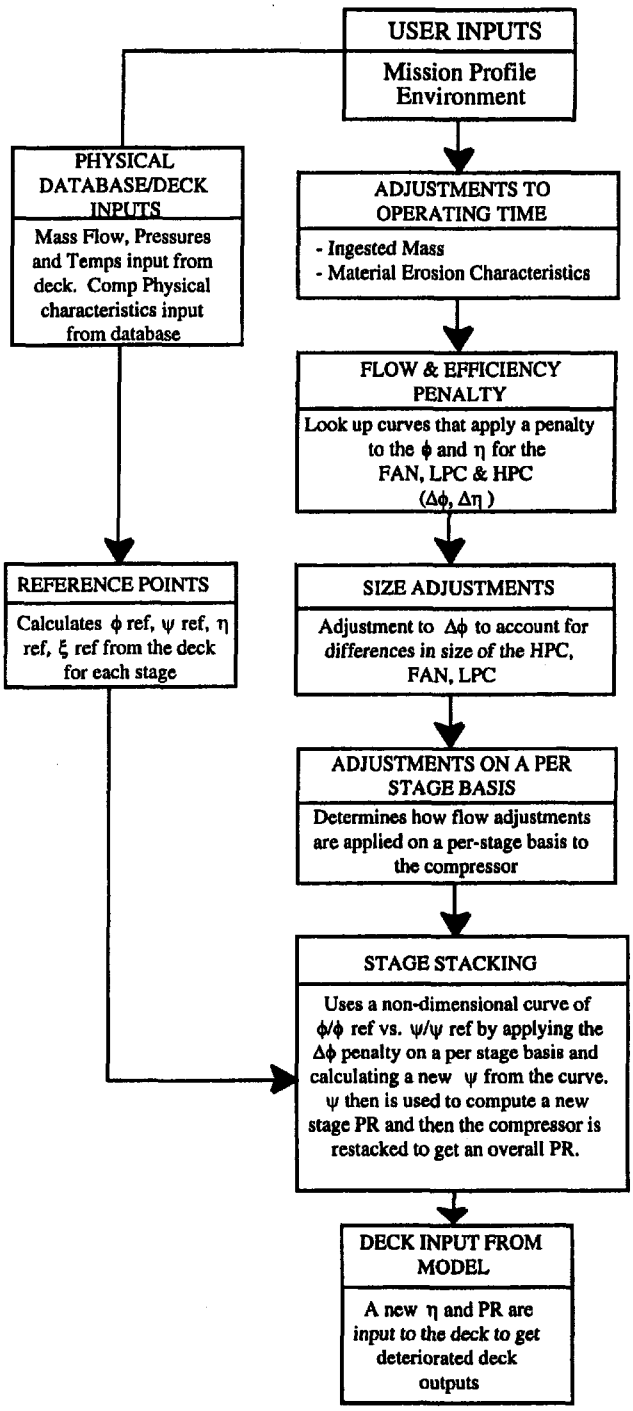

Fig. 2 Flowchart of compressor methodology

This procedure also considers the materials in the compressor. A ratio of the material erosion characteristic of the input engine to the material erosion characteristic of the basis engine used in the data correlations is generated using test data findings. The material erosion characteristics are represented by

$$\nu = K_1\left[1 + CK\left(K_{12}\sin\left(\frac{90}{\beta_0}\beta_1\right)\right)\right]^2 \times V_1^2\cos^2(\beta_1)(1 - R_1^2) + K_3(V_1\sin(\beta_1))^4. \quad (1)$$

The compressor materials are represented by generic aluminum, titanium, and steel alloys for the erosion properties. The ratio is then applied to the accumulated operating time at altitudes to increase or decrease the exposure time as appropriate.

Compressor Flow and Efficiency Adjustments. There is a separate correlation curve for the Fan, LPC, and HPC for each deterioration mechanism (fouling, erosion, and wear). The curves provide a correction factor that is applied to the flow and efficiency of a specific compressor section. For fouling, the corrections (adjustment) are a function of operating time below a certain altitude and overall compressor loading (ψ). An option is provided to water wash the engine every X (input) number of hours. After water wash, the operating hours for fouling will be zeroed. For wear, the corrections (adjustment) are a function of operating cycles and overall compressor loading. For erosion, the adjustments are a function of operating time below a certain altitude and overall compressor loading.

Data collected from deterioration studies, Naval Air Warfare Center (NAWC) test runs, and provided by the manufacturer were used to develop the deterioration curves. Because of the limited amount of source data, engineering assumptions were made to fill any data lapses. The model uses linear interpolation to calculate a reduction in flow capacity (i.e., adjustment to ϕ) and efficiency loss (adjustment to η) for each compressor component from each of the three deterioration mechanisms.

Adjustments on a Per Stage Basis. Because each loss mechanism (i.e., fouling, erosion, and wear) affects the compressor in a different manner, a representative adjustment is made to each stage of the compressor. This is accomplished using the stage stacking methodology developed by Muir et al. (1989). Work by Muir has shown that a common nondimensional curve of the nondimensional flow coefficient (ϕ/ϕ_{ref}) versus pressure loading (ψ/ψ_{ref}) can provide a representative performance characteristic for any compressor stage. The reference point is the design point or peak efficiency point of the compressor. Because the operating characteristics of each individual stage are only known by the manufacturer, this stage-stacking methodology is used to estimate the single stage performance. During the stage-stacking calculation, a generic nondimensional performance characteristic of ϕ versus ψ is used for each stage. The undeteriorated operating point for each stage is found in terms of flow coefficient (ϕ), pressure coefficient (ψ), and efficiency (η). Applying a per stage flow adjustment ($\Delta\phi$) to the flow coefficient ϕ, which when all adjustments summed would equal the previously determined total flow adjustment, simulates the deterioration effects due to flow loss. The deteriorated stage ϕ provides a deteriorated stage ψ from the generic performance characteristic, which can then be used to compute a deteriorated stage pressure ratio. By restacking the stages, a new overall pressure ratio is computed for the deteriorated compressor section. The η would not have to be applied on a per stage basis because the adjustment is applied directly to the η, and it is not looked up on an operational curve. Thus, applying the η adjustment on a per stage basis would give the same result as applying it overall.

Observed data is used to distribute the per stage flow adjustment. Fouling has been stated as occurring primarily in the first half of the compressor (Aker and Saravanamuttoo, 1989). However, no data has been found which can verify the typical distribution. For modeling purposes, a linearly declining distribution through the first half of the total compressor section, as defined by Eq. (2), is assumed.

$$\Delta\phi)_j^{\text{fouling}} = \frac{\Delta\phi_{\text{total}}^{\text{fouling}}}{\sum_{i=1}^{N/2}}\,[N/2 - (j-1)] \quad (2)$$

Erosion is shown to affect the rear stages more significantly than the early stages. Therefore, the distribution of this adjustment is

a straight line increase through the entire compressor as defined by

$$\Delta\phi)_j^{\text{erosion}} = \frac{\Delta\phi_{\text{total}}^{\text{erosion}}}{\sum_{i=1}^{N} i}\,[j]. \quad (3)$$

Wear occurs throughout the compressor. Under operational loads, the wear may occur more severely at the outer extremes of the compressor (i.e., bending of a cantilever beam); however, there is no data to support this. Under thermal cycles, wear would be expected to occur evenly throughout the compressor. Wear primarily appears in the compressor as tip clearance increases. The data in this region shows that the rear of the compressor has more severe tip-region deterioration than the front. This, however, may be due to the erosion factor. The model applies a straight line distribution of this wear adjustment throughout the compressor as defined by

$$\Delta\phi)_j^{\text{wear}} = \frac{\Delta\phi_{\text{total}}^{\text{wear}}}{N}. \quad (4)$$

Size Adjustments. The data correlations for the flow and efficiency adjustments are based on the dimensions of the Pratt & Whitney JT9D compressor sections. This is because the majority of the source data for the curves comes from JT9D data. To account for the difference between the compressor size of the user-selected engine and the compressor size of the data correlations, a correction is applied to the flow coefficient.

The model first computes the effect of deterioration on tip loss using Eq. (5) at the ϕ undeteriorated and the ϕ deteriorated with the source data engine size. The tip loss calculation is a function of the flow capacity and compressor physical characteristics.

$$\epsilon_{\text{tip}} = \frac{2\psi\tau R_t}{\eta(R_t^2 - R_h^2)}\left[0.759\left(\frac{\phi\sigma\varphi\lambda}{\sin^3(\beta_m)}\right)^{0.5} + 1.17\,\frac{\phi}{\sigma^2\tan(\beta_m)}\right] \text{(Batcho, 1986)} \quad (5)$$

The model then computes the effect of deterioration on tip loss using the physical characteristics of the actual engine being modeled. Taking the difference between the tip loss deteriorated and tip loss undeteriorated yields the tip loss effect. The size effect is determined by comparing the ratios of the tip loss effect of the actual engine to the tip loss effect of the source data. Thus, a relative percentage adjustment is determined. This adjustment reflects the effect of size on deterioration accumulation.

Once the pressure ratio is computed at the new deteriorated operating point, this information is fed back to the simulation model forcing it to converge to a new overall performance.

Turbine Methodology

To determine the causes of performance deterioration within the turbine section, the basic loss mechanisms that affect turbine performance were researched. The works of Mukhtarov and Krichakin (1969), Ainley and Mathieson (1951), Balje' and Binsley (1968) and an engine manufacturer's internal loss model, divide turbine losses into the following six categories: (1) Profile Loss; (2) Profile Incidence Loss; (3) Secondary Flow loss; (4) Blade Tip Clearance Loss; (5) Cooling Air Injection Aerodynamic Loss; and (6) Cooling Air Thermodynamic Loss. Although the loss correlations vary in form, they generally agree on the parameters that affect each loss.

Deterioration studies performed by Pratt & Whitney Aircraft and General Electric Corporation on the JT9D and CF6 commercial airline engines found that the major causes of turbine section performance deterioration were an increase in tip clearance and flow capacity. Figure 3 shows where this deterioration occurs in a typical high pressure turbine.

Tip clearances on all rotating blades were found to increase over time due to rubbing associated with thermal growth during power transients with small dwell times (less than 4 min). Clearances also increased more gradually after the initial rub clearance was reached due to erosion of the blade tips.

Both the JT9D and CF6 experienced flow capacity increases with operating time in the high pressure and low pressure turbines. This capacity change was caused by vane trailing edge bowing under thermal and pressure loads.

With these major deterioration sources, we again looked at which basic losses would be affected by deterioration. Profile incidence loss will change due to a mismatching of the turbine when vane bowing occurs. This deterioration causes the gas angles to change and results in changing incidence angles on the turbine airfoils, increasing losses.

Secondary flow losses are also a function of incidence, and, therefore, will be affected by the mismatching caused by vane bowing.

The most straight forward loss mechanism and the one that results in the largest decrease in turbine efficiency is the tip clearance loss. This loss, due to tip rubbing and erosion, is dependent upon the mission profile and the number of damaging cycles (i.e., cycles where tip rubs occur) versus operating time. Figure 4 provides a graphical illustration of how reburst cycles result in turbine blade tip rubs.

For the model, adjustments are made to three parameters to impose the effects of deterioration in the turbine. The stepwise sequence of the methodology is shown in Fig. 5. Adjustments are made to the turbine efficiency, flow parameter, and cooling air split for the operating point being computed—forcing the simulation model to converge to a new overall performance. Turbine efficiency is adjusted based on the results of the tip clearance model used to compute the amount of tip clearance increase due to blade rubbing. The turbine flow parameter and cooling air split are adjusted based upon data correlation curves.

Tip Clearance Loss Methodology. The decrease in turbine efficiency caused by increased tip clearances is modeled by first predicting the growth in tip clearances due to rubbing wear and erosion, and then using the Egli method to calculate the efficiency penalty associated with the new clearances. The Egli method calculates the leakage flow over a turbine blade based on pressure ratio and clearance height. The amount of turbine work is then reduced by this leakage flow to total gas flow ratio.

The following are the sequential steps that will be used to calculate the turbine performance penalty after a specified number of mission cycles and operating time.

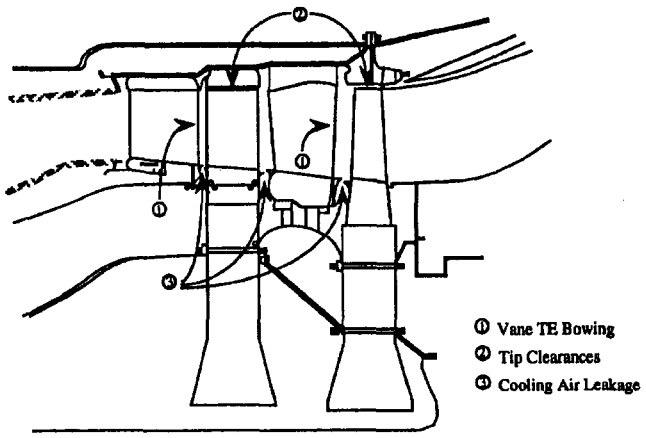

Fig. 3 Where deterioration occurs in turbines

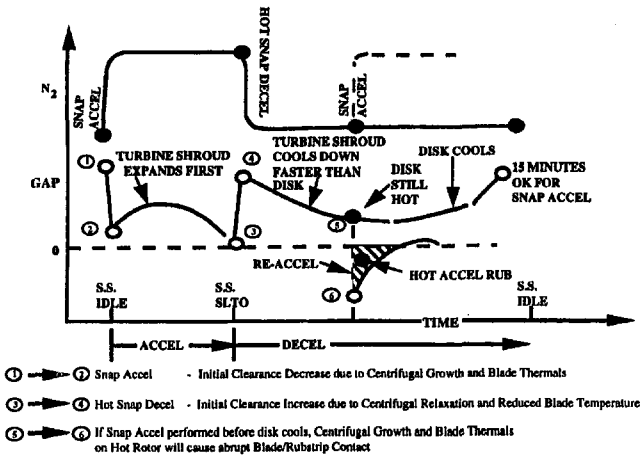

Fig. 4 How rebursts result in tip rubs

Step 1. The number of damaging cycles is calculated based upon the mission profile and the number of missions flown during the operating time. These cycles are the ones that consist of rebursts with less than 4 min of dwell time at the lower power setting.

Step 2. The maximum interference rub is predicted using the thermal expansion coefficients for each disk section and basic stress/strain formulas to calculate the thermal and centrifugal growth, respectively, of the blade and disk and compare it to the thermal growth of the turbine shroud. The maximum difference between the two is used to predict the maximum interference during reburst cycles.

Step 3. A clearance increase for each rub during a damaging cycle is imposed on the turbine up to the maximum interference predicted in Step 2. At this point, the clearance due to rubbing will have progressed to the maximum level. Historical data from the JT9D and CF6 studies show that 3–5 mils are typical of a single rub.

Step 4. This clearance for each rotating blade will be used to calculate the associated efficiency penalty using the Egli method. The Egli method is a simplified loss correlation that estimates the tip loss by assuming that leakage flow is excluded from doing work in the turbine (i.e., 1 percent leakage results in 1 percent drop in stage efficiency). This method was originally developed to estimate leakage flow across labyrinth seals. It calculates flow through an annular seal using the pressure ratio across the inlet and the exit of the seal.

$$W_L = A\alpha\mu\omega\sqrt{g\frac{P_{\text{inlet}}}{V_{\text{inlet}}}} \tag{10}$$

From this we can calculate the stage efficiency delta by

$$\Delta\eta_{\text{turb}} = \frac{W_L}{W_{\text{inlet}}}. \tag{11}$$

The Egli method was selected because of its excellent correlation to test data for a wide range of turbine sizes and loadings.

Flow Capacity Increase Methodology. Vane trailing edge bowing is the cause of the flow capacity increase in turbines with operating time. Thermal and pressure loads on the airfoils that are beyond the elastic limits for the materials cause trailing edge distortion. Since vane bowing is a nonelastic deformation of the airfoils, the growth in flow capacity is correlated with the operating time at Sea Level Take Off (SLTO) or higher power levels. These power levels are generally the only power conditions where nonelastic behavior of the vanes should occur. Therefore, mission profiles that have longer operating times at high power conditions will cause the flow capacity increase to occur more rapidly. The model uses curves developed for different turbine materials of flow capacity increases versus operating time at SLTO power conditions and higher. The curves were developed from studies of turbine deterioration causes.

This flow capacity increase is continued until the trailing edge distortion required to cause the flow capacity increase exceeds the normal limits set for airfoil removal. These limits are determined from the technical manuals for existing engines or from teardown inspection data from endurance test engines.

Model Implementation

The computer implementation of the deterioration methodology involved building and maintaining databases, numerical computation, and developing a graphical user interface (GUI). All numerical calculations for the deterioration methodology were developed using ANSI standard FORTRAN 77. This provided the ability to run the model on both the Navy's VAX and UNIX workstations as well as to be easily portable to any other computer or operating system. All database files are ASCII based to also allow for portability. The deterioration model makes extensive use of either manufacturer thermodynamic models or the NASA/Navy Engine Program (NNEP) for the determination of initial engine flow and thermodynamic parameters and calculation of overall performance deterioration effects.

The GUI was implemented using the C programming language and the Tcl/Tk scripting language on a UNIX workstation running X Windows and Motif. Tcl/Tk was chosen to allow for rapid development of prototype interfaces and portability among UNIX based workstations. This scripting language also allows for new capabilities and different engines to be added to the interface with ease. The GUI is a completely separate program which sets up all needed data files and then calls the deterioration calculation program. After the deterioration has been calculated, the user interface then provides the ability to view graphs of deteriorated specific fuel consumption and efficiencies versus number of missions.

The user of the model has the ability to input and edit mission profiles, material properties, and engine characteristics in the GUI. Missions are entered and edited using a spreadsheet win-

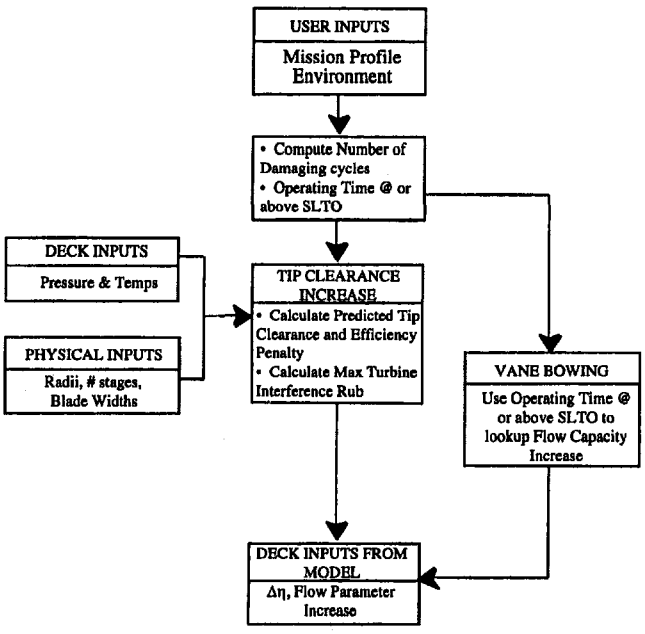

Fig. 5 Flowchart of turbine methodology

dow. They can be arbitrarily grouped to allow for the determination of deterioration on an aircraft with a number of different missions. Mission profiles may also be viewed graphically in the interface as well. Material properties and engine characteristics are entered or modified in dialog boxes.

The GUI also allows the user to specify the general environmental conditions in a graphical manner by pointing to a location on a world map. The interface then uses the geographic location that has been pointed to and assigns one of five predefined environmental conditions for the model to calculate deterioration. Currently, the model has definitions for temperate, desert, tropical, oceanic, and arctic. The user can also view a map of the regions for which the different environmental definitions have been defined.

After the user has set up all needed data files using either the graphical interface or in a text editor, the calculation of the deterioration is determined.

These performance adjustments are then used to modify the initial values of the performance parameters in the engine cycle deck and the overall engine efficiency and fuel consumption changes are determined. The program then saves the total number of missions that have been modeled, the total operating time, and the changes in efficiency and fuel consumption. If any additional missions are to be run, the program loops, using the deteriorated values for the initial input in the next mission.

Results

Data from NAWC and NAPC F404-GE-400 test reports (Georgiou, 1981; Marx, 1993) were used to verify the deteriorated results output from the model.

To simulate the F404 Sand Ingestion Test, the mission profile and sand concentration level used during the test were used as inputs to the model. However, due to model limitations, the anti-ice (A/I) system and customer bleed were not simulated. The model losses for thrust and the increase in TSFC exceeded the losses experienced during the actual engine test. The test engine was a CIP engine with a number of deviations from the QT design as listed in Appendix A of the report. The thrust loss for the model was 7.13 percent at IRP, and the TSFC increase was 2.86 percent. The thrust loss and TSFC increase experienced during the actual engine test were at 6.62 percent and 2.19 percent, respectively. A possible cause of the discrepancy in performance degradation could be due to the unavailability of measured thrust at the test cell. The performance degradation of the fan was the largest contributor to overall engine performance loss for both the model (5.46 percent loss in Fan efficiency) and the actual test (4.34 percent loss in Fan efficiency).

Next, the mission endurance test was simulated using the same mission profile as the test and a clean environment. The engine used in the test was a CIP engine that had accumulated various operating times on a number of components (e.g., A/B case, 4323 hours; HPT blades with times ranging from 178 to 776 hours prior to the test). To simulate the CIP engine used in the actual test, before running the mission endurance test the model was run to accumulate approximately 100 h of engine operation and 236 compressor cycles. The resultant thrust loss at IRP from the baseline taken at the start of the endurance test was 2 percent (compared to a 1.3 percent decrease from the test report). The total thrust loss experienced during the actual engine test and the model were both at 3.0 percent. However, previous ASMET IRP trend data indicates that the 150 hour QA Test exceeded the level of IRP thrust deterioration consistent with the characteristic deterioration of the F404 development database. The IRP thrust deterioration rate for a 660 hour ASMET done previously indicates that a 150 h endurance test should have about a 1 percent loss in IRP thrust. The difference between the thrust loss of the model (2.1 percent) to that of the IRP trend data (1 percent) can be attributed to the age and number of cycles accumulated by the engine. For example, if the model engine had accumulated 1000 compressor cycles, the resultant thrust loss over the test is 1.06 percent, which is similar to the ASMET IRP thrust loss trend data. The model thrust loss for this test is affected most by compressor wear, which is based on the number of cycles accumulated by the compressor. As wear begins to reach a maximum (point at which rubbing wear no longer occurs), the amount of thrust loss calculated by the model over the test period becomes less.

The limited results currently available to verify model data is due to the fact that engine manufactures are only willing to provide limited access to engine deterioration data. Data made available from the various engine manufactures and US Navy reports were used to develop the correlation curves for the model. Further testing will be conducted as additional data is made available through the Navy and other sources.

Conclusion

The resulting model provides the user the ability to assess the war fighting capability of an engine by evaluating the overall mission performance for various environments at any given point in its life. The methodology developed for our deterioration model was done in such a manner that as additional data becomes available, the models' correlation curves can easily be updated, and, therefore, improve the overall accuracy of the model. The simplicity of this type of deterioration model makes it readily available for integration with other manufacturer's baseline engine simulation models.

References

Ainley, D. G., and Mathieson, G. C. R., 1951, "A Method of Performance Estimation for Axial-Flow Turbines," British ARC, R&M 2974.

Aker, G. F., and Saravanamuttoo, H. I. H., 1989, "Predicting Gas Turbine Performance Degradation Due to Compressor Fouling Using Computer Simulation Techniques," ASME JOURNAL OF ENGINEERING FOR GAS TURBINES AND POWER, Vol. 111, No. 2, pp. 343.

Batcho, et al., 1986, "Interpretation of Gas Turbine Response Due to Dust Injection," DNA-TR-86-306, prepared for DNA under contract DNA 001-83-C-0182.

Balje', O. E., and Binsley, R. L., 1968, "Axial Turbine Performance Evaluation, Part A—Loss Geometry Relationships," *Journal of Engineering Power.*

Georgiou, C. C., 1981, "F404-GE-400 Sand Ingestion Test," Naval Air Propulsion Center Report Number NAPC-PE-62.

Marx, M. M., 1993, "F404-GE-400 Engine 150-Hour Quality Assurance Fighter Accelerated Mission Endurance Test," Report Number PE-255, Naval Air Warfare Center Aircraft Division, Trenton, NJ.

Muir, D. E., Saravanamuttoo, H. I. H., and Marshall, D. J., 1989, "Health Monitoring of Variable Geometry Gas Turbines for the Canadian Navy," *ASME Journal of Engineering for Power,* Vol. 111, No. 2, pp. 244–250.

Mukhtarov, M. Kh., and Kichakin, V. I., 1969, "Procedure for Estimating Flow Section Losses in Axial-Flow Turbines when Calculating Their Characteristics," Central Scientific Research Institute of Aircraft Engine Construction, Teploenergtika.

Sallee, G. P., 1980, "Performance Deterioration Based on Existing (Historical) Data: JT9D Jet Engine Diagnostic Program," NASA CR-135448, Pratt & Whitney Aircraft Group, Contract No. NAS3-20632, Cleveland, OH.

Tabakoff, W., 1986, "Compressor Erosion and Performance Deterioration," ASME Publication FED-Vol. 37, presented at the AIAA/ASME 4th Joint Fluid Mechanics, Plasma Dynamics, and Lasers Conference, Atlanta, GA.

Tabakoff, W., 1987, "Compressor Erosion and Performance Deterioration," *ASME Journal of Turbomachinery,* Vol. 112, No. 1, pp. 78.

Advanced Combined Cycle Alternatives With the Latest Gas Turbines

P. J. Dechamps
Cockerill Mechanical Industries,
Utility Boilers,
Ave. A. Greiner 1
4100 Seraing, Belgium

The last decade has seen remarkable improvements in industrial gas turbine size and performances. There is no doubt that the coming years are holding the promise of even more progress in these fields. As a consequence, the fuel utilization achieved by combined cycle power plants has been steadily increased. This is, however, also because of the developments in the heat recovery technology. Advances on the gas turbine side justify the development of new combined cycle schemes, with more advanced heat recovery capabilities. Hence, the system performance is spiraling upward. In this paper, we look at some of the heat recovery possibilities with the newly available gas turbine engines, characterized by a high exhaust temperature, a high specific work, and the integration of some gas turbine cooling with the boiler. The schemes range from classical dual pressure systems, to triple pressure systems with reheat in supercritical steam conditions. For each system, an optimum set of variables (steam pressures, etc.) is proposed. The effect of some changes on the steam cycle parameters, like increasing the steam temperatures above 570°C are also considered. Emphasis is also put on the influence of some special features or arrangements of the heat recovery steam generators, not only from a thermodynamic point of view.

Introduction

New gas turbine designs, based on higher than ever TETs, are now available on the market. These new machines hold the promise of even higher combined cycle efficiencies, for two reasons: When the gas turbine TET is increased, both the gas turbine efficiency and the gas turbine exhaust temperature are increased for the optimum pressure ratio under combined cycle operation (Brandt, 1992; Jericha et al., 1991). The latest ABB machines (GT24-GT26) (Jury and Luthi, 1994; Luthi, 1994; Van der Linden, 1995) adopt a different route in which reheat is used in order to maintain a very good exhaust temperature even for high pressure ratios.

The increase in gas turbine exhaust temperature allows the use of higher superheated steam temperatures, in the vicinity of the classical now 540°C, or even higher, up to 570°C, which is becoming common practice in classical steam power plants. A considerable improvement in combined cycle efficiency is obtainable under these circumstances, because the Rankine cycle efficiency is highly dependent on the steam superheat temperature.

There is also the possibility that some advanced combined cycle configurations, especially those comprising reheat, or reheat with supercritical steam conditions, come into force because of this increase in gas turbine exhaust temperatures. Such cycle configurations are usually thought to take better advantage of the amount of heat available above the highest pinch point temperature in the HRSG.

Moreover, the IGCC power plants that are now about to appear on the market very often incorporate advanced triple pressure (sometimes even more) reheat systems in order to fulfill the steam requirements on the gasification side (Dechamps and Mathieu, 1991, 1992a, b).

All this results in an important increase in the use of gas-fired combined cycle plants for power generation in many countries. This paper aims at presenting the relative merits of such advanced combined cycle options, from dual pressure systems to triple pressure reheat systems with supercritical steam conditions behind the ABB GT26 engine.

The Gas Turbine

The ABB GT26 machine has been selected for this study because it has particular characteristics due to the use of reheat. Its ISO performance is quoted in Table 1.

In combined cycle operation, this gas turbine is supposed to be operating on natural gas, with a 10 mbar pressure drop at the inlet to the compressor, and a 25 mbar back pressure at the turbine discharge, mainly due to the presence of the HRSG (Borglin, 1991). These adverse pressures reduce the gas turbine performances, as quoted in Table 1.

Generic Combined Cycle Characteristics

The various combined cycle options covered in this paper are characterized by some common features, so that the comparison between them really makes sense. These common assumptions, which are based on industrial practice for assisted circulation heat recovery boilers, are summarized in Table 2, while Fig. 1 gives the arrangement of a 2-2-1 configuration.

Optimization

All the combined cycle presented and compared in this paper have been optimized with the objective of maximizing the plant efficiency. Such an optimization process is however subject to various constraints, which are mainly technological:

- maximum HP steam superheat and reheat temperature: 570°C

This corresponds to advanced industrial practice for steam turbosets, and is achievable without supplemental firing only with the latest gas turbines.

- minimum pinch point temperature difference: 10°C

Contributed by the International Gas Turbine Institute and presented at Turbo Asia '96, Jakarta, Indonesia, November 5–7, 1996. Manuscript received at ASME Headquarters July 1996. Associate Technical Editor: J. W. Shinn. Paper No. 96-TA-55.

Table 1 Gas turbine characteristics

Design data	
inlet temperature (°C)	15
inlet pressure (bar)	1
compressor pressure ratio	30
exhaust mass flow (kg/s)	542
exhaust temperature (°C)	608
net efficiency (% LHV)	37.8
net power output (MW)	240
At Site Conditions	
inlet pressure drop (mbar)	10
HRSG back pressure (mbar)	25
ambient temperature (°C)	15
ambient pressure (bar)	1
fuel	natural gas (42 MJ/kg)
relative humidity (%)	80
exhaust mass flow (kg/s)	539.86
exhaust temperature (°C)	617.9
net efficiency (% LHV)	36.99
net output (MW)	236.31

- minimum approach point temperature difference: 2°C

These two values are common industrial practice for assisted circulation-type boilers, and are drawn from a compromise between performance of the plant and cost of the boiler, which can be primarily regarded as proportional to its surface.

- minimum temperature difference between superheated steam and gas: 20°C

This is of a similar nature to pinch and approach temperature differences and tends to keep the superheater surfaces at reasonable levels.

- minimum stack temperature: 75°C

The minimum acceptable stack temperature is dependent on the sulfur content of the fuel used, the value of 75°C being typical of sulfur-free natural gas, for which the dew point is not significantly different from that of pure CH_4 flue gases. Interestingly, the selected values never come into force for the considered steam cycles, as all of them turn out to give stack temperatures above 78°C.

- minimum steam quality at the outlet from the LP steam turbine: 0.88 kg of steam per kg of water–steam mixture

Table 2 Generic combined cycle characteristics

HRSG Data

type : assisted circulation design
pinch point temperature differences : 10°C
approach point temperature differences : 2°C
minimum temperature difference (gas - superheated steam) : 20°C
minimum stack temperature : 75°C (never a constraint in practice)
fuel for supplemental firing : natural gas (42 MJ/kg)
feedwater heating : econo-type circuit on the deaerator, with recirculation
maximum acceptable superheat steam temperature : 570°C

Steam Cycle Data

steam turbine isentropic efficiency : 85%
efficiency degradation for wet steam : -1% efficiency per % moisture by mass
condenser pressure : 50 mbar
feedwater pump efficiency : 75%
minimum acceptable steam outlet quality from the LP steam turbine : 0.88

The steam quality at the outlet from the LP steam turbine is usually maintained above that value, below which special devices are required to capture the water droplets and decrease the amount of damage caused by impingement on the blade surfaces.

- maximum working pressure for non-supercritical cycles: 160 b

The maximum working pressure is selected as the practical maximum pressure for assisted circulation design HRSG, above which a once-through design would certainly be used, as for the supercriticals.

The optimization process is conducted so that none of the above-mentioned constraints is violated, using the GTCALC and CCCALC codes developed at the University of Liège and at Cockerill Mechanical Industries, and devoted respectively to gas turbine and combined cycle calculations (Dechamps, 1991).

Options Considered for This Study

Seven different combined cycle schemes have been studied. These are:

- a dual pressure non-reheat cycle, hereafter named $2P$
- a triple pressure non-reheat cycle, hereafter named $3P$
- a dual pressure reheat cycle, hereafter named $2PR$
- a triple pressure with mild reheat cycle, hereafter named $3PM$
- a triple pressure reheat cycle, hereafter named $3PR$
- a dual pressure reheat supercritical cycle, named $2PRS$
- a triple pressure reheat supercritical cycle, named $3PRS$

Nomenclature

$2P$ = dual pressure combined cycle
$3P$ = triple pressure combined cycle
$2PR$ = dual pressure combined cycle with reheat
$3PM$ = triple pressure combined cycle with mild reheat
$3PR$ = triple pressure combined cycle with reheat
$2PRS$ = dual pressure combined cycle with reheat and supercritical steam conditions
$3PRS$ = triple pressure combined cycle with reheat and supercritical steam conditions
CC = combined cycle
cp = heat capacity at constant pressure, kJ/kgK
GT = gas turbine
HP = high pressure
HRSG = heat recovery steam generator
IGCC = integrated coal gasification in combined cycle plant
IP = intermediate pressure
is = pertaining to an isentropic process
LHV = lower heating value
LMTD = logarithmic mean temperature difference, °C
LP = low pressure
$\dot{m}$ = mass flow rate (kg/s)
mbar = millibar (100 Pascal)
MJ = megaJoule
MW = mega Watt
NTU = number of transfer units
Q = heat flux, kW
S = heat transfer surface, m^2
ST = steam turbine
T = temperature, °C
TET = turbine entry temperature
U = heat transfer coefficient, kW/m^2K
η = process efficiency
ϵ = process effectiveness

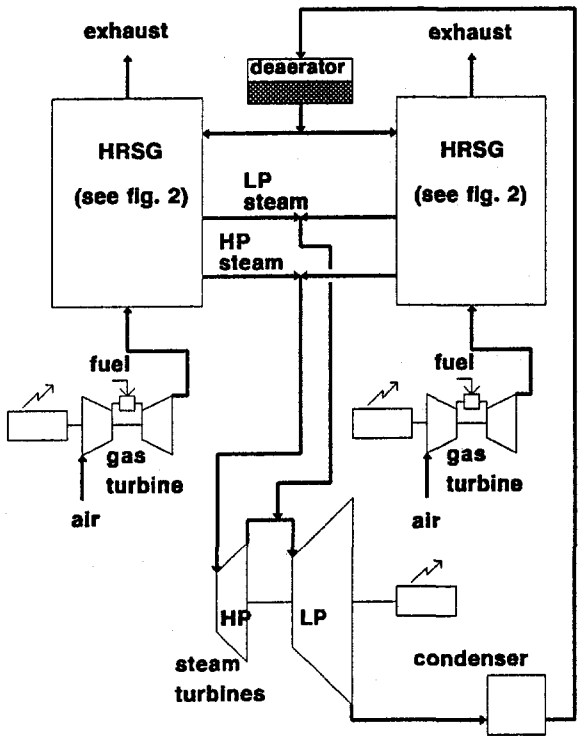

Fig. 1 Schematic diagram of a 2-2-1 combined cycle

The 3*PM* arrangement deserves an explanation: It is a scheme in which the *IP* steam is superheated up to the maximum superheat temperature (570°C) by means of an additional heat exchanger located in the gas path in parallel with the *HP* superheater. It actually gives some of the additional performance of reheat schemes, without the associated complexity.

All HRSG designs are incorporating feedwater preheaters before the deaerator (econo-type heat exchanger), an intertwined disposition of economizers when required, and intertwined *HP* superheater and reheater when reheat is to be used (Stecco et al., 1991). As an example, the 3*PR* HRSG schematic diagram is represented on Fig. 2.

Parameter Optimization

Objective. The objective when optimizing is to maximize the efficiency of the plant. This is a purely thermodynamic criterion, which does not account for any economic consideration. That is the reason why the parameters that could be optimized only using an economic objective are considered as constraints for this study (pinch point temperature differences, etc).

Optimized Parameters. A certain number of parameters are free to vary within constraints during the optimization process. These are:

- all superheat temperatures (*HP-IP-LP*)
- all drum pressures (*HP-IP-LP*)
- the reheat pressure
- the reheat temperature
- the deaerator pressure
- the supplemental firing temperature

With regard to these parameters, it is interesting to note that the previously mentioned constraints for optimization fall into two broad categories:

- those that can be checked before the calculation is actually performed with a set of variables (a priori constraints) (maximum superheat temperature of 570°C for example)
- those that require the calculation of the cycle before they can be checked (e.g., stack temperature and steam outlet quality)

Main Results. When the cycle is optimized with respect to the plant efficiency, the different parameters listed here are adapted and chosen in different manners because some of them are really at the optimum value, while, for some others, one or several constraints limit the values that can be used.

- all superheated and reheated steam temperatures are maximum, i.e., less than 570°C and less than the corresponding gas temperature in the HRSG minus 20°C;
- the supplemental firing decreases the efficiency of all cycles;
- the deaerator pressure has no influence on the thermodynamic performances of the cycle, except from a purely deaeration point of view, as it is fed by an econo-type heat exchanger;
- all *HP* drum and reheat pressures are brought to the maximum value of 160*b*, except for the *HP* pressures of the non-reheat 2*P*, 3*P*, and 3*PM* cycles, limited by the steam quality at the *LP* steam turbine exhaust, regardless of the gas turbine used.

Table 3 gathers the relevant design information for all the optimized cycles. Figure 3 illustrates the efficiency as a function of the highest pressure level in the system. The maximum pressure can actually be reached, with the exception of the 2*P*, 3*P*, and 3*PM* systems, when the absence of reheat produces a poor steam turbine outlet quality at high pressures.

Figure 4 gathers the relevant information in terms of efficiency for the optimized cycles only. In abscissa, the various configurations are ordered in increasing efficiency.

Figure 5 shows for the same optimized plants the LP steam turbine outlet quality (kg of steam per kg of water-steam mixture). One can observe that the limiting criterion when optimizing (quality = 0.88) has been active for the 2*P*, 3*P*, and 3*PM* cycles only. As expected, the steam outlet quality is substantially higher for reheat cycles (2*PR* and 3*PR*).

Figure 6 illustrates the stack temperatures achieved by the same optimized plants. The conclusion is that three pressure level systems always give a lower stack temperature than the corresponding two pressure level technology. In other words, the 3*P* options have lower stack temperatures that the 2*P* options, the 3*PR* than the 2*PR*, and the 3*PRS* than the 2*PRS*.

It should be noted that the influence of the efficiency degradation with moisture content in the steam turbine is substantial for the optimization process and the performances of the combined cycle. Figure 7 illustrates the efficiency of the 2*P* system based for various assumptions as far as efficiency degradation is concerned. The efficiency drop with turbine efficiency degradation

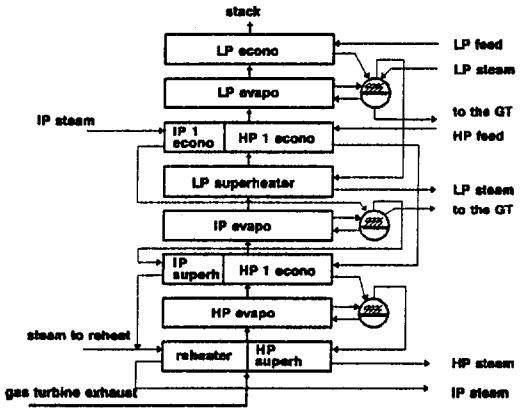

Fig. 2 Structure of a three pressure reheat HRSG

Table 3 Combined cycle plant characteristics optimized for maximum efficiency

	2P	3P	2PR	3PM	3PR	2PRS	3PRS
HP pressure (bar)	112.8	95.5	160	123.1	160	260	280
IP pressure (bar)	-	25	-	23.8	34	-	30
LP pressure (bar)	6.3	5.95	21	5.8	5.8	16	5.9
reheat pressure (bar)	-	-	21	-	34	16	30
HP superheat T (°C)	570	570	570	570	570	570	570
IP superheat T (°C)	-	238	-	570	271	-	285
LP superheat T (°C)	198	168	262	168	178	248	174
reheat T (°C)	-	-	570	-	570	570	570
stack temperature (°C)	78.3	78.1	120.4	78.9	88.3	111.5	86.2
outlet steam quality	0.88	0.88	0.977	0.88	.931	0.993	.938
total HRSG NTU	13.3	15.1	14.23	17	17	17.31	18.7
ST power (MW)	116.7	117.4	117.9	119.4	124.7	126.3	132.4
total output (MW)	351.7	352.6	352.9	354.3	359.58	360.32	366.2
net plant efficiency (%)	56.05	56.19	56.24	56.46	57.28	57.40	58.33

is huge, and interestingly, an optimum pressure ratio appears for efficiency degradations higher than 1 percent per percent moisture, with a flat optimum.

Heat Transfer Surfaces

To provide a complementary information to the performances, the heat transfer surface in the various considered configurations are a useful data, directly related to the HRSG cost.

Figure 8 presents the total NTUs for the various HRSGs used in the optimum cycles. Recall that NTUs (number of transfer units) are defined as:

$$\text{NTU} = DT_{\text{gas}}/\text{LMTD}$$

where: DT_{gas} is the temperature difference on the gas side of the heat exchanger; LMTD is the logarithmic mean temperature difference on the same heat exchanger.

The heat flux Q is equal to $S*U*\text{LMTD}$ and to $DT_{\text{gas}}*cp_{\text{gas}}*m_{\text{gas}}$ where: S is the heat transfer surface (m^2), U is the heat transfer coefficient ($\text{kW/m}^2\text{K}$), cp_{gas} is the average heat capacity of the gas (kJ/kgK), m_{gas} is the gas mass flow rate (kg/s). Hence, the NTU can be rewritten as $\text{NTU} = S*U/(cp_{\text{gas}}*m_{\text{gas}})$.

Therefore, if one can accept the assumption that the gas mass flow rate, properties, and the heat transfer coefficient are constant, the NTU is strictly proportional to the heat transfer surface.

Figure 8 shows how the heat transfer surface requirement increases with the complexity of the boiler and the cycle performance. Also, the supercritical configurations always require more surface than their non-supercritical counterparts. The reason for this is that the heat transfer in a supercritical boiler is

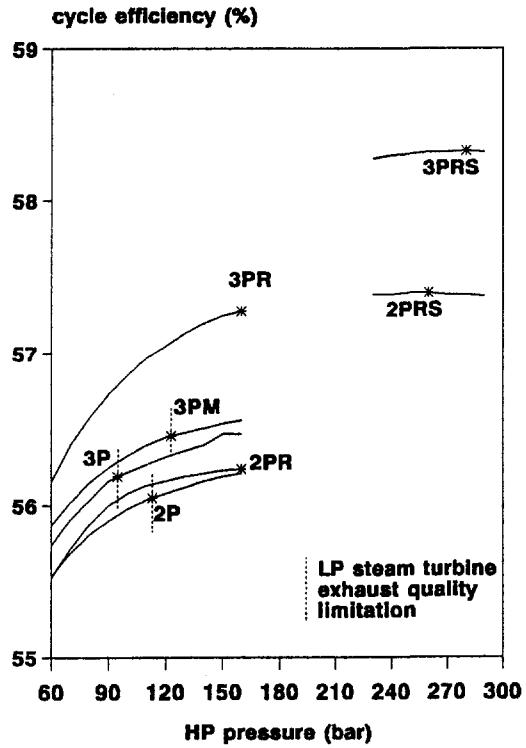

Fig. 3 Efficiencies as a function of cycle pressure

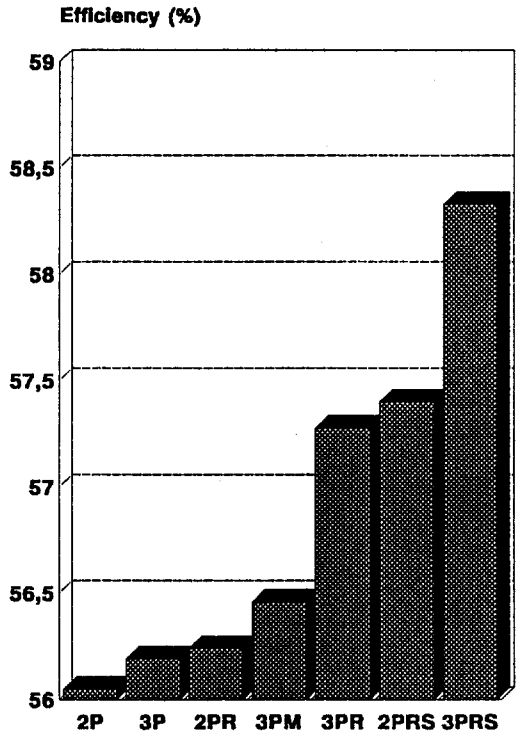

Fig. 4 Efficiencies of optimized cycles

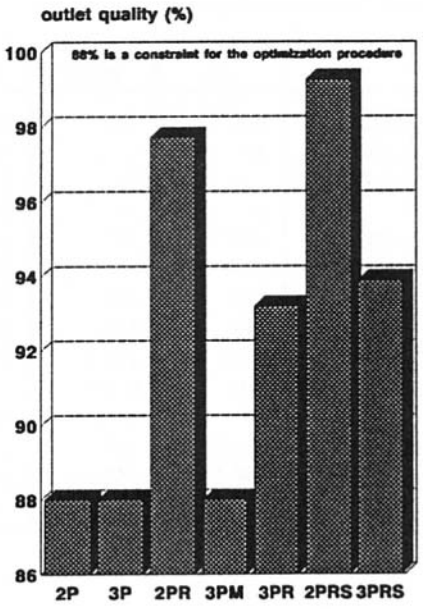

Fig. 5 LP steam turbine outlet qualities of optimized cycles

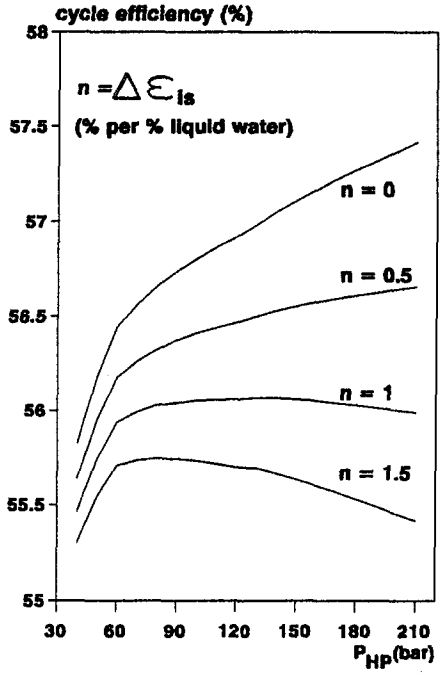

Fig. 7 Efficiency degradation with moisture content

characterized by the absence of a well-defined pinch point location, the pinch point being rather valid over a wide range of temperatures (there is no vaporization as such). Therefore, for a given pinch, the actual mean temperature difference encountered in a supercritical heat exchanger is less than that of non-supercritical ones, giving rise to larger surface requirements.

As a consequence of this, it is likely that different values for the pinch point will have to be selected when supercritical combined cycles configurations are used. Figure 9 presents the efficiency penalty encountered by the 3*PRS* scheme when the pinch is varied from 9°C up to 15°C. One can observe that a 15°C pinch turns into a loss of 0.2 percent point in efficiency, together with a 20 percent reduction in heat transfer surface requirement. It is certainly worth conceding a small efficiency penalty in order to recover a substantial heat transfer surface.

Stack Temperature Limitations

For all the preceding results, the minimum stack temperature had been set to 75°C, which is compatible with the use of sulfur-free natural gas and never came into force during the optimization process. Figure 10 presents for all the options the efficiency penalty, which results from a stack temperature limitation at 100°C, allowing for some sulfur in the fuel.

Not surprisingly, the cycles that have a low stack temperature when not constrained are more penalized. That is the case for all nonreheat options, compared to their reheat counterparts.

It is widely admitted that a dual pressure system does not make sense if the stack temperature is limited to 150°C (because of the use of high-sulfur fuel oil). Similarly, it can be deduced here that the use of a third pressure level does not make sense

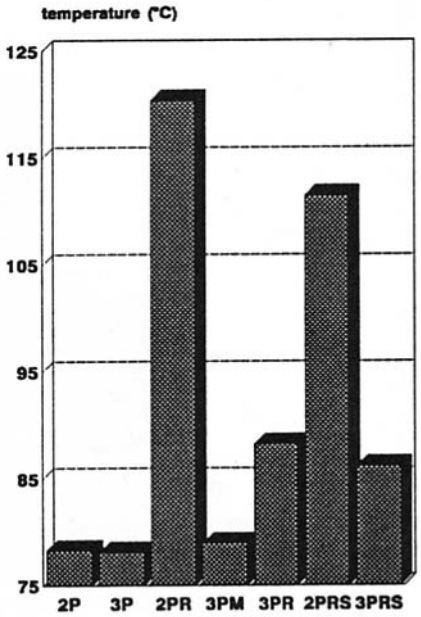

Fig. 6 Stack temperatures of optimized cycles

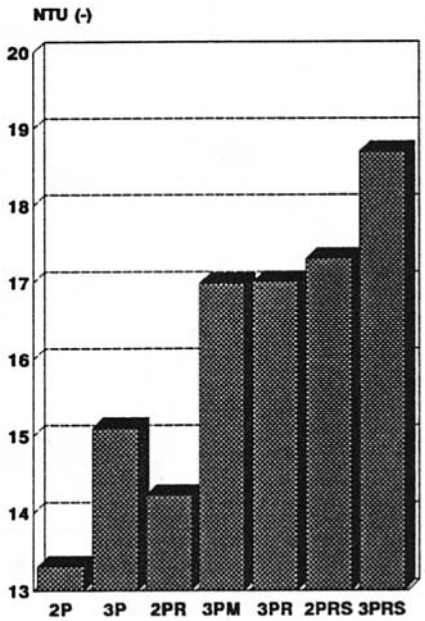

Fig. 8 Total NTUs of optimized cycles

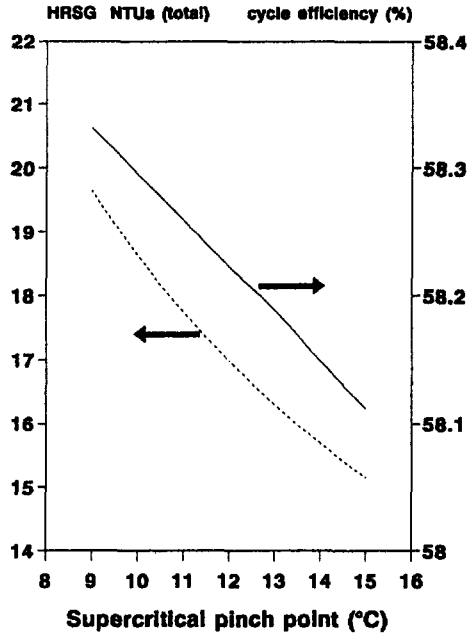

Fig. 9 Pinch selection in supercritical cycles

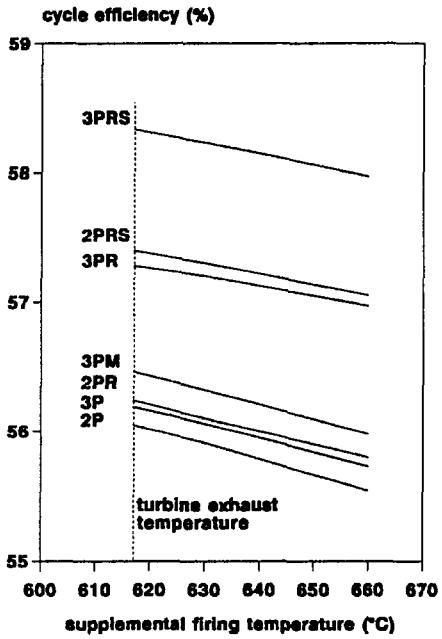

Fig. 11 Influence of supplemental firing

if the stack temperature is limited to 100°C, as it recovers energy from the gases at the lowest temperatures.

Supplemental Firing Considerations

From Fig. 11, it can be seen that the use of supplemental firing always decreases efficiency. The use of supplemental firing must then be regarded as one more tool for the regulation of the output level, or for the regulation of the steam generation in a cogeneration process.

It must be mentioned that a beneficial effect of supplemental firing on efficiency had already been established in repowering configurations, for single pressure level plants with reheat and high pressures (>100 bar) (Dechamps and Mathieu, 1992a, b). It is not the case here, because of the intrinsically high exhaust temperature of the gas turbine.

Reheat Versus Third Pressure Level

Starting with a $2P$ combined cycle scheme, there often is a discussion that attempts to compare the use of a third pressure level with the introduction of reheat. Different sources of information come to different conclusions as to which solution is best (Bolland, 1990; Dechamps et al., 1993).

It should, however, be kept in mind that these two improvements of the classical $2P$ combined cycle act on basically different parameters in order to improve the efficiency of the plant. Let us consider the following expression for the combined cycle efficiency η_{cc}:

$$\eta_{cc} = \eta_{GT} + (1 - \eta_{GT}) * \epsilon_{\text{HRSG}} * \eta_{\text{Rankine}}$$

where

η_{cc} = combined cycle net efficiency
η_{GT} = gas turbine net efficiency
η_{Rankine} = Rankine cycle efficiency = steam turbine output/heat transferred in the HRSG

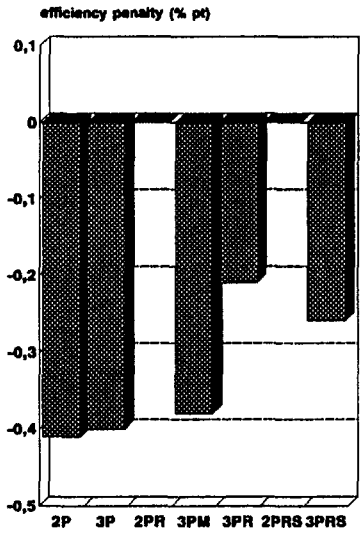

Fig. 10 Efficiency penalties for a stack temperature limit of 100°C

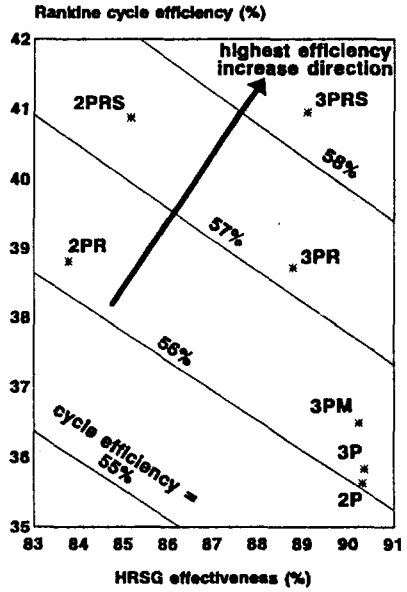

Fig. 12 Efficiency plane

ϵ_{HRSG} = HRSG effectiveness = heat transferred in the HRSG/ heat transferable in the HRSG

with the heat transferable in the HRSG defined as the amount of heat that would be transferred if the stack temperature was equal to the ambient temperature.

For a given gas turbine, η_{GT} is constant, so that the combined cycle efficiency η_{cc} varies as the product of η_{Rankine} and ϵ_{HRSG}. Figure 12 shows how the different cycles can be situated into the $(\eta_{\text{Rankine}} - \epsilon_{HRSG})$ plan.

Some iso-efficiency curves for the combined cycle are represented and are of course hyperbolic segments, with the product $\eta_{\text{Rankine}} * \epsilon_{HRSG}$ kept constant.

It can be observed that for reheat cycles, the introduction of a third pressure level acts on the HRSG efficiency, while the introduction of reheat and possibly of supercritical steam conditions acts on the Rankine efficiency.

Hence, the comparison of the introduction of reheat with the introduction of the third pressure level should always be conducted with great caution, especially with regard to what assumptions are made as far as stack temperature limits are made, for example, for such limits influence the HRSG effectiveness.

Sensitivity Analysis

Figures 13 and 14 present the results of a sensitivity analysis conducted on the $2P$ cycle. The influence of a change in some of the parameters that were fixed during the basic study are illustrated. One should note the high influence of the steam turbine isentropic efficiency on the combined cycle efficiency, of the condenser pressure and of the pinch point temperature differences. It is remarkable that the *LP* temperatures have a greater influence than the corresponding *HP* temperatures.

Not surprisingly, the total *NTU*s are found to be very sensitive to pinch point temperature differences, especially in the *LP* sections.

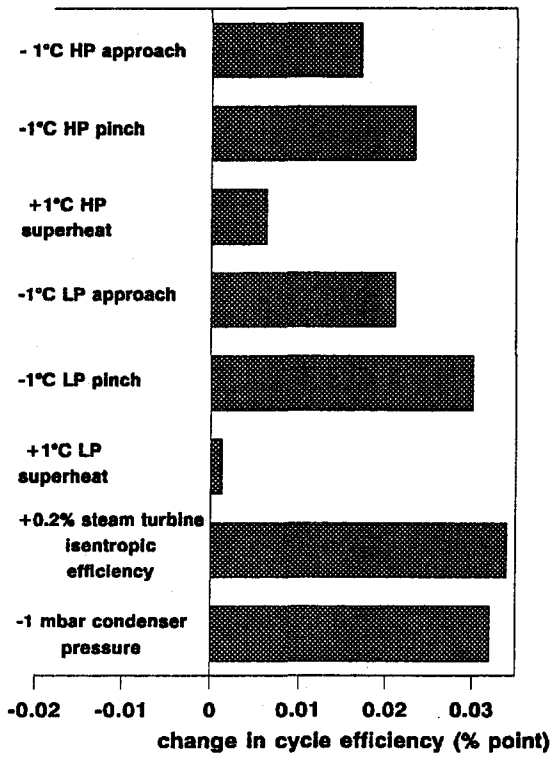

Fig. 13 Sensitivity analysis—efficiency

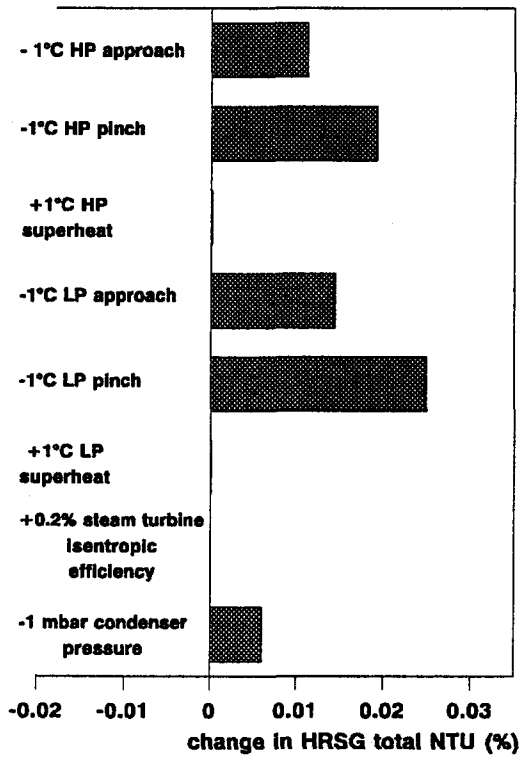

Fig. 14 Sensitivity analysis—NTUs

Conclusions

It has been demonstrated that advanced combined cycle schemes can be beneficial when used in conjunction with the more advanced gas turbines available.

Among all the improvements that can be done on a state-of-the-art $2P$ combined cycle, the introduction of reheat holds the greater promises in terms of fuel savings.

With the assumptions that where used, the introduction of a third pressure level does not provide any substantial advantage unless it is coupled with reheat ($3PM$ and $3PR$).

Taking into account the efficiency increase and the heat transfer surface requirements, an economic evaluation has to be carried out in order to decide whether or not the introduction of a higher complexity in the HRSG is valuable.

The supercritical steam cycles might need to be designed with greater than usual pinch point temperature differences if the heat transfer surface has to be kept comparable to what exists now.

Going toward supercritical steam conditions requires new HRSG designs and again, an economic analysis needs to be performed. This paper has provided some leading parameters for such a study in terms of efficiency increase and heat transfer surface requirements through the NTU parameter.

References

Bolland, O., 1991, "A Comparative Evaluation of Advanced Combined Cycle Alternatives," ASME JOURNAL OF ENGINEERING FOR GAS TURBINES AND POWER, Vol. 113, pp. 190–197.

Borglin, S., 1991, "A Contribution to the Thermodynamic Calculation of Open Gas Turbine Processes," ASME IGTI-Vol 6,

Brandt, D. E., 1992, "The Application of a Mature Gas Turbine Design Philosophy," ASME IGTI-Vol 7.

Dechamps, P. J., 1991, "Users Guide for the GTCALC, CCCALC and CASH-FLOW Programs," internal lecture notes, University of Liège, Mar.

Dechamps, P. J., and Mathieu, Ph., 1991, "IGCC Plants as Alternatives to Pulverized Coal Plants in Western Countries," presented at the First International Conference on Combustion Technologies for a Clean Environment, Portugal.

Dechamps, P. J., and Mathieu, Ph., 1992a, "Modelling of a Steam Power Plant Repowering Option: Replacement of the Conventional Boiler With a New HRSG," ASME IGTI-Vol 7.

Dechamps, P. J., and Mathieu, Ph., 1992b, "Phasing the Construction of an IGCC Plant for Fuel Flexibility," ASME Paper No. 92-GT-144.

Dechamps, P. J., Magain, D., and Mathieu, Ph., 1993, "Advanced Combined Cycle Alternatives With Advanced Gas Turbines," ASME IGTI-Vol. 8.

Jericha, H., Höller, F., and Kindlhofer, H., 1991, "Modular Combined Cycle Plant Enhanced for More Efficiency, Power and Maintainability," ASME IGTI-Vol. 6.

Jury, W., and Luthi, H. K., 1994, "Advanced GT's Call for Advanced CC's," ASME Paper No. 94-GT-303.

Luthi, H. K., 1994, "The ABB GT24/26 Gas Turbine Family With Sequential Combustion," *Proc. PowerGen Europe Conference,* Vol. 9, May 1994, Koln, Germany.

Stecco, S., Bidini, G., and Grimaldi, C., 1991, "Thermodynamic Insight in Designing or Selecting Recovery Boilers for Gas-Steam Combined Power Plants," ASME IGTI-Vol 6.

Van der Linden, S., 1995, "ABB's GT-24 Gas Turbine at GPU's Gilbert Station," *Proc. 1995 EPRI Conference on New Power Generation Technology,* San Francisco, CA.

Low-Leakage Modular Regenerators for Gas-Turbine Engines

J. A. Kluka
Pratt & Whitney,
Middletown, CT
klukaja@pwen.com

D. G. Wilson
Department of Mechanical Engineering,
Massachusetts Institute of Technology,
77 Mass. Ave, Rm. 3-455,
Cambridge, MA 02139

One of the significant problems plaguing regenerator designs is seal leakage resulting in a reduction of thermal efficiency. This paper describes the preliminary design and analysis of a new regenerative heat-exchanger concept, called a modular regenerator, that promises to provide improved seal-leakage performance. The modular regenerator concept consists of a ceramic-honeycomb matrix discretized into rectangular blocks, called modules. Separating the matrix into modules substantially reduces the transverse sealing lengths and substantially increases the longitudinal sealing lengths as compared with typical rotary designs. Potential applications can range from small gas-turbine engines for automotive applications to large stationary gas turbines for industrial power generation. Descriptions of two types of modular regenerators are presented including sealing concepts. Results of seal leakage analysis for typical modular regenerators sized for a small gas-turbine engine (120 kW) predict leakage rates under one percent for most seal-clearance heights.

Introduction

Regenerators are heat exchangers used to improve the thermal efficiency of gas-turbine engines. Regenerators recover some of the energy from the engine exhaust (turbine exit) by reintroducing it back into the cycle just prior to combustion (compressor exit). The compressed air now enters the combustor at a higher temperature. Therefore, less fuel is needed for the same amount of energy output. The result is an increase in thermal efficiency.

Most regenerators are periodic-flow heat exchangers which consist of a heat-transfer surface (ceramic material containing small passages in a honeycomb arrangement called a matrix) that is periodically transferred from the cold compressed-air flow to the hot exhaust flow. On the hot side (low pressure), heat is transferred from the exhaust gases to the ceramic material as it flows through the passages. On the cold side (high pressure), heat is transferred from the matrix material to the compressed-air flow.

Typical gas-turbine regenerators are rotary types which consist of a ceramic matrix disk. The hot turbine-exhaust flows through part of the disk and the cold compressed air flows through the rest in the opposite direction. The disk is rotated such that the hot portion is then periodically exposed to the cold side and vice versa. Most rotary concepts have intrinsic compressed-air-leakage problems. Face seals exist on both sides of the disk along the inner and outer circumference and along two radii to separate the compressed-air flow, exhaust-gas flow, and the surrounding atmosphere. The compressed air escapes under the seals resulting in a reduction of an engine's thermal efficiency. Some 4–14 percent of the compressor mass flow escapes for typical regenerator designs (Wilson, 1995). Wilson and MIT have patented a new regenerator concept (Wilson, 1993a), called the modular regenerator, that promises to offer substantially less leakage than current designs.

Modular Regenerator Conception and General Description

The rationale for the conception of the modular-regenerator concept was made by Wilson (1993b). The design goal for the modular regenerator is to decrease the area over which leakage occurs, thus reducing the leakage. This leakage area is the seal-clearance height multiplied by the transverse sealing length. The transverse sealing length is the length of the seals measured along the periphery of the regenerator's high-pressure side across both sides of the matrix disk. Assuming a fixed seal-clearance height, reducing the transverse sealing length will reduce the leakage. The inherent leakage problem with rotary designs is a long transverse sealing length and most of the leakage occurs over the radial seals. The transverse length of the radial seals can be reduced by increasing the inner radius of the disk, thus forming an annular matrix. The seals can then be relocated to encompass the cross-sectional area of the matrix which reduces the sealing length considerably. The relocated seals are illustrated in Fig. 1.

The matrix can then be broken up into smaller segments (called modules) and straightened to form blocks with rectangular flow passages, as shown in the Fig. 2. The modules are moved linearly within the passages such that modules exposed to one flow are periodically moved to the other exposed area. A void of at least one module volume is needed to allow movement. In addition, the two exposed areas could be separated further than is shown in Fig. 2, which would eliminate any special ducting of the flow that might be required for a particular gas-turbine application. The flow through the modules reverses (between the two exposed areas, as shown in Fig. 2) as in other regenerators, providing some degree of self cleaning. Furthermore, removal of modules (that are not located within the exposed areas) from the regenerator for periodic maintenance or replacement is possible. This can be performed during regenerator operation, a procedure not feasible with any other regenerator concepts.

The modular design has an additional leakage reduction benefit of having greater longitudinal sealing lengths over rotary concepts. The longitudinal sealing length is the seal length in the direction of leakage flow (and normal to the transverse sealing length). Therefore, increasing the longitudinal sealing length will decrease the leakage. The longitudinal sealing length can be as long as the distance separating the two areas exposed to the flow. A comparison of sealing lengths for the rotary and modular cases is shown in Fig. 3.

Since the total transverse sealing length has dramatically decreased and the longitudinal sealing length has substantially

Contributed by the International Gas Turbine Institute and presented at the International Gas Turbine & Aeroengine Congress & Exhibition, Orlando, FL, June 2–5, 1997. Manuscript received by the ASME Headquarters July 1997. Paper No. 97-GT-8. Associate Technical Editor: H. A. Kidd.

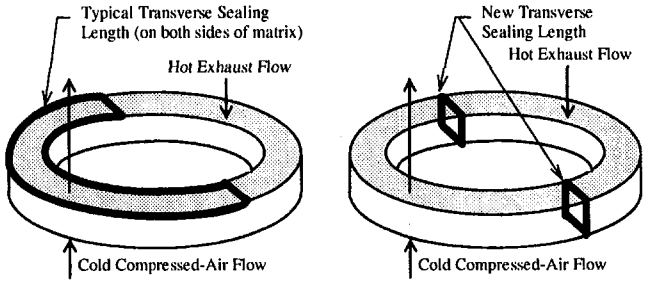

Fig. 1 Relocation of sealing lengths for an annular matrix

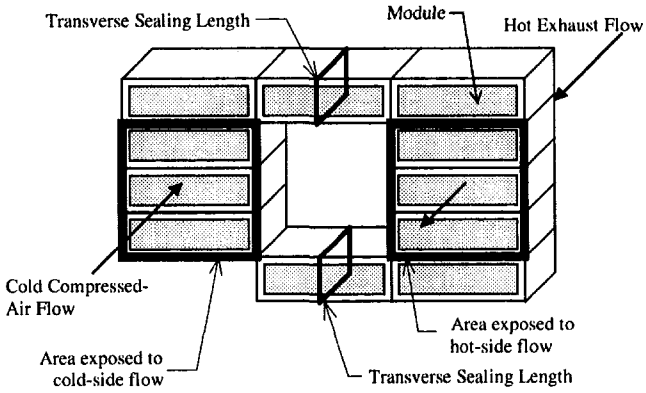

Fig. 2 General arrangement of a modular regenerator

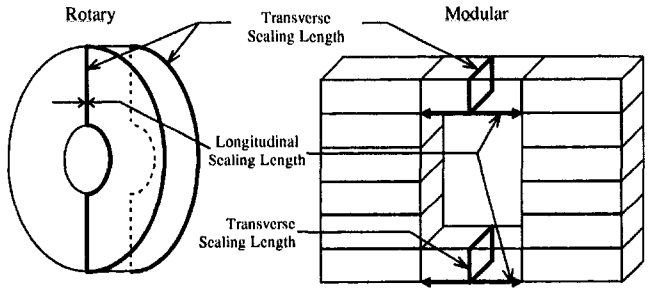

Fig. 3 Comparison of sealing lengths for rotary and modular regenerators

increased for the modular design, the seal leakage should be substantially lower than conventional rotary regenerators. In spite of the leakage performance benefits, the major consequence in making the transition to the modular case is an increase in mechanical complexity for matrix movement. Rotary concepts require a single device to rotate the matrix, whereas several devices, such as linear actuators, are required for module movement.

Applications

Breaking up the matrix into modules allows the exposed flow areas to have virtually unlimited size. If a larger heat-transfer area is needed, the designer can just add more modules to the exposed flow areas. Thus modular regenerators have numerous applications ranging from small gas turbines for vehicular use to large ground-based gas turbines for industrial power generation. In contrast, rotary regenerators have been designed primarily for vehicular applications since the size of the monolithic ceramic matrix disk is limited to a diameter of 1 m due to manufacturing and thermal-stress constraints (Wilson, 1993b). Furthermore, the modular concept could be used in exhaust-heated cycles to burn coal, wood, and refuse-derived fuels as

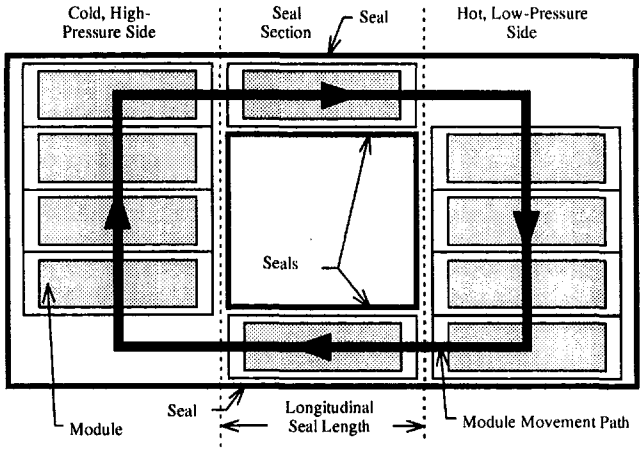

Fig. 4 General layout of the module-seal concept with a longitudinal seal length of one module

proposed by Wilson (1993c). These cycles burn "dirty" fuels in which combustion products can clog the matrix passages despite the inherent self cleaning of the matrix. Having the capability to replace the modules for cleaning during continuous engine operation makes the modular case attractive.

When competing with rotary applications, a modular regenerator's size might preclude its use on some small gas-turbine vehicles. The overall dimensions will be considerably greater than rotary designs due to the open space between the two areas exposed to the flow. The size might be too large to fit in a vehicle's engine compartment. Furthermore, analysis and testing should be conducted to ensure that module movement can withstand the vehicular environment.

Wilson states that regenerator designs would require very low leakage at pressure ratios of 8:1 for aircraft-engine applications (Wilson, 1993b). Rotary concepts have been unsuccessful thus far to provide this, but modular concepts might be able to achieve such performance.

Modular Regenerator Concepts

Basically, two different types of modular regenerators exist. Both concepts consist of separating the hot and cold sides with two rectangular passages containing seals, called the seal section. They differ in the type of sealing technique used. The first concept has a module acting as the seal. The second concept contains partitions to seal off the compressed air.

Module-Seal Concept. The module-seal concept essentially places modules within the passageway (called the seal section) that separates the two sides exposed to the flow, thus blocking the compressed air from entering the low-pressure side. Therefore, modules must always be present in the seal section. Leakage occurs when the compressed air travels through the seal section to the low-pressure side. Figure 4 illustrates the general layout. This concept provides the simplest modular configuration from a mechanical standpoint.

With the short transverse sealing length and the long longitudinal seal length, this option should provide very low leakage. The longitudinal seal length could be increased (by adding more modules in the seal section) to provide further leakage reduction or reduce any special ducting of the flow. Consequently, as the longitudinal seal length gets larger, the time for a module to travel from one side to the other will increase (if the speed of the modules remains constant). This may cause a reduction in effectiveness (a measure of the regenerator's thermal performance) due to heat conduction within the matrix material.

Mechanisms are required to translate the modules along the linear paths shown in Fig. 4. Linear actuators such as pneumatic

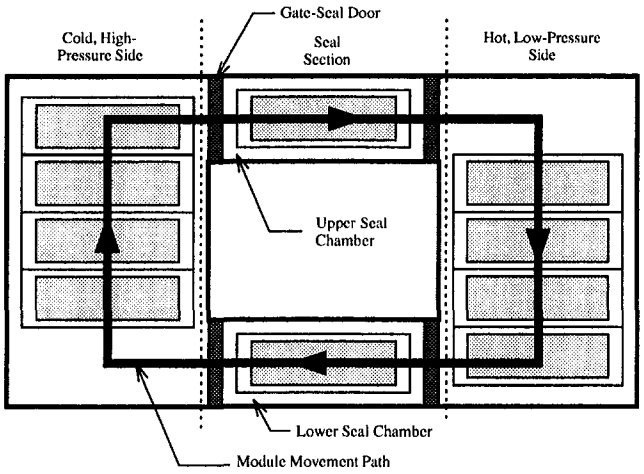

Fig. 5 General layout of the gate-seal concept with a chamber length of one module length

cylinders could be used to provide such movement. These mechanisms must account for the large pressure forces that act on the modules located within the seal section. These forces push the modules toward the low-pressure side. This will be advantageous for modules traveling in the direction of the pressure force; however, these forces must be overcome when modules are traveling towards the high-pressure side.

Gate-Seal Concept. The gate-seal concept seals the compressed air by partitioning the hot side, cold side, and seal section using gate-seal doors (also called gate valves) (Wilson, 1993a). These doors open and close to allow module movement. The basic layout has the seal section containing two seal chambers with gate-seal doors on either side. The general arrangement is shown in Fig. 5. Module movement through a seal section occurs when one of the two gate-seal doors opens for each seal chamber, thus letting modules enter and exit.

For this concept, the leakage consists of the transfer of compressed air when the door opens to the low-pressure side. This differs for each seal chamber where the upper chamber has less leakage than the lower chamber. This occurs because the upper-chamber door on the right opens to move a module out of the chamber to the low-pressure side, and the lower-chamber right door opens to let a module enter. Thus, part of the upper chamber's volume is occupied by a module, and the rest of the volume is air that is transferred as leakage. The other chamber is empty as the right door opens; therefore, the entire volume of air within this chamber is transferred as leakage. Note that the concept of transverse and longitudinal sealing lengths do not really apply for this regenerator because the leakage is dictated by the volume of air that can enter a seal chamber.

Mechanisms are required to move the modules within the hot and cold sides and in and out of each chamber. This concept will probably require more mechanisms than the module-seal concept because additional steps are made during module movement (due to the addition of the gate-seal doors). Furthermore, like the module-seal concept, the gate-seal regenerators can have a longer seal section by adding more chambers.

Seal Description

The modular regenerator's key performance advantage is potentially low leakage rates due to its seal lengths and sealing techniques. Descriptions of these sealing techniques for both types of modular regenerators are given below.

Seals for Module-Seal Regenerators. The seal leakage occurs along four module faces when a module is located within the seal section. The convention for naming the module sides

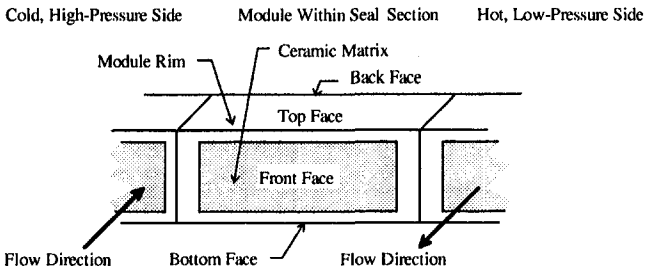

Fig. 6 Location of module faces where the leakage occurs

that form the seal is shown in Fig. 6. To minimize the leakage flow, labyrinth seals are used around all module faces. Each module contains a honeycomb matrix surface on two faces, front and back. When these faces are in close contact with the regenerator casing walls, a labyrinth seal inherently exists due to the matrix surface. The other two module faces, top and bottom, consist of smooth ceramic material which comprise part of the module rim that provides protection of the matrix material during module transit. A matrix-like surface incorporated into the regenerator casing walls that are in close contact with these two faces is needed to provide the labyrinth seal.

The seal leakage can be classified into two groups, gap and carry over. Gap leakage is the fluid flow traveling through the gaps created by modules in the seal section (i.e., the space between the regenerator casing walls and the module faces). Carry-over leakage consists of the transfer of trapped air within the matrix passages as modules travel from one side to the other. Recall that modular regenerators have reduced transverse sealing lengths over rotary concepts. This provides a reduction in gap leakage only.

The front and back module faces contain the matrix surface; therefore, the leakage along these faces consists of carry over and gap leakage. The layout of the seal across these faces is shown in Fig. 7. The top and bottom module faces are smooth surfaces due to the module rims which results in gap leakage only. The seal along these faces is illustrated in Fig. 8.

Seals for Gate-Seal Regenerators. The seal for the gate-seal regenerator is a seal chamber as shown in Fig. 9. The chamber consists of a volume enclosed by the regenerator casing walls and two gate-seal doors that open and close vertically. The sealing concept can be shown by an example of a module moving to the low-pressure side. First, the left door opens (with the right door closed) to allow a module to enter from the high-pressure side. Compressed air enters the chamber at this point. Then, the left door closes and the right door opens to allow the module to enter the low-pressure side. Therefore, the compressed air is transferred as leakage to the low-pressure side. Reducing the open space around a module within the chamber

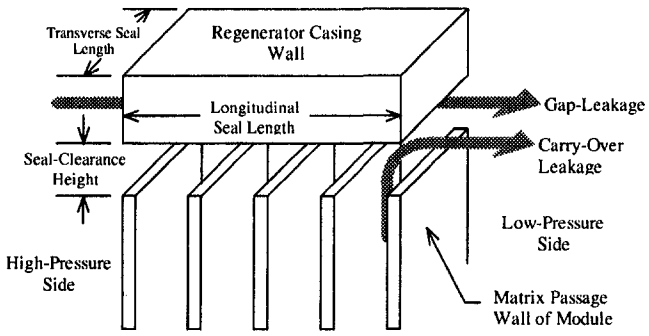

Fig. 7 Diagram of seal along the module front and back faces for module-seal regenerator

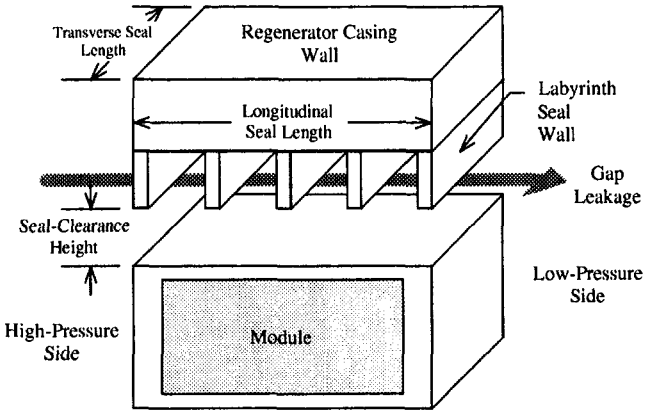

Fig. 8 Diagram of seal along the module top and bottom faces for module-seal regenerator

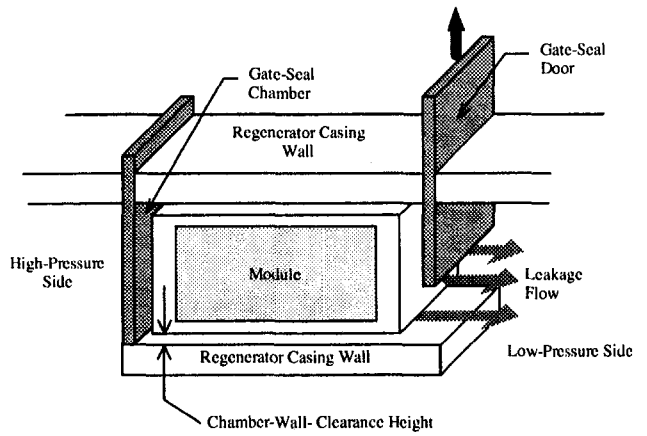

Fig. 9 Diagram of seal chamber for gate-seal regenerator (right-side door in process of opening for module entry into low-pressure side)

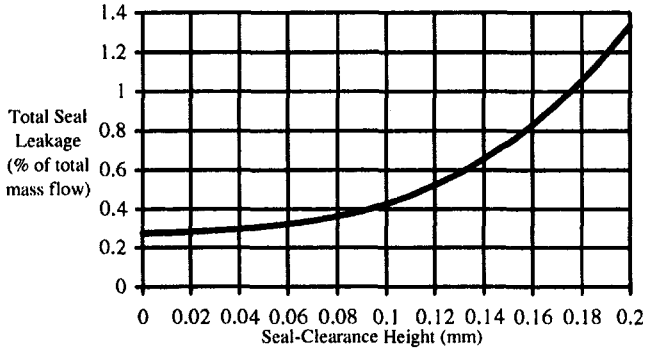

Fig. 10 Predicted net seal leakage from the high-pressure side for a typical module-seal regenerator sized for a 120 kW gas-turbine engine

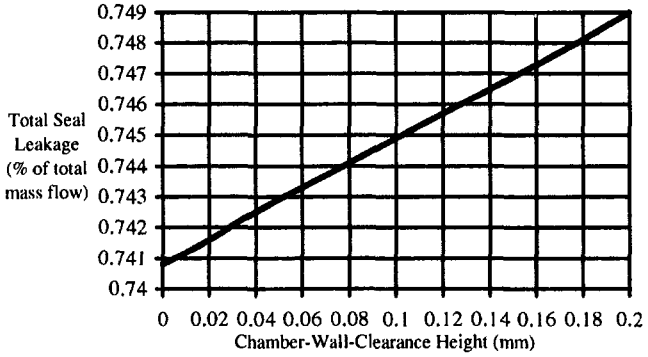

Fig. 11 Predicted net seal leakage from the high-pressure side for a typical gate-seal regenerator sized for a 120 kW gas-turbine engine

will reduce the leakage, but the volume must not be too small to preclude easy module entry/exit.

Seal-Leakage Rates

Leakage rates were determined by Kluka (1995) for typical modular regenerators sized for a small gas turbine (120 kW). The following presents a brief description of the leakage analysis method and the results obtained.

Module-Seal Regenerators. The leakage analysis for module-seal regenerators is based on the leakage method for rotary regenerators developed by Harper (1957) where Harper models the leakage flow through labyrinth seals. First, the general equations for gap and carry-over leakage were derived for the modular case. Then the equations were modified to determine the leakage across each module face.

The results of total leakage for a typical regenerator sized for a small gas turbine from Kluka (1995) are plotted in Fig. 10. Note that as the seal-clearance height approaches zero, the leakage approaches the carry-over leakage value, which is less than 0.3 percent of the total mass flow.

Gate-Seal Regenerators. The leakage rates for gate-seal regenerators were determined by calculating the mass of air located within the seal chambers and dividing it by the time interval when the air is transferred from one pressure side to the other (i.e., the total time for one module to move to the next module location).

The results of net seal leakage for a typical gate-seal regenerator sized for a small gas turbine are shown in Fig. 11 (Kluka, 1995). At zero chamber-wall-clearance height, the leakage is the flow from the volume of one empty chamber plus the volume of the voids of a module matrix (volume of air in a chamber containing a module). This is somewhat analogous to carry-over leakage.

Summary and Conclusions

Modular regenerators promise to offer improved leakage performance over rotary designs by reducing the transverse sealing lengths and increasing the longitudinal sealing lengths. Discretizing the ceramic matrix into rectangular modules allows a regenerator's heat transfer area to increase such that applications on a wide range of gas-turbine sizes are feasible. Furthermore, module replacement is possible during regenerator operation for periodic maintenance or repair. These advantages for the modular regenerator outweigh the main disadvantage, an increase in mechanical complexity for matrix movement. Mechanisms will have to be developed to provide efficient module movement without sacrificing any performance benefits. Addressing this disadvantage is a matter of mechanical design, an issue with possible resolutions; however, the disadvantages of the rotary designs are inherent; therefore, resolutions are not readily conceivable.

Leakage results for typical modular regenerators sized for a 120 kW gas-turbine engine were consistent with the claims of lower leakage rates by predicting leakage under one percent for most seal-clearance heights. Experimental sealing tests should be conducted in the future to corroborate these results.

More information on modular regenerators including module design, mechanical design analysis, design/performance calculations, and design optimization analysis can be found in MIT thesis by Kluka (1995).

References

Harper, D. B., 1957, "Seal Leakage in the Rotary Regenerator and its Effect on Rotary Regenerator Design for Gas Turbines," *Transactions of the ASME,* February, pp. 233–245.

Kluka, J. A., 1995, "The Design of Low-Leakage Modular Regenerators for Gas-Turbine Engines," Master of Science in Aeronautics and Astronautics thesis, Massachusetts Institute of Technology, Cambridge, MA, June.

Wilson, D. G., 1993a, United States Patent, Patent Number 5,259,444, November 9.

Wilson, D. G., 1993b, "Low-Leakage and High-Flow Regenerators for Gas Turbine Engines," *Proc. Instn. Mech. Engrs.,* Vol. 207, pp. 195–202.

Wilson, D. G., 1993c, "The Supplementary-Fired Exhaust-Heated Cycle for Coal, Wood and Refuse-Derived Fuel," *Proc. Instn. Mech. Engrs.,* Vol. 207, pp. 203–208.

Wilson, D. G., 1995, "Turbine Cars, Major Contender, Bumpy Road," *Technology Review,* February/March, pp. 50–57.

INCONEL® Alloy 783: An Oxidation-Resistant, Low Expansion Superalloy for Gas Turbine Applications

K. A. Heck

J. S. Smith

Inco Alloys International,
Huntington, WV 25705

R. Smith
Inco Alloys International,
Hereford, United Kingdom

INCONEL® alloy 783 is an oxidation-resistant low coefficient of thermal expansion (low CTE) superalloy developed for gas turbine applications. Turbine efficiency can be increased through the use of low-CTE shrouds and case components that maintain tight blade tip clearances at different turbine operating temperatures. To achieve low CTE, alloys based on Ni–Fe–Co compositions require Cr content be maintained at low levels. Added Cr lowers the Curie temperature and thereby increases thermal expansion rate over a wider temperature range. The necessary lack of Cr minimizes resistance to both general oxidation and stress-accelerated grain boundary oxygen enhanced cracking (SAGBO). Increased amounts of Al in alloys strengthened by γ' alone also promotes SAGBO. Alloy 783 is the culmination in the development of an alloy system with very high aluminum content that, in addition to forming γ', causes β aluminide phase precipitation in the austenitic matrix. It was discovered that this type of structure can be processed to resist both SAGBO and general oxidation, while providing low thermal expansion and useful mechanical properties up to 700°C. The high Al content also reduces density to 5 percent below that of superalloys such as INCONEL alloy 718. Key aspects of the alloy development are presented, including the assessment of SAGBO resistance by evaluating elevated temperature crack growth in air. The alloy, now commercially available, has been successfully fabricated and welded into gas turbine engine components.

Introduction

Over the years, gas turbine engine efficiency has been optimized in designs that exploit the characteristics of low coefficient of thermal expansion (low-CTE) superalloys. Such efficiency is achieved through tight control of blade tip clearances over the range of turbine operating conditions. Low expansion compressor cases and shrouds are currently made from superalloys INCOLOY® alloy 903, INCOLOY® alloy 907, and INCOLOY® alloy 909. The ferromagnetic characteristic below the Curie points of these alloys is responsible for thermal expansion coefficients (α) lower than observed in paramagnetic alloys. These Ni–Fe–Co base alloys also have very low chromium content, as added Cr lowers the Curie temperature and thereby increases overall thermal expansion rate [1]. Low Cr content makes this class of alloys sensitive to oxidation phenomena at elevated temperatures (see appendix, Table A).

Oxidation at elevated temperatures can manifest itself as both general oxidation seen in Fig. 1(a) (see appendix), and as the stress-accelerated grain boundary oxygen assisted intergranular cracking phenomena (SAGBO) seen in Fig. 1(b). The SAGBO phenomenon can be observed in many superalloys and is discussed elsewhere [1, 2]. Low-Cr age-hardenable superalloys and some intermetallics are particularly susceptible to SAGBO [3]. Alloy 783 is the result of an extensive low-CTE alloy development program aimed at improving resistance to both forms of oxidation. Alloy 783 property developments are discussed, then resulting behavior is compared to low-CTE alloy 909 and the higher α superalloy used as a benchmark, INCONEL alloy 718.

Contributed by the International Gas Turbine Institute and presented at the 41st International Gas Turbine and Aeroengine Congress and Exhibition, Birmingham, United Kingdom, June 10–13, 1996. Manuscript received at ASME Headquarters February 1996. Paper No. 96-GT-380. Associate Technical Editor: J. N. Shinn.

Aluminum Effect

Ni–Fe–Co base low-CTE superalloys are age hardenable through additions of Al, Ti, and Nb. Experience has shown that increased Al content is beneficial for creep resistance and stability, but has a profound negative effect on 540°C rupture ductility due to SAGBO. Alloy 903, for example contains 0.9 percent Al, and is susceptible to SAGBO in some orientations [1]. Earlier alloy developments to overcome this effect were based on reducing creep resistance (alloy 907) and adding Si-rich grain boundary precipitates (alloy 909)[4]. These alloys have much improved notch rupture ductility compared to alloy 903, but 538°C crack growth resistance is relatively poor compared to alloy 718. Alloys with enough Al added (>2.5 w%) for good general oxidation resistance are strengthened by γ' but have low ductility in air at 540°C. While SAGBO can manifest itself as low tensile or stress rupture ductilities, the effect is most stringently measured by its contribution to fast crack growth in a corresponding intergranular fracture mode.

It is known that a wide range of Ni–Fe–Co base compositions containing 5 or more weight percent Al can be processed to contain forms of a BCC β phase that improves rupture ductility of a γ' strengthened matrix [5]. The effect of Al content on 649°C rupture life and ductility of 42 percent Ni-18 percent Co-3 percent Nb-balance Fe alloys is shown in Fig. 2. The change in microstructure with increased Al correlates with the presence of a β phase that assists grain refinement during processing and contributes toward good rupture ductility [5]. A small 3 percent Cr addition, and heat treatments that precipitate grain boundary β phase, impart slow crack growth behavior at 540°C without sacrificing low-CTE characteristics. The alloy 783 composition is shown in Table A.

Alloy 783 can be heat treated a number of ways depending on desired property combinations. This paper focuses on optimizations for gas turbine applications. Figure 3 shows both γ' and β precipita-

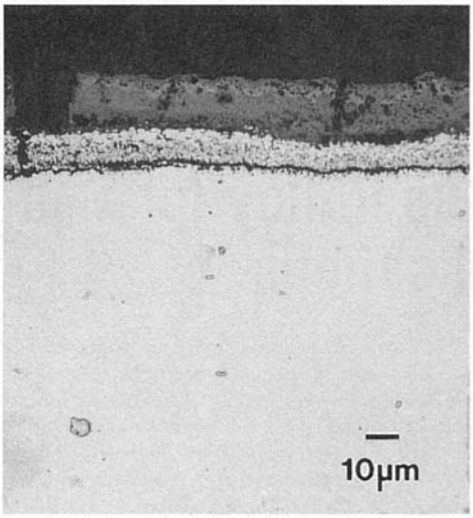

Fig. 1(*a*) Cross section of alloy 909 surface showing general surface oxidation after 500 hours at 704°C in air

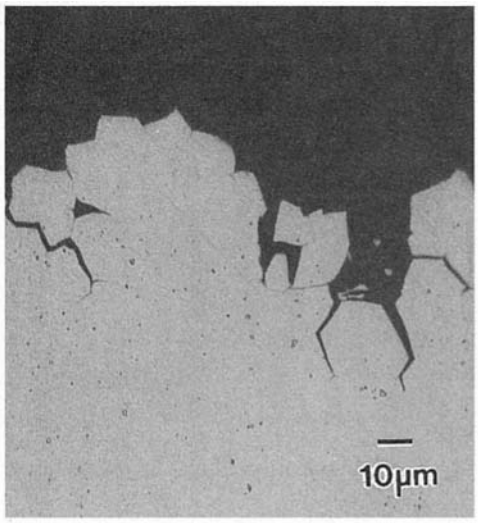

Fig. 1(*b*) Cross section of a 538°C stress rupture fracture of an alloy in a SAGBO-prone condition. Note the intergranular fracture mode.

tions that occur upon heat treatment of fully solution annealed alloy 783, and is useful for understanding heat treatment behavior.

Stress Rupture

The effects of various heat treatments on the 650°C and 586 MPa combination notched-smooth stress rupture life and ductility are shown in Table B. The notch Kt factor was 3.7. Also shown are room temperature tensile properties for reference purposes. Test specimens were obtained from a 51 mm thick by 102 mm high seamless hot rolled turbine engine ring produced from a 200 mm forged billet. All specimens were annealed at 1121°C for 1 hour and air cooled before the age-hardening heat treatments.

Isothermal aging heat treatment at 732°C for 8 h resulted in lower room temperature strength and high ductility. Notch fracture occurred in very short times. The two-step aging heat treatment compatible with alloy 718 for increased room temperature tensile strength alone results in notch rupture fractures after short life. Inserting a β-precipitating heat treatment of 843°C for 2 to 4 hours between the anneal and a 718°C/621°C two-step heat treatment, however, further increased tensile strength and provided good smooth bar life and ductility.

Isothermal aging at 788°C for 16 h provided notch ductility and adequate smooth bar rupture life with excellent ductility. Room temperature strength was inadequate. Coupling the 788°C for 16 h with a 55°C/h furnace cool to 621°C hold for 8 h and air cool heat treatment increased strength to acceptable levels and resulted in good stress rupture life and ductility.

The results from these heat treatments illustrate the combined use of gamma prime and beta heat treatments in attaining both adequate tensile and stress rupture strength and ductility. Isothermal aging heat treatments are inadequate for producing material with good tensile strength. Two-step aging heat treatments within the gamma prime precipitation temperature range (but below the β precipitation temperature range) result in good tensile strength, but fail to provide good notch rupture strength.

Combining β precipitation with gamma prime precipitation provides material with a good combination of tensile strength and notch ductile stress rupture behavior. This is done by using either a long time (16 h) low temperature β precipitation heat treatment at 788°C followed by furnace cooling through the gamma prime precipitation temperatures and a hold at 621°C, or using the short time (2 to 4 h) 843°C heat treatment before a two-step gamma prime precipitation heat treatment. Selection of the hold time at 843°C can be adjusted to compensate for variations due to grain size or prior thermomechanical history. The short time 843°C heat treatment permits flexibility in selecting gamma prime precipitation heat treatments. This feature allows alloy 783 heat treating to be compatible with nearly all other gamma prime strengthened superalloys.

Sustained Load Crack Growth

The experience accumulated in the development and application of controlled, low thermal expansion superalloys for gas turbines has clearly shown the need to incorporate crack growth resistance in the alloy design. Sustained load crack growth resis-

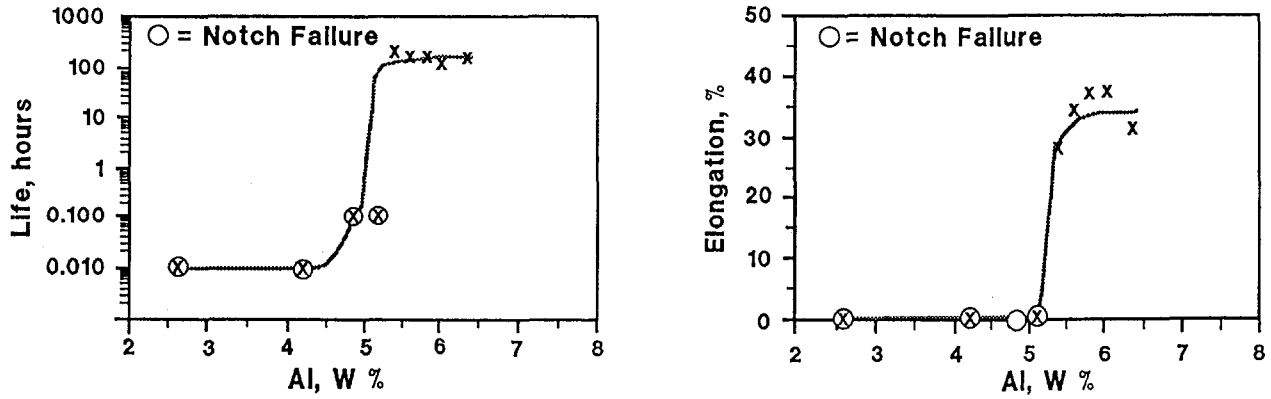

Fig. 2 Effects of Al content on the 649°C/510 MPa stress rupture life (left) and rupture ductility (right) of 42 percent Ni/18 percent Co/1.5 percent Ti/3 percent Nb/balance Fe alloys. The failures in the notched bar sections are SAGBO-related.

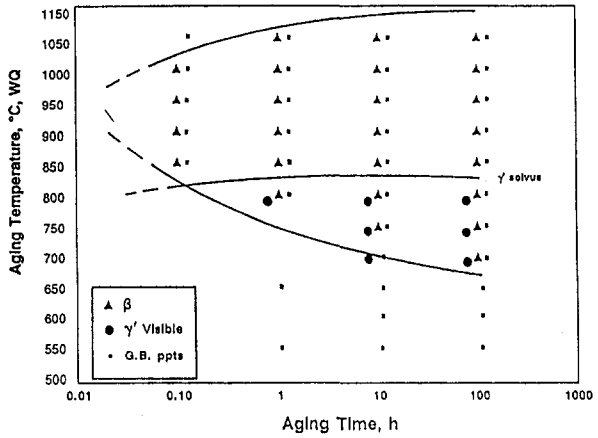

Fig. 3 T-T-T diagram for alloy 783. Isothermal heat treatments after 1150°C solution anneal, then water quenched.

tance equivalent to alloy 718 (at 540°C in air) was therefore established as a primary goal during the development of alloy 783.

The effect of annealing and aging treatments on alloy 783 crack growth behavior is shown in Fig. 4. The response is somewhat complex, but in general, crack growth rate is inversely proportional to volume percent β phase. Annealing temperature influences final crack growth properties by establishing grain size, fixing the amount of globular β phase retained from hot working operations, and affecting additional β precipitation in grain boundaries during lower temperature "β aging" treatments.

Figure 5 illustrates the effect of annealing heat treatment on the 33 MPa$\sqrt{m}$ crack growth rates in two orientations of a forged and rolled alloy 783 ring followed by an aging heat treatment of 760°C/12 h furnace cooled 55°C/h to 621°C/8 h and air cooled. This aging heat treatment is not considered optimal for property development, but permits β precipitation during the 760°C exposure and gamma prime precipitation during the furnace cool and 621°C hold.

At lower annealing temperatures crack growth rates in both the long transverse and short transverse orientations are relatively low and similar. Annealing temperatures of 1000°C or less do not solution β precipitated during the prior hot working cycles and tend to precipitate additional globular and fine intergranular β particles. Lower annealing temperatures also allow retained energy from the ring rolling operations to enhance fine intergranular β precipitation during the 760°C heat treatment cycle. Thermomechanically precipitated globular β tends to be

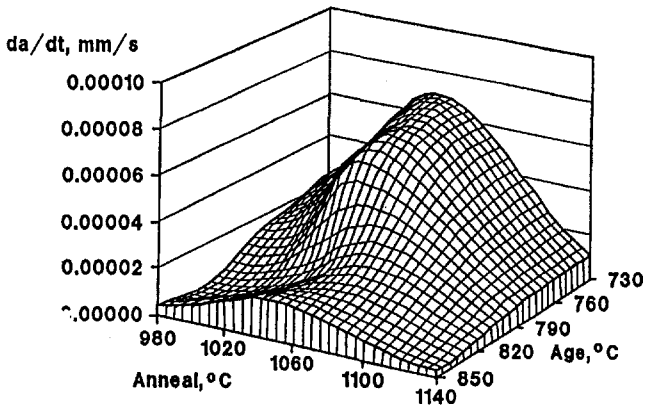

Fig. 4 Effect of heat treatment on alloy 783 538°C crack growth rate at K = 33 MPa$\sqrt{m}$ (in air)

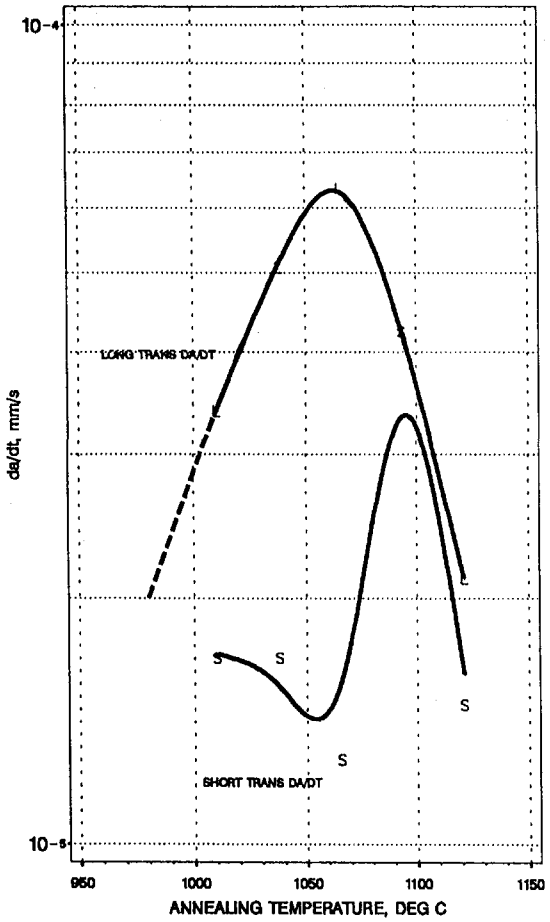

Fig. 5 Alloy 783 crack growth rates at K = 33 MPa$\sqrt{m}$ as a function of anneal and test orientation (note: non-standard aging treatment used). Note the alloy is most isotropic when either a low or a high-temperature anneal is utilized.

elongated and oriented in the hot working direction (in this case, parallel to the circumference of the seamless rolled ring).

As annealing temperature is increased above 1000°C, β begins to solution, and grain size increases. The associated lack of grain boundary β causes long transverse 538°C da/dt to increase. The large β particles precipitated during the prior thermomechanical processing do not completely solution. This β, which may be elongated, provides greater crack growth resistance in the short transverse orientation of the ring. This anisotropy disappears as annealing temperature increases.

Annealing temperatures above 1075°C solution most of the β, spheroidize remaining globular β, and increase grain size. The coarsened grain and spheroidized globular β morphologies establish isotropy. Solutioning provides more fine intergranular β to be precipitated during the 760°C heat treatment cycle, which results in improved da/dt resistance in both orientations.

Commercial Heat Treatment

In practice, a 1121°C annealing temperature (just below the β solvus) is utilized. This relatively high temperature is amenable to commercial brazing operations, yet the high β solvus inhibits grain growth. Material hot worked and annealed below the β solvus contains residual globular β phase particles among recrystallized grain. There is, however, additional Al available for grain boundary precipitation during the 843°C for 2 to 4 hour β-age treatment. Gamma prime age hardening of grain interiors occurs during the alloy 718 compatible heat treatment of 718°C/8 hours, furnace cool 55°C per hour to 621°C, hold

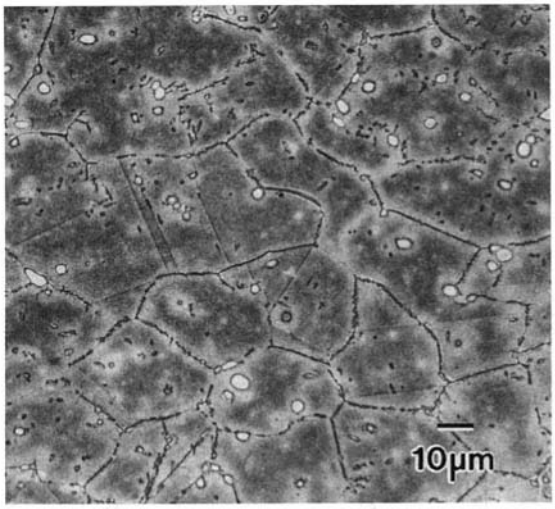

Fig. 6 Microstructure of fully heat treated alloy 783 (1121°C/1h, AC + 843°C/2 h, AC + 718°C/8 h, FC (55°C/h) to 621°C/8 h, AC). Note the globular β phase remaining from prior hot work and final anneal, and grain boundary β present from the 843°C heat treatment step. Kallings etch.

for 8 hours. Other aging schemes within the γ' precipitation range can be used. It has been found that peak yield strength is achieved if some amount of slow cooling is utilized between a high and a low aging temperature. Table C summarizes the behavior of alloy 783 during standard heat treatment. The fully heat treated microstructure is shown in Fig. 6.

For comparisons, crack growth tests were conducted on compact tension specimens obtained from three gas turbine rings made of alloy 909, alloy 718, and alloy 783, respectively. Alloy 909 specimens were heat treated at 982°C for one hour, air cooled, and age hardened at 746°C for 4 h, furnace cooled 55°C/h to 621°C for 4 h, and air cooled. Alloy 718 was annealed at 954°C and air cooled, followed by age hardening at 718°C/8 h furnace cooled 55°C/h to 621°C/8 h and air cooled. These are optimum commercial heat treatment cycles for producing crack growth resistance in the two alloys. Alloy 783 specimens from a 51 mm thick by 102 mm high seamless forged ring were annealed at 1121°C for one hour, air cooled, given a β precipitation heat treatment of 843°C for two hours, air cooled, followed by gamma prime precipitation at 718°C for 8 h furnace cooled to 621°C for 8 h and air cooled.

As seen in Fig. 7, alloy 783 exhibits crack growth behavior similar to alloy 718, and provides at least an order of magnitude reduction in crack growth rates over that of alloy 909. Moreover, the crack growth curves indicate that the crack propagation threshold stress intensity of alloy 783 is similar to alloy 718 and significantly greater than that of alloy 909. The high temperature 1121°C anneal for alloy 783 results in nearly isotropic grain and β precipitation structure providing crack growth resistance in various orientations.

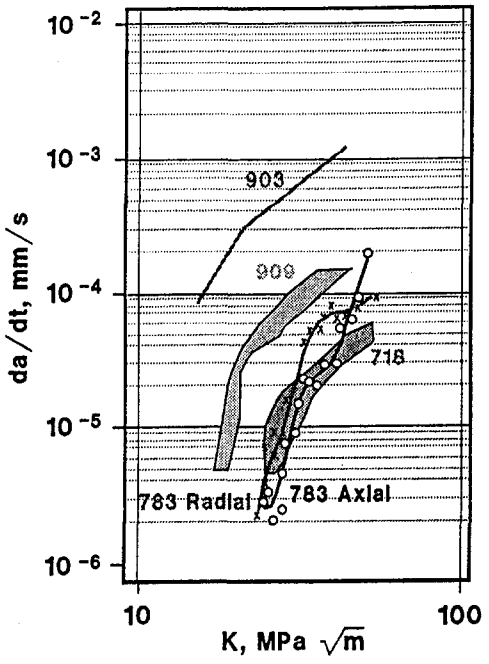

Fig. 7 538°C crack growth curves comparing behavior of alloys 783, 718, and 909 in air

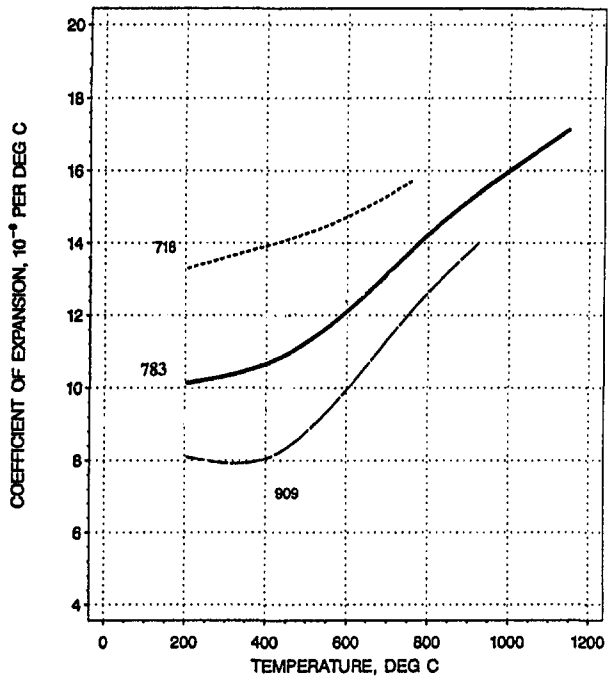

Fig. 8 Comparative thermal expansion data for fully heat-treated alloys 783, 718, and 909

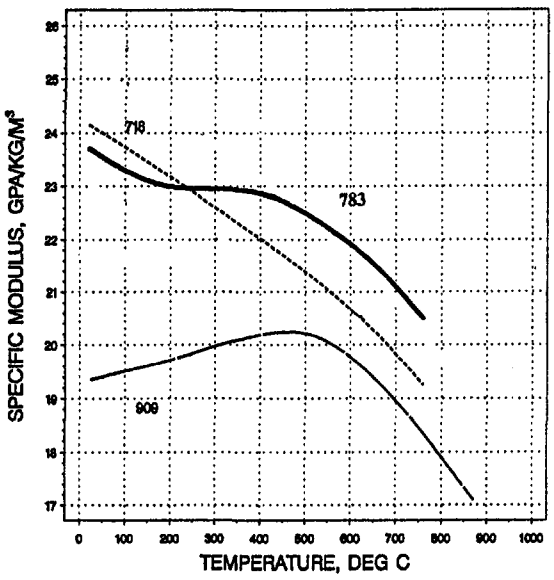

Fig. 9 Comparative specific modulus data for alloys 783, 718, and 909

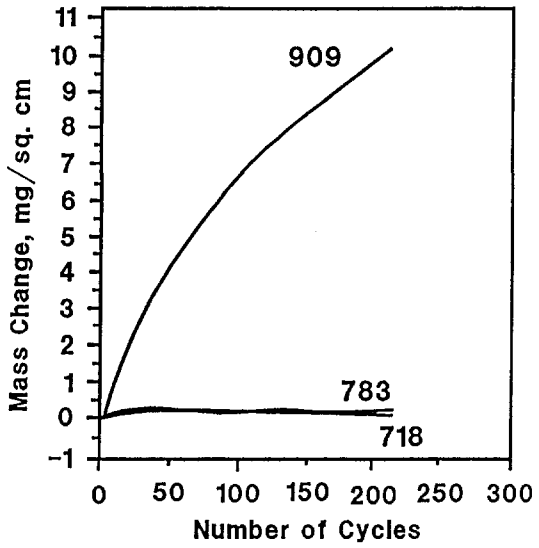

Fig. 10 Weight change of alloys 783, 718 and 909 after 704°C cyclic oxidation tests (60 min.in/20 min.out)

Thermophysical Properties

Thermal expansion data are shown in Fig. 8. The expansion versus temperature curve is 20 percent lower than that for alloy 718, and is parallel up to 700°C. Behavior is similar to that of alloys M-151/M-152. The optimized Ni–Co–Fe content results in an inflection (or Curie) temperature of about 600°C and allows for a smooth coefficient of thermal expansion curve over the operating temperature range.

Density of alloy 783 is lower than many superalloys due to the high Al content. For example, alloy 783 density is 7.78 kg/m^3 (0.281 lb/$in.^3$) compared to 8.19 kg/m^3 (0.296 lb/$in.^3$) for alloy 718, that is, 5 percent lower. Young's modulus of elasticity as a function of temperature is shown in Fig. 9. At room temperature the Young's modulus of alloy 783 is about 7 percent lower than that of alloy 718. The rate of modulus decrease with increasing temperature is small compared to alloy 718, however, and at temperatures above 400°C through gas turbine engine operating ranges alloy 783 modulus is essentially equivalent to alloy 718 modulus.

Oxidation and Salt Spray Resistance

Figure 10 provides a comparison of the cyclic oxidation resistance of alloys 783, 909, and 718 at 704°C. The oxidation rate of alloy 783 is slightly greater than alloy 718 at 704°C, but is still excellent compared to alloy 909.

The results of salt fog testing to ASTM B117-85 for duplicate tests of the three alloys are shown in Table D. The salt fog resistance of alloy 783 shows corrosion coverage and corrosion rate approaching those of alloy 718, and are superior to those of alloy 909. The end grain pitting observed on one alloy 783 specimen, but not the other, indicates marginal resistance to pitting on surfaces perpendicular to the worked direction.

Commercial Alloy Production

Alloy 783 is produced by standard vacuum induction melting (VIM) and vacuum arc remelting (VAR) methods. The alloy is readily forged into bar or ring products using processing steps similar to those used thoughout the industry for INCONEL alloy 718. Alloy 783 has hot working characteristics similar to alloy 718, and grain refinement is assisted by working within the β phase precipitation temperature range (see Fig. 3).

Summary and Conclusions

INCONEL alloy 783 is a low coefficient of thermal expansion superalloy whose Al and Cr content provides resistance to oxidation. The high Al content within its low-expansion Ni–Co–Fe matrix results in an austenitic (γ) matrix capable of γ' and β phase precipitation. The alloy is age hardenable by γ' precipitation heat treatments compatible with other superalloys, such as alloy 718. Control of β phase precipitation through processing and heat treatment results in reduced 538°C crack growth rates in air. This signifies a resistance to the SAGBO mechanism, which is often responsible for cracking of superalloys in this temperature regime. In current practice, β phase is utilized for grain refinement during processing, then is partially solutioned and re-precipitated at grain boundaries for a balance between rupture life and ductility. These mechanisms offer a solution to the oxidation and SAGBO problems that have plagued low-Cr, γ' strengthened superalloys since their inception.

The combination of both general oxidation and SAGBO resistance, low CTE, low density, and high yield and rupture strengths provides a useful combination of engineering properties for gas turbine applications.

®INCONEL and INCOLOY are trademarks of the INCO family of companies.

References

1 Smith, D. F., and Smith, J. S., "A History of Controlled, Low Thermal Expansion Superalloys," *Physical Metallurgy of Controlled Expansion Invar-Type Alloys,* TMS, Warrendale, PA, 1990, p. 253.

2 Sadananda, S., "Creep Crack Growth in Alloy 718," *Metallurgical Transactions,* Vol. 8A, Mar. 1977.

3 Liu, C. T., and Sikka, V., "Nickel Aluminides for Structural Uses," *Journal of Metals,* May 1986, pp. 19–21.

4 Heck, K. A., "The Effects of Silicon and Processing on the Structure and Properties of INCOLOY Alloy 909," *Physical Metallurgy of Controlled Expansion Invar-Type Alloys,* TMS, Warrendale, PA, 1990, p. 273.

5 Heck, K. A., Smith, D. F., Holderby, M. A., and Smith, J. S., "Three Phase Controlled Expansion Superalloys With Oxidation Resistance," *Superalloys 1992,* TMS, Warrendale, PA, 1992, p. 217.

APPENDIX

Table A Nominal alloy compositions (weight percent) and oxidation resistance comparison

Alloy	Ni	Fe	Co	Al	Nb	Ti	Cr	Si	704°C Ox. Resistance	538°C SAGBO Resistance
783	28.5	Bal.	34.0	5.4	3.0	0.1	3.0	-	Good	Good
909	38.0	Bal.	13.0	<0.1	5.0	1.5	<0.5	0.4	Poor	Marginal
907	37.4	Bal.	14.4	<0.1	4.8	1.5	<0.5	-	Poor	Marginal
903	38.8	Bal.	14.1	0.9	3.0	1.4	<0.5	-	Poor	Poor
718*	53.0	Bal.	-	0.6	5.1	0.9	19.0	-	Good	Good

* Not a low CTE alloy, but has benchmark properties used for comparison.

Table B Effect of heat treatment on room temperature tensile (RTT) and 649°C/586 MPa combination smooth-notched (Kt 3.7) stress rupture (SRU) properties: hot rolled seamless rings solution annealed 1121°C/1 h, air cooled + age hardened as shown below

Aging Heat Treatment	RTT YS, MPa	RTT EL, %	SRU Life, h	SRU EL, %
High Temperature Anneal, Air Cool + Isothermal Aging Heat Treatments				
732°C/8h, AC	644	31	2.1	Notch
788°C/16h, AC	591	29	60.7	34
843°C/8h, AC	505	34	34.7	34
High Temperature Anneal, Air Cool + Two-Step Aging Heat Treatments				
732°C/8h, FC to 621°C/8h, AC	749	27	10.1	Notch
788°C/16h, FC to 621°C/8h, AC	753	23	52.4	16
High Temperature Anneal, Air Cool + Three-Step Aging Heat Treatment				
843°C/2h, AC + 718°C/8h, FC to 621°C/8h, AC	780	24	54.3	26

Notes: AC = Air Cooled to room temperature; WQ = Water Quenched to room temperature
FC = Furnace Cooled 56°C/h to temperature shown; YS = 0.2% Offset Yield Strength;
EL = Elongation after fracture; Notch = Fractured in notched section at life hours shown

Table C Effect of each heat treatment step on alloy 783 structure

Step	Effect
1121°C/1h, AC	Full recrystallization Slight grain growth Partial solutioning and spheroidization of β phase Compatible with high temperature brazing
843°C/2-4h, AC	Precipitation of additional β phase in grain boundaries Stabilization
718°C/8h, FC to 621°C/8h, AC	γ' age for strength Compatible with INCONEL alloy 718 aging treatment

Table D Salt spray (fog) testing comparisons

Alloy	Specimen Code	Exposed Surface Corrosion Coverage, %	Corrosion Rate, 10^{-6} m/yr	Maximum Pit Depth, 10^{-6} m
718	1	0	2.5	No Attack
	2	0	2.5	No Attack
909	3	40	43.	80
	4	40	45.	50
783	5	6	8.	330
	6	1	5.	No Attack

Notes:

1. Tested to ASTM B117-85 for 720 hours at 35°C. All specimens with 120 grit sanded surface.
2. Specimens were nominally 12.7 mm dia. x 51 mm length cylinders.

Oxidation Resistance and Critical Sulfur Content of Single Crystal Superalloys

J. L. Smialek
NASA Lewis Research Center,
21000 Brookpark Rd.,
Cleveland, OH 44135
msmial@lims02.lerc.nasa.gov

Single crystal superalloys had greatly improved cyclic oxidation resistance when their sulfur content was reduced from impurity levels, typically 5–10 ppmw in past years, down to 1 ppmw or below currently. Excellent alumina scale adhesion has been documented for PWA 1480, PWA 1484, Rene'N5, Rene'N6, and CMSX 4, all without reactive element (Y) additions. Hydrogen annealing was used for effective desulfurization to below 0.1 ppmw, as well as for achieving controlled intermediate levels. This paper summarizes the direct relationship between cyclic oxidation behavior and sulfur content. An adhesion criterion has been proposed based on the concentration of sulfur needed to initiate spallation due to a monolayer of interfacial segregation. This suggests that a level down to ~0.2 ppmw would be needed to maximize adhesion for a 1 mm thick sample. It is in reasonable agreement with the experimental results.

Introduction

Historical Background. For many decades the dramatic effect of trace amounts of reactive elements on alumina and chromia scale adhesion has been recognized and widely studied. Various theories have been used to account for such behavior, such as pegging, vacancy sink, growth stress, and scale plasticity. About ten years ago, the connection between scale adhesion and sulfur segregation was reported independently by Smeggil et al. (1986), Lees (1987), Luthra and Briant (1986), and Ikeda et al. (1983). These studies found strong surface segregation of sulfur from very low levels in the bulk, which could then be curtailed by the addition of reactive elements. Subsequent studies confirmed that adhesion could be produced by just reducing the sulfur impurity level, without the need for reactive elements (Smialek, 1987; Smeggil, 1987; Melas and Lees, 1988; Ikeda et al., 1989). Discussion of the exact nature of sulfur segregation and its effects on alumina scale growth continues (Meier et al., 1995; Grabke et al., 1995). Nevertheless, there is general agreement that reducing the sulfur level produces a first order improvement in scale adhesion in the absence of reactive elements.

Historically, scale adhesion has been effectively achieved by the addition of reactive elements. For many commercial systems relying on protective alumina scales (e.g., polycrystalline NiCrAlY coatings or FeCrAlY heating elements), the direct addition of 0.1 percent Y was more practical than removing ppm levels of sulfur. It is assumed that the reactive elements, which are strong sulfide formers, preclude sulfur segregation by gettering it in the bulk.

Conventional wisdom has often held that advances in superalloy mechanical properties usually brought about a corresponding detriment in oxidation behavior due to nonprotective NiO, $NiCr_2O_4$, and TiO_2 scale growth. However, more recent alloys have become more oxidation resistant, due in part to high aluminum and refractory metal contents. Continuous, interfacial Al_2O_3 formation has allowed the manifestation of a strong reactive metal dopant effect. Unfortunately, high levels of Y were initially difficult to achieve in advanced single crystal superalloys because of nonuniform Y distributions and Y reactions with mold materials. Parallel approaches have produced low sulfur (1–3 ppmw) components through strictly controlled raw materials, melting and casting procedures. Recent advances have now produced low S, low Y, highly oxidation resistant superalloys. However, defining the acceptable sulfur level is still of prime importance.

This paper is not directed toward improved melting procedures for producing low-sulfur oxidation resistant superalloys. What it does address is the concept of a critical sulfur content, i.e., the maximum tolerable without degrading scale adhesion. To this end, the oxidation behavior of superalloys is described as a function of various sulfur contents, as controlled by a laboratory hydrogen annealing process. The success of this process was first demonstrated for PWA 1480, annealed in 1 atm hydrogen at 1200° and 1300°C (Tubbs and Smialek, 1989). The present paper puts forth new results and discusses them in light of many recent studies on hydrogen annealed superalloys. The fundamental approach toward defining the concept of a critical sulfur content is now described.

Fundamental Considerations.

Sulfur Segregation. The crux of the adhesion mechanism is the tendency for sulfur to segregate at the oxide metal interface at very high levels. This occurs even when sulfur is present in the alloy at very low (ppm) levels. Both interface and surface segregation of sulfur has been found on alumina-forming systems (Grabke et al., 1995; Hou and Stringer, 1992; Smeggil et al., 1986; Luthra and Briant, 1986; Smialek and Browning, 1986; Walker and El Gomati, 1988). Furthermore, such behavior has been observed for single crystal PWA 1480 and Rene'N6 superalloys (Jayne and Smialek, 1993; Smith et al., 1995).

Equilibrium surface segregation has been treated theoretically by McLean (1957) and measured on nickel surfaces by Miyahara et al. (1985). The McLean equation for sulfur segregation on nickel was determined from the data of Miyahara (Smialek et al., 1994) to be

$$\theta/(1-\theta) = 0.19\, C_s/(1-C_s)\exp(137\ \text{kJ}/RT), \quad (1)$$

where θ is the surface coverage, relative to an assumed maximum of 0.5 atom fraction, C_s is the bulk concentration of sulfur, and T is temperature in Kelvin.

Surface segregation isotherms have been calculated from Eq. (1) and are shown in Fig. 1 for various bulk levels of sulfur.

Contributed by the International Gas Turbine Institute and presented at the 41st International Gas Turbine and Aeroengine Congress and Exhibition, Birmingham, United Kingdom, June 10–13, 1996. Manuscript received by the ASME Headquarters February 1996. Paper No. 96-GT-519. Associate Technical Editor: J. N. Shinn.

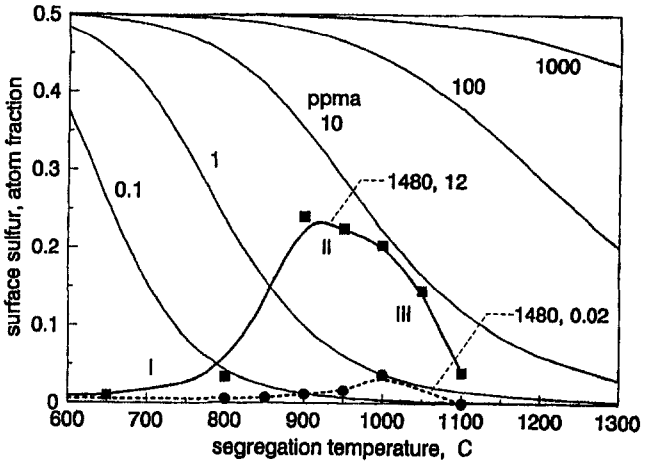

Fig. 1 Temperature dependence of sulfur surface segregation on nickel for bulk contents of 0.1 to 1000 ppma (from Eq. 1); Miyahara et al. (1985); as determined in Smialek et al. (1994)). Also shown is actual high temperature XPS data for PWA 1480 (adapted from Jayne and Smialek (1993)).

For a typical alloy impurity level of 10 ppma sulfur (~6 ppmw), high levels of surface segregation can be expected for normal turbine operating regimes of 900°–1150°C. Conversely, at very low bulk sulfur levels (0.1 ppma), very little segregation is predicted. Thus, a bulk level of 0.1 ppma would be expected to prevent spalling caused by sulfur segregation.

The bold curve represents actual hot stage XPS data for a single crystal PWA 1480 sample with 12 ppma (7.5 ppmw) bulk sulfur (Smialek, et al., 1994 as adapted from Jayne and Smialek, 1993). The three regimes observed by Miyahara et al. (1985) are also seen here: (1) below 775°C where slow diffusion prevents saturation, (2) maximum saturation at ~24 at. %, and (3) above 975°C where equilibrium saturation decreases with temperature and evaporation effects take place. Furthermore, little or no segregation was observed for a sample that was hydrogen annealed, (dashed curve) to a resultant sulfur content of only 0.015 ppma, i.e., 0.01 ppmw (Jayne and Smialek, 1993).

Similarly, Smith et al. (1995), later verified high sulfur levels (up to 27 at. percent) at the scale-metal interface of Rene'N6 oxidized at 1100°C for 1 h. Spalling was induced in the scanning Auger microscope by an impact apparatus, allowing direct interfacial sulfur measurements. This is significant in that the previous discussion applied to free surfaces, which generally show a stronger tendency for segregation. Nevertheless, in most cases, a strong parallel trend exists between segregation at free surfaces and interfaces.

Hydrogen Annealing. The desulfurization of metals by hydrogen annealing has been assumed to be a diffusion controlled surface segregation process (Smialek, 1991), in which rapid cleaning occurs by evaporation or formation of H_2S gas. Hydrogen atmospheres are required to prevent alumina scale formation, which obstructs the removal of sulfur. In order to have a range of sulfur contents over which to observe oxidation effects, samples of various thicknesses of PWA 1480 were hydrogen annealed over a range of times and temperatures. (Thickness also plays a role in defining a specific critical sulfur content, as will be describe later). Using the thin slab diffusion solution, the following approximation applies for values of $Dt/L > 0.05$:

$$C_s/C_o = 8/\pi^2 \exp(-\pi^2 D_s t/L^2), \qquad (2)$$

where C_s and C_o are the final and original average sulfur contents, D_s is the diffusion coefficient of sulfur in nickel, t is time, and L is thickness. The projected average sulfur contents for some of the test matrix conditions are shown in Fig. 2, assuming a starting level of about 10 ppm. It can be seen that very low sulfur levels are expected for a number of realistic exposures. For example, reductions to below 0.01 ppm sulfur are predicted for 0.5 mm samples, annealed at 1200°C, for 20 h. Also, the sulfur content can be varied within an intermediate range. (This paper presents the results for 0.5 mm (20 mil) samples only).

Previously, chemical analyses of sulfur in hydrogen annealed PWA 1480 samples were compared to the results calculated by the thin slab diffusion equation, using the diffusivity of sulfur in nickel. Reasonable agreement was obtained (Smialek and Tubbs, 1995). However, the annealing process appears to become less efficient at about 0.1 ppmw sulfur (Smialek et al., 1994), below which desulfurization is much slower than that predicted from diffusion kinetics.

Experimental Procedure

The new data was obtained from polycrystalline bar stock of PWA 1480, electrodischarge machined to 0.5 × 12 × 25 mm coupons. These were polished through 600 grit emery, cleaned in detergent, and rinsed in ethanol. The starting sulfur content was determined to be about 11 ppmw by GDMS, glow discharge mass spectroscopy (Tubbs and Smialek, 1989). Hydrogen annealing was performed in a flowing H_2/Ar mixture in high purity alumina tubes. Times and temperatures varied from 8–100 h and 1000°C to 1300°C, respectively. All samples appeared clean and metallic, with less than ±0.03 mg/cm^2 weight change after annealing.

Cyclic oxidation was performed in air in a vertical tube furnace, with automatic timers, counters, and pneumatically controlled specimen insertion. The test was performed at 1100°C (2012°F) with a cycle frequency of 1 h; the samples were weighed at various intervals up to 1000 h. Scales were characterized by X-ray diffraction and SEM.

Results and Discussion

Gravimetric Data. The effect of annealing temperature on the 1100°C cyclic oxidation weight change curves is shown in Fig. 3. Here, the specimen thickness was 0.5 mm (20 mils) and the annealing time was 20 h. For these conditions, the 1000° and 1100°C anneals did little to improve the cyclic oxidation resistance over that of the as-received (unannealed) control sample. All three conditions exhibited more than 20 mg/cm^2 weight loss after 500 1 h cycles. The 1200° and 1300°C annealing treatments, however, resulted in 1000 h weight changes of +0.10 and −3.4 mg/cm^2, respectively. This represents a very

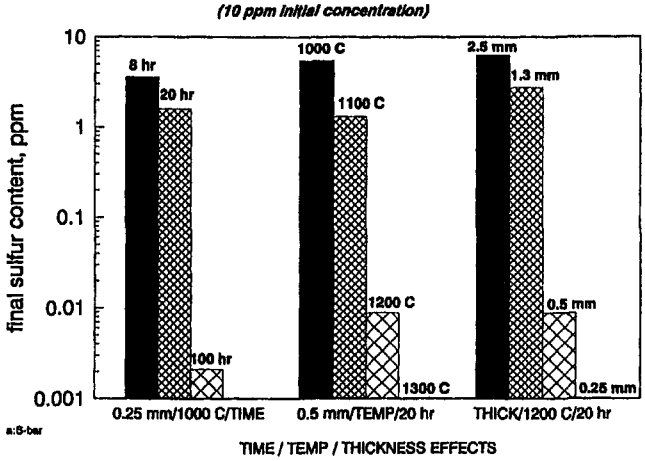

Fig. 2 Effect of hydrogen annealing parameters on desulfurization, as predicted by Eq. (2)

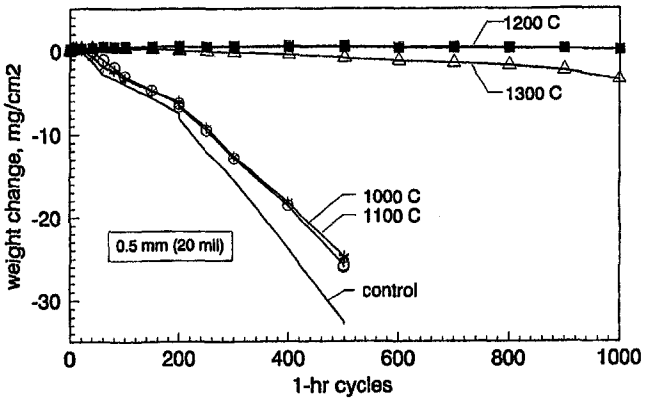

Fig. 3 Effect of hydrogen annealing temperature (for 20 h anneals) on the 1100°C cyclic oxidation behavior of PWA 1480

significant improvement. (It should be noted that the degradation of the 1300°C sample was related to the partial melting that occurred upon annealing and the attendant modification of oxidation behavior).

The effect of annealing time on oxidation behavior is shown in Fig. 4. These were also 0.5 mm samples and were all annealed at 1200°C. Here, a significant improvement was noted by only an 8 h anneal, producing a weight loss of only 6.7 mg/cm^2 after 1000 h. The 1000 h weight changes of the 20, 50, and 100 h samples were all excellent (+0.10, +0.36, and +0.16 mg/cm^2, respectively).

These results are in complete agreement with prior studies on hydrogen annealed PWA 1480 (Smialek and Tubbs, 1995; Meier et al., 1995). The weight change after 200 and 1500 oxidation cycles at 1100°C was +0.33 and −1.0 mg/cm^2, respectively. Furthermore, similar results have been obtained for PWA 1484, Rene'142, Rene'N5 and Rene'N6 without *Y*, and CMSX 4. These results are summarized in Table 1 along with all pertinent references. In these studies, hydrogen annealing was performed at 1200° to 1280°C for 30–100 h, which resulted in remarkable benefits in cyclic oxidation at 1100° to 1200°C for times ranging from 200 to 1500 h.

X-Ray Diffraction. Scale phases were identified from X-ray diffractometer scans. The results are shown in Table 2. The major phases are Al_2O_3, $Ni(Al,Cr)_2O_4$, and $CrTaO_4$. A greater relative amount of Al_2O_3 is noted for the more oxidation resistant samples, and more $NiCr_2O_4$ and $CrTaO_4$ for the samples with poor oxidation resistance. This is substantially the same result obtained previously for hydrogen annealed PWA 1480 (Smialek and Tubbs, 1995). Similarly, the scale on as-received Rene'N5 (without *Y*) contained similar amounts of $CrTaO_4$-$NiTa_2O_6$, $NiAl_2O_4$, and Al_2O_3 after 500 1 h cycles at 1150°C. With hydrogen annealing, the scale was primarily Al_2O_3 after 1000 h (Smialek et al., 1994).

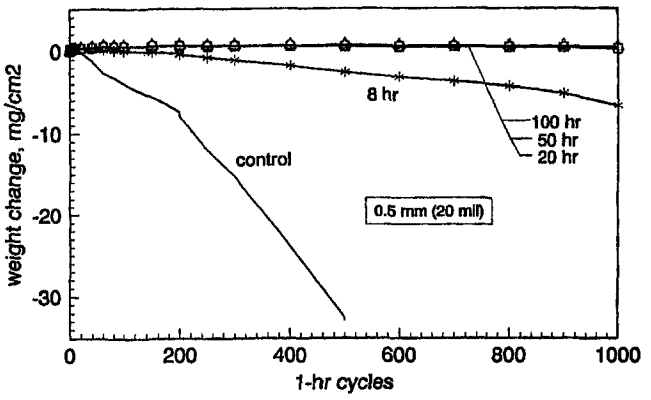

Fig. 4 Effect of hydrogen annealing time (for 1200°C anneals) on the 1100°C cyclic oxidation behavior of PWA 1480

Table 1 Summary of cyclic oxidation improvements for superalloys by hydrogen annealing and desulfurization

ALLOY anneal T / t	sulfur, ppmw	temp., C	time, hr	weight, mg/cm2	reference
PWA 1480	8.8	1100	200	-7.6	Tubbs, Smialek, 1989
1300 C/100 hr	0.04	1100	200	+0.33	(Smialek, Tubbs, 1995)
PWA 1480	11	1100	500	-32.9	Smialek, 1996
1200 C/100 hr	N.A.	1100	900	+0.31	(this study)
PWA 1480	6	1100	400	-20.0	McVay et Al, 1992
1200 C/100 hr	N.A.	1100	1500	-1.0	(Meier et al., 1995)
PWA 1484	5	1100	1000	-20.0	McVay et al., 1992
1200 C/100 hr	N.A.	1100	1200	+0.15	(Meier et al., 1995)
PWA 1484	8-10	1180	180	-10.0	Allen et al., 1994
1300 C/50 hr	1	1180	800	+0.95	
(MgO coated)					
Rene'142	6.3	1150	1000	-19.9	Smialek et al., 1994
1280 C/100 hr	0.3	1150	1000	+0.96	
Rene'N5	3.2	1150	500	-23.3	Smialek et al., 1994
1280 C/100 hr	0.2	1150	1000	+0.87	
Rene'N6	4.3	1200	200	-39.3	Smith et al., 1995
1250 C/30 hr	0.08	1200	200	-0.76	
CMSX 4	2.8	1200	240	-6.0	Kircher et al., 1991
1200 C/10 hr	0.1	1200	690	+0.18	

Table 2 Effect of hydrogen annealing parameters on scale phases formed on PWA 1480 after cyclic oxidation at 1100°C for 500 h

20 hr anneals	control	1000 C	1100 C	1200 C	1300 C
(effect of temp.)	CrTaO4	CrTaO4	CrTaO4	Al2O3	Al2O3
	NiCr2O4	Al2O3	NiCr2O4	NiAl2O4	NiAl2O4
	NiAl2O4	NiCr2O4	NiAl2O4	CrTaO4	CrTaO4
		NiAl2O4	Al2O3		
1200 C anneals	control	8 hr	20 hr	50 hr	100 hr
(effect of time)	CrTaO4	Al2O3	Al2O3	Al2O3	Al2O3
	NiCr2O4	NiAl2O4	NiAl2O4	NiAl2O4	NiAl2O4
	NiAl2O4	CrTaO4	CrTaO4	CrTaO4	CrTaO4

A more detailed characterization of as-received Rene'N6 (without *Y*) oxidized at 1200°C for 200 cycles showed coarse grained NiO surface scales, with inner $NiAl_2O_4$ and Al_2O_3 layers eventually replaced by $NiCr_2O_4$ and Cr_2O_3 (Smith et al., 1995). With hydrogen annealing, an outer NiO layer was still formed, an inner layer of $CrTaO_4$ changed to $NiTa_2O_6$, and a mixed $NiAl_2O_4$ + Al_2O_3 layer remained at the metal interface.

Effect of Sulfur Content. The 500 h weight change of all the samples tested is shown in Fig. 5 as function of the sulfur content predicted from Eq. (2), assuming an initial sulfur content of about 10 ppmw. The sulfur level of the 1000° and 1100°C annealed samples was predicted to be >1 ppmw, and their performance was only marginally improved. The sulfur level of the sample annealed at 1200°C for 8 h is predicted to be 0.3 ppmw, and its performance was notably improved. Finally, the annealing treatments for longer times or higher temperatures

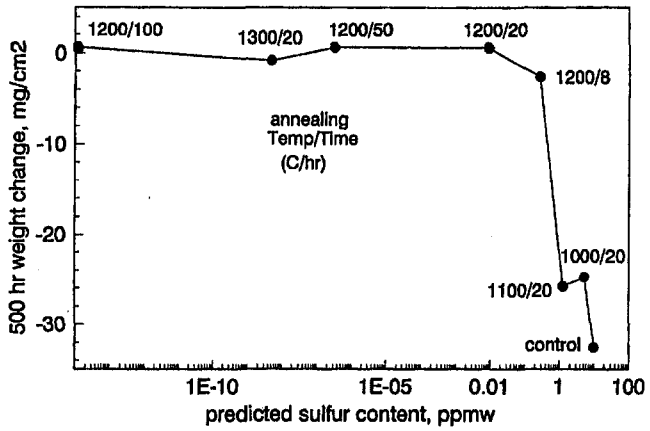

Fig. 5 Relationship between 1100°C cyclic oxidation behavior and the sulfur content predicted by Eq. (2)

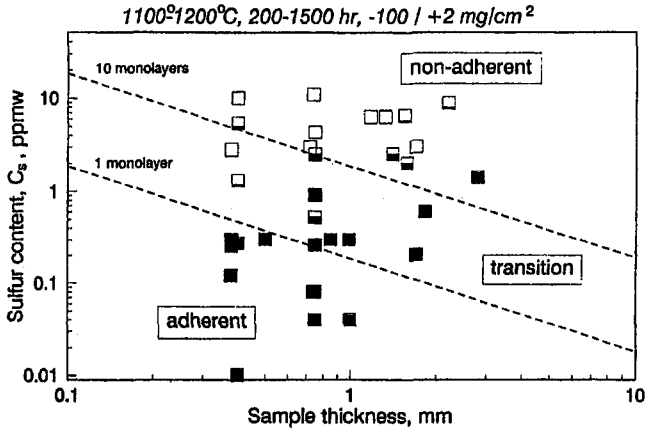

Fig. 7 Adhesion map showing proposed critical sulfur content based on 1 monolayer segregation criterion. Solid symbols represent actual data for adherent hydrogen annealed superalloy samples; open symbols represent nonadherent behavior of unannealed samples. (Adapted from Smialek et al. (1994).

produced excellent behavior for predicted residual sulfur contents of <0.01 ppmw.

It is emphasized that these are only predicted sulfur levels intended to illustrate the primary trend. Critical values can only be unequivocally determined after analysis by GDMS is obtained. Prior experience suggests that 0.01 ppmw will be near the minimum sulfur level obtained for any condition and that those predicted above 1 ppmw will be in approximate agreement with the analyzed value.

Various intermediate sulfur values were obtained by GDMS in the studies of Table 1. Cyclic oxidation weight change is plotted against these actual analyzed sulfur values in Fig. 6. The dashed curves indicate the band within which data from all various alloys and oxidation exposures lie. At the high sulfur (unannealed) side of the plot, the band is quite wide. But at the low sulfur end (extensive annealing), the band contracts considerably to a tight range of small weight changes. Because of the various test temperatures and durations, there is a spread in the weight change data from one investigation to the other. However, each test series follows a similar trend: as the sulfur content is reduced below an initial value (3–10 ppmw), the final weight change diminishes from a relatively large loss, becoming much less severe at about 1 ppmw. Below 1 ppmw, most of the test programs reported small weight gains, suggesting minimal, if any, spalling. Indeed, visual observations reported negligible spalling to bare metal for low sulfur alloys (Smialek and Tubbs, 1995; Smith et al., 1995).

Adhesion Criteria. The underlying motivation of this study is to define an upper limit to the sulfur level, that would still allow maximum oxidation performance (scale adhesion)

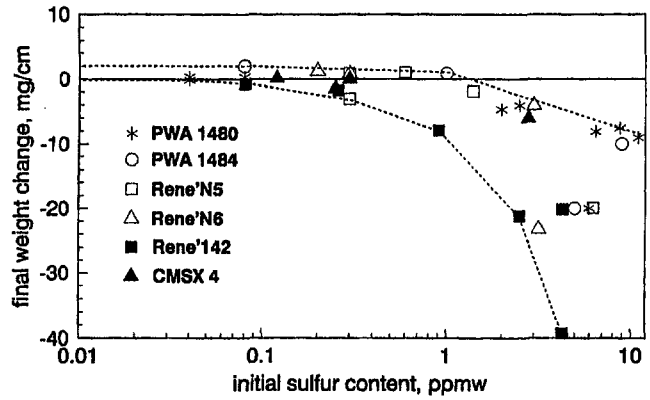

Fig. 6 Summary plot of cyclic oxidation weight change versus analyzed sulfur contents of various hydrogen annealed superalloys (from the studies of Table 1)

for actual turbine hardware. The data of Figs. 5 and 6 indicate that values between 0.2–1 ppmw give all the benefits attained by samples of the same alloy with even lower sulfur contents. This provides one useful empirically derived specification.

A more fundamental approach has been suggested to define a critical sulfur content (Smialek, 1991). This concept holds that the limit of an adhesion benefit would be obtained if the sample contains a total amount of sulfur less than that required to produce 1 monolayer of segregation. The implication is that about one monolayer is required to cause a significant spallation event; but, with no replenishment, it is unable to sustain repetitive degradation. The equivalence between bulk sulfur content and segregated monolayers has been approximated by Smialek (1991) as follows:

$$C_s = (8.27 \times 10^{-2}\ \text{gm/cm}^2) * N_m A/W \qquad (3)$$

where,

C_s = bulk sulfur content in ppmw
N_m = number of segregated monolayers
A = sample surface area in cm^2
W = sample weight in gm

The one monolayer criterion is shown on the "adhesion map" of Fig. 7 for a thin infinite plate of density = 9 gm/cm^3. All conditions above this line contain more than the indicated one monolayer of sulfur; all those below contain less than one monolayer. According to the criterion, a 1 mm sample should have less than 0.2 ppmw bulk sulfur to achieve the maximum adhesion benefit. Thicker samples require lower concentrations because they have more sulfur available for segregation at the same bulk concentration. Actual data are represented by the symbols: solid symbols represent adherent annealed samples; open samples represent nonadherent unannealed behavior; and partially filled symbols represent partially adherent behavior of samples with intermediate sulfur levels (from Smialek et al., 1994). The proposed criterion did not strictly define the boundary between adherent and nonadherent behavior. However, the experimentally determined transition (data points) did fall in the vicinity of a few monolayer equivalents. Future work will actually address the proposed adhesion effect of different sample thicknesses (0.25, 0.5, 1, 2, and 5 mm) at constant sulfur contents.

It should also be noted that the thermodynamic equilibrium surface concentration of sulfur at 0.2 ppmw (0.3 ppma) is predicted to be only 11 percent of a monolayer at 800°C from Eq. (1) (see Fig. 1). This is the temperature below which slow kinetics prevent attaining surface saturation at 50 percent. Therefore, this low bulk sulfur criterion (one monolayer equiva-

lent) also translates into a low equilibrium segregation level of sulfur.

Concluding Remarks

This summary has shown the strong dependence of single crystal superalloy oxidation resistance on low levels of sulfur impurity contents. Extraordinary improvements are possible from desulfurization by hydrogen annealing. Typical sample thicknesses ~1 mm may be easily desulfurized to <1 ppmw by annealing at 1200°–1300°C. Sulfur segregation in hydrogen annealed superalloys is essentially eliminated. This in turn produces excellent cyclic oxidation behavior at 1100°–1150°C with very small weight changes of only 0.5 to 1 mg/cm^2 after 1000 hours. Both empirical and fundamental criteria of scale adhesion suggest that a critical sulfur content of 0.1–1 ppmw is required to obtain the maximum adhesion for alloys without *Y*. The benefit of low sulfur superalloys may be taken by reducing the amount of *Y* required and by operating without a coating or by enabling extended oxidative lives with coatings.

Acknowledgments

The author is grateful to D. Humphrey and J. Wagner for performing hydrogen annealing treatments. This study draws from the major contributions of and collaborations with previous coauthors: B. K. Tubbs, D. T. Jayne, R. V. McVay, G. H. Meier, F. S. Pettit, M. C. Stasik, J. C. Schaeffer, and W. H. Murphy.

References

Allen, W. P., Bornstein, N. S., Chin, S., DeCrescente, M., Duhl, D. N., Pike, R. A., and Smeggil, J. G., 1994, "Method for Removing Sulfur from Superalloy Articles to Improve Their Oxidation Resistance," U.S. Patent 5,346,563, September 13, 1994.

Fox, P., Lees, D. G., and Lorimer, G. W., 1991, "Sulfur Segregation During High Temperature Oxidation of Chromium," *Oxidation of Metals,* Vol. 36, pp. 491–503.

Grabke, H. J., Kurbatov, G., and Schmutzler, H. J., 1995, "Segregation Beneath Oxide Scales," *Oxidation of Metals,* Vol. 43, pp. 97–115.

Hou, P. Y., and Stringer, J., 1992, "Oxide Scale Adhesion and Impurity Segregation at the Scale Metal Interface," *Oxidation of Metals,* Vol. 38, pp. 323–345.

Ikeda, Y., Nii, K., and Yoshiihara, K., 1983, "High Temperature Oxidation and Surface Segregation of Sulfur," *Proceedings JIMIS-3: High Temperature Corrosion Transactions of the Japan Institute of Metals,* Supplement 24, pp. 207–214.

Ikeda, Y., Tosa, M., Yoshihara, K., and Nii, K., 1989, "Detrimental Effect of S Segregation to Adherence of Al_2O_3 Coating Layer on Stainless Steels and Superalloys," *ISIJ International,* Vol. 29, pp. 966–972.

Jayne, D. T., and Smialek, J. L., 1993, "A Sulphur Segregation Study of PWA 1480, NiCrAl, and NiAl Using X-ray Photoelectron Spectroscopy with In-Situ sample Heating," *Microscopy of Oxidation 2,* S. B. Newcomb and M. J. Bennett, eds., Institute of Metals, London, pp. 183–196.

Kircher, T. A., Khan, A., and Pregger, B., 1991, paper presented at Aeromat 91, Long Beach, CA, ASM, 1991.

Lees, D. G., 1987, "On the Reasons for the Effects of Dispersions of Stable Oxides and Additions of Reactive Elements on the Adhesion and Growth-Mechanisms of Chromia and Alumina Scales—The Sulfur Effect," *Oxidation of Metals,* Vol. 27, pp. 75–81.

Luthra, K. L., and Briant, C. L., 1986, "Adhesion of Oxide Films on MCrAlY Alloys," *Fundamental Aspects of High Temperature Corrosion—II,* D. Shores and G. Yurek, eds., *The Electrochemical Society,* Pennington, NJ, 86-9, pp. 187–199.

McLean, D., 1957, *Grain Boundaries in Metals,* Clarendon Press, Oxford.

McVay, R. V., Williams, P., Meier, G. H., Pettit, F. S., and Smialek, J. L., 1992, "Oxidation of Low Sulfur Single Crystal Nickel-Base Superalloys," *Superalloys 1992,* S. D. Antolovich et al., eds., TMS-AIME, Warrendale, PA, pp. 807–816.

Meier, G. H., Pettit, F. S., and Smialek, J. L., 1995, "The Effects of Reactive Element Additions and Sulfur Removal on the Adherence of Alumina to Ni- and Fe-Base Alloys," *Werkstoffe und Korrosion,* Vol. 46, pp. 232–240.

Melas, I., and Lees, D. G., 1988, "Factors Effecting Adhesion of Chromia Scale on Chromium," *Mater. Sci. and Techn.,* Vol. 4, pp. 455–456.

Miyahara, T., Stolt, K., Reed, D. A., and Birnbaum, H. K., 1985, "Sulfur Segregation on Nickel," *Scripta Met.,* Vol. 19, pp. 117–121.

Smeggil, J. G., Funkenbusch, A. W., and Bornstein, N. S., 1986, "A Relationship Between Indigenous Impurity Elements and Protective Oxide Scale Adherence Characteristics," *Metall. Trans.,* Vol. 17A, pp. 923–932.

Smeggil, J. G., 1987, "Some Comments on the Role of Yttrium in Protective Oxide Scale Adherence," *Mater. Sci. and Engineer.,* Vol. 87, pp. 261–265.

Smialek, J. L., 1987, "Adherent Al203 Scales Produced on Undoped NiCrAl Alloys," *Metall. Trans.,* Vol. 18A, pp. 164–17.

Smialek, J. L., 1991, "Effect of Sulfur Removal on Al_2O_3 Scale Adhesion," *Metall. Trans.,* Vol. 22A, pp. 739–752.

Smialek, J. L., and Browning, R., 1986, "Current Viewpoints on Oxide Adherence Mechanisms," *High Temperature Materials Chemistry III,* R. Rapp, ed., The Electrochemical Society, Pennington, NJ, pp. 259–271.

Smialek, J. L., Jayne, D. T., Schaeffer, J. C., and Murphy, W. C., 1994, "Effects of Hydrogen Annealing, Sulfur Segregation and Diffusion on the Cyclic Oxidation Resistance of Superalloys: A Review," *Thin Solid Films,* Vol. 253, pp. 285–292.

Smialek, J. L., and Tubbs, B. K., 1995, "Effect of Sulfur Removal on Scale Adhesion to PWA 1480," *Metall. and Mat. Trans.,* Vol. 26A, pp. 427–435.

Smith, M. A., Frazier, W. E., and Pregger, B. A., 1995, "Effect of Sulfur on the Cyclic Oxidation Behavior of a Single Crystalline Nickel-Based Superalloy," *Mat. Sci. and Engineer.,* Vol. 203, pp. 388–398.

Tubbs, B. K., and Smialek, J. L., 1989, "Effect of Sulfur Removal on Scale Adhesion to PWA 1480," *Corrosion and Particle Erosion at High Temperatures,* V. Srinivasan and K. Vedula, eds., TMS-AIME, Warrendale, PA, pp. 459–487.

Walker, C. G. H., and El Gomati, M. M., 1988, "The Role of Zirconium and Sulphur in the Adherence of Oxides on Superalloys," *Appl. Surf. Sci.,* Vol. 35, pp. 164–172.

GTD111 Alloy Material Study

J. A. Daleo

J. R. Wilson

Wilson & Daleo Inc.,
Ancaster, Ontario,
Canada

Very few property data on this common turbine blade alloy have been published. As longer hours of service are accumulated, maintenance considerations such as developing optimum component life strategies and repair processes become important. The lack of specific material data hampers the effort of users and repair facilities to achieve optimum service from this alloy. This study measured some of the basic mechanical and metallurgical characteristics of this polycrystalline nickel base superalloy. Tensile and short-term creep rupture properties as well as microstructural and fracture characteristics are presented. Both the as-heat-treated and thermally exposed characteristics at two different temperatures are examined.

Introduction

The polycrystalline nickel base superalloy, GTD111, developed by General Electric (GE) is used extensively for high-temperature rotating buckets in land-based gas turbines. At present, for a standard gas turbine material, only a minimum amount of information detailing the metallurgical and mechanical properties of the alloy has been published. General Electric has published the nominal chemistry and has indicated that the alloy has approximately a 20°C creep rupture advantage over the industry standard blading material IN-738LC alloy [1, 6]. Beyond this no other technical information is available on the alloy.

Examination of the published GTD111 alloy composition suggests that the alloy is a derivative of the successful aircraft blade alloy René 80. The chemical compositions are the same except for slight modifications to the proportions of the elements C, Ta, and Mo, which were modified to improve the hot corrosion properties.

Evaluation of service-exposed GTD111 components as to their suitability for repair or re-use is hampered by the lack of published microstructural and mechanical property data and by limited experience with this particular material outside the manufacturer. This research program was developed to understand the material's long-term metallurgical aging characteristics and to generate enough basic material properties to reliably provide engineering services. The information gained from the experiments is directly applicable to the analysis and repair of General Electric rotating buckets in Frame 3, 5, 6, 7, and 9 engine models.

Experimental Program

The experiments and tests conducted were designed to identify some of the basic mechanical and metallurgical property characteristics of the GTD111 alloy. The material was characterized in the standard heat treated condition and after thermal exposures that bracket the operating temperature of the material in typical gas turbine rotating bucket applications. Sample material was aged at 816°C (1500°F) and 899°C (1650°F) for 5000 hours. The test program was designed to determine the effect of the thermal exposures on the mechanical properties of the alloy and to determine the microstructural stability of the material. The results, including the aging characteristics, were then compared to René 80 alloy. If the alloy had similar mechanical and aging properties to René 80, the extensive published data base for René 80 could be substituted for this alloy with reasonable confidence. If the alloy showed significant differences, further work would be required to understand the long-term aging effects and mechanical properties.

Investigation

1 GTD111 Literature Search. A literature and patent search for relevant published data did not reveal any useful information. Apparently no U.S. or Canadian patents have yet been issued for the alloy (1994).

2 Acquisition of Sample Material. The root forms of MS6001B engine run first-stage buckets were used as starting material for the study. The metal temperatures experienced by the root forms during operation are relatively low (<538°C), thus the microstructural features and starting mechanical properties do not significantly change during service. This makes the root form material representative of the original chemistry and manufacturing process used to make the buckets and suitable starting material for the experiments. A photograph of a typical bucket used in the study is illustrated in Fig. 1.

Nine buckets were used in the program. The buckets were selected so that different heats of material would be represented in the testing program, providing as broad a cross section of initial starting conditions as possible. The following buckets were made available for the study:

Serial Number	Heat Code
EIFM204757	VAF141
EIFM179744	VAF125
EIFM193232	VAF135
EIFM203610	VAF136
EIFM203785	VAF136
EIFM192260	VAF135
EIFM203939	VAF140
EIFM185892	VAF125
EIFM174645	VAF124

3 Chemical Analysis. Quantitative chemical analysis of bucket serial number EIFM174645 was performed (Table 1). The acceptable chemistry range was estimated from the published René 80 composition. The remaining GTD111 first-stage buckets used in the program were characterized by their heat codes and in the Scanning Electron Microscope, using an Energy Dispersive X-ray Analyzer.

4 Microstructural Analysis. Knowledge of the alloy microstructure is fundamental to understanding the mechanical property behavior of the material. Superalloy microstructures never reach a state of equilibrium. They continually change with time at the operating temperatures experienced in most gas turbine applications.

The starting microstructure of the GTD111 buckets is a product of the chemistry, the casting parameters, coating, and heat

Contributed by the International Gas Turbine Institute and presented at the 41st International Gas Turbine and Aeroengine Congress and Exhibition, Birmingham, United Kingdom, June 10–13, 1996. Manuscript received at ASME Headquarters February 1996. Paper No. 96-GT-520. Associate Technical Editor: J. N. Shinn.

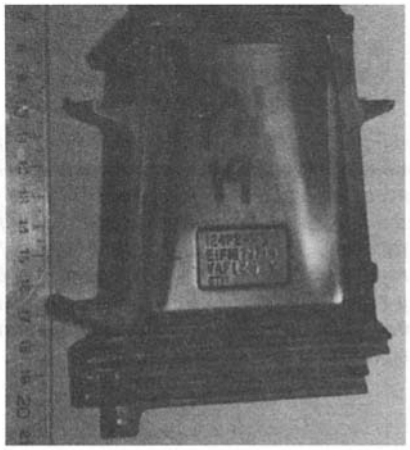

Fig. 1 A photograph of a typical Frame 6 root form used for sample material in the experiments

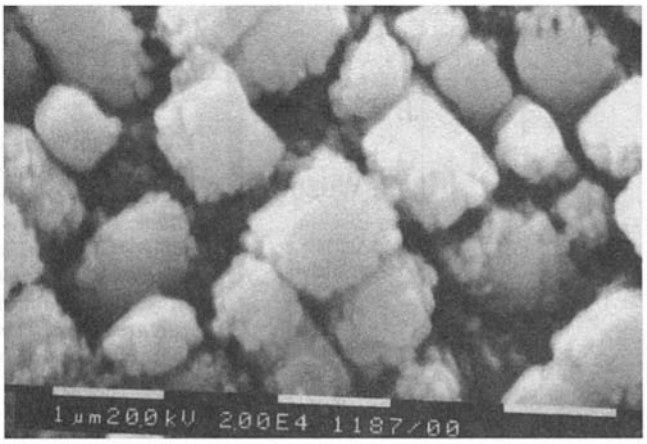

Fig. 2 A scanning electron micrograph of the GTD111 microstructure in the standard heat-treated condition illustrating the duplex gamma prime precipitates in the gamma matrix

treatment steps used to manufacture the component. The buckets used in this study were vacuum investment cast, hot isostatically pressed, machined, and processed through the General Electric GT29PLUS INCOAT coating process and the General Electric GTD111 alloy standard heat treatment.

The microstructural features generated by the processing were similar to other nickel-based superalloy casting alloys previously described by Sims et al. [2]. In general, all of the bucket castings examined appeared to be of high quality. No excessively large grains, porosity, or areas of gross shrinkage were observed. The lack of porosity in the microstructure indicates that the buckets were hot isostatically pressed as part of the original manufacturing sequence.

Samples examined from bucket serial number EIFM174645 in the SEM revealed that the GTD111 microstructure in the standard heat-treated condition consisted of a duplex gamma prime (γ') ($Ni_3(Al, Ti)$ precipitate evenly distributed in the face centered cubic (FCC) gamma (γ) matrix (Fig. 2). The average size of the primary γ' precipitates was 0.86 μm and the average size of the secondary γ' precipitates was 0.1 μm. The grain boundaries were decorated with a very thin, discontinuous $\gamma'/M_{23}C_6/M_6C$ carbide layer (Fig. 3). Scattered throughout the matrix and occasionally on the grain boundaries were eutectic γ' nodules and MC carbides (Ta, Ti, W). The grain boundaries were not finely serrated; however, they were wavy on a macro scale. Eutectic γ' and MC carbides were present both along the grain boundaries and evenly distributed throughout the matrix.

Table 1 Chemical composition

ELEMENT	EIFM174645 WEIGHT (%)	ESTIMATED GTD-111 ALLOY LIMITS (%) ***		NOMINAL RENÉ 80 ALLOY LIMITS (%)	
		MINIMUM	MAXIMUM	MINIMUM	MAXIMUM
Carbon	0.103	0.08	.12	.15	.19
Boron	0.015	0.01	.02	0.01	0.02
Chromium	13.78	13.7	14.3	13.7	14.3
Cobalt	9.21	9.0	10.0	9.0	10.0
Nickel	Remainder		Remainder		Remainder
Molybdenum	1.54	1.3	1.7	3.7	4.3
Tungsten	3.70	3.5	4.1	3.7	4.3
Tantalum	2.88	2.5	3.1	-	0.01
Aluminum	3.02	2.8	3.2	2.8	3.2
Titanium	4.81	4.7	5.1	4.8	5.2
Zirconium	0.01	0.02	0.08	0.02	0.10
Hafnium	0.04	0.02	0.08		

***Limits based on nominal GTD111 composition and René 80 tolerances.

The stability of the various microstructural phases at the operating temperatures experienced by gas turbine buckets is extremely important. In service the γ' phase increases in size with time and temperature and complex carbide reactions occur. The most important of the carbide reactions is the continued growth of the $M_{23}C_6$ carbide phase along the grain boundaries. The migration of chromium to the boundary leaves the matrix locally enriched in the γ'-forming elements nickel, aluminum, titanium etc., allowing a film of γ' to form along the boundary. Degeneration of MC carbides into $M_{23}C_6 + \gamma'$ in the matrix and along the grain boundaries accelerates the process. Examples of these phase changes were observed in the microstructure of the buckets aged at 816°C (1500°F) and 899°C (1650°F) for 5000 hours as well as in service-exposed material.

A Scanning Electron Micrograph of bucket EIFM192260 illustrating the microstructure after a 5000 hour thermal exposure at 816°C (1500°F) is presented in Fig. 4. While the primary γ' particles had not significantly grown in size during the thermal exposure, they had started to transform from cube-shaped particles to a more rounded morphology. The size of the primary γ' precipitates had grown from an average size of 0.86 μm to 0.95 μm. The secondary γ' precipitates were dissolved. The grain boundary carbides were starting to coarsen and coalesce. Continuous $\gamma'/M_{23}C_6$ films had formed.

The microstructure of bucket EIFM204757 after a 5000 hour thermal exposure at 899°C (1650°F) is presented in Fig. 5. The primary γ' precipitates had transformed from cubic shaped

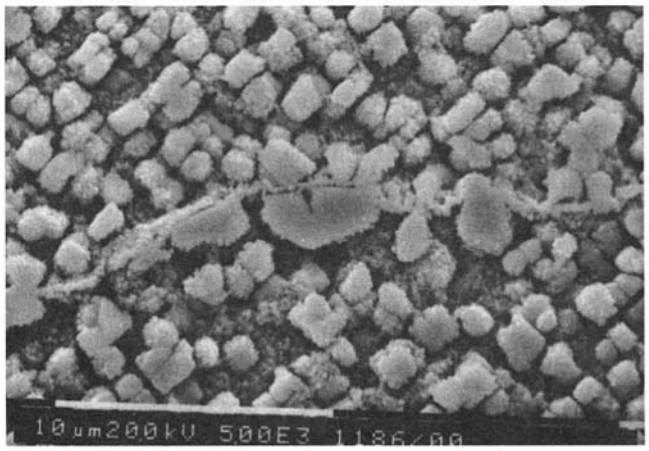

Fig. 3 A scanning electron micrograph of the GTD111 microstructure in the standard heat-treated condition illustrating a typical grain boundary

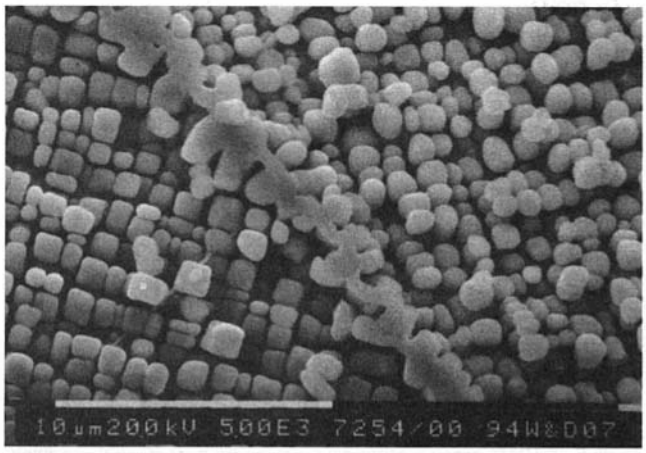

Fig. 4 A scanning electron micrograph illustrating the GTD111 microstructure after a 5000 hour thermal exposure at 816°C (1500°F)

Fig. 6 A scanning electron micrograph of the GTD111 microstructure after a 5000 hour thermal exposure illustrating eutectic gamma prime nodules and MC carbides present along the grain boundaries

particles to a rounded morphology. The size of the primary γ' precipitates had grown from an average size of 0.86 μm to 1.16 μm. The secondary γ' precipitates were consumed. The grain boundary carbides had coarsened and coalesced. Thick continuous $\gamma'/M_{23}C_6$ films had formed. Figure 6 illustrates the eutectic gamma prime and MC carbides present along the grain boundaries as well as throughout the matrix. Note the degeneration of the MC carbide along the grainboundary.

The microstructure of a GTD111 turbine bucket removed from service after approximately 23,000 hours is presented in Figs. 7 and 8. Note that the growth of matrix γ', the grain boundary carbides, and the formation of γ' films along the boundaries is continuing. Although γ' formation along grain boundaries is normal and in most cases beneficial, when the films become too thick, the boundary is imbrittled, becomes notch sensitive and is prone to cracking (Fig. 9). Continued growth of the γ' phase reduces the creep resistance of the material.

5 Mechanical Testing

5.1 Tensile Testing. Tensile samples from bucket serial numbers EIFM179744 and EIFM193232 were tested at the following parameters per ASTM E8 [3]:

21°C (70°F) 649°C (1200°F)
732°C (1350°F) 816°C (1500°F)
982°C (1800°F)

The ultimate tensile strength, 0.2 percent offset yield strength, percent elongation, and percent reduction of area were measured and are reported in Table 2.

5.2 Creep Rupture Testing. Creep rupture samples from bucket serial numbers EIFM179744, EIFM193232, and EIFM174645 were tested at the following parameters per ASTM E139 [4]:

816°C/565.4 MPa (1500°F/82 KSI)
816°C/482.6 MPa (1500°F/70 KSI)
871°C/372.3 MPa (1600°F/54 KSI)
871°C/296.5 MPa (1600°F/43 KSI)
982°C/189.6 MPa (1800°F/27.5 KSI)

Comparative creep rupture properties at the same test parameters were generated from buckets serial numbers EIFM192260 and EIFM204757 after 5,000 hour thermal exposures at 816°C (1500°F) and 899°C (1650°F).

The hours to failure, percent elongation, percent reduction of area, minimum creep rate, and resulting Larson Miller parameters of the samples tested in the standard heat treated condition are reported in Table 3. The creep rupture properties of the thermally exposed material are presented in Table 4.

Plots of percent creep deformation (strain) versus time for the creep rupture samples tested are illustrated in Figs. 10–14.

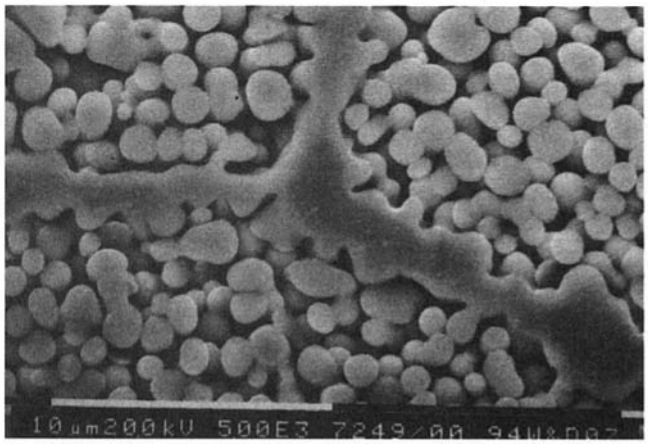

Fig. 5 A scanning electron micrograph illustrating the GTD111 microstructure after a 5000 hour thermal exposure at 899°C (1650°F)

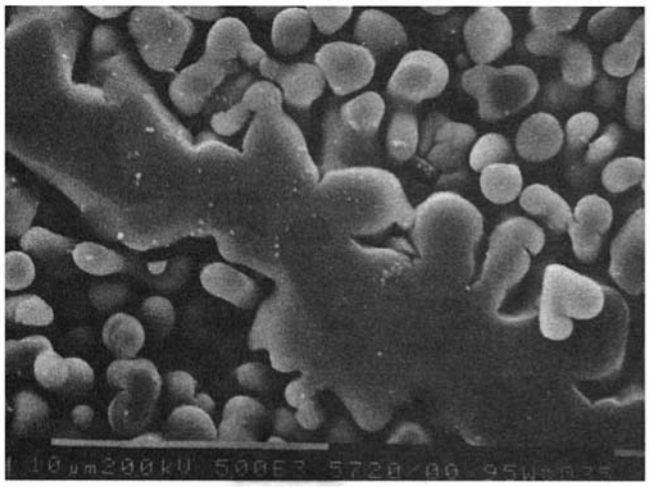

Fig. 7 A scanning electron micrograph illustrating the GTD111 microstructure observed at the leading edge of a MS6001 first-stage turbine bucket after approximately 23,000 hours of service

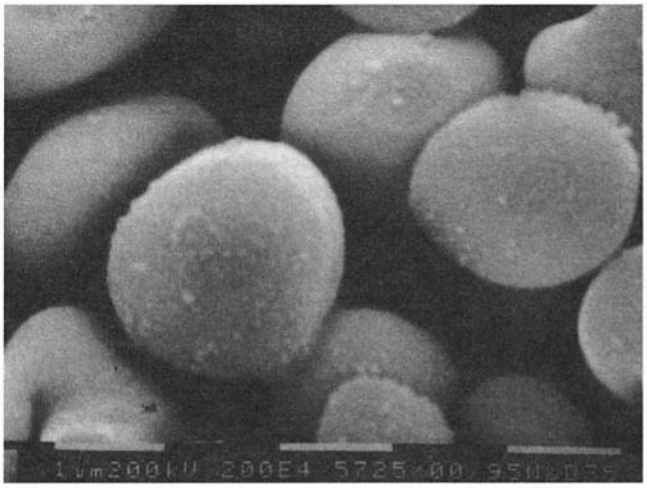

Fig. 8 A scanning electron micrograph illustrating the GTD111 microstructure observed at the leading edge of a MS6001 first-stage turbine bucket after approximately 23,000 hours of service

Compared to the material properties in the standard heat-treated condition, the creep rupture properties of GTD111 alloy had significantly degraded after the 5000 hour thermal exposures at both 816°C and 899°C with the rupture life and minimum creep rates decaying more after the 899°C exposure. The creep ductilities, however, were still acceptable. The difference in the drop in properties between the 816°C and 899°C test points was not as large as one might expect considering the extent of microstructural changes that had occurred at 899°C compared to the 816°C exposure. In GTD111 material that has received the appropriate heat treatments, the gamma prime particles and grain boundary carbides are arranged in a structure that results in the optimum creep properties. When the alloy is exposed to gas turbine operating conditions, or in this case during laboratory exposures, microstructural changes occur. The dissolution of the secondary gamma prime precipitates and the increase in the size of the strengthening gamma prime particles tends to lower the creep strength and possibly the fatigue resistance of the material. The thick continuous $\gamma'/M_{23}C_6$ films weaken the grain boundaries and act as primary pathways for fracture. Similar aging effects have been reported to reduce mechanical properties in René 80 alloy [7].

The GTD111 alloy creep rupture samples tested at the René 80 qualification parameters 982°C/189.6 MPa (1800°F/27.5 KSI) in the standard heat-treated condition passed the minimum requirements of the test. While the creep rupture properties of the thermally exposed samples had dropped significantly, the test samples both passed the minimum requirements of the test. The inability of the test parameters to discriminate between the material conditions indicates that testing GTD111 alloy at the common René 80 qualification parameters would not be a valid acceptance test to re-qualify refurbished material that has been coated and re-heat treated.

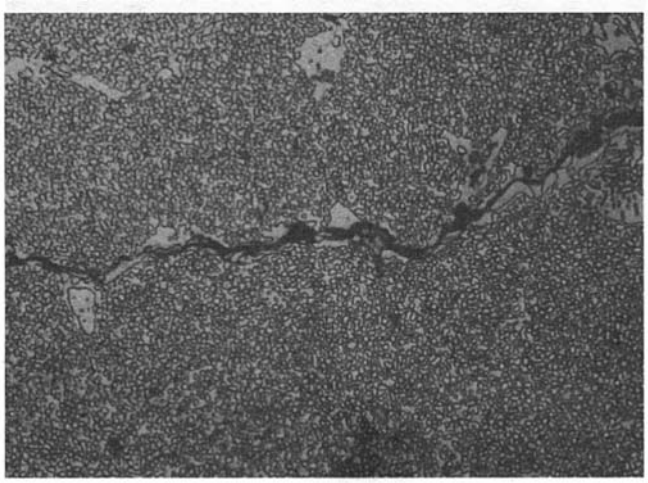

Fig. 9 A photomicrograph illustrating a fractured grain boundary observed in a MS6001 first-stage turbine bucket after approximately 23,000 hours of service (×500)

Table 2 GTD111 tensile test data

SERIAL NUMBER	TEST TEMP(°C)	UTS (MPa)	0.2% YS (MPa)	% ELONG	%R A
EIFM179744	21	1011	819	10.5	15.7
EIFM193232	21	953	836	8.8	17.7
EIFM179744	649	1109	756	12.6	18.5
EIFM193232	649	1143	724	13.7	14.7
EIFM179744	732	1031	783	13.0	21.0
EIFM179744	816	854	717	29.7	29.2
EIFM193232	816	860	678	22.8	38.1
EIFM193232	982	429	297	22.3	30.2

Table 3 GTD111 creep rupture data—standard heat-treated condition

SERIAL NUMBER	TEMP (°C)	STRESS (MPa)	LIFE HOURS	% ELONG	% R/A	MCR %ε/hr	LMP
EIFM174645	982	189.6	37.2	7.6	12.1	0.057	48,750
EIFM174645	982	189.6	38.2	9.2	10.6	0.079	48,780
EIFM179744	816	565.4	9.4	13.4	26.2	0.379	41,107
EIFM193232	816	565.4	18.4	13.9	24.2	0.310	41,679
EIFM179744	816	482.6	83.4	12.2	28.1	0.046	42,965
EIFM193232	816	482.6	111.4	14.0	19.3	0.037	43,212
EIFM179744	871	372.3	59.7	14.9	19.6	0.064	44,859
EIFM193232	871	372.3	58.6	12.9	16.7	0.071	44,842
EIFM179744	871	296.5	339.0	10.7	13.7	0.0139	46,412
EIFM193232	871	296.5	406.0	9.9	12.9	0.0084	46,574

The René 80 stress rupture qualification test parameters were originally designed as quality control tests to screen out chemistry lots/heat treatment cycles that produce material outside of the René 80 material scatter band. The stress rupture specification [4], for René 80 material, given the standard heat treatment requires a minimum time to rupture of 23 hours with 5 percent reduction in area. The GTD111 alloy acceptance test parameters are not currently available.

6 Fracture Characteristics. The fracture surfaces of the creep rupture samples were examined in the SEM and by metallographic methods. The primary fracture mode of all of the

Table 4 GTD111 creep rupture data after 5000 hour thermal exposures

SERIAL NUMBER	EXPOSURE TEMP °C	TEMP (°C)	STRESS (MPa)	LIFE HOURS	% ELONG	% R/A	MCR %ε/hr	LMP
EIFM192260	816	816	565.4	4.5	17.5	34.5	1.274	40,480
EIFM204757	899	816	565.4	2.1	7.3	7.0	1.174	39,831
EIFM192260	816	816	482.6	34.6	12.1	25.0	0.150	42,217
EIFM204757	899	816	482.6	22.0	12.3	11.9	0.226	41,813
EIFM192260	816	871	372.3	38.5	10.7	13.6	0.155	44,466
EIFM204757	899	871	372.3	16.2	13.8	23.3	0.440	43,692
EIFM192260	816	871	296.5	165.5	6.9	7.3	0.012	45,770
EIFM204757	899	871	296.5	163.1	8.3	16.2	0.023	46,757
EIFM192260	816	982	189.6	26.4	6.9	11.1	0.082	48,413
EIFM204757	899	982	189.6	26.0	7.9	13.1	0.109	48,398

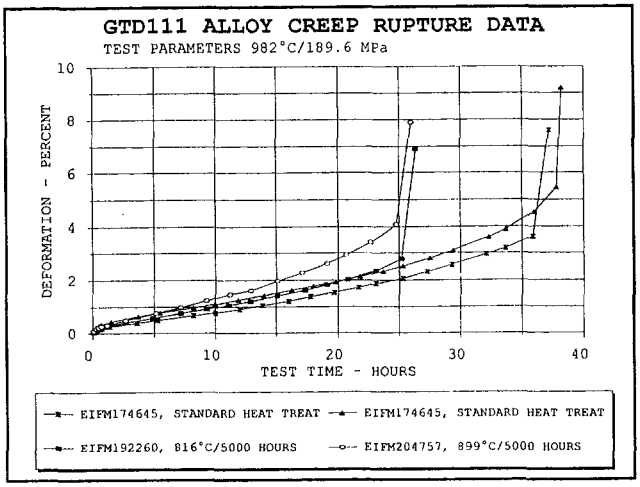

Fig. 10 A plot of percent creep deformation (strain) versus time for the creep rupture samples in the standard heat-treated condition and after thermal exposures at 816°C and 899°C

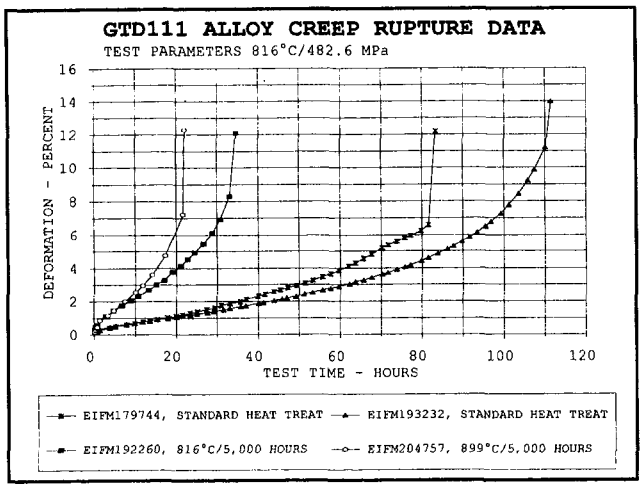

Fig. 12 A plot of percent creep deformation (strain) versus time for the creep rupture samples in the standard heat-treated condition and after thermal exposures at 816°C and 899°C

samples examined was wedge cracking along intergranular fracture paths with the cracks linking up to form shear walls during the final overload failure (Figs. 15 and 16). At the 871°C (1600°F) test temperature, the cracking mechanism was assisted by oxidation of the grain boundaries (Figs. 17 and 18). The occasional cracked MC carbide was observed at or just below the fracture surfaces. Very little secondary cracking was observed in all of the samples examined except for the samples tested at 871°C/296.5 MPa (1600°F/43 KSI). These samples were failing along multiple intergranular fracture paths.

Discussion

1 Mechanical Property Analysis. A tensile test property versus temperature plot comparing René 80 alloy and the GTD111 alloy test data in Table 2 is illustrated in Fig. 19. The tensile curves are almost identical, indicating that GTD111 alloy behaves similarly to René 80. Using René 80 tensile properties for GTD111 alloy appears to be an acceptable procedure for new material given the standard heat treatment.

A Larson–Miller curve [5] constructed from the GTD111 alloy test data in Table 3 is plotted in Fig. 20. A Larson–Miller Plot comparing the GTD111 alloy test points and René 80 data from the literature with points picked off the GTD111 Larson Miller curve published by General Electric [6] is presented in Fig. 21. The GTD111/René 80 alloy Larson–Miller curves appear to be identical.

A least-squares regression model ($Y = \beta_0 + \beta_1 X + e$) was fitted to the GTD111 creep rupture data presented in the Larson–Miller form. The least-squares fit, the 95 percent confidence intervals about the mean and the 95 percent prediction interval for an individual observation were calculated and plotted in Fig. 22. For a first-order estimate of the confidence limits using limited data, the model was a good fit of the experimental and published data. More low stress, intermediate temperature (816°C to 899°C), long term creep data points are needed to accurately fit the lower end of the curve.

The creep rupture data points measured after the 5000 hour laboratory thermal exposures at 816°C and 899°C are also plotted in Fig. 22. The creep rupture properties have dropped below the 95 percent confidence interval of the mean as well as the individual prediction levels at the 816°C/565.4 MPa (1500°F/82 KSI) and 816°C/482.6 MPa (1500°F/70 KSI) parameters. As the test temperature was increased and the testing stress reduced, the deterioration of the aged properties did not appear to be as significant. The wide discrepancy in the rate of creep

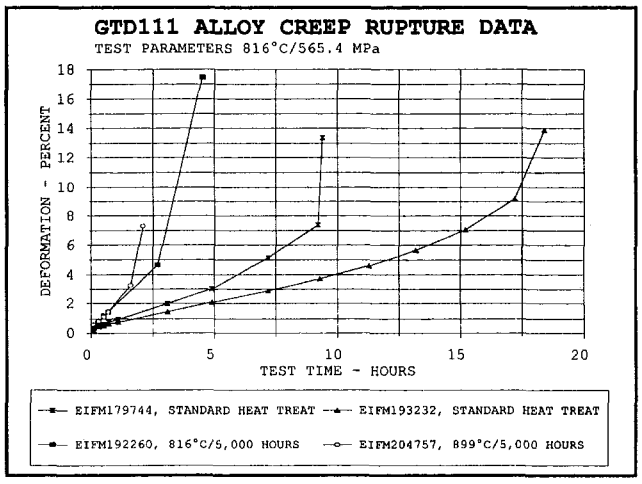

Fig. 11 A plot of percent creep deformation (strain) versus time for the creep rupture samples in the standard heat-treated condition and after thermal exposures at 816°C and 899°C

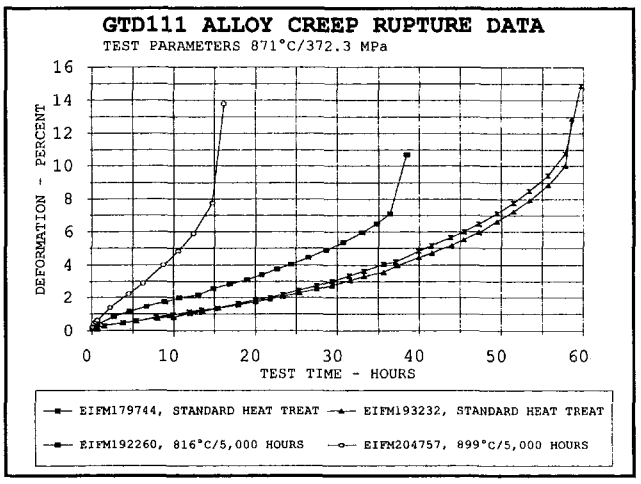

Fig. 13 A plot of percent creep deformation (strain) versus time for the creep rupture samples in the standard heat-treated condition and after thermal exposures at 816°C and 899°C

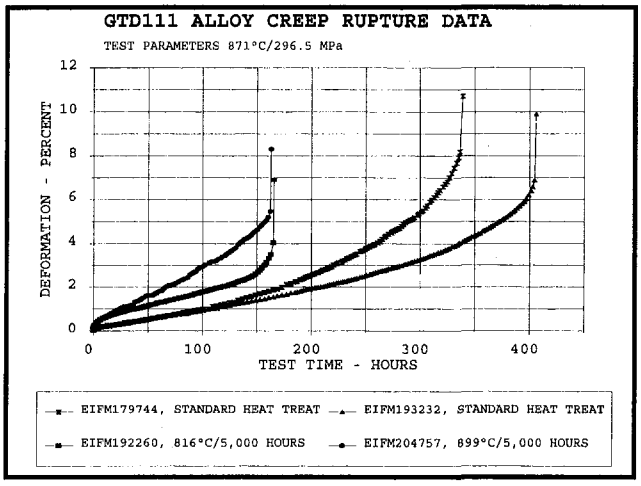

Fig. 14 A plot of percent creep deformation (strain) versus time for the creep rupture samples in the standard heat-treated condition and after thermal exposures at 816°C and 899°C

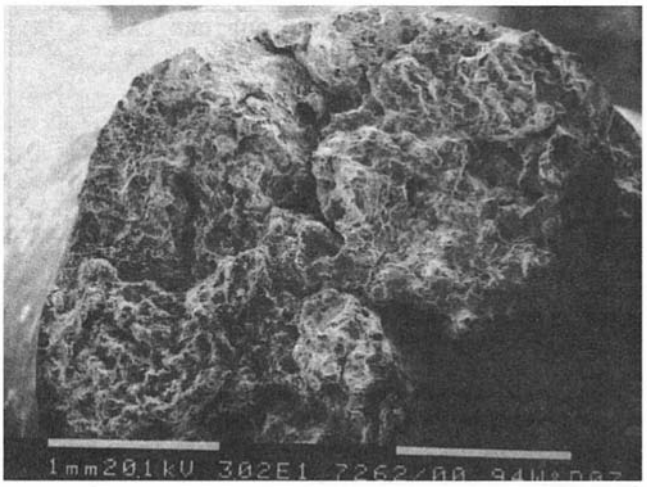

Fig. 16 A scanning electron fractograph of GTD111 alloy in the standard heat-treated condition creep tested at 871°C/296.5 MPa

rupture property deterioration between the lower temperature, higher stress creep rupture properties and the high temperature, lower stress properties was likely due to the nature of the test. At the higher test temperatures, the secondary gamma prime particles are quickly dissolved and their strengthening effect is not included in the test result either before or after the thermal exposure. However, at the lower temperature, higher stress parameters, the secondary gamma prime precipitates are not dissolved during the short duration of the test. The difference in the mechanical properties before and after the thermal exposures can be attributed to the dissolution of the secondary gamma prime precipitates.

Stress rupture data points measured from service exposed GTD111 Frame 6 and Frame 7 first stage buckets are also plotted in Fig. 22. Note that some of the service exposed points are well outside the 95 percent confidence interval of the mean. Experience with GTD111 material removed from service has revealed a loss in creep ductility as well as creep life. This may imply that the material is being imbrittled by oxygen effects previously described by Woodford [8].

2 Temperature Estimation Using the γ' Growth Rate Method. The rate of gamma prime (γ') coarsening in superalloys including René 80 [9] has been reported to follow diffusion-controlled coarsening kinetics. The data generated from the experiments define the GTD111 γ' coarsening kinetics and allowed the rate constants to be calculated. The model was then adapted to estimate metal temperatures of service run components.

The rate of gamma prime (γ') coarsening follows the diffusion controlled coarsening kinetics described by Chellman and Ardell [10]:

$$(r_F^3 - r_S^3)^{1/3} = Kt^{1/3} \tag{1}$$

where t is time in seconds, r_F is the average γ' radius in nanometers at time t, r_S is the average starting γ' radius at time 0, and K is a constant.

The rate constant K is independent of volume fraction and contains many important quantities including the temperature information. In its simplest form the rate constant can be expressed as follows [11]:

$$\ln K^3T = B - Q/RT \tag{2}$$

where T is absolute temperature, Q is the activation energy for diffusion, R is the gas constant, and B is a constant. A plot of $\ln (K^3T)$ versus $1/T$ results in a straight line with Q/R as the slope. Once Q is known, T can be estimated.

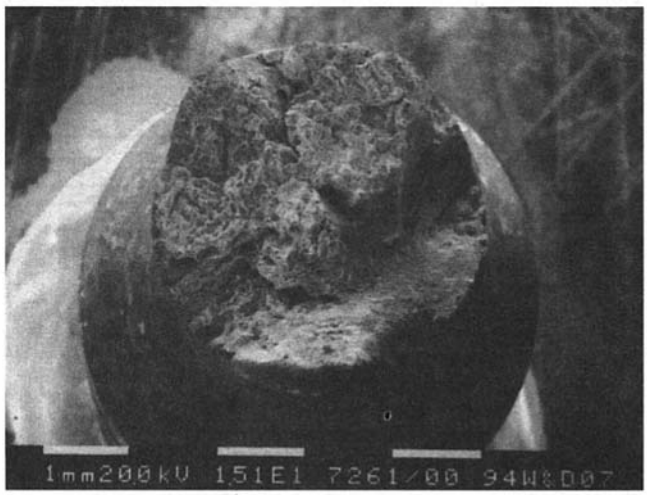

Fig. 15 A scanning electron fractograph of GTD111 alloy in the standard heat-treated condition creep tested at 871°C/296.5 MPa

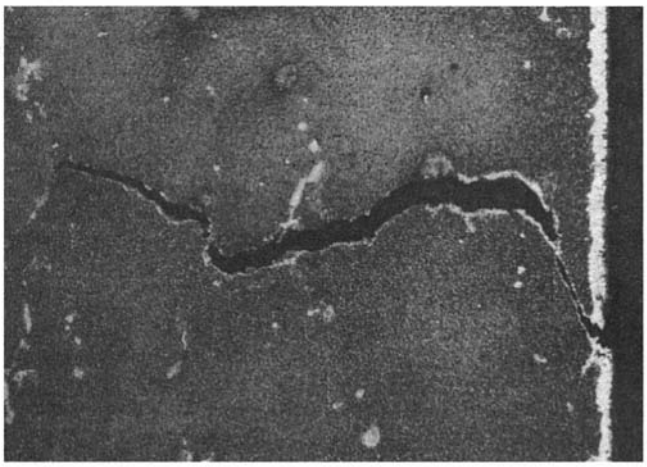

Fig. 17 A photomicrograph of GTD111 alloy, exposed at 816°C for 5000 hours, creep tested at 871°C/296.5 MPa, illustrating that the intergranular fracture mechanism was assisted by oxidation of the grain boundaries (×150)

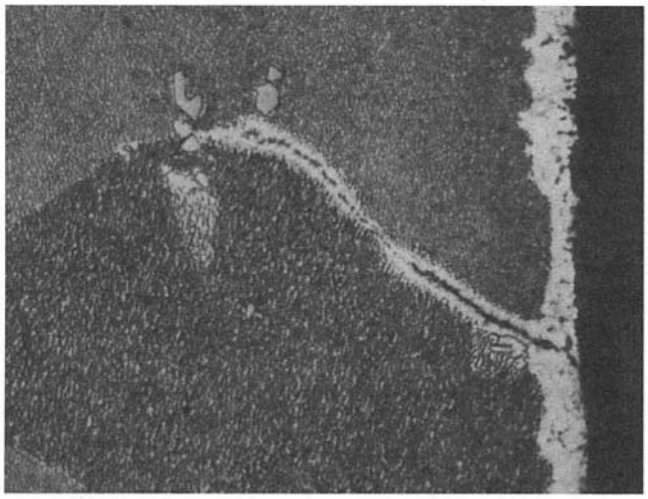

Fig. 18 A photomicrograph of GTD111 alloy, exposed at 816°C for 5000 hours, creep tested at 871°C/296.5 MPa, illustrating that the intergranular fracture mechanism was assisted by oxidation of the grain boundaries (×500)

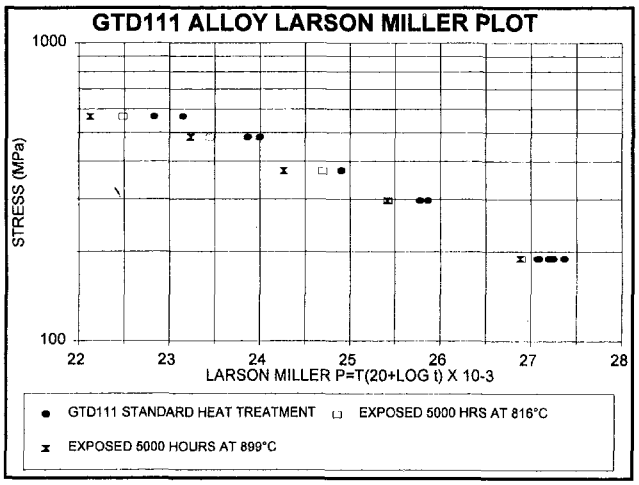

Fig. 20 A GTD111 alloy Larson–Miller Curve constructed from the test data presented in Tables 3 and 4

The activation energy for diffusion has been reported in the literature for both simple systems such as Al in Ni and Ti in Ni as well as complex superalloys such as IN-738, U500 etc. The reported activation energy ranged from 2.57 to 2.83 × 10^5 Joules/mole. The activation energy for diffusion calculated for GTD111 alloy in this experiment was 2.59 × 10^5 Joules/mole. This compares favorably with the published data, indicating that this material behaves similarly to the other basic superalloy systems and that temperature estimation based on gamma prime growth laws is a viable tool using this alloy system.

In practice this model has been used effectively to estimate metal temperatures of service run components manufactured from GTD111, IN-738LC, Udimet 520 and Udimet 710/720 alloy systems.

Conclusions

The creep rupture and tensile data generated indicate that the strength of GTD111 material is virtually identical to the published René 80 data. This indicates that until a more thorough GTD111 alloy data base is generated or becomes available in the open literature, René 80 alloy properties can be substituted for GTD111 alloy provided that the GTD111 material is in the standard heat treated condition.

Compared to GTD111 alloy, in the standard heat treated condition, the short-term creep rupture properties of the material had degraded after 5,000 hour thermal exposures at both 816°C (1500°F) and 899°C (1650°F). The creep rupture lives and minimum creep rates decayed slightly more after the 899°C exposure than the 816°C exposure.

The experimental data indicated that testing GTD111 alloy at the common René 80 stress rupture qualification parameters designed for accepting René 80 material would not be a valid acceptance test to re-qualify refurbished GTD111 material.

The rate of GTD111 gamma prime coarsening observed in the experiments compared favorably with the published data for other basic $Ni_3(Al, Ti)$ superalloy systems. Temperature estimation based on gamma prime growth laws was evaluated and proved to be a viable tool in evaluating GTD111 alloy. Temperature estimates accurate to approximately ±20°C are possible assuming that the aging rate is independent of gamma prime volume fraction and that material is exposed at relatively constant temperature.

Recommendations

The GTD111 alloy material study should be continued. The thermal exposures at typical bucket operating temperatures

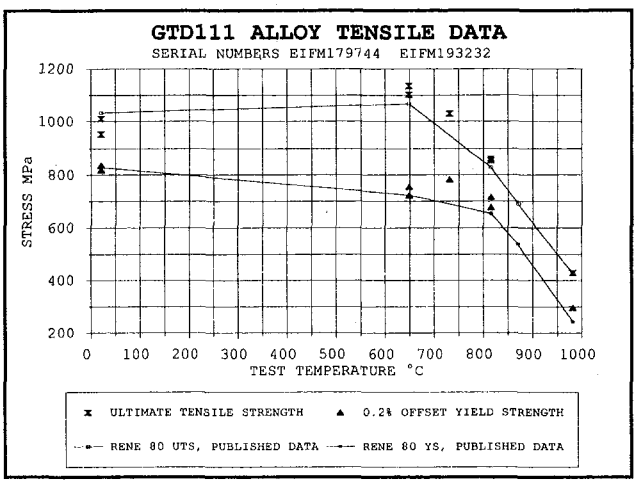

Fig. 19 A tensile test property versus temperature plot comparing the GTD111 test data with the René 80 alloy

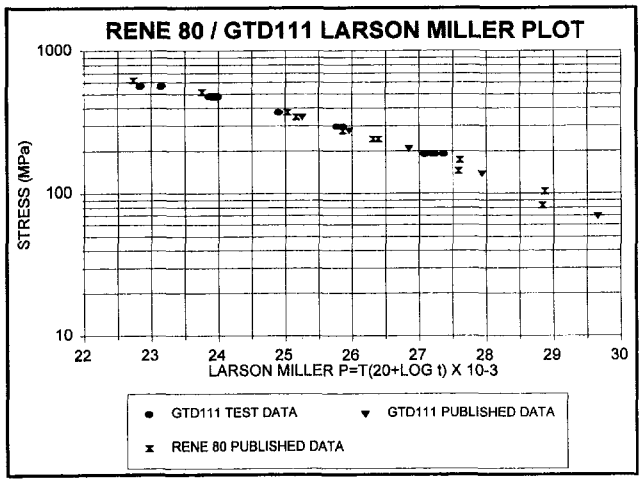

Fig. 21 A Larson–Miller plot comparing the GTD111 alloy test points with René 80 data from the literature and the GTD111 Larson–Miller curve published by General Electric

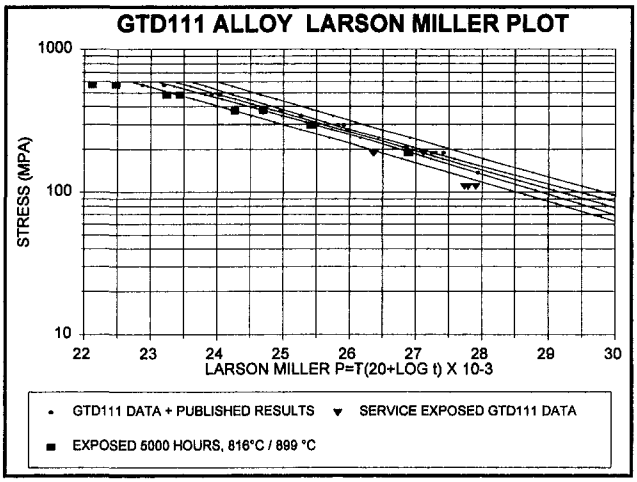

Fig. 22 A least-squares regression model ($Y = \beta_0 + \beta_1 X + e$) fitted to the GTD111 creep rupture data illustrating the fit, the 95 percent confidence intervals about the mean and the 95 percent prediction interval for an individual observation. Test data from the thermally exposed GTD111 material and select service exposed GTD111 data points are plotted.

should be continued past 10,000 hours and the metallurgical and mechanical properties re-evaluated using standard methods.

Long-term creep rupture tests should be conducted on material in the standard heat treated condition to improve the Larson Miller Curve and to further assess the long term aging characteristics of the material.

Regenerative heat treatments to restore the metallurgical and mechanical properties of service run GTD111 buckets should be developed and evaluated. Complete sets of used components should be processed and returned to service as part of the program.

A second testing program designed to develop coated and thin wall GTD111 alloy mechanical properties should also be started.

Acknowledgments

This work was partially funded by the National Research Council of Canada's Industrial Research Assistance Program. The contributions of Ron Natole of Natole Turbine Enterprises and David Hodgson and Chris Butcher of McMaster University's Institute for Materials Research are also greatly appreciated.

References

1 GE Power Systems, Turbine Technology Reference Library, GER-3569.

2 Sims, C. T., Stoloff, N. S., Hagel, W. C., eds., *Superalloys II,* A Wiley-Interscience publication, 1987.

3 "Standard Test Methods of Tension Testing of Metallic Materials," ASTM E8.

3 Standard Practice for Conducting Creep, Creep Rupture, and Stress Rupture Tests," ASTM E139.

4 Aerospace Structural Metals Handbook Specification #4217, Rene 80 alloy.

5 Larson, F. R., and Miller, J., *Trans. ASME,* Vol. 74, 1952, p. 765.

6 Schlike, P. W., Foster, A. D., Pepe, J. J., and Beltran, A. M., "Advance Materials Propel Progress in Land-Base Gas Turbines," *Advanced Materials and Processes,* April 1992.

7 "Low Cycle Fatigue of René 80 as Affected by Prior Exposure," Antolovich, S., Domas, P., J. Strudel, *Metallurgical Transactions A,* Vol. 10A, Dec. 1979.

8 Woodford, D. A., "Environmental Damage of a Cast Nickel Base Superalloy," *Metallurgical Transactions A,* Vol 12A, Feb. 1981.

9 Kolkman, H. J., "Creep, Fatigue and Their Interaction in Coated and Uncoated René 80," *Materials Science and Engineering,* Vol. 89, 1987, pp. 81–91.

10 Chellman, D. J., and Ardell, A. J., "The Coarsening of γ' Precipitates at Large Volume Fractions," *Acta Met.* Vol. 22 1974, pp. 577–588.

11 Stevens, R. A., and Flewitt, P. E. J., "The Effects of γ' Precipitate Coarsening During Isothermal Ageing and Creep of the Nickel-Base Superalloy IN-738," *Mat. Sci. and Eng.,* Vol. 37, 1979, pp. 237–247.

Aerodynamically Induced Radial Forces in a Centrifugal Gas Compressor: Part 1—Experimental Measurement

J. J. Moore

M. B. Flathers

Solar Turbines Inc.,
San Diego, CA 92123

Net radial loading arising from asymmetric pressure fields in the volutes of centrifugal pumps during off-design operation is well known and has been studied extensively. In order to achieve a marked improvement in overall efficiency in centrifugal gas compressors, vaneless volute diffusers are matched to specific impellers to yield improved performance over a wide application envelope. As observed in centrifugal pumps, nonuniform pressure distributions that develop during operation above and below the design flow create static radial loads on the rotor. In order to characterize these radial forces, a novel experimental measurement and post-processing technique is employed that yields both the magnitude and direction of the load by measuring the shaft centerline locus in the tilt-pad bearings. The method is applicable to any turbomachinery operating on fluid film radial bearings equipped with proximity probes. The forces are found to be a maximum near surge and increase with higher pressures and speeds. The results are nondimensionalized, allowing the radial loading for different operating conditions to be predicted.

Introduction

Evaluation of radial forces on the rotor is important to assess the static load margin of the shafting, bearing, and supporting structure of the machine. Furthermore, the dynamic force coefficients (K_{xx}, C_{xx}, etc.) of fluid film bearings are a strong function of radial load. If not properly designed, the radial forces may overly stiffen the bearings, thereby lowering the logarithmic decrement of the vibration modes. The result of this degradation is increased imbalance response and reduced stability of the machine. The need for accurate prediction and experimental verification of radial forces is important for sound mechanical design.

Radial loading in centrifugal pumps has been studied experimentally as early as 1936 by Binder and Knapp (1936). Stepanoff (1957) made significant contributions to the understanding of the radial loads and presented empirically based relationships to predict the forces. Stepanoff investigated the use of double tongue volutes to promote a more symmetric pressure field in the pump volute. He found a reduction, but not elimination, of the net radial force. Some efficiency improvement at off-design flows is also recorded. Agostinelli et al. (1960) investigated 16 different pump designs with specific speeds ranging from 25 to 165 (English units) using strain gages on the bearing supports to measure radial load. The authors noted that radial loading for higher specific speed pumps increases at a higher rate when operating off design. Furthermore, they reported that at higher specific speeds (>100) the flow at minimum radial load is greater than the design flow.

More modern experimental techniques use Laser-Doppler Anemometers (LDA) to observe both the steady-state and dynamic flow patterns in the pump volutes (Miner et al., 1989). The findings revealed asymmetric flow fields even at a design flow that worsened at off design. Odeja and Flack (1992) utilized LDA techniques to investigate the pressure and momentum forces for both single- and double-tongue volutes. Reductions near 50 percent were reported for a double-tongue volute at low flows.

While the radial loading of pumps has been studied extensively, little work in the area of radial loads with compressible flow has been published. Most of the experimental techniques to measure the radial forces described above employ either static pressure taps around the circumference of the volute, strain gages at the bearing supports, or measurement of the electrical current delivered to radial magnetic bearings. For a typical industrial high-pressure compressor equipped with tilting-pad oil bearings, none of these techniques are easily implemented.

Most industrial compressors are equipped with a set of orthogonally mounted (X-Y), eddy-current proximity probes adjacent to the radial bearings to measure shaft vibration. Shaft centerline position may be monitored in a two-dimensional plane by capturing the DC gap voltage from the probes. Tilting-pad bearings by design contain essentially no cross-coupled stiffness; therefore, a force vector applied to such a bearing will yield a displacement in that direction. For a given speed, the magnitude of the deflection is a function of the bearing running clearance, the load direction relative to the pad pivots, any pad deflection, and the bearing Sommerfeld number defined as:

$$S = \left(\frac{R}{C_b}\right)^2 \frac{\mu}{60}\left(\frac{N}{F_r}\right) \tag{1}$$

The smaller the Sommerfeld number, the greater the eccentricity ratio.

The experimentally obtained shaft centerline locus may be used to determine the bearing eccentricity ratio (ϵ_b), defined as the shaft eccentricity from center divided by the bearing clearance. By comparing the measured eccentricity ratios to a commercial tilting-pad bearing code (THPAD, Branagan and Barrett, 1993), the total reaction force magnitude and phase may be determined. Vectorially subtracting shaft journal weight and summing the resulting force vector at the two bearings yields the applied aerodynamic load on the centrifugal impeller. This semi-empirical technique may be easily applied to other turbo-

Contributed by the International Gas Turbine Institute and presented at the 41st International Gas Turbine and Aeroengine Congress and Exhibition, Birmingham, United Kingdom, June 10–13, 1996. Manuscript received at ASME Headquarters February 1996. Paper No. 96-GT-120. Associate Technical Editor: J. N. Shinn.

machinery operating on fluid film bearings where calculation of static radial loads is desired.

THPAD shows an almost exact correlation to the experimental data on a five-pad tilting pad bearing code presented by Gardner and Ulschmid (1974) for babbitt temperature, friction loss, and bearing drain temperature as demonstrated by Branagan and Barrett (1993). THPAD underpredicts the measured bearing eccentricity ratio of 0.66 by 8 percent for this case study even though accurate values for pad pivot stiffness, which has an effect on eccentricity, were not available when the comparison was made.

The force contribution from gas labyrinth seals and impeller cross-coupled stiffness for the gas compressor was calculated to be less than 5 percent of the aerodynamic force under all operating conditions. The influence from these components may be significant in other turbomachinery and should be verified when using this technique. The force arising from a nonuniform static pressure distribution in the inlet duct is minimized through the use of inlet guide vanes and represents less than 2 percent of the total aerodynamic load using data provided by Flathers et al. (1996). The disk-pack couplings used to drive the compressor generate less than two pounds (9 Newtons) of radial load due to misalignment. Therefore, the majority of the radial load reacted by the journal bearings arises from the impeller-volute interaction. Since the signal from the proximity probes is low-pass filtered, the results are not a function of journal vibration amplitude. Therefore, the method may be applied to both rigid and flexible rotor designs, even while operating near critical speeds.

Test Facility

The test facility used in this study is a closed-loop arrangement capable of testing in accordance with ASME PTC-10, which outlines the arrangement and location of compressor piping and instrumentation. A schematic of the closed-loop test facility is shown in Fig. 1. The test compressor is driven by a slave gas turbine engine capable of delivering greater than 3500 hp (2600 kW). A gearbox is used to provide proper speed matching to the test compressor. The test skid is fully instrumented for operation and control, as well as capturing compressor mechanical and aerodynamic performance. Standard compressor instrumentation includes temperature, pressure, flow, speed, vibration, and gas properties.

Temperature measurements include: four resistance temperature detectors (RTDs) at both compressor suction and discharge; two RTDs five diameters downstream of orifice plate; one RTD for ambient conditions; and type-K thermocouples at inlet and outlet for bearing lube oil and discharge of seal gas vent.

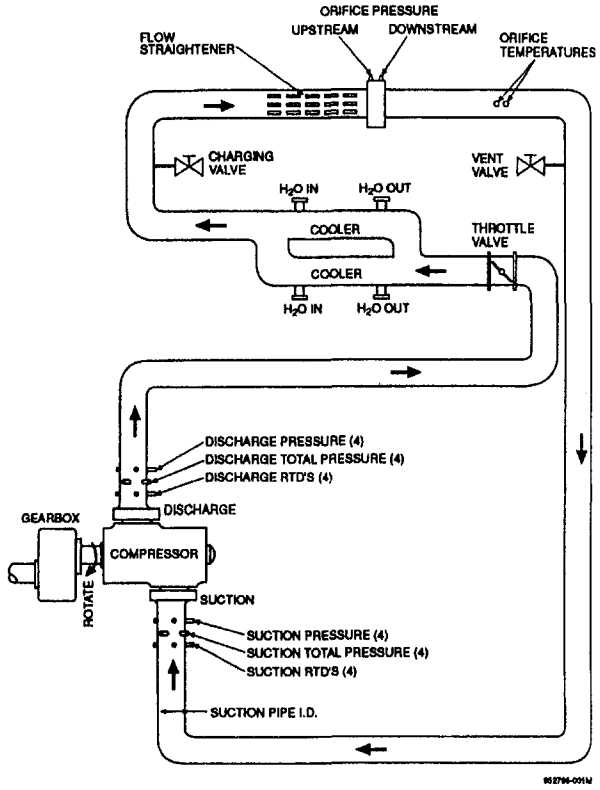

Fig. 1 Schematic of closed-loop facility

Total pressure is measured using four Kiel® probes at both compressor suction and discharge pipes required by ASME PTC-19.5 test specification. Compressor flow is calculated using orifice pressure, delta-P, and temperature as input. Lube oil flow for both suction and discharge bearings is measured with turbine flow meters and seal gas vent flow at both ends is recorded using rotometers.

Gas properties are calculated from the gas composition. A continuous gas analyzer is used to measure the oxygen content in the nitrogen gas used for testing. All testing is conducted with pure nitrogen.

Vibration measurements include both X and Y proximity probes located adjacent to both radial bearings. State-of-the-art data gathering is employed including a micro-Vax based data acquisition system and Bently-Nevada's ADRE for Windows vibration analysis system capable of performing digital signal

Nomenclature

C_b = assembled radial bearing clearance with undeformed pads
D = diameter of impeller
F_p = force exerted on bearing pad pivot
F_r = volute induced radial force
K_{eff} = effective pivot stiffness in vertical plane
K_p = pad pivot stiffness
K_r = nondimensional radial load coefficient
L = stage length of impeller
N = compressor speed, rpm
N_{pads} = number of pads in bearing
P_1 = suction pressure
P_2 = discharge pressure
Q = compressor flow, ACFM
R = bearing journal radius
S = Sommerfeld number
t = pad thickness from bearing surface to pivot
V_x, V_y = X and Y proximity probe voltage change from geometric center to contacting bottom bearing pads
W = weight on journal bearing
X_{geom} = shaft drop from bearing center to between pads (no pad deformation)
Δe = shaft centerline drop during run-down
ΔV_x, ΔV_y = change in X and Y probe gap voltage during run-down
ΔY_{geom} = distance shaft drops between pads beyond bearing clearance
ϵ_b = calculated bearing eccentricity ratio relative to undeformed bearing clearance
ϵ_{mc} = ϵ_b at maximum continuous speed under influence of gravity loading only
θ_x, θ_y = angle from vertical of X and Y proximity probe
μ = absolute oil viscosity, reyn
ϕ = inlet flow coefficient
ψ = isentropic head coefficient

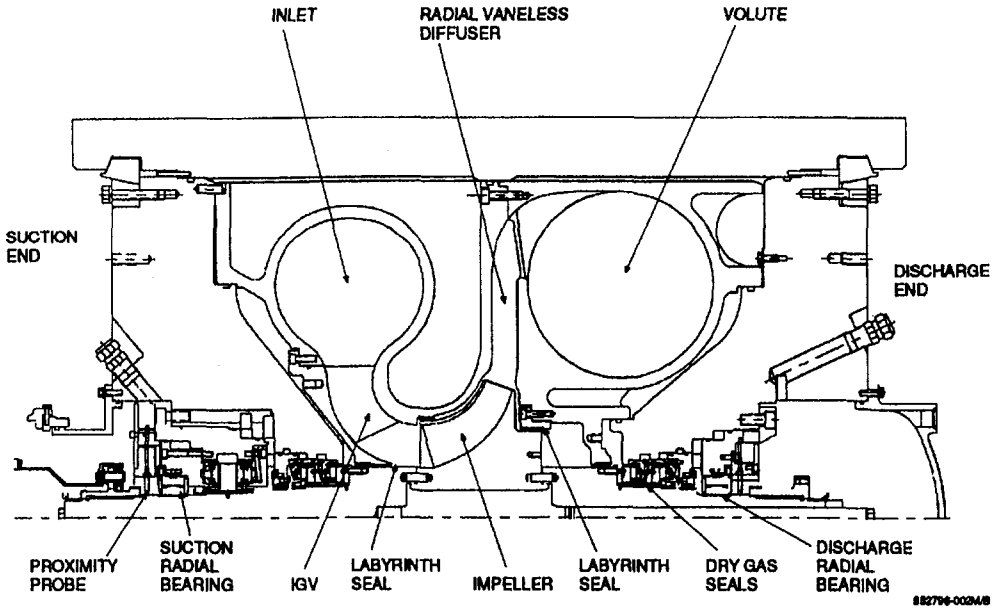

Fig. 2 C401 compressor cross section

processing of the dynamic signal from the eddy-current proximity probes, as well as capturing DC probe gap voltage using low-pass filters to eliminate the AC component. Bently-Nevada's 7200 series proximity probes are employed, yielding 200 mV/mil over the entire operating range and are installed 45 deg either side of vertical. Speed is measured using a Keyphasor® probe.

Test Article

The test compressor is a single-stage, centrifugal pipeline boost compressor with a maximum case pressure of 1600 psi (11.0 MPa) (Fig. 2). The aerodynamic components include: a radial inlet with radial inlet guide vanes, a mixed flow impeller, a vaneless diffuser, and a discharge volute. Further information on the radial inlet guide vane is provided by Flathers et al. (1996). The tested configuration is a high flow ($\phi = 0.12$), low head ($\psi = 0.75$) design with a specific speed of approximately 180 (English units). Other design features include tandem dry gas seals, tilting-pad journal bearings, and self-equalizing, tilting-pad thrust bearings. The journal bearings contain five pads with journal weight between the pads and a length to diameter ratio (L/D) of 0.5 initially. Figure 3 is a photo of the tilting-pad bearing showing the centered, spherical pivots, and pad RTD leads.

This design was later altered to an L/D of 0.6 with weight on pad to accommodate better the aerodynamic radial loading. All results presented utilize bearings with an L/D ratio of 0.5, except those given in Figs. 15 and 16, which have an L/D of 0.6.

Experimental Methodology

Experimental Calculation of Bearing Clearance. The running bearing clearance and geometric center must be determined before bearing eccentricity ratios may be evaluated. Although measured prior to compressor build, bearing clearance is determined experimentally to eliminate the effect of sensor inaccuracy. Since the measured eccentricity relative to the measured clearance is nondimensional, the results are no longer a function of transducer accuracy, only repeatability. Experimental determination of bearing clearances is performed by noting the shaft centerline change during a coastdown of the machine from its maximum speed.

The compressor is operated unpressurized at $P1 = 5$ psig (34 kPa) so that the aerodynamic loading is negligible. Only the gravity loading of $W = 199$ lb (885 N) due to shaft weight is reacted at the bearings. An example is shown in Fig. 4 and is annotated with shaft speed in rpm. Figure 5 defines each parameter as the shaft drops in its bearings (highly exaggerated). Notice that the shaft locus is purely vertical since tilting-pad bearings contain essentially no cross-coupled stiffness. From Fig. 5 the total shaft drop is equal to:

$$C_b + \Delta Y_{\text{geom}} + \frac{W}{K_{\text{eff}}} = \epsilon_{mc} C_b + \Delta e \tag{2}$$

grouping terms yield:

$$C_b(1 - \epsilon_{mc}) = \Delta e - \frac{W}{K_{\text{eff}}} - \Delta Y_{\text{geom}} \tag{3}$$

Finally, the running bearing clearance may be solved for:

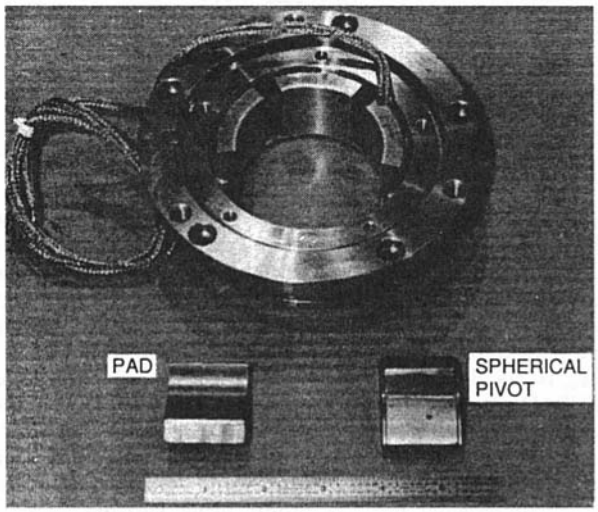

Fig. 3 Tilting-pad radial bearing ($L/D = 0.5$)

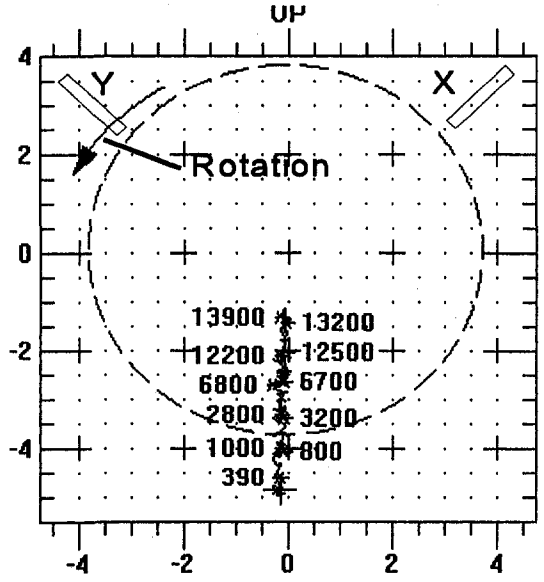

Fig. 4 Shaft centerline *X-Y* position (in mils) during run-down

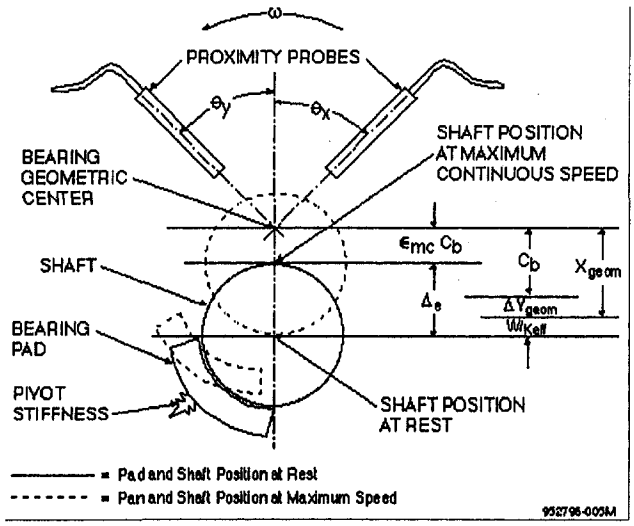

Fig. 5 Schematic of shaft centerline drop

$$C_b = \frac{\Delta e - \dfrac{W}{K_{\text{eff}}} - \Delta Y_{\text{geom}}}{1 - \epsilon_{mc}} \tag{4}$$

where (for load between pads):

$$\Delta e = \frac{\sqrt{\Delta V_x^2 + \Delta V_y^2}}{\text{Probe Sensitivity } (V/\text{mil})} \tag{5}$$

Δe is the measured shaft centerline drop during the rundown of the machine obtained by capturing the change in gap voltage (ΔV) for the X and Y probes. Since tilting-pad bearings contain little cross-coupling, the attitude angle of the journal from vertical due to gravity loading is approximately 180 deg, resulting in a pure vertical drop during shutdown as shown in Fig. 4.

ϵ_{mc} is calculated using a commercial tilting-pad bearing code (THPAD, Branagan and Barrett, 1993) given the journal weight, shaft speed, lube oil grade and temperature, assembled bearing clearance (obtained from machine build records), and pad preload. This code solves the Reynold's equation to produce the circumferential pressure profile using variable viscosity, heat conduction, and pad deformation. Including pad pivot deformation proved especially important for accurate eccentricity prediction.

K_{eff} is defined as the effective pad pivot stiffness in the vertical plane and is equal to the lower pad pivot stiffness (K_p) for a machine with journal weight on the bearing pad. For load between pads, K_{eff} is:

$$K_{\text{eff}} = 2 \cdot K_p \cos\left(\frac{360 \text{ deg}}{2 \cdot N_{\text{pads}}}\right) \text{(Load between pads)} \tag{6}$$

Hertzian contact theory is used to determine K_p for both point and line contact pad pivot designs. For spherical pivots used in the compressor, the pivot stiffness is a function of the radial load on that pad. Therefore, iteration must be used when running THPAD for a particular journal load until the assumed load and the calculated loads on the pads match. The pivot force (F_p) used to calculate K_p in Eq. (6) is equal to the gravity load (W) for load on pad designs. For load between pads, the pivot force is:

$$F_p = \frac{W}{2 \cos\left(\dfrac{360 \text{ deg}}{2 \cdot N_{\text{pads}}}\right)} \text{(load between pads)} \tag{7}$$

The final parameter in Eq. (4), ΔY_{geom}, represents the geometric distance the shaft drops between the pads beyond the bearing clearance. For a load on pad design, $\Delta Y_{\text{geom}} = 0$. For a load between pad design, ΔY_{geom} is given as:

$$\Delta Y_{\text{geom}} = C_b \cdot \left(\frac{X_{\text{geom}}}{C_b} - 1\right) \text{(Load between pads)} \tag{8}$$

where X_{geom} is the shaft drop from bearing center to resting on the bottom two pads (Fig. 5) and is determined using the law of cosines from Fig. 6:

$$X_{\text{geom}} = (t + R + C_b) \cdot \cos\left(\frac{360 \text{ deg}}{2 \cdot N_{\text{pads}}}\right) - \sqrt{(t + R + C_b) \cdot \cos\left(\frac{360 \text{ deg}}{2 \cdot N_{\text{pads}}}\right)^2 - C_b \cdot (2 \cdot t + 2 \cdot R + C_b)} \tag{9}$$

Calculations show that the quantity ($X_{\text{geom}}/C_b - 1$) is not a strong function of C_b. Therefore, the nominal bearing clearance may be used in Eq. (5). For the gas compressor, the quantity ($X_{\text{geom}}/C_b - 1$) = 0.236 for a five-pad, load between pad bearing with a nominal radial bearing clearance of 0.00245 in. (0.062 mm). The undeformed bearing clearance (C_b) in Eq. (4) may now be solved for as a closed-form expression:

$$C_b = \frac{\left(\Delta e - \dfrac{W}{K_{\text{eff}}}\right)}{(1.236 - \epsilon_{mc})} \tag{10}$$

The clearance of both bearings is determined with this procedure. For future calculations, all eccentricity ratios will be referenced to the undeformed bearing clearance. When applying this methodology to bearings other than the tilting-pad type, the effect of attitude angle of the journal must be considered.

Determination of Bearing Geometric Center. In order to determine the bearing eccentricity ratio during operation by use of proximity probe gap voltage, reference voltages must be established representing the geometric center of the bearing. This procedure corrects for any DC drift of the proximity probes from when the bearing clearance is determined to when the

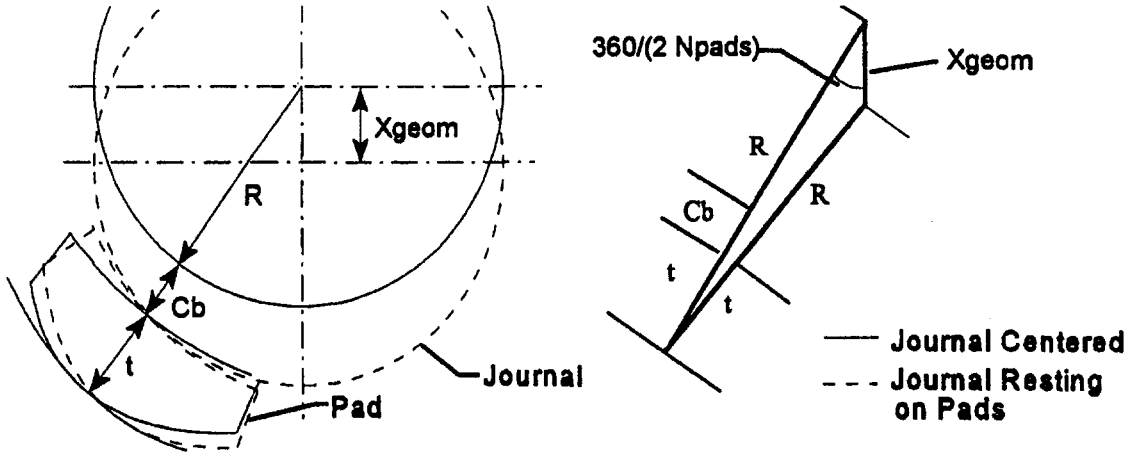

Fig. 6 Schematic of X_{geom}

radial loading test is performed. From the shutdown run (Fig. 4), the total distance from the geometric center to the bottom of the bearing (equivalent to $\Delta e + \epsilon_b C_b$ represented in voltage) may be calculated by:

$$V_{\text{geom}} = \sqrt{\Delta V_x^2 + \Delta V_y^2} + \epsilon_{mc} \cdot C_b \cdot \text{Probe Sens.} \quad (11)$$

This voltage may be resolved into components in the direction of the probe position as:

$$V_x = V_{\text{geom}} \cdot \cos(\theta_x) \quad (12)$$

$$V_y = V_{\text{geom}} \cdot \cos(\theta_y) \quad (13)$$

where θ_x and θ_y represent the probe angle from vertical.

The geometric center is recalculated for each loading study. Following each test, the machine is shut down and the gap voltage (Vr_x, Vr_y) with the rotor at rest in the bearings is noted. The gap voltage (Vgc_x, Vgc_y) representing the journal geometrically centered is:

$$Vgc_x = Vr_x + V_x, \quad Vgc_y = Vr_y + V_y \quad (14)$$

Using this procedure, Fig. 4 has been adjusted to represent the geometric center at the origin of the graph and C_b is shown as the dotted circle. The shaft eccentricity during operation may now be determined by comparing the operating X and Y gap voltage to Vgc_x and Vgc_y.

Experimental Shaft Centerline Locus Capture. The shaft centerline locus is captured by monitoring the proximity probe gap voltage while slowly changing operating conditions of the machine at a constant speed. The gas compressor is traversed continuously from surge (minimum flow) to choke (maximum flow) while maintaining constant speed. The aerodynamic radial loading changes as the flow is reduced and contains a minimum value near the best efficiency point (BEP).

Figures 7 and 8 show the shaft centerline at 5 psig (34.5 kPa) and 150 psig (1034 kPa) suction pressure, respectively, captured with the vibration data acquisition system. The bearing clearance and center have been determined as shown above. Figure 7 shows essentially no influence, while the aerodynamic loading in Fig. 8 is evident. The highest radial loads are near surge where the aerodynamic load adds to the weight of the rotor and, for this suction pressure, produces a bearing eccentricity ratio over 50 percent of the bearing clearance. The eccentricity ratio (e/C_b) may be calculated for each point captured and is a complex value with both amplitude and phase. Other important parameters such as compressor flow, head, and bearing temperature are simultaneously being captured with the computer data acquisition system.

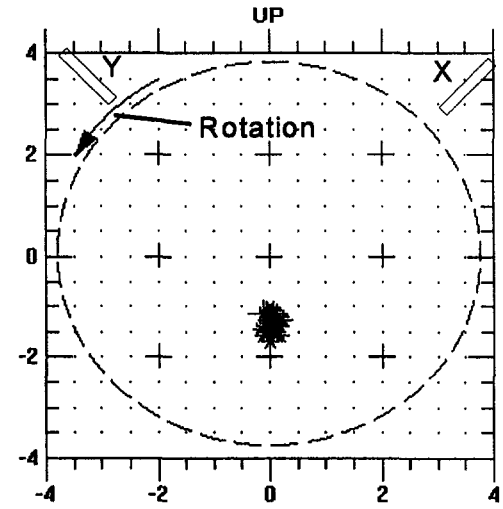

Fig. 7 X–Y shaft centerline locus, P_1 = 5 psig (34.5 kPa), discharge bearing

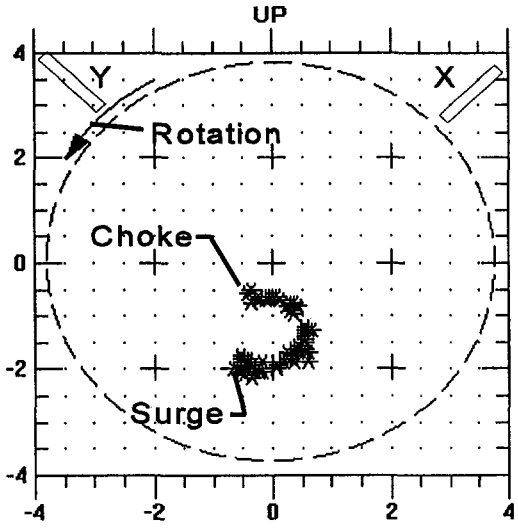

Fig. 8 X–Y shaft centerline locus, P_1 = 150 psig (1034 kPa), discharge bearing

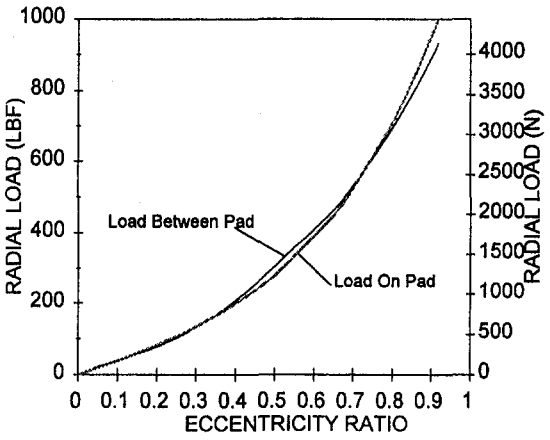

Fig. 9 Calculated bearing load versus eccentricity ratio (L/D = 0.5)

Radial Force Calculation. Using the experimental bearing eccentricity ratios, the radial force may be determined by calculating the force/eccentricity relation using a commercial bearing code. For this study, THPAD (Branagan and Barrett, 1993) again is employed. The calculated force versus eccentricity ratio for the gas compressor bearings (L/D = 0.5) is given in Fig. 9 and shows essentially an identical relationship for both load between and load on pad. As previously discussed, the assumed and calculated loads on the pad pivots must be iterated for each radial load. The maximum pad temperature, pressure, and safety factor may also be calculated versus ϵ_b. Again, ϵ_b is the eccentricity ratio relative to the undeformed bearing assembled clearance.

Method Validation

Before the methodology presented above is used for radial force calculation, the technique is validated. To verify the bearing code's ability to predict shaft eccentricity ratio while changing Sommerfeld number, the measured and predicted shaft eccentricity ratios are compared versus shaft speed with only gravity loading present (operating unpressurized). Figure 10 shows good correlation over the entire speed range and for eccentricity ratios approaching 0.9.

The speed decrease from 14,300 to 1000 rpm causes a 14:1 reduction in the Sommerfeld number (see Eq. (1)). This reduction is analogous (same value of S) to an increase in radial load (F_r) from the journal weight of 199 lb (885 N) to over 2800 lb (12,500 N). This exercise validates the load-eccentricity technique over the entire range of radial loading measured.

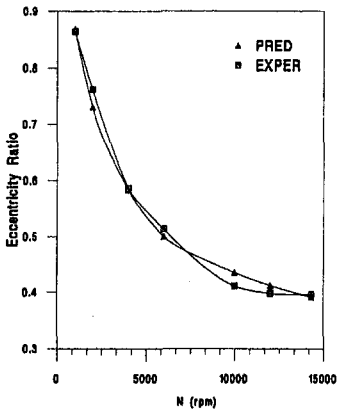

Fig. 10 Eccentricity ratio versus speed comparison

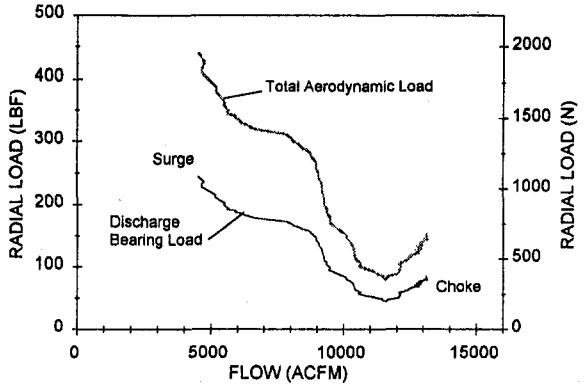

Fig. 11 Aerodynamic radial load versus Q (NS180, $P1$ = 150 psig, 14,300 rpm)

Experimental Results

Factory Data. The radial load may now be calculated for each point in Fig. 8 using the eccentricity ratio to load relationship in Fig. 9. The weight due to gravity may be vectorially subtracted from each bearing and the result added together to yield the true external load on the rotor. The result is shown in Fig. 11 where the aerodynamic radial load on the discharge end bearing and the total load is plotted versus compressor flow. The shape of the curve agrees with the results of Agostinelli et al. (1960), where the maximum force lies at a minimum flow, and the minimum force is at a flow greater than the design flow of 10,200 ACFM (4.83 m^3/s). These aerodynamically induced radial forces are plotted on the polar graph shown in Fig. 12.

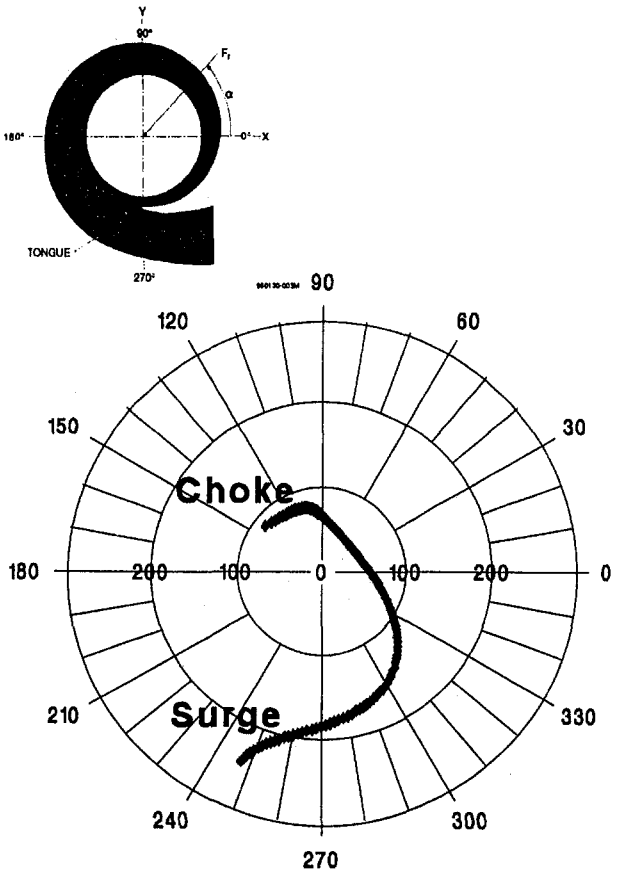

Fig. 12 Aerodynamic radial load on discharge bearing (α in deg) (NS180, $P1$ = 150 psig, 14,300 rpm)

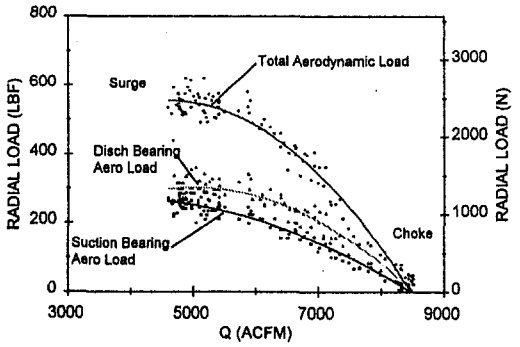

Fig. 13 Radial load in field at NS 180, P_2 = 750 to 810 psi (5.17 to 5.52 MPa), 11,000 rpm

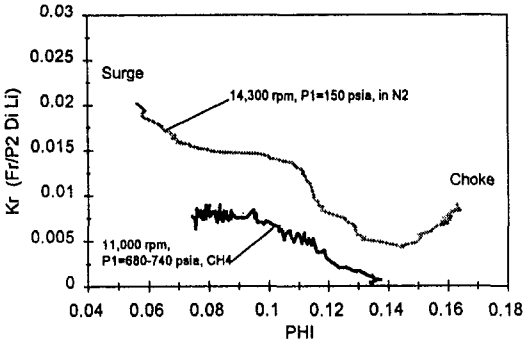

Fig. 14 Nondimensional Kr versus ϕ (NS 180)

The forces actually lift the rotor when operating near choke and reach their maximum force of 240 lb (1068 N) near surge for a suction pressure of 150 psia (1034 kPa). Agostinelli et al. (1960) also show for higher specific speed pumps, the force vector approaches the volute tongue opposite the direction of rotation as the flow is decreased. Figure 11 shows this same phenomenon, but the force vector actually travels past the tongue (located at 270 deg) as the flow is decreased.

Field Data. Pump theory (Stepanoff, 1957) suggests that the radial force will increase linearly with discharge pressure. A field test was performed at suction pressures in excess of 600 psi (4.14 MPa) with discharge pressures over 800 psi (5.52 MPa). Operation of the machine unpressurized was not possible, preventing an accurate calculation of the bearing geometric center. The maximum flow coefficient (ϕ) obtained corresponds to the ϕ with minimum force based on the factory test. Therefore, the aeroload at this flow is assumed to be small and the only load on the bearing is due to gravity. The resulting radial loading at the bearings and the net aerodynamic load is plotted versus compressor flow as the flow is reduced at constant speed given in Fig. 13. Again, the radial loading increases as the machine operates toward surge. The total aerodynamic load on the rotor exceeds 600 lb (2670 N). Higher flows and speeds were not possible due to pipeline conditions and horsepower restrictions.

Nondimensionalization of Results. Stepanoff (1957) suggests that the volute-induced radial force is described by the following relationship:

$$F_r = K_r \cdot P_2 \cdot D \cdot L \tag{15}$$

K_r may be solved for and used to compare the radial force of different operating conditions for a particular machine. In order to reduce out the effect of speed on compressor flow, the flow coefficient may be used and is defined as:

$$\phi = \frac{700.3}{D^3} \cdot \frac{Q}{N} \tag{16}$$

The dimensionless radial loading results for the factory and field tests are shown in Fig. 14 using total aerodynamic load. The results show a similar trend for the two results. Both results show a minimum force near the design flow of 0.127. The data also suggest that compressor speed, which does not appear in Eq. (15), is an important parameter in describing the radial force.

Additional Results. Additional testing was later performed on a lower specific speed impeller (NS 80). The operating conditions of the three tests are described in Table 1.

Figure 15 summarizes the reduced test results. K_r is plotted versus the ratio of the machine flow to the design flow (Q/Q_n). The term Q/Q_n is used to allow comparison of different specific speed impellers.

Cases 1 and 2 clearly show that K_r effectively reduces out the effect of suction pressure on the results. For a fixed flow and speed, P_1 and P_2 are linearly related by the pressure ratio across the impeller. Therefore, Cases 1 and 2 will yield the same K_r for a given flow if the radial loads increase linearly with suction pressure. Indeed, this is the case as shown in Fig. 15 for a speed of 11,150 rpm.

In comparing Cases 2 and 3, the effect of speed may be shown. As demonstrated with Cases 1 and 2, the effect of increased P_2 due to the increase in speed from 11,150 to 13,500 rpm is reduced out by K_r. However, K_r does not fully explain the relationship of radial load with speed. Case 3 at 13,500 rpm also yields a minimum force at higher flow than for Case 2 at 11,150 rpm.

Figure 16 compares the results of the K_r of Case 3 for a NS80 impeller with the previous results for an N S180 impeller. The lower specific speed impeller delivers a higher K_r at its minimum flow. The results of Agostinelli et al. (1960) shows an opposite trend for specific speed from 20 to 120 but presents little data beyond 120. The point of minimum load for the NS80 is at a greater flow relative to the design flow than for the NS180.

Table 1 Case Studies

Case	Speed (rpm)	Suction Pressure, psia (MPA)
1	11,150	600 (4.14)
2	11,150	315 (2.17)
3	13,500	315 (2.17)

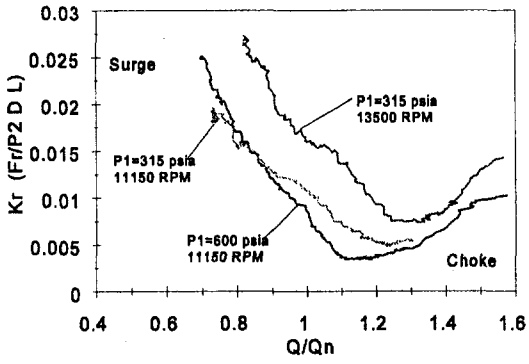

Fig. 15 Effect of speed and pressure changes on Kr (NS80)

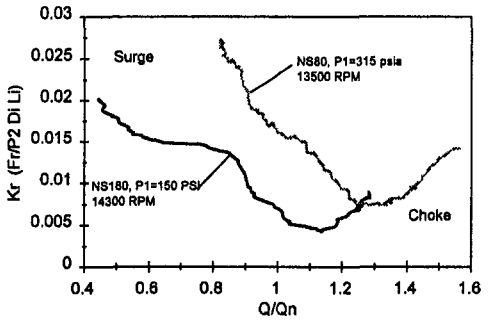

Fig. 16 Comparison of different specific speed impellers

The K_r parameter may be used to predict the radial forces at higher pressures for a given speed and even machines of different scale. However, to characterize the loading fully for a given specific speed impeller, tests must be performed at varying flows and speeds.

Summary and Conclusion

A novel technique has been presented to quantify the radial force arising from the process fluid of turbomachinery operating on fluid film bearings. This technique is used to characterize the magnitude of aerodynamically induced loading in a centrifugal compressor arising from nonuniform pressure distributions in the diffuser and volute when operating at off-design conditions. Characterization of these forces during factory testing can verify that adequate safety margins exist for static load capacity of the tilting-pad bearings, as well as rotordynamic stability prior to field implementation. Quantifying these forces also provides an avenue for CFD model verification, which is the topic of Part 2 of this paper.

Future work includes completing the data base on radial load patterns for additional specific speed impellers. Investigations of the radial load on machines with scaled (larger and smaller) aerodynamic flow paths will also be studied. Using the nondimensional relations presented, the inclusion of radial forces at the rotordynamic design stage of new equipment will provide more accurate assessments of dynamic stability leading to more robust mechanical designs.

Acknowledgments

The authors would like to acknowledge the efforts of Dr. Chester Lee and Mr. Bert Edlebeck for their contributions to this testing program. Our appreciation also goes to Solar Turbines Inc. for permission to publish this paper.

References

Agostinelli, A., Nobles, D., and Mockridge, C. R., 1960, "An Experimental Investigation of Radial Thrust in Centrifugal Pumps," ASME JOURNAL OF ENGINEERING FOR POWER, Vol. 82, pp. 120–126.

Binder, R. C., and Knapp, R. T., 1936, "Experimental Determination of the Flow Characteristics in the Volutes of Centrifugal Pumps," *Transactions of the ASME,* Paper No. HYD-58-4, pp. 649–661.

Branagan, L. A., and Barrett, L. L. E., 1993, "A Manual for Use With the Tilting-Pad Bearing Program THPAD," Version 2.23b, ROMAC Report No. 284, University of Virginia.

Flathers, M. B., Baché, G. E., and Rainsberger, R., 1996, "An Experimental and Computational Investigation of Flow in a Radial Inlet of an Industrial Pipeline Centrifugal Compressor," ASME *Journal of Turbomachinery,* Vol. 118, pp. 371–384.

Flathers, M. B., and Baché, G. E., 1998, "Aerodynamically Induced Radial Forces in a Centrifugal Gas Compressor: Part 2—Computational Investigation," ASME JOURNAL OF ENGINEERING FOR GAS TURBINES AND POWER, Vol. 120, No. 2, pp. 000–000.

Gardner, W. W., and Ulschmid, J. G., 1974, "Turbulence Effects in Two Journal Bearing Applications," ASME *Journal of Lubrication Technology,* pp. 15–21.

Miner, S. M., Beaudoin, R. J., and Flack, R. D., 1989, "Laser Velocimetry Measurements in a Centrifugal Flow Pump," ASME *Journal of Turbomachinery,* Vol. 111, No. 3, pp. 205–212.

Odeja, W., and Flack, R. D., 1992, "Experimental Pressures and Momentum Forces on the Impeller of Single and Double Volute Centrifugal Pumps," ROMAC Report No. 338, University of Virginia.

Stepanoff, A. J., 1957, *Centrifugal and Axial Flow Pumps—Theory, Design, and Application,* 2nd ed., Wiley, New York.

H. Kanki
Department of Mechanical Engineering,
Kobe University,
Kobe, Japan

Y. Kaneko
Takasago R&D Center,
Mitsubishi Heavy Industries, Ltd.,
Takasago, Japan

M. Kurosawa

T. Yamamoto

Headquarters,
Mitsubishi Heavy Industries, Ltd.,
Yokohama, Japan

Prevention of Low-Frequency Vibration of High-Capacity Steam Turbine Units by Squeeze-Film Damper

The cause of the low-frequency vibration (subsynchronous vibration) of a high-pressure turbine was investigated by the analytical study and vibration exciting test for the actual machine in operation. From the results, it is found that the low-frequency vibration is caused by the decrease of the rotor system damping at high-loading operating conditions. As a countermeasure, a squeeze-film damper is designed in order to increase the damping of the rotor system. After the verification test of the squeeze-film damper's capability in the workshop, it was installed on the actual turbine. Vibration exciting tests for the high-pressure turbine under the actual operating conditions were carried out. These field tests confirmed that the damping of the rotor system was increased as expected in the design and consequently the low-frequency vibrations disappeared completely under all operating conditions.

Introduction

Recently, the low-frequency vibrations of high-pressure (HP) turbine rotors have become an important problem to be overcome in developing the high-capacity and advanced steam condition turbine units. The low-frequency vibrations are the non-synchronous vibrations of the high-pressure turbine rotor, which occur when the unit's load is increased. According to studies performed by the author et al., these vibrations can be classified into the following categories, as shown in Fig. 1:

(*i*) steam whirl
(*ii*) forced vibration caused by the flow disturbance of the control stage
(*iii*) forced vibration caused by the rubbing between the rotor and the casing

The steam whirl is a self-excited vibration of the first vibrational mode of the rotor system under the high-loading operation condition, and is similar to the oil whip but it is not as severe. Furthermore, the steam whirl can occur, even if the tilting-pad type bearings are used to prevent the oil whip. It is well known that the steam whirl is caused by the steam exciting forces, which are generated due to the blades and seals; however, extensive studies carried out by turbine manufacturers and researchers all over the world haven't sufficiently clarified the details yet.

In Russia, the seal exciting force of the control stage, which is the main cause of the steam whirl, has been investigated extensively and Olimpiev (1978) reported the outlined results of investigation. Recently, Childs and Gansle (1996) reported the exciting force for various types of seal. However, as reported by McClosky and Adams (1992), the steam whirl frequently causes a trouble for a HP rotor of large capacity steam turbine at present and has not been exactly estimated at the design stage still now. On the other hand, both the vibration caused by the flow disturbance of the control stage and the vibration caused by rubbing are forced vibrations, and the first vibrational mode of the rotor system is also excited in these cases. Wu and Flowers (1993) carried out an analytical study for the vibration caused by rubbing, but most of this vibration cannot be analytically estimated till now. No effective way to exactly estimate the vibration caused by the flow disturbance of the control stage is available at present. Since the low-frequency vibration experienced in an actual high-pressure turbine is so complex, it is essential to discriminate which type of the vibrations mentioned in Fig. 1 appears to take the suitable corrective action for the phenomenon.

In this work, in order to solve the low-frequency vibration problem experienced in the large-capacity turbine unit, at first, the analytical study and vibration exciting test of the turbine rotor under actual operating conditions were carried out. Results show that the low-frequency vibration occurs due to the decrease of the rotor system damping under high-loading operation conditions. This reduction is caused by the instability force in the control stage. In the second step, as a countermeasure, a squeeze-film damper was designed and tested in the workshop in order to verify its damping capability. Finally, after this verification, the squeeze-film damper was installed on the actual turbine unit, and the vibration exciting tests under the actual operating conditions were carried out again. From these field tests, it is confirmed that the damping of the rotor system is increased as expected in the design and the low-frequency vibrations completely disappear under all operating conditions.

Low-Frequency Vibration of the High-Pressure Turbine

The situation of the low-frequency vibration, which had been experienced in the high-pressure rotor of the 450 MW steam turbine, is outlined as follows. This unit comprises two rotational drive lines, each with a 225 MW, 3000 rpm generator as shown in Fig. 2. While one drive line is driven by one HP (High-Pressure) turbine and one LP (Low-Pressure) turbine, the other drive line is driven by one IP (Intermediate Pressure) turbine and one LP turbine. Eight governing valves for adjusting the steam flow are connected to the inlet of the HP turbine. The turbine output power is controlled by the opening of these governing valves.

After several months of operation since overhaul, the HP drive line began to experience a strong low-frequency (27 Hz)

Contributed by the International Gas Turbine Institute and presented at the 42nd International Gas Turbine and Aeroengine Congress and Exhibition, Orlando, Florida, June 2–5, 1997. Manuscript received at ASME Headquarters February 1997. Paper No. 97-GT-11. Associate Technical Editor: H. A. Kidd.

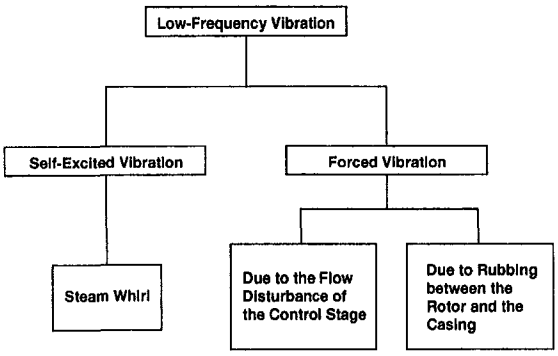

Fig. 1 Classification of low-frequency vibration of high-pressure steam turbine

vibration of the HP turbine rotor. Figure 3 shows the typical situation of the experienced low-frequency vibration. The low-frequency vibration started around 300 MW of output, and rapidly increased with the rise of load. The spectrum of the shaft vibration of the HP rotor is also shown in Fig. 3. Figure 4 shows the measured results on the direction of the whirling vibration. It was found from these results that the low-frequency vibration had the following features:

1 It occurs at high-loading operation only.
2 The dominant frequency is 27 Hz, the natural frequency of the first bending mode of the HP rotor (Fig. 3).
3 The direction of the whirl is forward (Fig. 4).
4 The occurrence condition and the threshold of the low-frequency vibration may be changed if the eight-valve opening sequence is changed.

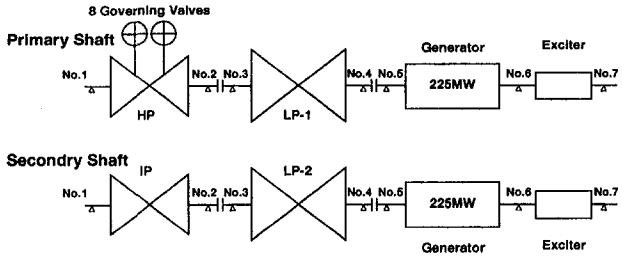

Fig. 2 Shaft system of steam turbine unit experienced low-frequency vibration

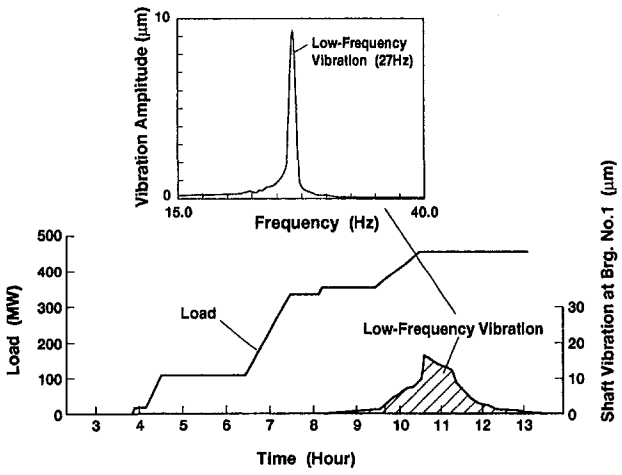

Fig. 3 Low-frequency vibration and turbine output power

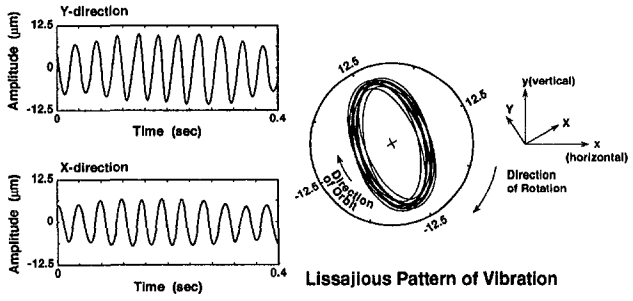

Fig. 4 Trajectory of the low-frequency vibration at bearing No. 2 (450 MW)

Vibration Exciting Test

In order to judge whether the low-frequency vibration occurring in the actual turbine is a self-excited vibration or a forced vibration, the damping ratio of the first vibrational mode of the HP rotor in operation was measured by using the vibration exciting test method developed by Kanki et al. (1986a, b). In this method, the inertia-type exciter is mounted on the bearing of the turbine rotor through a jig, and the natural frequency and the damping ratio of the rotor system can be obtained by measuring the frequency response. The stability of the rotor system in operation can be evaluated in accordance with the following procedure:

1 Operate the machine under the required test condition.
2 Excite the bearing pedestal by sinusoidal exciting force, sweep the exciting frequency, and measure the frequency response through an appointed natural frequency.
3 Analyze the data and evaluate the natural frequency and the damping ratio of the appointed mode.
4 Repeat the steps from (1) to (3), for all test conditions such as speed and load of machine.

Figure 5 shows the experimental feature of the vibration exciting test in operation, and Fig. 6 shows the exciter mounted on the bearing of the HP turbine. In order to carry out the vibration exciting test in operation for the actual turbine, a compact exciter with easy operation and large power is required.

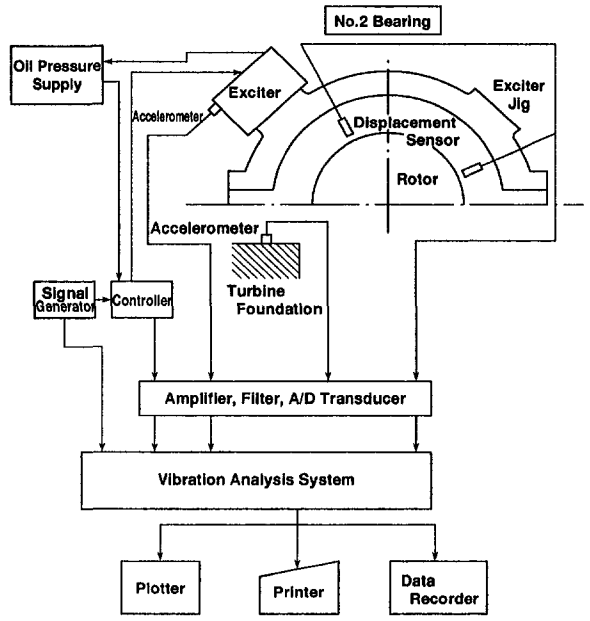

Fig. 5 Block diagram of vibration exciting test of HP turbine

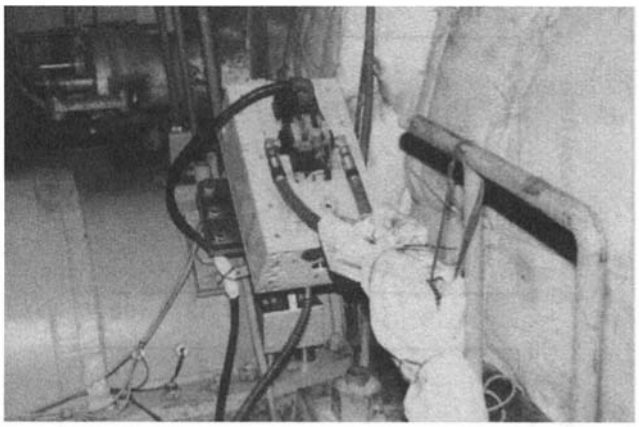

Fig. 6 Electrohydraulic vibration exciter attached to HP turbine

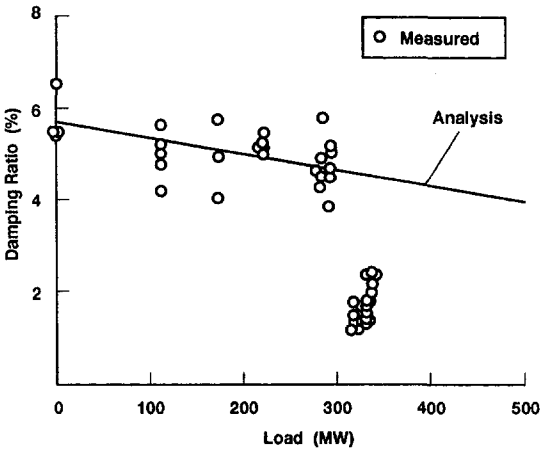

Fig. 7 Damping ratio of HP rotor first mode

In this test, the inertia-type electrohydraulic exciter developed by the author et al. was used.

Figure 7 shows the relationship between the turbine output power and the damping ratio of the HP rotor first mode, obtained from the vibration exciting test in operation. As shown in Fig. 7, it is found that the damping ratio of the HP rotor first mode decreases gradually with the increase of the turbine output power up to approximately 300 MW but suddenly decreases at the point where the load exceeds 300 MW. That is, it is clarified from the results of the vibration exciting test in operation that the low-frequency vibration that occurred in the load range over 300 MW is a self-excited vibration, i.e., steam whirl, caused by the decrease of the damping of the HP rotor first mode. In addition, it is clarified that the damping of the HP rotor first mode is closely related to the valve opening sequence (i.e., admission of the control stage) because the seventh governing valve always begin to open just prior to the sudden decrease of the damping ratio.

Analysis of Destabilizing Force

The exciting forces that cause the steam whirl on a HP rotor of a steam turbine have been mainly considered to be the following two forces until now:

1 Stage excitation force (Alford force)
2 Labyrinth seal excitation force

As is well known, those exciting forces can be generally expressed by eight dynamic coefficients (four stiffness coefficients and four damping coefficients), and assuming that the rotor is located at the center of labyrinth seal, those forces can be expressed by only four dynamic coefficients:

$$K_{xx} = K_{yy},\ K_{xy} = -K_{yx},\ C_{xx} = C_{yy},\ C_{xy} = -C_{yx} \qquad (1)$$

In order to evaluate the effects of those exciting forces on the stability of the HP rotor first mode, at first, the dynamic coefficients were calculated by using the method developed by Kanki et al. (1986a, b). Then, the stability of the HP rotor first mode was evaluated by carrying out the vibration analysis, in which those coefficients were incorporated into the whole turbine rotor model (Fig. 8) by using the same way as that for the bearing coefficients. In this analysis, the whole primary rotor was modeled by a sequence of beam elements as shown in Fig. 8, and the vibration analysis was carried out using the transfer matrix method.

The solid line in Fig. 7 indicates the calculated results of the HP rotor first mode damping ratio. As shown in this figure, the gradual decrease of the HP rotor first mode damping ratio with load increase can be detected analytically; however, the analytical model used doesn't express the sudden fall of the damping ratio at 300 MW load as detected by the experiment. Namely, the gradual decrease of the damping can be attributed to the well-known stage excitation force and labyrinth seal excitation force, but the reason for the sudden decrease under high-loading condition can not be explained thoroughly at present. To bring the analytical solution closer to the experimentally detected results, it is deemed necessary to establish a precise mechanical model for which the effects of the partial admission of the control stage, nozzle alignment (alignment between the control stage and nozzle), etc., can be quantitatively taken into account.

Design of Squeeze-Film Damper

Since it was found that the low-frequency vibration of the actual turbine is caused by the decrease of the HP rotor first mode damping ratio, the HP rotor bearing No. 2 was replaced by a squeeze-film damper bearing. This corrective action was taken in order to increase the damping of the HP rotor. Figure 9

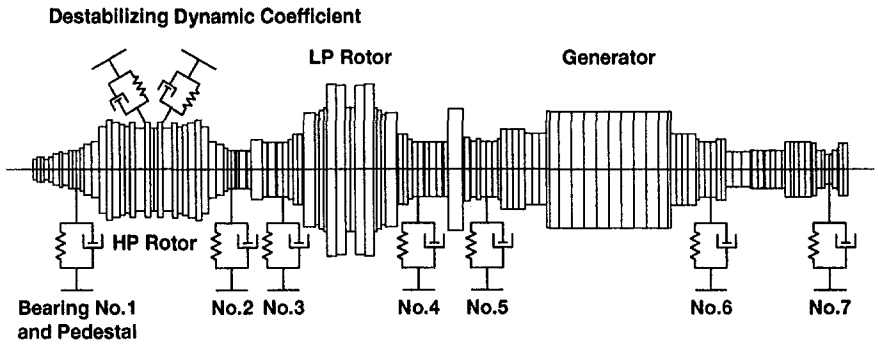

Fig. 8 Analysis model for calculating damping ratio of HP rotor first mode

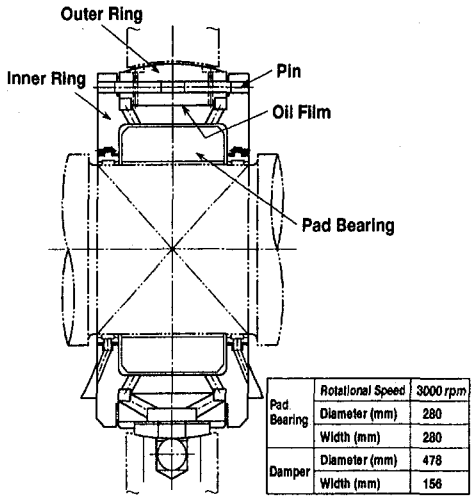

Fig. 9 Squeeze-film damper bearing

shows the developed squeeze-film damper bearing. The bearing inner ring is fitted to the outer ring by 36 pins and the damping effect is obtained by the existence of the squeeze oil film between them.

The squeeze-film damper bearing design procedure was as follows. The squeeze-film damper bearing is modeled according to the right side of Fig. 10, and this model replaced bearing No. 2 in the rotor model (Fig. 8) to carry out vibration analysis. The pins spring constant (ke) and the squeeze-film damping coefficient ($c\omega$) were selected taking the following points into consideration:

1 The damping ratio of the HP rotor first mode should be as large as possible.
2 The inner ring should not contact with the outer ring under the effect of the weight and the partial admission of the control stage.

The calculated results are shown in Fig. 11, where the damping of the HP rotor first mode was analyzed by using the ratio of spring constant (ke) to the damping coefficient ($c\omega$) as a parameter. In this analysis, the HP rotor first mode damping ratio was adjusted by acting the exciting force (cross spring kxy) on the control stage, so as to meet the measured results of the original rotor system, where the HP rotor first mode damping ratio was approximately 2 percent at the high-loading condition (Fig. 7). As shown in Fig. 11, the HP rotor first mode damping ratio can be increased by about 2 percent if the ratio ($c\omega/ke$) is selected to be in the optimal range.

In the next step, the film thickness and the eccentricity necessary for obtaining the optimum damping coefficients of the squeeze-film shown in Fig. 11 were calculated in accordance with the method of Szeri et al. (1983). Figure 12 is an example

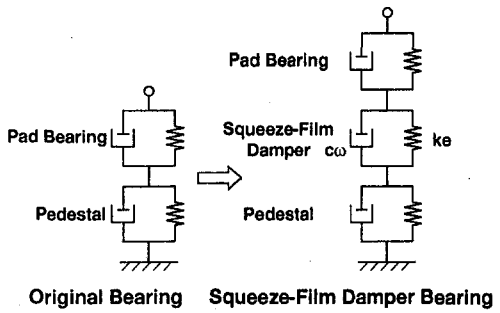

Fig. 10 Dynamic model of the squeeze-film damper bearing

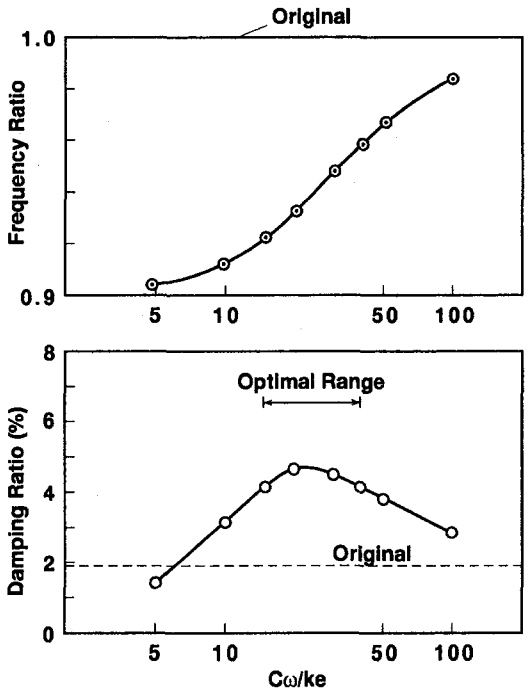

Fig. 11 Calculated frequency and damping ratio of the HP rotor first mode with squeeze-film damper ($ke = 6 \times 10^5$ kgf/cm)

of the calculated results, which shows the relationship between the eccentricity and the squeeze-film damper damping coefficients. As shown in this figure, setting the bearing clearance (Cr) to be 0.25 mm and the eccentricity (ϵ) to be zero, the optimum damping coefficients can be obtained even if the static bearing displacement produced in operation is taken into consideration. The spring constant (ke) and the static displacement in operation shown in Fig. 12 were analyzed in details by using the three-dimensional finite elements model shown in Fig. 13.

Verification Test

1 Shop Test. In order to verify the damping effect of the developed squeeze-film damper bearing, the verification test was carried out by utilizing the rotational test facilities in the shop after the HP rotor of the actual turbine was transported to

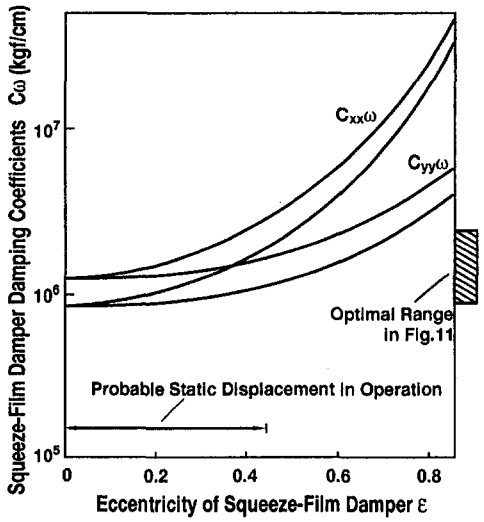

Fig. 12 Calculated damping coefficients of the squeeze-film damper (clearance Cr = 0.25 mm)

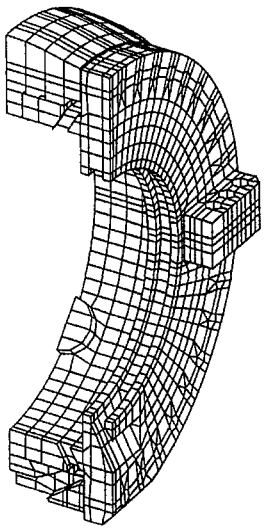

Fig. 13 Finite element model of the squeeze-film damper for calculating static deformation

the shop from the power station during the outage. In the shop verification test, the vibration exciting test of the HP rotor first mode was carried out in rotation for two cases, the original No. 2 bearing case and the squeeze-film damper case. From the shop test, it was confirmed that the damping ratio was increased as expected in the design. Figure 14 shows the results of the exciting test carried out in the shop.

2 Field Test. After the verification test in the shop, the squeeze-film damper bearing was installed on the HP rotor at the actual site, and the low-frequency vibrations at various loads were measured. In addition, the HP rotor first mode damping ratio was measured by carrying out the vibration exciting test in operation. Figure 15 shows the spectrum of shaft vibration at rated load and Fig. 16 shows the relationship between the load and the HP rotor first mode damping ratio. From these results, it was confirmed that the low-frequency vibration was completely eliminated under all operating conditions because the damping ratio in load operation was increased by about 2 percent as expected in the design stage by using the squeeze-film damper bearing.

This turbine unit has been satisfactorily operated without low-frequency vibration for 2 years after the squeeze-film damper bearing was installed.

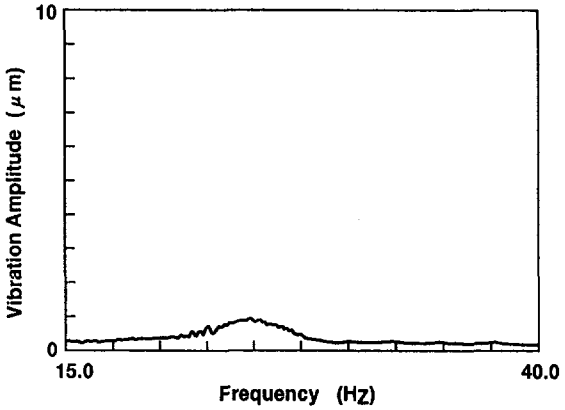

Fig. 15 Spectrum of the shaft vibration at bearing No. 2 after installing the squeeze-film damper (450 MW)

Conclusion

In order to solve the problem of the low-frequency vibration that occurred on the HP rotor of the steam turbine, the vibration exciting test in operation and the analysis were carried out. As a result, it was clarified that the low-frequency vibration of this turbine unit was a self-excited vibration (steam whirl) caused by the decrease of the HP rotor first mode damping ratio in high-loading operation. Therefore, the squeeze-film damper was designed as a countermeasure, and it was verified by the shop test that the HP rotor first mode damping ratio was increased as expected in the design. Furthermore, the squeeze-film damper bearing was installed on the HP rotor at the actual site after the verification test in shop, then the vibration exciting test in operation was carried out to measure the damping ratio in load operation. As a result, it was confirmed that the HP rotor first mode damping ratio was increased by about 2 percent due to the effect of squeeze-film damper and the low-frequency vibration was completely eliminated.

In this paper, it is shown by using an actual example that the vibration exciting test in operation developed by the author et al. is very effective for obtaining a solution of nonsynchronous vibration problems such as the low-frequency vibration. The precise analysis method that includes the effects of Curtis force and the nozzle alignment at the control stage has been developing, and in the future, the accuracy of the calculated steam exciting force will be improved.

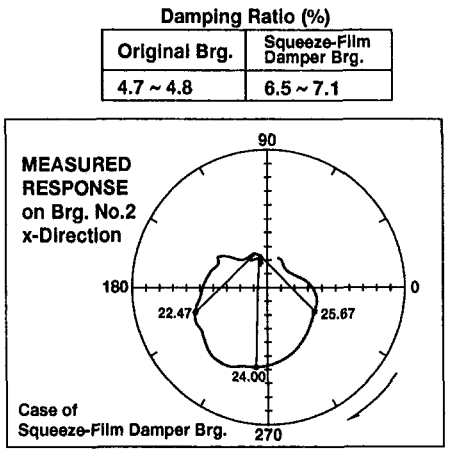

Fig. 14 Measured HP rotor first mode damping ratio in shop test

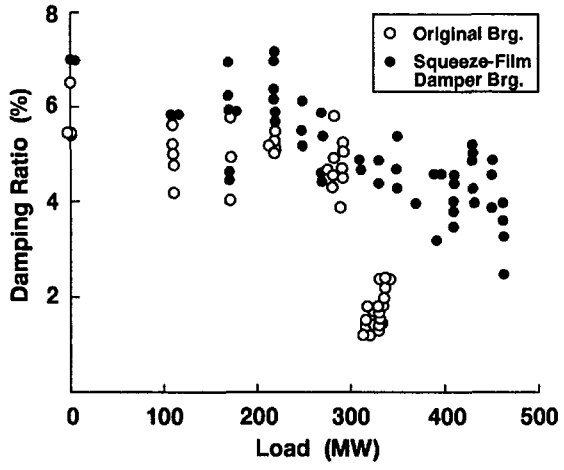

Fig. 16 Measured HP rotor first mode damping ratio in field test

References

Childs, D. W., and Gansle, A. J., 1996, "Experimental leakage and rotor dynamic results for helically grooved annular gas seals," ASME JOURNAL OF ENGINEERING FOR GAS TURBINES AND POWER, Vol. 118, pp. 389–393.

Kanki, H., Fujii, H., Hizume, A., Ichimura, T., and Yamamoto, T., 1986a, "Solving nonsynchronous vibration problems of large rotating machineries by exciting test in actual operating condition," *Proc. International Conference on Rotordynamics,* JSME, IFToMM, pp. 221–225.

Kanki, H., Morii, S., and Hizume, A., 1986b, "Theoretical and experimental study of the destabilizing force by labyrinth seal," *Proc. International Conference on Rotordynamics,* JSME, IFToMM, pp. 603–608.

McCloskey, T. H., and Adams, M. L., 1992, "Trobleshooting power plant rotating machinery vibration problems using computational techniques: case histories," *IMech E,* C432/137, pp. 233–244.

Olimpiev, V. I., 1978, "Problem of preventing low-frequency vibration of the shafting of high-capacity steam turbine units," *Teploenergetika,* Vol. 25, pp. 8–14.

Szeri, A. Z., Raimondi, A. A., and Giron-Duarte, A., 1983, "Linear force coefficients for squeeze-film dampers," ASME *Journal of Lubrication Technology,* Vol. 105, pp. 326–334.

Wu, F., and Flowers, G. T., 1993, "A study of the influence of rubbing on the dynamics of a flexible disk rotor system," ASME Paper No. 93-GT-35.

Imbalance Response of a Test Rotor Supported on Squeeze Film Dampers

L. San Andrés
Associate Professor.

D. Lubell
Research Assistant.

Mechanical Engineering Department,
Texas A&M University,
College Station, TX 77843-3123

Squeeze film dampers (SFDs) provide vibration attenuation and structural isolation to aircraft gas turbine engines which must be able to tolerate larger imbalances while operating above one or more critical speeds. Rotor-bearing-SFD systems are regarded in theory as highly nonlinear, showing jump phenomena and even chaotic behavior for sufficiently large levels of rotor imbalance. Yet, few experimental results of practical value have verified the analytical predictions. A test rig for measurement of the dynamic forced response of a three-disk rotor (45 kg) supported on two cylindrical SFDs is described. The major objective is to provide a reliable data base to validate and enhance SFD design practice and to allow a direct comparison with analytical models. The open-ends SFD are supported by four-bar centering structures, each with a stiffness of 3.5 MN/m. Measured synchronous responses to 9000 rpm due to various imbalances show the rotor-SFD system to be well damped with amplification factors between 1.6 and 2.1 while traversing cylindrical and conical modes critical speeds. The rotor amplitudes of motion are found to be proportional to the imbalances for the first mode of vibration, and the damping coefficients extracted compare reasonably well to predictions based on the full-film, open-ends SFD. Tight lip (elastomeric) seals contribute greatly to the overall damping of the test rig. Measured dynamic pressures at the squeeze film lands are well above ambient values with no indication of lubricant dynamic cavitation as simple theoretical models dictate. The measurements show absence of nonlinear behavior of the rotor-SFD apparatus for the range of imbalances tested.

Introduction

Squeeze film dampers (SFDs) provide viscous damping to rotating structures, allowing for reduction in rotor-bearing lateral vibration amplitudes and providing safe isolation to other structural components. SFDs have been used primarily in aircraft jet engines where rolling element bearings provide little damping to the rotor-bearing system and in high performance compressors as retrofit elements in series with tilting pad bearings to soften bearing supports, reduce critical speeds, and allow for an extra margin of system stability (Zeidan et al., 1996).

Squeeze film dampers derive their action from a lubricant being squeezed in the annular space between a nonrotating journal and a bearing housing. The journal, typically mounted on the outer race of rolling element bearings, precesses due to the forces exerted on the rotating shaft. Conventional SFDs consist of a cylindrical journal and bearing with an elastic support connecting the journal to ground and preventing its rotation. This support, in the form of a squirrel cage, must be sufficiently soft to allow journal motions and to bring an effective damping action. The required low stiffness of the damper supports demands spaces two or three times longer than the journal axial length. Numerous archival references present the analysis and design of simple geometry SFDs based on solutions to the classical Reynolds equation of hydrodynamic lubrication. The most popular being the short length SFD with open ends. The squeeze film action generates hydrodynamic pressures and damping forces at the film locations where the instantaneous gap is decreasing. Analysis also predicts suction pressures in the regions where the film thickness is locally increasing. In these zones, the simple models assume the lubricant to cavitate, i.e., to undergo an instantaneous phase change since an ideal fluid is unable to sustain tension. The theoretical models are yet to account for the physical aspects of bubble dynamics with local mass conservation. Widely varying test results in research and practice have demonstrated that the design of SFDs is based on overly simplified analytical models which either fail to incorporate or simply neglect distinct structural and fluid-related features which greatly affect the dynamic force response of SFDs. The lack of adequate understanding of the mechanics of squeeze film flows stems from the near absence of fundamental experimental evidence and sound rationale that directly address the issues and problems of interest (San Andres, 1995). Zeidan et al., (1996) provide a detailed account on the history and evolution of SFD design practices, describe practical cases and novel SFD technologies, and discuss the major issues yet to be addressed in SFD analysis. Zeidan (1994) also introduces the concept of compact integral SFDs, which may replace current damper configurations in the near future. The interested reader should consult the cited references for further details.

Rotordynamic analyses regard SFDs as nonlinear mechanical elements providing film forces ranging from small to unlimited depending on the instantaneous journal position and velocity within the clearance circle (Vance, 1988). The models, as given by Mohan and Hahn (1974), Li and Taylor (1987), and San Andres and Vance (1988), consider the lubricant dynamic cavitation phenomena as governed purely by the kinematics of journal motion and render a no pressure variation zone of 180 deg extent around the journal circumference, i.e., the SFD π-film model. Analytical and computer-based predictions of the dynamic response of rotor-bearing systems supported on SFDs show a rich nonlinear behavior with multiple valued responses, jump phenomena, and zones evidencing chaos. The dynamic response is highly sensitive to the rotor imbalance, which, if large enough, can lock-up the bearing supports and give rise to excessive vibration amplitudes at the most flexible points of

Contributed by the International Gas Turbine Institute and presented at the International Gas Turbine & Aeroengine Congress & Exhibition, Orlando, FL, June 2–5, 1997. Manuscript received by the ASME Headquarters July 1997. Paper No. 97-GT-12. Associate Technical Editor: H. A. Kidd.

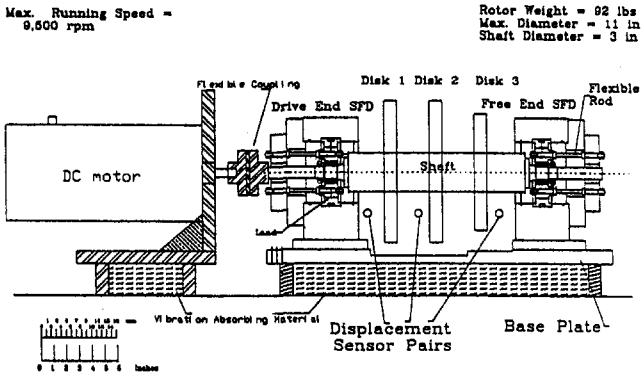

Fig. 1 Schematic view of test rig with open end squeeze film dampers

the structure, while passing through critical speeds. In general, theoretical predictions of rotor responses have correlated poorly with test results since dampers in practice operate with a number of features that affect their performance. The most important are the level of external pressurization, type of feed mechanism, and end-seal restrictions, fluid inertia, and most notably air ingestion from the gaseous environment surrounding the SFDs. Theory is yet to provide a sound set of results of practical value for the design and operation of SFDs.

This paper introduces a test rig for measurement of the imbalance response of a rotor supported on SFDs. The major objectives are (*a*) to provide reliable measurements in a rotor-SFD configuration similar to an aircraft engine, (*b*) to develop an experimentally validated analytical model to predict the forced dynamic performance of SFDs operating with a bubbly air/oil mixture due to air ingestion, and (*c*) to develop a nonlinear fluid-structural model, should the test results evidence deviations from linear behavior. The first objective is addressed in this publication, and it includes the prediction and measurement of the system fundamental parameters and the coast-down tests for various levels of rotor imbalance. As is far too common in research work, the experimental results depend greatly on the test rig, and, thus, a detailed account of the system and its fundamental parameters becomes mandatory.

Description of Test Rig and Major Components

Figure 1 shows a schematic view of the rotor-SFD test apparatus resting on a base plate isolated from a heavy work table with a elastomeric vibration absorbing pad. A 10 HP (7.5 kW) DC power supply and DC motor drive the test rotor through a flexible coupling. The motor is also mounted on elastomeric pads providing vibration isolation from/to the work table. A drawn cup roller clutch in the coupling allows the motor to bring the rotor to a top speed of ~9,000 rpm and then be shut off without applying a torque to the rotating shaft. This feature of the coupling insures free coast-down tests of the test rig as the motor drag friction does not affect rotor deceleration rate. A DC battery (12 volts, 900 A) connected in parallel with the power supply provides a boost in current for start-up acceleration of the test rotor.

The rotor consists of a shaft, 26.5 in (673 mm) long and main diameter 3 inches (76.2 mm), and three 1 inch (25.4 mm) thick disks shrunk fitted at evenly spaced intervals of 2.5 inches (63.5 mm). Two of the disks are of 11 inches (279.4 mm) in diameter, and the third is 9 inches (228.6 mm) in diameter. Each disk has 10–32 threaded holes spaced 30 deg apart and at radii equal to 4.5 inches (large disks) and 3.5 inches (small disk). At these locations, calibrated imbalance masses are inserted. The weight of the rotor (shaft and disks) is 92 pounds (41.7 kg). The bearing support housings are split elements with a 1.42 inches (36 mm) wide groove at mid length of their inner bore. This groove is the seat for the damper housings, and on installation of each damper bearing, it becomes a circumferential chamber that allows lubricant feeding to the damper film lands and ball bearings. A lubricant feed port is located on the side (horizontal plane) of the support, and ports at the bottom sides collect the oil discharge from the ball bearings and squeeze film elements. The outside face of the support housings holds the displacement sensors. The opposite face holds the structure for support and centering of the dampers.

Each squeeze film damper, depicted in Fig. 2, consists of a cylindrical housing and a journal. The damper housing rests on the groove of the split bearing support and contains six feed holes of $\frac{1}{16}$ inch (1.6 mm) diameter connecting the circumferential groove to the damper squeeze film lands. The journal is of diameter (D) and length (L) equal to 3.72 inches (95 mm) and 0.91 inches (23.0 mm), respectively. The journal also contains a port for installation of a pressure transducer facing the middle plane at the bottom of the circumferential squeeze film land. The nominal radial clearance (c) on the damper film lands is equal to 0.009 inches (0.229 mm). Note that the damper slenderness ratio (L/D) and clearance to journal radius ratio ($2C/D$) are equal to 0.243 and 0.005, respectively. The journal is connected to the bearing support with four steel rods of 0.235 inch (6 mm) diameter and 1.97 inches (50.2 mm) length. The support is designed for a nominal radial stiffness k_s = 20,000 lb/in (3.5 MN/m). Alignment and centering of the damper journal within its housing is provided by four fine positioning screws mounted on brackets also attached to the bearing support. A pair of high precision ball bearings is mounted inside each damper journal. A thin spacer ring separates the ball bearing pairs, and a nut and collar allows the application of a speci-

Nomenclature

B = SFD bearing parameter, $\mu D(L/c)^3/(M_{eq} f_n 2\pi)$
c = SFD radial clearance [m]
C_{crit} = critical damping coefficient for first mode, $2 \cdot (K_{eq} M_{eq})^{1/2}$, [N·s/m]
C_V, C_H = system damping coefficients for vertical and horizontal motions [N·s/m]
C_{SFD} = SFD theoretical direct damping coefficient [N·s/m]
C_{seals} = damping coefficient from lip seals [N·s/m]
D = SFD diameter [m]
e = amplitude of rotor motion [m]
f_{Vn}, f_{Hn} = first natural frequencies for vertical and horizontal motions [Hz]
k_s = SFD elastic lateral support stiffness [N/m]
K_{Veq}, K_{Heq} = system equivalent stiffness coefficients for vertical and horizontal motions [N/m]
L = SFD length [m]
m = imbalance mass [kg]
M_{eq} = equivalent rotor mass for first mode, 45.8 kg
P = squeeze film pressure [bar]
Q = amplification factor at first critical speed
r = radius for location of unbalance mass [m]
u = $m \cdot r/M_{eq}$, imbalance displacement [m]
t = time [s]
ε = e/c, dimensionless SFD journal center displacement
θ, z = circumferential and axial coordinates
μ = fluid viscosity [Pa·s]
ξ = system damping ratio, $C/C_{crit} = 1/2Q$

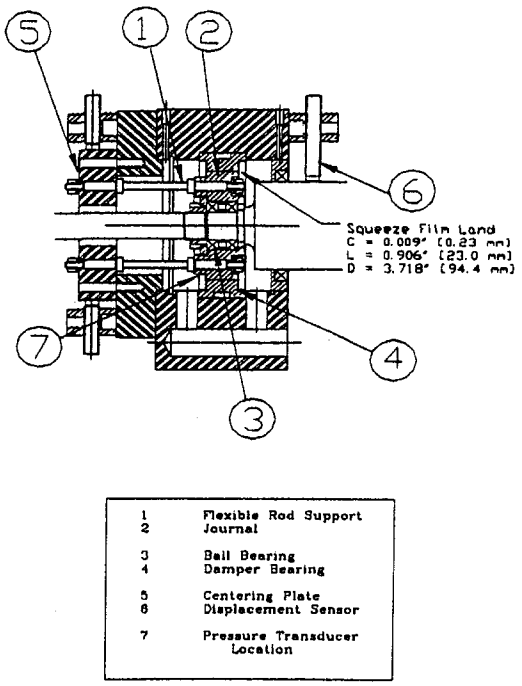

Fig. 2 Open ends—squeeze film damper and flexible support

fied preload. Lubrication to the ball bearings is drawn from the flow through the damper film lands via a radial hole of $\frac{1}{16}$ inch (1.6 mm) diameter discharging to the annular space between the ball bearings.

The split supports holding the shaft and dampers have lip seals (3 inch (72.8 mm) diameter) on each side preventing the leakage of lubricant to the base table. These elastomeric seals are tightly installed and provide additional damping to the system. On installation at room temperature (70°F (21°C)) the SFD radial clearance was measured to be 0.0078 inches and 0.0096 inches (0.198 mm and 0.244 mm) in the horizontal and vertical directions, respectively, for the damper installed at the rotor free end. The measured radial clearances for the damper facing the drive motor are equal to 0.0077 (0.196 mm) inches (horizontal) and 0.0093 inches (0.236 mm) (vertical). The distortion of the damper clearances may be due to the compression exerted when fastening the bearing top supports.

A lubrication system delivers oil to the bearing housings from a 40 gallon (151 liter) reservoir through a variable frequency gear pump. The temperature in the reservoir is controlled using a 1.5 kW electrical heater. The lubricant discharged from the bearing supports flows through a forced air convection cooler with a thermostat control, and then it is pumped back to the main reservoir. A turbine flow meter displays the flow rate supplied to the bearing supports and Bourdon-type pressure gauges indicate the static supply pressure to each squeeze film damper. Three pairs of noncontact, eddy-current displacement sensors are mounted to measure directly the rotor displacements at locations next to the damper on the motor drive end, the middle disk, and the damper at the rotor free end (see Fig. 1). The displacement sensors are mounted in the horizontal and vertical directions. Piezoelectric dynamic pressure sensors are installed at the bottom of the middle section of the damper journals. An optical keyphasor facing the drive motor coupling detects the rotor speed. Temperature measurements are performed with type-K thermocouples at the pump discharge and return oil lines, on the drive motor, and for room temperature. Most importantly, thermocouples cold welded to the side faces of the damper housing provide direct measurements of the operating temperature at the discharge sections of the damper squeeze film lands.

An eight-channel simultaneous sampling 20 kHz data acquisition interface unit records signals from the six displacement sensors and the two pressure transducers, and with an additional channel for the rotor speed sensor. The acquisition system includes slow-roll subtraction, order tracking, and synchronous response filtering. An instrumentation console contains digital displays of the operating rotor speed, flow rate, supply, and damper discharge temperatures, and includes the controls for operation of the lubrication pumps and the oil cooling and heating elements. Three oscilloscopes display the rotor orbits at the measurement locations. A fourth oscilloscope shows the damper film pressures, and a frequency analyzer depicts the FFT of selected vibration signals.

System Parameter Identification

A linear rotordynamics software (Murphy, 1995), based on the transfer matrix method, is used for prediction of the rotor system natural frequencies, mode shapes, and imbalance response. The measured rotor weight including the damper journals and coupling is 101 lb (45 kg). The estimated center of mass of the rotor-bearing system is located 13.1 inches (333 mm) from the drive end, i.e., about 25 mm (1 inch) to the left from the middle disk.

Identification of Rotor Free-Free Modes. The rotor (shaft and press fitted disks) was hung with nylon ropes for identification of its elastic unconstrained modes. A miniature (1 gram) piezoelectric accelerometer was installed at different locations along the rotor, and subsequently, the rotor was excited in the horizontal direction with a calibrated impulse hammer. The measurements showed two elastic modes, natural frequencies at 630 Hz and 930 Hz (±4 Hz). The computed predictions are equal to 622 Hz and 941 Hz, with a percent difference in the measurements of −1.3 percent and +1.2 percent, respectively.

Dampers' Lateral Support Stiffness. Precise knowledge of the "squirrel cage" lateral stiffness is needed for accurate determination of the rotor-bearing critical speeds (Zeidan et al., 1996). Each damper journal and its four flexural rods were assembled and rigidly connected to the bearing supports. All parts were weighed before assembly. Two methods were used for measurement of the damper lateral stiffness. Method (a) consisted of loading the damper journal and then measuring the journal deflection using a dial gauge. Method (b) was based on impacting the damper journal with a calibrated piezoelectric load hammer and measuring the ensuing vibration with a miniature accelerometer. The second method has the advantage of providing an indication of the structural damping of the elastic support. A summary of the measurements is provided in Table 1. The load versus displacement method shows the most reliable results as evidenced by the correlation coefficients (0.98 and higher) of the test data.

Identification of Natural Frequencies for the Test Rotor-Bearing System. The rotor supported on the SFDs was excited with a calibrated impact hammer at the coupling (most sensitive to show the elastic modes), and the rotor motion was measured with a miniature accelerometer attached magnetically to the middle disk. The system was free of any lubricant. Table 2 presents a summary of the measurements and the predictions, including a percent difference. The test rotor shows different vertical (f_{Vn} = 62 Hz) and horizontal (f_{Hn} = 56 Hz) fundamental natural frequencies indicating the bearing split supports to be softer in the horizontal direction. It is worth noting that the addition of the flexible coupling at the rotor end determines a dramatic reduction of the first elastic mode from 630 Hz to just 194.7 Hz.

The first natural mode indicates a rotor motion close to a rigid body cylindrical mode. An equivalent system stiffness and critical damping coefficients are therefore likely to be found.

Table 1 Radial stiffness of conventional damper flexible support (squirrel cage). Design value = 20,000 lb/in (3.5 MN/m)

Method	(1) Support free end	(2) Support drive end
(a) Vertical	18,421 lb/in ± 135 lb/in (3.21 MN/m)	20,420 lb/in ± 160 lb/in (3.55 MN/m)
Horizontal	18,510 lb/in ± 1020 lb/in (3.22 MN/m)	20,781 lb/in ± 1174 lb/in (3.62 MN/m)
(b) Vertical & Horizontal	18,829 lb/in ± 38 lb/in (3.28 MN/m)	19,684 lb/in ± 39 lb/in (3.23 MN/m)
Natural frequency	254 Hz	260 Hz
Equivalent mass	2.86 lb (1.30 kg)	2.85 lb (1.29 kg)
Damping ratio (ξ)	0.012	0.012
Structural damping	0.28 lb·s/in (49 N·s/m)	0.29 lb·s/in (50.5 N·s/m)

Using a system mass M_{eq} = 101 lb (45.8 kg) and the measured fundamental natural frequencies (f_n) of 62 Hz (vertical) and 56 Hz (horizontal), determines the equivalent parameters for the fundamental mode as

Vertical Direction.

$$K_{Veq} = (f_{Vn}2\pi)^2(M_{eq}) = 39.666 \text{ klb/in } (6.94 \text{ MN/m})$$

$$C_{V\text{crit}} = 2(K_{Veq}M_{eq})^{1/2} = 203.6 \text{ lb}\cdot\text{s/in } (35.6 \text{ kN}\cdot\text{s/m}) \quad (1)$$

Horizontal Direction.

$$K_{Heq} = (f_{Hn}2\pi)^2(M_{eq}) = 32.361 \text{ klb/in } (5.67 \text{ MN/m})$$

$$C_{H\text{crit}} = 2(K_{Heq}M_{eq})^{1/2} = 184.0 \text{ lb}\cdot\text{s/in } (32.2 \text{ kN}\cdot\text{s/m}) \quad (2)$$

with uncertainties of ±0.17 MN/m and ±0.45 kN·s/m, respectively.

Measurements of System Damping at Zero Rotational Speed. Transfer functions of rotor acceleration versus impact load were obtained using a frequency analyzer, and from these, values for the system damping coefficient were extracted. The impulse excitations at the middle disk showed transfer functions with a single peak at the fundamental (rigid body) mode. On the other hand, impulses at the other disks excited also the conical and first bending modes. The measurements revealed significant damping coefficients for the "dry" or oil-free, rotor-bearing system, mostly attributed to the tight elastomeric (lip) seals. The identified system "*dry*" damping values at two different temperatures (21 and 38°C) are

$$C_{V\text{seals}} = 21.7; 17.8 \text{ lb}\cdot\text{s/in } (3.80; 3.11 \text{ kN}\cdot\text{s/m})$$

$$C_{H\text{seals}} = 17.0; 13.8 \text{ lb}\cdot\text{s/in } (2.98; 2.41 \text{ kN}\cdot\text{s/m}) \quad (3)$$

in the vertical and horizontal directions, respectively.

The lubricant (ISO VG 10) at preset temperatures and a feed pressure of 10 psig (0.7 bars) was next circulated through the SFDs and ball bearings. The identified values of system damping coefficients for the fundamental mode representing the averages of at least six impact tests are given in Table 3. The theoretical SFD damping coefficients for the two dampers combined ($2 \times C_{SFD}$) are also given in Table 3, and are based on the short length-open ends SFD model without lubricant cavitation or fluid inertia (Vance, 1988):

$$C_{SFD} = \pi\mu(D/2)(L/c)^3/(1 - \varepsilon^2)^{1.5}. \quad (4)$$

The viscosity (μ) is determined from the measured oil temperature at the damper discharge and a journal orbit radius $\varepsilon = 0$ (centered operation) is assumed for the predictions. The measurements also indicated a slight increase (<2 percent) in the damped natural frequencies. Note that the test system damping coefficients include not only the damping from the SFDs, but also the significant "dry" damping from the lip seals and coupling. Note that the damping coefficient (C_H) for horizontal motions is smaller than the one in the vertical direction (C_V). It appears that the impulse excitations in the horizontal plane had a larger degree of uncertainty, as later verified by the imbalance coast down tests.

In the design of SFDs a bearing parameter (B) is defined as

$$B = \mu D(L/c)^3/(M_{eq}f_n2\pi) = (2/\pi)(C_{SFD}/C_{crit}) = (2/\pi)\xi, \quad (5)$$

which denotes the amount of squeeze film damping for small amplitude centered motions ($\varepsilon \to 0$) at the first critical speed. The experimental bearing parameter (B) ranges from 0.050 to 0.12 for the range of lubricant temperatures tested.

Test Rig Synchronous Imbalance Responses

Small calibrated masses (m) were inserted in the middle disk at a radius r = 4.5 inch (114.3 mm). The rotor, after a 45 minute warm up period at 3000 rpm, was brought rapidly to a top speed of approximately 9000 rpm, the power was shut down, and the coast down response measured. Table 4 provides a summary of the test peak-to-peak amplitudes of synchronous response while passing through the first critical speeds. The table includes the lubricant temperature and the imbalance displacement ($u = m\cdot r/M_{eq}$). All tests were conducted with a feed pressure to the SFDs equal to 15 psig (1 bar) and a total flow rate of approximately 2.4 GPM (9 liter/min).

Table 2 Natural frequencies of test rotor-bearing system. Measurements from rap tests and predictions at zero rotational speed. (No lubricant in ball bearings or dampers).

Mode	Measured		Predictions	Percent difference
	Vertical	Horizontal		
1. Cylindrical	62 Hz	56 Hz	60.5 Hz	2.5% / 7.0%
2. Conical	100 Hz	110 Hz	94.5 Hz	5.5 %
3. Elastic$_1$	200 Hz	204 Hz	194.7 Hz	4.5 %
4. Elastic$_2$	888 Hz (± 4 Hz)		914.0 Hz	3.0%

Uncertainty in measurements: ± 2 Hz. **Predictions based** on $K_{XX} = K_{YY} = 20{,}420$ lb/in for the drive end, and $K_{XX} = K_{YY} = 18{,}421$ lb/in for free end, $C_{XX} = C_{YY} = 3.2$ lb·s/in (557.5 N·s/m) at both bearing supports.

Table 3 Estimated and measured 1st mode system damping coefficients from rap tests. Lubricant temperature increases. Lubricant ISO VG 10. SFD: D = 3.72 in (94.5 mm); L = 0.9 in (23 mm); and c = 8.75 mils (0.222 mm).

Oil Temperature		Viscosity	Theory	Horizontal	Vertical
			$2 \times C_{SFD}$	C_H	C_V
°F	°C	centipoise	lb·s/in	lb·s/in	lb·s/in
70	21.1	18.55	34.27	30.63	47.72
80	26.6	14.87	27.47	28.70	42.00
90	32.2	11.86	21.91	27.06	38.80
100	37.7	9.50	17.60	26.50	36.30
104	41.1	8.78	16.14	26.40	34.30
Uncertainty in measurements: ~1 lb·s/in				C_{Hcrit} = 184.0	C_{Vcrit} = 203.6
				f_{Hn} = 56 Hz	f_{Vn} = 62 Hz

Table 4 Summary of rotor synchronous responses at first critical speed. Imbalance at middle disk. Notation: D—drive end; M—middle disk; F—free end; A—Average; and M_{eq} = 101 lb (45.8 kg).

Imbalance	Imbalance	Vertical P-P (μm)				Horizontal P-P (μm)				Temp
(g·in)	u (μm)	D	M	F	A	D	M	F	A	°F
residual	0.0	24	25	26	25	30	29	26	28.3	99
65.7	36.3	163	155	143	153	147	155	150	150	99
65.7	36.3	162	155	147	154	144	152	148	148	98
104	57.5	248	232	209	230	225	232	224	227	102
104	57.5	249	235	218	234	227	236	228	230	100
128.25	70.9	292	264	242	266	259	265	256	260	96
128.25	70.9	269	242	232	247	248	256	255	253	92
148.5	82.1	307	263	240	270	281	281	275	279	91
Critical Speeds:		3,500 to 4,000 rpm				3,100 to 3,160 rpm				

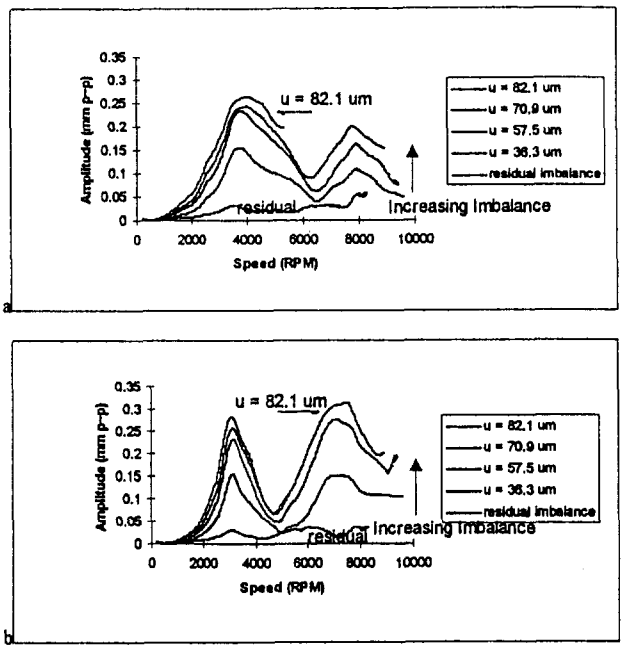

Fig. 3 Test synchronous imbalance responses at middle disk (slow roll compensated): (*a*) vertical; (*b*) horizontal

Each experimental coast down was performed twice to verify the repeatability of the tests. Note that the tests with the larger imbalance masses were performed at lower lubricant temperatures. Figure 3 depicts the vertical and horizontal synchronous rotor responses at the middle disk. Similar responses measured at the drive and free ends are not shown here for brevity (San Andres and Lubell, 1996). The highest speed for the test with the largest imbalance mass (u = 82.1 μm) was only to 5300 rpm for safety considerations. The measurements show the rotor amplitudes of motion to be nearly proportional to the imbalance displacements. The cylindrical critical speeds are approximately 3100 rpm and 3800 rpm for the horizontal and vertical directions, respectively, while the forward conical critical speed is around 7600 rpm. Note also that the critical speeds do not shift as the rotor imbalance and peak vibration increase.

Excitation of the conical critical speed was thought unlikely since the imbalance masses were located at the middle disk closest to the rotor mass center. It is important to note that while passing through the forward-mode conical critical speed, the response at the middle disk showed frequency component equal to three times the rotor speed and with a magnitude slightly smaller to that of the synchronous frequency. Later, this (supersynchronous) motion was determined to be that of the support holding displacement sensors, which resonated at these operating conditions.

At this time, only the rotor responses through the cylindrical mode critical speeds have been analyzed with some detail. The results from Table 4 demonstrate the SFDs to operate as linear mechanical elements, and, hence, the system amplification factor (Q) at the first critical speed is easily determined by the ratio of the rotor amplitude of motion to the imbalance displacement (u). From these results, values of the system damping ratio ($\xi = Q/2$) are also extracted. Finally, system damping coefficients, as given in Table 5, are determined by multiplying the damping ratio (ξ) times the critical damping coefficients (C_{crit}). The test results demonstrate a linear operation of the SFDs at the first critical speed in spite of the large journal amplitudes at the drive end SFD of up to 70 percent of its nominal clearance. The identified system damping coefficients agree well with the impact excitation values in the vertical direction (Table 3).

Figure 4 shows the SFD damping coefficients in the vertical and horizontal directions as determined from the tests and from the formulae for the full film, short length SFD open ends model (Eq. 4). The SFD theoretical values are calculated with

Table 5 Amplification factors (Q) and extracted system damping coefficients from rotor synchronous responses at first critical speed. Imbalance at middle disk. C_{Vcrit} = 203.6 lb·s/in, C_{Hcrit} = 184.0 lb·s/in.

Imbalance u (μm)	u/c c = 0.222 mm	Vertical Amp/c	Q_V	ξ_V	C_V lb·s/in	Horiz. Amp/c	Q_H	ξ_H	C_H lb·s/in	Viscosity (cp)
36.3	0.164	0.346	2.11	0.24	48.1	0.339	2.07	0.24	44.4	10.2
36.3	0.164	0.348	2.12	0.23	47.8	0.333	2.04	0.24	45.2	10.4
57.5	0.259	0.517	2.00	0.25	51.0	0.511	1.97	0.25	46.6	9.8
57.5	0.259	0.527	2.04	0.25	50.0	0.519	2.00	0.25	45.9	10.0
70.9	0.319	0.599	1.88	0.27	54.3	0.586	1.83	0.27	50.2	10.8
70.9	0.319	0.558	1.75	0.29	58.3	0.570	1.78	0.28	51.6	11.7
82.1	0.370	0.608	1.64	0.30	61.9	0.628	1.70	0.29	54.1	11.9

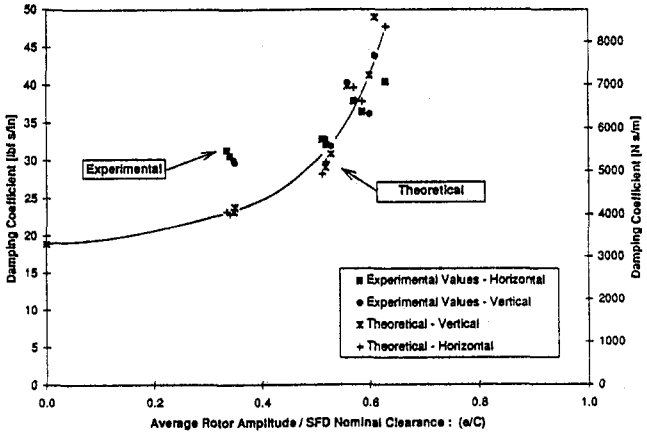

Fig. 4 Squeeze film damping coefficients ($2 \times C_{sfd}$) extracted from imbalance responses

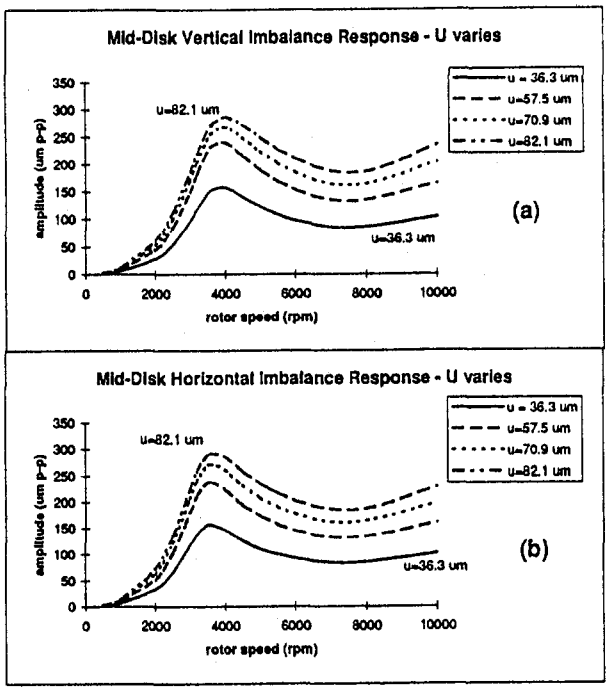

Fig. 5 Predicted linear rotor response at middle disk versus rotor speed. Imbalance increases (*a*) vertical and (*b*) horizontal.

a viscosity based on the oil test temperature and the measured amplitudes of motion at the near-damper locations. Note that the test SFD damping values reflect the subtraction of the "dry" elastomeric damping coefficients (C_{seals}). In general, the theoretical damping coefficients increase nonlinearly with the rotor amplitude of motion. The large tests damping coefficients for the measurements with the largest imbalances are probably due to the lower oil temperature rather than a direct consequence of the rotor vibration amplitude.

Figure 5 shows the calculated synchronous imbalance response at the middle disk for increasing imbalance levels. The linear responses, based on the identified system damping coefficients (Table 5), predict well the first critical speed ($V\&H$) and its peak amplitudes, but fail to show the excitation of the conical mode for speeds above 5000 rpm.

In the imbalance test measurements, the shaft centerline position changed as speed increased, thus indicating a severe thermal bow amounting to approximately 0.0024 inches (0.061 mm) at the middle disk and 0.002 inches (0.051 mm) at the damper supports. Measurements of the shaft surface temperature at the disk locations as well as closer to the damper housings were performed. Temperatures at the disks were slightly higher than ambient, so excessive windage effects were not important. However, the shaft ends were much hotter at the sides of the support housings, approximately 130°F (73°C), pointing out to insufficient lubrication to the ball bearings which (presumably) also had excessive assembly preloads. This thermal bow may explain the excitation of the conical mode on the imbalance responses. Another possible cause currently being studied is related to a resonant excitation of the bearing solid supports and test rig base.

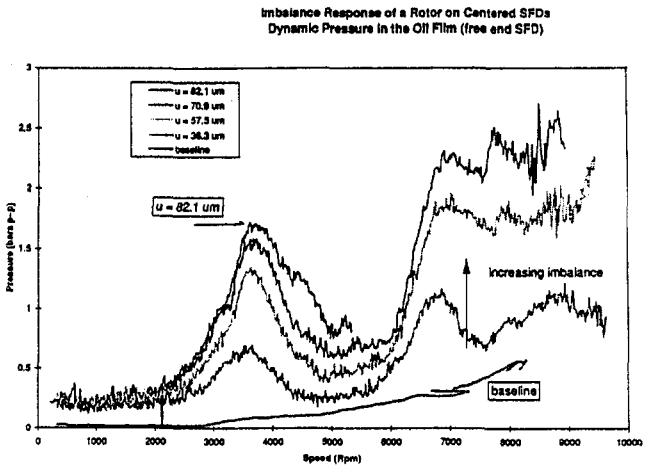

Fig. 6 Peak-peak (dynamic) film pressures at free end SFD for increasing levels of imbalance

The measurements of squeeze film pressures at the SFD on the rotor free-end provide no evidence of lubricant cavitation in any of the tests. Figure 6 shows the (unfiltered) amplitudes of peak-to-peak dynamic pressure for the coast down tests with increasing levels of imbalance at the middle disk. The p-p dynamic pressures show maximum values while passing through the critical speeds. It is presumed that there was enough lubricant flow through the SFDs in all tests so that no air inges-

tion was likely to occur. Later tests with reduced supply pressures to the dampers have confirmed this assertion.

A unique experiment was performed to verify the benefit of the SFD supports on the response of the test rotor. An imbalance mass of 14.7 grams was inserted on the disk closest to the rotor free end (r = 3.5 inch (89 mm), u = 28.3 μm). Figure 7 shows the rotor synchronous response near the middle disk for a run-up to 5000 rpm without any lubricant supply to the damper, then the pump was turned on and lubricant was delivered at a pressure of 10 psig (0.7 bar) and at a temperature of 79°F (26.1°C). The coast down curve shows the response with the SFDs filled with lubricant. The large differences in responses for the coast up without lubricant and the coast down are dramatic and demonstrate the action of the SFDs. From this test and at the passage through the first critical speed, system damping ratios (ξ) for inactive and active dampers are estimated to be 0.12 and 0.28, respectively. The damping ratio for the active SFDs is larger than for the tests presented in Table 5 since the lubricant is at a lower temperature, and its viscosity is larger (~14.9 cp). Note that the damping ratio for the inactive SFDS is still large since some remnant lubricant was still within the thin film lands and also due to the damping action of the elastomeric (lip) seals. Figure 8 dramatically depicts the measured pressures with no oil circulating (SFD inactive) and with oil flowing through the dampers (coast down). Large film pressures are generated by the "no oil" inactive SFD condition as the rotor crosses its critical speed. The test then demonstrates that just a few drops of lubricant enable the SFDs to effectively attenuate rotor vibrations.

Conclusions

A test apparatus and measurements of the imbalance response of a rotor-bearing system supported on squeeze film dampers (SFDs) are presented. A massive three-disk rotor is supported on high-precision ball bearings in series with cylindrical SFDs and centering elastic structures. A data acquisition system records the rotor motion versus shaft speed at three axial rotor locations. In addition, squeeze film pressures are also measured at the bottom film land of one of the dampers.

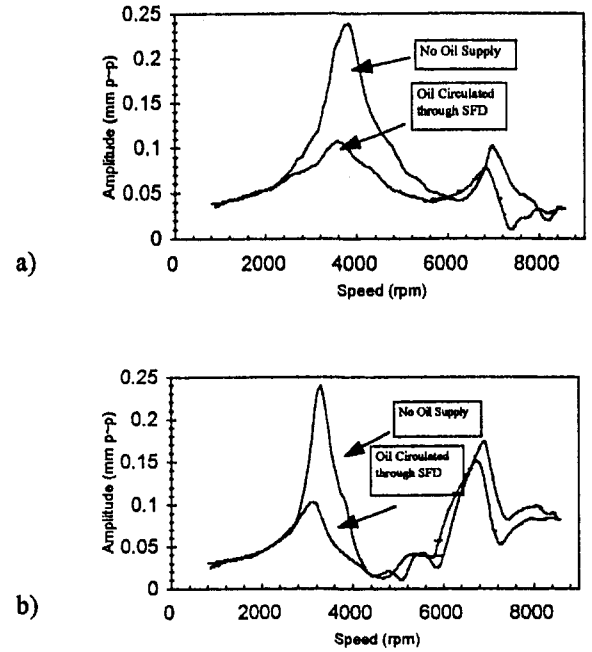

Fig. 7 Imbalance response for run-up (no oil on SFDs) and coast-down (oil at *Ps* = 10 psig (0.7 bar)). Imbalance 28.3 μm at free end disk: (*a*) vertical; (*b*) horizontal.

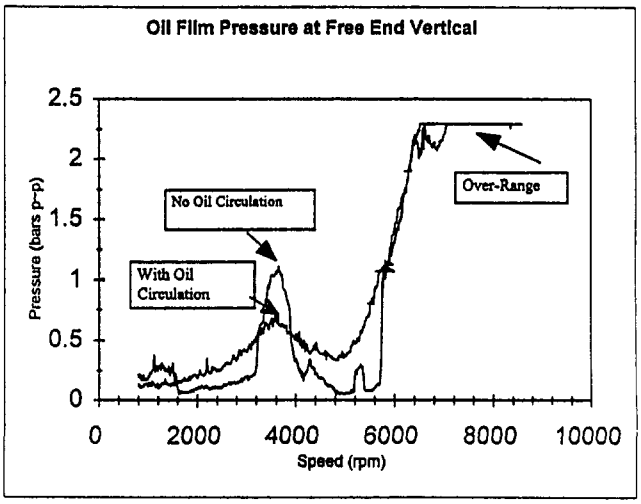

Fig. 8 Squeeze film pressure in free end (vertical) SFD for test conditions of Fig. 7

Systematic tests were performed to identify the rotor-bearing parameters of importance. Rotor free-free mode natural frequencies were measured and were validated by computed predictions. The stiffness coefficients for the SFD elastic supports were also measured and verified the design values. Measurements of the rotor undamped natural frequencies on its bearing supports show a cylindrical mode (~60 Hz), a conical mode (~100 Hz), and a first bending mode (~200 Hz). The first two natural frequencies are within the rotor speed operating range (<10 kcpm).

The system damping coefficients, extracted from impact load (rap) excitations at zero speed, vary greatly with the lubricant temperature and include a significant contribution from the lip (elastomeric) at the bearing supports. Measurements of the synchronous rotor response with different imbalance masses show the SFDs to damp well the rotor response for the cylindrical and conical modes of vibration. The rotor coast down responses demonstrate a linear behavior relative to the magnitude of the imbalances inserted at the rotor middle disk and without shifts of the critical speeds. Large rotor motions to 70 percent of the nominal SFD clearance have been measured and with peak-peak squeeze film pressures as large as 3.0 bars (43 psi). However, lubricant dynamic cavitation (vapor or gaseous) has not yet been observed. The test system damping coefficients are relatively constant and not strongly dependent on the amplitude of rotor motion through the first critical speed. The SFD damping coefficients extracted from the tests agree reasonably well with predictions from the full-film open ends SFD model.

Measurements of the test rotor-SFD responses to coupled mass imbalances and with the SFD journals statically off-centered will be reported shortly.

Acknowledgments

The support of National Science Foundation and the TAMU Turbomachinery Research Consortium are gratefully acknowledged. Thanks to Dr. J. Larsen-Basse of NSF for his interest in this work. Thanks also to Dr. Juan Oliveras of Universidad Simón Bolívar (Venezuela) for performing tests on the identification of damping coefficients from the lip seals.

References

Li, X. H., and Taylor, D., 1987, "Nonsynchronous Motion of Squeeze Film Damper Systems," *ASME Journal of Tribology,* Vol. 109, pp. 169–176.

Mohan, S., and Hahn, E. J., 1974, "Design for Squeeze Film Damper Supports for Rigid Rotors," *ASME Journal of Engineering for Industry,* Vol. 96, pp. 976–982.

Murphy, B. T., 1995, XLROTOR, Rotating Machinery Analysis, Inc., Austin, TX.

San Andres, L., and Vance, J. M., 1988, "Effect of Fluid Inertia on the Performance of Squeeze Film Damper Supported Rotors," ASME JOURNAL OF ENGINEERING FOR GAS TURBINES AND POWER, Vol. 110, pp. 51–57.

San Andres, L., and Lubell, D., 1996, "Unbalance Response of a Test Rotor Supported on Squeeze Film Dampers," Report TRC-SFD-2-96, TAMU Turbomachinery Research Consortium. Texas A&M University, College Station, TX.

San Andres, L., 1995, "Theoretical and Experimental Comparisons for Damping Coefficients of a Short Length Open-End Squeeze Film Damper," presented at the *ASME Turbo Expo '95 Land, Sea and Air Conference,* Houston, TX, ASME Paper 95-GT-98.

Vance, J., 1988, *Rotordynamics of Turbomachinery,* John Wiley & Sons, Inc. NY.

Zeidan, F. Y., 1994, "Applications of Squeeze Film Dampers," *Turbomachinery International,* Sept/Oct., pp. 50–53.

Zeidan, F., San Andres, L., and Vance, J., 1996, "Design and Application of Squeeze Film Dampers in Rotating Machinery," *Proceedings of the 25th Turbomachinery Symposium,* Turbomachinery Laboratory, Texas A&M University, College Station, TX, pp. 169–188.

Transient Thermoelasto-hydrodynamic Study of Tilting-Pad Journal Bearings Under Dynamic Loading

P. Monmousseau

M. Fillon

J. Frêne

Université de Poitiers, URA CNRS,
Laboratoire de Mécanique des Solides,
S.P.2M.I., BP 179,
86960 Futuroscope Cedex, France
email: fillon@lms.univ-poitiers.fr

Nowadays, tilting-pad journal bearings are submitted to more and more severe operating conditions. The aim of this work is to study the thermal and mechanical behavior of the bearing during the transient period from an initial steady state to a final steady state (periodic). In order to study the behavior of this kind of bearing under dynamic loading (F_{dyn}) due to a blade loss, a nonlinear analysis, including local thermal effects, realistic boundary conditions, and bearing solid deformations (TEHD analysis) is realized. After a comparison between theoretical results obtained with four models (ISO, ADI, THD, and TEHD) and experimental data under steady-state operating conditions (static load W_s), the evolution of the main characteristics for three different cases of the dynamic load ($F_{dyn}/W_s < 1$, $F_{dyn}/W_s = 1$ and $F_{dyn}/W_s > 1$) is discussed. The influence of the transient period on the minimum film thickness, the maximum pressure, the maximum temperature, and the shaft orbit is presented. The final steady state is obtained a long time after the appearance of a dynamic load.

1 Introduction

The purpose of this paper is to study the transient effect in the bearing due to a sudden unbalancing of the load, which occurs when a blade is lost in steam and gas turbines.

Choy et al. (1992) showed the importance of a theoretical nonlinear analysis for a plain journal bearing tested in conditions of unbalance mass. An isoviscous theory has been applied in this transient analysis. Paranjpe and Han (1995) performed a transient thermohydrodynamic study for a plain journal bearing submitted to a sinusoidal load. The cavitation boundary conditions (which conserve mass flow across the film rupture) and the reformation boundary conditions have been introduced. But two different time scales (for the film and for the bushing) have been used in order to determine the temperature fields. Paranjpe (1996) performed a study of a dynamically loaded engine bearing. He showed the great differences between the results obtained with the thermal theory and those with the isothermal theory. Desbordes et al. (1994) demonstrated the influence of two-dimensional pad deformation, and Desbordes et al. (1995), the influence of three-dimensional pad deformation for a tilting pad journal bearing submitted to high unbalance mass. Gadangi and Palazzolo (1995) analyzed tilting-pad journal bearings submitted to unbalance mass. They studied separately the influence of the thermal effect with an adiabatic boundary condition, and the influence of pad flexibility. In a second study, Gadangi et al. (1996), completed a transient thermal analysis for plain and tilting-pad journal bearings: The thermal effect has to be taken into account. Fillon et al. (1996) solved the transient thermal problem with a global approach, which is not appropriate in the case of a large unbalance mass.

Moreover, all these studies do not take into account the real transient phenomenon generated by the large change in bearing load due to a sudden blade loss. The subject of this paper is to analyze the behavior of a tilting-pad journal bearing submitted to a sudden dynamic load. A comparison between four theoretical cases is performed. The first case we will study is an isothermal theory (ISO) for which the fluid film and the bearing temperatures are equal to the feeding temperature. The second one we will consider is an adiabatic theory (ADI) without heat transfer in the pads while the third case is based on the realistic boundary conditions with heat transfer into the pads (THD). The last case is identical to the third with the exception that it has been created to include the solid bearing deformations (TEHD). Further on in our study, we will also examine the transient phenomenon generated by a blade loss from an initial steady state to a final steady state (periodic). Finally, an examination of the unbalance mass on the bearing performance will be conducted.

2 Analysis

In order to find realistic results, it will be necessary to use a local model of the thermal effects (Monmousseau et al., 1997). However, in order to reduce the CPU time, the thermal problem will be solved in the midplane of the bearing. In addition, the thermomechanical displacements of the pads are obtained by using the thick shell theory. The temperature in the pads will be varied with the time but that of the housing will be assumed to be constant.

2.1 Governing Equations. Using the classical lubrication hypotheses, it is assumed that the flow is laminar and that inertia in the film is neglected. The fluid is Newtonian and incompressible. The lubricant viscosity is only dependent on the temperature. The following four characteristics—density, specific heat, thermal conductivity and heat transfer coefficient—are assumed to be constant. The bearing geometry is presented in Fig. 1. The film thickness is defined by:

$$h(\theta) = C - (C - C_b)\cos(\theta - \psi^i) - (R + d)\delta^i \sin(\theta - \psi^i) + x_s \cos\theta + y_s \sin\theta + \delta_h(\theta) \quad (1)$$

where C is the radial pad clearance, C_b is the radial bearing clearance, R is the shaft radius, d is the pad thickness, δ^i is the

Contributed by the International Gas Turbine Institute and presented at the 42nd International Gas Turbine and Aeroengine Congress and Exhibition, Orlando, Florida, June 2–5, 1997. Manuscript received at ASME Headquarters February 1997. Paper No. 97-GT-400. Associate Technical Editor: H. A. Kidd.

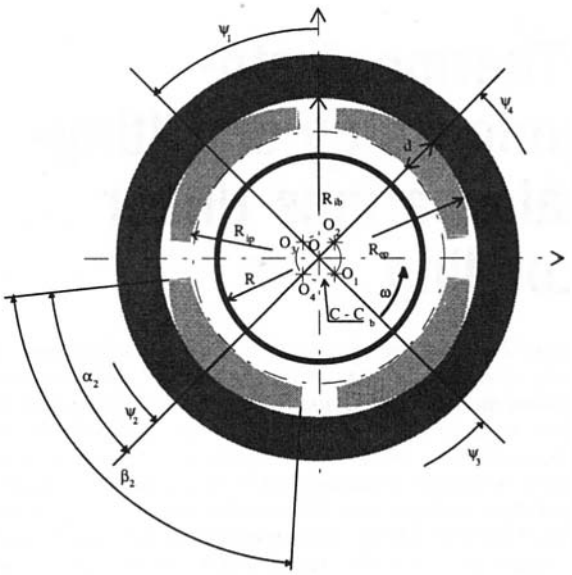

Fig. 1 Bearing geometry

rotation of the pad i, ψ^i is the pivot location of the pad i, x_s and y_s are the coordinates of the shaft center, and $\delta_h(\theta)$ is the film thickness variation due to the mechanical and thermal displacements.

The pressure is determined by solving the generalized Reynolds equation:

$$\frac{1}{R^2}\frac{\partial}{\partial\theta}\left(G\frac{\partial p}{\partial\theta}\right)+\frac{\partial}{\partial z}\left(G\frac{\partial p}{\partial z}\right)=\omega\frac{\partial}{\partial\theta}\left(h-\frac{I_2}{J_2}\right)+\frac{\partial h}{\partial t} \quad (2)$$

where

$$I_2=\int_0^h\frac{y}{\mu}dy;\quad J_2=\int_0^h\frac{dy}{\mu}\quad\text{and}\quad G=\int_0^h\frac{y}{\mu}\left(y-\frac{I_2}{J_2}\right)dy$$

We assumed that the rotor is rigid, symmetric, and supported by two identical tilting-pad journal bearings. Under the static load, the journal center is located on a stable equilibrium position. Under both static and dynamic loads, the motion of the journal center is governed by the dynamic equations:

$$M\ddot{x}_s=F_x+Me_b\omega^2\cos(\omega t)+W_{static} \quad (3a)$$

$$M\ddot{y}_s=F_y+Me_b\omega^2\sin(\omega t) \quad (3b)$$

where M is the part of the rotor mass acting upon the bearing,

Table 1 Geometric characteristics of the bearing at 20°C and operating conditions

Journal radius	R	(10^{-3} m)	50
Bearing length	L	(10^{-3} m)	70
Radial pad clearance	C	(10^{-3} m)	0.148
Radial bearing clearance	C_b	(10^{-3} m)	0.079
Preload ratio	m	-	0.47
Pad thickness	d	(10^{-3} m)	20
Angular amplitude of pad i	β^i	(°)	75
Pivot position of pad i	α^i/β^i	-	0.5
Pivot position in bearing	ψ_i	(°)	45 - 135 225 - 315
Static load	W_s	(N)	2,000
Rotor mass	M	(Kg)	1,000
Shaft speed	N	(rpm)	4,000

Table 2 Lubricant characteristics

Inlet temperature	T_0, T_{bath}	(°C)	40
Inlet pressure	P_0	(MPa)	0.05
Dynamic viscosity at 40°C	μ_o	(Pa.s)	0.0277
Density at 40°C	ρ_o	($Kg.m^{-3}$)	860
Thermal conductivity	k_o	($W.m^{-1}.K^{-1}$)	0.13
Specific heat	c_o	($J.Kg^{-1}.K^{-1}$)	2,000

e_b the unbalance eccentricity, F_x and F_y the components of the hydrodynamic force, ω the angular speed, and t the time.

The temperature in the film is obtained by solving the transient energy equation:

$$\rho_o c_o\left(\frac{\partial T}{\partial t}+\frac{u}{R}\frac{\partial T}{\partial\theta}+v\frac{\partial T}{\partial y}\right)=k_o\frac{\partial^2 T}{\partial y^2}+\mu\left(\frac{\partial u}{\partial y}\right)^2 \quad (4)$$

where ρ_o is the fluid density, c_o is the specific heat of lubricant, μ the viscosity, u and v are the velocity components, and k_o the lubricant thermal conductivity.

In the pads, the temperature is obtained by the transient heat transfer equation

$$\rho_p c_p\frac{\partial T}{\partial t}=k_p\left(\frac{\partial^2 T}{\partial r^2}+\frac{1}{r}\frac{\partial T}{\partial r}+\frac{1}{r^2}\frac{\partial^2 T}{\partial\theta^2}\right) \quad (5)$$

where ρ_p is the pad density, c_p is the specific heat of the pad, and k_p the pad thermal conductivity.

2.2 Boundary Conditions. All the boundary conditions have been developed in a previous study (Monmousseau et al., 1997).

The Reynolds classical boundary conditions are applied to the Reynolds equation.

At the film-shaft interface, the temperature is calculated according to the assumption that the global heat exchange at the interface is zero. At the film-pad interface, the temperature is obtained through the heat flux continuity condition. On the outer parts of the pads, free convection and radiation hypotheses are applied. In the inlet zone of the film, the temperature is assumed to be constant across the film thickness. The average film temperature is determined by using the flow continuity condition and the heat flux continuity equation.

2.3 Pad Displacements. The calculation of the pad displacements has been presented in detail in a previous article (Monmousseau et al., 1997). Both thermal and mechanical displacements are taken into account: thermal expansion of the shaft and the pads and pad displacements due to the temperature gradient and the hydrodynamic pressure. In addition, the pivot deflection induced by the Hertzian contact between the pads and the housing is taken into account. These displacements

Table 3 Solid characteristics

Coefficient of thermal expansion of the shaft	α_s	(K^{-1})	$12\ 10^{-6}$
Coefficient of thermal expansion of the pads	α_p	(K^{-1})	$12\ 10^{-6}$
Pad thermal conductivity	k_p	($W.m^{-1}.K^{-1}$)	45
Pad convective heat transfer coefficient	h_p	($W.m^{-2}.K^{-1}$)	100
Specific heat of pads	c_p	($J.Kg^{-1}.K^{-1}$)	400
Density of pads at 40°C	ρ_p	($Kg.m^{-3}$)	7,800
Young's modulus	E	(MPa)	210,000
Poisson's ratio	ν	-	0.30

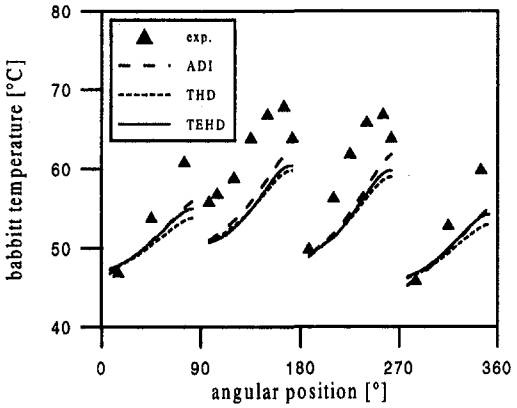

Fig. 2 Babbitt temperature versus angular position

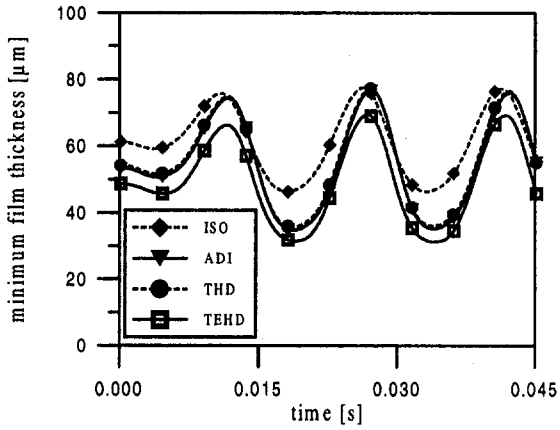

Fig. 4 Minimum film thickness for an unbalance eccentricity e_b = 22.8 μm

allow us to define the operating radial bearing clearance needed at each time step.

3 Numerical Procedure

The finite difference method solves the constitutive equations. The Gauss–Seidel iterative scheme with overrelaxation is used for the generalized Reynolds equation, while an explicit method is called for to solve the energy and heat transfer equations. Last, the pad positions are determined by the integration (implicit Euler method) of the momentum equations applied to each pad.

The general process is as follows:

- (*a*) Give initial data ($t = 0$) while $t < t_{end}$
- (*b*) Solve Reynolds equation, until convergence on pad position is not achieved, then determine hydrodynamic forces
- (*c*) Solve energy equation and deduce the viscosity field in the film
- (*d*) Solve heat transfer equation in the pads
- (*e*) Calculate bearing deformations
- (*f*) Establish new journal position
- (*g*) Receive final results ($t = t_{end}$)

The ISO theory proceeds through only the (*a*), (*b*), (*f*), and (*g*) steps whereas the ADI theory uses the (*a*), (*b*), (*c*), (*f*), and (*g*) steps. We also notice that the THD theory goes through all the steps except (*e*) and that the TEHD theory functions in all the steps.

4 Results and Discussion

4.1 Static Load Without Unbalance Mass. In order to validate the theoretical results of our study, a comparison between experimental data and such theoretical findings will be conducted. The test bearing and other experimental data have been presented in earlier journal publications (Monmousseau et al., 1997; Fillon et al., 1992). The data of the bearing at 20°C are shown in Table 1. Here in these operating conditions we should mention that the shaft rotational speed is 418.9 rad/s (4000 rpm) and the static load is equal to 2000 N.

Next, the lubricant characteristics are given in Table 2, followed by the solid characteristics seen in Table 3.

The babbitt temperatures determined by using three theoretical cases (ADI, THD, and TEHD) and experimental data are presented in Fig. 2.

In our efforts, we have found that the maximum discrepancy between experimental and theoretical results is about 5°C. The influence of the theory (ADI, THD, and TEHD) is not striking because the static load is low.

4.2 Static Load With Unbalance Mass. An unbalance eccentricity of 22.8 μm (dynamic load = 4000 N) has been established in order to compare the findings obtained based on the four theoretical results (ISO, ADI, THD, and TEHD). In Fig. 3, the journal trajectories are defined. Here, the nondimensional eccentricities before the application of the dynamic are respectively 0.13 for the ISO theory, 0.24 for the ADI theory, 0.22 for the THD theory, and 0.18 for the TEHD theory. In this

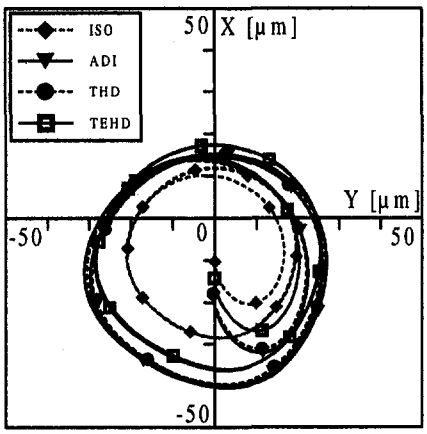

Fig. 3 Shaft orbit for an unbalance eccentricity e_b = 22.8 μm

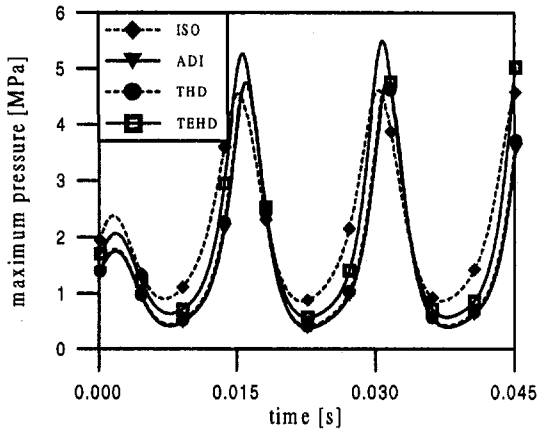

Fig. 5 Maximum pressure for an unbalance eccentricity e_b = 22.8 μm

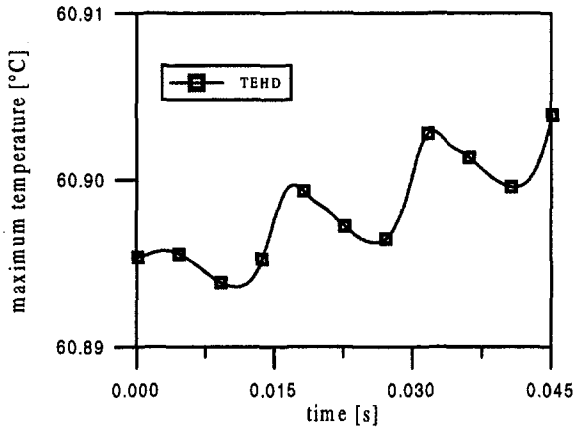

Fig. 6 Maximum temperature for an unbalance eccentricity e_b = 22.8 μm

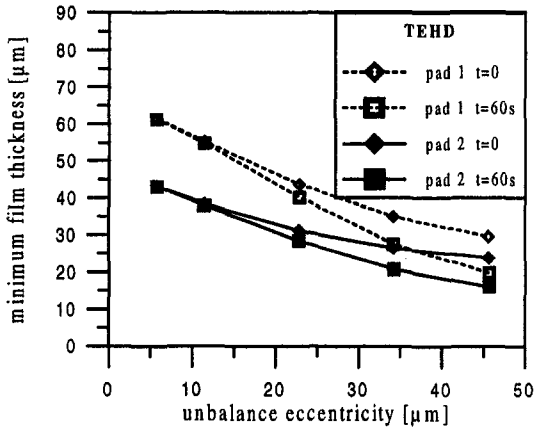

Fig. 8 Minimum film thickness versus unbalance eccentricity

case, the shaft orbit of the ADI theory and the THD theory are very similar.

Because of the bearing clearance reduction, the TEHD theory ensures a shaft orbit smaller in amplitude than the ADI and THD theories. This trajectory is larger than the one obtained by the ISO theory since the thermal effects decrease the viscosity.

Figure 4 is included to demonstrate the variations of the minimum film thickness versus time for a loaded pad (pad number 2) just after application of the dynamic loading.

The ISO case sets a minimum film thickness of 46.4 μm while the ADI and THD cases provide 34.9 and 35.7 μm, respectively. Being at the lowest value, the TEHD theory is 31.1 μm. The influence of thermal effects on minimum film thickness is not negligible: Realistic results are predicted using nonisothermal models. The bearing element displacements must also be accounted for in order to predict more accurate results.

In Fig. 5, we see the maximum pressure versus time for the same loaded pad. The TEHD theory gives a maximum pressure of 5.5 MPa. The other theories give a maximum value of almost 4.7 MPa. Both thermal effects and bearing element displacements have to be considered: Compared to the TEHD results, the ISO model leads to the greatest minimum film thickness (+50 percent) and the lowest maximum pressure (−15 percent).

Figure 6 shows us the variation of the maximum bearing temperature versus the time for a loaded pad (TEHD theory). The increase in maximum temperature is very slow because the thermal time scale is approximately one hundred times larger than the mechanical time scale. In Fig. 7, the variations of the maximum temperature for a loaded pad include testing several unbalance eccentricities in order to analyze the influence of the dynamic loading.

Until the time $t = 0$, the tilting-pad journal bearing operates under an initial steady state. At $t = 0$, a sudden dynamic loading is applied. It ensures a total modification of the thermal and the mechanical behavior of the bearing. After 60 seconds, the increase in the temperature becomes negligible: the bearing operates under a final (periodic) steady state. For a dynamic loading of 1000 N (e_b = 5.7 μm), no significant increase in temperature is detected whereas, for a dynamic loading of 4000 N (e_b = 22.8 μm), the increase in temperature is 3.5°C, and this reaches 14°C for a dynamic loading of 8000 N (e_b = 45.6 μm).

In our study, we underline there is a transient period from the initial steady state to the final (periodic) steady state. The increase in the maximum temperature, for high unbalance mass, leads to significant modifications in the behavior of the tilting-pad journal bearing. For example, in Fig. 8, we see the variations of the minimum film thickness versus unbalance eccentricities for a loaded pad (number 2) and an unloaded pad (number 1) just after the application of the dynamic loading as well as these two a long time after the application of the dynamic loading (60 s). Under a ratio dynamic loading/static load of 1 ($e_b \leq$ 11.4 μm), no significant discrepancies between initial and final steady-state are noticeable.

The same phenomenon is observed in Fig. 9, concerning maximum pressure. Thus, when this ratio is greater than 1, significant discrepancies appear. For example, for a ratio equal to 4 (eb = 45.6 μm), the minimum film thickness of an unloaded pad decreases from 29.6 to 19.8 μm (−33 percent), that de-

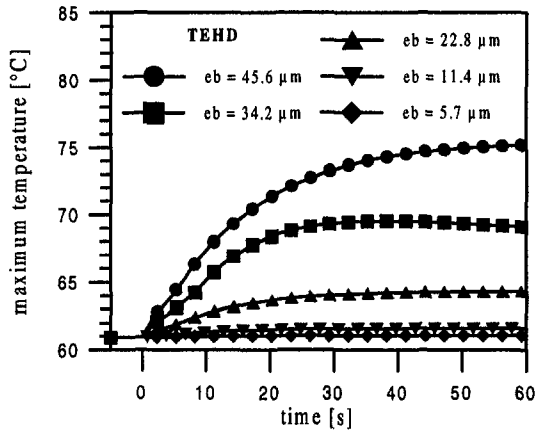

Fig. 7 Maximum bearing temperature versus time

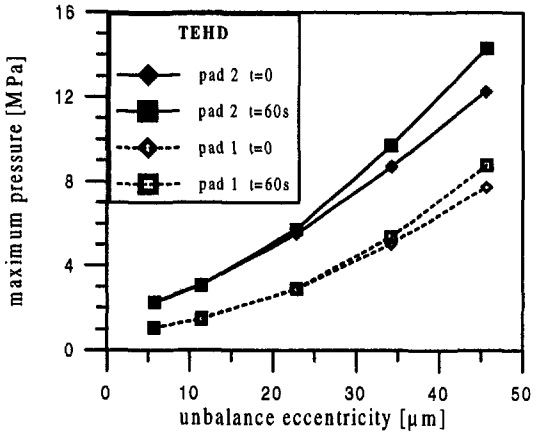

Fig. 9 Maximum pressure versus unbalance eccentricity

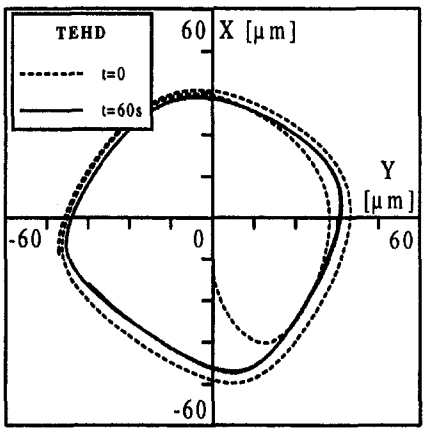

Fig. 10 Shaft orbit for an unbalance eccentricity e_b = 45.6 μm

crease is from 23.8 to 16.1 μm (−32 percent) for a loaded pad. At the same time, the maximum pressure increases, for an unloaded pad, from 7.73 to 8.77 MPa (+13 percent) and, for a loaded pad, from 12.26 to 14.30 MPa (+17 percent). These modifications on the minimum film thickness and the maximum pressure lead to a change in the shaft orbit. Figure 10 shows the trajectory of the shaft center just after the application in the dynamic loading ($0 \leq t \leq 0.030$ s) and a long time after (60 s $\leq t \leq$ 60.015 s) for an unbalance eccentricity e_b = 45.6 μm. In this figure, it is evident that because of the reduction of the bearing clearance, the discrepancy between the initial and the final orbit (−5 percent) is not as great as the difference in the minimum film thickness and in the maximum pressure.

5 Conclusion

A transient analysis of a tilting pad journal bearing submitted to a dynamic loading has been analyzed and performed in our study. Therefore, some concluding remarks can be made:

1 A realistic study must take into account all the thermal phenomenon: the results given by the isothermal theory (ISO) are not realistic.
2 The bearing element displacements have to be accounted for in order to predict more accurate results (TEHD theory).
3 The sudden application of a dynamic loading leads to a mechanical transient period and a thermal transient period, from the initial steady state to the final periodic steady state.
4 The elapsed time of the mechanical transient period is short (one revolution), but the elapsed time of the thermal transient period is longer (several seconds) and this difference depends largely on the dynamic load intensity.
5 When the ratio between dynamic load to static load is lower than 1, the behavior of the bearing is dominated by the static load thus the transient period is short and the change in the bearing characteristics is not well marked.
6 When the ratio between dynamic load to static load is greater than 1, the bearing behavior is dominated by the dynamic load and thus the transient period is large and the change in the bearing characteristics is significant.

References

Choy, F. K., Braun, M. J., and Hu, Y., 1992, "Nonlinear Transient and Frequency Response Analysis of a Hydrodynamic Journal Bearing," ASME *Journal of Tribology,* Vol. 114, pp. 448–454.

Desbordes, H., Fillon, M., Chan Hew Wai, C., and Frêne, J., 1994, "Dynamic Analysis of Tilting-Pad Journal Bearing—Influence of Pad Deformations," ASME *Journal of Tribology,* Vol. 116, pp. 621–628.

Desbordes, H., Fillon, M., Chan Hew Wai, C., and Frêne, J., 1995, "The Effects of Three-Dimensional Pad Deformations on Tilting-Pad Journal Bearings Under Dynamic Loading," ASME *Journal of Tribology,* Vol. 117, pp. 379–384.

Fillon, M., Bligoud, J. C., and Frêne, J., 1992, "Experimental Study of Tilting-Pad Journal Bearings—Comparison With Theoretical Thermoelastohydrodynamic Results," ASME *Journal of Tribology,* Vol. 114, pp. 579–588.

Fillon, M., Desbordes, H., Chan Hew Wai, C., and Frêne, J., 1996, "A Global Approach of Thermal Effects Including Pad Deformation in Tilting-Pad Journal Bearings Submitted to Unbalance Load," ASME *Journal of Tribology,* Vol. 118, pp. 169–174.

Gadangi, R. K., and Palazzolo, A. B., 1995, "Transient Analysis of Tilt Pad Journal Bearings Including Effects of Pad Flexibility and Fluid Film Temperature," ASME *Journal of Tribology,* Vol. 117, pp. 302–307.

Gadangi, R. K., Palazzolo, A. B., and Kim, J., 1996, "Transient Analysis of Plain and Tilt Pad Journal Bearings Including Fluid Film Temperature Effects," ASME *Journal of Tribology,* Vol. 118, pp. 423–430.

Monmousseau, P., Fillon, M., and Frêne, J., 1997, "Transient Thermoelastohydrodynamic Study of Tilting-Pad Journal Bearings—Comparison Between Experimental Data and Theoretical Results," ASME *Journal of Tribology,* Vol. 119, pp. 401–407.

Paranjpe, R. S., and Han, T., 1995, "A Transient Thermohydrodynamic Analysis Including Mass Conserving Cavitation for Dynamically Loaded Journal Bearings," ASME *Journal of Tribology,* Vol. 117, pp. 369–378.

Paranjpe, R. S., 1996, "A Study of Dynamically Loaded Engine Bearings Using a Transient Thermohydrodynamic Analysis," STLE *Tribology Transactions,* Vol. 39, pp. 636–644.

Characterization of Contact Kinematics and Application to the Design of Wedge Dampers in Turbomachinery Blading: Part 1—Stick-Slip Contact Kinematics

B. D. Yang

C. H. Menq

Department of Mechanical Engineering,
The Ohio State University,
Columbus, OH 43210

Friction dampers are often used in turbine design to attenuate blade vibration to acceptable levels so as to prolong blades' service life. A wedge damper, also called a self-centering, blade-to-blade damper, can provide more design flexibility to meet various needs in different operating conditions when compared with conventional platform dampers. However, direct coupling of the two inclined friction interfaces of the wedge damper often leads to very complex contact kinematics. In Part I of this two-part paper, a dual-interface friction force model is proposed to investigate the coupling contact kinematics. The key issue of the model formulation is to derive analytical criteria for the stick-slip transitions that can be used to precisely simulate the complex stick-slip motion and, thus, the induced friction force as well. When considering cyclic loading, the induced periodic friction forces can be obtained to determine the effective stiffness and damping of the interfaces over a cycle of motion. In Part II of this paper, the estimated stiffness and damping are then incorporated with the harmonic balance method to predict the forced response of a blade constrained by wedge dampers.

Introduction

Dry friction has long been recognized to be an effective and simple means of increasing the mechanical damping level of turbine bladed disk systems. In particular, dry friction is often applied to attenuate blade vibration to acceptable levels so as to prolong blades' service life by preventing high-cycle fatigue. Examples of such application include platform dampers like blade-to-ground and blade-to-blade dampers, and shroud contacts. Although the design of dampers or shroud contacts still mainly depends on experience and lab testing, many studies have been conducted to establish analytical approaches to predict the dynamic behavior of frictionally constrained blade systems [1–10]. For this class of problems, three issues are important: friction law, contact kinematics, and nonlinear dynamics analysis.

It is well known that friction is such a complex process that there is no unique law that can completely explain the phenomenon associated with friction. Thus, depending on the applications of interest, different friction laws may be applied. For the problem of turbomachinery blading, it is desired to have a friction law that can render a tractable mathematical interface model while the influence of the friction contact can still be well characterized. This demand becomes more prominent when a computationally efficient method is required to deal with the dynamic analysis of frictionally constrained structures. Among various friction laws, the Coulomb friction law has prevailed in this class of problems. While the Coulomb friction law has many limitations [11, 12, 13], it has been shown to be useful in such applications [3, 4, 15].

Contact kinematics is known to be how the contacting surfaces move with respect to each other. Because the induced friction force is completely characterized by the relative motion between the contacting surfaces, the contact kinematics plays important role in determining the effective damping and stiffness of the friction interface. The contact kinematics can be divided into two different components that have distinctive effects on its influenced structures: tangential components that induces friction slip and a normal component that causes the normal load variation. The simplest contact kinematics is that the contacting surfaces move back and forth with respect to each other and are held by a constant normal load. This contact kinematics has been intensively examined in the literature [1, 3, 4, 5, 7, 14]. The two-dimensional contact kinematics in which the contacting surfaces undergo two-dimensional relative motion has also been studied in [16, 17, 18]. The normal load variation may appear in shroud contact because the protruding shrouds constrain the blade motions not only along the contact surface but also along the normal direction of the surface [10, 19].

Friction contacts have inherently nonlinear characteristics and their interactions with overall system dynamics often lead to very complex dynamic behaviors. In predicting the nonlinear forced response of frictionally constrained complex structures, such as turbine blades, the closed solution, if possible, frequently becomes impractical [20, 21]. The time-domain solution procedure using the numerical integration technique has been shown to be a feasible approach [13, 22]. Although the detailed analysis of stick-slip may not be necessary for the numerical integration approach, it often leads to lengthy computation. The problem of the computation load is even worsened

Contributed by the International Gas Turbine Institute and presented at the International Gas Turbine & Aeroengine Congress & Exhibition, Orlando, FL, June 2–5, 1997. Manuscript received by the ASME Headquarters July 1997. Paper No. 97-GT-19. Associate Technical Editor: H. A. Kidd.

by the requirement of a small step size for avoiding the numerical instability. On the other hand, the frequency-domain solution procedure using the harmonic balance technique has been proven to be effective in solving this type of nonlinear problem [5, 6, 10, 14, 22]. The harmonic balance method transforms the governing differential equations of motion into the algebraic equations that can be solved using an efficient numerical solver such as the Newton-Raphson method. Although the harmonic balance method is an approximate method and has several limitations, its accuracy has been shown to be sufficient for such applications [22, 23].

In developing the friction force model, the work cited above considered that dampers and shroud contacts are characterized by the friction force model involving only a single friction interface; that is, the evaluation of the friction force is decoupled from the influence of other interfaces. This work focuses on a different type of friction force model having two coupled interfaces. In turbomachinery blading, a wedge damper is an example of a damper having two coupled interfaces; the configuration is shown in Fig. 1. It can be seen that the inclined platforms form a V-shape between the adjacent blades. During the operation, engine rotation causes the centrifugal force to load the wedge damper against the adjacent blades, and the wedge damper is designed in such a way that it remains in contact with each adjacent blade at any instant. Hence, the vibration of the blades results in a predictable damper motion for dissipating energy, and at the same time the damper can seal the passway of the gas stream to increase the aerodynamic efficiency of the turbine. Besides, the inclined interfaces can be aligned with the vibration direction to better use the relative motion for dissipating energy and, thus, can provide more design flexibility to meet various needs in different operating conditions. By neglecting the inertial effect, the damper remains in force balance at any instant, and, thus, the induced friction force at one of the inclined friction interfaces can affect the normal load of the other interface through this force balance, and subsequently, alter the friction force as well. This direct coupling of the two interfaces of the damper can lead to very complex contact kinematics.

This work consists of two parts. In Part I, the contact kinematics of a wedge damper is investigated. A dual-interface model is proposed to analyze the stick-slip motion at the two coupled friction contacts of the damper. Based on the proposed model, a set of two force balance equations is derived to establish the coupling relationship among the induced friction forces and the contact normal loads at the two friction interfaces of the damper. Using these two force balance equations, a diagram of stick-slip configuration is developed. This diagram can be used to visualize the stick-slip motions of the two interfaces, and, thus, facilitate the analysis of the stick-slip motion. It can also be used to evaluate the effectiveness of the geometric design of a wedge damper. Based on the diagram of stick-slip configuration, analytical criteria predicting the stick-slip transitions are derived. With these stick-slip transition conditions, the induced friction forces and the contact normal loads of the two interfaces of the damper can be predicted in terms of the resulting relative motion between adjacent blades. In Part II of this paper, the proposed friction force model is incorporated with the harmonic balance method to predict the forced response of a blade constrained by wedge dampers.

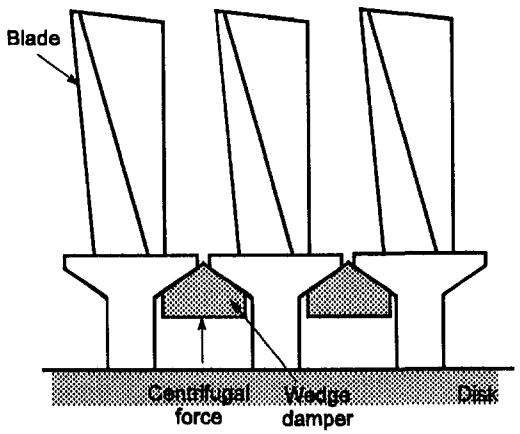

Fig. 1 Wedge dampers

Contact Kinematics

Figure 2 shows the detailed configuration of a wedge damper whose geometry is characterized by the damper angle between the two inclined surfaces. The centrifugal force caused by engine rotation loads the damper against the inclined platforms of the neighboring blades, whose motions, $\mathbf{d}_1$ and $\mathbf{d}_2$, can be expressed in a u-v coordinate frame, an oblique coordinate frame defined along the inclined surfaces as follows:

$$\mathbf{d}_1 = d_{1,u}\hat{\mathbf{u}} + d_{1,v}\hat{\mathbf{v}} \tag{1}$$

$$\mathbf{d}_2 = d_{2,u}\hat{\mathbf{u}} + d_{2,v}\hat{\mathbf{v}} \tag{2}$$

where $\hat{\mathbf{u}}$ and $\hat{\mathbf{v}}$ are unit vectors. Depending on the damper geometry and the vibratory motions of the two neighboring blades, there may exist two types of contact kinematics: nonrotational and rotational.

Nonrotational Contact Kinematics (Fig. 3(a)). It will be shown later that if the damper angle does not exceed a certain value, the platforms and the damper will remain in (surface) contact during the course of vibratory motion. If this is the case, it can be assumed that the damper does not rotate with respect to the platforms of the blades. In this situation, the contact kinematics is called nonrotational, and the damper motion can be characterized by the motions of the blades as follows:

$$\mathbf{d}_{\text{damper}} = d_{2,u}\hat{\mathbf{u}} + d_{1,v}\hat{\mathbf{v}} \tag{3}$$

Thus, the relative motions at both contacts can be expressed as

$$d_u = d_{1,u} - d_{2,u} \tag{4}$$

$$d_v = d_{2,v} - d_{1,v}. \tag{5}$$

This type of contact kinematics results in a predictable damper motion and is the main focus of this research.

Rotational Contact Kinematics (Fig. 3(b)). If the damper angle is too large, the damper may rotate to maintain the necessary force balance of the damper. When this situation occurs, point contacts take place, and Fig. 3(b) shows two possibilities of rotation that depend on how the neighboring blades vibrate. If the corner of the inclined platform is close to the apex of the damper, the contact force at contact point A (shown as the big arrow) is much larger than that at contact point B (shown as the small arrow). In this situation, contact point B tends to separate, and contact point A remains in stick condition, resulting in two undesired features of no sealing effect and no slip to dissipate energy. By properly designing the configuration of the damper, the occurrence of the rotation of the damper can be prevented. It is noted that the tendency of the separation at contact point B (i.e., when the contact force tends to vanish) provides a way to predict when this rotational contact kinematics occurs.

Model of a Wedge Damper

Figure 4 shows a model of a wedge damper in which two inclined friction interfaces are on both sides of a wedge object that is assumed to be rigid and subjected to a centrifugal force N. The inclined angles, α and β, are the angles from the direction of

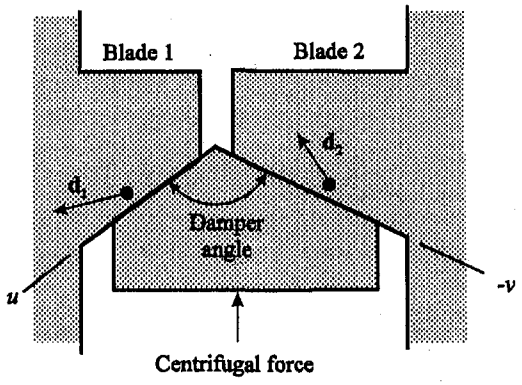

Fig. 2 Configuration of a wedge damper

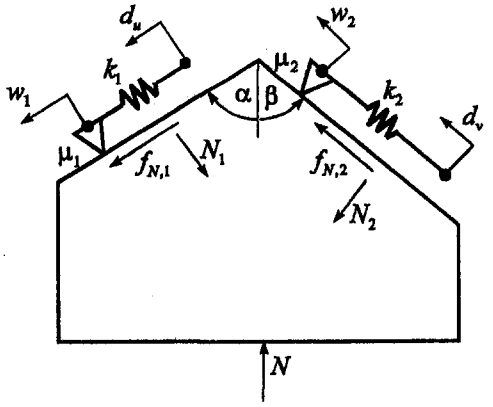

Fig. 4 Model of a wedge damper

the centrifugal force, and the angle $\alpha + \beta$ is the damper angle of the wedge damper. In this model, each interface is modeled as the one proposed by Griffin [3], which consists of one flexible element of stiffness $k_1(k_2)$ and one friction contact point of friction coefficient $\mu_1(\mu_2)$. In this work, only the nonrotational contact kinematics are considered, and, thus, the relative motions of the interfaces, d_u and d_v, can be calculated from the blade motions using Eqs. (4) and (5). d_u and d_v are termed the input motions in the following discussion. The slip motions of the contact points, w_1 and w_2, characterize the stick/slip condition of the interfaces. When the contact point reverses the direction ($\dot{w}_1 = 0$ or $\dot{w}_2 = 0$), the slip-to-stick transition takes place. However, $\dot{w}_1$ and $\dot{w}_2$ are not explicitly known, and how to relate these two slip motions to the input motions becomes important when analyzing the stick-slip phenomenon. It should be pointed out that this complexity does not appear when the single-interface model with constant normal load is considered. It can be shown that, in the single-interface model, the contact point reverses the direction when the input motion reverses the direction.

In order to simplify the formulations, the following nondimensionalized variables are used:

$$\bar{f}_{N,1} = \frac{f_{N,1}}{N} \quad \bar{N}_1 = \frac{\mu_1 N_1}{N} \quad \bar{u} = \frac{k_1 d_u}{N} \quad \bar{w}_1 = \frac{k_1 w_1}{N}$$

$$\bar{f}_{N,2} = \frac{f_{N,2}}{N} \quad \bar{N}_2 = \frac{\mu_2 N_2}{N} \quad \bar{v} = \frac{k_2 d_v}{N} \quad \bar{w}_2 = \frac{k_2 w_2}{N}. \quad (6)$$

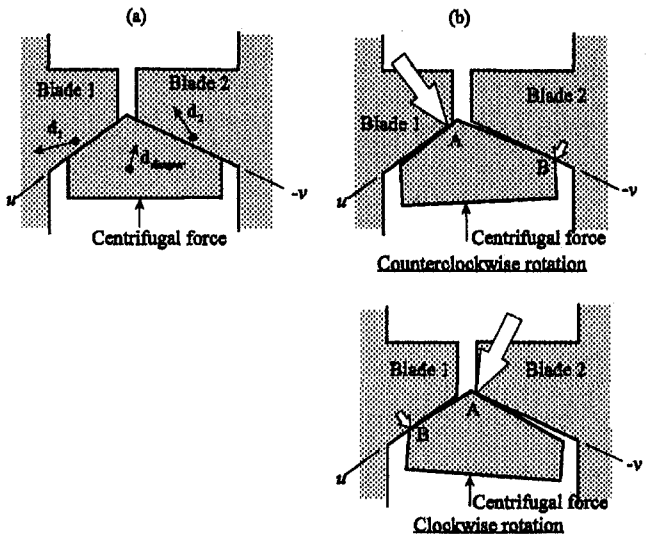

Fig. 3 Contact kinematics (*a*) nonrotational, (*b*) rotational

In this model, the friction forces are equal to the spring forces at any instant, and can be expressed as

$$\bar{f}_{N,1} = \bar{u} - \bar{w}_1 \quad (7)$$

$$\bar{f}_{N,2} = \bar{v} - \bar{w}_2. \quad (8)$$

Furthermore, each friction contact obeys the Coulomb friction law:

Stick Condition.

$$-\bar{N}_1 \le \bar{f}_{N,1} \le \bar{N}_1 \quad \text{and} \quad \dot{\bar{w}}_1 = 0 \quad \text{for interface 1} \quad (9)$$

$$-\bar{N}_2 \le \bar{f}_{N,2} \le \bar{N}_2 \quad \text{and} \quad \dot{\bar{w}}_2 = 0 \quad \text{for interface 2} \quad (10)$$

Positive Slip Condition.

$$\bar{f}_{N,1} = \bar{N}_1 \quad \text{and} \quad \dot{\bar{w}}_1 \ge 0 \quad \text{for interface 1} \quad (11)$$

$$\bar{f}_{N,2} = \bar{N}_2 \quad \text{and} \quad \dot{\bar{w}}_2 \ge 0 \quad \text{for interface 2} \quad (12)$$

Negative Slip Condition.

$$\bar{f}_{N,1} = -\bar{N}_1 \quad \text{and} \quad \dot{\bar{w}}_1 \le 0 \quad \text{for interface 1} \quad (13)$$

$$\bar{f}_{N,2} = -\bar{N}_2 \quad \text{and} \quad \dot{\bar{w}}_2 \le 0 \quad \text{for interface 2} \quad (14)$$

Under the influence of the normal load $\bar{N}_1$, the input motion $\bar{u}$ can induce the friction force $\bar{f}_{N,1}$, which affects the normal load of $\bar{N}_2$ through the force balance of the damper, and, subsequently, alters the friction force $\bar{f}_{N,2}$. As a result, the friction force depends on not only the input motion of its associated interface, but also the input motion of the other interface. The force balance of the damper, the center role of the coupling, can be formulated as follows by neglecting the inertia of the damper:

$$\bar{N}_1 = -\frac{\mu_1 \cos(\alpha + \beta)}{\sin(\alpha + \beta)} \bar{f}_{N,1} + \frac{\mu_1}{\sin(\alpha + \beta)} \bar{f}_{N,2} + \frac{\mu_1 \cos\beta}{\sin(\alpha + \beta)} \quad (15)$$

$$\bar{N}_2 = -\frac{\mu_2}{\sin(\alpha + \beta)} \bar{f}_{N,1} + \frac{\mu_2 \cos(\alpha + \beta)}{\sin(\alpha + \beta)} \bar{f}_{N,2} + \frac{\mu_2 \cos\alpha}{\sin(\alpha + \beta)}. \quad (16)$$

From the above equations, it is clear that the normal loads $\bar{N}_1$ and $\bar{N}_2$ are affected by both friction forces $\bar{f}_{N,1}$ and $\bar{f}_{N,2}$.

In this dual-interface friction force model, the coupling through the force balance of the damper leads to a complex stick-slip mechanism in which the stick-slip motions of the interfaces interact with each other. As a result, the estimation

of the friction damping and effective stiffness becomes more difficult when compared to the single-interface model. For harmonic input motions, say $\bar{u} = A \sin \omega t$ and $\bar{v} = B \sin(\omega t + \phi)$, the friction forces are approximated by the first fundamental terms of their Fourier series as

$$\bar{f}_{N,1} \approx \bar{f}_{s,1}(A, B, \phi) \sin \omega t + \bar{f}_{c,1}(A, B, \phi) \cos \omega t \quad (17)$$

$$\bar{f}_{N,2} \approx \bar{f}_{s,2}(A, B, \phi) \sin(\omega t + \phi) + \bar{f}_{c,2}(A, B, \phi) \cos(\omega t + \phi), \quad (18)$$

where $\bar{f}_s$'s are the stiffness terms for they are in phase with the motion, and $\bar{f}_c$'s are the damping terms for they are out of phase by 90 deg with the motion.

Stick-Slip Configuration

According to the Coulomb friction law, each interface of the damper may stick, slip towards the positive direction, or slip towards the negative direction. Since only the nonrotational contact kinematics is of interest, the separation of the interfaces is not considered here. Thus, the state of the wedge damper can be defined as the combination of the stick-slip motions of the two friction interfaces. There are nine possible states, which can be classified into three types: one stick state; four single-slip states; and four double-slip states. The stick state denotes the condition of both interfaces sticking. The single-slip state denotes the condition of one interface sticking and the other slipping. The double-slip state denotes the condition of both interfaces slipping. These states are summarized in Table 1, in which the letter E designates the stick condition, the letter P the positive-slip condition, and the letter N the negative-slip condition. The state of the damper is represented by a two-letter symbol, the first letter of which is referred to as the condition of interface 1 and the second letter as the condition of interface 2. It can be shown later that when the damper angle is large, the separation of the interfaces may be included in the stick-slip configuration. Although the separation of the interfaces will not be considered in the stick-slip analysis, this provides a way to design a damper configuration free of the separation.

When considering the Coulomb friction law and the force balance of the damper (Eqs. (9)–(16)), the stick-slip configuration of a wedge damper can be graphically represented by the sketch of Fig. 5. In this configuration, the friction forces limited by the slip load lie within a range that is shown as the shaded area and consists of the nine states that are mentioned above. For interface 1, the two projective lines ($\bar{f}_{N,1} = \bar{N}_1$ and $\bar{f}_{N,1} = -\bar{N}_1$) represent the positive and negative slip conditions, and the region between these two lines is the stick condition for interface 1. Interface 2 also has a similar situation of its stick-slip conditions being bounded within the two projective lines ($\bar{f}_{N,2} = \bar{N}_2$ and $\bar{f}_{N,2} = -\bar{N}_2$). Considering the two interfaces simultaneously, the double-slip state of the damper is shown as the intersection of the projective lines of different interfaces,

Table 1 State of a wedge damper

Type of state	Symbol	Stick-slip condition (interface 1)	Stick-slip condition (interface 2)
stick	*EE*	stick	stick
single-slip	*PE*	positive slip	stick
	NE	negative slip	stick
	EP	stick	positive slip
	EN	stick	negative slip
double-slip	*PP*	positive slip	positive slip
	NN	negative slip	negative slip
	PN	positive slip	negative slip
	NP	negative slip	positive slip

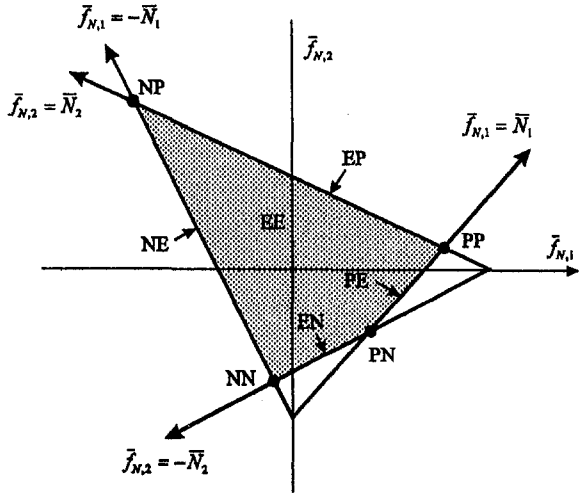

Fig. 5 Stick-slip configuration of a wedge damper

the single-slip state is shown as the line segment between two double-slip states, and the stick state is the region bounded by the four line segments of the single-slip state. The stick-slip configuration can be used to visualize the stick-slip motions, and, therefore, help analyze the stick-slip phenomenon. Another usage of this configuration is to help design an efficient damper configuration.

Depending on the damper angle, three different types of stick-slip configuration may exist. When a damper has a large damper angle, its stick-slip configuration can be shown in Fig. 6(*a*). It can be seen that the separation points of $\bar{N}_1 = 0$ and $\bar{N}_2 = 0$, namely the intersections of the projective lines ($\bar{f}_{N,1} = \bar{N}_1$ and $\bar{f}_{N,1} = -\bar{N}_1$, and $\bar{f}_{N,2} = \bar{N}_2$ and $\bar{f}_{N,2} = -\bar{N}_2$), are included in this stick-slip configuration. This indicates that the rotational contact kinematics may take place during the course of vibration. As mentioned previously, the rotational contact kinematics may give rise to the unwanted features of no seal effect and no slip to dissipate energy. When a damper has a small damper angle, the stick-slip configuration may have a open stick region as shown in Fig. 6(*c*). This open stick-slip configuration is inefficient in dissipating energy because a significant portion of the

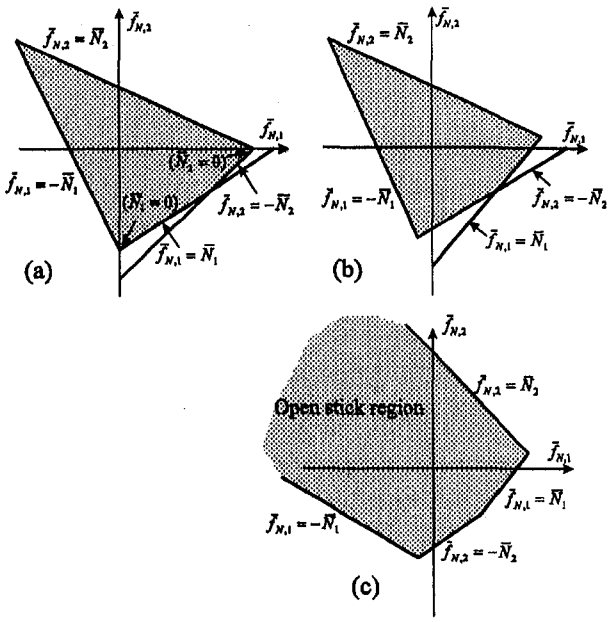

Fig. 6 Three types of stick-slip configuration

motion may reside in the stick region. In between these two cases, a moderate damper angle can result in an efficient damper configuration, whose stick-slip configuration is shown in Fig. 6(*b*). Its effectiveness in dissipating energy arises from the fact that the rotational contact kinematics will not occur and the stick-slip configuration has a closed stick region.

A complete discussion about the design of an efficient damper configuration can be found in [24]. This paper is devoted to the stick-slip analysis for the efficient damper configuration and its effect on the forced response of turbine blades.

Transition Criterion Between States

For the proposed friction force model, model formulations have to be derived to evaluate the induced friction force so as to estimate its equivalent damping and effective stiffness. However, due to the complexity of the coupled stick-slip motions in the dual-interface model, the establishment of the friction force is far more complicated than that in the single-interface model employed by Griffin [3]. The main difficulty of the model formulations is that the determination of the transitions between various states is not straightforward. Take the transition from the slip condition to the stick condition for example. In the single-interface model with constant normal load, this transition occurs when the input motion reverses its direction. However, in the dual-interface model, this transition occurring at one interface may be postponed to some instant after the reversion of the motion or hastened to some instant before the reversion, because the transition depends on the input motions of this interface and the other interface as well.

To solve this problem, analytical transition criteria are developed to predict when the transitions take place between states. Before developing these criteria, the friction forces ($\bar{f}_{N,1}$ and $\bar{f}_{N,2}$) and the slip velocities of the contact points ($\dot{\bar{w}}_1$ and $\dot{\bar{w}}_2$), which characterize the stick-slip conditions of the interfaces as implied by the Coulomb friction law, have to be addressed in analytical forms.

Stick-Slip Characteristic. For the stick state of the damper (*EE*), both interfaces stick. One can conclude that

$$\bar{f}_{N,1} = (\bar{u} - \bar{u}_0) + \bar{f}^0_{N,1} \quad \text{and} \quad \dot{\bar{w}}_1 = 0 \tag{19}$$

$$\bar{f}_{N,2} = (\bar{v} - \bar{v}_0) + \bar{f}^0_{N,2} \quad \text{and} \quad \dot{\bar{w}}_2 = 0, \tag{20}$$

where $\bar{u}_0$, $\bar{v}_0$, $\bar{f}^0_{N,1}$, and $\bar{f}^0_{N,2}$ are the displacements and friction forces at the beginning of the stick state.

For the single-slip state (*PE*), interface 1 slips towards the positive direction and interface 2 sticks. Therefore, the stick-slip characteristics of interface 2 are the same as Eq. (20) but the friction force of interface 1 equals to the positive slip load, i.e., $\bar{f}_{N,1} = \bar{N}_1$ and, considering Eqs. (7), (8), (15), and (16), $\dot{\bar{w}}_1$ can be expressed in terms of the input motions

$$\dot{\bar{w}}_1 = \dot{\bar{u}} - \frac{\mu_1}{\sin(\alpha + \beta) + \mu_1 \cos(\alpha + \beta)} \dot{\bar{v}}. \tag{21}$$

It can be seen that $\dot{\bar{w}}_1$ depends on $\dot{\bar{u}}$ and $\dot{\bar{v}}$. This indicates that the slip-to-stick transition of interface 1 (when $\dot{\bar{w}}_1 = 0$) seldom occurs when its input motion reaches the extreme ($\dot{\bar{u}} = 0$). Using similar procedures, the stick-slip characteristics of the other three single-slip states (*NE*, *EP*, *EN*) can also be obtained, which are listed in Table 2.

For the double-slip state (*PP*), both interfaces slip towards the positive direction. Hence, their friction forces equal to the positive slip load, i.e., $\bar{f}_{N,1} = \bar{N}_1$ and $\bar{f}_{N,2} = \bar{N}_2$, and considering Eqs. (7), (8), (15), and (16), $\dot{\bar{w}}_1$ and $\dot{\bar{w}}_2$ can be expressed as

$$\dot{\bar{w}}_1 = \dot{\bar{u}} \quad \text{and} \quad \dot{\bar{w}}_2 = \dot{\bar{v}}. \tag{22}$$

Table 2 Stick-slip characteristics

State	$\bar{f}_{N,1}$	$\dot{\bar{w}}_1$	$\bar{f}_{N,2}$	$\dot{\bar{w}}_2$
EE	$(\bar{u} - \bar{u}_0) + \bar{f}^0_{N,1}$	0	$(\bar{v} - \bar{v}_0) + \bar{f}^0_{N,2}$	0
PE	$\bar{N}_1$	$\dot{\bar{u}} - \frac{\mu_1}{s + \mu_1 c}\dot{\bar{v}}$	$(\bar{v} - \bar{v}_0) + \bar{f}^0_{N,2}$	0
NE	$-\bar{N}_1$	$\dot{\bar{u}} + \frac{\mu_1}{s - \mu_1 c}\dot{\bar{v}}$	$(\bar{v} - \bar{v}_0) + \bar{f}^0_{N,2}$	0
EP	$(\bar{u} - \bar{u}_0) + \bar{f}^0_{N,1}$	0	$\bar{N}_2$	$\frac{\mu_2}{s - \mu_2 c}\dot{\bar{u}} + \dot{\bar{v}}$
EN	$(\bar{u} - \bar{u}_0) + \bar{f}^0_{N,1}$	0	$-\bar{N}_2$	$\frac{-\mu_2}{s + \mu_2 c}\dot{\bar{u}} + \dot{\bar{v}}$
PP	$\bar{N}_1$	$\dot{\bar{u}}$	$\bar{N}_2$	$\dot{\bar{v}}$
PN	$\bar{N}_1$	$\dot{\bar{u}}$	$-\bar{N}_2$	$\dot{\bar{v}}$
NP	$-\bar{N}_1$	$\dot{\bar{u}}$	$\bar{N}_2$	$\dot{\bar{v}}$
NN	$-\bar{N}_1$	$\dot{\bar{u}}$	$-\bar{N}_2$	$\dot{\bar{v}}$

$s = \sin(\alpha + \beta)$, $c = \cos(\alpha + \beta)$

The other three double-slip states (*PN*, *NP*, *NN*) can be obtained by using similar procedures. They are also listed in Table 2.

Analytical Transition Criterion. For the dual-interface friction force model, it is found that there are 28 possible transitions whose criteria need be derived. This variety indeed reflects the complexity of this problem. However, these criteria have one thing in common; that is, each criterion requires one equation to prescribe when the transition takes place and a number of constraints to guarantee the transition to be satisfied. In general, the criteria can be set up by considering when the friction force reaches the slip load for the stick-to-slip transition or when the contact point reverses its direction for the slip-to-stick transition, and if the stick-slip conditions after the transition are satisfied.

To better illustrate how to establish these criteria, two cases are considered to exemplify the procedure. The first case is the transition from state *EP* to state *EE*. Before the transition, interface 1 sticks and interface 2 slips towards the positive direction; after the transition, interface 1 remains stuck, but interface 2 becomes stuck. Thus, the transition occurs when the contact point of interface 2 reverses the direction, i.e., $\dot{\bar{w}}_2 = 0$ and $\ddot{\bar{w}}_2 \leq 0$; the latter one is required to ensure the contact point of interface 2 has a tendency towards the negative direction when it reaches the extreme. Using the stick-slip characteristic of state *EP*, the transition criterion becomes

$$[\mu_2/(\sin(\alpha + \beta) - \mu_2 \cos(\alpha + \beta))]\dot{\bar{u}} + \dot{\bar{v}} = 0$$

$$[\mu_2/(\sin(\alpha + \beta) - \mu_2 \cos(\alpha + \beta))]\ddot{\bar{u}} + \ddot{\bar{v}} \leq 0. \tag{23}$$

The second case considered is the transition for state *EP* to state *PP*. The transition occurs when the friction force at interface 1 reaches the slip load, i.e., $\bar{f}_{N,1} - \bar{N}_1 = 0$; at the same time, the friction force must have a tendency to exceed the slip load that results in the constraint $\dot{\bar{f}}_{N,1} - \dot{\bar{N}}_1 \geq 0$. By considering force balance equations (15) and (16) and the stick-slip characteristics of state *EP*, this constraint becomes $\ddot{\bar{u}} \geq 0$. Another constraint can be established by examining the stick-slip conditions of state *PP*, i.e., $\dot{\bar{w}}_1 \geq 0$ and $\dot{\bar{w}}_2 \geq 0$. Using the stick-slip characteristics of state *PP*, these constraints become $\dot{\bar{u}} \geq 0$ and $\dot{\bar{v}} \geq 0$. Finally, the transition criterion can be summarized as

$$\bar{f}_{N,1} - \bar{N}_1 = 0, \quad \dot{\bar{u}} \geq 0, \quad \text{and} \quad \dot{\bar{v}} \geq 0. \tag{24}$$

Using similar procedures, the other transition criteria can be obtained and they are summarized in Table 3.

Equivalent Damping and Effective Stiffness

For given cyclic input motions, the periodic friction forces can be attained using a "state-by-state simulation" by applying the developed transition criteria. One example of the resulting friction forces by the state-by-state simulation is shown in Fig. 7 as a trajectory, along with the diagram of the stick-slip configuration of the damper. The simulation starts from the origin that corresponds to the stick state with the zero friction forces. Then, from the transition criteria listed in Table 3, the next state can be predicted by calculating the four possible transition instants starting from the stick state *EE* and then selecting the one that is first encountered. In this case, the single slip state

Table 3 Analytical transition criteria

State (from)	State (to)	Transition criterion
EE	*EP*	$\bar{f}_{N,2} - \bar{N}_2 = 0, \quad \dot{\bar{f}}_{N,2} - \dot{\bar{N}}_2 \geq 0$
	EN	$\bar{f}_{N,2} + \bar{N}_2 = 0, \quad \dot{\bar{f}}_{N,2} + \dot{\bar{N}}_2 \leq 0$
	PE	$\bar{f}_{N,1} - \bar{N}_1 = 0, \quad \dot{\bar{f}}_{N,1} - \dot{\bar{N}}_1 \geq 0$
	NE	$\bar{f}_{N,1} + \bar{N}_1 = 0, \quad \dot{\bar{f}}_{N,1} + \dot{\bar{N}}_1 \leq 0$
EP	*EE*	$\left[\mu_2/(s-\mu_2 c)\right]\dot{\bar{u}} + \dot{\bar{v}} = 0, \quad \left[\mu_2/(s-\mu_2 c)\right]\ddot{\bar{u}} + \ddot{\bar{v}} \leq 0$
	NP	$\bar{f}_{N,1} + \bar{N}_1 = 0, \quad \dot{\bar{u}} \leq 0, \quad \dot{\bar{v}} \geq 0$
	PE	$\bar{f}_{N,1} - \bar{N}_1 = 0, \quad \dot{\bar{u}} \geq 0, \quad \dot{\bar{v}} \leq 0$
	PP	$\bar{f}_{N,1} - \bar{N}_1 = 0, \quad \dot{\bar{u}} \geq 0, \quad \dot{\bar{v}} \geq 0$
EN	*EE*	$\dot{\bar{v}} - \left[\mu_2/(s+\mu_2 c)\right]\dot{\bar{u}} = 0, \quad \ddot{\bar{v}} - \left[\mu_2/(s+\mu_2 c)\right]\ddot{\bar{u}} \leq 0$
	PE	$\bar{f}_{N,1} - \bar{N}_1 = 0, \ \dot{\bar{u}} \geq 0, \ \dot{\bar{v}} \geq 0, \ \dot{\bar{u}} - \left[\mu_1/(s+\mu_1 c)\right]\dot{\bar{v}} \geq 0$
	PN	$\bar{f}_{N,1} - \bar{N}_1 = 0, \quad \dot{\bar{u}} \geq 0, \quad \dot{\bar{v}} \leq 0$
	NN	$\bar{f}_{N,1} + \bar{N}_1 = 0, \quad \dot{\bar{u}} \leq 0, \quad \dot{\bar{v}} \leq 0$
PE	*EE*	$\dot{\bar{u}} - \left[\mu_1/(s+\mu_1 c)\right]\dot{\bar{v}} = 0, \quad \ddot{\bar{u}} - \left[\mu_1/(s+\mu_1 c)\right]\ddot{\bar{v}} \leq 0$
	EN	$\bar{f}_{N,2} + \bar{N}_2 = 0, \ \dot{\bar{u}} \leq 0, \ \dot{\bar{v}} \leq 0, \ \dot{\bar{v}} - \left[\mu_2/(s+\mu_2 c)\right]\dot{\bar{u}} \leq 0$
	PN	$\bar{f}_{N,2} + \bar{N}_2 = 0, \quad \dot{\bar{u}} \geq 0, \quad \dot{\bar{v}} \leq 0$
	PP	$\bar{f}_{N,2} - \bar{N}_2 = 0, \quad \dot{\bar{u}} \geq 0, \quad \dot{\bar{v}} \geq 0$
NE	*EE*	$\dot{\bar{u}} + \left[\mu_1/(s-\mu_1 c)\right]\dot{\bar{v}} = 0, \quad \ddot{\bar{u}} + \left[\mu_1/(s-\mu_1 c)\right]\ddot{\bar{v}} \geq 0$
	NP	$\bar{f}_{N,2} - \bar{N}_2 = 0, \quad \dot{\bar{u}} \leq 0, \quad \dot{\bar{v}} \geq 0$
	EN	$\bar{f}_{N,2} + \bar{N}_2 = 0, \quad \dot{\bar{u}} \geq 0, \quad \dot{\bar{v}} \leq 0$
	NN	$\bar{f}_{N,2} + \bar{N}_2 = 0, \quad \dot{\bar{u}} \leq 0, \quad \dot{\bar{v}} \leq 0$
PP	*EP*	$\dot{\bar{u}} = 0, \quad \ddot{\bar{u}} \leq 0, \quad \ddot{\bar{v}} \geq 0$
	PE	$\dot{\bar{v}} = 0, \quad \ddot{\bar{u}} \geq 0, \quad \ddot{\bar{v}} \leq 0$
PN	*EN*	$\dot{\bar{u}} = 0, \quad \ddot{\bar{u}} \leq 0, \quad \ddot{\bar{v}} \leq 0$
	PE	$\dot{\bar{v}} = 0, \quad \ddot{\bar{u}} \geq 0, \quad \ddot{\bar{v}} \geq 0$
NN	*EN*	$\dot{\bar{u}} = 0, \quad \ddot{\bar{u}} \geq 0, \quad \ddot{\bar{v}} \leq 0$
	NE	$\dot{\bar{v}} = 0, \quad \ddot{\bar{u}} \leq 0, \quad \ddot{\bar{v}} \geq 0$
NP	*EP*	$\dot{\bar{v}} = 0, \quad \ddot{\bar{u}} \leq 0, \quad \ddot{\bar{v}} \geq 0$
	NE	$\dot{\bar{v}} = 0, \quad \ddot{\bar{u}} \leq 0, \quad \ddot{\bar{v}} \leq 0$

$s = \sin(\alpha+\beta), \quad c = \cos(\alpha+\beta)$

$$EE \rightarrow EP \rightarrow PP \rightarrow EP \rightarrow EE \rightarrow NE \rightarrow EN \rightarrow PE \rightarrow$$
$$\longrightarrow PP \rightarrow EP \rightarrow EE \rightarrow NE \rightarrow EN \rightarrow PE \rightarrow \cdots$$

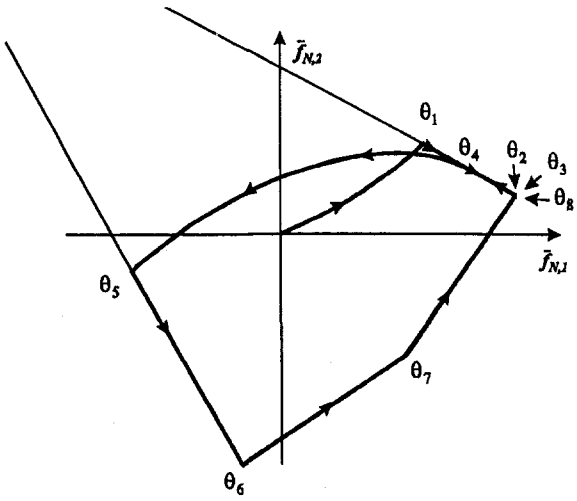

Fig. 7 Friction force trajectory

EP is the next state, and the transition occurs at the instant θ_1. This state-by-state simulation proceeds in the same manner to find the following transitions (θ_2, θ_3, θ_4, . . . , etc.) and their associated states until the periodic (steady state) friction forces are reached. As can be seen from this resulting trajectory, the periodic friction forces are always obtained within a few cycles because there is no inertial term in the model formulation. Thus, the state-by-state simulation can be an effective way to evaluate the induced friction forces.

There exist four types of steady-state friction force trajectory as shown in Fig. 8. When the input motions are small, the induced friction forces will not exceed the slip load to cause the interfaces to slip; as a result, both interfaces remain fully stuck all the time, and the resulting trajectory of the two friction forces becomes an ellipse within the stick region, as shown in Fig. 8(*a*). As the input motions increase, one of the interface may begin to slip and stick alternately, but the other still remains fully stuck. One example of the trajectory is shown in Fig.

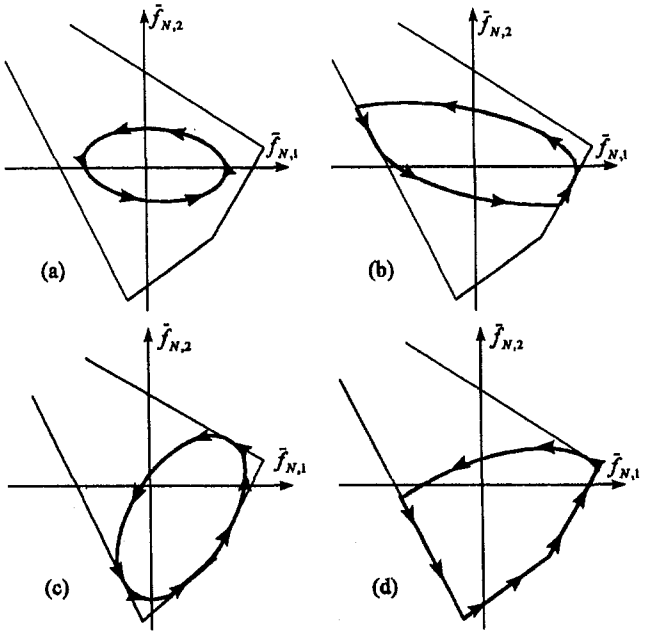

Fig. 8 Steady-state friction force trajectory

8(*b*). In some situations, both interfaces may undergo alternating stick-slip motions without the double-slip condition. As can be seen in Fig. 8(*c*), the trajectory of this case swings between the stick region and the single-slip condition. When the input motions become large, both interfaces slip most of the time to result in the double-slip condition. One example of the trajectory is shown in Fig. 8(*d*).

It is interesting to note for the same input motions that different initial states and initial values of the friction forces at the beginning of the simulation may result in different friction force trajectories when their steady states are reached. This indicates that the nonunique trajectories may physically exist. In fact, this situation can occur when one interface is fully stuck and the other undergoes an alternating stick-slip motion. As shown in Fig. 9 for the case that interface 2 is fully stuck and interface 1 experiences an alternating stick-slip motion, the nonunique trajectories lie between two limit cases, trajectory *A* and trajectory *B*. The trajectory *A* is referred to as the upper limit of the trajectories because it has the least portion of the motion residing in the slip region and, thus, can impose the least attenuation effect on its influenced structures, causing the largest response. In the opposite way, the trajectory *B* is referred to as the lower limit of the trajectories, which can cause the smallest response. Since the state-by-state simulation has difficulty in getting both limits of the trajectories, an analytical method using the geometric relations between the stick-slip configuration and the ellipse representing the input motions is developed to determine these two extreme trajectories if they exist. The detailed derivation of this method can be found in [24].

Once the periodic friction forces are identified using the state-by-state simulation or the analytical method for the limit cases of the nonunique trajectories, Fourier series expansion is then applied to estimate the damping and stiffness of the friction interfaces. Typical results of the damping and stiffness are shown as the continuous lines in Fig. 10. In this case, the ratio of the amplitude A of $\bar{u}$ to the amplitude B of $\bar{v}$ is kept constant ($A/B = 2.5$), and the phase angle between them is 45 deg. From the results, one thing to be noted is that for interface 1 the varying levels of the damping and stiffness, shown by its upper and lower limit cases, exist over the range of A from 0.22 to 0.54. As mentioned previously, this uncertainty is the result of the existence of the nonunique friction force at interface 1,

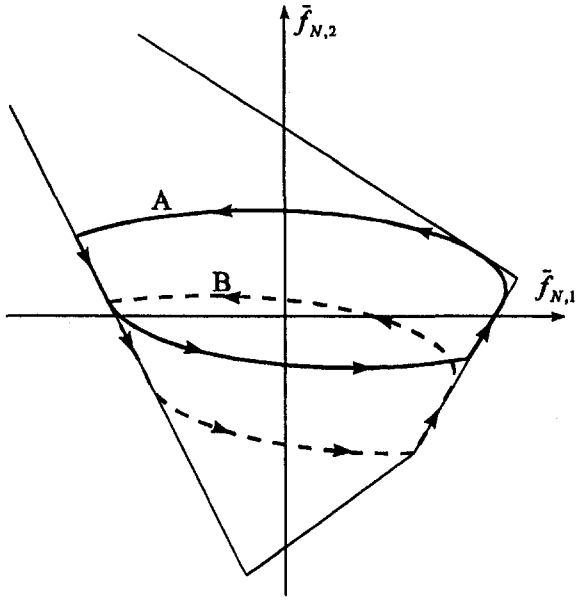

Fig. 9 Upper limit (*A*) and Lower limit (*B*) of non-unique friction force trajectories

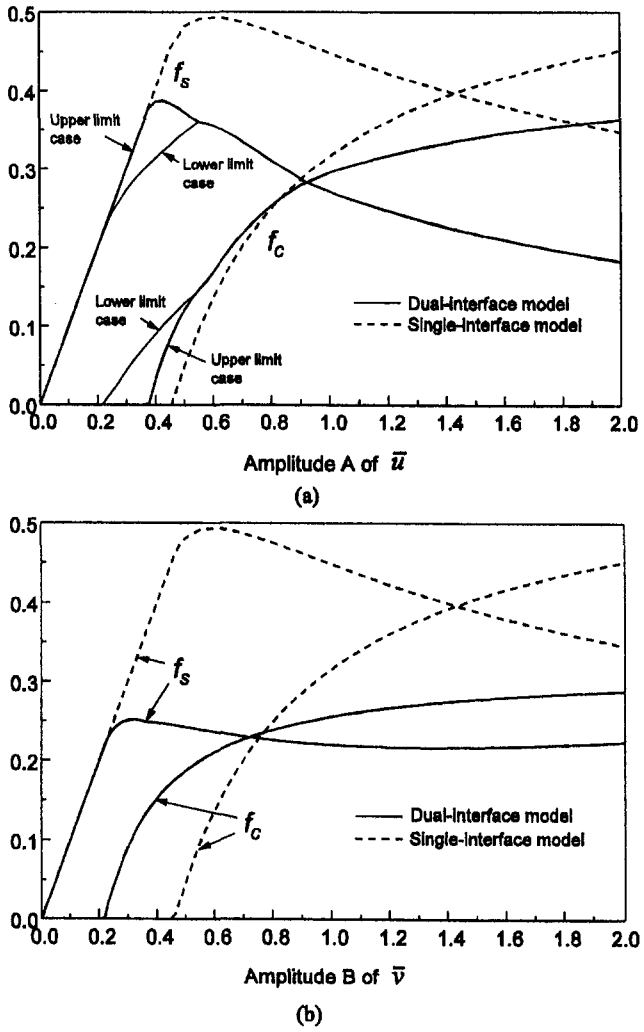

Fig. 10 Fourier coefficients (damping and stiffness) (*a*) interface 1, (*b*) interface 2

which undergoes an alternating stick-slip motion while interface 2 remains stuck all the time.

For comparison, the damping and stiffness estimated using the single-interface model under the same input motion conditions are also shown in both figures as dotted lines. In these estimations, the normal loads are assumed constant and calculated as $N \sin \alpha$ and $N \sin \beta$ for interface 1 and interface 2, respectively. These results show that for the region of small input motions, the predictions from both friction force models are the same; that is, the stiffness is the stiffness of the interface and the friction damping does not exist. This is because the input motions are not sufficiently large to cause either of the two interfaces to slip, and, as a result, both remain in the stick condition. When the slip motion becomes larger, the prediction of the single-interface model exhibits a large difference from that of the dual-interface model, indicating that the coupling effect of the interfaces can not be neglected and has to be taken into account.

It is noted that, besides the friction forces, the normal loads $\bar{N}_1$ and $\bar{N}_2$ also vary in response to the input motions of the interfaces. Therefore, they can also contribute damping and stiffness to influenced structures, which can be calculated using the force balance equations (15) and (16) once the damping and stiffness of the friction forces are obtained.

Conclusions

Although the wedge damper has many advantages over the conventional platform damper, the direct coupling of the two

inclined interfaces through the force balance of the damper often gives rise to complex contact kinematics. In this work, a dual-interface friction force model was developed to analyze the stick-slip motion at the two coupled interfaces of the damper. The key issue of the model formulation was to establish the analytical transition criteria that are used to exactly predict the stick-slip transitions. Based on the transition criteria, a simulation procedure was developed to attain the induced steady-state friction forces. This simulation is very effective because it is performed in a "state-by-state" manner. Besides, the steady-state condition is often reached within a few cycles since the interfaces are assumed massless.

The predicted damping and stiffness by the proposed dual-interface model were compared with that by the single-interface model under the same input motion condition but an assumed constant normal load. The comparison indicates that when the stick-slip motions take place, the simple single-interface model gives erroneous estimation on the damping and stiffness. This result supports the argument that the coupling effect through the force balance of the damper can not be neglected when the friction force model for the wedge damper is developed.

In Part II of this paper, the application of the proposed friction force model to the prediction of the forced response of a blade constrained by wedge dampers will be presented.

Acknowledgment

This material is based on work supported by the GUIde Consortium and the U.S. Air Force under contract No. F33615-92-C-2212. Any opinions, findings, and conclusions or recommendations expressed in this material are those of the authors and do not necessarily reflect the views of the GUIde Consortium or the Air Force.

References

1 Goodman, L. E., and Klumpp, J. H., 1956, "Analysis of Slip Damping with Reference to Turbine Blade Vibration," *ASME Journal of Applied Mechanics,* Vol. 23, Sept., pp. 421–429.

2 Earles, S. W. E., and Williams, E. J., 1972, "A Linearized Analysis for Frictionally Damped Systems," *Journal of Sound and Vibration,* Vol. 24, No. 4, pp. 445–458.

3 Griffin, J. H., 1980, "Friction Damping of Resonant Stresses in Gas Turbine Engine Airfoils," *ASME Journal of Engineering for Power,* Vol. 102, Apr., pp. 329–333.

4 Srinivasan, A. V., and Cutts, D. G., 1983, "Dry Friction Damping Mechanisms in Engine Blades," *ASME Journal of Engineering for Power,* Vol. 105, Apr., pp. 332–341.

5 Muszynska, A., and Jones, D. I. G., 1983, "A Parametric Study of Dynamic Response of a Discrete Model of Turbomachinery Bladed Disk," *ASME Journal of Vibration, Acoustics, Stress, and Reliability in Design,* Vol. 105, Oct., pp. 434–443.

6 Menq, C. H., Griffin, J. H., and Bielak, J., 1986, "The Forced Response of Shrouded Fan Stages," *ASME Journal of Vibration, Acoustics, Stress, and Reliability in Design,* Vol. 108, Jan., pp. 50–55.

7 Cameron, T. M., Griffin, J. H., Kielb, R. E., and Hoosac, T. M., 1990, "An Integrated Approach for Friction Damper Design," *ASME Journal of Vibration, Acoustics, Stress, and Reliability in Design,* Vol. 112, Apr., pp. 175–182.

8 Wagner, L. F., and Griffin, J. H., 1990, "Blade Vibration With Nonlinear Tip Constraint: Model Development," *ASME Journal of Turbomachinery,* Vol. 112, Oct., pp. 778–785.

9 Pfeiffer, F., and Hajek, M., 1992, "Stick-Slip Motion of Turbine Blade Dampers," *Philosophical Transactions of the Royal Society of London, A,* Vol. 338, pp. 503–517.

10 Yang, B. D., and Menq, C. H., 1996, "Modeling of Friction Contact and Its Application to the Design of Shroud Contact," ASME JOURNAL OF ENGINEERING FOR GAS TURBINES AND POWER, Vol. 119, No. 4, pp. 472–477.

11 Oden, J. T., and Pires, E. B., 1983, "Nonlocal and Nonlinear Friction Law and Variational Principles for Contact Problems in Elasticity," *ASME Journal of Applied Mechanics,* Vol. 50, Mar., pp. 67–76.

12 Menq, C. H., 1989, "Modeling and Vibration Analysis of Friction Joints," *ASME Journal of Vibration, Acoustics, Stress, and Reliability in Design,* Vol. 111, Jan., pp. 71–76.

13 Anderson, J. R., and Ferri, A. A., 1990, "Behavior of a Single-Degree-of-Freedom System With a Generalized-Friction Law," *Journal of Sound and Vibration,* Vol. 140, No. 2, pp. 287–304.

14 Dowell, E. H., and Schwartz, H. B., 1983, "Forced Response of a Cantilever Beam With a Dry Friction Damper Attached, Part I: Theory," *Journal of Sound and Vibration,* Vol. 91, No. 2, pp. 255–267.

15 Dowell, E. H., and Schwartz, H. B., 1983, "Forced Response of a Cantilever Beam with a Dry Friction Damper Attached, Part II: Experiment," *Journal of Sound and Vibration,* Vol. 91, No. 2, pp. 269–291.

16 Griffin, J. H., and Menq, C. H., 1991, "Friction Damping of Circular Motion and its Implications to Vibration Control," *ASME Journal of Vibration and Acoustics,* Vol. 113, April, pp. 225–229.

17 Menq, C. H., Chidamparam, P., and Griffin, J. H., 1991, "Friction Damping of Two-Dimensional Motion and Its Application in Vibration Control," *Journal of Sound and Vibration,* Vol. 144, No. 3, pp. 427–447.

18 Sanliturk, K. Y., and Ewins, D. J., 1996, "Modeling Two-Dimensional Friction Contact and Its Application Using Harmonic Balance Method," *Journal of Sound and Vibration,* Vol. 193, No. 2, pp. 511–523.

19 Menq, C. H., Griffin, J. H., and Bielak, J., 1986, "The Influence of a Variable Normal Load on the Forced Vibration of a Frictionally Damped Structure," ASME JOURNAL OF ENGINEERING FOR GAS TURBINES AND POWER, Vol. 108, April, pp. 300–305.

20 den Hartog, J. P., 1931, "Forced Vibration with Combined Coulomb and Viscous Friction," *Transactions of the ASME,* APM-53-9, pp. 107–115.

21 Yeh, G. C. K., 1964, "Forced Vibrations of a Two-Degree-of-Freedom System With Combined Coulomb and Viscous Damping," *Journal of the Acoustical Society of America,* Vol. 39, 1966, pp. 14–24.

22 Menq, C. H., and Griffin, J. H., 1985, "A Comparison of Transient and Steady State Finite Element Analyses of the Forced Response of a Frictionally Damped Beam," *ASME Journal of Vibration, Acoustics, Stress, and Reliability in Design,* Vol. 107, Jan., pp. 19–25.

23 Bindemann, A. C., and Ferri, A. A., 1992, "Characteristics of Passive Damping in Build-Up Structures," *Friction-Induced Vibration, Chatter, Squeal, and Chaos,* DE-Vol. 49, R. A. Ibrahim and A. Soom, eds., ASME, NY.

24 Yang, B. D., 1996, "Contact Kinematics of Friction Interfaces and Applications to the Prediction of Resonant Response of Frictionally Constrained Turbine Blades," Ph.D. dissertation, Ohio State University, Columbus, OH.

Characterization of Contact Kinematics and Application to the Design of Wedge Dampers in Turbomachinery Blading: Part 2—Prediction of Forced Response and Experimental Verification

B. D. Yang

C. H. Menq

Department of Mechanical Engineering,
The Ohio State University,
Columbus, OH 43210

In the second part of this paper, the application of the proposed dual-interface model to the prediction of the forced response of a blade constrained by wedge dampers will be presented. When considering cyclic loading, the induced friction forces and contact normal loads are combined so as to determine the effective stiffness and damping of the friction interfaces over a cycle of motion. The harmonic balance method is then used to impose the approximate stiffness and damping of the friction interfaces to a linear structure model of the blade. This approach results in a set of nonlinear algebraic equations that can be solved to yield the forced response of the blade excited by harmonic external forces. The predicted forced response can then be used to optimize a given damper design, namely to determine the dynamic weight at which the maximum reduction of resonant response is obtained. In order to illustrate the capacity of the proposed method and to examine its accuracy, the forced response of a test beam is examined. The prediction is also compared with the results of lab tests to validate the proposed dual-interface friction force model.

Introduction

In the second part of this paper, the application of the proposed dual-interface model to the prediction of the nonlinear forced response of a blade constrained by wedge dampers will be presented. Three issues, namely structure modeling, dynamic coupling, and nonlinear resonant response, are examined.

It has been demonstrated in [1] that a simplified spring-mass system model, either single or few degrees of freedom, may not be sophisticated enough to capture the dynamic characteristics of a beam-like structure, such as a blade, under the influence of friction interfaces. It is because the mode shape of the beam-like structure may vary significantly as the constrained force increases, so that a simple model often over-estimates the dynamic stiffness of the whole system. This raises a need of using a more accurate structure model, such as a finite element model. Based on an accurate structure model, the forced response of the structure can then be characterized by the receptances [2], which can be calculated from a standard harmonic finite element analysis of the structure.

Using the concept of receptance along with the estimated stiffness and damping of the friction interfaces, based on the proposed dual-interface model, the dynamic coupling between the dampers and the linear structure can be established via the use of the harmonic balance method[1], which has been widely used in the application of friction damping design [1, 3, 4, 5, 6]. The method of harmonic balance is employed based on the assumption that, when the external excitation is harmonic, except for the case of subharmonic resonance, the displacement and, thus, the induced nonlinear friction force are periodic and have the same fundamental period as the external excitation. Hence, the displacement and the friction force can be exactly described by infinite Fourier series. By assuming that the displacement to be dominated by the fundamental harmonic and keeping only the fundamental terms of the Fourier series of the induced friction force, the estimated stiffness and damping can then replace the nonlinear friction force and be integrated with the linear structure to transform the nonlinear differential equations of motion into a set of nonlinear algebraic equations that can be solved to yield the forced response of the frictionally constrained blade excited by harmonic external forces.

This approach eliminates most of the linear degrees of freedom of the structure from the nonlinear dynamic analysis so that the nonlinear vibration problem can be solved in a separate algorithm with less degrees of freedom that involves only the constrained portion of the structure. As a result, a computationally efficient method can be obtained for predicting the forced response of frictionally constrained structures which are so complex that they require finite element models to adequately represent their dynamic behaviors.

The harmonic balance method along with receptance representation has been successfully applied to the prediction of the forced response of shrouded fan blades [5, 6] and turbine blades constrained by the blade-to-ground damper [1]. In this work, this method will be applied to the case of the turbine blade constrained by wedge dampers. In order to illustrate the capacity of this method and to examine its accuracy, the forced response of a test beam is investigated. The prediction is also compared

Contributed by the International Gas Turbine Institute and presented at the International Gas Turbine & Aeroengine Congress & Exhibition, Orlando, FL, June 2–5, 1997. Manuscript received by the ASME Headquarters July 1997. Paper No. 97-GT-20. Associate Technical Editor: H. A. Kidd.

[1] The harmonic balance method is also referred to as the describing function method in control literature [7].

with the results of lab tests to validate the proposed dual-interface friction force model.

Nonlinear Response

The major source of excitation in a turbomachine usually arises from inevitable circumferential variation in the pressure of the working fluid. When the blades rotate through this variation in the flow field, it may be shown that each blade experiences a periodic excitation with a frequency of the rotating speed Ω. This periodic excitation can be decomposed into a number of Fourier components, each of which has a frequency $n\Omega$ and is often referred to as an nth engine order excitation. Each engine order excitation, which can be separately used to study the forced response of a bladed system, acts on different blades with a constant phase shift from blade to blade. This type of harmonic excitation has been widely used in the literature [5, 8, 9] and can be expressed, for the blade k, as:

$$\mathbf{f}_E^k(t) = \mathbf{f}_E e^{(j\omega t + (k-1)\varphi)} \tag{1}$$

where $\mathbf{f}_E$ is the force vector on a single blade, ω is the excitation frequency, and φ is the interblade phase angle. The excitation frequency and the interblade phase angle can be related to the rotating speed Ω as

$$\omega = n\Omega \tag{2}$$

$$\varphi = \frac{2\pi n}{N_b}, \tag{3}$$

where n is the engine order of the excitation, and N_b is the number of blades on the disk.

In the structural analysis of a bladed disk system, a great simplification can be obtained by assuming the system is tuned, i.e., each blade has exactly the same dynamic characteristics. Under the excitation condition described in Eq. (1), each blade of the tuned system vibrates in the same matter but with the interblade phase difference (φ) from its adjacent blades. As a result, the whole response of the bladed system can be described by the response of a single representative blade. In addition, if each blade is constrained by friction contacts, the induced constrained force will also have the interblade phase difference from the corresponding constrained force on the adjacent blades.

Figure 1 shows a tuned bladed disk system constrained by wedge dampers. Using the finite element modeling, the governing equation of motion of blade k, a representative blade of the tuned system, can be expressed as

$$\mathbf{M}\ddot{\mathbf{u}}^k(t) + \mathbf{C}\dot{\mathbf{u}}^k(t) + \mathbf{K}\mathbf{u}^k(t) = \mathbf{f}_E^k(t) + \mathbf{f}_N^k(\mathbf{u}^k, \dot{\mathbf{u}}^k, t), \tag{4}$$

where $\mathbf{M}$ is the mass matrix, $\mathbf{C}$ is the damping matrix, $\mathbf{K}$ is the stiffness matrix, $\mathbf{f}_E^k$ is the external harmonic excitation, and $\mathbf{f}_N^k$ is the nonlinear constrained force, which includes the induced friction force and the varying normal force and is a function of the motion at the contact point. The finite element model is three-dimensional, and, if the model contains n nodes, the matrices will be $3n \times 3n$ matrices and the vectors will be $3n$-element vectors. It is noted that the elements of $\mathbf{f}_N^k$ are all zero except for the elements associated with the pth and qth nodes that contact with the wedge damper. It is clear that the nonlinear aspect of this dynamic problem is embedded in the term $\mathbf{f}_N^k$, whose relationship with the desired solution $\mathbf{u}^k(t)$ has to be established.

From linear vibration theory, without the friction coupling, the forced response of the blade due to external harmonic excitation can be attained by a standard harmonic analysis for the frequencies of interest. For the representative blade of the tuned system, the harmonic excitation forces acting on the blade are expressed as

$$\mathbf{f}_E^k(t) = \mathbf{f}_E^k e^{j\omega t}, \tag{5}$$

where ω is the frequency of excitation, and $\mathbf{f}_E^k$ is a complex vector representing the magnitude and phase of the excitation force. The complex receptance matrix of the system can be calculated as

$$\mathbf{R} = [\mathbf{r}_{ij}] = (\mathbf{K} - \omega^2\mathbf{M} + j\omega\mathbf{C})^{-1}, \tag{6}$$

where $\mathbf{r}_{ij}$, a 3×3 matrix, is defined as the steady state response of the ith node due to unit harmonic excitation force at the jth node. With this complex receptance matrix, the steady-state response of the structure under the harmonic excitation force of Eq. (5) can be formulated as follows:

$$\mathbf{u}_{Ei}^k = \sum_{j=1}^{n} \mathbf{r}_{ij}\mathbf{f}_{Ej}^k, \tag{7}$$

where $\mathbf{u}_{Ei}^k$ is the response of the ith node due to the external excitation, $\mathbf{f}_{Ej}^k$ is the external force acting on the jth node of the structure, and both are three-element vectors.

When the blade is constrained by wedge dampers, the induced constrained forces at the contact points can be considered as feedback forces that come to influence the response of the whole blade, including that of the contact points. Using the method of harmonic balance, the constrained force including the friction force and the varying normal force is approximated to have the same frequency as the external excitation, and its amplitude and phase are nonlinear functions of the contact points' displacements. Integrating with the receptance representation of the blade, this approach results in a set of nonlinear algebraic equations that can be solved iteratively to yield the desired steady-state response of the structure. Due to the use of the finite element model for the complex structure of the blade, the number of the nonlinear algebraic equations can be large, and the equations involve the unknowns of each nodal displacement (in this case, $3n$ unknowns). However, these nodal displacements can be divided into two groups. The first one consists of the displacements of all the friction contact points and the second includes the others. This allows one to separate the friction contacts from the otherwise linear part of the system and condense the nonlinear equations to the degrees of freedom of the friction contacts only. This can be illustrated by the block diagram shown in Fig. 2 for the considered example. In this example (see Fig. 1), because the tuned system is assumed, the motion of the wedge damper between blade k and blade $k+1$ is sufficient to characterize the constrained forces $\mathbf{f}_{Np}^k$ and

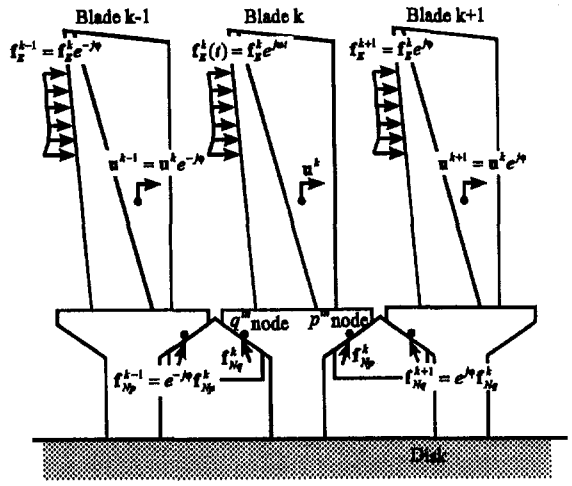

Fig. 1 Tuned bladed disk system

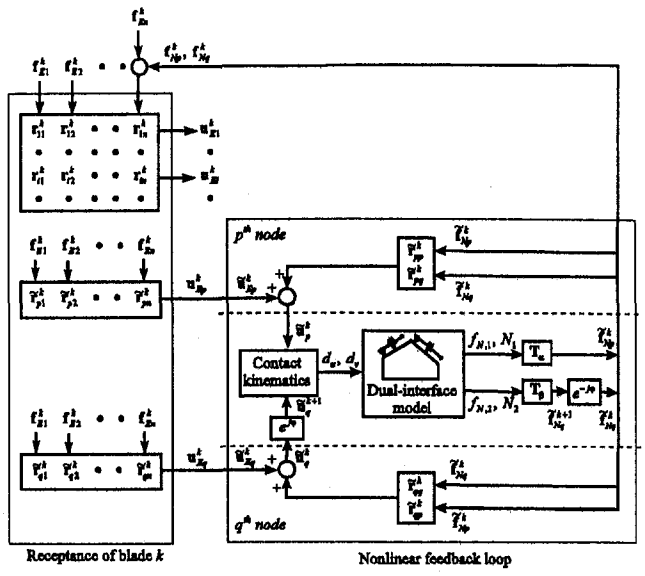

Fig. 2 Separation of nonlinear constrained force from the linear structure model

$\mathbf{f}_{Nq}^{k}$ that act on the contact points of blade k (the pth and qth nodes, respectively).

It can be seen that although the nonlinear constrained forces $\mathbf{f}_{Np}^{k}$ and $\mathbf{f}_{Nq}^{k}$ are fed back to the blade's structure and affect the motion of every node point, one can focus on the nonlinear feedback loop of the contact points (the pth and qth affect the motion of every node point, one can focus on the nonlinear feedback loop of the contact points (the pth and qth nodes). As noted, to solve this nonlinear problem, the relationship of the constrained forces $\tilde{\mathbf{f}}_{Np}^{k}$ and $\tilde{\mathbf{f}}_{Nq}^{k}$ with the displacements of the contact points $\tilde{\mathbf{u}}_{p}^{k}$ and $\tilde{\mathbf{u}}_{q}^{k}$ has to be established[2]. This can be obtained through the contact kinematics and the dual-interface friction force model, which was presented in the first part of this paper. First, the relative motions of the inclined interfaces, d_u and d_v, can be calculated from $\tilde{\mathbf{u}}_{p}^{k}$ and $\tilde{\mathbf{u}}_{q}^{k+1}$ ($\tilde{\mathbf{u}}_{q}^{k+1}$ having an interblade phase difference φ from $\tilde{\mathbf{u}}_{q}^{k}$, i.e., $\tilde{\mathbf{u}}_{q}^{k+1} = e^{j\varphi}\tilde{\mathbf{u}}_{q}^{k}$) through the contact kinematics. Special attention should be paid to that $\tilde{\mathbf{u}}_{p}^{k}$ and $\tilde{\mathbf{u}}_{q}^{k+1}$ are in complex (number) representation but d_u and d_v are in harmonic (function) representation. The conversion of $\tilde{\mathbf{u}}_{p}^{k}$ and $\tilde{\mathbf{u}}_{q}^{k+1}$ into their harmonic representation need be carried out before the analysis of contact kinematics. Once the relative motions are known, using the proposed dual-interface model, the induced friction forces as well as the varying normal loads ($f_{N,1}$, N_1, $f_{N,2}$, and N_2) can be estimated as harmonic functions in terms of the relative motions. Note also that the conversion of $f_{N,1}$, N_1, $f_{N,2}$, and N_2 into their complex representation need be performed to make them compatible with the following mathematical manipulations. Since these forces are in the inclined coordinate frames associated with the inclined surfaces, the coordinate transformations $\mathbf{T}_\alpha$ and $\mathbf{T}_\beta$ (the former is associated with the angle α, and the latter with the angle β, see Fig. 4 of Part I of this paper) have to be applied to obtain the constrained forces $\tilde{\mathbf{f}}_{Np}^{k}$ and $\tilde{\mathbf{f}}_{Nq}^{k+1}$. Furthermore, the constrained force at the qth node on blade k, $\tilde{\mathbf{f}}_{Nq}^{k}$, can be calculated from $\tilde{\mathbf{f}}_{Nq}^{k+1}$ by considering the phase difference between them (i.e., $\tilde{\mathbf{f}}_{Nq}^{k} = e^{-j\varphi}\tilde{\mathbf{f}}_{Nq}^{k+1}$).

[2] In this nonlinear feedback loop, the tilde symbol (~) is used to indicate that the matrices and vectors do not include the elements related to the axial component (the component along the axial direction of the turbomachine). Because the axial component does not participate in the evaluation of the friction forces occurring at the interfaces of the wedge damper, it can be excluded from this nonlinear analysis. Therefore, the vectors, such as $\tilde{\mathbf{u}}_{Ep}^{k}$, are two-element vectors, and the matrices, such as $\tilde{\mathbf{r}}_{pq}^{k}$, are 2×2 matrices.

Once the functions $\tilde{\mathbf{f}}_{Np}^{k}(\tilde{\mathbf{u}}_{p}^{k}, \tilde{\mathbf{u}}_{q}^{k})$ and $\tilde{\mathbf{f}}_{Nq}^{k}(\tilde{\mathbf{u}}_{p}^{k}, \tilde{\mathbf{u}}_{q}^{k})$ are known, the displacements of the pth and qth nodes can be expressed by the nonlinear algebraic equations as

$$\tilde{\mathbf{u}}_{p}^{k} = \tilde{\mathbf{u}}_{Ep}^{k} + \tilde{\mathbf{r}}_{pp}^{k}\tilde{\mathbf{f}}_{Np}^{k}(\tilde{\mathbf{u}}_{p}^{k}, \tilde{\mathbf{u}}_{q}^{k}) + \tilde{\mathbf{r}}_{pq}^{k}\tilde{\mathbf{f}}_{Nq}^{k}(\tilde{\mathbf{u}}_{p}^{k}, \tilde{\mathbf{u}}_{q}^{k}) \quad (8)$$

$$\tilde{\mathbf{u}}_{q}^{k} = \tilde{\mathbf{u}}_{Eq}^{k} + \tilde{\mathbf{r}}_{qp}^{k}\tilde{\mathbf{f}}_{Np}^{k}(\tilde{\mathbf{u}}_{p}^{k}, \tilde{\mathbf{u}}_{q}^{k}) + \tilde{\mathbf{r}}_{qq}^{k}\tilde{\mathbf{f}}_{Nq}^{k}(\tilde{\mathbf{u}}_{p}^{k}, \tilde{\mathbf{u}}_{q}^{k}), \quad (9)$$

where $\tilde{\mathbf{u}}_{Ep}^{k}$ and $\tilde{\mathbf{u}}_{Eq}^{k}$ are the displacement vectors that contain the tangential and radial components of $\mathbf{u}_{Ep}^{k} = \sum_{j=1}^{n} \mathbf{r}_{pj}\mathbf{f}_{Ej}^{k}$ and $\mathbf{u}_{Eq}^{k} = \sum_{j=1}^{n} \mathbf{r}_{qj}\mathbf{f}_{Ej}^{k}$ respectively, which are the displacements of the friction contact points without the friction coupling, and can be calculated using the given external force and the receptances. Equations (8) and (9) now have only two unknown variables $\tilde{\mathbf{u}}_{p}^{k}$ and $\tilde{\mathbf{u}}_{q}^{k}$, which can be solved using a numerical solver, such as the Newton-Raphson method. After knowing $\tilde{\mathbf{u}}_{p}^{k}$ and $\tilde{\mathbf{u}}_{q}^{k}$, the constrained forces can be calculated using the functions $\tilde{\mathbf{f}}_{Np}^{k}(\tilde{\mathbf{u}}_{p}^{k}, \tilde{\mathbf{u}}_{q}^{k})$ and $\tilde{\mathbf{f}}_{Nq}^{k}(\tilde{\mathbf{u}}_{p}^{k}, \tilde{\mathbf{u}}_{q}^{k})$, and the constrained forces along with the receptances of the blade can be used to calculate the whole response of the blade. As can be seen, the nonlinear feedback loop consists of only the receptances of the contact points of the structure to result in an algorithm for the nonlinear vibration problem with less degrees of freedom. As a result, this harmonic balance method along with receptance representation becomes computationally efficient.

When there are multiple wedge dampers to constrain the blade, the above-mentioned procedure can still be applied. In this case, each wedge damper will lead to two nonlinear algebraic equations, similar to Eqs. (8) and (9), and two unknown variables, which are the displacements of the two contact points.

It is then clear that the solution procedure for predicting the nonlinear forced response of a bladed system constrained by wedge dampers using this receptance approach can be separated into two stages. The first stage is to solve the nonlinear feedback loop, as formulated in Eqs. (8) and (9) that involve the dual-interface friction force model and the contact points of the structure, to obtain the displacements of the contact points and, thus, the induced constrained forces. Then, in the second stage, using the receptance formulation, the response of the whole structure can be accurately calculated by considering the resulting constrained forces as an additional excitation to the structure.

Dynamic Analysis of a Test Beam

To investigate the influence of wedge dampers on the resonant response of the constrained turbine blade, a test beam used by GE Aircraft Engines in a friction damping experiment is studied in this paper. The experimental set-up is depicted in Fig. 3. The test beam simulated a turbine blade geometry with

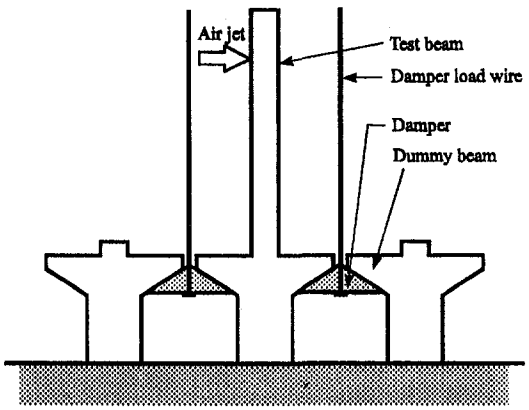

Fig. 3 Experimental set-up

inclined platforms. Two wedge dampers positioned on each side of the test beam were retained by two "dummy" beams with their simulated airfoils removed. The damper load, which is the counterpart of the centrifugal force in the actual engine operation, was controlled over a wide range by varying the tensile load in the wire. The test beam was excited by means of a pulsing air jet, whose excitation level was controlled by the air jet supply pressure and carefully calibrated. The dummy beams can be assumed motionless because of the removal of their simulated airfoils. A strain gage was placed at the root of the airfoil to measure the vibratory stress.

Receptance. Since this experimental set-up contains only one test beam, the harmonic balance method along with receptance representation that is developed for a representative blade of a tuned system can be readily applied by letting $\varphi = 0$. Moreover, one side of each wedge damper is assumed to contact with the ground (since the dummy beams are assumed motionless), whose receptance is assigned to be zero. To calculate the nonlinear forced response of the test beam, modal analysis using the finite element package ANSYS was first performed on the test beam to obtain the structural representation suitable for the nonlinear analysis, including the modal masses, the modal frequencies, the modal displacements of some critical points, such as the contact points with the dampers. Using this modal information, the receptance of these critical points can be calculated. It is sometimes desired to use as few vibration modes as possible to save the computation effort, and this demand can be achieved by examining the contribution of individual vibration modes to the receptance of the contact point. Because the total receptance of the contact point is the summation of the receptances from individual modes, the comparison among these individual receptances can give an indication of how many modes are dominant and should be included in the analysis. All the receptances of the two contact points were examined, and similar results were obtained. Therefore, in this paper, only the result for the receptance of the left contact point that relates the response in the x (horizontal) direction to the excitation in the x-direction is shown in Fig. 4(a), where the individual receptances from the first four flexural modes are plotted[3]. To clearly see the comparison among different modes, the receptance within the frequency range of interest are detailed in Fig. 4(b). It should be pointed out that the comparison has to be made on the accumulation basis; that is, the receptance from a specific mode has to be compared with the accumulative receptance of its lower modes. Take the frequency of 1.50 in Fig. 4(b) for example. The addition of the receptance from the fourth mode into the accumulative receptance of the first three modes causes the total receptance of a 7 percent increase (3.0/(8.6 + 17.5 + 12.0 + 3.0)). In fact, for this frequency range of interest, the participation of the fourth mode does not cause the total receptance to increase significantly. Therefore, the first three modes are sufficient to capture the dynamic behavior of the frictionally constrained beam. The conclusion of the above structural analysis, which does not involve the nonlinear friction coupling, was further confirmed by the fact that the inclusion of the fourth mode does not change the resulting forced response significantly in the nonlinear analysis. This can be illustrated by a series of damped responses under a strong influence of the dampers, as shown in Fig. 5, that are obtained by keeping increasing the number of the participating modes up to the fourth mode.

In the analysis, the structure damping was simulated by a linear viscous element. The value of the damping coefficient was selected so that the amplitude of the resonant response was comparable to that observed in the experiment. The friction coefficients of the interfaces were estimated by measuring the friction force when the contact surfaces slip. The stiffness of the friction interfaces were set to obtain the same amount of the frequency shift as observed in the experiment.

In the following discussion, the response of the beam refers to the vibratory stress at the airfoil root, and the data is presented in the normalized form.

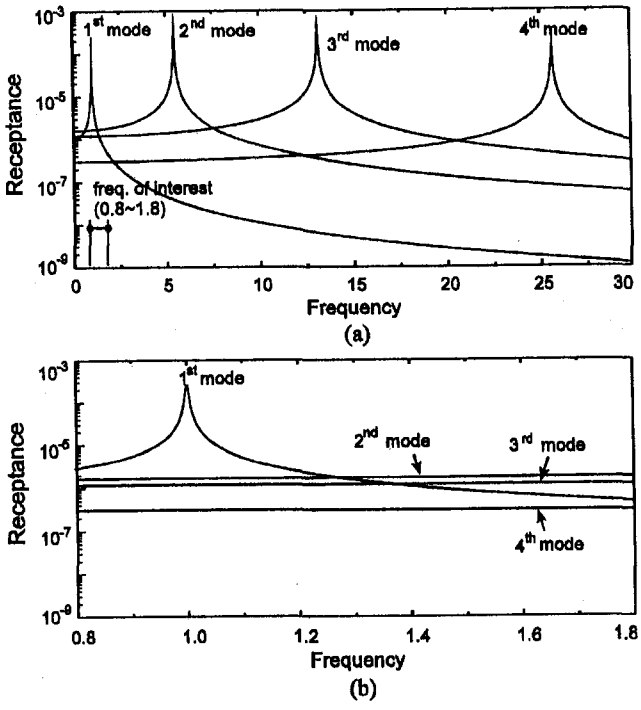

Fig. 4 Receptances from individual vibration modes: (a) wide frequency range: 0.0 ~ 30.0; and (b) frequency range of interest: 0.8 ~ 1.8.

Frequency Response. Figure 6 shows predicted tracking curves of the test beam under a specific excitation level and different levels of applied damper load. A tracking curve is a curve of the response amplitude of the test beam as a function of the excitation frequency. It can be seen that the resonant responses are bounded within two linear cases: fully slipping case and fully stuck case. This is similar to the situation when the single-interface friction force model is considered [1, 5, 6]. The fully slipping case occurs when the damper load is zero, and, therefore, the damper is not ineffective at all. As the damper load increases to a certain large value, the friction interfaces are completely stuck. In this case, the friction interfaces do not dissipate energy at all but provide additional stiffness to the test beam to cause a higher resonant frequency. In between, the resonant response of the test beam is damped and the resonant frequency increases as the damper load increases. In these damped responses, one interesting thing to note is that an "optimal" damper load, designated as N^*, exists to minimize the resonant amplitude.

The calculation indicates that there exist nonunique responses for moderate damper loads; among them, three cases of damper load $6N^*$, $15N^*$, and $35N^*$ are considered, and the predicted responses are shown in this figure. It is noted that the nonunique response does not appear in the case of the single-interface model. As mentioned previously, when one interface of the damper sticks but the other undergoes an alternating stick-slip motion, the interfaces may provide varying levels of damping and stiffness, depending on the initial condition of the friction forces. As a result, the response of the structure becomes nonunique. Since the upper and lower limits of the friction forces that give the least and largest attenuation effects respectively

[3] The frequency has been normalized with respect to the first natural frequency of the structure.

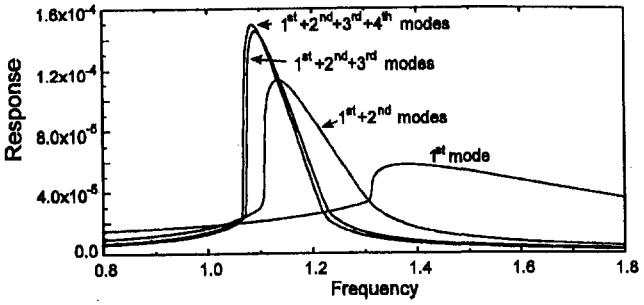

Fig. 5 Participation of vibration modes

can be identified, the upper and lower bounds of the nonunique response can be obtained.

Optimal Curve. An optimal curve is a curve of the resonant amplitude as a function of the applied damper load. It can be of substantial aid for the design of friction damping in two aspects. The first one is that it can determine an "optimum" of damper load that minimizes the resonant response. For platform dampers such as wedge dampers, this optimal damper load can be used to design the optimal weight of the damper since the damper is held in place by centrifugal acceleration during the operation. The second aspect is that the optimal curve can be normalized with respect to the excitation; that is, for a specific damper configuration, one normalized curve is sufficient for any level of excitation. This can greatly reduce the nonlinear analysis in optimizing the design of friction damping to only establishing the normalized optimal curve.

The predicted normalized optimal curve for the test beam is shown in Fig. 7. Actually, this optimal curve can be established by picking the peaks of the tracking curves shown in Fig. 6, and this was done by employing a peak-searching algorithm in the developed computer code to obtain the peak amplitude once a frequency response is calculated. It can be seen that the peak amplitude reduces remarkably as the damper load increases from zero; after the optimal damper load, it tends to increase gradually towards the peak amplitude of the fully stuck case. As mentioned previously, nonunique response may exist for moderate damper loads; as a result, the peak responses in this range of damper load can have different values that are within the upper and lower optimal curves. However, this uncertainty of the peak response is not of much interest to the designer because the damper load is much larger than the optimum.

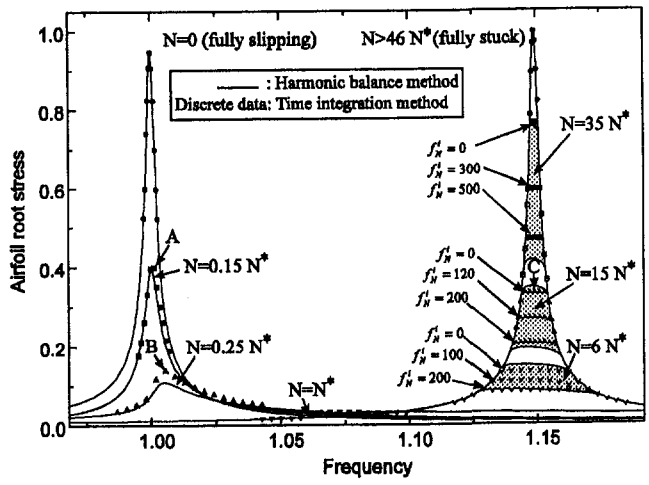

Fig. 6 Tracking curves of the test beam

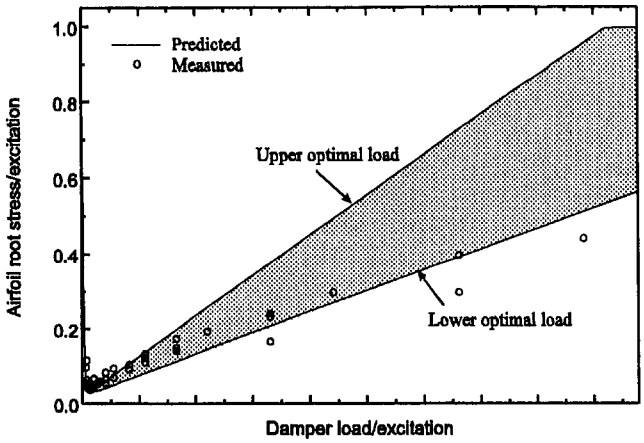

Fig. 7 Normalized optimal curve of the test beam

Comparison With Time Integration Method. In this section, the accuracy of the approximate procedure using the harmonic balance method in predicting the nonlinear frequency response of the test beam is examined by comparing the predictions with those obtained from the direct time integration method. The comparisons are shown in Fig. 6. All the comparisons are made in the range of frequency near resonance.

From the results, one can observe that the approximate solutions for both the fully slipping and fully stuck cases are exact. This is because the system is linear under both conditions. For the cases between these two extreme cases, the test beam's vibration induces the friction slip at the contact points. This makes the problem become nonlinear. However, the approximate procedure, in general, can still provide close solutions for these conditions. Special attention should be paid to the cases of the moderate damper load that leads to the nonunique response. For these conditions with possible nonunique solutions, the simulation of the time integration procedure was performed using different values of the initial friction force f_N^i. As can be seen from the figure, the solutions from the time integration procedure lie within the bounds predicted by the harmonic balance method. Besides, it can be found that, through the intensive simulation, the solutions using the zero initial friction force ($f_N^i = 0$) form the upper bound of other solutions using different initial friction forces.

Although the approximate solutions are sufficiently accurate in this application, one can still observe the discrepancy between the approximate solutions and the time simulation solutions under some conditions where the friction nonlinearity becomes significant. To understand the reasons that cause the discrepancy, the steady state displacement (x component only) of the contact point of the test beam under the conditions corresponding to the three points (A, B, and C), as shown in Fig. 6, was simulated and is depicted in Fig. 8. Since the harmonic balance method assumes that the response is harmonic, the fundamental harmonic of the steady-state displacement was also calculated and is shown as the dotted line in the figure for the purpose of reference. Under the condition at point A, the harmonic assumption is reasonably true, and, as a consequence, the two solutions agree very well as shown in Fig. 6. Under the condition at point B the slip load increases to cause the friction nonlinearity to become significant, and, thus, the resulting displacement becomes off-harmonic due to the existence of the super-harmonic components. Because the transition conditions of the interfaces of the wedge damper are complicated and the induced friction force is very sensitive to the input relative motion, the slightly off-harmonic displacement can cause a noticeable difference between approximate solution from the harmonic balance method and the time integration solution. The existence of the super-harmonic components is more evident in

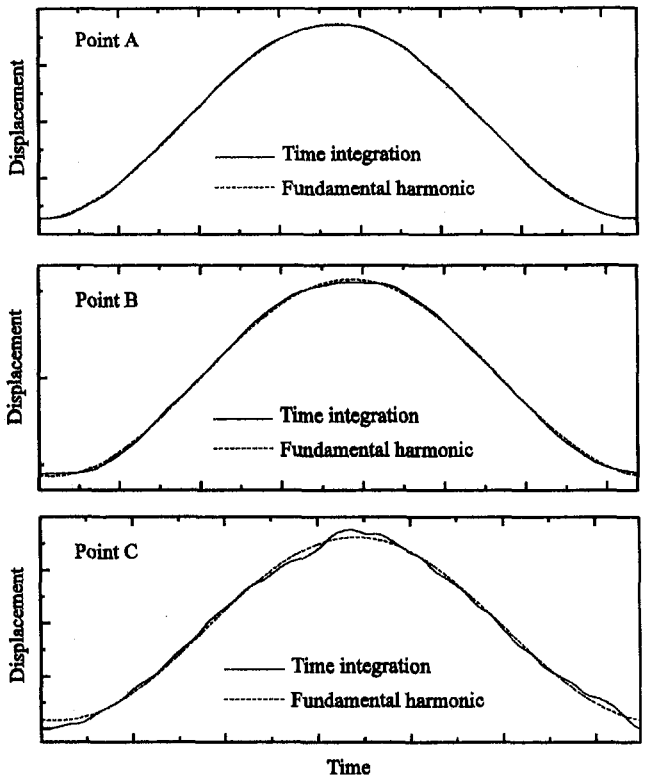

Fig. 8 Steady-state displacement of the contact point

the displacement under the condition at point C. Since the harmonic assumption is not entirely accurate, the apparent deviation of the approximate solution from the time integration solution is expected.

Comparison With the Experiment Result

The friction damping experiment discussed in this section was conducted at GE Aircraft Engines, and the experimental set-up has been described in the previous section. In this experiment, the peak amplitudes of the airfoil root stress were recorded for different combinations of the damper load and the excitation level. In comparing these results with the predicted normalized optimal curve, the measured stress and the damper load are normalized with respect to the excitation and depicted in Fig. 7. From this comparison, it is seen that the analytical predictions agree reasonably well with the experimental data near the optimal damper load. However, two differences are evident. The first is that the data has a trend to lie on a single curve, instead of scattering within the upper and lower bounds as predicted. This discrepancy is due to the experimental procedure that always reloaded the damper for each run and caused "free" interfaces at the beginning of the test (i.e., zero initial friction force), and, consequently, as described previously, the response would lie on the upper bound of the nonunique response. The second difference observed in the experimental data is that for high damper loads the test has much lower amplitudes than those calculated using the theoretical friction force model. As a matter of fact, this discrepancy is expected for the proposed model that assumes point contacts at the interfaces and does not account for the microslip phenomenon [10, 11, 12]. While the proposed friction force model is inadequate in predicting the response for high damper loads, these loads are much larger than the optimal damper load and usually would not be of much interest to the designer.

Conclusions

The nonlinear forced response of a bladed disk assembly constrained by wedge dampers was investigated under the tuned system assumption. This assumption was found useful in such applications because it can reduce the formidable analysis of the entire structure to a much simpler analysis of a single representative blade. To predict the nonlinear response of the frictionally constrained blade, a harmonic balance method along with receptance representation was proposed. The proposed method is an approximate method, which uses the harmonic balance technique to approximate the nonlinear constrained force and uses the receptances, calculated from a standard finite element analysis of the structure, to subsequently solve the nonlinear vibration problem is a separate algorithm involving the degrees of freedom of friction contacts only. As a result, this method in computationally efficient.

In order to illustrate the capacity of the proposed method, the resonant response of a test beam constrained by two wedge dampers was examined. The predicted resonant response can be used to optimize a given damper design, namely to determine the dynamic weight at which the maximum reduction of resonant response is obtained. To evaluate the feasibility of using the harmonic balance method, the predicted results were compared with the solutions of the direct time integration method. The results show that the harmonic balance method is adequate to the needed application. The prediction was also compared with the results of lab tests to validate the proposed dual-interface friction force model. The comparison shows excellent agreement over the range of damper load, which is between the zero damper load and the optimal damper load. Discrepancy is observed for the region of higher damper load, which may cause microslip, not included in the proposed model, at the contact surfaces.

Acknowledgments

This material is based on work supported by the GUIde Consortium and the U.S. Air Force under contract No. F33615-92-C-2212. Any opinions, findings, and conclusions or recommendations expressed in this material are those of the authors and do not necessarily reflect the views of the GUIde Consortium or the Air Force. The authors would like to thank Mr. Joe Panovsky of GE Aircraft Engines for providing the experimental data.

References

1 Menq, C. H., and Griffin, J. H., "A Comparison of Transient and Steady State Finite Element Analyses of the Forced Response of a Frictionally Damped Beam," *ASME Journal of Vibration, Acoustics, Stress, and Reliability in Design,* Vol. 107, Jan. 1985, pp. 19–25.

2 Bishop, R. E. D., and Johnson, D. C., *The Mechanics of Vibration,* Cambridge University Press, London, UK, 1960.

3 Caughey T. K., "Sinusoidal Excitation of a System with Bilinear Hysteresis," *ASME Journal of Applied Mechanics,* Vol. 27, Dec. 1960, pp. 640–643.

4 Dowell, E. H., and Schwartz, H. B., "Forced Response of a Cantilever Beam with a Dry Friction Damper Attached, Part I: Theory," *Journal of Sound and Vibration,* Vol. 91, No. 2, 1983, pp. 255–267.

5 Menq, C. H., Griffin, J. H. and Bielak, J., "The Forced Response of Shrouded Fan Stages," *ASME Journal of Vibration, Acoustics, Stress, and Reliability in Design,* Vol. 108, Jan. 1986, pp. 50–55.

6 Yang, B. D. and Menq, C. H., "Modeling of Friction Contact and Its Application to the Design of Shroud Contact," ASME JOURNAL OF ENGINEERING FOR GAS TURBINES AND POWER, Vol. 119, No. 4, Oct. 1997, pp. 958–963.

7 Gelb, A., and Vander Velde, W. E., *Multiple-Input Describing Functions and System Design,* McGraw-Hill, NY, 1968.

8 Fabunmi, J. A., "Forced Vibration of a Single Stage Axial Compressor Rotor," ASME JOURNAL OF ENGINEERING FOR GAS TURBINES AND POWER, Vol. 102, No. 2, 1980, pp. 322–329.

9 Griffin, J. H., and Hoosac, T. M., "Model Development and Statistical Investigation of Turbine Blade Mistuning," *ASME Journal of Vibration, Acoustics, Stress, and Reliability in Design,* Vol. 106, Apr. 1984, pp. 204–210.

10 Menq, C. H., "Modeling and Vibration Analysis of Friction Joints," *ASME Journal of Vibration, Acoustics, Stress, and Reliability in Design,* Vol. 111, Jan. 1989, pp. 71–76.

11 Menq, C. H., Bielak, J., and Griffin, J. H., "The Influence of Microslip on Vibratory Response, Part I: A New Theoretical Model," *Journal of Sound and Vibration,* Vol. 107, June, 1986, pp. 279–293.

12 Menq, C. H., Griffin, J. H., and Bielak, J., "The Influence of Microslip on Vibratory Response, Part II: A Comparison with Experimental Results," *Journal of Sound and Vibration,* Vol. 107, June, 1986, pp. 295–307.

Structural Analysis of Cylinder Head Cracking in a Heavy-Duty Diesel Engine

J.-Y. Luo

C. J. Korte

Cummins Engine Company, Inc.,
Box 3005,
Columbus, IN 47202-3005

There were fatigue cracking problems at the intake ports of a prototype heavy-duty six-cylinder head. Several proposals of design change were evaluated by finite element and reliability analysis. Constant amplitude loading and monotonic temperature-dependent properties of the head material are assumed. An equivalent stress-strain parameter (ESSP) is proposed to consider multiaxial stress/strain effect on fatigue cracking. A significant reliability improvement was predicted with cost savings and verified by limited engine tests.

Introduction

It has been reported that in the testing of a prototype heavy-duty, in-line six-cylinder diesel engine, more than 25 cylinder heads had a cracking problem at the lower portion of the intake port fillet in their early service life. The intake port wall and surrounding portions of the head are complicated in geometry and subjected to a complicated load path predominated by bending in the vertical direction and shearing along the wall fillet line as the cylinder fires. Such effects are enhanced by the initial bending caused by the assembly load of the adjacent short head cap screw bolt. The crack initiates at the fillet corner on the upper side of the intake port in a I-II mixed mode, and then extends through the wall thickness along the fillet line during a cyclic bending-shearing history. Among possible structural solutions are to (1) increase local bending-shearing stiffness by increasing the fillet radius and/or the wall thickness along the fillet kink line, (2) reduce the assembly compression effects by increasing wall thickness and/or height of the short cap screw boss, and (3) change the global load path around the intake port wall by reducing top deck thickness over the injector bore and exhaust port and/or enhancing the in-plane stiffness around the intake inlet area. However, all of the structural proposals are subjected to manufacturing, performance, and cost limits, and may be effective individually or simultaneously, depending on how much reliability improvement can be obtained from changes. It requires finite element and fatigue analysis to evaluate their effects on stress/strain and reliability at the critical location under the engine operating conditions for each option. Our analytical work is summarized in this paper.

There has been a lot of research work on the fatigue mechanisms of cast irons such as in reference [1]. The alloyed gray iron used for the head contains graphite flake cells distributed in a pearlitic matrix. Subjected to cyclic loading, fatigue micro-cracks are initiated at graphite flake cell/matrix interfaces, and then propagated and linked through the matrix. The critically oriented graphite flakes with weak strength and interface would be cracking at low tensile stress level in early life stages, and become micro-notches affecting local plasticity and crack growth in the matrix which consumes the majority part of fatigue life of gray iron. Multiaxial fatigue is one of the predominant failure modes in engine components with complex geometries and/or subjected to complex cyclic loading. The equivalent stress/strain approach [2] is one of the most acceptable ideas in engineering sense due to its scalar simplicity to implement and to be related to uniaxial material testing, despite some fundamental weaknesses. More research work of multiaxial fatigue theories and modeling may be seen in the literature [3, 4].

Three-Dimensional Finite Element Modeling

The ANSYS finite element package [5] was used to build a three-dimensional head model. A representative volume of half of cylinder 3 and half of cylinder 4 was modeled with 39,000 ten-node tetrahedral elements. Valve guides and seat inserts were included in the model. Cap screw bolts were modeled with spar elements to transmit assembly loads. The joint stiffness of the block, liner, and head gasket was calculated using a simplified spring system and modeled with spar elements. The solid FE mesh is shown in Fig. 1. The total active degrees of freedom of 185,700 were solved by a preconditioned conjugate gradient (PCG) processor.

All of the materials were assumed as linear thermo-elastic in a preliminary FEA. However, for the head gray iron, a so-called "nonlinear-bimodulus" material, significant nonlinear behavior with different tensile and compressive slopes was shown in its uniaxial tests even at lower stress level and room temperature. It is attributed to its graphite-cells effect. Tensile and compressive stress-strain curves at three different temperatures are provided from monotonic uniaxial tests. Because the ANSYS program is limited to handle materials with the same tensile and compressive modulus, an average-modulus curve between tension and compression at each of three temperatures was calculated. The resulting "single-modulus" nonlinear stress-strain curves are shown in Fig. 2 and used in the analysis. No cyclic stress-strain data for the head gray iron was available.

The finite element procedure consists of steady-state thermal analysis and linear or nonlinear elastic analysis at assembly and torque-peak operating conditions. The torque peak temperature distribution obtained in the thermal analysis is symmetrically imposed on both cylinder regions as the steady-state thermal load. In the fatigue loading history, both thermal load and assembly load of head cap screw bolts are considered as initial loads for the model. The only cyclic load is the combustion pressure on the combustion face of the head bottom deck. In a 1-5-3-6-2-4 cylinder firing cycle, the pressure reaches a peak value (PCP) of 15.86 MPa (2300 psi) in each cylinder when it is firing. Assuming a constant-amplitude, combustion pressure history when cylinder 3 fires, a peak, stress/strain point occurs at its intake port fillet, while a valley point occurs at the symmetric location of the intake port fillet in adjacent cylinder 4, and vice versa (as illustrated in Fig. 3).

Based on available data from heat transfer/fluid dynamics calculation and temperature measurements under torque-peak conditions, various pairs of film coefficients and bulk tempera-

Contributed by the International Gas Turbine Institute and presented at the Fall Technical Conference of the ASME Internal Combustion Engine Division, Springfield, OH, October 20–23, 1996. Manuscript received by the ASME Headquarters August 1996. Associate Technical Editor: D. Assanis.

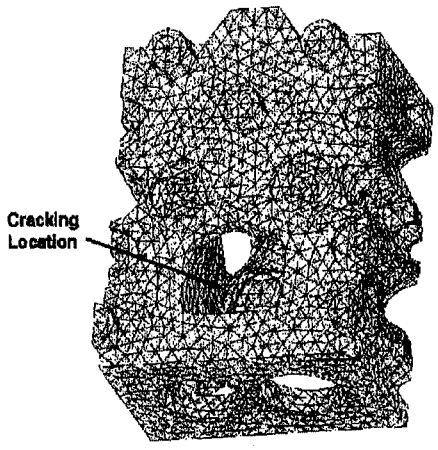

Fig. 1 Finite element mesh

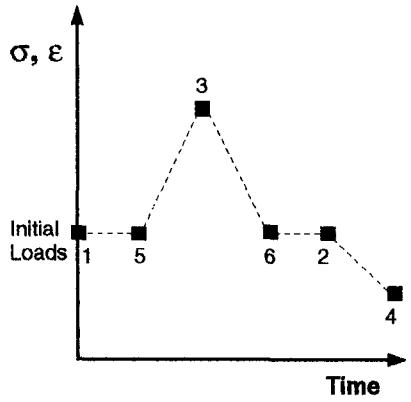

Fig. 3 Load history at the intake port fillet of cylinder 3 for a firing cycle

tures were set up in different areas of the head combustion face, injector bores, intake and exhaust port walls, and water jacket walls. Adiabatic conditions were assumed on all cutting surfaces due to symmetric heat distribution in the cutting direction.

To simulate load variation of the cap screw bolt fixture during an operating cycle, the measured assembly force on the bolt was applied at its bottom end node first. The resulting nodal displacement was held in the next load step of cylinder firing. Thus, elastic variation of cap screw bolt deflection and load, due to combustion pressure, can be automatically compensated. Using the same method to set up load on the head-gasket joint, an initial strain equivalent to the assumed total sealing press load was imposed on the spars that simulate stiffness of the gasket combustion seal-liner-block midstop joint that resulted in nonuniform liner pressure along the circumference of the seal. The corresponding nodal displacements were held in the cylinder's firing load case so that pressure on the seal decreased. Similarly, thermal deflection on the combustion seal, due to the liner thermal expansion, was calculated and added on the assembly deflection. The total thermal-mechanical load on the cap screw bolt and the gasket is the combined results from liner thermal expansion, bolt thermal expansion, and combustion pressure with the joint stiffness effect. Also, injector load was applied on the cone-shaped contact surface near the tip.

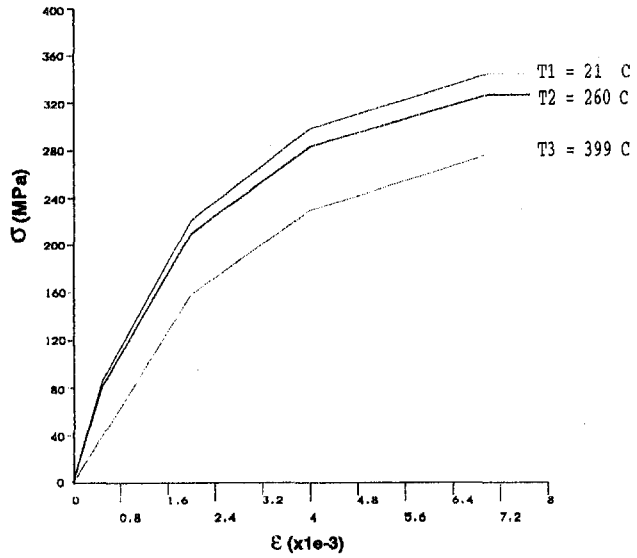

Fig. 2 Average stress-strain curves of head material

FEA Results and Discussions

Figure 4 shows the temperature distribution over the head model at the torque-peak condition. Its high gradient from combustion deck to upper potion results in thermal loading at the intake port fillet, even though local temperature distribution over there is quite uniform.

A preliminary, linear elastic FEA indicated relative effects of proposed design changes of the local configuration at the intake port fillet. As a baseline, case 1 is the initial configuration of the prototype head with tapered fillet radii from the top 8 mm through the middle 3.5 mm, to the bottom 2 mm. In cases 2 and 3, the fillet radius in its middle portion at the port side is increased to 6 mm and 8 mm, respectively. In case 4, head material is filled in the water jacket groove of the short cap screw boss to make its wall of 11 mm a uniform thickness. Case 5 uniformly increases the port wall thickness from 6.5 mm to 10 mm. Case 6 uniformly increases the top deck to 12 mm. Resulting maximum tensile stresses and their locations along the fillet corner line are summarized in Table 1.

As seen in Table 1, the larger middle fillet radii of cases 2 and 3 could significantly reduce both assembly and operating stresses at the critical region due to a direct reduction of stress concentration. The enhanced short and thick cap screw boss reduces its assembly compression and related bending of the intake port wall so as to reduce maximum assembly stress, but gives more restriction to operating thermal-mechanical deflection so as to keep the operating maximum stress unchanged. The thicker port wall could help to significantly reduce both stresses due to its stronger bending stiffness. The thicker top deck over the port increases global stiffness to restrict the port deformation, but this effect is not significant for stress reduction at the critical location due to the longer distance between them. This linear analysis selected two of the five proposals as the most promising changes: case 3 of 8 mm large fillet, and case

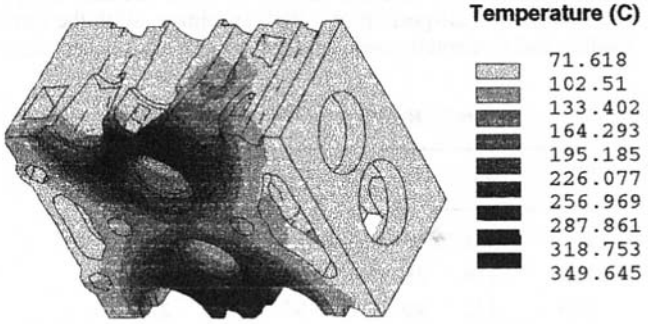

Fig. 4 Temperature contour under torque-peak loading

Table 1 Linear maximum stress at the fillet

Case	Assembly σ1		Operating σ1	
	MPa	location	MPa	location
1 (initial design)	159	middle	248	lower
2 (6 mm fillet)	124	middle	214	middle
3 (8 mm fillet)	97	middle	200	lower-middle
4 (enhanced CS boss)	117	lower	248	lower
5 (10 mm wall)	117	middle	200	middle
6 (12 mm TD)	143	middle	245	middle

5 of 10 mm thick wall, with other casting and performance considerations.

However, assuming constant modulus in the linear FEA overestimates the stress level; this misleads fatigue/reliability analysis as compared with measured material strength. Therefore, besides the baseline of case 1, case 3 and case 3 plus case 5 (3 + 5) were recalculated, using a nonlinear FE process with the average temperature-dependent, stress-strain curves of the gray iron.

Nonlinear stress/strain results at the critical location of intake port fillet are listed in Tables 2 and 3 and are used for the following fatigue/reliability analysis.

It is noted in Tables 2 and 3 that the state of stress and strain at the critical location is multiaxial, with compatible normal and large shear components. Also, significant biaxial compressive residual stress in the critical surface layer was induced in a head casting process and measured from section and *X*-refraction tests. Therefore, a uniaxial loading assumption may not be valid for the following fatigue analysis.

For the initial design (case 1), measured strain gage data at the intake port fillet was available and used to correlate the nonlinear FE results. It is noted that a strain gage measures an average value over the area it covers, while the FEA gave a range of nodal strain values in the same region.

It is shown in Table 4 that the nonlinear FE model overestimates the assembly strains, but does quite well at predicting PCP firing strains. Therefore, the average multilinear assumption is acceptable. It gives lower stress but larger strain with much more solution time than the linear analysis. The maximum principal stress ($\sigma 1$) distribution on the surface of the intake port for each of the three cases is shown in Fig. 5, respectively. It is seen that the peak point of $\sigma 1$ is always located in the lower region along the fillet corner for every case, but its level is gradually lowered down by the local geometric enhancements.

Current gray iron fatigue *S-N* curves are based on rotating beam fatigue (RBF) test data calibrated by a linear elastic beam formula, $\sigma = Mz/I$. It does not include nonlinear-bimodulus effects of gray iron, and it may bring in significant errors in determination of *S-N* curves. Such error was evaluated using a FE model of a half-portion of a RBF specimen. With the same loading and constraint conditions, three cases with linear, average multilinear, and "bimodulus" multiliner properties were run, respectively. The stress/strain results are compared in Table 5.

It is indicated that the linear beam theory overestimates maximum stress by 9–10 percent. This effect was considered in the following fatigue/reliability analysis. More generally, for gray irons or any other lower-stress nonlinear materials, it is more accurate to establish strain-life curves by running strain-controlled fatigue tests to include their nonlinearity effects. When using *S-N* curves resulting from the linear RBF calibration for such materials, some reduction should be imposed on the fatigue strength data and could be evaluated by a nonlinear FE simulation to the test.

Table 2 Nonlinear peak stress at the fillet

Case	σx	σy	σz	σxy	σyz	σzx (MPa)
1	181	68	-1	129	42	2
3	178	39	-7	98	17	-4
3+5	142	40	-2	93	34	22

Table 3 Nonlinear strain amplitudes at the fillet

Case	εx	εy	εz	εxy	εyz	εzx (1e-6)
1	712	-118	12	3923	233	-754
3	694	-37	-101	2414	-168	-683
3+5	533	-45	-6	1918	-28	-221

Fatigue Criterion for Gray Iron

Using stress/strain data resulting from the nonlinear FEA, traditional uniaxial stress and strain-based fatigue theories predicted unexpected high unreliability rates for case 1, case 3, and case (3 + 5). The discrepancy may be attributed to neglecting the multiaxial stress/strain effects. Also, it was impossible to include inhomogeneous effects of graphite cells in the macro FE model, but such weak inclusions are critical for microcrack initiation and propagation in gray iron. Therefore, a new fatigue criterion is developed to include these damage factors.

Considering the nonzero mean stress effects on fatigue damage, the Smith-Watson-Topper (SWT) parameter [6], a scalar product of maximum stress and strain amplitude has been widely used in uniaxial elastic-plastic fatigue analysis. For multiaxial loading cases, it is extended by defining an equivalent stress-strain parameter (ESSP) as a fatigue criterion:

$$\text{ESSP} = (\sigma\_\text{eqv\_max}) \times (\epsilon\_\text{eqv\_alt}). \quad (1)$$

The σ_eqv_max is the von Mises maximum stress including mean and residual stress effects, and it is formulated as

$$\sigma\_\text{eqv\_max} = 0.7071((Sx - Sy)^2 + (Sy - Sz)^2 + (Sz - Sx)^2 + 6(Sxy^2 + Syz^2 + Szx^2))^{0.5} \quad (2)$$

with

$$Sx = \sigma x\_\text{max} + \sigma x\_\text{res}, \quad Sxy = \sigma xy\_\text{max}$$
$$Sy = \sigma y\_\text{max} + \sigma y\_\text{res}, \quad Syz = \sigma yz\_\text{max}$$
$$Sz = \sigma z\_\text{max} + \sigma z\_\text{res}, \quad Szx = \sigma zx\_\text{max}.$$

The ϵ_eqv_alt is the von Mises total strain amplitude formulated as

Table 4 Comparison of FE and measured strain

Loading	FEA	Strain Gage (1e-6)
Assembly + Thermal	1066 - 1944	894
PCP + Assembly + Thermal	1449 - 2432	2247

Table 5 Linear and nonlinear stress and strain for RBF

Calibration Method	σ1 (MPa)	ε1 (1e-6)	σ3 (MPa)	ε3 (1e-6)
Linear Beam Theory	126.9		-126.9	
Multilinear FEA(ave)	115.1	820	-115.1	-820
Multilinear FEA(bi)	116.4	881	-116.8	-951

$$\epsilon\_eqv\_alt = 0.4714((EPx - EPy)^2 + (EPy - EPz)^2 + (EPz - EPx)^2 + 6(EPxy^2 + EPyz^2 + EPzx^2))^{0.5} \quad (3)$$

with

$$EPx = 0.5(\epsilon x\_max - \epsilon x\_min)$$

$$EPy = 0.5(\epsilon y\_max - \epsilon y\_min)$$

$$EPz = 0.5(\epsilon z\_max - \epsilon z\_min)$$

$$EPxy = 0.5(\epsilon xy\_max - \epsilon xy\_min)$$

$$EPyz = 0.5(\epsilon yz\_max - \epsilon yz\_min)$$

$$EPzx = 0.5(\epsilon zx\_max - \epsilon zx\_min).$$

The maximum and minimum value of stress/strain components are corresponding to the peak and valley point in a constant-amplitude proportional loading path, respectively.

The uniaxial fully reversed loading is a special case in which all mean stress components are zero, and the σ_eqv_max is equal to the axial stress amplitude σ_alt and the ϵ_eqv_alt is the axial strain amplitude ϵ_alt. Its ESSP is simplified as

$$\text{ESSP\_uni} = (\sigma\_\text{alt}) \times (\epsilon\_\text{alt}). \quad (4)$$

Special care must be taken into account of the notch effect of graphite flakes in gray iron. Generally, on casting surfaces the notch effect is negligible because little graphite cells are distributed in the surface layer. But on machined surfaces, opening flake-like notches exist and cause local stress/strain concentration and plasticity in the matrix under cyclic loading. The notch effects may be determined from nominal axial stress and strain amplitudes using Neuber-Topper-type rules. Mitchell [7] has proposed a relation:

$$(\sigma\_\text{alt\_notch} \times \epsilon\_\text{alt\_notch} \times E\_m)^{0.5} = Kf(\sigma\_\text{alt\_nomi} \times \epsilon\_\text{alt\_nomi} \times E\_g)^{0.5} \quad (5)$$

with

$$Kf = 1 + 0.1(D\_c)^{0.5}(\text{BHN})^{0.9}, \quad (6)$$

where Kf is the fatigue notch factor of the matrix and depends on graphite cell diameter D_c and matrix hardness in BHN, and E_g and E_m are the Young's modulus of the gray iron and the matrix, respectively.

Since

$$\text{ESSP\_notch} = \sigma\_\text{alt\_notch} \times \epsilon\_\text{alt\_notch}$$

and

$$\text{ESSP\_nomi} = \sigma\_\text{alt\_nomi} \times \epsilon\_\text{alt\_nomi},$$

we have

$$\text{ESSP\_notch} = Kf^2 \times (E\_g/E\_m) \times \text{ESSP\_nomi}. \quad (7)$$

Thus, the notch ESSP may be calculated from the nominal stress and strain amplitude data that can be obtained from measurement or finite element simulation for standard uniaxial material tests.

It is noted that more general notch correction for proportional and nonproportional multiaxial loading have been developing based on equivalence assumption of notch-tip strain energy density in reference [8, 9] that may be applied to evaluate graphite cell effects in gray iron more accurately.

Intake Port Reliability Prediction

For the head, applied ESSP was calculated using thermomechanical stress and strain data from the nonlinear FEA, as shown in Tables 2 and 3. Biaxial residual stress induced in casting at the critical location was measured as −232 and −206 MPa in the x and y-direction, respectively, and added on the FE stress. The micronotch effect was neglected on the casting surface of the intake port fillet.

The RBF test was calibrated by a FE simulation using the average multilinear elastic curves. It provides a fully reversed fatigue stress amplitude of 115 MPa and a strain amplitude of 820e-6 at a fatigue life of 500,000 miles to calculate the nominal material ESSP. To consider the graphite flake effect on a cut surface of the specimen, the fatigue strength is further corrected. Assuming $D\_c = 0.06$ inch and $BHN = 276$, Eq. (6) determines a Kf value of 4.85. With E_g = 15e6 psi and E_m = 30e6 psi, the notched ESSP resulting from Eq. (7) is 1.112 MPa.

Reliability prediction is based on probability analysis of interference between applied ESSP at the intake port fillet and material ESSP from the RBF test. In statistical consideration of loading and material data, normal distribution is assumed for both. A coefficient of variation (COV), defined as (standard deviation)/(mean), is assumed as 0.15 for the applied ESSP and 0.20 for the material, based on the statistics of loading and

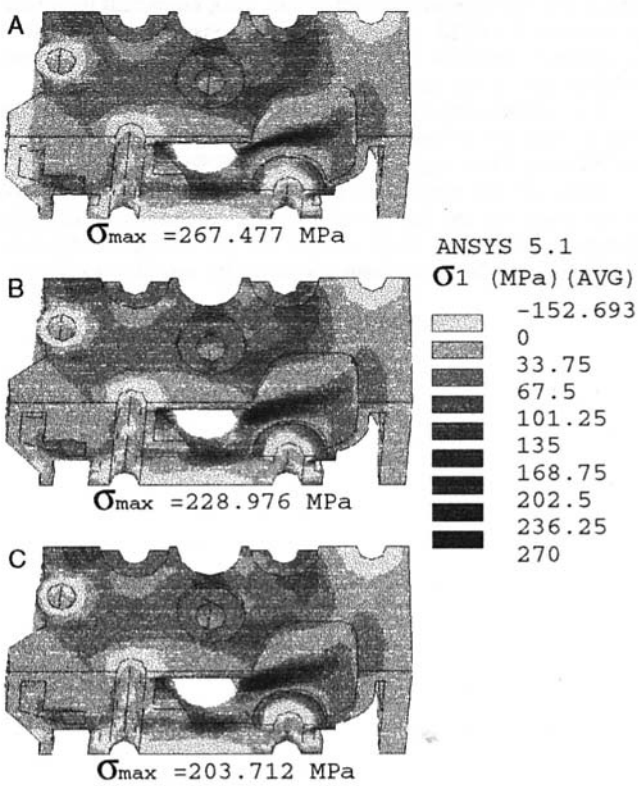

Fig. 5 Maximum stress contours at the intake port fillet: (A) current design (case 1); (B) 8 mm fillet radius (case 3); and (C) 8 mm fillet radius and 10 mm thick wall (case 3 + 5).

Table 6 ESSP and fatigue cracking rates at the fillet

Case	σ_eqv_max	ε_eqv_alt	ESSP		Unreliability
			appli	mater	
	(MPa)	(1e-6)	(MPa)		(%)
1	264.0	2367	0.625	1.112	4.36
3	223.8	1539	0.344	1.112	0.08
3+5	226.1	1176	0.266	1.112	0.02
Good Head	337.7	1053	0.356	1.112	0.09

material data. The results are summarized in Table 6. Here, the last case of "good head" is an established product in a similar application as planned for this prototype head. It does not exhibit intake port cracking when it is subjected to engine test and field loading history. It may be used as a benchmark to compare its ESSP evaluation with those for the proposed design changes.

It indicated that case 3, with the 8 mm radius fillet, alone could lower the cracking rate from case 1 to a compatible level of 0.08 versus 0.09 of the "good head". Case (3 + 5), with additional thicker port wall, could provide more safety margin to reduce cracking rate, but it may not be necessary due to a trade-off of higher cost.

It is noted that the equivalent maximum stress of case (3 + 5) is higher than in case 3, but its cracking rate is lower due to a smaller equivalent strain amplitude. It illustrates why such a product function of stress and strain as the SWT parameter or ESSP is a more proper criterion to control inelastic fatigue behaviors than stress or strain alone. Also, numerical tests indicated that the ESSP criterion is not as sensitive as the Mode-I criterion to residual stress, which may relieve possible errors introduced by uncertainty, of residual stress measurement.

It has been reported from recent engine tests for two modified heads with the 8 mm fillet alone that no intake port cracking was found. That seems to support the ESSP prediction.

However, the equivalent stress and strain concept originated from plasticity and has some inherent weaknesses to describe fatigue phenomena. Such criteria do not include hydrostatic stress effect which has been shown to be sensitive to fatigue, and can not predict cracking orientation which would be related to maximum stress, strain, or strain energy density directions. Also, such criteria are inconvenient to be used for out-of-phase and nonproportional loading path due to complexity of equivalent maximum stress and strain amplitude. Experimental evidence suggests that some caution may have to be exercised.

Conclusions

There were intake port cracking problems of prototype cylinder heads of a heavy-duty diesel engine. Several structural proposals for design improvement were evaluated by FEA and experiments, and their data was interpreted using fatigue/reliability analysis.

Using ANSYS, finite element modeling techniques are developed to build an accurate mesh of complex head geometry, to set up thermal-mechanical loading conditions, and to simulate gray iron nonlinearity.

An equivalent stress-strain parameter (ESSP) is extended from the SWT criterion for the multiaxial fatigue cases and is applied to the head intake port reliability prediction with a micronotch correction of gray iron. It evaluated more reasonable fatigue cracking rates than traditional fatigue criteria, as compared with limited engine testing results and expectations.

It is concluded that a 8 mm radius fillet could significantly reduce the intake port cracking rate to 0.08 percent from prototype 4.36 percent. In addition, a 10 mm thick wall would further improve the port reliability with only 0.02 percent cracking risk with trade-off of higher cost, which may not be necessary.

References

1 Socie, D. F., Fash, J. W., and Dowing, S. D., "Fatigue of Gray Iron," FCP Report No. 44, UIUC, 1982.

2 Bannantine, J. A., Comer, J. J., and Handrock, J. L., "Fundamentals of Metal Fatigue Analysis," Prentice-Hall, Inc., Englewood Cliffs, NJ, 1990.

3 Glinka, G., Shen, G., and Plumtree, A., "A Multiaxial Fatigue Strain Energy Density parameter Related to the Critical Fracture Plane," *Fatigue Fract. Engng. Mater. Struct.*, Vol. 18, 1995, pp. 37–46.

4 Chu, C. C., "Fatigue Damage Calculation Using the Critical Plane Approach," *ASME J. Engng. Mater. Tech.*, Vol. 117, 1995, pp. 41–49.

5 ANSYS User's Manual for Revision 5.1, Swanson Analysis Systems, Inc., 1994.

6 Smith, K. N., Watson, P., and Topper, T. H., "A Stress-Strain Function for the Fatigue of Metals," *J. Mater.*, Vol. 5, 1970, pp. 767–778.

7 Mitchell, M. R., "A Unified Predictive Technique for the Fatigue Resistance of Cast-Ferrous Based Metals and High Hardness Wrought Steels," Ph.D. thesis, TAM UIUC, 1976.

8 Moftakhar, A., Buczynski, A., and Glinka, G., "Calculation of Elasto-Plastic Strains and Stresses in Notches Under Multiaxial Loading," *Intl. J. Fracture*, Vol. 70, 1995, pp. 357–373.

9 Chu, C. C., "Incremental Multiaxial Neuber Correction for Fatigue Analysis," SAE Tech. Paper No. 950705, 1995.

Performance and Compatibility of California Reformulated Gasoline in On-Road, Off-Road, and Non-Vehicle Engines

A. R. Bevan
abevan@cleanair.arb.ca.gov

K. M. Nolan

State of California,
California Environmental Protection Agency
Air Resources Board,
Mobile Source Control Division,
P.O. Box 2815,
Sacramentao, CA 95812

As part of its comprehensive program to reduce air pollution, California has mandated the use of a cleaner burning reformulated gasoline introduced in March 1996. In 1995 the Air Resources Board, with oversight from an industry, public interest, and governmental advisory committee, undertook an extensive study of the performance and compatibility characteristics of California reformulated gasoline in on-road, off-road, and non-vehicle engines. The evaluation included in-use comparison of California reformulated gasoline to conventional gasoline in normal fleet operations. Fleets totaling 829 test and 637 control vehicles were studied. Additionally, off-road and non-vehicle in-use testing was conducted covering engine technologies in the following uses: utility, lawn and garden applications; pleasure craft and small marine vessels; agricultural and industrial engines; and recreational snowmobiles and personal watercraft. California reformulated gasoline was found to perform as well as conventional gasoline in terms of driveability, starting, idling, acceleration, power, and safety.

Introduction

California's air quality problems are among the worst in the nation. A large part of those problems are caused by motor vehicles. The Air Resources Board estimates that in California, mobile sources contribute significantly to the emissions of smog-forming pollutants, with a 45 percent contribution to volatile organic compounds (VOCs) emissions and a 72 percent contribution to emissions of oxides of nitrogen (NOx). Similarly, mobile sources account for 68 percent of carbon monoxide (CO) emissions. (California Air Resources Board, 1991a) Gasoline is also a source of known and suspected toxic air contaminants. Gasoline powered vehicles are responsible for 90 percent of the benzene emissions in the state and almost 80 percent of the 1,3-butadiene emissions.

In March 1996, the Air Resources Board (ARB) took a large step toward controlling emissions from motor vehicles by implementing the California Reformulated Gasoline requirements. California Reformulated Gasoline (CaRFG) has been shown to reduce emissions of VOCs, NOx, and CO, as well as the risk from exposure to toxic air contaminants (California Air Resources Board, 1991a). Table 1 shows the emission reductions attributable to CaRFG (California Air Resources Board, 1991b). CaRFG accomplishes these emission reductions by regulating the properties shown in Table 2. The regulation also provides for averaging or use of a predictive model to meet property specifications.

In 1994, prior to CaRFG's implementation, the ARB formed an advisory committee to oversee the introduction of CaRFG. One of the primary roles of this industry, governmental, and public interest member committee was to oversee a thorough in-use performance evaluation of CaRFG. The advisory committee provided oversight on the design and protocol of the test program and also approved the findings at the termination of the study.

Contributed by the International Gas Turbine Institute and presented at The Spring Technical Conference of the ASME Internal Combustion Division, Fort Collins, CO, April 27–30, 1997. Manuscript received by the ASME Headquarters September 25, 1997. Paper No. 97-ICE-29. Associate Technical Editor: D. Assanis.

The ARB recognized a need to demonstrate the performance and compatibility of CaRFG prior to its introduction and subsequent use by over 20 million vehicles in California. It was recognized that in-use testing under real-world conditions was necessary to demonstrate this for both on and off-road vehicles and equipment.

Background

The scope of this performance study included evaluation of vehicle components that may be affected by changes in gasoline composition, and vehicle or engine performance. Materials that may be affected by property changes include elastomers, composites, and metals. Elasticity, durability, and swelling characteristics of elastomers such as acrylonitrile, nitrile butyl rubber, epichlorohydrin copolymer, and fluoroelastomers can be affected by oxygenates and aromatic content of gasoline. Composite and metal materials in engine fuel systems may be affected by the corrosive nature of the fuel or a reaction between the fuel and the material. Lubricity characteristics of the fuel will also affect the wear rate of engine fuel system components.

Driveability, defined as how well the engine starts, idles, accelerates, and resists stalling, characterizes running performance. These performance characteristics have been correlated with the driveability index (DI) calculated by Eq. (1) (Barker et al., 1988):

$$DI = 1.5 \times [T10] + 3.0 \times [T50] + [T90] \quad (1)$$

A lower DI generally correlates to better driveability of vehicles. Since CaRFG lowers T50 and T90, it is expected that engine performance will be improved over conventional gasoline.

Test Procedure

Fleets of vehicles and equipment were operated using either the CaRFG test fuel or a conventional control fuel. In total, 829 on-road vehicles comprised the CaRFG test fleet, and 637 vehicles comprised the control fleet. Fleets of utility, lawn and garden equipment, marine engines, personal watercraft, snow-

Table 1 predicted emission benefits of California reformulated gasoline

Market Segment	VOC	NOx	CO
On-Road	17%	11%	11%
Off-Road	10%	--	--
Marketing Operations	7%	--	--
Total	15%	11%	11%

mobiles, and agricultural, and industrial equipment were also tested. Testing took place between February and September 1995.

Fleet Selection. Participation of fleets was invited based on a set of criteria which allowed for controlled data collection while maintaining normal operating conditions. Fleet selection criteria included: centralized refueling with a high level of confidence that test vehicles were refueled from only that facility; single ownership of the fleet to facilitate communication with maintenance and management staff; a centralized location for periodic engine inspections; access to maintenance and fueling records; appropriately matched control fleet under the same ownership if available; and systematic fueling and mileage records for computation of fuel economy for on-road fleets.

Test Fuel. The CaRFG test fuel specifications were designed to represent the average expected CaRFG on the market in California, based on information provided by and aggregated from refiners supplying California. In addition to setting the specifications for the test fuel, ranges were established for the blendstocks used to make the fuel. Both summer and winter fuels were tested during the six month program. The specifications of the two fuels, as set by the CaRFG Advisory Committee, are listed in Table 3. Table 4 lists the limits set for the blendstocks used to make the test fuel.

Fleets designated as control fleets used locally available conventional unleaded fuel that would normally be supplied to the refueling facility.

Categories of Engines Tested. The test program included a wide range of engine types from the on and off-road categories. On-road engine technologies included carbureted and fuel injected fuel delivery systems from light, medium, and heavy-duty vehicle classes. Model years ranged from 1961 to 1995. Tables 5 and 6 illustrate the on-road fleet make-up, and compare the test fleet to the on-road California vehicle population.

The off-road and non-vehicle categories tested included both two-stroke and four-stroke engine technologies. Of the two-stroke engines, both oil-injection and premix oil/fuel systems were tested. Utility, lawn, and garden engines included two and four-stroke engines. Applications in this category included lawn mowers, edgers, trimmers, blowers, chainsaws, tree trimmers, and hedgers. The pleasure craft and small marine engine category included one inboard 454 cubic inch Chevrolet engine used in a parasailing application, and outboard two-stroke engines ranging in output from 5 to 150 horsepower. Two-stroke personal watercraft engines tested ranged in size from 639 to 644 cc and used oil injection for oil/fuel mixing. Two-stroke snowmobiles were tested with engine sizes ranging from 440 to 550 cc. The snowmobiles also utilized oil injection. Engines used in the agricultural and industrial applications included generators, forklifts, utility carts, and tractors. This category included both two-stroke and four-stroke engine types. Table 7 describes the off-road test fleets by use category. Only the pleasure craft and small marine engine category utilized a control fleet, with 5 outboard motors representing the control group.

Table 2 specifications for California reformulated gasoline

Property	Flat Limit
Reid Vapor Pressure, psi (kPa)	7.0 (48)[1]
Sulfur, ppmw	40
Benzene, vol%	1.00
Aromatics, vol%	25
Olefins, vol%	6.0
Oxygen, wt%	1.8 to 2.2
T50, °F (°C)	210 (99)
T90, °F (°C)	300 (149)

(1) Summer specification only.

Table 3 specifications for CaRFG test fuel

Specification	Winter Test	Summer Test
RVP, psi	11 to 12	6.5 to 6.9
RVP, (kPa)	(76 to 83)	(45 to 48)
Aromatic content, vol. %	18 to 20	18 to 20
Olefinic content, vol. %	3.0 to 5.0	3.0 to 5.0
Sulfur content, ppm	15 to 25	15 to 25
Benzene content, vol. %	0.5 to 1.0	0.5 to 1.0
Oxygen content, wt. %	~2	~2
T50 °F	190 to 210	190 to 210
T50 (°C)	(88 to 99)	(88 to 99)
T90 °F	280 to 300	280 to 300
T90 (°C)	(138 to 149)	(138 to 149)

Table 4 limits on test fuel composition by blending material

Blendstock Component	Range
Reformate, vol.%	20 to 30
MTBE, vol. %	10.8 to 11.2
Cracked stocks, FCC & hydro.	20 to 35
Alkylate, vol. %	15 to 20
Isomerate, vol. %	2 to 10
Straight-run naphtha, vol. %	as approved[1]
Other: as approved	as needed[2]

(1) None was used to make test fuels.
(2) Butane was added to the winter test fuel.

Table 5 test program fleet distribution by model year compared to California in-use vehicle population

Model Year	Test Fleet	Control Fleet	California Population
Pre 1981	8.0%	0.8%	12.7%
1981 to 1984	10.1%	6.3%	11.6%
1985 to 1989	48.5%	54.8%	29.6%
Post 1989	33.4%	38.1%	46.1%

Table 6 test program fleet distribution by weight class compared to California in-use vehicle population

Weight Class	Test Fleet	Control Fleet	California Population
Light-Duty	47.3%	51.5%	91.8%
Medium-Duty	30.8%	28.3%	5.7%
Heavy-Duty	22.0%	20.3%	2.5%

Table 7 off-road and non-vehicle test fleets

Category	Test Fleet Size	California Population
Utility, Lawn and Garden	49	4,644,000
Pleasure Craft	102	782,000
Personal Watercraft	11	151,000
Snowmobiles	10	14,000
Ag, Industrial, & Construction	23	82,000

Test Protocol. The on-road test fleets operated on the CaRFG test fuel for a period of six months. (One of the test fleets, with 112 vehicles, started late, only operating on the CaRFG test fuel for 4 months due to fuel storage difficulties.) The off-road test programs operated using test fuels for periods of time appropriate to their seasonal use. For example, snowmobiles were operated for 6 weeks, which was the duration allowable under the test period based on available snow; likewise, utility, lawn, and garden equipment were operated for 10 weeks through the most productive months of the landscape maintenance season.

Vehicles and equipment were inspected prior to the start of testing to establish the baseline condition of the engines. Engines were then inspected every two months to log continued engine condition. (Marine and personal watercraft engines were inspected every 2 weeks.) Inspections included visual, start, and idle tests. Fuel system component conditions were noted with attention to any leaks, seeps, or wear to fuel system parts.

Repair incidents (i.e., any engine or fuel system repair for which the vehicle or equipment was taken out of service and which could be fuel related), were reported and recorded for investigation. The ARB staff worked with the fleet maintenance staff to screen out non-fuel related repairs such as transmission work, electrical problems, or scheduled routine maintenance, such as oil changes and tune-ups. The ARB staff then worked with the fleet staff, Advisory Committee members, and the original equipment manufacturers to classify fuel system incidents as fuel related or not fuel related.

Data Collected

Fuel Analysis. To ensure the integrity of the test fuel properties throughout the delivery, storage, and dispensing process, one liter samples were taken at regular intervals. Samples were analyzed for the CaRFG regulated properties, ASTM gasoline specifications, specific gravity, and hydrocarbon composition.

Throughout the test program a total of 436 fuel samples were taken for analysis. Table 8 shows the average fuel properties for all the fleet sites separated by winter and summer fuel types, as well as the range of measured properties for control sites.

Table 8 measured average properties of test fuels

Property	Winter Test	Summer Test	Conventional (Range)
RVP, psi	n/a	6.6	n/a
RVP, (kPa)		(46)	
Aromatic content, vol. %	19.9	18.4	21.1-39.5
Olefinic content, vol. %	5.6	5.7	4.0-16.2
Sulfur content, vol. %	21	52	61-227
Oxygen content, wt. %	2.03	2.09	0.58-3.51
Benzene content, vol. %	0.6	0.89	0.02-2.12
T50 °F	191	190	182-229
T50 (°C)	(88)	(88)	(83 - 109)
T90 °F	303	298	308-351
T90 (°C)	(151)	(148)	(153 -177)

Table 9 repair incidents

Incident Type	Test	Control
Fuel Pumps	12	6
Carburetors	8	9
Fuel Lines	3	0
Fuel Injectors	0	0
Fuel Tanks	0	5
Other	1	0
Total	**24**	**20**

Table 10 historical fleet composition by model year and vehicle weight class, in vehicle-years

Model Year	Light-Duty	Medium-Duty	Heavy-Duty
Pre 1981	90	21	397
1981 to 1984	255	225	894
1985 to 1989	3315	1713	1707
Post 1989	4301	2679	1123
Total	**7961**	**4638**	**4121**

Table 11 Historical fleet distribution by odometer reading and vehicle weight class, in vehicle-years

Odometer Reading ($x10^{-3}$ miles)	Light-Duty	Medium-Duty	Heavy-Duty
<50	3455	2274	1091
50 - 100	3236	1421	1466
100 - 150	1108	753	1110
>150	162	190	454
Total	**7961**	**4638**	**4121**

Inspection Data Intermediate inspections were conducted at test sites at least three times during the test program. A database was created to store and report inspection log results. This database was used to track the condition of vehicles and equipment throughout the program.

Repair Incidents Over the course of the test program, 44 repair incidents were reported. Table 9 shows the rate of observed incidents for the on-road test program. To assist in the analysis of the cause of the incident, affected fuel system parts were collected whenever possible for tear-down analysis.

Historical Data. In order to make a comparison between the repair incident rate encountered during the test program and a normal rate of repairs for the fleet, baseline historical data were collected from participating fleets where available. In addition to fleet historical records, the maintenance records from the California Department of Transportation's fleet of 7000 vehicles were made available for analysis. Records were collected for the fleet maintenance years of 1993 and 1994. Only fuel-system-related repairs were tracked; specifically, repairs involving fuel pumps, fuel injectors, fuel lines, fuel tanks, carburetors, and fuel filters. Tables 10 and 11 describe the vehicles represented in the historical data set by model year, odometer reading, and weight class (all in vehicle-years).

Data Analysis

Determination of the effect of CaRFG on fuel system components was made with two comparisons. First, the test fleet repair

Table 12 expected repair rates from baseline data

Incident Type	Test Fleet	Control Fleet
Fuel Pumps	2.1%	1.7%
Carburetors	2.2%	1.5%
Fuel Lines	1.9%	1.6%
Fuel Injectors	0.7%	0.8%
Fuel Tanks	1.4%	1.2%
Overall	**8.3%**	**6.8%**

incident rates were compared to the control fleet repair incident rates. Second, both the test and control fleets were compared to the repair rates seen in historical baseline data.

Historical Repair Rates. Baseline data were analyzed in vehicle groups that allowed for useful comparisons to the on-road test fleets. Repair rates were established for each fuel system component and for total incidents by model year group, odometer reading, and by weight class.

Three steps were applied to the data to extrapolate the repair rates seen in the baseline data to the expected or predicted repair rates for the test and control fleets. First, the number of vehicles from the test fleets in a group was counted. Groups were defined by vehicle weight class, odometer reading, and model year. Second, for each group, counts were multiplied by their respective baseline incident rates from the same group in the baseline fleet to produce the expected number of repairs for each combination. Third, the expected repairs were summed to determine the overall incident repair rates that were expected annually for each group.

This methodology accounted for differences in fleet composition between test and control fleets. Table 12 shows that the overall expected repair rate for the test fleet was 8.3 percent, compared to 6.8 percent for the control fleet. These rates are for a six month test period.

Observed Incident Rates. By the nature of the test, none of the fuel system repairs observed during the test program could be definitively said to be caused by the fuel used. Rather, incidents were either defined as "may be fuel related" or "not fuel related." Twelve incidents occurred during the test program that were defined as "not fuel related" after investigation; these included faulty electrical components, loose fuel fittings, and other miscellaneous incidents.

Those incidents labeled as "may be fuel related" were characterized as either normal or unusual with consideration of the age and service of the component. Table 13 summarizes the incidents by component and by designation as normal or unusual.

During the test program inspections, 131 "seeps" were identified in test vehicles. In the control vehicles, 45 seeps were identified. Seeps were defined as a wet spot or stain near a gasket, seal, or fitting, which suggested that fuel may have "seeped" from this area during operating conditions. To determine the nature of the seeps, a task group was formed by the technical review panel to review the seeps. From their investigations, the panel concluded that the reported seeps were "normal" and were not attributed to the test fuel.

Table 13 number of component and total incidents

Incident Type	Normal Incidents		Unusual Incidents	
	Test	Control	Test	Control
Fuel Pump	7	4	5	2
Carburetor	3	3	5	6
Fuel Line	1	0	2	0
Fuel Injectors	0	0	0	0
Fuel Tank	0	2	0	3
Other	1	0	0	0
Total	**12**	**9**	**12**	**11**

Table 14 observed and expected incident repair rates

Incident	Test		Control	
	Observed	Expected	Observed	Expected
Fuel Pump	1.4%	2.1%	0.9%	1.7%
Carburetor	1.0%	2.2%	1.4%	1.5%
Fuel Line	0.4%	1.9%	0.0%	1.6%
Fuel Injectors	0.0%	0.7%	0.0%	0.8%
Fuel Tank	0.0%	1.4%	0.8%	1.2%
Total	**2.9%**	**8.3%**	**3.1%**	**6.8%**

Table 15 incident rates by odometer reading

Odometer Reading (x 10^{-3} miles)	Test Fleet		Control Fleet	
	Observed Rate	Expected Rate	Observed Rate	Expected Rate
< 50	1.2 %	4.4 %	1.1 %	4.2 %
50 to 100	1.7 %	9.1 %	3.5 %	7.9 %
> 100	14.3 %	18.9 %	15.8 %	16.1 %

Table 16 incidents by model year

Model Year	Test Fleet		Control Fleet	
	Observed Rate	Expected Rate	Observed Rate	Expected Rate
Pre-1981	3.0%	19.8%	0%	11.8%
1981- 1984	4.7%	19.1%	12.2%	17.3%
1985 - 1989	4.2%	8.1%	3.7%	8.5%
Post 1989	0.4%	2.5%	0.8%	2.4%

To evaluate the effect of the fuel on incident rates in the test and control fleets, the observed rates were adjusted to compensate for differing proportions of weight classes, model years, and odometer readings. Table 14 compares the observed and expected repair rates in the test and control fleets. Table 14 also shows that the observed rate is much lower than the expected rate when comparing total incidents. The expected rate could be higher because the historical data set may include non-fuel related and routine maintenance incidents. The agreement between observed and expected incident rates was much better for parts such as fuel pumps that do not have a routine maintenance schedule.

Incidents By Odometer Reading. Incident rates were also analyzed as a function of odometer readings to evaluate the impact of mileage accumulation. Table 15 compares the observed incident rates in the test and control fleets with the expected incident rates as calculated from the baseline data.

Incidents by Model Year. A comparison of incident rates as a function of vehicle age was also made. It should be noted that the most recent model-year vehicle to experience an incident was 1990. Generally, older vehicles showed higher incident rates. However, as shown in Table 16, the incident rates for

pre-1981 vehicles was lower than for 1981 to 1984 vehicles. Two possible reasons for this include (1) the sampling error due to the relatively small sample size of the pre-1981 vehicles and (2) the possibility that original fuel system components in pre-1981 vehicles may have already reached the end of their useful life and were replaced with new components.

Off-Road and Non-Vehicle Engine Programs. With the exception of the marine category, the off-road and non-vehicle engine test programs did not have control fleets available for comparison. Historical repair records were also not available to compare expected incident rates to observed incident rates. Analysis of CaRFG's compatibility was made on an incident-by-incident basis. Each incident was reviewed by ARB staff, fleet staff, and the original equipment manufacturers to determine the probability that the incident was caused by the fuel. Below, each category tested is described.

Utility, Lawn, and Garden. In the utility, lawn, and garden category, 42 units were operated for a period of 10 weeks in a commercial landscaping environment. Included in this fleet were seven new units meeting California's 1995 emission certification standards. These standards require significantly reduced emissions and the use of limited-adjustment carburetors. It is estimated from hourly logs kept by equipment users that the entire fleet of 42 engines was operated for a total of 3100 hours. No significant deterioration was noted during ARB inspections. Similarly, no increase in maintenance practices was reported.

During the test period, two incidents were reported. One incident involved a backpack blower. The other involved a weed trimmer. The backpack blower incident was designated possibly fuel related, but normal considering the age and condition of the unit. The repair involved the need to rebuild the carburetor. The weed trimmer experienced a scored cylinder. It was determined by the engine manufacturer that the failure was not caused by fuel, but rather by the conditions of use and age of the unit.

Pleasure Craft and Small Marine Engines. Boat engines were tested in two separate fleets. The first fleet comprised boats used in parasailing, recreational water-skiing, and cruising applications at high altitude (6200 feet above sea level). This fleet comprised one inboard engine (335 horsepower) and seven outboard engines (ranging from 15 to 150 horsepower). The outboard engines had a matched control fleet, also tested at high altitude, with five engines ranging in horsepower from 70 to 150. The test program was conducted for 10 weeks.

Interim test program inspections did not reveal deterioration of engine condition. Fleet operators reported no difference in performance between the test and control fleets. During the test program, four repair incidents were reported from the control fleet, and four incidents were reported from the test fleet. Of the eight incidents reported from both fleets, only one was determined to possibly be fuel-related. This repair incident involved a leaking carburetor that was described as normal for the age and condition of the engine; it was reported from a boat in the control group.

The second test fleet comprised 95 boats used in a recreational rental environment. The fleet was made up of 88 small fishing boats with 5 to 9.9 horsepower outboard engines and 7 pontoon boats with 25 horsepower outboard engines. Model years of these engines ranged from 1983 to 1994. This test program was conducted for 10 weeks. Boats averaged 20 to 30 hours per week, and the fleet used 3570 gallons of test fuel.

During the test period, 7 inspections were conducted. Inspections revealed signs of seepage from engines. However, after further investigation, the seeps were determined to be non-fuel related and to be the result of fleet operating practices. (Boats were tipped 90 deg for pressure washing, spilling fuel from the carburetor bowl into the engine compartment.) No incidents were reported at this site, and the fleet manager and operators did not report any abnormal performance or maintenance problems.

Table 17 summary of off-road and non-vehicle incidents

Equipment	Repair	Fuel Related?
Backpack Blower	Rebuild Carburetor	Possibly
Weed Trimmer	Scored Piston	No
Boat 1	Rod through cylinder	No
Boat 2	Broken piston ring	No
Boat 3	Broken piston ring	No
Boat 4	Broken piston ring	No
Boat 5 (Control)	Broken piston ring	No
Boat 6 (Control)	Broken piston ring	No
Boat 7 (Control)	Broken piston ring	No
Boat 8 (Control)	Leaking carburetor	Possibly
Personal Watercraft	Broken piston ring	No

Personal Watercraft. The personal watercraft test program was also conducted at high elevation. The test fleet comprised 11 units operated for 10 weeks. Of the eleven units, 10 were 1995 model year, and one was a 1994 model year. Hour meters installed on the units showed that during the test period, units were operated for 964 hours. Approximately 750 gallons of fuel were consumed by the test fleet.

Engine inspections did not show any deterioration of the units through the course of the test program. This fleet incorporated pressure tests of the cylinders to gauge deterioration of engine performance. The results of the pressure tests were within normal variations expected. One repair incident was reported during the test program involving a failed piston ring. It was determined by the engine manufacturer that the ring failed due to normal wear and not to the fuel used.

Snowmobiles. A fleet of 10 snowmobiles was tested for a period of 6 weeks. All of the snowmobiles used CaRFG test fuel for the duration of the evaluation. The test was conducted at 7500 feet above sea level. During the test program, the fleet accumulated 25,475 miles of use.

The test fleet was inspected twice during the test program. These inspections did not reveal any deterioration in engine condition during the course of the program. Similarly, no repair incidents were reported during the test period. The fleet operators noted a decrease in smoke from the engines, and this was identified as a benefit of the CaRFG test fuel. The fleet operators noticed a slight loss in acceleration.

Industrial and Agricultural Vehicles and Equipment. The industrial and agricultural test fleets included forklifts, concrete mixers, utility carts, generators, tractors, a sweeper, a skip loader, a bobcat, and a hi-jet. Equipment was tested in two locations for periods of 10 weeks to 5 months. Both fleets were operated by organizations also participating in the on-road test program.

At both test sites inspections of engines did not reveal any deterioration of engine components, and no repair incidents were reported during the test period.

Summary of Off-Road and Non-Vehicle Test Programs. Table 17 summarizes the incidents reported during the off-road and non-vehicle test programs, and lists the conclusions regarding the possible cause of the incidents.

Findings

Results of the performance test program indicated that CaRFG performed as well as conventional gasoline in terms of driveability, starting, idling, acceleration, power, and safety.

In the on-road test program, both test and control fleets experienced similar fuel system problems on a small percentage of vehicles (3 percent). These problems involved the following: fuel pumps, carburetors, leakage from fuel hoses and gaskets, and fuel tank and tank components.

Comparison of the overall problem frequency rate between test and control fleets indicated that there was no meaningful difference between the frequency of problems in the fleets operated with test fuel versus fleets operated with conventional gasoline.

Newer vehicles in the test and control fleets (1991 and newer) did not experience fuel system problems. The repair incidents that did occur were seen in both the test and control fleets in older vehicles, generally with higher mileage. The average model year of vehicles experiencing fuel system problems was 1986, and the average odometer reading was at 95,000 miles, with a range of 24,000 to 202,000 miles.

Evaluation of the historical baseline maintenance and repair data showed an increasing rate of failures in fuel system components associated with aging. The overall frequency of problems for the test and control fleets (3 percent) was well below the expected frequency determined from baseline historical data, which showed an expected rate of 6.8 to 8.3 percent. The repair incidents documented in the baseline data were the same type of repairs seen in the test and control vehicles during the test program.

Review of the data from all of the off-road and non-vehicle test programs showed that the change to, and the long-term use of, CaRFG was not expected to adversely affect off-road vehicles and non-vehicle equipment. None of the repair incidents reported during the test program were identified as unusual or positively linked to the use of CaRFG. Operators did not note differences in performance, including starting, idle, or acceleration.

Acknowledgments

ARB Staff and Divisions. Testing was conducted through the cooperation of eight divisions and over 80 staff members including the following: engineering and technical staff who designed test procedures and coordinated test fleets; automotive technicians who inspected vehicles and equipment; compliance staff who coordinated and conducted fuel sampling; laboratory staff who conducted analysis of fuel samples; and technical support staff who provided software programming and statistical analysis assistance. Internal review was conducted by J. Behrmann, Manager, Strategy Evaluations Section and D. Simeroth, Chief, Criteria Pollutants Branch of the Stationary Source Division.

Participating Fleets. Fleets that provided vehicles and equipment for testing as well as time and assistance from their staff during the test program included:

- Bank of America
- California State University, Fresno
- California Department of Transportation
- City of Sacramento
- County of Sacramento
- General Telephone & Electronics
- Pacific Bell Telephone, Northern and Southern California
- Paradise Watercraft Boat Rentals and South Shore Parasailing
- Lake Cachuma Boat Rentals
- Lake Tahoe Winter Sports Center

Vehicle and Equipment Manufacturer Involvement. The following companies contributed to the test program with technical assistance and resources: Andreas Stihl; Arctco Incorporated; Chevron, U.S.A. Products Company; Echo-Kioritz; Ford Motor Company; General Motors Corporation; Holley Performance Products Company; Homelite, Division of Textron, Inc.; Husqvarna AB; Mercedes-Benz of North America; Mercury Marine; Mitsubishi Motors of America, Inc.; Nissan Motors Company; Poulan/Weed Eater; Shell Oil Products; Texaco Refining and Marketing Inc.; and Toyota Technical Center, U.S.A.

Technical Review Committee. Repair incidents for the on-road test program were evaluated by a technical review committee comprised of the following people: R. Barber and K. Carabell, Chevron Research and Technology Company; L. Beard, Chrysler Corporation; B. Benjaminson, California Department of Consumer Affairs, Bureau of Automotive Repair; N. Chan, D. Chernich, J. Courtis, and P. Jacobs, California Air Resources Board; D. DonLevy and B. Rippon, Ford Motor Company; P. Dorn and M. Kulakowski, Texaco Research and Development; A. Hochhauser, Exxon Research and Engineering Company; L. Olejnik and T. Sprik, Shell Oil Products; G. Barnes, General Motors Corporation; J. Stott, J. Trost, and A. Wong, General Motors Service Technology Group.

References

California Air Resources Board, Stationary Source Division, 1991a, "Proposed Regulations for California Reformulated Gasoline, Vol. 1, California Phase 2 Reformulated Gasoline Specifications," Staff Report, Sacramento, CA, pp. 13–21.

California Air Resources Board, Stationary Source Division, 1991b, "Proposed Regulations for California Reformulated Gasoline," Technical Support Document, Sacramento, CA, pp. 14–31.

California Air Resources Board, Stationary Source Division, 1996a, "CaRFG Performance and Compatibility Test Program, Report of the Performance Subcommittee of the California Reformulated Gasoline Advisory Committee," Sacramento, CA.

California Air Resources Board, Stationary Source Division, 1996b, "CaRFG Performance and Compatibility Test Program," Appendices, Sacramento, CA.

Barker, D. A., Gibbs, L. M., and Steinke, E. D., 1988, "The Development and Proposed Implementation of the ASTM Driveability Index for Motor Gasoline," Paper Number 881668, Society of Automotive Engineers, Warrendale, PA.